STRUCTURE AND RHEOLOGY OF POLYMER NANOCOMPOSITES AT LARGE DEFORMATION

By

Matthew Melton

A DISSERTATION

Submitted to
Michigan State University
in partial fulfillment of the requirements
for the degree of

Materials Science and Engineering—Doctor of Philosophy

2022

ABSTRACT

STRUCTURE AND RHEOLOGY OF POLYMER NANOCOMPOSITES AT LARGE DEFORMATION

By

Matthew Melton

Over the past century, polymer nanocomposites (PNCs), formed through dispersing nanosized inorganic particles in polymer matrices, have become increasingly important functional and structural materials with various applications in energy, environment, healthcare, and infrastructure. Among the most fundamental aspects of PNCs for industrial purposes are the relationships between PNC processing, the microstructure of the composite material, and the macroscopic properties. However, some aspects of these relationships, including their origins, are still poorly understood and it remains a complex challenge to unravel the fundamental characteristics connecting these relationships.

In this dissertation, the aim is to develop new techniques through a combination of small-angle scattering (SAS) and advanced microscopes to develop understandings of how external deformation influences the dispersion state of nanoparticles (NPs) in various industrially relevant processing conditions. Specifically, the target is to show how Scanning Electron Microscopes (SEMs) can be a powerful complimentary technology to aid in the understanding of spatial rearrangement of the NPs in high viscoelastic polymer medium. By breaking down how SEM adds an underutilized manner of inspecting the NP dispersion in direct space for PNCs, and adapting analytical techniques from other disciplines, this work develops a novel methodology with regard to polymers to study how NPs rearrange on the microscopic scale as a result of macroscopic deformation.

In order to provide a more complete understanding, both tensile and shear deformation modes have been explored. In tensile deformation, the PNCs have been uniaxially extended to a series of elongation ratios acting as different stages of the NP rearrangement progress for rates well above and below a Weissenberg number, $Wi = \dot{H}\tau_d = 1$, where $\dot{H}$ is the Hencky strain rate and τ_d is the polymer's terminal relaxation time. Delaunay Triangulation analysis has been applied to quantify the spacing of the NPs relative to their nearest neighbor, and the results for NP rearrangement have been compared against projections of the macroscopic uniaxial deformation fields believed to hold microscopically for PNCs. This work shows strong deviation from the affine predictions, pointing to important long-missing features in understanding the relationship between the microstructural rearrangement and the macroscopic deformation of PNCs.

Complex shear deformation has also been performed through capillary rheometry and the SEM has been used to observe the characteristics of the NP clustering of extruded PNCs. These results show a clear breakdown in the Cox-Merz rule for the flow behaviors of PNCs under capillary extrusion. Moreover, interesting features of microstructural rearrangement of PNCs have been observed, highlighting the strong influence of capillary flow to the final dispersion state of PNCs that also changes with the NP loadings and the applied stress. Given the high relevance of capillary extrusion to advanced manufacturing, the revealed results should have strong implications to future manufacturing of polymer nanocomposites with desired properties.

ACKNOWLEDGEMENTS

The author would like to acknowledge the following individuals for their support: Kathleen Melton – for making the sacrifices to allow me to complete this program. I could not have done this without you. Rich and Ruth Melton and Ray and Pauline Boeman – for their constant support. Dr. Shiwang Cheng – for the guidance, teaching, and patience provided across these 5 years and for the uncounted hours spent helping me to succeed. Dr. S. Ross Glandon – for assisting with the troubleshooting of numerous MATLAB® codes. Dr. Per Askelund – for sharing his knowledge and expertise in SEM usage for polymers. Dr. Andre Lee – for his mentorship and teaching provided in group meetings and elsewhere. Dr. Quinn Sun – for being my partner in the foundation of our research group and being a friend throughout our shared time here. Danielle DeJonge, Tyler Johnson, Dr. Yang Lu, Aditya Patil, Shalin Patil, Dr. David Vogelsang, Dr. Yuelin Wu, Zipeng Xu, Dr. Jie Yang, and Yuxiang Zhong – for making the group fun and creating a positive research environment. JoAnn Ballor, Harish Chakravarty, Madeline Mackinder, Affan Malik, Dr. Adam Marsh, and Chauncey Splichal – for helping me keep my sanity outside of research. Dr. Martin Crimp, Dr. Lawrence Drzal, Dr. Robert C. Ferrier Jr., and Dr. Pengpeng Zhang – for their guidance and willingness to serve as doctoral committee members. Dr. Katy Colbry, Heather Dainton, Donna Fernandez, Jessica Gallegos, Jennifer Keddle, Kim McClung, Tiffany Owen, and Brad Tobin – for helping me navigate graduate student life and the many deadlines, forms, and other necessities required by the department and university to complete this degree. To the other CHEMS department and MSU faculty, staff, and graduate students and other family and friends for their support, thank you.

TABLE OF CONTENTS

LIST OF FIGURES

KEY TO SYMBOLS

A	Mean atomic weight of a compound
A_0	Area
D	Diameter
D_{NP}	Center-of-the-mass diffusion time of a nanoparticle
d	Distance
d_{cc}	Center-to-center distance of nanoparticles
d_{IPS}	Interparticle spacing distance
$d_{\parallel}$	Nanoparticle distance in stretching direction
$d_{\perp}$	Nanoparticle distance transverse to stretching direction
E	Young's modulus (bulk modulus)
E_0	Incident electron beam accelerating voltage in Scanning Electron Microscope
F_p	Force along a plane
G	Shear modulus
G'	Storage modulus
G"	Loss modulus
G*	Complex modulus
H	Hencky strain
$\dot{H}$	Hencky strain rate
h	Thickness
I(q)	Intensity in scattering experiments
k_b	Boltzmann constant
L	Length

M_W	Molecular weight of a polymer
N	Number of monomers in a polymer chain
n	Number of nanoparticles
P	Pressure
P(d)	Probability density of a distance
Pe	Péclet number
Q	Volumetric flow rate in extrusion
q	Scattering wave vector in small-angle scattering
r	Radius
Re	Reynolds number
R_g	Polymer radius of gyration
R_{NP}	Radius of nanoparticle
t	Time
T	Temperature
T_g	Glass transition temperature
T_{ref}	Reference temperature
W	Width
Wi	Weissenberg number
Wi_R	Rouse Weissenberg number
Δx	Displacement in shear deformation
V	Volume
v	Velocity
Z_{eff}	Effective atomic number of a compound
tan(δ)	Loss factor

γ	Strain
$\dot{\gamma}$	Strain rate
ζ	Friction coefficient
η	Zero-shear viscosity of polymer
Θ	Angular rotation
θ	Angle, in extrusion the angle of the die entry
λ	Elongation ratio
λ_{in}	Inelastic mean free path
λ_w	Wavelength of x-ray scattering beam
μ	Viscosity of a liquid
ρ	Density
$\frac{d\boldsymbol{\Sigma}(\boldsymbol{Q})}{d\boldsymbol{\Omega}}$	Differential cross section in scattering experiments
σ	Stress
σ_{eng}	Engineering stress
τ_d	Disentanglement or terminal relaxation time
τ_e	Rouse time of entanglement strain
τ_R	Rouse time
τ_α	Segmental relaxation time
φ_{NP}	Volume fraction of filler nanoparticles
$\boldsymbol{\Omega}_v$	Angular velocity
ω	Angular frequency

KEY TO ABBREVIATIONS

AFM	Atomic Force Microscope
BSE	Backscattered electrons
DIC	Digital Image Correlation
DT	Delaunay Triangulation
EIV	Electron Interaction Volume
FIB-SEM	Focused Ion Beam Scanning Electron Microscope
FFT	Fast Fourier Transform
IMFP	Inelastic Mean Free Path
MEK	Methyl ethyl ketone
NP	Nanoparticle
P2VP	Poly(2-vinyl pyridine)
PMA	Poly(methyl acrylate)
PNC	Polymer Nanocomposite
PS	Polystyrene
PTFE	Poly(tetrafluoroethylene)
PVAc	Poly(vinyl acetate)
SAS	Small-angle scattering
SANS	Small-angle Neutron Scattering
SAOS	Small Amplitude Oscillatory Shear
SAXS	Small-angle X-ray Scattering
SE	Secondary electrons
SEM	Scanning Electron Microscope
TEM	Transmission Electron Microscope

TGA	Thermogravimetric Analysis
TTSP	Time-temperature Superposition Principle
v%	Volume percent, φ

CHAPTER 1: INTRODUCTION

1.1 Research Motivation

Over the past several decades, polymer nanocomposites (PNCs) have emerged as increasingly important materials due to their widespread application potential. Ever since Toyota discovered that exfoliated montmorillonite particles dispersed in a nylon-6 matrix could increase the modulus while simultaneously increasing the heat deflection temperature,[1] the industrial race to discover what other improvement PNCs could provide has incentivized the scientific community to increase their understanding of PNCs. Today, the applications for PNCs are spread across numerous fields ranging from aerospace to dentistry and from water purification to lithium-ion batteries.[2-5] This plethora of fields is directly a result of the variety of properties within PNCs that can be manipulated including, but not limited to, electrical and thermal conductivities, as well as optical, mechanical, and barrier properties.[6-11, 21] Combined with the fact polymers can be both a lighter and cheaper raw material, relative to common structural materials,[12, 13] and the supposition that increased demand for nanomaterial processing is expected to decrease the production costs,[13, 14] it is no wonder that PNCs are globally in such high demand and continuing to grow in industrial usage.[11, 15]

Regardless of the polymer matrix or nanofiller materials and their shape, the macroscopic properties are dependent on both the amount of filler present[16, 17] and their microstructure.[18-21] It is therefore fitting that the nanoparticle (NP) filler fraction and microstructure are the frequent target of studies. While the optimization of different polymer properties is a well-researched topic,[21] the final properties are also influenced through the use of processing techniques that take advantage of polymer behaviors.[22, 23] Polymers are typically processed industrially by introducing deformation, which could involve a tensile mode, shear mode, or some combination of both

depending on the end applications and desired properties.[13, 24] It is well-known that polymer processing can affect the microstructure of PNCs. The NP rearrangement has been linked to the polymer-nanoparticle and nanoparticle-nanoparticle interactions, which are not well studied; moreover, the origin of the relationship between the deformation in PNC processing and the final NP microstructure is even less understood.

1.2 Current Understanding in the Scientific Community

1.2.1 Basic Polymer Dynamics

Polymers exist in many forms, both natural and synthetic, but share characteristic dynamic behaviors, which are well covered by many polymer textbooks.[25, 26] To describe these dynamics, the Rouse model and reptation model are used. The Rouse model applies to polymers in an unentangled state and describes the behavior of a polymer chain in a manner like a bead and spring. In an equilibrium state, the polymer wiggles around, mostly contained within a volume known as the radius of gyration, R_g. If the ends of the unentangled polymer chain are subjected to a force pulling them apart, it increases the tension within the chain by forcing higher energy conformations as the chain deforms. When released, the polymer will retreat back into its original state with time; however the Rouse model also states that if the ends of the chain are held, and not pulled apart, the chain will still experience entropy fluctuations due to the transfer of net moment forces onto the ends of the chain as the rest of the chain wiggles. Furthermore, the ends do not need to be the source of the strain, rather any 2 arbitrary points within the chain can be used instead, and the Rouse model describes the dynamic response of the chain between these 2 points. Consequently, even when the polymer chain becomes entangled, the Rouse model describes the parts of the chain between entanglement points, although it can no longer be utilized to describe the full dynamic response of the entire chain. In order to describe the entire chain in an entangled polymer, the

reptation model is proposed. The reptation model assumes the motion of the polymer chain is constrained by other nearby chains, with two different components describing the motion. First, the Rouse model still describes the faster motions of the polymer between constraints. The averaged motion, traced back to the relative position of individual monomers, is used to define a line called the primitive path, which is the averaged shortest path between the two endpoints following the chain. In reality, the chain is constantly wiggling around this path and the result is that it occupies a volume resembling a tube. The second component is that as energy moves within the system and time progresses, the polymer chain disentangles itself from the tube in a diffusive process called reptation, giving the model its name. For a bulk polymer sample, individual chains cannot truly be disentangled from one another; instead, they diffuse to new areas constantly working into and out of entanglements with other chains. The amount of time required for the chain to move itself fully outside of the original tube depends on the polymer's bulk appearance.

Polymers exist primarily in three different appearances: glassy, rubbery, and liquid-like (sometimes called either the terminal flow or melt flow regime), or the cross-over points between appearances, and each exhibits different properties. These states are governed by the various timescales polymers exhibit, of which a several are noteworthy: τ_d, the disengagement or terminal relaxation timescale; τ_R, the Rouse timescale; τ_e, the Rouse time of entanglement strain; and τ_α, the segmental relaxation timescale. Fig. 1.1 depicts an example master curve, specifically the master curve of a polystyrene (PS) sample with molecular weight (M_W) of 100,000 g/mol at a reference temperature, T_{ref} = 423 K. The different states and timescales are presented alongside the curves of the elastic storage modulus, G', and the viscous loss modulus, G", plotted against angular

frequency, ω. These timescales are in reciprocal seconds relative to ω and describe specific aspects of the dynamics in polymer models.

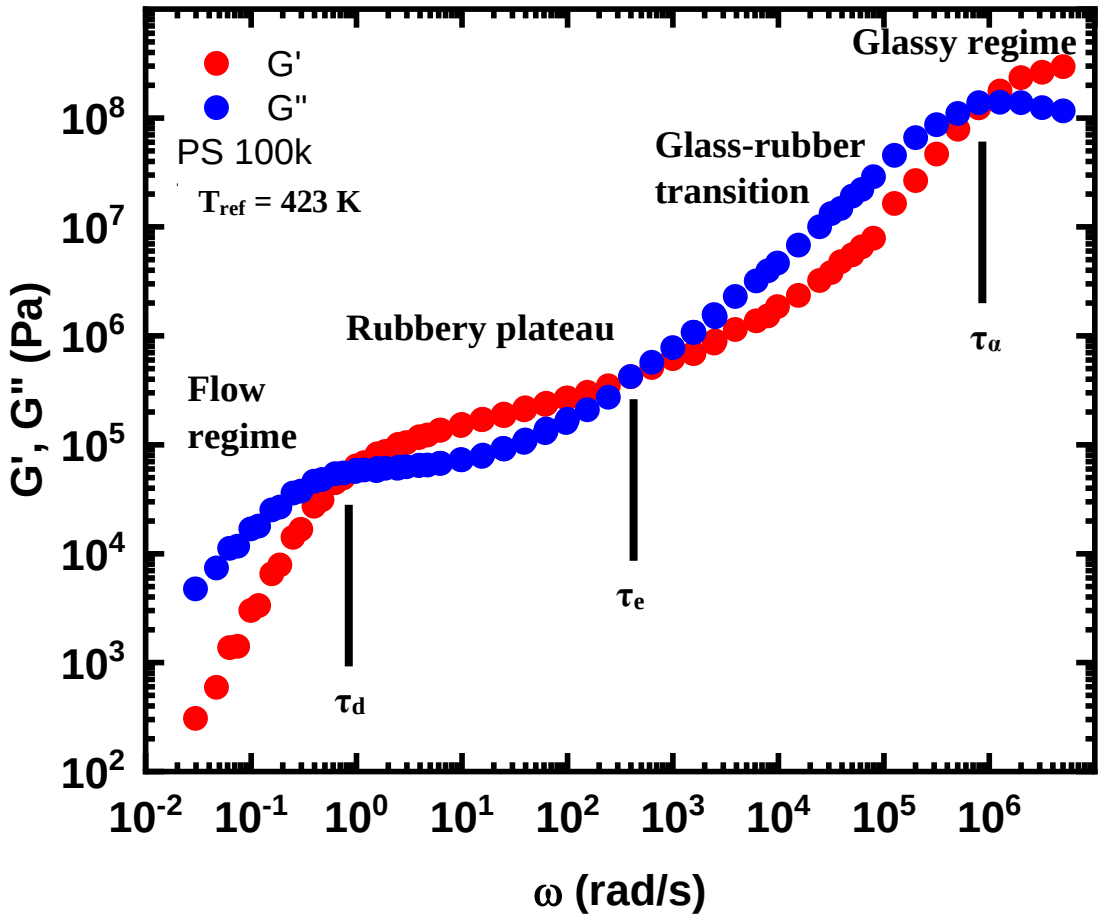

Figure 1.1: Example master curve. Storage modulus, G', and loss modulus, G", vs angular frequency, ω, for a polystyrene sample. Different appearance regimes and timescales are noted corresponding to polymer behavior at a reference temperature of 423 K.

The terminal relaxation time is located at the cross-over from the rubbery plateau to the terminal flow regime, and represents the average time required for the polymer chain to fully diffuse from the initial tube depicted by the reptation model into a new tube environment. For polymer systems with a true flow regime, defined by having $G' \propto \omega^2$ and $G'' \propto \omega^1$, when probed at timescales longer than τ_d the energy dissipation behavior dominates the polymer response, and the polymer is observed to behave as a simple liquid. The Rouse timescale corresponds to the average relaxation time between entanglements as described by the Rouse model. It is unique

among timescales noted here because there is not an exact spot on the figure that can be observed, and is instead described through a mathematical relationship to the diffusive characteristics of the polymer chain:[26]

$$\tau_R = \frac{\zeta}{k_b T} N {R_g}^2 \qquad (1)$$

where ζ is the friction coefficient of the monomer beads, k_b is the Boltzmann constant, T is the temperature, N is the number of monomers in the polymer chain, and R_g is the radius of gyration of the polymer chain. This allows further relationships to τ_d and τ_e to be derived, allowing calculation directly from the master curve. The Rouse time of entanglement strain corresponds to the onset of polymer entanglement effects and is located at the beginning of the rubbery plateau. It often correlates closely with the cross-over frequency between G' and G" separating the glass-rubber transition of non-Newtonian viscoelastic response and the more linear-elastic response of the plateau. The segmental relaxation, or α-relaxation, process corresponds with the polymer movement at the monomer level, primarily their diffusion and viscosity. The segmental relaxation behavior is also responsible for the glass transition in the polymer. When probed at timescales smaller than τ_α, the chain is observed as a solid in which the polymer is effectively motionless.

The timescales associated with each of these regions and relaxation processes are highly temperature dependent; however, a principle known as the time-temperature superposition principle (TTSP) makes use of the assumption that every relaxation timescale within the polymer has identical temperature dependence. This allows for the construction of polymer master curves at a reference temperature based on a limited ω testing window by shifting subsets of data, as will be discussed later. Consequently, polymer behaviors across different dynamics regimes can be accessed rather easily, by manipulating either the temperature or effective frequency range, and

both polymers research and processing utilize this principle to great effect. While powerful, TTSP will only hold for a PNC when the polymer motion is not significantly constrained by the NPs, as the changes in segmental length scale of filled PNCs can cause the breakdown in TTSP applicability.[27] This shifts the discussion to how the addition of the NPs to the polymer matrix changes the polymer behavior, and the theories explaining the nanoreinforcement effect in PNCs.

1.2.2 The Debate of Microscopic Mechanisms for Mechanical Reinforcement of Polymer Nanocomposites

Even before Toyota industrialized early polymer nanocomposites, it was well established that polymer mechanical properties were enhanced by filler materials.[28] The basis of the improvement is simple enough: a polymer such as poly(vinyl acetate) (PVAc) has an experimentally determined Young's modulus of E = 5.1 GPa.[29] The glassy state has the highest modulus for a polymer, but while this is the peak modulus of PVAc it is still less than one-sixth of an example 33.5 GPa value for silica (SiO_2) NPs available commercially[30] and silica NPs are far from the strongest available. The origin of the improvements to the mechanical properties have remained elusive though, and several theories currently exist to attempt to provide that answer. From a simulation or modeling perspective, it is usually best to begin with the simplest case. If one were to add only 1 NP to an otherwise neat polymer, the improvement generated would be small, but mapping that result to generate a mathematical model describing the overall elastic response of a perfect rubber could provide a basis for expansion to other dilute systems. Fortunately, researchers have already created such a simulation with the goal of

> "generat(ing) a rigorous analytical result for the fundamental problem of the overall elastic response of rubber reinforced by a

dilute distribution of rigid particles under arbitrarily large 3D deformations,"[31]

thereby proving the understand of the hydrodynamic amplification effect that had been developed over the previous century, beginning with Smallwood's quantification of the NP reinforcement.

In 1944, Smallwood proposed the following relation:

$$E^* = E(1 + 2.5\varphi) \qquad (2.1)$$

where E is the original modulus of the matrix, E* is the modulus of the composite, and φ is the volume fraction of the filler material.[32] Because of the identical form of Smallwood's proposed relation to that of Einstein's derivation for the viscosity, μ, of a colloidal suspension in Newtonian fluids: [33,34]

$$\mu^* = \mu(1 + 2.5\mu) \qquad (2.2)$$

this phenomenon is termed "hydrodynamic amplification" despite the lack of hydrodynamics within materials in the solid state. This solution makes the assumption of spherical filler particles with complete adhesion with the matrix, without chemical changes to the matrix, under small amounts of deformation and was believed to be independent of filler particle size as long as the particle is large enough to neglect the molecular structure of the matrix.[32] Two decades later, Mullins and Tobin became the first to suggest "strain amplification" as the reason for the improved reinforcement and provided a description of the strain field immediately around the particle. Due to the increased moduli, they argued the NP can be treated as an non-deformable solid and when the matrix undergoes deformation the surface of the NP experiences a non-uniform strain-field.[35] Under uniaxial deformation, the two poles on the NP surface oriented parallel to the stretching directions will experience significantly increased tension, with a transition across the surface of

the NP to a zero net force that becomes significantly increased compression forces at the four perpendicular poles. Therefore, the mechanical reinforcement of the PNC is the result of overstraining in the polymer as it fills the "missing" deformation from the filler material. While the simulation referenced above showed a favorable comparison to the understanding proposed by Mullins and Tobin, allowing for a model to explain all isotropic distributions of rigid particles in a perfect rubber, not all derivations and empirical work have fit these assumptions.

A 2012 derivation suggested the assumption of amplified strain caused the conservation of energy law to be violated.[36] Additionally, the result of two separate Small-angle Neutron Scattering (SANS) experiments within rubber/silica and polystyrene/silica PNCs found no evidence of molecular overstraining and instead attribute the increased mechanical properties to nanoparticle-nanoparticle interactions.[37, 38] Yet these results directly contradict an earlier SANS study that purportedly observed molecular overstraining in a polystyrene-polyisoprene-polystyrene tri-block copolymer that treated the microphase separation of the polyisoprene block as a filler.[39] Unfortunately, filler type and fraction are not the only influencing factors for mechanical improvement because shape and size also play an important role alongside loading in mechanical reinforcement, contrary to Smallwood's size assumption.[40, 41] These results show that smaller diameter particles have an increased reinforcement effect than larger diameter particles at similar volume fractions, and that rod-like particles outperform spherical and triangular particles in mechanical improvement tests. These combined results have led researchers to the conclusion that the increased surface-area-to-volume ratio, and thereby increased interfacial polymer-NP interaction volume are the origin of reinforcement and not polymer overstraining.[29, 41]

These mechanical reinforcement beliefs break down the PNCs interactions into 2 types: the polymer-mediated interactions and the direct nanoparticle-nanoparticle interactions, referred

to as the nanoparticle network. The nanoparticle network changes the dynamic response of the polymers, as evidenced by the restricted polymer mobility near NPs and shifted temperature dependencies within the dynamic response timescales.[27, 42] Even prior to a complete packed PNC, the nanoparticle network will begin to form via polymer bridges. This can be manipulated in the case of a well-dispersed PNC with suitable mechanical reinforcement to effectively decouple the polymer-mediated response from the nanoparticle network response during strain and creep tests.[43] By decoupling the responses, it was determined that the polymer relaxation spectra were identical regardless of nanoparticle loading in the sample; however, the total sample rheological response was heavily influenced by NP loading. Therefore, it was concluded that the emergence of the nanoparticle network was the primary influence in the change of PNC dynamics that eventually caused the breakdown of TTSP at higher loadings. While the evidence for the hydrodynamic enforcement effect continues to mount,[44-46] it has yet become conclusive enough to alter the perception of the strain amplification theory. The contradictory results supporting both differing theories has yielded continued uncertainty with regards to the origin of the relationship between NP microstructure and the macroscopic PNC mechanical properties, despite myriad efforts to reveal the cause. As such, the continued efforts to understand this origin remain critical to the understanding of PNC deformation behaviors and the underlying philosophies for how to best control PNC mechanical properties within modern industrial practices.

1.3 Classical Quantification of Nanoparticle Dispersion

1.3.1 Small-Angle Scattering and Nanoparticle Dispersion

One of the key challenges to understanding the structure-property relationship during deformation is comprehending how the macroscopic flow field generated by the external deformation influences the microstructural rearrangement of the embedded NPs. While the ability to directly track individual particles is an existing technical challenge, polymer science has found success studying the averaged movements of a mass of particles through the combination of advanced imaging and small-angle scattering techniques. The fundamental understanding of small-angle scattering, using either neutrons or x-rays, is well documented[47] and both simulation efforts exploring the dispersion of the NPs as a function of polymer-nanoparticle interaction[18] as well as scattering measurement focused on the changes in nanoparticle dispersion[37, 48] are readily available.

The way Small Angle X-ray Scattering (SAXS) and SANS generate meaningful NP dispersion data across an entire sample is through the fact that in the reciprocal space system large-scale structures are found within the smallest angles – $2\theta < 2^{o}$. This can be shown through the evaluation of Bragg's law

$$\sin(\theta) = \frac{\lambda}{2d} \qquad (3)$$

where if the spacing distance of the represented structure, d, is similar to the incident beam's wavelength, λ, then the scattering angle, 2θ, would be 30º. If the scattering wavelength is on the order of 1 Å, then only information on the scale > 10 Å is visible in the small-angle scattering spectrum. Fortunately, PNCs typically have spatial features in the nm – μm scale; therefore, the

powerful tool of small-angle scattering is perfectly suited to probe any ordered microdomains within the sample, such as the NP distribution.

Small-angle experiments directly measure an intensity profile, I(q), which holds the spatial information relative to many different aspects of the PNC system. Whenever performing analysis on the spacing of the filler material, it is useful to first subtract the scattering profile of both an empty cell and the polymer matrix without any filler material. Fig. 1.2 shows the unnormalized 2-D I(q) vs q_x and q_z. Panel a) shows the detector's reading without any sample present, which is representative of the background readings that should be subtracted from all subsequent images during analysis. Panel b) shows the reading from the neat polymer, poly(2-vinyl pyridine (P2VP). The scattering of the neat polymer serves as a control for the signal response of the dust and other possible sample impurities contained within the PNC as well. Panel c) shows the scattering response from the PNC, which is a much stronger signal than that of the neat polymer. The baseline inhomogeneity of the neat polymer and the empty cell are both subtracted from the measured composite sample's signal prior to analyzing the signal to determine NP spacing measurements.

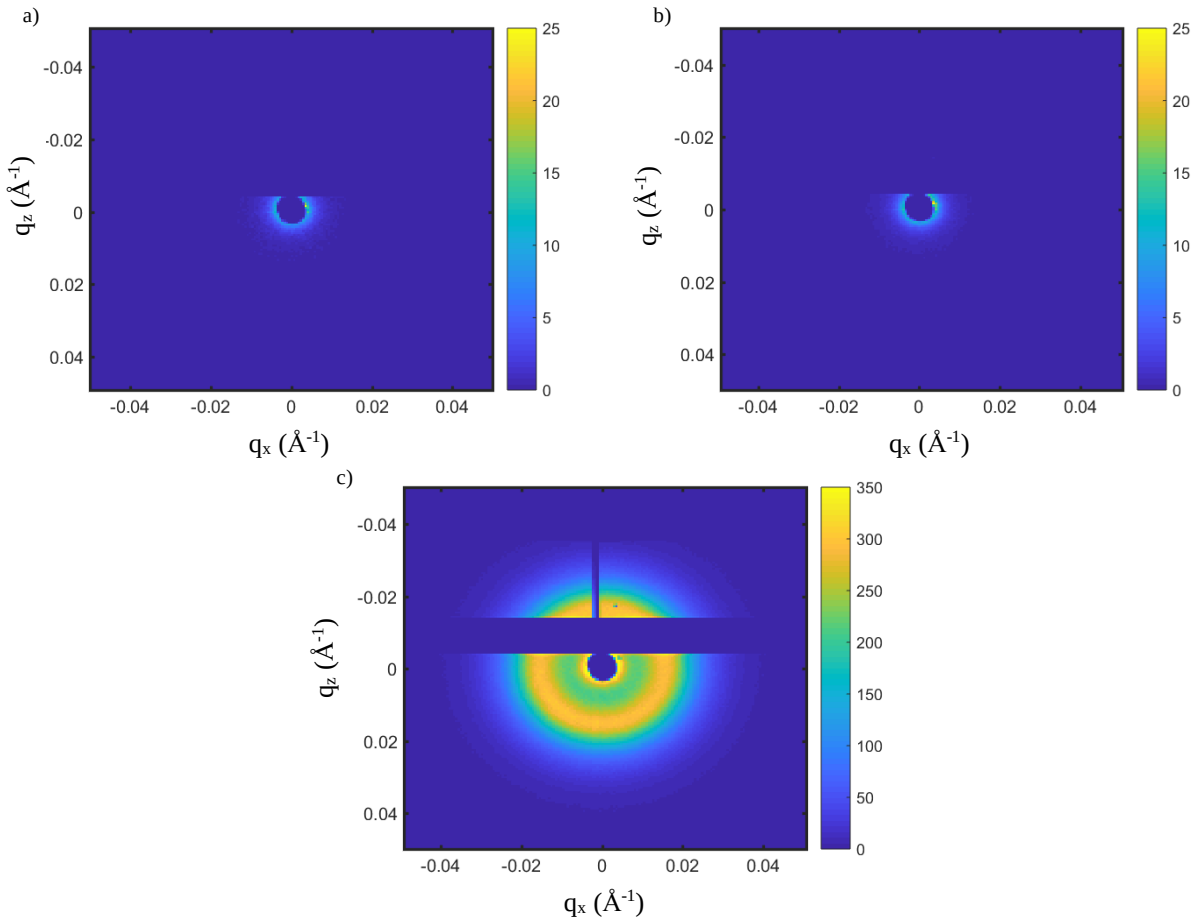

Figure 1.2: I(q) vs q_xq_z 2-D intensity profiles for a) an empty cell, b) neat P2VP, and c) 7 vol% PNC sample from unpublished work of Dr. Quinn Sun.

When performing the analysis, the results of several short exposure windows to the x-ray beam are averaged, allowing sufficient data generation while minimizing systematic errors and detector saturation that could occur if a single continuous exposure for the same total interaction duration was used. After reduction of the signal noise and the subtraction of the relevant measurements, the data should be normalized by the thickness of the sample to enable accurate comparisons and graphed as I(q) vs q (Å^{-1}). As shown in fig. 1.3,[49] the differences in scattering length density, called contrast, create an intensity profile that can be broken down into several different aspects. To measure the NP form factor, scattering is performed on a PNC with a dilute concentration of the NPs such that the positions of individual particles are entirely uncorrelated.

This results in an intensity curve related to individual NPs, detailing both the shape and size range of the NPs present in the PNC. As more NPs are added to the system, the shape of the curve changes in the low q region to describe the NP spacing relative to one another while the high q region still represents the individual NPs and has a similar intensity profile. As the NPs begin to form aggregates, the high q region moves towards 10^0 (cm^{-1}) in I(q) and provides the intra-aggregate structure factor of aggregates throughout the sample, while the lower q region shows the mass/size of individual aggregates, and the intermediate q region provides information on the spacing between aggregates. Additionally, the number of the NPs within an aggregate can be discerned by a ratio between the intensity of the isolated aggregate to the plateau value of the form factor of individual NPs, which holds as long as aggregates are isolated from one another.[49]

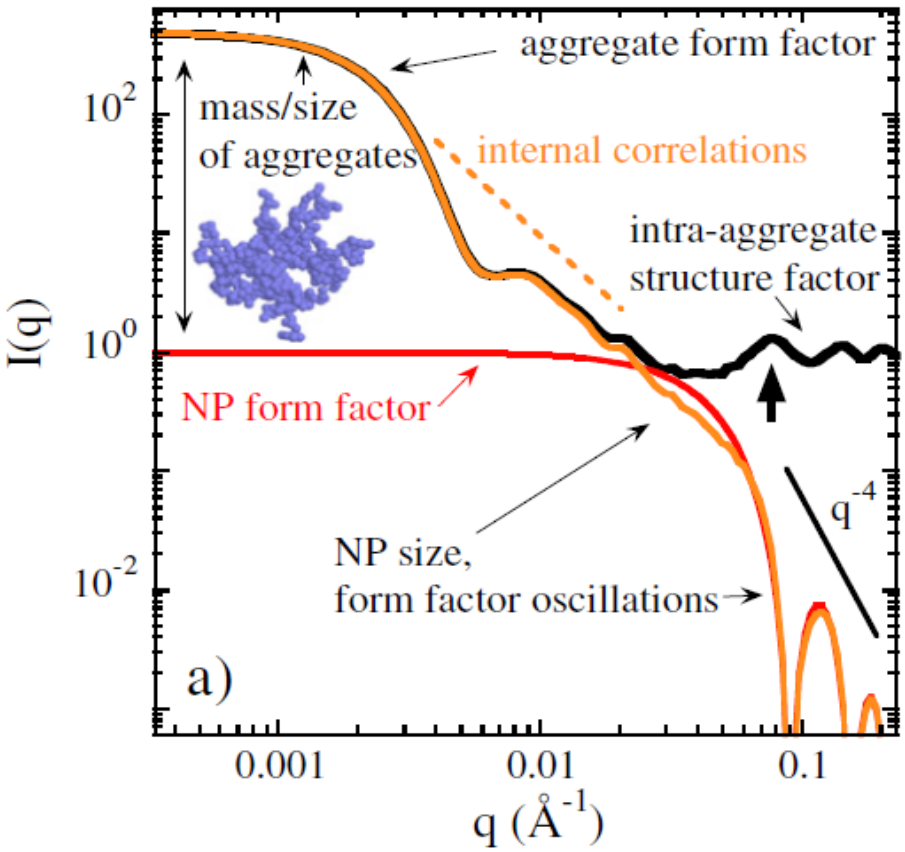

Figure 1.3: I(q) vs q ($Å^{-1}$) illustration. Illustration detailing the SAXS results for a variety of the NP arrangements within a PNC. Figure from reference 49.†

†Reprinted from Current Opinion in Colloid & Interface Science, 20, Genix A.-C.; Oberdisse, J., Structure and dynamics of polymer nanocomposites studied by X-ray and neutron scattering techniques, 293-303, 2015, with permission from Elsevier.

It is inherent that this information is extremely valuable to understanding the structure-property relationship; however, coupling the external deformation field to the resulting microstructural relationship has proven difficult through SAS alone. For one, the analysis of PNC SAXS can become complex as NPs begin interacting with one another. A major challenge is to extract 3D information from the 2D measurement. Additionally, the fact that the data provides an averaged response across the entire sample in reciprocal space – as opposed to a direct-space imaging method – is another limitation despite the powerful information gained. Another observation is that the results have not matched the affine deformation expectations, as seen in fig. 1.4.[50] Here, the nanoparticle spacings (y-axis) are compared against the performed extension (x-axis) where the dashed lines represent the movement of the NPs following the macroscopic deformation, the affine deformation prediction, but the data points reveal the actual rearrangement of the NPs in both the parallel (blue) and perpendicular (red) directions to be much smaller than expected. Unfortunately, the underlying cause of this phenomena and a concrete theory to describe it are currently non-existent, and the limitations of current SAXS capabilities suggest that a complimentary technique could be extremely valuable in probing localized areas in direct-space.

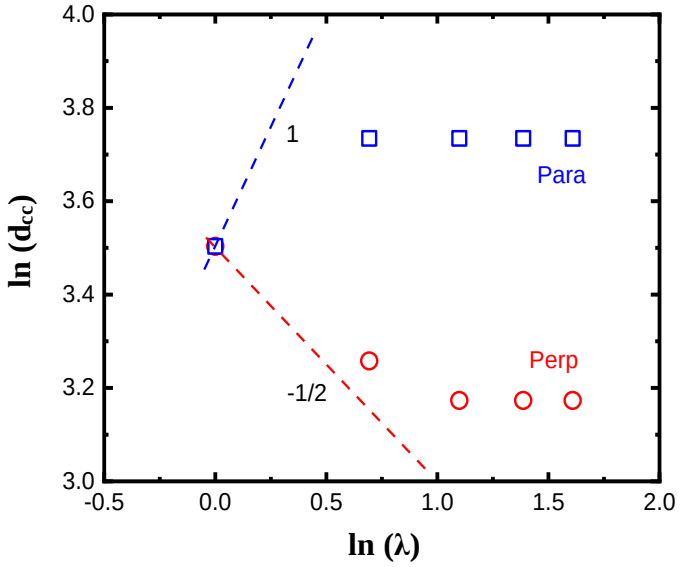

Figure 1.4: ln(d_{cc}) vs ln(λ). Affine deformation predictions for NP spacing in parallel and perpendicular directions compared to results from SAXS experimentation. Figure from reference 50.†

1.3.2 Potential Complimentary Techniques

While SAXS may not be able to provide localized data in direct-space, it has been used in coordination with several different technologies to study the behaviors of polymers and polymer composites. A Transmission Electron Microscope (TEM) can provide a localized view on the μm^2 scale with resolution on the nm scale, directly imaging the physical spacing of the NPs within the sample. Additionally, it has a wide compliment of available characterization techniques, such as electron energy loss spectroscopy or 3-D analysis, which can be used to provide additional information.[51, 52] TEMs have been widely used to characterize the fracture surfaces of PNCs and elucidate the fracture mechanics;[53] however, the observation of a non-linear deformation flow field is a tricker proposition. *In-situ* tensile deformation studies have been performed for nanofiber-filled polymers to analyze the reorientation; fracture; and matrix pull-out of fibers during deformation,[54] but for a non-linear test a specialized holder capable of precisely controlling the rate must be available. While there is limited space in a TEM column, the small sample size should yield a large enough elongation ratio to be valuable, although the tradeoff is increasingly difficult sample generation and placement as the size of the sample becomes miniscule but must be uniform while the sides must be properly orientated to generate accurate results. Although proven not to be impossible,[55] it is no wonder that this experiment is not widely performed. Additionally, *ex-situ* deformation studies could produce dubious results since the process of TEM sample generation involves actions that could deform the PNC in a difficult to quantify manner. Ultimately, since the 3-D reconstruction of data (or the generation of micro-thin film to reduce flow behavior to 2-D geometry) with physical significance is possible, the TEM is a viable alternative, or at the very least a powerful complimentary tool.

Another alternative capable of a physical observation is an Atomic Force Microscope (AFM). AFM is a surface-level technique capable of examining deformation flow fields while simultaneously measuring the mechanical properties and interfacial boundaries of a PNC,[29] as well as perform *in-situ* tensile testing.[56] Additionally, since the AFM cantilever device is relatively small it can be leveraged to create interesting set-ups combining AFM with other techniques.[57] However, AFM is not without several potential drawbacks: it only measures particles at the surface, the sample surface must be relatively flat, it will be difficult to survey large areas of the sample, and *in-situ* deformation will be limited to a single location that may or may not be representative of the entire sample. Therefore, while *ex-situ* examination of pre- and post-deformation properties would provide intriguing evidence of the surface response to deformation, the overall observation would be lacking, and it would be used best in conjunction with other technologies for this research.

Another advanced imaging option, including potential methodologies, has been provided by metals research and adapted to polymers for *in-situ* SEM experiments.[55, 57, 58] While the use of electron microscopes for polymers research is widespread, the SEM appears to be underutilized compared to TEM, and is typically used for NP size and dispersion analysis or other basic sample characterizations, or for imaging fracture mechanics.[59, 60] Macroscopically, polymer deformation has been imaged in a manner consistent with the methodologies laid out by metals researchers,[61-64] but the expansion of these techniques to probing PNC deformation flow fields on a micro- or nano-scale have not been widely utilized, despite the SEM possessing the necessary conditions of both a large μm^2 field of view with nm resolution. Additionally, the sample preparation requirements are not as stringent as on the TEM, with less unintended deformation and a much larger sample area, and the surface is not required to be as smooth as on AFM, with a greater ability

to probe multiple large areas efficiently to generate a statistically relevant observation of the NP structure and rearrangement across deformation of the PNC. While it can be used to observe topographical information, it also penetrates beneath the surface to a degree to allow the measurement of the NPs within the polymer bulk, while at the same time limiting the depth to only a single layer of the NPs to remove the necessity of 3-D reconfiguration. Of course, the stage could still be tilted to allow 3-D reconfiguration if desired, and, similar to the TEM, there are a variety of additional characterization techniques available on SEM columns. It is this expanded use of the SEM technology that will be explored in detail in Chapter 2.

1.4 Research Philosophy and Approach

1.4.1 Potential Impact and Overall Philosophy

Polymer research and the polymer industry are intrinsically linked to one another and increased scientific understanding usually leads to increased material performance in some way, providing ample motivation for researchers to address areas where multiple theories to explain phenomena exist. Polymer processing relies on the manipulation of polymer dynamics during deformation in either a tensile or shear manner. Within these modes, there are numerous different techniques utilized to generate finished products, with various strategies to optimize the results. Industrial practices have needed to continuously evolve with the understanding of polymer dynamics, as the link between different procedures and final properties is well documented.[65, 66] It is established that driving a PNC out of equilibrium can be used to manipulate the arrangement of the NPs.[67] Therefore, polymer deformation mechanics, and consequently industrial processing practices, intrinsically result in the movement of nanoparticles within the polymer matrix. The study of how these nanoparticles rearrange during deformation could provide valuable information crucial to unlocking the origin of the processing-structure-property relationships. Previous studies

have relied on scattering data to characterize the 3D NP distribution across deformation;[38, 39] however, this averaged data can only be used to describe the sample as a whole, without phase information or the ability to identify localized variances with no direct physical observations of the PNC – a key shortcoming found within most common polymer research methods.

Therefore, this research aims to utilize a Scanning Electron Microscope (SEM) to image the physical space of a PVAc/SiO_2 sample across deformation. The captured micrographs will display nanoparticles near the surface of the PNC sample on a nanometer length scale to be used in a manner largely unutilized in polymers research, although possible templates are well established within metals research and continue to be widely used.[61-63, 68] Since polymers are often processed in both tensile and shear modes, the effects of both will be studied herein. In order to accurately portray the volume fraction of filler nanoparticles, φ_{NP}, all PNC samples are verified using Thermogravimetric Analysis (TGA).

With regard to tensile deformation, a well-dispersed PNC without significant mechanical reinforcement will be stretched using extensional rheology procedures. The NP spacing distributions will be compared before and after deformation to observe the deformation flow behavior relative to the macroscopic deformation of the system via SEM images. The analysis of these behaviors is important to understanding the processing-structure-properties relationships during polymer processing practices such as film-blowing and hot pressing. With respect to shear deformation, PNCs of various φ_{NP} and NP sizes will undergo complex shear deformation via a capillary rheometer probing different response regimes. The extrudate cross-sections will be observed via SEM images to analyze phase separation as a result of strain rates applied. The analysis of these behaviors is important to understanding the processing-structure-properties

relationships during polymer processing practices such as 3D printing, fiber spinning, and various extrusion processes.

1.4.2 Overview of Tensile Deformation Experimentation

Considering the importance of the processing-structure-property relationships and their intrinsic connection to the microstructure of the NPs during PNC deformation, it comes as no surprise that it is a common research topic.[48, 69, 70] Despite the widespread research on the issue, the effect of the macroscopic deformation field on the NP microstructure on a nanoscale has proven to be a difficult challenge to unravel because different polymer matrices and different NP combinations have varied interactions on a microscopic level resulting in complicated polymer-NP and NP-NP balances to account for.[69]

On the macroscopic level, uniaxial extension is well-defined: consider a sample with dimensions length, L_0, width, W_0, and thickness, h_0, as pictured in fig. 1.5. As the sample is stretched the dimensions become L, W, and h. In uniaxial deformation, as L changes the elongation ratio is defined by the relationship:

$$\lambda = L / L_0 \qquad (4)$$

where λ is the elongation ratio as it is deformed at a specified rate. As L is increased by a factor of λ, in order to conserve volume the width and thickness must decrease by a factor of $\lambda^{0.5}$. The engineering stress, σ_{eng}, can be found as the force at a given time over the initial cross-sectional area of the sample prior to deformation. The results of engineering stress against elongation ratio are typically plotted to compare the mechanical properties of PNCs. Extensional rheometry can be completed in a number of different ways,[71] with 2 methods used in this research. In one, the sample is fixed at one end and pulled at the other with velocity, v, according to the relationships:

$$v = \dot{H} L_0 e^{\dot{H}t} \qquad (5.1)$$

$$H = \dot{H}t = \ln(\lambda) \qquad (5.2)$$

where $\dot{H}$ is the rate of Hencky strain, H. From this equation, it is seen that the velocity increases exponentially during the test, and the experimental limits are defined by both the cross-head movement speed range and the maximum length between the two fixtures. The other method applied here is to use a pair of counter-rotating drums, which shifts into the angular velocity, Ω_v, with the relationships:

$$\Omega_v = \frac{\dot{H} L_0}{r} \qquad (5.3)$$

$$H = \frac{\Theta r}{L_0} \qquad (5.4)$$

where r is the radius of the drums and Θ is the angular rotation. Here, the length of the sample is held constant while the area decreases exponentially with time, allowing for control at constant Ω_v, with larger λ achievable without the same apparatus limitations. In either technique, uniaxial extension of the polymer is achieved. Classically, polymer networks are often assumed to deform in an affine manner, which means that the macroscopic deformation applied to the sample can be uniformly translated throughout all sublevels of the sample down to a microscopic level.[72] If the positional change of the NPs follows the deformation flow field of the polymer, for a PNC system with well-dispersed NPs undergoing macroscopic affine deformation it is expected that the NPs should also follow the same conditions. That is, the center-to-center distance, d_{cc}, between nanoparticles should increase by $d_{cc}\lambda$ in the direction of stretching, $d_{\parallel}$, and decreases by $d_{cc}/\lambda^{0.5}$ in the two transverse directions, $d_{\perp}$. For the spacing between any to NPs relative to one another there

exists both a $d_{\parallel}$ and $d_{\perp}$ component that will be separated during analysis. For this experiment, d_{cc} will be determined via scaling the SEM images by their inherent pixel/nm ratio.

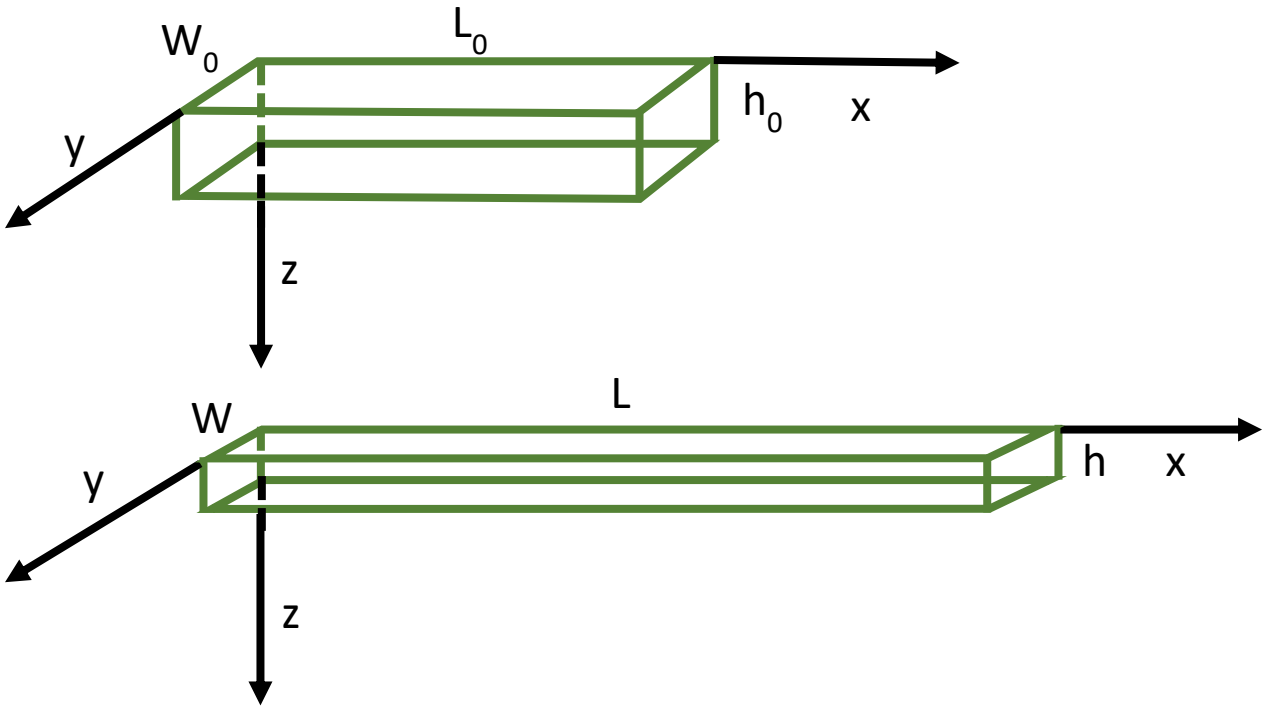

Figure 1.5: Schematic of uniaxial extension. Sample is shown before (top) and after (bottom) deformation in the +x direction with coordinate system and dimensions width (W), length (L), and thickness (h). The '0' subscript refers to the initial dimensions of the sample.

To check that the PNC is well-dispersed, a linear rheological technique known as Small-Amplitude Oscillatory Strain (SAOS) is used. SAOS applied a sinusoidal strain pattern:

$$\gamma(\omega, t) = \gamma_0 \sin(\omega t) \qquad (6)$$

where γ_0 is a constant strain value, ω is angular frequency, and t is time. The sample, mounted between a configuration of parallel plates of a defined radius, experiences a shear stress, σ:

$$\sigma(\omega, t) = G' \gamma_0 \sin(\omega t) + G'' \gamma_0 \cos(\omega t) \qquad (7)$$

The sample is tested across a frequency range, such as from 100 to 0.01 rad/s, at different temperatures $T > T_g$, where T_g is the glass transition temperature. TTSP is then utilized to construct a master curve where the data is all shifted relative to T_{ref}, taken as any one of the temperatures

measured. Another way to evaluate the mechanical performance of the PNC compared to the neat polymer is to construct the TTSP master curves on the same plot. One indication of nanoreinforcement is whether the shift factors for each temperature, relative to T_{ref} (which should be taken as the same value), are different. Another indication is whether there are substantial differences between the G' and G" curves – as the emergence of a nanoparticle network will increase the rubber plateau value and eventually prevent the cross-over into a terminal flow regime – instead behaving more like a gel than a liquid.[44]

These details from the SAOS master curve can provide, among other information, an indication of whether a nanoparticle network exists in the PNC; however, they cannot provide any information on the dispersion state. In order to determine the dispersion state, it desirable to survey the entire sample to measure the full spread of values that can be averaged. Due to the electron density difference between the SiO_2 nanoparticles and the polymer, as well as the ability to cover a large sample area, SAXS is typically performed to characterize the dispersion statistics;[59] but this technique still has shortcomings, notably a lack of physical observation. In lieu of scattering experimentation, an SEM will be used as the primary method to enable direct physical observations and subsequent analyses of the images will be used to determine the NP spacing across the sample. To observe different stages of deformation under varied dynamic responses, the process will be stopped at varied λ for multiple deformation rates. Image analysis will be used to produce results both comparable and complimentary to the analysis afforded by scattering experiments.

1.4.3 Overview of Shear Deformation Experimentation

Similarly, the concept of PNC phase separation under shear deformation has also been the topic of research for quite some time.[73, 74] This earlier research goes so far as to propose a mathematical representation for the timescale of microphase separation for polyurethane PNC

systems with nanofillers, and are not the only example of discussing these dynamics.[75] Considering the growing importance of PNC 3D printing in additive manufacturing, a comprehensive understanding of these polymer dynamics under shear deformation is crucial to design processes to create the best products.[76]

Simple shear deformation is also well-defined: consider a sample with dimensions thickness, h, sandwiched between two parallel planes with contact area, A_0, as pictured in fig. 1.6. A force, F_p, applied along the top plane causes displacement, Δx, of the top plane while the bottom plane is held stationary by an equal resistive force of $-F_P$. The shear strain in the sample is then defined as the ratio of Δx over h; similarly, the shear stress is defined as the ratio of F_p over A_0, the area the force is applied to. The shear modulus, G, is then defined as the ratio of shear stress over shear strain.

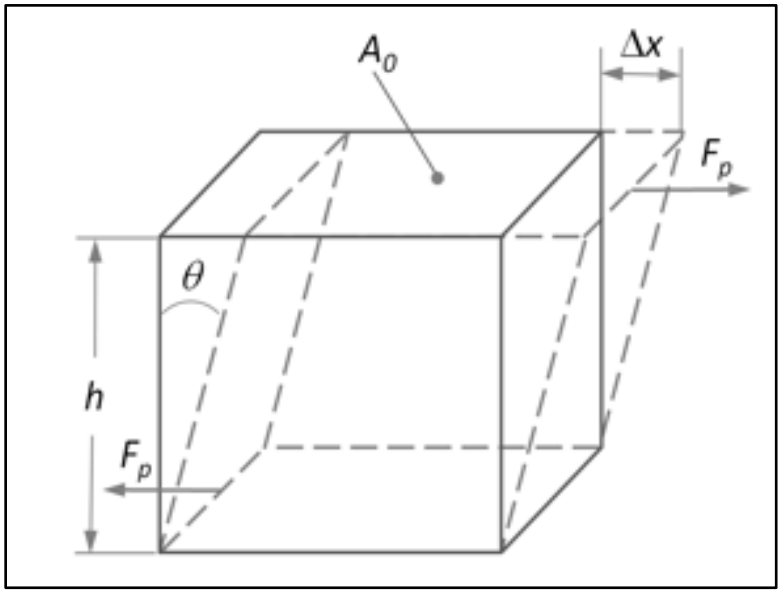

Figure 1.6: Schematic of simple shear deformation. The force applied on one edge of the sample causes a displacement across the sample and resistive force on the other edge.

In order to probe the phase separation behavior of PNCs during shear deformation, a variety of sample loadings of PVAc/SiO_2 PNCs for 2 distinct NP sizes were extruded through a capillary rheometer. In a capillary rheometer, force is applied to the sample via a piston that pushes the PNC

through a die with characteristics of length, L, diameter, D, and entry angle, θ. The cross-section schematic of an extruder die is presented in fig. 1.7. While this process is highly dependent on the shear-deformation behavior at the wall, there are also extensional flow components to the process, creating a complex system that can be challenging to breakdown the origin of behaviors. Varying either θ or the L/D ratio will result in varied flow mechanics as θ influences the flow field entering the die and the L/D ratio controls the timescale of the polymer response allowed during the process. The inlet pressure, P, experienced by the PNC is measured and can be converted into the shear stress, σ. The mass of the PNC extruded across a measured amount of time is used to calculate an apparent shear rate, $\dot{\gamma}_{app}$, which is plotted against σ to generate a flow curve across the varied pressure datapoints. Multiple dies with varied L/D at the same θ can be used to correct the inlet and outlet pressure loss factors of the flow, and the Weissenburg-Rabinowitsch correction can be used to calculate $\dot{\gamma}_{true}$ from $\dot{\gamma}_{app}$; however, for the purpose of comparing flow behaviors and imaging NP rearrangement between samples extruded on an identical system this correction is not strictly necessary.[77, 78] The diameter of the extrudate is also measured, as its ratio over D, called die swell, provides information on the PNC elasticity and the stress relieved during the extrusion process.

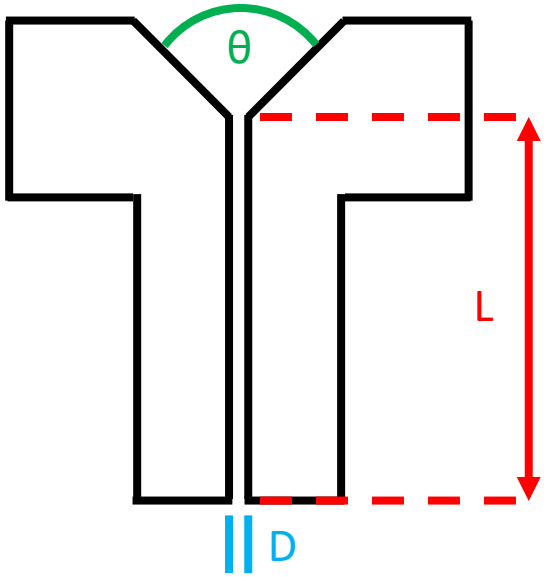

Figure 1.7: Schematic of extruder die.

Cross-section faces of the resultant extrudate samples are then imaged using a SEM to visualize flow separation behaviors. The physical observations can be linked to the changing flow regimes on the $\dot{\gamma}_{app}$ versus σ plot and related to die swell measurements as well. Additional information is provided by SAOS measurements of the PNC relaxation spectra and evaluation of TTSP master curves compared to the neat polymer.

1.5 Outline of Subsequent Chapters

The current understanding and competing theories that work to explain the polymer behaviors crucial to the processing-structure-property relationships within the polymers community have now been discussed. Additionally, the current characterization techniques used to determine NP spacing in efforts to support those theories have been introduced. Therefore, it is now beneficial to outline the ensuing chapters to show in brief how this dissertation aims to help define the understanding of the processing-structure relationship through a physical basis via SEM imaging technology.

After briefly covering the fundamentals of the SEM, Chapter 2 will detail how existing SEM understandings and methodologies can be leveraged for a novel use of the SEM imaging with respect to PNC systems. This includes how the limits of the physical information gathered can be utilized as an advantageous restriction to the benefit of the resulting image analysis. It will do this by showing the calculation of a sample's electron interaction volume (EIV), which is related to the maximum escape depth, as a function of the column's accelerating voltage and PNC material properties. This information, combined with some basic information related to SEM operating principles, allow for reasonable assumptions regarding the information gathered with regards to the 3D layout of the PNC microstructure.

In Chapter 3, the method outlined in Chapter 2 will be applied to a PNC undergoing tensile deformation. The physical representation of the NPs acquired via SEM imaging will be used to quantify NP rearrangement across different stages of deformation, investigating the origin of the processing-structure relationship. It will be discussed how the results of these analyses offer observations both comparable to and complimentary to the results of SAS, proving the value and validity of this methodology. These analyses will then be used to show how the microstructural rearrangement of the NPs under different deformation rates deviate from the macroscopic deformation field. This discovery defies the prevalent understanding of the NP motion under affine tensile deformation and reveals interesting features of the rearrangement of the NPs under polymer deformation.

In Chapter 4, SEM images of extruded polymer will be used to discuss the phase-evolution of the PNC under shear deformation. The PNC is examined at various pressures involving multiple flow regimes, with groups of images captured at various regions across the cross-sectional face of the extrudate showcasing the differences in NP concentrations visible along the surface.

Contrasting the edge of the sample against the bulk of the material allow interesting observations between multiple sample sets of varied NP size and loading within a similar polymer base. The results provide a fascinating window into the other half of the processing-structure relationship and reinforce the challenges present in decoupling the origin of PNC behaviors.

Chapter 5 summarizes the main conclusions of the previous chapters, discusses the work still ongoing, and explores the next steps that can be taken to advance the understanding of the processing-structure-property relationships. It serves to bring the dissertation back into a single frame of reference to discuss the importance of the discoveries contained herein.

CHAPTER 2: SCANNING ELECTRON MICROSCOPE IMAGING FOR PHASE QUANTIFICATION OF POLYMER NANOCOMPOSITES

2.1 Scanning Electron Microscope Background

2.1.1 Introduction to Scanning Electron Microscopy

An SEM works by creating a highly focused electron beam and detecting different interactions from that beam's interaction with the near surface of an object. The basics of the SEM and its polymer applications are readily available.[79, 80] The beam is emitted from a cathode at an accelerating voltage, E_0, that can be controlled between a typical range of 0.1 to 30 keV for many SEMs, although some possess higher and lower energies. As it passes through the column towards the sample, the electron beam is refined by a combination of magnetic and electrostatic coils – used as lenses to bring the beam into focus – and apertures – which aid focusing efforts by only allowing certain angles of travelling electrons to pass through their opening, thereby reducing the beam to a more-refined cone. Once the beam reaches the sample, the electrons can interact with the sample in many different ways, as depicted in fig. 2.1. Different detectors are required to process the different signals, with the exception that a secondary electron (SE) detector will also detect backscattered electrons (BSE). The reason for this is due to the nature of the interactions that create the secondary and backscattered electrons, which will be detailed below. The beam is focused in a discrete x-y pattern that is measured in sequence, generating an image by digitizing the detected response into corresponding X-Y locations on the display screen with a gray level generated by the intensity of the signal response at that location. In SEM, magnification is controlled not by the strength of the magnetic lenses (as it is in a TEM), but rather the ratio of the X-Y display field over the x-y locations on the sample. This means the working distance of the sample (the distance between the sample and the objective lens), the voltage supplied to the x-y

scanning coils, and the dwell time (the amount of time spent detecting the signal at an x-y coordinate) all play crucial roles in the image obtained. Fortunately, the sample stage movement allows control of the working distance, the SEM will control the voltage changes automatically (although this value can also be tuned manually for high resolution imaging), and the image cycle time (the total time spent composing the image) can be manipulated through the selection of a scanning speed. Additionally, scans can be performed in parallel and integrated together to improve image quality – which it should be made clear is not the same as parallel imaging: it is parallel computation of the sequential process of imaging.

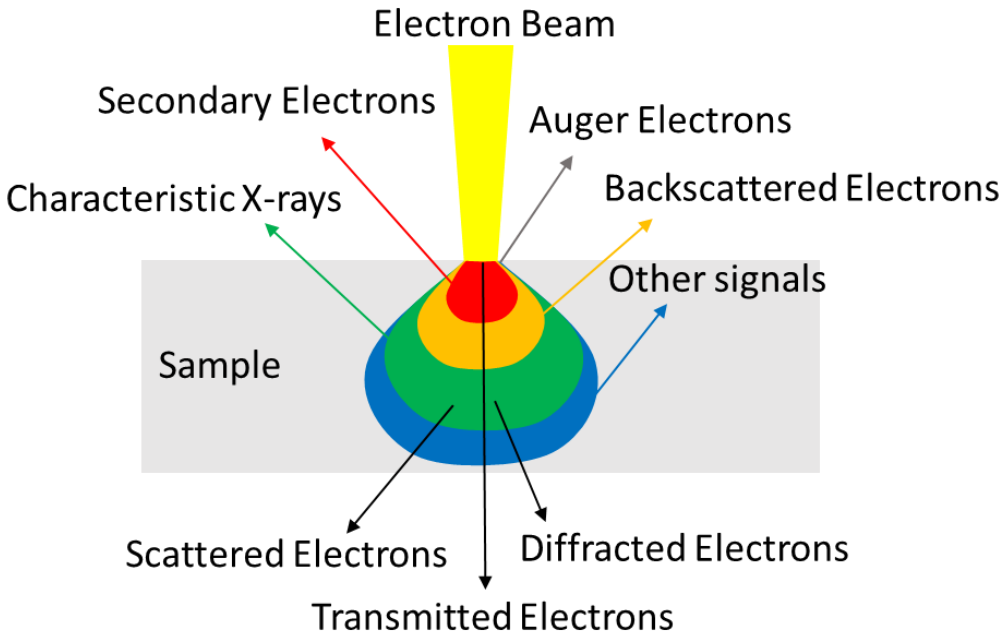

Figure 2.1: Sample interactions of an electron beam. Several different types of interactions happen between the beam and the sample, although an SEM will only detect signals that return through the surface of the sample. Specialized detectors are required to process different signals, with the main exception that a secondary electron detector will also pick up Backscattered Electron signals.

When imaging a sample, key factors the equipment user must determine are the proper aperture, type of signal detected for the image, and the accelerating voltage of the incident electron beam. When selecting an aperture, the main consideration is the depth of focus desired, i.e. the length of space in the z-direction that is in focus. A smaller aperture will create a narrow cone with a larger depth of focus, or a reduced x-y frame with greater $\pm z$ before objects begin to blur, and a

larger aperture will create a wider cone with a smaller depth of focus, or an increased x-y frame with lesser $\pm$z before objects begin to blur. When imaging with secondary electrons, the SEM uses an electrode with a positive bias to 'collect' the scattered electrons from the sample's surface, regardless of the nature of the interaction. This is because SEs are inelastically scattered and have low energies ($\leq$ 50 eV) once they escape the sample surface – and only inelastic interactions near the surface can even escape – and require the voltage bias to attract the emitted electrons into the detector. As a result, SE-mode images typically result in an intensity bias towards surface-driving information, such as topography, which can be amplified by tilting the sample to artificially increase the 'depth' of surface-driven interactions from the incident electron beam – a manipulation of the phenomena known as the 'edge effect.' Meanwhile, BSEs are the result of elastic interactions with the sample and are therefore much higher energy (analogous to the energy magnitude of the incident electron beam). When using the SEM to image BSEs, the bias on the scintillator is either switched to a negative charge or turned off (or a different detector with a bias altogether is used), meaning the low-energy signals are effectively filtered out and the image only includes the high-energy signals of BSEs with intensity differences based on the interaction materials' density instead of the depth of their interaction. It is important to note that while BSE detection eliminates SE detection, the inverse is an impossibility and SE detection will always include BSE detection as well. If the desired information is surface driven, such as surface topography or limited planes of sub-surface artifacts, then SE is likely to be the appropriate choice. However, BSE are more useful for material characterization purposes when there are large differences between material densities within a sample, and topographic contrast with BSEs can also be a powerful tool. Additional specialized detectors can be used to study characteristic x-rays, fluorescent x-rays, and cathodo-luminescence among other signals within a sample for varied

characterization purposes, but for this work the main decision lies in choosing between SE and BSE detection. The optimum accelerating voltage is also dependent on the application of the SEM. If BSEs are the primary objective, higher accelerating voltages, $E_0 \geq 10$ keV, are often desirable because the relationship between the atomic number and BSE energy is a nearly monotonic increase beyond $E_0 = 5$ keV and therefore a higher voltage corresponds with increased contrast between materials. For high-resolution imaging, there are actually 2 competing thoughts to selecting the accelerating voltage. If $E_0 \geq 25$ keV, the lateral spread of BSEs will degrade their detected signal into background noise and the remaining SE signal will be strong; however, this strategy requires longer cycle time to account for the increased signal-to-noise ratio in weakly contrasting systems, such as PNCs. Alternatively, when $E_0 \leq 5$ keV, as the beam energy is reduced the EIV also decreases by a factor of $E_0^{1.67}$ and eventually reduces the signal of BSEs into the same interaction 'footprint' of the SEs; therefore, BSEs contribute to the high-resolution signal and can aid in image contrast at the expense of overall brightness and depth of information gathered. The determination of the EIV and selection of accelerating voltages for PNC systems will be addressed in a subsequent section.

2.1.2 Imaging a Polymer Nanocomposite

With respect to PNC samples, there are several additional challenges, such as the insulating nature of the sample, that must also be addressed. As shown in fig. 2.1, when the electrons of the primary beam make contact with the sample there are many different interactions that take place. In reality, a large number of these electrons are absorbed by the sample during this process – for instance, in any inelastic interaction that is well below the surface. Additionally, electrons can take complicated pathways through the sample, interacting with numerous different electrons both elastically and inelastically in a process that can drastically alter their trajectories in unpredictable

manners. In order to understand this process, researchers perform Monte Carlo simulations of electron interactions. Fig. 2.2[80] shows the simulated results for elemental carbon, silicon, copper, silver, and gold on the same scale for an E_0 = 20 keV. The electron pathways are indicated by a line colored either red, indicating an electron that escaped the surface and is detectable by the SEM, or blue, indicating an electron absorbed by the sample. Clearly, there are far more blue pathways than red, indicated most electrons are absorbed by the sample. For conductive samples, the absorbed electrons are passed through the sample to the stage and the sample experiences no net charge; however, many polymers and PNCs are insulating materials and the net effect is a large build-up of negative charge in the sample when the outgoing current cannot match the incoming current of the beam. This charge build-up causes interference in the imaging process by distorting the picture, washing out the contrast with increasingly high intensity areas, and even altering the incident beam due to the repulsion cause by the magnitude of the negative charge. Eventually, the magnitude of the potential becomes too large and the sample discharges back to a neutral state, but the sample will then begin charging again and could suffer damage or chemical changes, such as cross-linking the polymer matrix, due to the excessive energy involved in the build-up. To avoid these imaging issues, it is common practice to coat insulating materials with a conductive material, such as carbon; gold; platinum; or other suitable metals, but this coating must be consistent across the surface of the sample and form a continuous pathway to the stage to prevent localized charging from occurring. Because coating the sample could alter how the surface is imaged, among other effects, sometimes it is desirable to reduce charging using other methods. Additional options to reduce charging are to lower the accelerating voltage to $E_0 \leq 1$ keV, thereby significantly decreasing the rate of charge build-up in the sample, or using an environmental SEM (ESEM) or low vacuum SEM (LVSEM), which both suppress charging by allowing the sample chamber to

include ionized particles thereby relieving the surface of some of the burden of charge accumulation. Choosing the right method to alleviate charging is important but is not the only concern for imaging insulating materials.

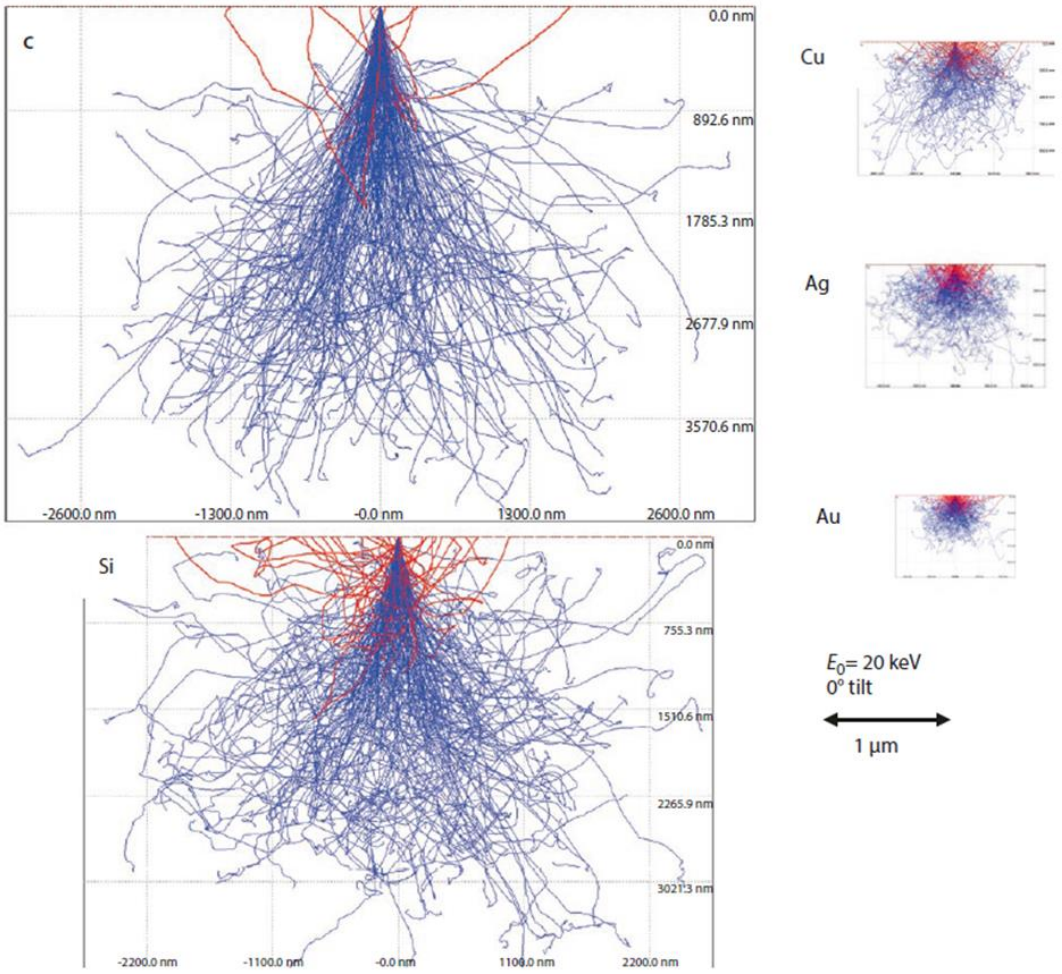

Figure 2.2: Monte Carlo simulation results for different elemental materials. The electron interaction volumes are shown on the same scale for the elements carbon, silicon, copper, silver, and gold for an accelerating voltage of 20 keV. Figure from reference 80.

Even after countering the PNC's insulating nature, the amount of energy entering the sample can still cause issues. Just as polymer chains are always moving and increased energy results in more movement, increased energy on the polymer surface can cause the appearance of the polymer "shrinking" away from the beam, and staying on a spot too long can also result in contrast distortions known as a "burn box." While the presence of nanoparticles appears to reduce

these responses, in low φ_{NP} samples, or even just particle-sparse regions of higher φ_{NP} samples, these effects can be detrimental to the imaging process. The source of this challenge is a disadvantage of the SEM's inherent imaging process. During the sequential imaging process, no 'true image' of the complete field of view actually exists, so as the polymer sample appears to move or drift randomly the image is distorted in a manner that can prevent analysis. Additionally, because this is an artifact of the sample's behavior and not the beam's behavior, the imaging features to account for 'beam drift' are sometimes ineffective; however, that does not imply there is no ability to adjust the imaging process to reduce the impact. To reduce the impact of polymer motion, the goal is to manipulate the total cycle time of the imaging process. Previously, it was discussed how the image cycle time can be increased to improve image resolution: by reducing the scan speed to allow the detector to spend a longer amount of time collecting the information for each pixel and/or allowing multiple pictures to be sequenced in parallel to be integrated together to increase the signal-to-noise ratio. This imaging process is used in both line integration and frame integration modes, and while it usually improves resolution, the longer cycle time means more energy supplied to the polymer and can sometimes have the opposite effect. When that is the case, the imaging process can be switched to a frame average technique at very fast scan speeds. This strategy severely limits the amount of energy locally provided to small areas of the sample by significantly increasing the scan speed so that the total cycle time is minimized, then taking the average of a large number of images produced in this manner to create a higher-resolved image. A comparison of these techniques for various PVAc composite samples is offered in fig. 2.3. In images a) and c), the frame average technique was used with a total cycle time of 6.6 s, while images b), d), and e) were formed using a line integration and a total cycle time of 26.0 s. Ergo, images a) and c) were formed more quickly, with lower interaction energies provided to each

pixelized area of the sample. Despite the consistency within each formation technique, in both equal comparisons one does not obviously outperform the other overall. On the one hand, image b) appears to have greater resolution than image a), with well-defined nanoparticle edges and less general blurriness in the surface markings. Alternatively, image c) appears to have better resolution than image d), which suffers from spatial distortion and as a result actually exhibits a slightly reduced field of view (compare the lower right corners of the two images). Image e) provides a higher nominal magnification of a low-concentration PNC with 40-50 nm NPs with areas of visible distortion caused by the apparent movement of the sample during line integration imaging, seen as lines passing horizontally across the image distorting that line, which would cause errors in the measurement of the NPs on opposite sides. The important conclusions to note from fig. 2.3 are that closely monitoring the behavior of the sample under the beam and that knowing when to apply each technique, which are not listed exhaustively here, are the keys to capturing the best images. Similarly, during the course of imaging a sample, allowing for variances in the scan speed and the adjustment of the signal-to-noise ratio through increased parallel sequencing or number of averaged frames will grant more success than attempting to define a single set of scanning variables to be used for every image.

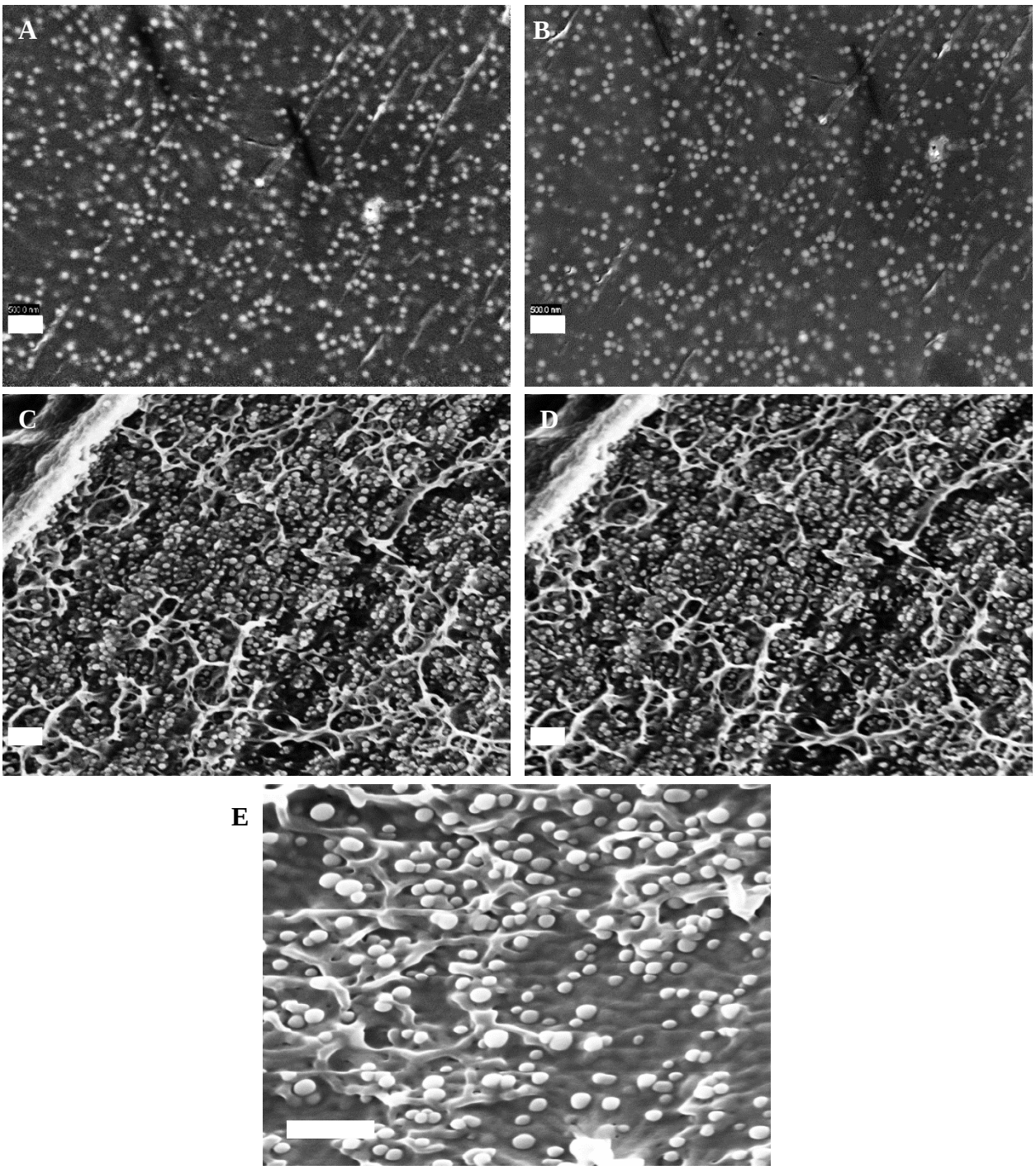

Figure 2.3: Comparison of the SEM imaging techniques. a) Frame average of 3v% PVAc with 70-90 nm NPs. b) Line average of same location as a). c) Frame average of 12v% PVAc/SiO_2 with 40-50 nm NPs. d) Line average of same location as c). e) Line integration of 2.8v% PVAc/SiO_2 with 40-50 nm NPs. Scale bars are 500 nm.

2.1.3 Determination of the Electron Escape Depth for Polymer Composites

Although not directly a challenge presented by imaging PNCs, this work also faced the challenging task of determining the escape depth of the detected signals in order to elucidate the nature of the physical observations provided by the images. Specifically, if it can be shown that only 1 complete layer of the NPs is present in an image, it greatly simplifies the analysis through an assumption of 2-D deformation fields and phase regimes. In order to determine the validity of a 2-D assumption, the escape path of the electrons must be estimated. One method of estimating the escape depth is through the calculation of the inelastic mean free path (IMFP). The IMFP is calculable through a readily available analytical formula reliant on the optical energy-loss function of a given material:[81]

$$\lambda_{in}^{-1} = \frac{1}{\pi a_0 v^2}\left[A \ln\left(\frac{2v^2}{I}\right) - \frac{7}{2v^2}C\right] \qquad (8)$$

where a_0 is the Bohr radius in nm; v is the electron velocity; and A, I, and C are material parameters from the optical energy-loss function $\mathrm{Im}[-1/\varepsilon_M(\omega)]$ with Mermin dielectric function ε_M. Once determined, the IMFP is generally estimated to be one-third of the total depth of the signal detected via SEM; however, this method involves additional experimentation require for each individual PNC system with results that cannot be generalized from one sample to another.

Alternatively, the EIV can be view as a symmetrical shape in the x- and y- planes, with deepest penetration in the z-direction roughly three times the maximum escape depth of the electron signal detectable by SEM. A simple exercise referring back to fig. 2.2 can confirm this: the shape of the EIV can be generalized by tracing a perimeter consisting of the blue lines travelling further from the sample entry point and the escape depth can be performed for the red lines. One trend from fig. 2.2 is that the higher a material's atomic weight, the smaller the maximum depth

of electron penetration in the sample. In fig. 2.4[80] it is shown that the accelerating voltage also significantly influences the EIV and escape depth of the electron, which remains about one-third of the total EIV. Therefore, any equation for estimating the EIV must account for both the material composition and accelerating voltage.

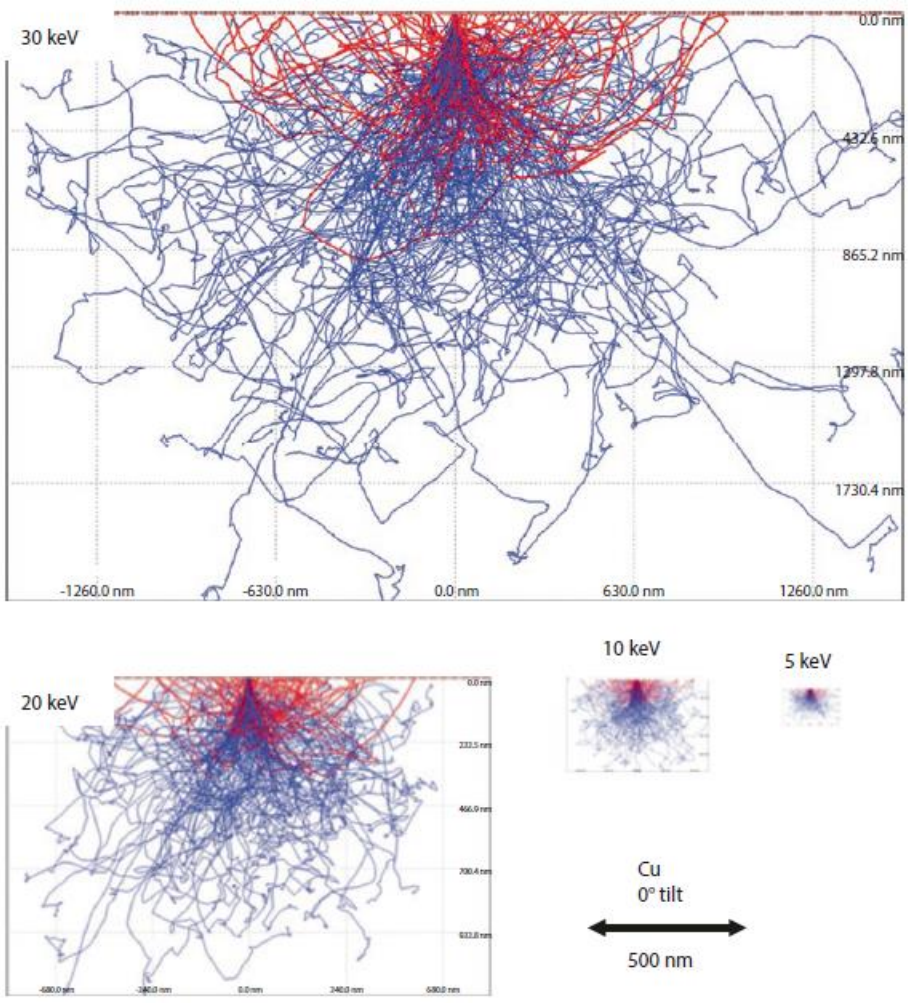

Figure 2.4: Monte Carlo simulation results for different accelerating voltages. The electron interaction volumes are shown on the same scale for the element copper at accelerating voltages of E_0 = 5, 10, 20, and 30 keV. Figure from reference 80.

There are two accepted relationships to guide the estimation of an EIV for any sample. The first was proposed Bethe in 1930:[82]

$$\frac{dE}{ds}\left(\frac{eV}{nm}\right) = -7.85\left(\frac{Z_{eff}\rho}{AE_0}\right) * \ln\left(1.166\frac{E_0}{J}\right) \quad (9.1)$$

where E_0 is the incident beam energy (in keV), Z_{eff} is the effective atomic number, ρ is the density (g/cm^3), A is the mean atomic weight (g/mol), and J is the mean ionization potential (keV) given by:

$$J\ (keV) = (9.76Z + 58.5Z^{-0.19})*10^{-3} \quad (9.2)$$

One noteworthy aspect of this equation is that the logarithmic decay suggests that the further into the sample the electron penetrates the quicker it loses energy (ie, electron interactions near the surface retain most of the energy, while those reaching deeper have lost a considerably greater amount of energy and therefore a much lower chance of escaping). This matches well with the theory that only electrons interacting within the top third of the total EIV are able to escape the sample and be detected.

Bethe's approximation is based solely on the elastic interaction pathways as a function of the possibly trajectories determined by scattering angles, while sample interactions with electrons can also be inelastic in nature. While the detection of inelastic scattering is only capable for interactions at or very near to the surface, as mentioned earlier these interactions will occur throughout the sample and serve to alter the actual EIV of the sample. In 1972, Kanaya and Okayama reviewed the existing fundamental theories of electron scattering and proposed the following range equation:[83]

$$R_{K-O}(nm) = 27.6\left(\frac{A}{Z_{eff}^{0.89}\rho}\right)E_0^{1.67} \quad (10)$$

where variables are consistent with equation 9 and this discussion. These results are comparable to modern Monte Carlo simulations, as shown in fig. 2.5.[80] Here, the $R_{K\text{-}O}$ range is shown as a gold

arrow superimposed on the Monte Carlo simulation for the EIV of carbon, aluminum, copper, and gold for an E_0 = 20 keV. It is important to note that neither result should be treated as a hard value, but rather an estimation of the maximum electron penetration for a combination of specific sample and beam conditions. For instance, in addition to the aforementioned relationship between atomic weights and accelerating voltages, it is also inherent to the range equation that sample density plays an important role. Elemental carbon could have a density of 1.8-2.1 g/cm^3, 2.267 g/cm^3, or 3.515 g/cm^3 depending on whether the current allotrope is amorphous, graphite, or diamond, respectively.[84] Despite identical beam conditions and similar elemental composition, uniform samples of these allotropes would be expected to produce varied EIV results, even without considering the phenomenon known as 'channeling' where the electron interaction length varies based on the crystal orientation relative to the electron beam.[85] This reality also applies to semi-crystalline polymer samples, as well as polymer composites with any filler material periodically distributed with a long-range order through the medium. Not only should one expect different results for a well-dispersed field of individual particles versus a field of aggregated groups of particles randomly distributed, but the volume fraction and filler type, shape, and orientation will also impact the actual EIV.

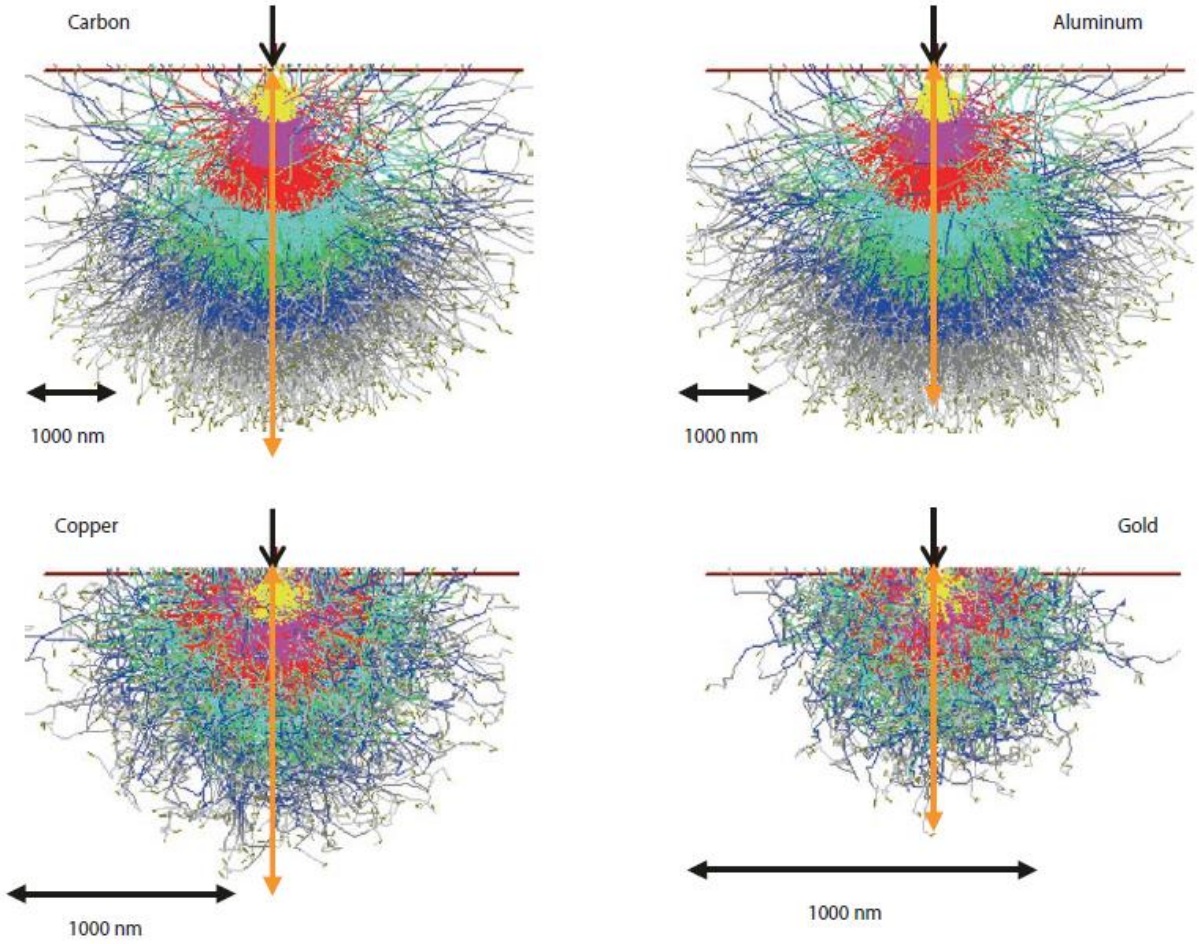

Figure 2.5: Kanaya-Okayama range comparison. The results of the Kanaya-Okayama range equation are depicted by a gold arrow superimposed over the Monte Carlo results for carbon, aluminum, copper, and gold at E_0 = 20 keV. Figure from reference 80.

With respect to PNCs, the sample coating must also be accounted for in addition to the morphology of the sample itself. In addition to negating surface charges, a thin coating of a conductive material serves to improve the signal-to-noise ratio of the imaging process because it reduces the spread of the interaction volume. This is related to the differing nature of high-Z electron pathways, which often increase the yield of surface-related secondary electrons and produce a more uniform hemispheric response area, whereas low-Z pathways move more laterally under the surface and generate a "pear" or "teardrop" shape with higher "background" noise from the further-reaching primary electrons.[80] Therefore, the coating material is also important, and a

platinum or gold coating will reduce the energy spread and result in higher resolution of insulating materials than a carbon coating, for example.

2.2 Application of Scanning Electron Microscope Methodologies

2.2.1 Procedural Challenges

While *in-situ* SEM methodologies have been around for some time, a methodlogy that could potentially be suitable for PNCs was described for tracking grain boundary motion during the deformation of metals by Kammers and Daly at the 2011 conference for the Society for Experimental Mechanics.[58] In this methodology, gold NPs were deposited onto the surface of a polished aluminum sample to create a strong contrast against the aluminum background. The area of interest was physically marked in a manner that it could easily be located, and, after deformation, the same area of the surface was imaged again. Digital Image Correlation (DIC) was then used to map the movement of individual gold NPs on the surface and allow grain boundaries to be determined based on the movement of the NPs in the same slip planes. The result was an accurate depiction of the surface strains resulting from tensile deformation of aluminum.

The initial experimentation aimed to achieve the transition to PNCs using Poly(methyl acrylate) (PMA) as the polymer base due to having a low T_g = 10º C, meaning rubbery behavior was accessible at room temperature. Imaging was performed on a Tescan MIRA 3 SEM due to an accessible *in-situ* screw-driven tensile frame from Ernest F. Fullam, Inc. A PNC with φ_{NP} = 12.8v% of SiO_2 NPs with radius, R_{NP}, = 7 nm was imaged at E_0 = 20 keV, with a thin platinum coating to resolve charging issues. The small NPs of the PNC require a high magnification to resolve clearly, which correspondingly limited the field of view used to determine long-range patterns in the visible NPs, so gold NPs of size R_{NP} = 30 nm were deposited on the surface of the

PMA composite to be tracked, much like the aforementioned methodology. The larger NPs allowed a wider field of view with well-resolved particles and a high contrast in BSE mode. The E_0 was later reduced to 15 keV to limit the energy input into the polymer system. To allow the gold NPs to experience the polymer bulk deformation field, the sample was placed into a vapor chamber to induce the diffusion of the gold NPs to just below the surface through the manipulation of polymer movement in the solvent vapor. Through the Stokes-Einstein relation, $d = \frac{k_b T}{6\pi\eta}$, where η is the viscosity, the diffusion coefficient was determined and the relationship $x = \sqrt{2dt}$ was used to determine the time required for the 1-dimensional diffusion distance with the knowledge that the BSE detection was possible at ~100 nm under these SEM imaging conditions. A comparison of the PNC in SE detection mode without the gold NPs and the PNC in BSE detection mode with the gold NPs is presented in fig. 2.6. This procedure was deemed sufficient to perform an *in-situ* particle tracking experiment; however, as the Fullam tensile stage performed deformation, the polymer sample began to charge as a result of the platinum surface layer not deforming along with the polymer. While significant elongation ratios, up to $\lambda \approx 8$, were reached prior to charging interference becoming too prominent, the sample also suffered from defects resulting in deformation not being true uniaxial extensions. To test whether this was caused by an influence in the PNC properties due to the inclusion of gold nanoparticles that were not uniformly dispersed throughout the matrix or platinum coating on the surface, 3 sequential modulus measurements were performed. First the neat PMA was tested, then gold NPs were added, and after following the diffusion process the sample was re-tested. Finally, the sample was platinum sputtered and re-tested. These results yielded no conclusive evidence that either the NPs or coating influences the mechanical properties of the PNC, as indicated by the shifted factors for the untreated and treated polymer dynamics curves shown in fig. 2.7.

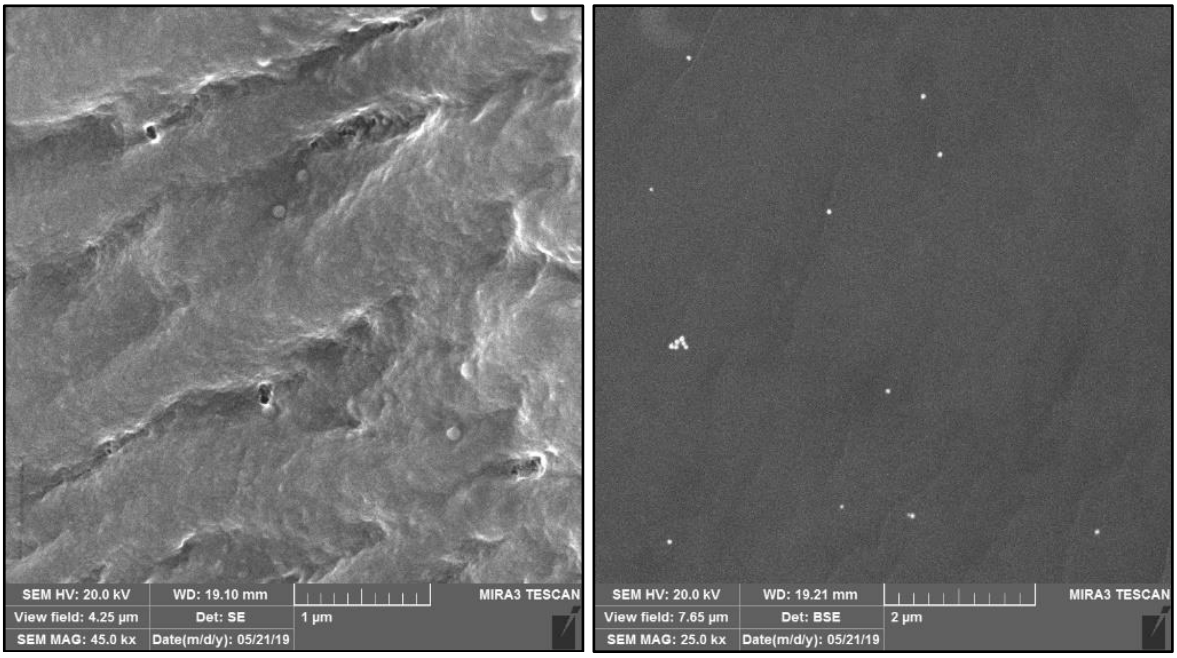

Figure 2.6: SEM images of 12.8v% PMA. SEM images of 12.8v% PMA in a) SE mode without Au NPs on surface. Note the difficulty in discerning patterns of SiO_2 NPs. b) BSE mode with Au NPs on surface. Note the drastically improved contrast of the NPs and increased 'View field.'

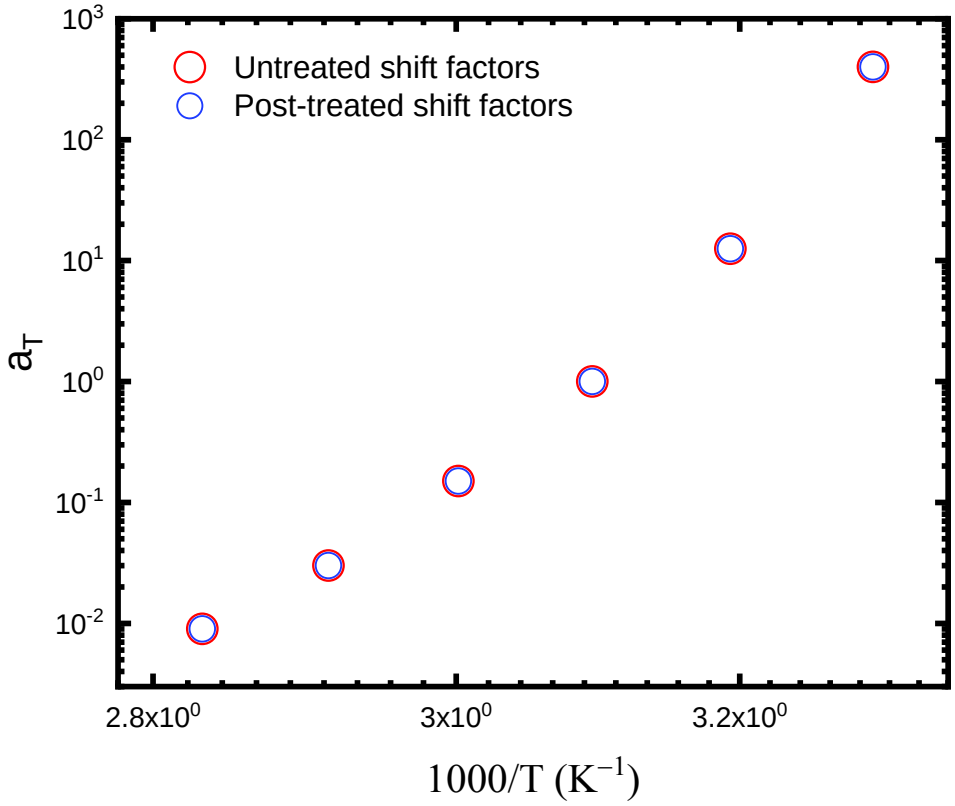

Figure 2.7: Determination of mechanical improvement from sample preparation. Shift factors of 6.7 v% PMA before and after addition of gold nanoparticles and platinum sputtering match, indicating no significant mechanical improvement to the PNC from the sample preparations for SEM imaging.

At this point, it was questioned whether a polymer in the glassy state would show uniaxial deformation better, and the switch was made from PMA to PVAc, which still suffered from non-uniform macroscopic deformation. To ensure macroscopic uniaxial extension, *ex-situ* testing on multiple different polymer systems were performed and imaging was performed on a Zeiss Auriga Focused Ion Beam (FIB) Scanning Electron Microscope (FIB-SEM). With the ability to further minimize the working distance, increased magnification was easier to achieve and with the use of larger NPs, R_{NP} = 40 nm, the E_0 could be reduced to 5 keV to resolve the SiO_2 NPs directly without the need for the gold NPs deposited on the surface. While a 1:1 tracking of the NPs at the same location before and after uniaxial stretching proved difficult due to the beam possibly cross-linking the polymer matrix at the locations in question, the ability to image localized NPs within a single layer of the PNC near the surface and quantify their spacing in direct space was still a valuable achievement. Additionally, further experimentation with varied E_0, magnification, and dwell time were successful in limiting, or negating altogether, the cross-linking effect in the PVAc PNC showing that, if careful consideration for the imaging conditions is performed, *in-situ* testing might still be viable – especially as technologies improve.

2.2.2 Determining Nanoparticle Spacing Within a Specific Polymer Nanocomposite

The immediate consequence of the PNC possibly cross-linking under the electron beam was that exact NP matching across deformation was unsolved. This caused a shift in the process to determine how to analyze NP spacing without 1:1 matching, where the same individual NPs would have been measured relative to their surroundings both before and after deformation. While large SiO_2 NPs, R_{NP} = 40 nm, were easily resolved within the PNC bulk on the Auriga, a concern remained as to how many layers of the NPs were viewed in a single image – or rather, what the maximum escape depth for electron signal detection was for this exact system. If the NPs could be

shown to approximately lie in the same x-y plane, then 2-D analysis of generalized NP spacing could be matched against the affine expectations of the macroscopic deformation flow field as detailed in section 1.4.2 with negligible z-direction motion due to sample dimensions probed. Without 1:1 matching, it is important that a generalized spacing analysis for a randomly located field on nanoparticles should also be comparable to SAXS results, which already produce such values, with the added benefit of a direct-space observation of localized flow fields available.

As previously discussed, the simplest way to estimate the depth of the detected signal is to provide an estimate for the EIV. For this example, a Zeiss Auriga FIB-SEM was used to image a 7v% PVAc/SiO_2 sample with a thin platinum coating on the surface estimated to be ~1 nm thick. For the Zeiss Auriga FIB-SEM in question, because SEMs will vary based on column set-up and type of electron emitter, it was determined that the incident beam accelerating voltage for best results was 5 keV. This was determined by taking a series of micrographs of a high volume fraction PVAc sample viewing the same sample area while varying the accelerating voltage until the surface polymer began to leave focus while retaining the focus on the nanoparticles just below the surface. The higher volume fraction was used in part to mitigate possible polymer imaging issues in this exercise and the comparison images are provided in fig. 2.10. The difference between the 4 quadrants illustrates the changes in both surface information and NP resolution that are the direct result of voltage selection. Initially, at the relatively lower E_0 in the top left the polymer topography is vividly captured. This topographical detail becomes less prominent with increased energy, although the initial trade-off is increased NP visibility within a complete sub-layer of the PNC sample. Eventually, at higher E_0 the beam is passing further into the sample – even passing through the first NPs – and the entire image of the PNC loses resolution. Therefore, the proper E_0 must be carefully considered for each PNC system and SEM to optimize the results for analytical purposes.

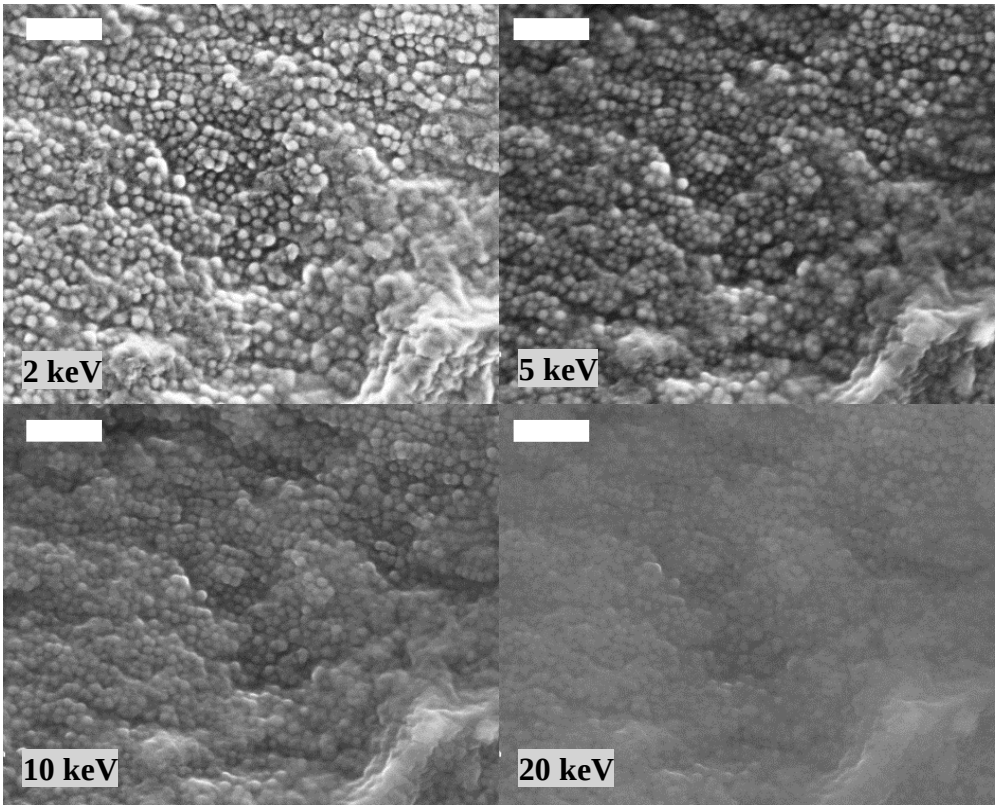

Figure 2.8: Comparison of E_0 for PNC sample. Comparison of different accelerating voltages at same location of a 36.7 v% PVAc/SiO_2 sample. Scale bars are 500 nm.

To estimate the electron maximum escape depth, equations 9.1 and 10 will be required. For PVAc, the 86.09 g/mol repeat unit becomes 7.17 g/mol averaged across the 12 atoms of the repeat unit ($C_4H_6O_2$). The density of the polymer is 1.19 g/cm^3 and the Z_{eff}, based on the most applicable literature results,[86] is being taken as 3.75. Using E_0 = 5 keV, equation 10 for a neat PVAc sample becomes:

$$R_{K-O,\ PVAc} = 27.6\left(\frac{7.17}{3.75^{0.89} * 1.19}\right)5^{1.67} = 754\ nm$$

To consider the interactions between the beam and both the platinum coating and silica NPs respectively, the equation 9.1 energy loss approximations are:

$$-\frac{dE}{ds}_{Pt} = 7.85\left(\frac{195 * 21.45}{78 * 5}\right) * \ln\left(1.166\frac{5}{(9.76 * 78 + 58.5 * 78^{-0.19}) * 10^{-3}}\right)$$

$$= 168.7\left(\frac{eV}{nm}\right)$$

$$-\frac{dE}{ds}_{SiO_2} = 7.85\left(\frac{20.02\bar{6} * 2.196}{14 * (5 - 0.1687)}\right) * \ln\left(1.166\frac{(5 - 0.1687)}{(9.76 * 14 + 58.5 * 14^{-0.19}) * 10^{-3}}\right)$$

$$= 17.8\left(\frac{eV}{nm}\right)$$

Accounting for the radius of the NPs, R_{NP} = 40 nm, as an average interaction depth yields 17.8*40 = 712 eV, a recalculated estimate for the PVAc composite sample would be:

$$R_{K-O,\ PNC} = 27.6\left(\frac{7.17}{3.75^{0.89} * 1.19}\right)(5 - 0.168 - 0.712)^{1.67} = 545\ nm$$

Recalling that the EIV is roughly three times the maximum escape depth yields an estimation of ~182 nm for the escape depth of a primary electron interacting with a nanoparticle and coming back out of the sample. If no NP is present the information retrieved could be from deeper penetration, but this is of little consequence for determining whether or not imaged NPs lie in a similar 2-D plane. This calculation neglects the fact that to escape the PNC the electron must once again pass through the platinum surface layer, which would yield a maximum escape depth of ~170 nm. Even this result is likely an overestimation due to ignoring the continuous energy loss model of the electrons travelling through the polymer. If treated as a linear loss function, a simplification to ease the complexity of the estimation process, the range equation results for platinum and silica NPs can be applied to determine the amount of energy lost per nm directly and result in a maximum escape depth estimation of ~114 nm for the composite. Acknowledging that this only accounts for the first NP encountered and likely underestimates the actual value due to not increasing the energy loss as penetration distance increases, the final estimated maximum escape depth of the electron is taken as the average of the two results, which yields ~142 nm. While a more precise model or more stringent calculations could be produced, since the final value is still merely an estimation, further efforts were deemed unnecessary. Since this value is already less

than 4*R_{NP}, or the length of two NPs stacked directly on one another with the first edge placed at the surface of the PNC, and only accounts for the energy loss of the interaction with the first NP, it is reasonable to assume that the NPs visible in the SEM images for this sample under these beam conditions lie within similar depths and can be treated as existing within the same 2-D plane. This assumption is boosted by the use of the SE detection as well, due to the contrast bias of information due to increased signal detection within the first <50 nm under the surface.

Now that it is reasonable to treat the NPs as a single plane, the spacing must be determined in a robust way. There are many different tools available, but a combination of ImageJ[87] and MATLAB®[88] proved one sufficient method. ImageJ software was used to import the initial image and set the scale into nanometers using the image's known pixel/nm ratio from the SEM image file. While brightness and contrast settings can be manipulated, it was often unnecessary, and the image was next converted into a binary image with black spots representing the NPs on a white field. Because the scale was set into nanometers, when the ImageJ "Analyze Particles…" option was used the NP coordinates were returned in real space relative to one another. Additionally, a downloaded macro was used to perform initial radial distribution analysis as a check for sufficient sample size of the NPs observed.[89] These coordinates were then used in MATLAB® in conjunction with the Delaunay triangulation (DT) algorithm to determine NP spacing relative to one another. The DT algorithm discretely analyzes positional information of points relative to their nearest neighbors, constructing a series of non-intersecting triangle edges by maximizing the minimum angles.[90] These edges each represent the d_{cc} of the NPs nearest to one another relative to the entire field and a field of randomly located NPs will always generate the same solution from the algorithm, which is why such analysis is used for fingerprint identification.[91] DT has also been widely used alongside DIC to study mechanical and deformation flow fields,[92, 93] proving its

robustness for this purpose. The sample alignment in the SEM is also known, so the d_{cc} can be broken into the components for $d_{\parallel}$ and $d_{\perp}$ in a way that allows direct comparison against the affine deformation expectations. The distribution of edge lengths also provides a statistical spread of the NP spacing, similar to the data revealed in SAXS measurements. Furthermore, the unaltered images can be imported directly into MATLAB® for 2-D fast Fourier transformation (FFT) analysis that is directly analogous to the SAXS experimental output and other MATLAB® codes were written to provide further analyses of the NP spacing based on the SEM images and NP coordinates.

2.2.3 Building on What is Known

Alternatively, had this assumption proven unreasonable, a shift in E_0 would have produced a new set of calculations as the dependence of estimated EIVs and associated maximum escape depths on E_0 for this PVAc/SiO_2 PNC follow the previously shown and utilized equations. Combining this with the observations in fig. 2.10, the proper conditions for this PNC system could be determined. More importantly, following this combination of varying the accelerating voltage to image the desired PNC system and following this relatively simplistic estimation procedure, these results provide the guidelines for expansion to any other PNC system. At E_0 = 5 keV, these conditions fall under one of the strategies for high-resolution imaging, where the reduced 'footprint' of BSEs works to the advantage of the imaging process. If the SiO_2 NPs were replaced by Au or TiO_2 NPs for example, which have a significant density increase, the BSE would immediately act to significantly increase contrast between the NPs and the polymer matrix. In turn, E_0 could then be lowered further to both improve the resolution; mitigate polymer imaging issues; and allow the reduction in the variance of the NP depth detected, further strengthening the assumption of a single 2-D layer analyzed. While the exact values of E_0 and the maximum escape

depth would still be dependent on the sample and SEM, this ability to improve the resolution and simultaneously tune the quality of the analytical assumption is extremely valuable. With the right polymer matrix, a relatively low E_0 ($\leq$ 5 keV), the enhanced contrast afforded by heavy NPs, and a stage that places the PNC at the highest point to allow optimized working distance, and therefore magnification, *in-situ* experimentation should be achievable to directly observe the rearrangement of the NPs under tensile deformation in real time.

CHAPTER 3: QUANTIFYING THE PHASE BEHAVIOR OF POLYMER NANOCOMPOSITES UNDER UNIAXIAL EXTENSION

3.1 Introduction

Polymer nanocomposites are important building blocks for structural materials for various modern applications with a wide array of tunable mechanical, optical, thermal, electrical, and barrier properties.[6-11, 21, 94] These advanced macroscopic properties of PNCs correlate strongly with the dispersion state of the NP phase that is one key parameter to control in polymer processing.[22, 23] Among many processing methods, PNC processing involving external deformation is most widely adopted both in traditional polymer industry as well as the emerging field of advanced manufacturing.[13, 24, 94-96] Therefore, understanding the correlation between external deformation and the microstructural rearrangement of PNCs is crucial for catalyzing future manufacturing practices of PNCs.

External deformation processes have been widely applied to control the microstructures of the NPs.[95, 96] Both shear and extension can strongly regulate the dispersion state of the NPs, leading to unconventional dispersion states in PNCs. Decades of intense industrial practices have demonstrated a crucial role of external deformation to control the properties of tire rubber that tie closely to the dispersion state of filler particles.[1, 95, 97, 98] Despite the wide acknowledgement of the important role of external deformation, an explicit understanding of the relationship between the external deformation and the microstructural rearrangement in polymer medium remains to be explored. Early studies of small-angle scattering showing interesting scattering patterns from the NP phase in deformed PNCs, such as “double wings” or “butterfly” patterns, highlighting a complex correlation between external deformation and the spatial rearrangement of the NPs in PNCs.[38, 67] Reverse Monte-Carlo simulation has been proposed to analyze the details of the

microstructural rearrangement of the NPs under deformation.[99, 100] Quantifying the 3D nanoscale NP motion from the 2D macroscopic scattering measurements present a grand scientific challenge, however. In addition to small-angle scattering, advanced microscopy, such as scanning probe microscopy and electron microscopy, has been actively employed to characterize the dispersion state or morphology of PNCs.[79, 101] These measurements provide real-space characterization of the NP phases and should serve as an ideal platform to study the structure of PNCs. However, their applications so far are limited to offer structural information to implement small-angle scattering measurements for the dispersion state of PNCs due to a few technical challenges with regards to sample preparation and data interpretation. It is rare to see their applications used for quantifying the microstructural rearrangement of PNCs during deformation.

The lack of a clear characterization of the microstructural rearrangement of PNCs during deformation has generated confusion regarding its influence on mechanical properties when strong mechanical enhancement has been observed. For instance, Tobin and Mullins argued the high mechanical enhancement of PNCs at large deformation is primarily due to an enhancement in matrix polymer deformation, i.e. the so-called molecular overstraining.[35] Although some earlier SANS measurements and nuclear magnetic resonance measurements claimed signs of molecular overstraining,[39] more recent SANS experiments showed an absence of molecular overstaining in deformed PNCs.[37, 38] Alternatively, these studies argue either the deformation of an NP-NP network or the hydrodynamic effect of the NPs are the leading contribution to the mechanical reinforcement of PNCs. On the other hand, a careful examination of the molecular overstraining proportion revealed a strong underlying assumption that the center-of-mass of individual NPs (or NP clusters) should follow the macroscopic deformation field, i.e. the affine deformation assumption.[35] From this perspective, a clear quantification of the microstructural rearrangement of

the NP phases in deformed PNCs can help clarify the molecular mechanism of the high mechanical strength of PNCs at large deformation.

To quantify the relationship between external deformation and the spatial rearrangement of the NPs, a model PNC with well-separated NPs is investigated through a combination of the SEM and rheology. This has allowed an investigation of the influence of the NP distribution on mechanical properties of the PNC during deformation. It was found that the microstructural rearrangement of the NPs in the large NP Péclet number limit, $Pe >> 1$, depends strongly on both the deformation and the dimensionless deformation rate, Weissenberg number, $Wi = \dot{H}\tau_d$, of the matrix polymer in uniaxial extension. Specifically, at $Wi >> 1$, the characteristic spatial rearrangement of the NPs follows excellently with the macroscopic deformation field up to $\lambda \approx 4.0$, both along with and perpendicular to the stretching direction. On the other hand, the spatial rearrangement of the NPs at $Wi << 1$ deviates from the external deformation field almost at the beginning of deformation, $\lambda \approx 1.5$. Detailed analyses reveal the deviation primarily from the breakdown of the affine deformation of the NPs along the stretching direction, whereas the motion of the NPs follow the affine deformation up to $\lambda \approx 4.0$ perpendicular to the stretching direction. These observations highlight the intriguing effect of the polymer viscoelasticity to the microstructural rearrangement of the NPs. Moreover, NP nanoscale movement falls significantly short at $\lambda > 4.0$ in comparison with the macroscopic external deformation at both $Wi << 1$ and $Wi >> 1$, exhibiting an interesting deformation-induced NP clustering in PNCs. Linear viscoelastic measurements show negligible mechanical reinforcement of the PNC; however, nonlinear stress-strain measurements at $Wi < 1$ show obvious mechanical reinforcement of PNC at intermediate strains that reduces to the classical hydrodynamic limit at large strains. On the other hand, strong mechanical reinforcement is observed for the PNC at all strains $Wi > 1$. Given the clear sign of a

lack of the NP network in deformed PNCs, these results suggest the hydrodynamic effect of the NPs as a major driving force for the microstructural rearrangement as well as the high mechanical strength of the deformed PNCs, whose magnitude depends strongly on the transient polymer viscoelasticity during deformation.

3.2 Materials and Methods

3.2.1 Materials

PVAc was used as the polymer matrix for this study, with SiO_2 nanoparticles with a radius of R_{NP} = 40 ± 5 nm (Nissan Chemical, MEK-AC-5140Z). The PVAc (Spectrum Chemical MFT Corp.) has a M_w of 100 kg/mol and a polydispersity of 1.76. The PVAc/SiO_2 nanocomposite was prepared through solution casting following a previously published protocol.[102] Specifically, a dilute solution of PVAc/methyl ethyl ketone (MEK) with a concentration of 0.05 g/mL was first prepared and filtered through a poly(tetrafluoroethylene) (PTFE) filter with $20\ \mu m$ pore sizes. After that, the desired amount of SiO_2 nanoparticles (suspended in MEK) were added into the PVAc/MEK solution in a dropwise manner under magnetic stirring. A continuous stirring of 2 hours was applied after the completion of the addition of the NPs before transferring the PVAc/SiO_2/MEK mixture to a PTFE petri-dish for drying 24 hours in a fume hood, where transparent, thin polymer films with 0.1 mm in thickness were formed. A subsequent drying at 40º C for 24 hours and at 60º C for 48 hours in a vacuum oven was performed before measurements. The mass fraction of nanoparticles was determined through thermogravimetric analysis (TGA Q50, TA instrument) in air from 293 K to 1073 K at a heating rate of 20 K/min, which was converted to the volume loading of nanoparticles as φ_{NP} = 7.4v%.

3.2.2 Small-Angle X-ray Scattering

SAXS was employed to characterize the dispersion state of the NPs in the PNC. The SAXS measurements were performed at the 12-ID-B beamline at the Advanced Photon Source at Argonne National Lab. The wavelength of the x-ray was $\lambda_w = 0.9347$ Å. The sample to distance was $2.011\ m$ and a two-dimensional (2-D) Pilatus 2M detector was used in the measurement. The sample thickness was $h = 0.2\ mm$. The 2-D isotropic scattering images were converted to 1-D SAXS intensity curves, $I(q)$ vs q, through the azimuthally average after solid angle correction and then normalized with the intensity of the transmitted x-ray beam flux using the beamline software, where $q = 0.003 - 0.9\ \text{Å}^{-1}$ was the scattering wavevector.

3.2.3 Scanning Electron Microscopy

SEM images of the PNCs were taken on a Zeiss Auriga FIB-SEM. Secondary electron scattering detection mode was used at an accelerating voltage of 5 keV to observe the spatial distribution of the NPs near the surface of PNCs films before and after elongation ratios of $\lambda \approx 1.5$, 2.5, 4.0, 5.0, 7.0, and 9.0. The stretching was performed on a Rheometric Scientific RSA III rheometer using a uniaxial extension fixture with Hencky strain rates of $\dot{H}$ = 0.025 s^{-1} and $\dot{H}$ = 0.097 s^{-1} at T = 353 K and T = 333 K, respectively. These values correspond to $Wi = \dot{H}\tau_d = 0.06$ and 20, respectively, where τ_d is the measured terminal relaxation time of the PNC. The samples were coated with an ultrathin layer (~ 1 nm) of platinum using a Denton Vacuum Desk II XLS sputtering device before imaging to reduce charging. Using the Kanaya-Okayama range equation in conjunction with the Bethe continuous energy loss approximation,[78, 79] the maximum escape depth of this PNC sample coated with an ultrathin platinum layer imaged at E_0 = 5 keV was estimated to be ~142 nm. Additionally, the use of the SE detection mode worked to contrast bias

the resolved images to NPs just under the surface (<< 50 nm) due to the high concentration of weak signals received via inelastically scattered electrons (< 50 eV). These factors allowed for the reasonable assumption that all analyzed NPs were within a single layer near the surface and analysis could treat the images as 2D planes with respect to NP arrangement.

3.2.4 Rheology

The linear and nonlinear rheological measurements were performed on an Anton Paar MCR302 Rheometer with a CTD 600 environmental oven. The accuracy of the oven is ±0.1 K. SAOS measurements were performed on a pair of parallel plates with a diameter of 4 mm at temperatures from 318 K to 393 K. The strain amplitude was varied from 0.01% near the glass transition temperature ($T_g = 313\ K$) and gradually increasing to 1.7% at the highest temperature ($T = 393\ K$). The frequency range of all SAOS measurements was 0.1 – 100 rad/s. The linear viscoelastic master curves were constructed for both the neat PVAc and the PVAc/SiO_2 nanocomposite through the time-temperature superposition principle. The terminal relaxation time, τ_d, of the neat PVAc was determined from the low frequency crossover between the storage modulus, G'(ω), and loss modulus, G"(ω). The stress-strain curves of neat PVAc and PVAc/SiO_2 nanocomposites at large deformation were collected using a third generation Sentmanat Extensional Rheometer fixture (SER-3) mounted on the MCR302 rheometer, with rates chosen at either 333 K or 353 K to correspond with Wi = 0.01, 0.06, 0.1, 0.6, 20, and 100.

3.3 Preliminary Nanoparticle Spacing Measurements

3.3.1 The Dispersion State of Polymer Nanocomposites from SAXS

SAXS and SEM were utilized to characterize the dispersion state of a PVAc/SiO_2 nanocomposite. Fig 3.1 shows the scattering intensity, I(q), of isotropic PVAc/SiO_2-7v% over a range of q = 0.003 – 0.04 $Å^{-1}$ that covers a length scale up to 200 nm. To identify the NP-NP center of mass correlation, Kratky representation[103] was adopted as $q^2I(q)$ vs q (bottom inset fig. 3.1), where a weak peak shows up at q ~ 0.004 $Å^{-1}$ that corresponds with an average center-to-center distance of the NPs d_{cc} ~ 157 nm. Given the average NP size of R_{NP} = 40 nm, the average interparticle distance is therefore $d_{IPS} = d_{cc} - 2R_{NP}$ = 77 nm, which is much larger than the radius of gyration of the polymer matrix of R_g = 9.3 nm. Thus, the individual NPs were well-separated with little chance for polymer bridge formation. Additionally, SEM measurements were performed to directly image the dispersion state of the NPs. As shown in the top inset of fig. 3.1, individual NPs are clearly seen and well-separated with no sign of the NP network formation. Interestingly, detailed analysis of the SEM images (in a following section) demonstrated d_{cc} ~ 180 nm, which is comparable to the SAXS measurements. Thus, both SAXS and SEM measurements support the individual dispersed state of the NPs in the polymer matrix.

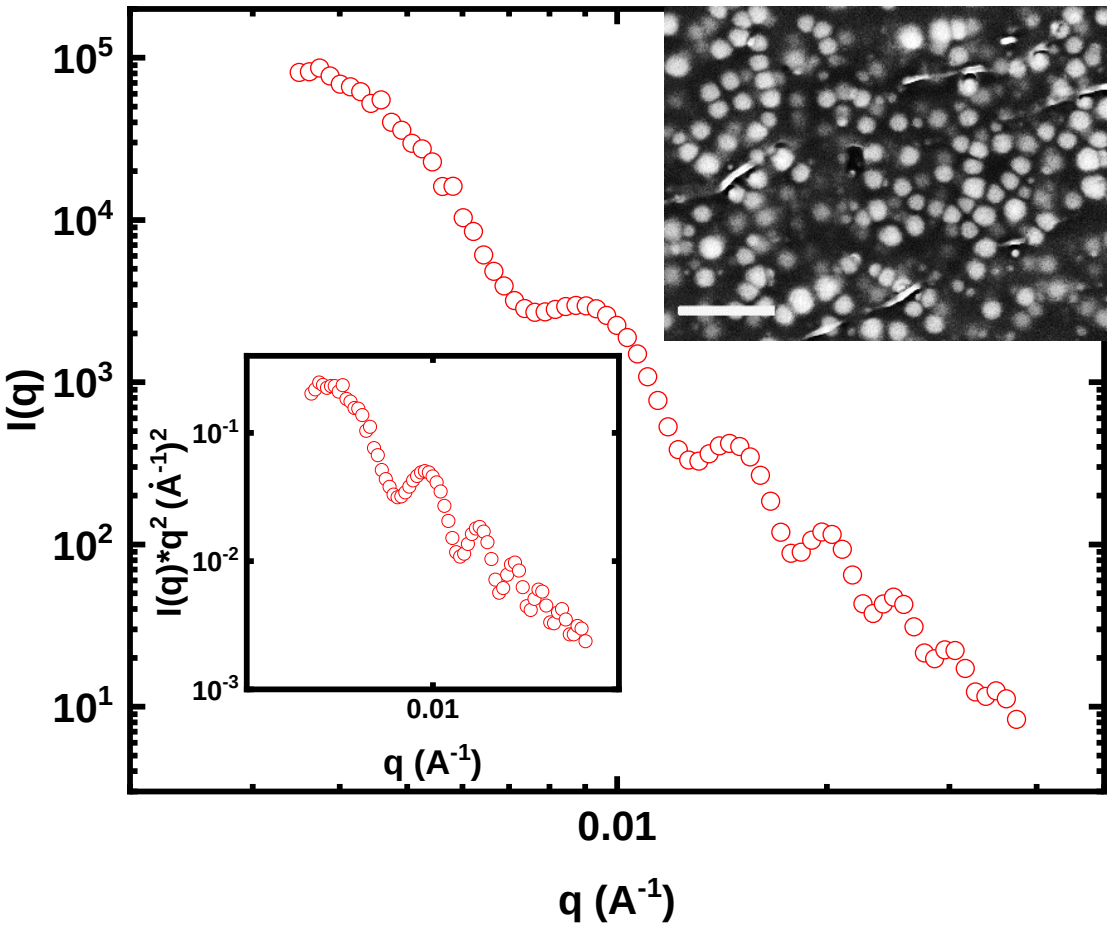

Figure 3.1: I(q) vs q with SEM image and Kratky plot insets. The SEM image has a scale bar of length 500 nm. The Kratky plot and SEM measurements show comparable dispersion states of the NPs well-dispersed in the polymer matrix

3.3.2 Preliminary Rheological Results

Linear rheology has been performed to quantify the viscoelastic properties of the polymer nanocomposites, including the terminal relaxation time of the matrix polymer and the mechanical properties at intermediate time scale. Fig. 3.2 shows the linear viscoelastic master curves of the neat PVAc and the PVAc/SiO_2 composite at T = 353 K. Interestingly, the viscoelastic spectrum of the PNC is almost identical with the neat polymer over the entire frequency range from rubbery plateau regime to the flow regime. The loss factor, tan(δ) = G"/G', of the PNC and the neat polymer

is almost identical over the entire frequency range (inset of fig. 3.2). Clear flow regimes are observed for both the neat PVAc and the PVAc/SiO_2 composite that have a terminal relaxation time of $\tau_d \approx 2.5$ s and zero-shear viscosity of $\eta \approx 10^5$ Pa*s. The identical loss factor between the neat polymer and the nanocomposite along with a clear flow regime indicates the absence of an extensive nanoparticle network in the PNC, which is consistent with the SAXS and SEM measurements. Only very weak mechanical reinforcement at the intermediate frequency region has also been observed for the PNC. These observations are consistent with the hydrodynamic effect of nanoparticles. The negligible influence of the NPs on the polymer dynamics is especially notable since it can help exclude the influence of polymer bridging or other slow modes on the microstructural rearrangement during deformation.

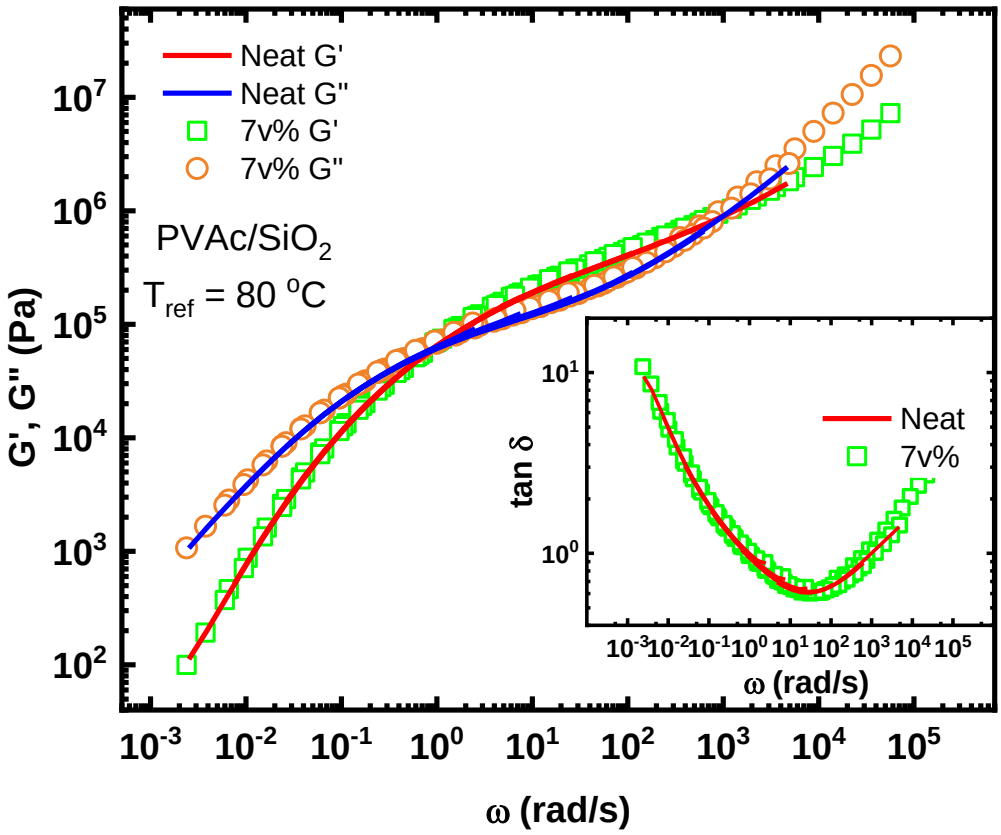

Figure 3.2: Linear rheology results. SAOS master curves for neat PVAc and the PVAc/SiO_2 composite with loss factor inset. The similar terminal flow regimes and loss factors across the angular frequency range indicate a negligible influence of the NPs on the dynamics.

The linear rheology of the PNCs provides crucial information to estimate the characteristic time of the center-of-the-mass diffusion time of the NP, $D_{NP} \approx \frac{6\pi\eta R_{NP}^3}{k_B T} \approx \frac{6\pi G_e R_{NP}^3}{k_B T}\tau_d \approx 5 \times 10^4\, \tau_d$, with $G_e \approx 0.2$ MPa being the plateau modulus of the matrix polymer and T = 353 K is the testing temperature. Thus, the Péclet number of the NP, $Pe = \dot{H} D_{NP} \approx 5*10^4\, Wi$, can be determined. At the slowest deformation rate of $Wi = 0.01$, $Pe >> 1$ is fulfilled, indicating a negligible influence of Brownian motion to the microstructural rearrangement of the NPs within the PNC during deformation and the spatial rearrangement of the NPs are completely enslaved by the deformation field of its surrounding polymer matrix.

Fig. 3.3 presents σ_{eng} versus λ of neat PVAc (red symbols) and the PNC (blue symbols) at Wi = 0.6, 20, and 100. The inset shows the stress-strain curves at Wi = 0.01, 0.06, and 0.1. Different from the negligible mechanical reinforcement of the PNC in the linear viscoelastic region, here the PNC shows clear high stresses at large deformation that also exhibit interesting strain and strain rate dependence. For instance, for $Wi < 1$, significant mechanical reinforcement is only observed in the elastic deformation ($\lambda < 2$) region, evidenced as a higher stress-overshoot of PNC compared to the neat matrix. However, for $Wi > 1$, strong mechanical reinforcement is present over the entire deformation, up to $\lambda \sim$ 8-9. These observations highlight a strong nonlinearity of the roles of the NPs with regards to the mechanical reinforcement of PNCs at large deformation, which will be discussed further in a later section.

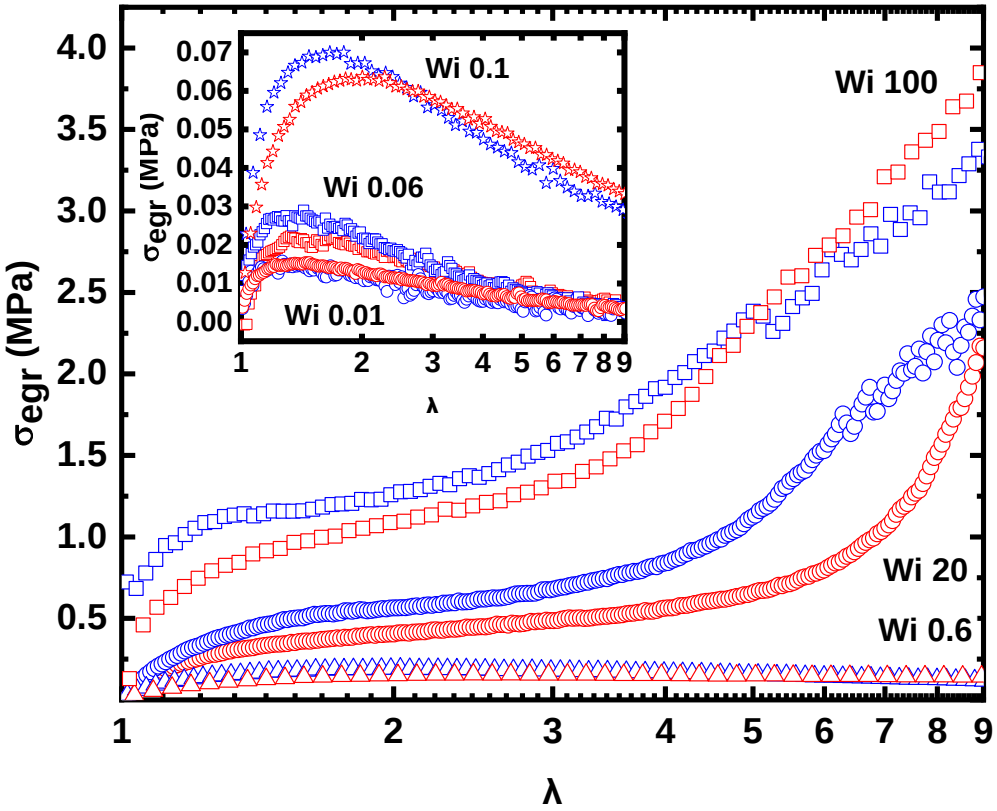

Figure 3.3: Stress-strain curves. Stress-strain curves for neat PVAc (red symbols) and the composite (blue symbols) at deformation rates corresponding with *Wi* = 0.6, 20, and 100. Inset shows the curves for rates *Wi* = 0.01, 0.06, and 0.1.

3.3.3 Spatial Distribution of Nanoparticles Through Scanning Electron Microscopy

An SEM in SE detection mode was utilized to quantify the spatial distribution of the NPs near the surface of the PNC. The best condition for imaging a single layer of well-resolved NPs within the PNC was determined to be under a beam with E_0 = 5 keV. Fig. 3.4 shows a representative SEM image of the PNC with a scale bar of 1000 nm. There is a dramatic contrast in brightness observed between the NPs at the surface layer compared to NPs further inside the polymer bulk and the polymer bulk itself. The individual dots are confirmed to be NPs by increasing the magnification, as shown in the inset of fig. 3.4 where the scale bar is 500 nm for roughly the middle of the larger image. An advantage of utilizing the lower magnification is the

increased field of view, in this case 22.7 by 17.0 μm (length by width). This is especially valuable for quantifying the large-scale microstructural rearrangements that are beyond the capability of conventional small-angle scattering techniques.

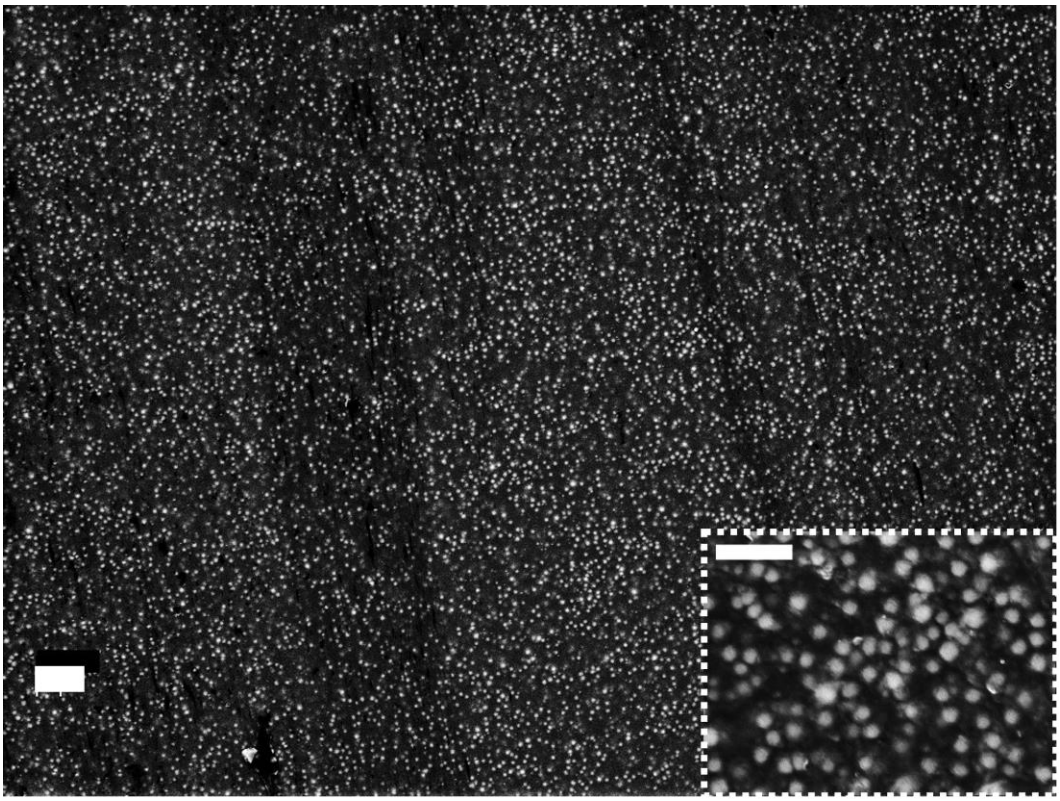

Figure 3.4: Representative SEM image. The image shows a 22.7 by 17.0 μm field of view, with a scale bar of 1000 nm present. The inset, taken at roughly the middle of the image, confirms the individual dots to be nanoparticles and has a scale bar of 500 nm.

To be more quantitative, the surface layer of the NPs is extracted from the SEM images using ImageJ software to filter out the background. Using the variance in brightness between the surface NPs and the background, the image is converted into a binary image where the NPs appear as black dots against the white background of the polymer phase as depicted in fig. 3.5. Note that many of the subsequent structural analyses are based on the binary images where the NP positions are well quantified on an appropriate length scale and the NP positional changes reflect directly the influence of macroscopic deformation.

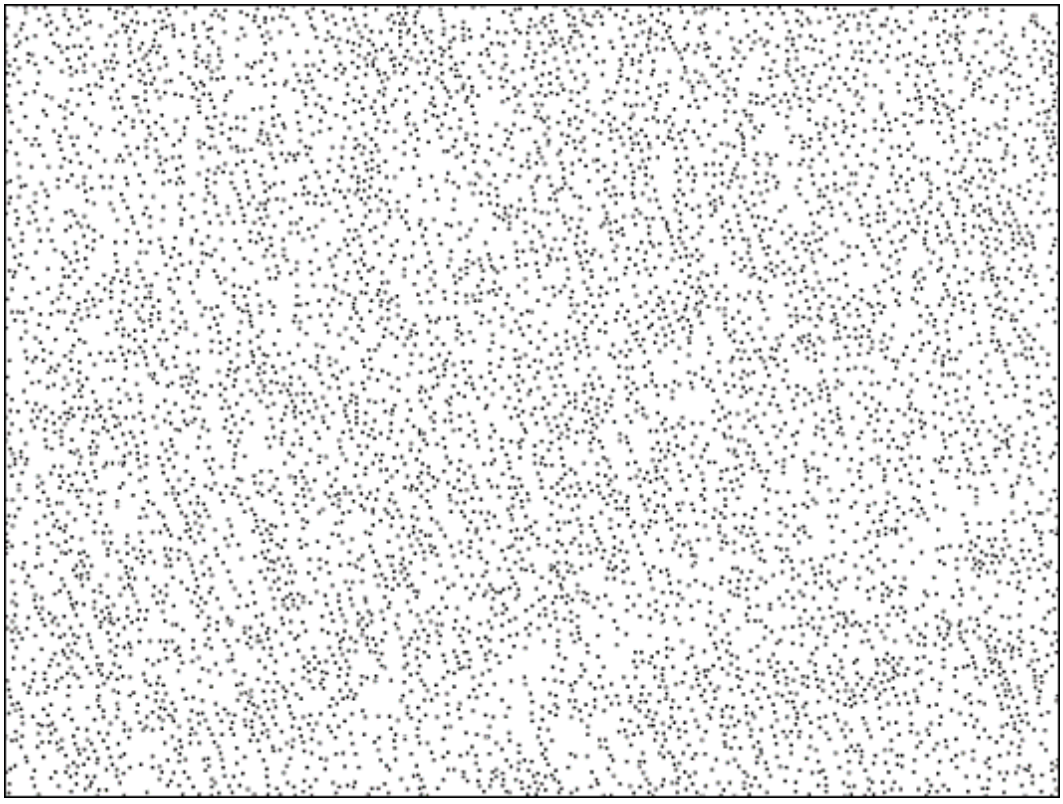

Figure 3.5: Representative binary SEM image. The image shows a 22.7 by 17.0 μm field of view. Each of the black dots represents individual nanoparticles.

Several different methods were used to analyze the structure of the NPs. One was the 2D-FFT of the raw SEM image, which is analogous to a scattering experiment. This method provides the average correlation of the NPs. Fig. 3.6 presents the 2D-FFT of the composite in the absence of deformation. Interestingly, even the 2D pattern obtained for the undeformed PNC is anisotropic, which suggests the non-isotropic dispersion of the NPs near the surface of the PNC locally. It is conceivable that large-scale anisotropy in the NP dispersion state might be due to residual structural anisotropy of the NPs during sample preparation. Note that the small residual structural anisotropy of the NPs will not affect the results since the deformation-induced structural anisotropy will be overwhelming and the focus is placed on the relative changes of the microstructures as a result of the deformation.

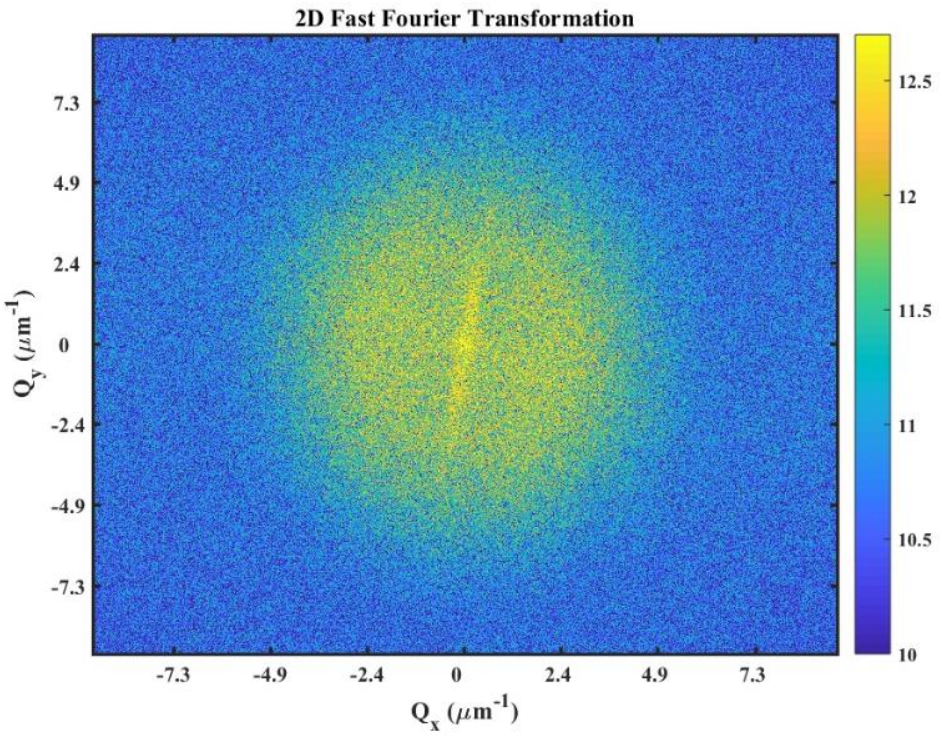

Figure 3.6: Example 2D-FFT. Fast Fourier transformation of the undeformed composite sample.

Additional analyses emphasize the relative positions of the NPs. Since the nearest neighbors are the most important for a quantification of the local spatial rearrangement of the NPs, the Delaunay triangulation algorithm was selected to analyze the relative position of the NPs that reflects the information of nearest neighbors. Specifically, DT analysis creates a discrete set of triangles by maximizing the minimum angles while avoiding any crossed edges to map the field of nanoparticles in a reproduceable manner for randomly located NPs, where each edge of a triangle represents the real center-to-center distance between particles nearest to one another relative to the entire field at proper scaling. Fig. 3.7 shows the results of the DT analysis for fig. 3.5, where blue lines represent real center-to-center distances between neighboring NPs closest to one another relative to the entire field. From this data, the total count of edges among neighboring NPs with d_{cc}, $n(d_{cc})$, as well as the count of their projections to the stretching direction $d_{\parallel}$, $n(d_{\parallel})$ and perpendicular to the stretching direction $d_{\perp}$, $n(d_{\perp})$ can be computed. In this specific case, 7,116

NPs are involved in fig. 3.7, which produces a resultant 21,295 edges from DT mapping. To examine a representative sample using the proposed DT analysis, the results of 5 randomly selected areas imaged across the sample for a given set of conditions (*Wi* and λ) were combined. In the case of the undeformed PNC, this resulted in a total of 31,791 NPs and 95,149 edges across the 5 images. Despite variations in local φ_{NP}, among images from the same sample, there is ample statistical agreement between the analysis of individual images, the averaged analysis, and the measured TGA results. This indicates an appropriate field of view and sample size for analytical purposes.

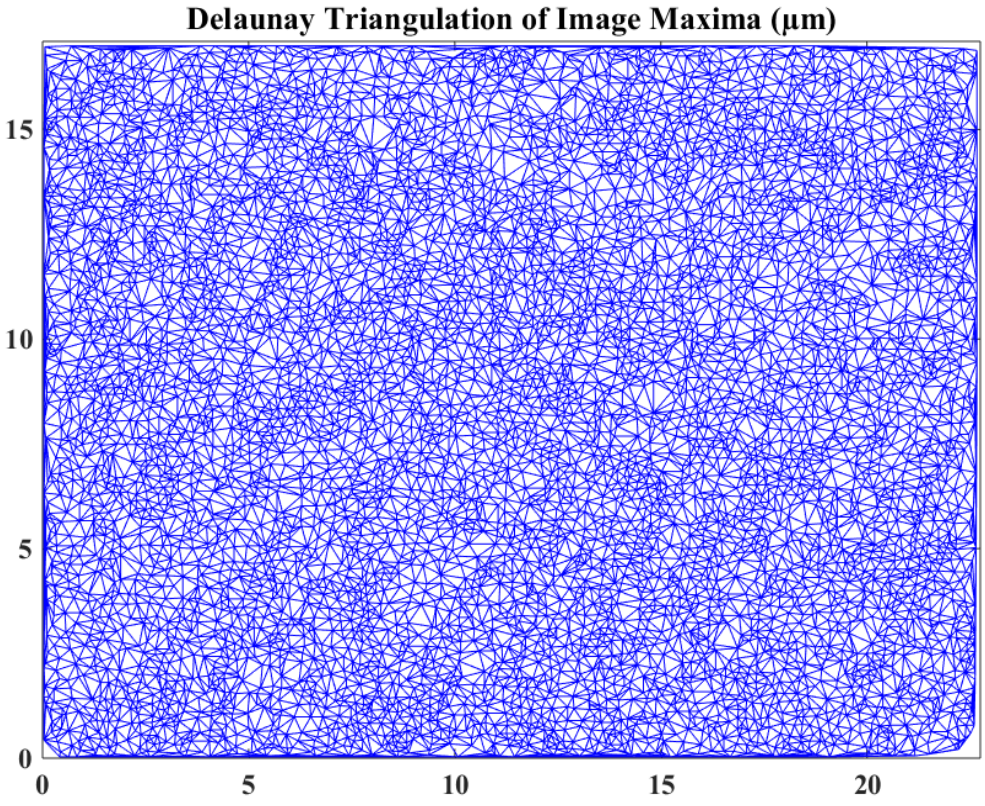

Figure 3.7: Example Delaunay triangulation output. Delaunay triangulation of the binary image in fig. 3.5 where each blue line represents a real center-to-center distance between a pair of nanoparticles. Here, there are 21,295 edges connecting 7,116 nanoparticles present in the image.

Quantitative analysis can therefore be made. For instance, the spatial distribution of the NPs can be characterized through probability densities, $P(d) = \frac{n(d)}{\sum n(d)}$. Fig. 3.8 presents plots of P(d), $P(d_{\parallel})$, and $P(d_{\perp})$ for the PVAc/SiO_2 composite prior to deformation. The total edge length

represents the true d_{cc} between NPs in the field, and the resulting projections into the directions parallel and perpendicular to the direction of stretching are necessary to compare against affine deformation principles. Note that while the total edge length is never less than $2*R_{NP}$, the length of the x- and y- component projections can be zero as that implies the two NPs lie on the same x- or y- coordinate and the corresponding y- or x- direction length between the NP pair must be greater than $2*R_{NP}$, respectively. The distribution of the NPs follows roughly a log-normal distribution $X = e^{\mu+\sigma Z}$, where μ is the expected value and σ is the standard deviation for the distribution of the random variable X with standard normal variable Z. The mean distance between NPs for the undeformed PNC is $\exp(\mu + \frac{\sigma^2}{2}) \approx 180$ nm and polydispersity standard deviation of $\sigma = 0.77$ as shown by the solid line. Interestingly, this mean average distance is very close to the characteristic d_{cc} of the PNC as determined by SAXS measurement and supports the newly proposed SEM analysis on quantifying the nanoscale spatial distribution of the NPs.

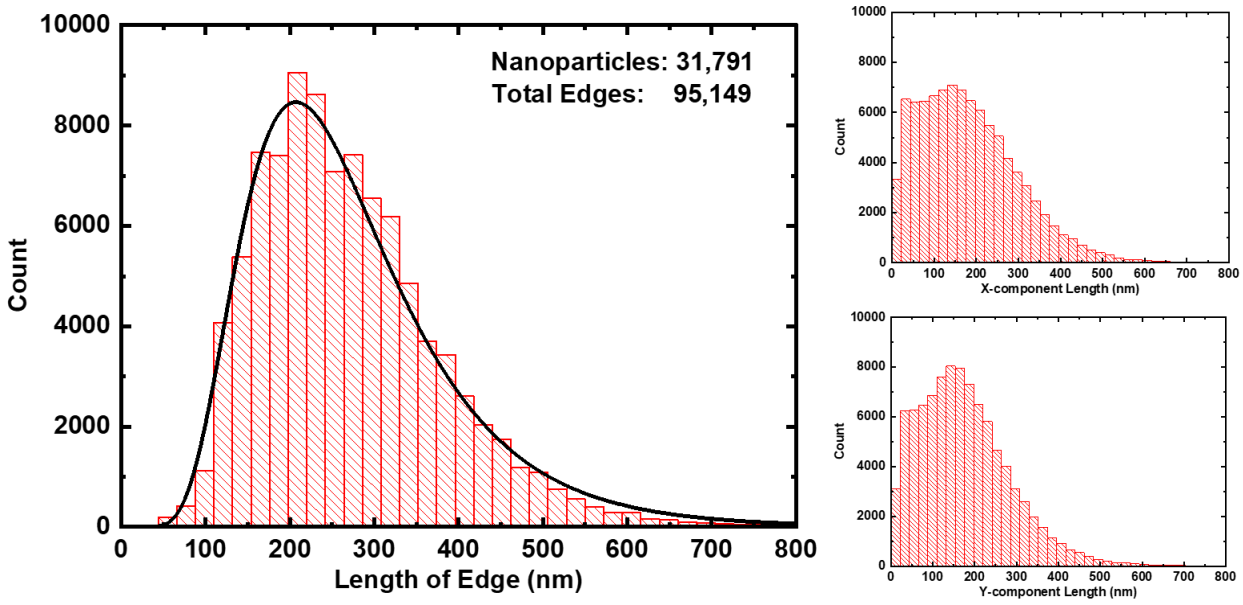

Figure 3.8: Distribution analysis for undeformed PNC. Results from the Delaunay triangulation analysis of the undeformed PNC are presented as histograms comparable probability densities. The total edge length represents the true d_{CC} between nanoparticles, with the vectors able to be projected into the directions parallel and perpendicular to the direction of stretching.

Further analysis of the NP field involved investigating the immediate environment of numerous randomly selected NPs, limited to NPs a specified distance from any edge to incorporate a full view of possible neighbors, to determine the autocorrelation function, radial distribution function, and nearest neighbors in the direct stretching or perpendicular to stretching direction. The autocorrelation function results indicated that beyond 500 nm, the distribution of the NPs was random across all samples; however, other results implied significant trends between the deformation and microstructural rearrangement of the NPs.

3.4 Analytical Results and Discussion

3.4.1 Microstructural Rearrangement of Polymer Nanocomposites at Deformation: The Strain Amplitude Effect

Uniaxial extension is employed to study the influence of deformation on the microstructure rearrangement.[67] In an ideal uniaxial extension, the length of a sample increases as a function of the elongation ratio and the width of the sample decreases proportional to $\lambda^{0.5}$as $W/W_0 = \lambda^{-0.5}$, where W_0 is the initial length and width of the sample and W is the length and width of the sample after an elongation of λ. Fig. 3.9 plots the $\ln(\lambda)$ against $-2\ln(W/W_0)$ identified from digital camera at different $\ln(\lambda)$ with *Wi* = 0.01, 0.6, and 100. A scaling of one is obtained up to $\lambda = 15$, validating the macroscopic uniaxial extension for the deformation rates and the elongation ratios covered in the experiments. Moreover, the uniaxial extension requires the length increases by a factor of λ and the width decreases by a factor of $\lambda^{0.5}$, implying a total increment in the surface area scaling with $\lambda^{0.5}$ because $(L*W)/(L_0*W_0) = \lambda* \lambda^{-0.5} = \lambda^{0.5}$. Assuming the total number of surface nanoparticles, *n*, remains the same during deformation, one should anticipate the number density of nanoparticles at deformation λ as $n(\lambda) \sim \lambda^{-0.5}$. Therefore, when ideal uniaxial extension holds macroscopically, we expect to see a reduction in NP number density per area with increasing λ.

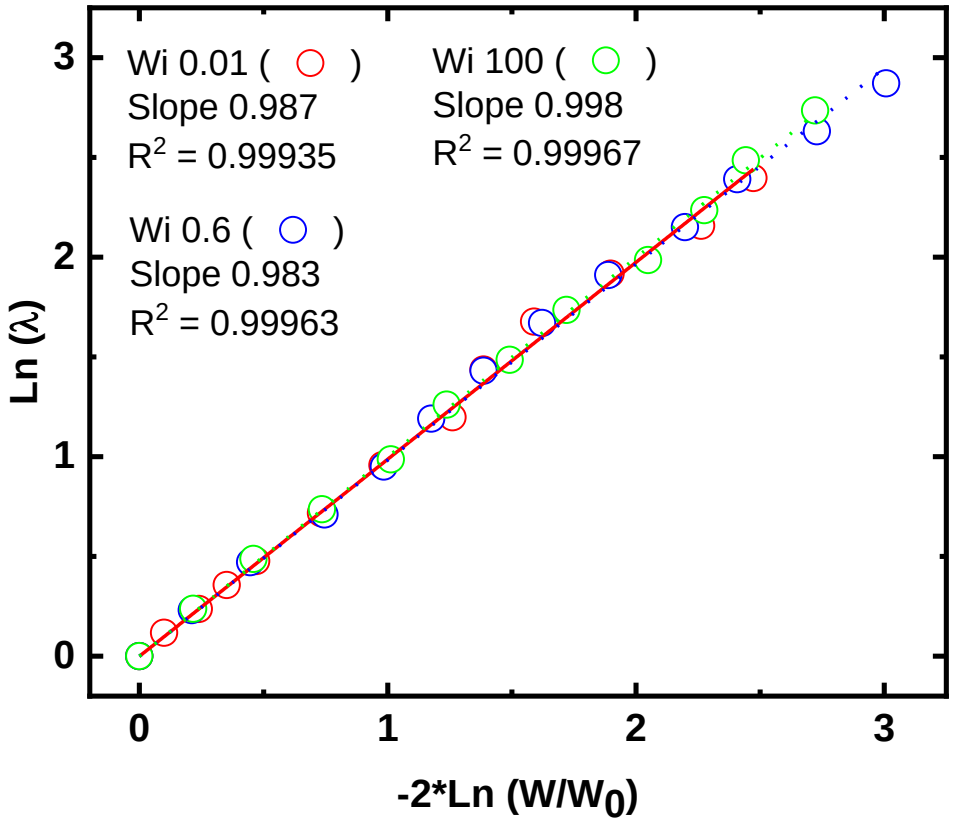

Figure 3.9: Check for uniaxial extension. Ln(λ) vs -2ln(W/W_0) shows uniaxial extensions hold affine properties macroscopically through $\lambda \approx 15$ across the full range of strain rates used.

Figs. 3.10 A), B), and C) show the representative SEM images of PVAc/SiO_2 at $\lambda = 1.5$, 4.0, and 7.0, respectively, for a deformation rate of $Wi = 0.06$. The coordinate system depicts the stretching direction, X, and the perpendicular direction, Y, with arrows above a scale bar of 500 nm. Figs. 3.10 D), E), and F) are the corresponding binary images of the NPs at the top surface layer. Several features are notable: (i) The breakdown of the residual anisotropic NP arrangement is evident immediately during deformation as the binary image for $\lambda = 1.5$ does not have an obvious, consistent pattern to the NPs as was the case for fig. 3.5. (ii) A noticeable reduction in the NP population is observed within the field of view as elongation ratio increases, consistent with the uniaxial extension geometry discussed above. (iii) Clear NP separation along the

stretching direction is observed with stretching, signifying the effect of stretching for the microstructural rearrangement of the PNC.

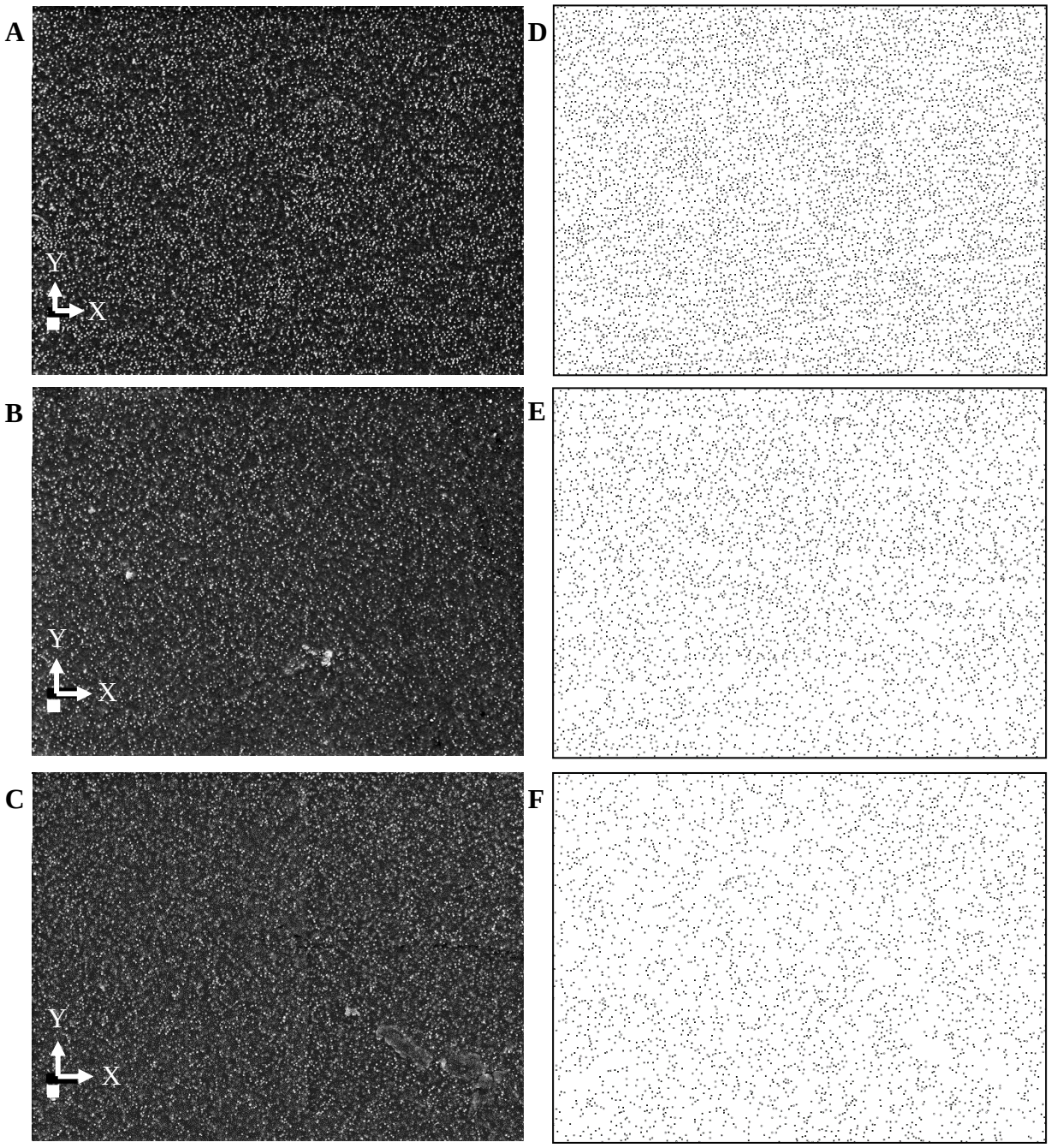

Figure 3.10: *Wi* = 0.06 SEM images with corresponding binary images. Sample SEM images for λ A) 1.5, B) 4.0, and C) 7.0 at deformation rate of *Wi* = 0.06 and their corresponding binary images, D), E), and F), respectively. Scale bars are 500 nm and X is the direction of stretching with perpendicular direction Y.

Two-dimensional FFT is applied to quantify the spatial correlation of the NPs. As shown in figs. 3.11 A), B), and C), clear structural anisotropy from the scattering of the NP phases has built up with deformation. From $\lambda = 1.0$ to $\lambda = 4.0$, the intensity correlation moves to a lower q along the stretching direction and a larger q perpendicular to the stretching direction, indicating the separation and convergence of the NPs along and perpendicular to the stretching direction respectively. These observations are consistent with the observation shown in the binary images. Intriguingly, the outer contour of the anisotropic images remain little changed beyond $\lambda = 4$, suggesting an interesting decoupling between the macroscopic deformation and the nanoscale nanoparticle movement. Recall that the Péclet number of the NPs is much larger than one at the testing deformation rate. It is therefore interesting to see such large decoupling between the macroscopic deformation and the nanoscale nanoparticle movement.

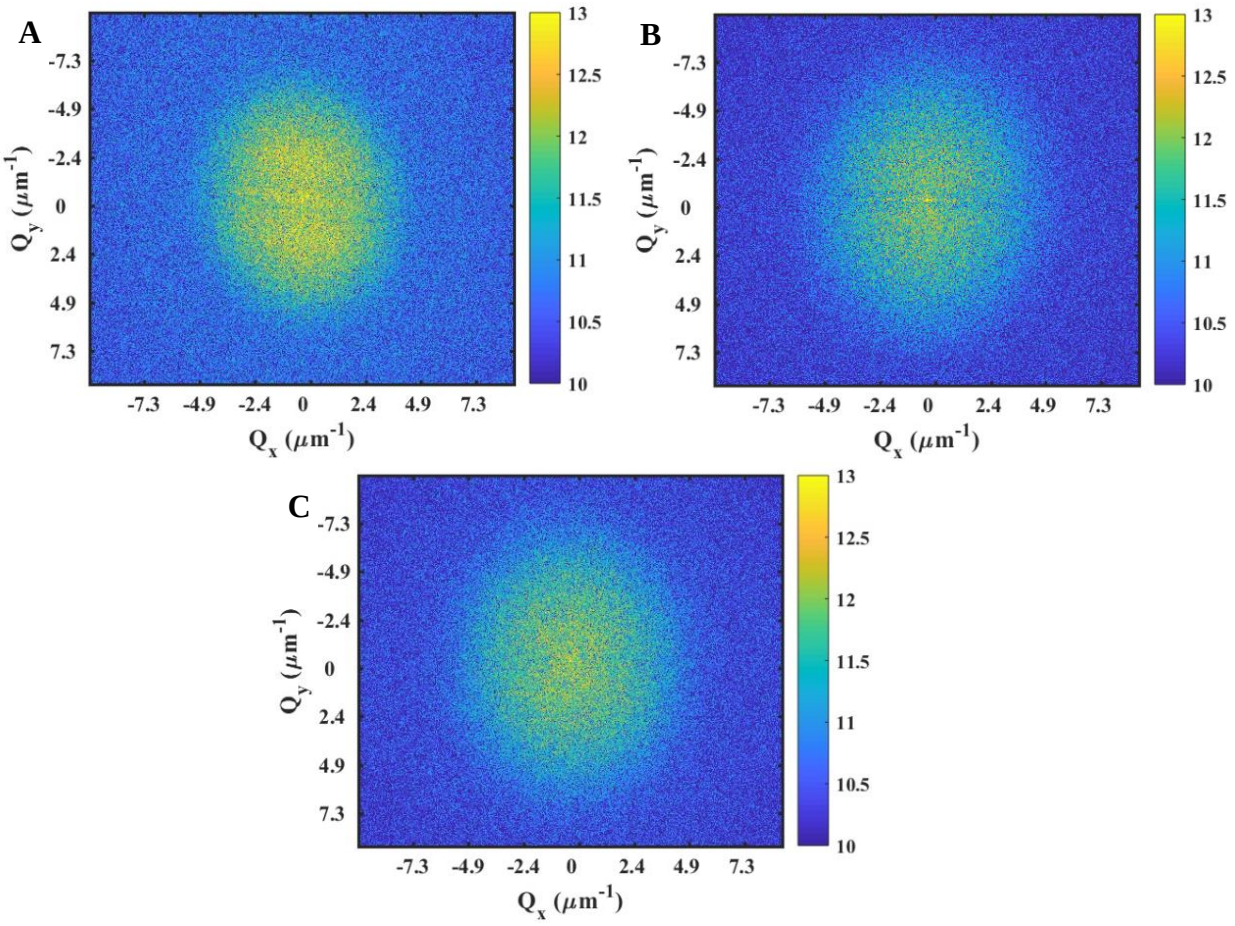

Figure 3.11: *Wi* = 0.06 2D-FFT results. 2D FFT of PNC at A) λ = 1.5, B) λ = 4.0, and C) λ = 7.0 deformed at Wi = 0.06.

To gain better insight on the microstructural rearrangement of the NPs with macroscopic deformation, the distribution of interparticle distances is further analyzed. Figs. 3.12 A), B), and C) present the analysis of P(d), P($d_{\parallel}$), and P($d_{\perp}$), respectively, at λ = 1.0 (reference), 1.5, 4.0, and 7.0. It is emphasized that the analyses are from five different sets of measurements at randomly chosen locations of the stretched samples. The dashed lines are the prediction of the expected positional distribution of the NPs if they follow affine positional change, i.e. each nanoparticle follows strictly the macroscopic deformation field. Note that the affine positional change of the NPs in elastomer is an important assumption of the prevailing viewpoint of the molecular overstraining in PNCs that is responsible for the mechanical reinforcement of PNCs. Several

features are worth pointing out: (i) The deformation leads to a shift in the characteristic peak position of P(d) and $P(d_{\parallel})$ to larger and $P(d_{\perp})$ to lower values, which are consistent with the uniaxial extension, the SEM imaging, and their 2D FFT analysis. (ii) The shapes of P(d), $P(d_{\parallel})$, and $P(d_{\perp})$ are significantly broadened with a pronounced tail at large d_{cc} side and the peak heights reduces indicating a strong separation in the distance between neighboring nanoparticles. (iii) The distribution functions of the NPs show significant changes at $\lambda < 5$, and only limited changes for $\lambda > 5$. This observation agrees with the 2D FFT analysis where the shapes of the 2D FFT remain almost the same beyond a certain elongation ratio. The origin of these phenomena is not clear and might be due to the deformation-induced NP clustering rather than further separation. Indeed, our SEM measurements observed clustering of the NPs at large deformation that is fundamentally against the affine deformation of the NPs in PNCs.

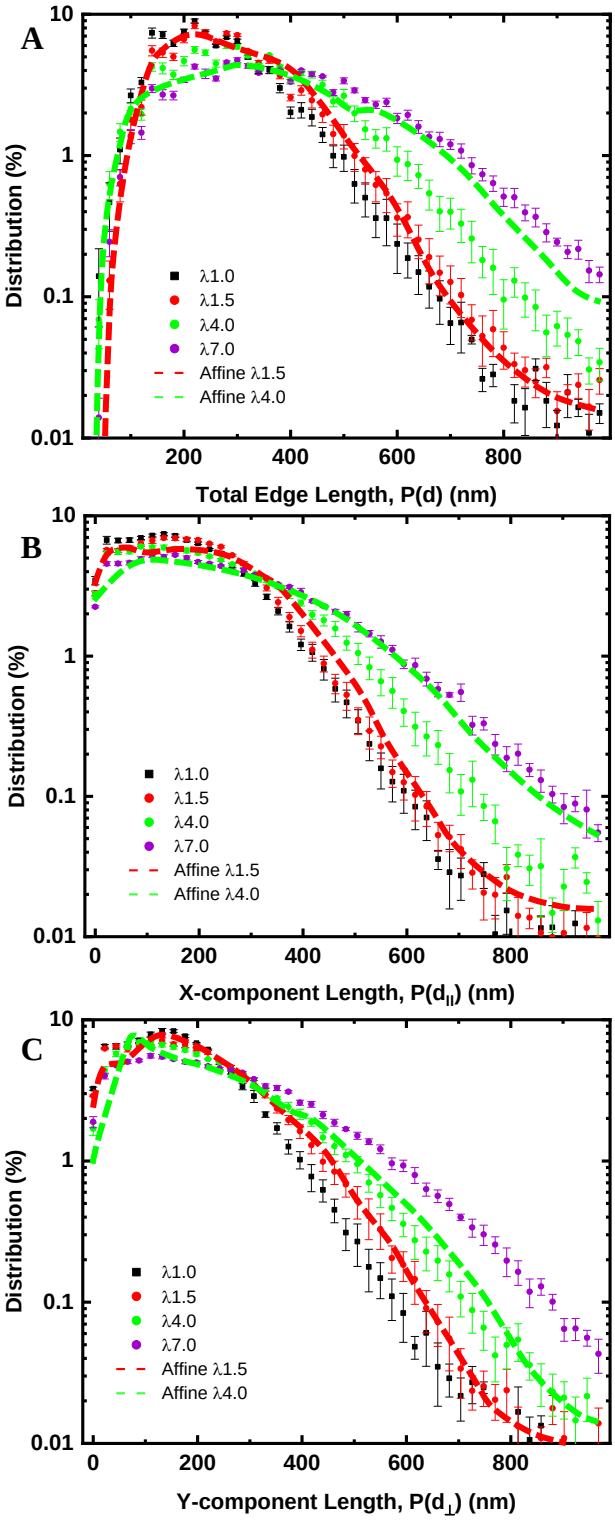

Figure 3.12: Nanoparticle spacing distributions for *Wi* = 0.06. NP spacing distributions for Delaunay triangulation results from 5 images averaged with error bars at elongation ratios λ = 1.0, 1.5, 4.0, and 7.0 for Wi = 0.06 with affine predictions based on λ = 1.0 spacing expanded to λ = 1.5 and λ = 4.0. A) $P(d)$, B) $P(d_{\parallel})$, and C) $P(d_{\perp})$.

Comparing experiments with their affine prediction offers several new insights. An interesting observation is the astonishingly small range of the validation of the affine prediction. As shown in Figs. 3.12 A), B), and C), experiments agree well with the affine prediction only at $\lambda \leq 1.5$ for P(d), $P(d_{\parallel})$, and $P(d_{\perp})$, while clear deviation between experiments and affine prediction is observed for P(d), $P(d_{\parallel})$, and $P(d_{\perp})$ at $\lambda > 4$. Another intriguing observation here is the affine prediction has a much higher values of P(d) and $P(d_{\parallel})$ at the large d and $d_{\parallel}$ limit at $\lambda = 4.0$, while a much better agreement is observed between the affine prediction and $P(d_{\perp})$ at the same elongation ratio. Moreover, the affine predictions for P(d) and $P(d_{\parallel})$ at $\lambda = 4.0$ happen to agree well with experiments at much higher elongation ratios of $\lambda = 5.0 – 7.0$, indicating an interesting retardation of the NP separation along the stretching direction. These observations clearly suggest a decoupling between microscopic strain field and the applied macroscopic deformation that has directional dependence. The strong deviation between experiments and the affine predictions points to a complex interplay between the external deformation and the microstructural rearrangement of the NPs in high polymer matrix. Given the high *Pe* of the NPs and the dilute NP loading, these observations unambiguously demonstrate the presence of long-range NP-NP interactions in PNCs that are mediated by the polymer matrix.

The strong deviation from affine expectations in the stretching direction is particularly interesting. Normalized autocorrelation function results from a downloaded ImageJ macro,[89] presented in fig. 3.13, suggest that individual NPs have no long-range interaction, as expected, and oscillate around 0 well before 2000 nm away from the origin NP's coordinates. Therefore, the variations in the immediate surroundings < 2000 nm from the origin NP are of interest in determining how NP spacing is affected by deformation. To further analyze the rearrangement of the NPs the scope was accordingly restricted to consider only the NPs closest to one another. For

each NP imaged under a set of conditions *Wi* and λ, the coordinates were analyzed to determine the first neighbor particle directly in the stretching direction, $d_{\parallel}$; to avoid double-counting distances between a pair of the NPs, distances were always measure in a unidirectional manner corresponding with the positive $d_{\parallel}$ direction with respect to the image's coordinate system. If no neighbor exists within the image in that direction, as is the case for the final NP of each row, the result is null and the NP is not factored into the statistics as an origin particle; this typically resulted in ~770 edges lost per image compared to the DT results, which is < 5% of the total edges counted and leaves sufficient statistical basis for analytical purposes. Fig. 3.14 presents the curves for *Wi* = 0.06 of both the first and second nearest neighbors in the pure $d_{\parallel}$ direction with the data truncated to within 5000 nm of the origin NP due to the increased noise as the limits of the field of view are approached, but as allowed by the observations of the autocorrelation function results. The dashed lines again represent the predictions of affine NP rearrangement at designated λ via uniaxial expansion of the undeformed cases. Interestingly, these lines feature an initial peak and curve that has smoothed into a linear slope beyond 2000 nm, and the peak has shifted to both a lower distribution and greater distance as λ increases. Additionally, the slope becomes more horizontal from $\lambda = 1.5$ to $\lambda = 4.0$, as the NP field expands and the expectation is that the average $d_{\parallel}$ is increasing by a factor of λ; however, the analysis of slope values was not performed as the data did not match the affine predictions. The transformation of the curve into a linear slope could be related to the lack of long-range network and the expected relationship between randomly located NPs in an expanding field, although this is merely a speculative observation. More interesting is the lack of true peak in the $\lambda = 7.0$ data; while the overall percentage of the NPs located within that distance to the origin NP has decreased from $\lambda = 4.0$, a broad plateau of similar values exists from a few hundred to nearly 1500 nm suggesting similar likelihood that the first neighbor is

located anywhere in that range. If one imagined the effect of the NP agglomeration, the random grouping of particles may have a similar effect on the distribution of the first neighbor: the peak would be smeared into a wider range as for every NP moved closer to another NP's location it simultaneously moves further from the NP neighbor in the opposite direction. While total agglomeration was not observed by SEM, localized population density variances are clearly visible at $\lambda = 7.0$ in fig. 3.10, possibly indicating local networks beginning to form, although this is again a speculative observation without more concrete evidence. The inset provides further information, using the second nearest neighbor – skipping the first nearest neighbor to provide an enhanced view of potential aggregation. While the results for $\lambda = 7.0$ appear to indicate increased probabilities of the second nearest neighbor existing within 500 nm compared to $\lambda = 4.0$, the data is too noisy to be relied on for an absolute conclusion.

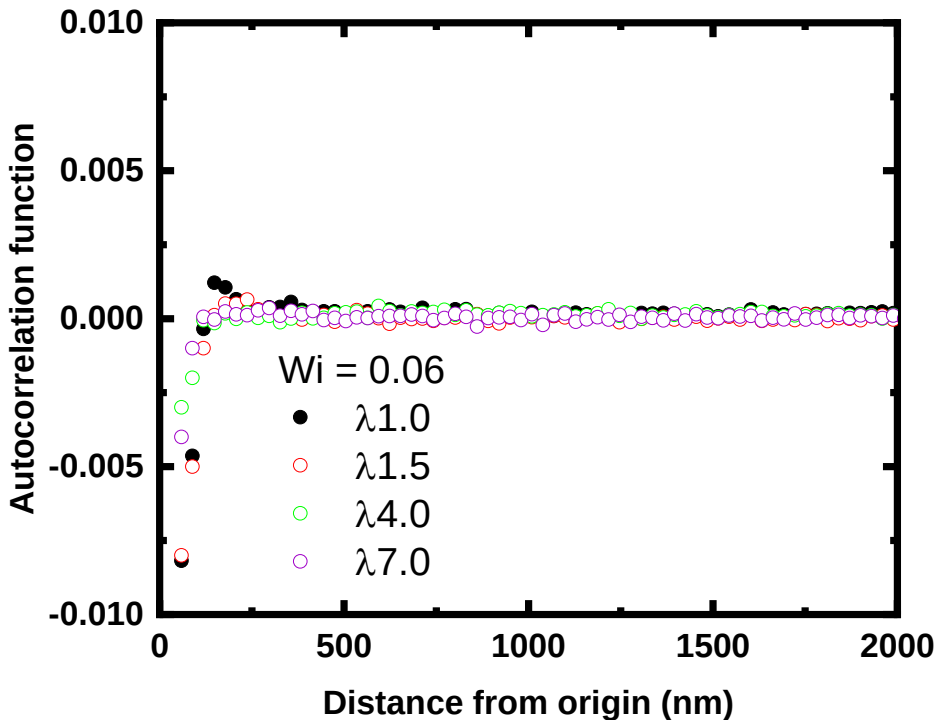

Figure 3.13: Autocorrelation function results for *Wi* = 0.06.

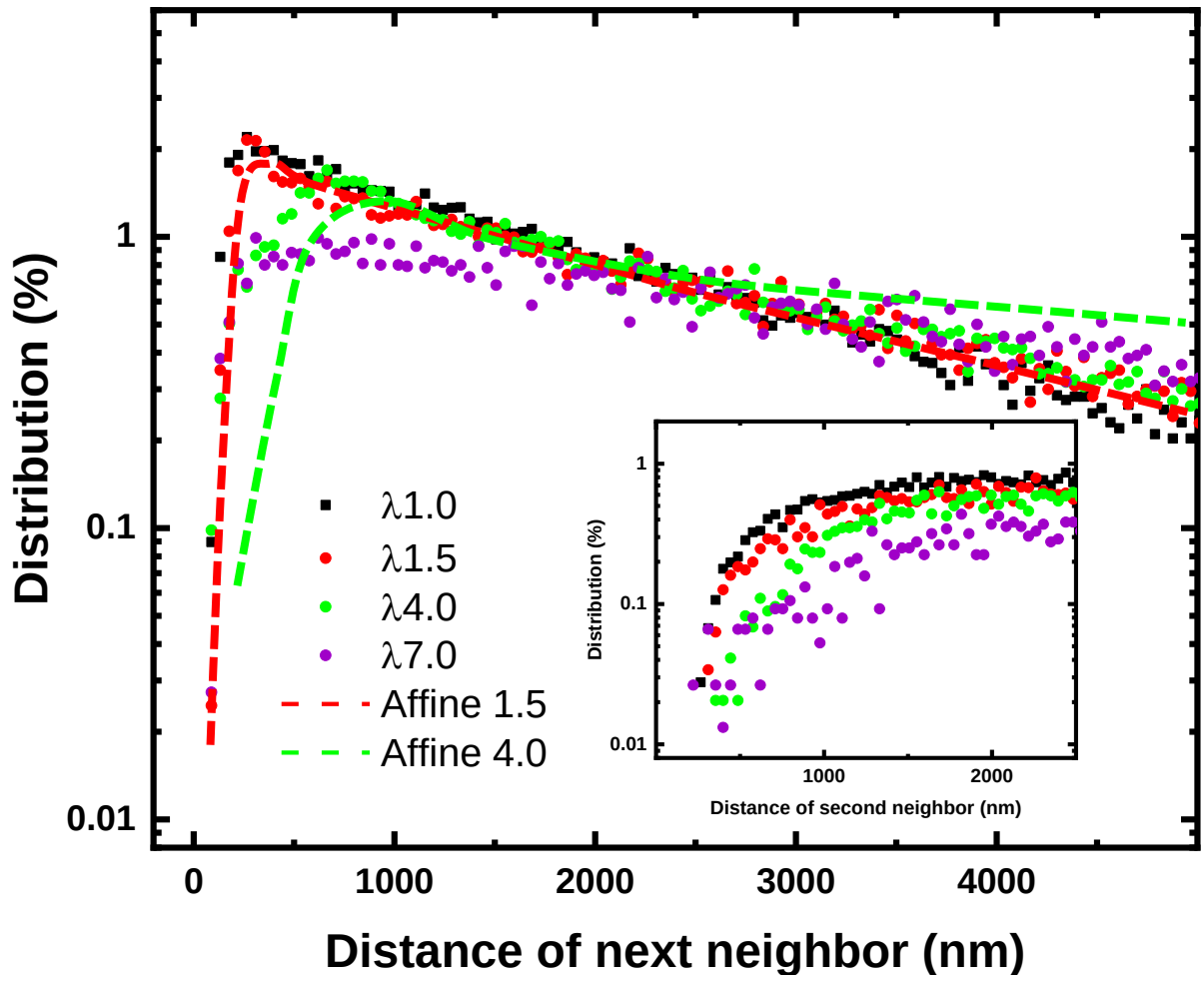

Figure 3.14: Nearest neighbor in direction of stretching for *Wi* = 0.06. The distribution of the distance from a nanoparticle to its nearest neighbor in the positive stretching direction is provided in contrast to the predictions of affine deformation. The inset provides the distribution to the second nearest neighbor in the positive stretching direction – an indication of clustering among nanoparticles.

In an attempt to further investigate these observations, the radial distribution of an NP's environment was randomly sampled in both $d_{\parallel}$ and $d_{\perp}$ directions, with a variance of $\pm$100 nm allowed for the coordinates to be considered within that direction. These results in fig. 3.15 show similar tendencies to the observations made with regards to the nearest neighbors, plotted against d_{cc} over R_{NP} to estimate how many NP distances are required to reach an independent correlation. Panel A) depicts the stretching direction, where it appears that after increasing the separation between NPs up to $\lambda = 4.0$, the spacing decreases dramatically by the time $\lambda = 9.0$ is reached. Meanwhile, in the y-direction the expected shift to closer values is observed in panel B), where

individual λ appear similar after deformation is performed. Unfortunately, these results are also too noisy to claim as clear evidence of agglomeration. Despite this drawback, they offer intriguing initial observations that warrant further investigation for understanding the deformation-induced rearrangement of the NPs.

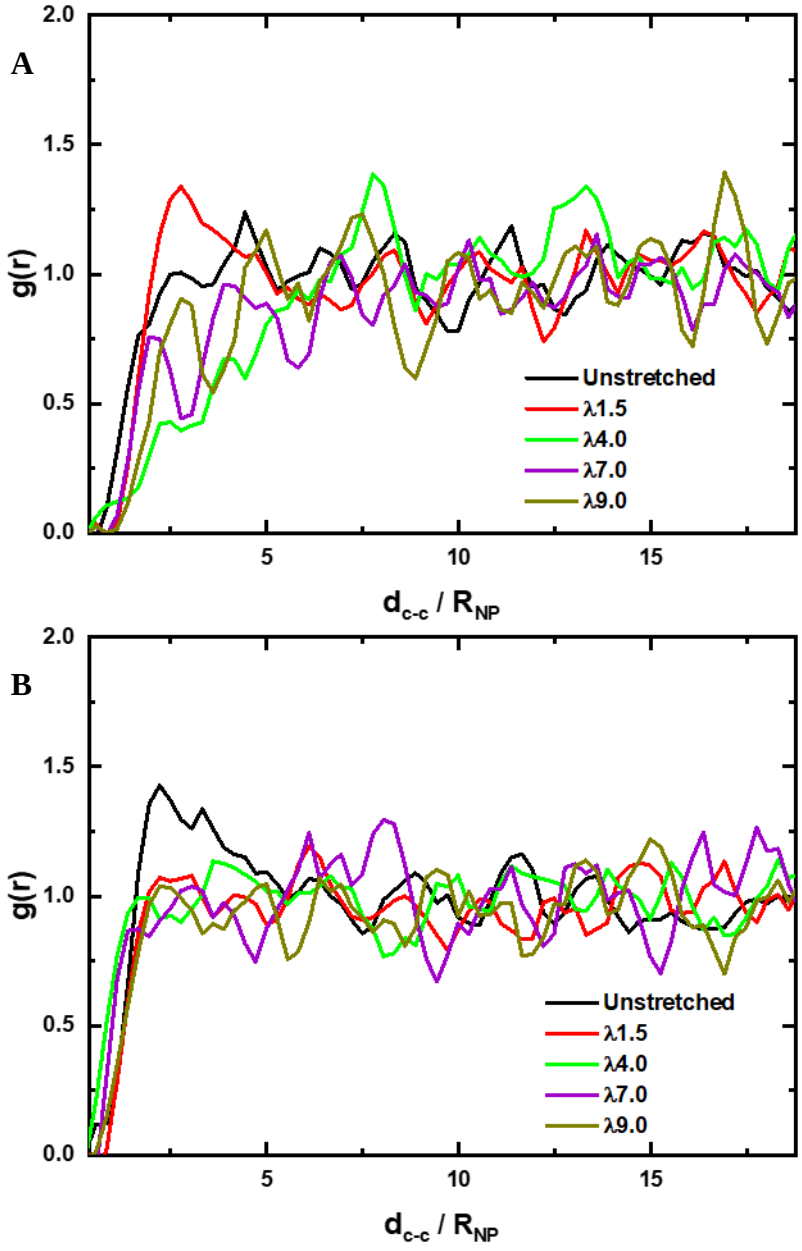

Figure 3.15: Radial distribution function for *Wi* = 0.06. The results for the radial distribution function, g(r), is provided for various λ at *Wi* = 0.06 in directions A) parallel to stretching and B) perpendicular to stretching.

3.4.2 Microstructural Rearrangement of Polymer Nanocomposites at Deformation: The Strain Rate Effect

The above analyses focus on the flow region of matrix polymer at $Wi = 0.06 << 1$. To study the effect of viscoelasticity on the positional rearrangement of the NPs, measurements and imaging of PVAc/SiO_2 was also performed at $Wi = 20 >> 1$. The stress-strain curves of PVAc/SiO_2 and the neat PVAc at $\dot{H} = 0.097\ s^{-1}$ ($Wi = 20$) has been presented in fig. 3.3, where a strong strain hardening is observed at large λ. Figs. 3.16 A), B), and C) present the representative SEM images at elongation ratios, $\lambda = 1.5$, 4.0, and 7.0 and figs. 3.16 D), E), and F) show the corresponding binary images of the spatial distribution of the top layer NPs. Interestingly, discernably less NP clustering can be observed in the binary image in comparison with the $Wi = 0.06$ images at higher λ, indicating a strong influence of the deformation rate on the spatial rearrangement of the NPs.

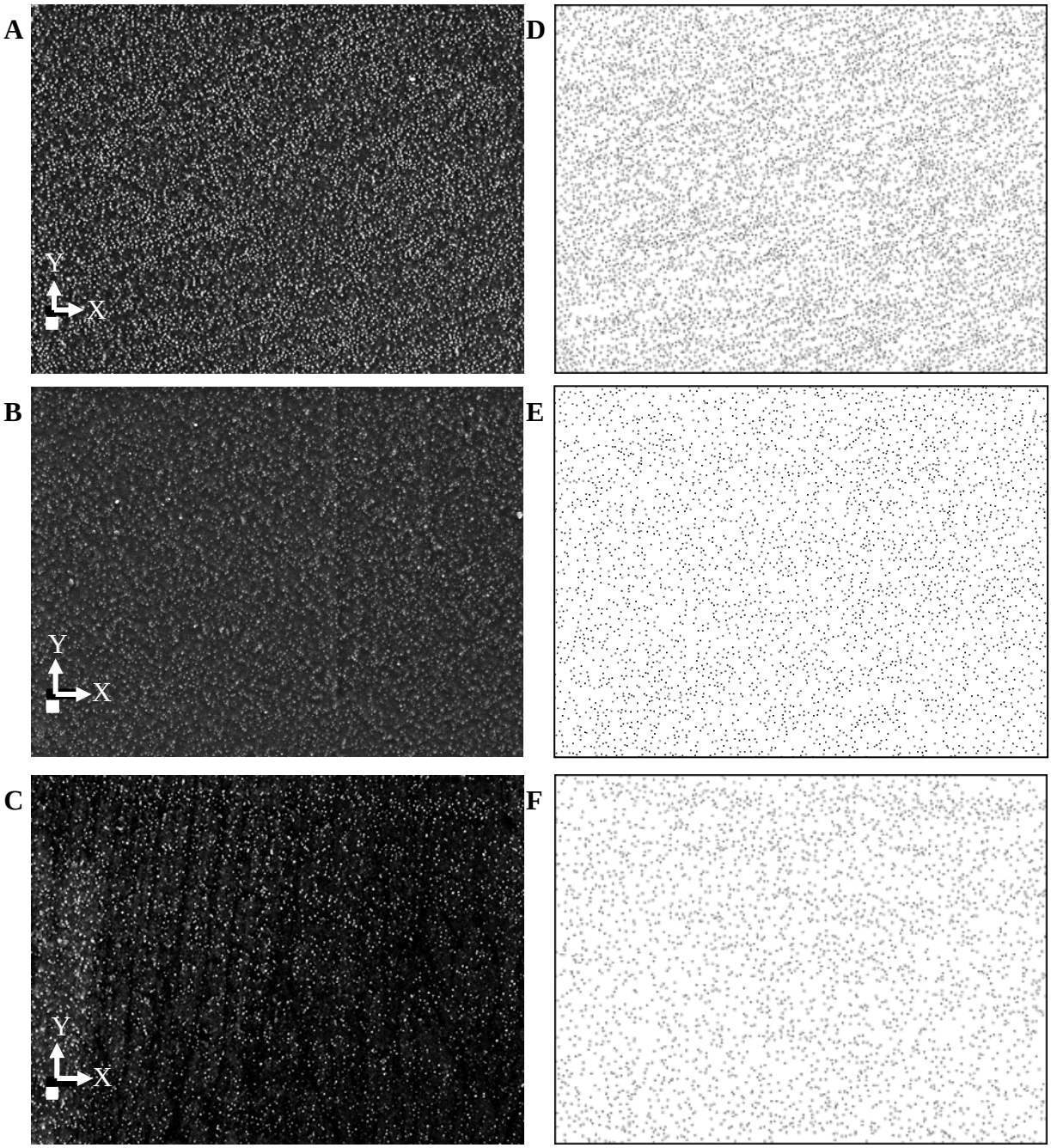

Figure 3.16: *Wi* = 20 SEM images with corresponding binary images. Sample SEM images for λ A) 1.5, B) 4.0, and C) 7.0 at deformation rate of *Wi* = 20 and their corresponding binary images, D), E), and F), respectively. Scale bars are 500 nm and X is the direction of stretching with perpendicular direction Y.

Figs. 3.17 A), B), and C) present the 2D FFT analysis of the SEM images at *Wi* = 20 with strong structural anisotropy of the NP distribution. The larger the strain, the stronger the structural anisotropy that has also been observed at *Wi* =0.06 at $\lambda \leq 4.0$. Interestingly, a continuous increment of the structural anisotropy is observed for $\lambda > 4.0$ at *Wi* = 20, in sharp contrast to the observation at *Wi* = 0.06 and highlighting the rate effect for the NP rearrangement. To be more quantitative, the distance distribution among NPs is again analyzed, as well as their comparison with the affine predictions in figs. 3.18 A), B), and C). The basic characteristics at *Wi* = 20 are similar to *Wi* = 0.06: (i) The peak positions of P(d) and $P(d_{\parallel})$ shift to higher d_{cc} values, implying the separation of the NPs with deformation. The peak position of $P(d_{\perp})$ shifts to smaller $d_{\perp}$ values, suggesting the tendency of the NPs moving towards each other transverse to the stretching direction. (ii) There are reductions in the peak heights of P(d), $P(d_{\parallel})$, and $P(d_{\perp})$ and significant enhancement of their values at the large d_{cc} region. (iii) Both P(d) and $P(d_{\parallel})$ at *Wi* = 20 agree well with the affine prediction at least up to $\lambda \approx 4.0$, implying a much better coupling between the microscopic strain field and the macroscopic deformation at *Wi* = 20 than at *Wi* = 0.06. Note that the matrix polymer dynamics exhibit a far stronger elastic behavioral response at *Wi* = 20 than the negligible elastic effect of the matrix polymer at *Wi* = 0.06. The interesting rate effect clearly indicates a strong correlation between the long-range NP-NP interactions and the elastic response of the matrix polymer. Fig. 3.19 presents the comparison of the P(d) at both low and high deformation rates for λ = 1.5, 4.0, and 7.0. The dashed lines are the affine prediction of the λ = 1.5 and 4.0 by assuming the same initial NP dispersion state as λ = 1.0. At λ = 1.5, no significant differences are observed for *Wi* = 0.06 and 20, thereby showing reasonable agreement with the affine prediction at that stage. While it bears recalling that the distributions are based on different localized loading

densities, it is interesting that the shape of the total length distribution P(d) for λ = 7.0 appears similar across deformation rates.

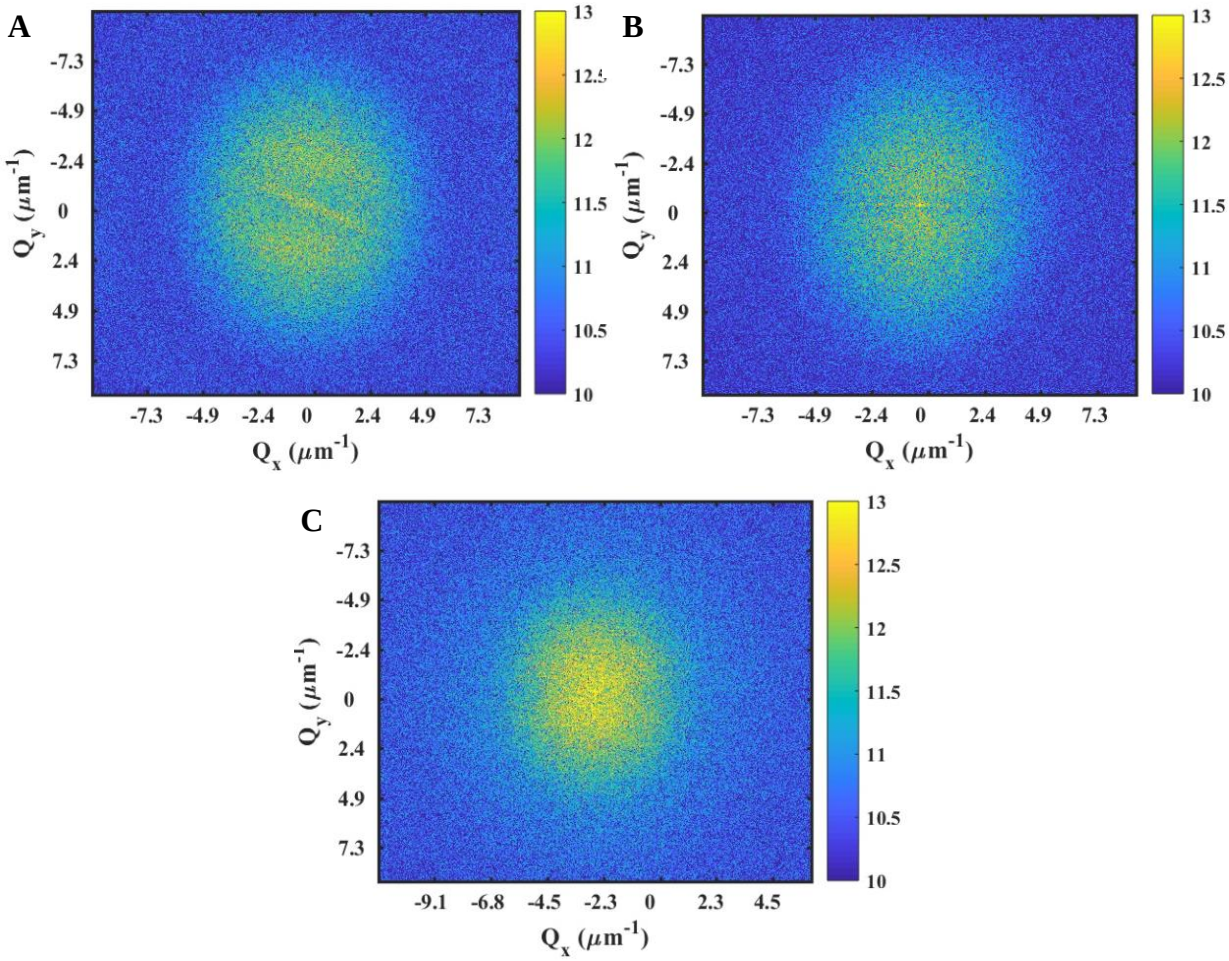

Figure 3.17: *Wi* = 20 2D-FFT results. 2D FFT of PNC at A) λ = 1.5, B) λ = 4.0, and C) λ = 7.0 deformed at Wi = 20.

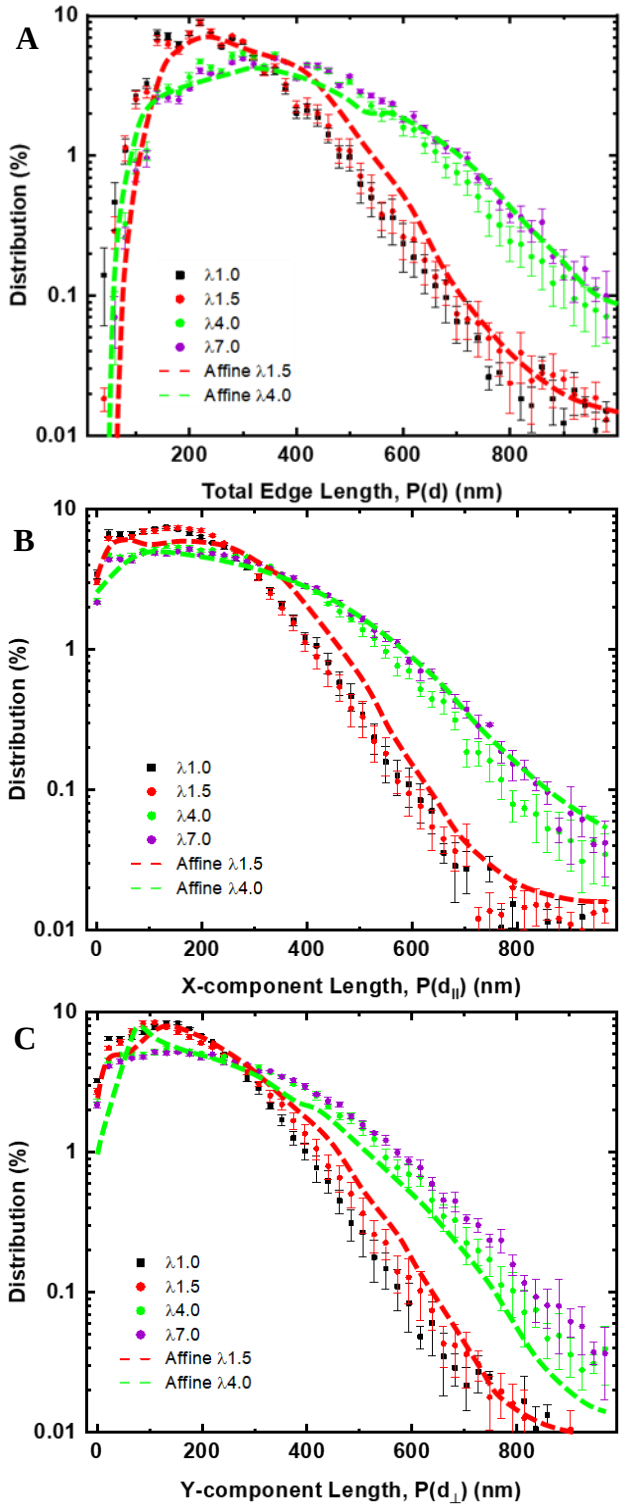

Figure 3.18: Nanoparticle spacing distributions for *Wi* = 20. NP spacing distributions for Delaunay triangulation results from 5 images averaged with error bars at elongation ratios λ = 1.0, 1.5, 4.0, and 7.0 for Wi = 20 with affine predictions based on λ = 1.0 spacing expanded to λ = 1.5 and λ = 4.0. A) $P(d)$, B) $P(d_{\parallel})$, and C) $P(d_{\perp})$.

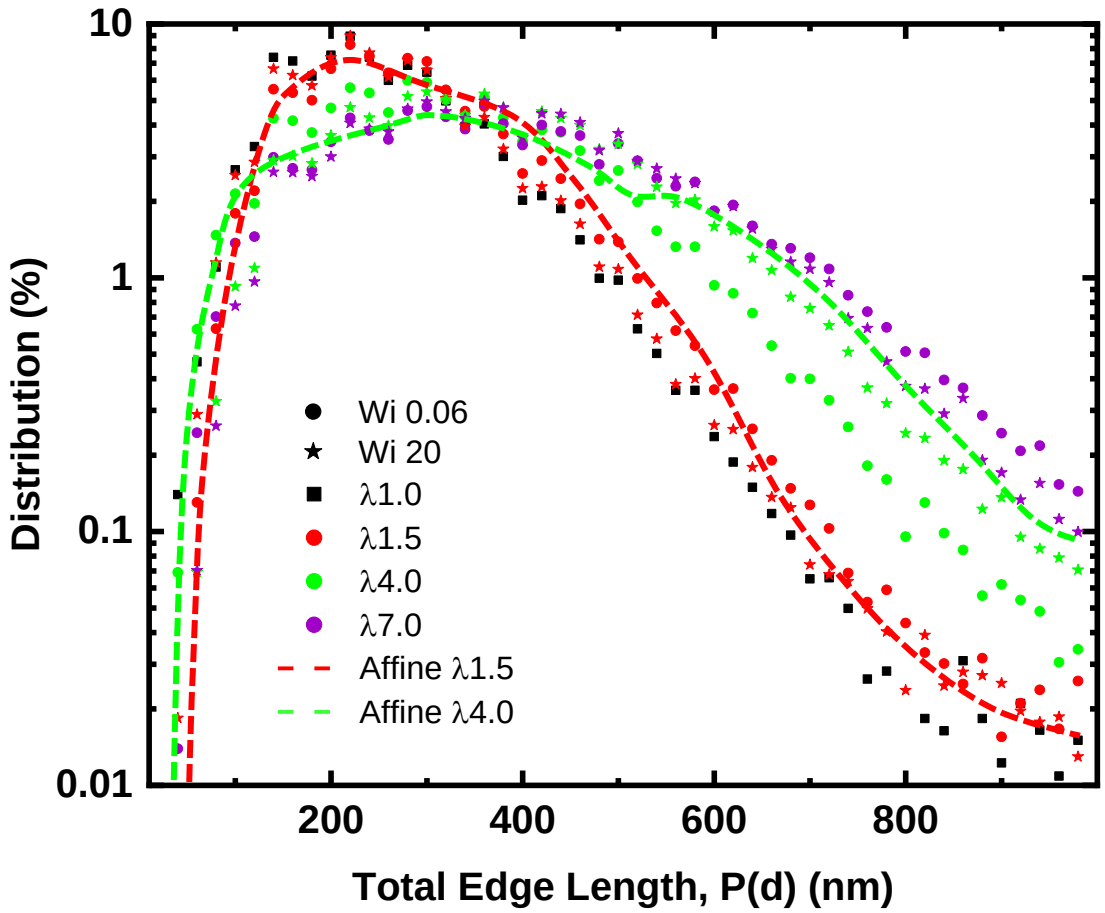

Figure 3.19: Comparison of the NP spacings at both deformation rates. NP spacing distributions, P(d), for Delaunay triangulation results from 5 images averaged at elongation ratios λ = 1.0, 1.5, 4.0, and 7.0 for Wi = 0.06 and 20 with affine predictions based on λ = 1.0 spacing expanded to λ = 1.5 and 4.0.

With respect to the analysis of the nearest neighbors, the similarities are no longer maintained. Fig. 3.20 shows the results for *Wi* = 20, where λ = 7.0 now more closely resembles the shape of the affine prediction for λ = 4.0: the curve has a sharp peak with a moderate descent that transforms into a seemingly linear relationship, albeit somewhat noisy beyond 2000 nm. Additionally, the second nearest neighbor lacks the <500 nm data points altogether, implying significantly fewer clustered particles immediately adjacent to the origin NP. Although still not conclusive, it is encouraging that the analysis is at least self-consistent with the observed results from figs. 3.16 through 3.18 that imply a larger expansion of the NPs in response to the higher deformation rate. The radial distribution function results also maintain this trend, as shown in fig.

3.21. Although there is a brief lag in the expansion of the NPs in $P(d_{\parallel})$ at $\lambda = 7.0$, there is no regression in spacing through $\lambda = 9.0$ as NPs are always moving away from one another. Once again, with respect to $P(d_{\perp})$ the results show an immediate reduction in spacing after deformation beings, but remains relatively stagnant across increasing λ. At this point, it is useful to compare the variations in total NP counts among the immediate environments of randomly selected NPs. Prior to the separation of only $P(d_{\parallel})$ and $P(d_{\perp})$ counts of the radial distribution function, the full radial profile provided the averaged count of nearby NPs a specified distance away from the origin point irrespective of direction. As shown in fig. 3.22, these results clearly indicate that $Wi = 0.06$ resulted in closer-packed areas within the sample than $Wi = 20$ through at least a range of $d_{cc} = 1000$ nm. Macroscopically, the φ_{NP} remains similar across the samples, despite the local variances in density. It stands to reason that at $Wi = 20$ the field maintains high homogeneity, while at $Wi = 0.06$ both particle rich and particle sparse regions are created locally within the matrix. The ultimate result of these different NP rearrangements will influence the respective mechanical properties of the samples; however, without clearer analytical results, any complete understanding of the mechanisms for these apparent rate-dependent deformation-induced agglomeration behaviors will remain elusive.

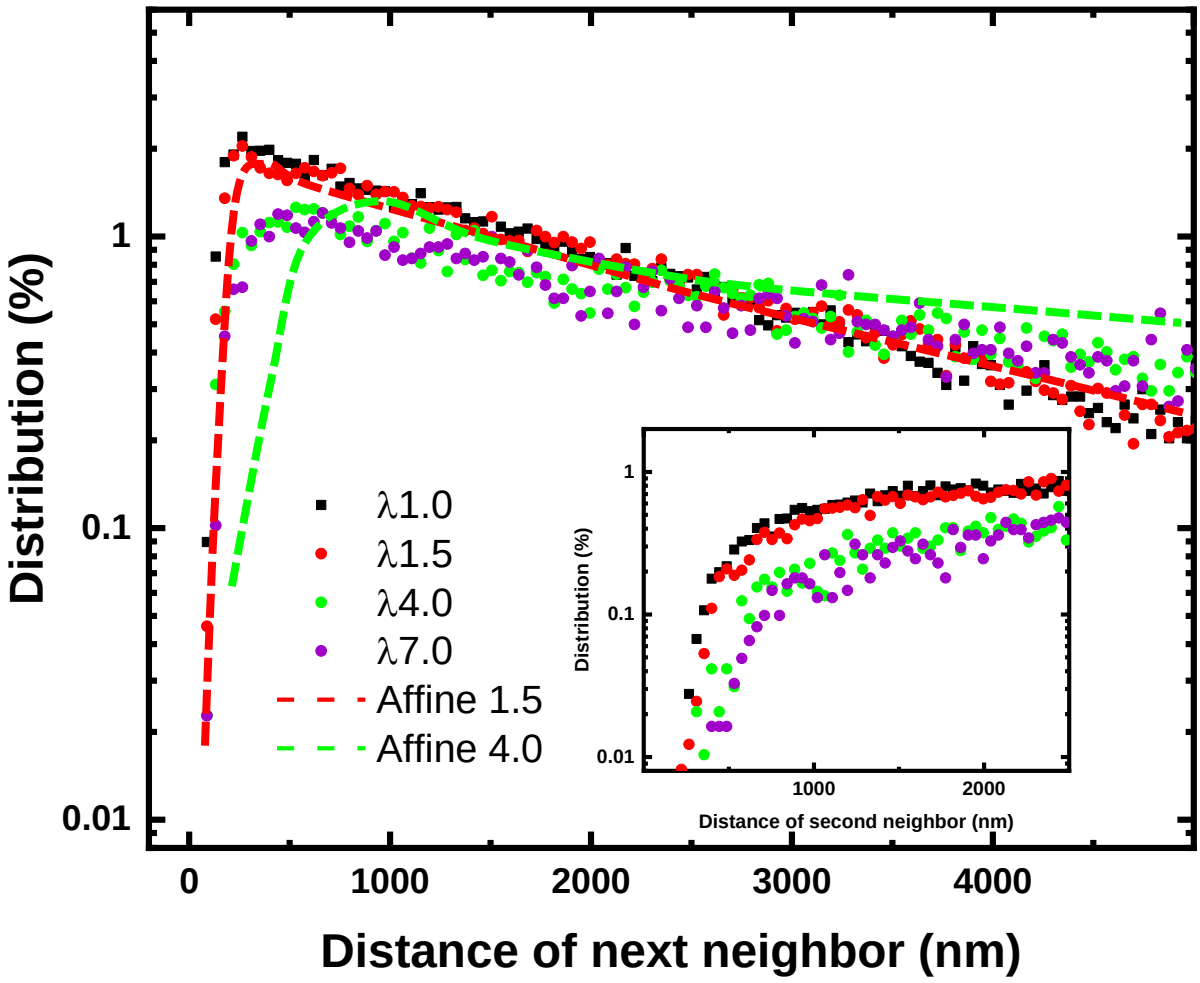

Figure 3.20: Nearest neighbor in direction of stretching for *Wi* = 20. The distribution of the distance from a nanoparticle to its nearest neighbor in the positive stretching direction is provided in contrast to the predictions of affine deformation. The inset provides the distribution to the second nearest neighbor in the positive stretching direction – an indication of clustering among nanoparticles.

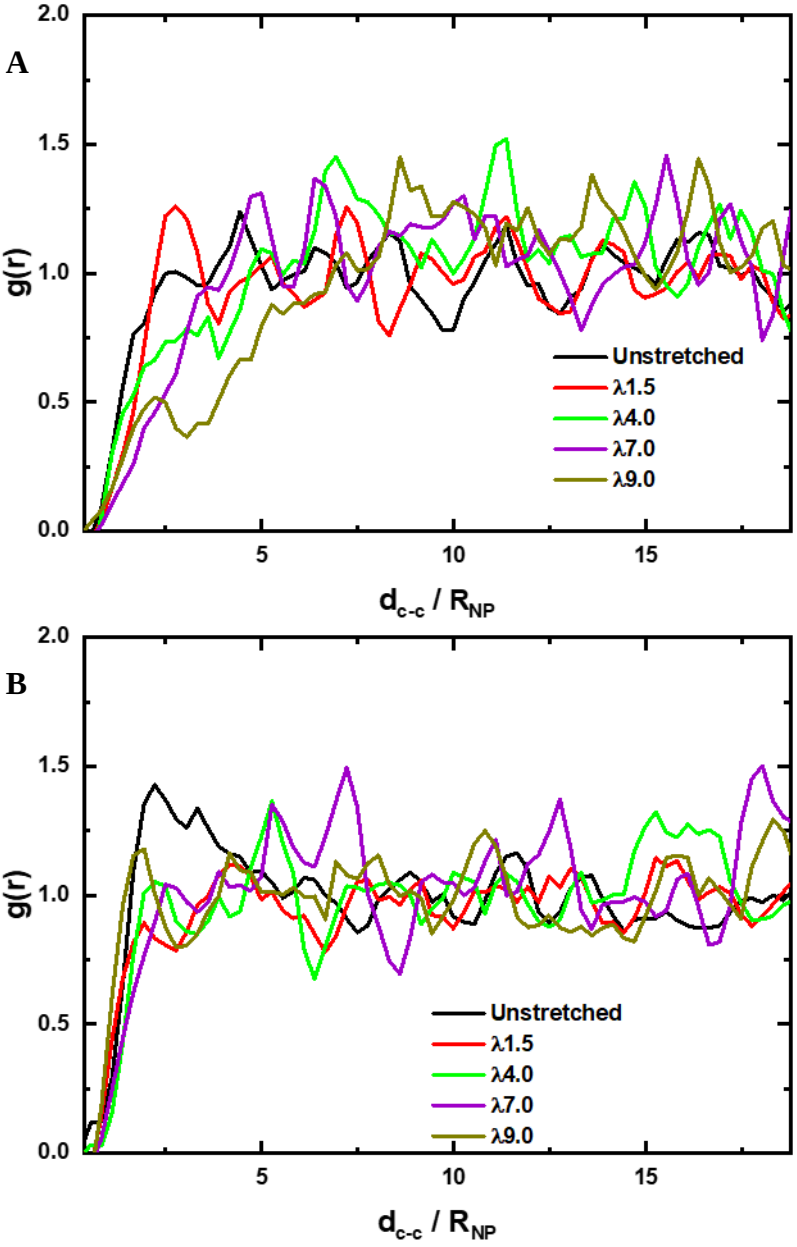

Figure 3.21: Radial distribution function for *Wi* = 20. The results for the radial distribution function, g(r), is provided for various λ at *Wi* = 20 in directions A) parallel to stretching and B) perpendicular to stretching.

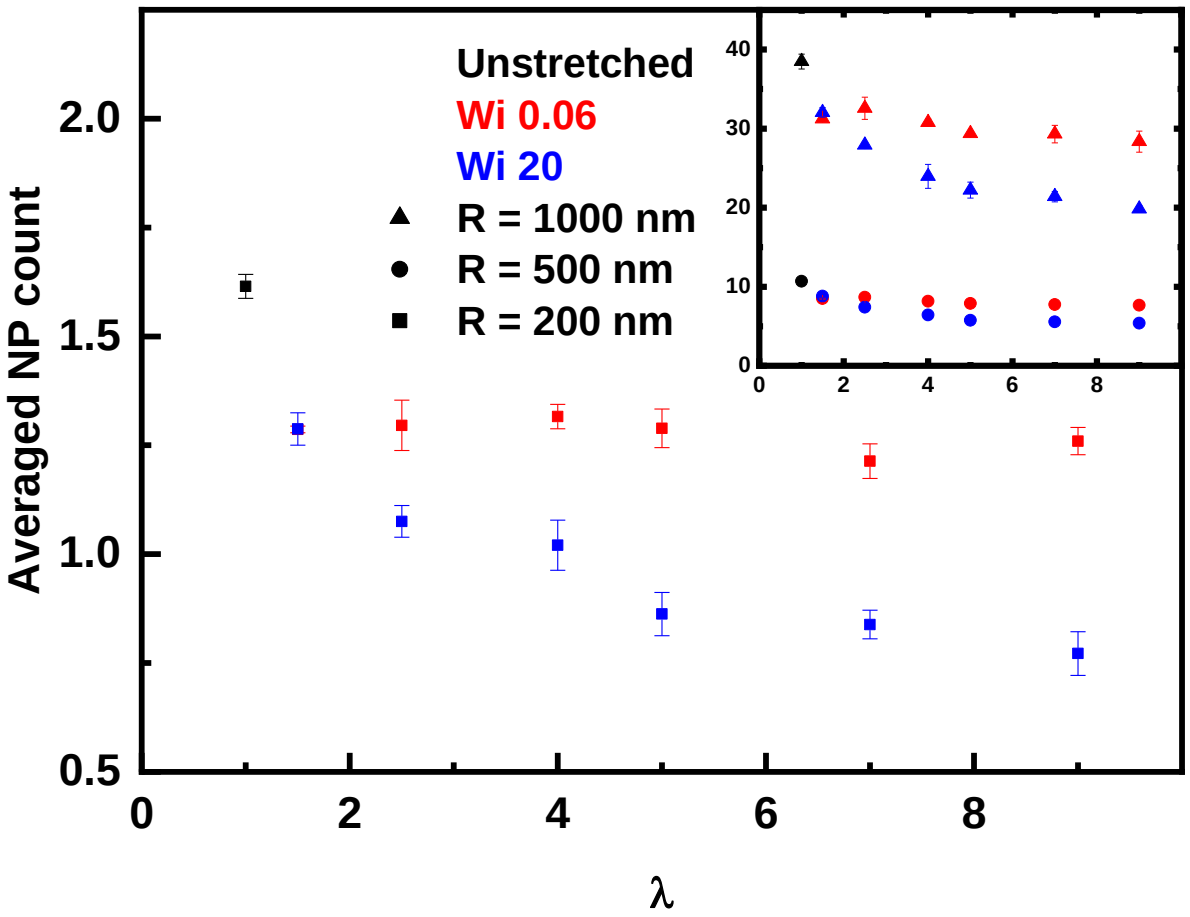

Figure 3.22: Count of neighbors surrounding nanoparticle of interest. Nanoparticles a certain distance from the edge, affording a full account of nearby particles, are randomly selected to determine the number of particles within a specific radial distance of 200 nm. The averaged neighbor count with associated error bars is shown for both *Wi* = 0.06 (red symbols) and *Wi* = 20 (blue symbols). The inset expands the radial distance to 500 nm (circles) and 1000 nm (triangles).

3.4.3 The Connection Between the Microstructural Rearrangement and Mechanical Properties of the Polymer Nanocomposite

The PVAc/SiO_2 exhibits a very weak mechanical enhancement in the linear response (fig. 3.3). In contrast, significant mechanical reinforcement has been observed in the PNC at large deformation (fig. 3.23), highlighting the strong nonlinear effect of the impact of the NPs to the polymer dynamics. Two important molecular viewpoints have been proposed for the mechanical reinforcement of PNCs at large deformation in addition to the classical hydrodynamic effect of the NPs. One proposes the presence of the enhanced polymer deformation to accommodate the non-

deformable NPs; the other is the deformation of the NP network. The former assumes affine positional change of the NPs and the latter requires the formation of an NP network. These SEM analyses demonstrate unambiguously the failure of affine positional change both at Wi = 0.06 and Wi = 20 at large deformation. Additionally, the SEM analyses show the absence of nanoparticle separation beyond $\lambda \approx 5.0$ for both Wi = 0.06 and Wi = 20, which acts against the requirement of a continuous separation of the NPs for the molecular overstraining perspective to be valid. On the other hand, our SEM analysis clearly show the lack of percolated NP networks over the whole range of deformation. Therefore, both the molecular overstraining and the deformation of the NP network cannot be the origin of the strong mechanical reinforcement of PNCs at large deformation in this case. The observed mechanical enhancement of the PNC is most likely due to the hydrodynamic effect of the NPs.

Could the hydrodynamic effect of the NPs explain the characteristics of the mechanical reinforcement of the PNC with a strong disparity between the linear response region and at large deformation? According to a recent small-angle neutron scattering study, the hydrodynamic effect of the NPs will lead to a redistribution of strain field surrounding the NPs rather than a net gain of molecular deformation.[104] Note that the hydrodynamic effect of the NPs is a long-range interaction that prevails several times longer than the radius of an NP. A strong interference of hydrodynamic effects of the NPs could emerge, which should depend on the dispersion state of the NPs. These SEM measurements clearly show the microstructure of PNCs has a strong strain dependence. Thus, one should anticipate a strain dependence in the mechanical reinforcement. On the other hand, the strong interference of hydrodynamic effects of neighboring NPs in PNCs can couple with the viscoelastic nature of the matrix, leading to a strong nonlinear effect resulting in the mechanical reinforcement depending on both the deformation amount and rate of deformation. Thus, the

hydrodynamic effect of the NPs could qualitatively explain the strain and strain rate dependence of the mechanical enhancement of PNC. Experimentally, the instantaneous mechanical reinforcement factors, $\sigma_{eng}^{PNC}(\lambda)/\sigma_{eng}^{matrix}(\lambda)$, shown in fig. 3.23 indeed exhibit strong strain and strain rate dependence.

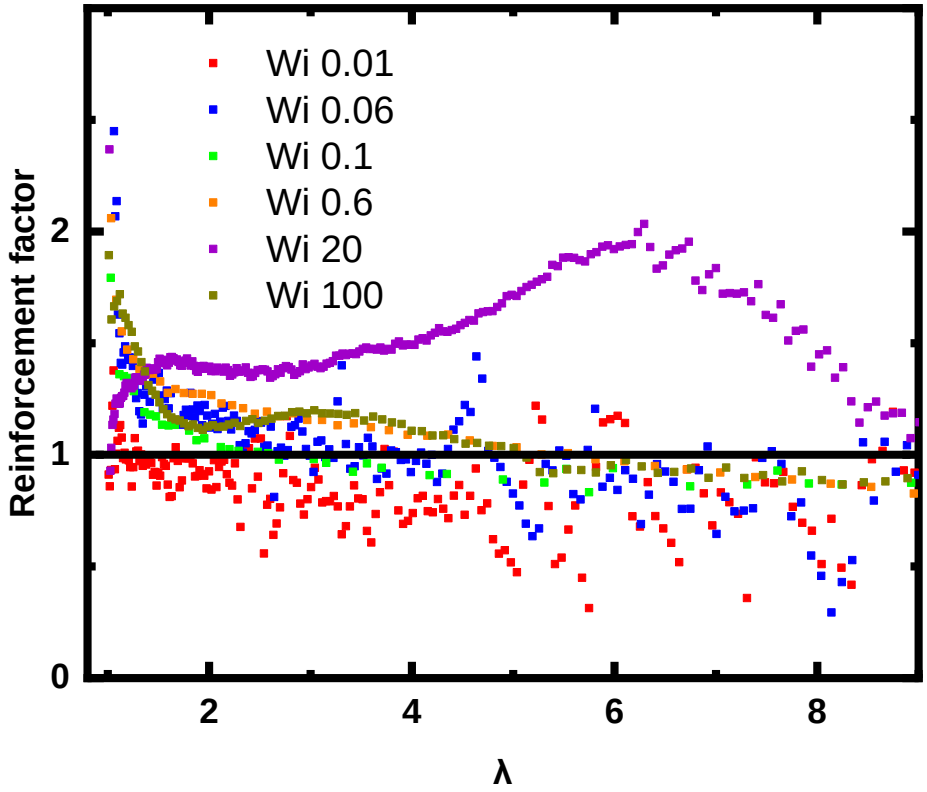

Figure 3.23: Reinforcement factor versus elongation ratio for varied strain rates.

3.5 Conclusions and Outlook

The above observations reveal several interesting features of positional changes of the NPs in PNCs at large deformation that have not been reported before. Additionally, no previous studies attempting the quantification of the strain and strain rate dependence of the microstructural rearrangement of the NPs in PNCs were found. These experiments are all in the high *Pe* number of nanoparticles. The following is a summary of the leading phenomenology uncovered by this research: (i) The NP positional change in polymer has a strain dependence. The positional

rearrangement of the NPs follows the external deformation only at small or intermediate strain. Strong evidence of the NP clustering is observed both from the 2D binary image and the detailed NP distance distribution analysis. (ii) The NP positional change depends strongly on the applied strain rate. At $Wi << 1$, the positional changes of the NPs deviate from the external deformation at an early stage of the deformation, $\lambda \sim 1.5$, along the stretching direction, which is much smaller than that in the direction perpendicular to the stretching direction where it is maintained until $\lambda \sim 4.0$. At $Wi >> 1$, the deviation of the NP positional changes from the external deformation have been pushed to $\lambda \sim 4.0$ both along and perpendicular to the stretching direction. These observations indicate an intriguing influence of polymer elasticity on the microstructural rearrangement of PNCs.

These important observations bring to mind the important characteristics of hydrodynamic interactions of particles where long-range interactions among NPs are present. A leading effect of the hydrodynamic interactions among particles is the collective motion of particles resulting from a coupling of the hydrodynamic forces and the flow field. As a result, the trajectory of individual particles does not necessarily align with the external deformation field, which might explain the observed non-affine positional change of the NPs at large deformation. At high *Pe*, the NP rearrangement is independent of Brownian motion and the hydrodynamic forces can dominate the whole stress and drive the formation of the NP clusters, which has been widely observed in colloidal suspensions.[105, 106] Thus, the hydrodynamic interactions among NPs can qualitatively explain (i) the non-affine positional change of the NPs, and (ii) the clustering of the NPs. Given that the details of the hydrodynamic interactions among NPs could be strongly mediated by the viscoelasticity of the matrix polymer, one would anticipate the explicit form of the hydrodynamic interactions among NPs has a strain rate dependence, which could explain the observed strain rate

dependence of the microstructure rearrangement of PNCs. In fact, a major challenge to understand the influence of external deformation on the microstructural rearrangement is the lack of detailed understanding of the hydrodynamic interactions among NPs in polymer matrix, which render it impossible to explicitly calculate the trajectory of the NPs under deformation. Nevertheless, the experimental observation of the non-affine positional change of the NPs seems to point to a hydrodynamic effect in origin.

Looking forward, several interesting, yet simple, modifications of this work could provide additional evidence of this phenomenon and shed light on the nature of the polymer response and its influence on the rearrangement of the NPs. First, the spatial redistribution of the NPs under deformation should be performed for all deformation rates to determine whether the effects of all $Wi << 1$ and $Wi >> 1$ are similar to better understand the effect of the influence of the polymer matrix elastic response. The response of a PNC with $\varphi_{NP} \approx 30$v%, over four times the v% of this PNC, where polymer bridging and direct NP-NP interactions are increased thereby allowing a comparison of whether long-range NP networks will overpower the polymer elastic effect on NP rearrangement, would also be valuable. Finally, remaining within the well-dispersed regime but varying the dispersion state of the NPs to be either well-dispersed or aggregated prior to deformation would also serve to confirm the effect of hydrodynamic interactions among NPs in the polymer matrix. In this case, it is predicted the altered hydrodynamic volumes of pre-clustered particles should increase local variability in NP rearrangements under deformation. While not an exhaustive list, this selection of alternative studies could employ the same basic characterization methods to provide direct comparisons to these results, while shedding additional light on the key aspects of the hydrodynamic interactions and elastic response of a PNC undergoing uniaxial deformation and the resulting effect on the macroscopic mechanical properties.

CHAPTER 4: THE MICROSTRUCTURAL REARRANGEMENT OF POLYMER NANOCOMPOSITES UNDER SHEAR

4.1 Polymer Shear Flow Introduction

As PNCs continue to grow in industrial use due to their wide range of applications,[6-11, 15] the relationship between polymer processing and PNC properties is an increasingly important concept to understand. Since processing relies on polymer dynamics and deformation behaviors and the final properties are heavily linked to the final microstructure of the filler materials, the relationship between polymer deformation and the microstructural changes is inherently tied to this understanding.[18-24] As a result, the study of how NPs are affected by polymer flow fields remains a crucial aspect of understanding how to optimize the best industrial practices for various polymer applications.

One of the most important industrial processing practices is extrusion, due to the wide variety of practical applications and shape of final materials such as rods, tubes, fibers, films, foams, and compounded mixtures that can be performed.[107] The extrusion processes shape materials by pushing it through a channel and a die conforming the material into the desired final shape. During the extrusion of a PNC, the viscous shear deformation response of the sample is not uniform. This is because the polymer experiences a non-homogenous melt-flow and dynamics response dependent on the location within the channel directing the flow field of the polymer sample that is surveyed.[108] Even during steady-state flow, this creates a complex system that has proven difficult to understand due to the non-equilibrium nature of entangled melts. While several constitutive models exist to describe the molecular-level response of polymers,[109-111] their predictions only adequately describe the low-rate deformation response, $\dot{\gamma}_{app} * \tau_R < 1$ (where $\dot{\gamma}_{app} * \tau_R$ is defined as the Rouse Weissenberg number, Wi_R), and have recently been challenged when

high deformation rates induce chain stretching.[112-114] It is equally important to understand how the polymer chain behaves in the resulting shear-thinning regimes of increased stress, and how the NPs rearrange.

It is known in viscoelastic flows, as is the case in extrusion, that NPs are subject to the polymer flow field, but the affected particle migration can be non-homogenous.[115] This creates concentration gradients as a result of the combination of pressure-driven flow through the channel with transverse-to-flow rearrangement across shear planes.[115] To understand the behavior of PNCs, observations from the dynamics of uniform spheres migrating during the shear deformation of a Newtonian fluid are expanded into systems involving the channel flow of viscoelastic fluids.[105, 106, 115, 116] In Newtonian fluids during laminar flow, numerous experiments have recorded a phenomenon called "tubular pinch," where well-dispersed NPs will form a ring-like high-concentration regime approximately 0.3*D away from the center of a tube with diameter, D.[116] This was found to be true for tubes of varying round and rectangular shapes, and was determined to be caused by a balance of the 'shear-gradient lift force' and 'wall repulsive force;' however, it was also shown that the distance from the center was dependent on the Reynolds number, *Re*, of the flow, and with high enough *Re* the particles would always migrate completely to the center of the channel.[116] However, polymer nanocomposites do not flow like Newtonian fluids. There is a more complex system of forces within PNC flow that includes the inertial force and shear-thinning behaviors of the PNCs, which push particles towards the wall, and the elastic force, which pushes particles towards the center. Therefore, it is a challenging task to describe the complex flow systems from shear-induced mixing and its effect on NP migration in the nonlinear flow regime. Localized flow instabilities can cause the anisotropic evolution of phase-separated regions and in shear-thinning regimes, the NP migration could be towards either the center or the edge depending

on the original position of the NP and the forces present.[106, 116] It was suggested that since the particle migration is heavily dependent on both the characteristic flow viscosity as well as the viscoelasticity of the polymer, a measurement dependent only on the channel dimensions and fluid response dynamics would more accurately characterize the NP migration. To that end, the "elasticity number" was defined as the ratio of the dimensionless Weissenburg number, *Wi*, which quantifies the elastic effects, and the dimensionless Reynolds number, *Re*, which quantifies the inertial effects.[116] These numerical results found that when the elastic force overcomes the inertial forces, i.e. at high enough elasticity numbers, the particle will always migrate towards the center of the channel; however, the elasticity number is highly sensitive to small changes in *Re* even within the laminar regime of *Re* = 0-100, since the elasticity number can drastically change for low *Wi*. Otherwise, if the forces balance one another, then the migration meets an equilibrium location somewhere between the center and the wall, similar to the Newtonian fluid results, whereas migration towards the wall will occur when the elastic forces are small. While experimental results have observed NP migration in the shear-thinning regime, despite several proposed theoretical efforts to explain the phenomena, the results have thus far been inconclusive.[106] Additionally, the recent emergence of an additional shear-thinning regime at high shear stress that deviates from the Cox-Mertz rule, which suggests that there is a linear proportionality between the solution viscosity and strain rate ($\eta \sim \dot{\gamma}^{(1-\beta)/\beta}$, where β is a material dependent scaling factor), further complicates the matter.[117, 118] Finally, while it is suggested that both decreasing the size of the NPs and increasing the φ_{NP} can decrease the phase separation, due to their effect on the viscosity, the relative degree of these effects in PNCs are not well studied.[119]

Scattering experiments performed on co-polymer melts, colloidal suspensions, and swollen gels have provided intriguing results that average the data between the entire sample but lack the

ability to observe localized areas and often do not focus directly on the NP migration.[105] Therefore, it is proposed to image the cross-sectional face of the extrudate under varied flow conditions via SEM to observe the resulting NP phases to provide key observations crucial to aid in the unraveling of the particle migration phenomenon.

4.2 Materials and Methods

4.2.1 Materials

As with the previous experiment, PVAc was used as the polymer matrix with SiO_2 nanoparticles of a radius of $R_{NP} = 40 \pm 5$ nm (Nissan Chemical, MEK-AC-5140Z) and $R_{NP} = 23 \pm 3$ nm (Nissan Chemical, MEK-AC-4130Y) used to make composites of various filler fractions. The PVAc (Spectrum Chemical MFT Corp.) has a M_w of 100 kg/mol and a polydispersity of 1.76. The PVAc/SiO_2 nanocomposite was prepared in the previously documented manner. The mass fraction of the NPs was determined through thermogravimetric analysis (TGA Q50, TA instrument) in air from 293 K to 973 K at a heating rate of 20 K/min, which was converted to the volume loading of nanoparticles, φ_{NP}. For $R_{NP} \approx 40$ nm, sample PNCs prepared and extruded by an undergraduate researcher of our lab, Mr. Zipeng Xu, were determined to be φ_{NP} = 2.6v%, 11.1v%, and 33.3v%. For $R_{NP} \approx 23$ nm, sample PNCs were determined to be φ_{NP} = 2.4v%, 14.5v%, and 35.3v%, which are comparable values to the $R_{NP} \approx 40$ nm samples.

4.2.2 Rheology

The extrusion measurements were performed on a pressure-controlled automated Monsanto Capillary rheometer at 100º C, with temperature of the channel controlled by a homemade Omega CN740 temperature box and verified independently by thermocouple (Omega HH506RA) prior to measurements. Flow curves were generated by measuring volumetric flow

rate of the sample, Q, at an applied pressure range, P. The mass flow rate is directly related to the apparent strain rate, $\dot{\gamma}_{app}$, based on the dimensions of the die used and the pressures can be converted into shear stress using equations 11 and 12. The linear rheological measurements were performed on an ARES Rheometer with an environmental oven and an accuracy of ±0.1 K. SAOS measurements were performed on a pair of parallel plates with diameter of 8 mm at temperatures from 323 K to 393 K. The strain amplitude was varied from ~0.01-0.05% near the glass transition temperature ($T_g = 313\ K$) and gradually increasing to ~1.5-2.0% at the highest temperature ($T = 393\ K$) dependent on sample loading. The frequency range of all SAOS measurements is 0.1 – 100 rad/s. The linear viscoelastic master curves were constructed for both the neat PVAc and the PVAc/SiO_2 nanocomposites through the time-temperature superposition principle.

In the capillary extrusion experiment, the volumetric flow rate and applied barrel pressure are the directly measured quantities, with the stress experienced by the sample given by the equation

$$\sigma = \frac{P - \Delta P_e}{\frac{4L}{D}} \qquad (11)$$

where ΔP_e is the end pressure loss, and L and D are dimensional characteristics of the extrusion die. The shear rate at the wall is given by the equation

$$\dot{\gamma}_{app} = \frac{32Q}{\pi D^3} \qquad (12)$$

where Q is the volumetric flow rate. Samples of varying φ_{NP} and R_{NP} were subjected to a range of driving pressures to provide observations from the linear viscoelastic regime and the shear-thinning regimes. Samples were also characterized by TGA to determine φ_{NP} values as well as SAOS for basic polymer dynamics. While extrusion was performed for the pressure range of P =

5 – 90 psi applied to the piston, SEM images were only performed at 5, 10, 20, 40, 60, and 80 psi pressures, but still adequately represent each of the flow regimes observed.

4.2.3 Scanning Electron Microscopy

SEM images of PNC extrudates were taken on a Zeiss Auriga FIB-SEM. Secondary electron scattering detection mode was used at an accelerating voltage of 5 keV to observe the phase distribution of the NPs across the cross-sectional face of extrudate samples. The samples were coated with an ultrathin layer (~ 1 nm) of platinum using a Denton Vacuum Desk II XLS sputtering device before imaging to reduce charging. Locations of interest around the edge of the sample and within the core of the cross-section were further imaged for localized observations based on the appearance of the face, with at least 4 randomly selected areas surveyed per sample.

4.3 Analytical Results and Discussion

4.3.1 Characteristics of Polymer Nanocomposites Under Extrusion

Capillary rheometers are frequently used to measure the shear viscosity as a function of shear rate. The extrusion flow curves can be directly compared to the SAOS master curves through the complex modulus $G^* = (G'^2 + G''^2)^{0.5}$ as a function of ω. Therefore, it is relevant to begin the discussion with a comparison of SAOS curves between the neat polymer and the PNC, φ_{NP} = 11.1v%, as shown in fig. 4.1. There is very little difference between the master curves, as there appears to be minimal mechanical reinforcement from the dispersed NPs. Based on these observations, the PNC flow should be similar under extrusion to that of the neat polymer and the nanoparticles should be subject to the surrounding flow fields created by the shear stress. An example image from these conditions is provided in fig. 4.2. Imaging the microstructural phase evolution of the NPs within the extrudate as the applied pressure is manipulated is therefore

extremely useful to understanding how the flow fields affect the microstructural rearrangement of PNCs.

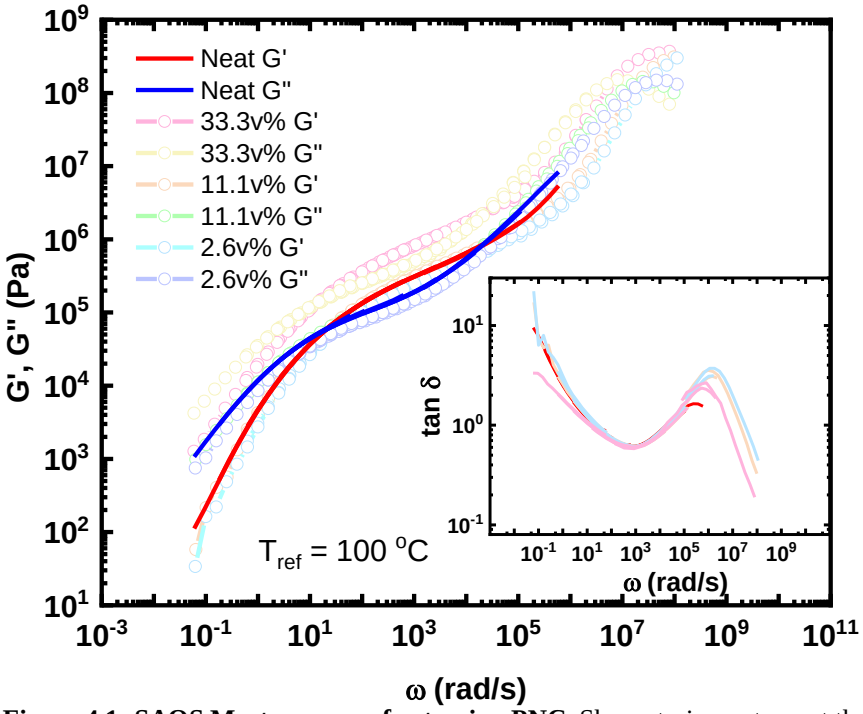

Figure 4.1: SAOS Master curve of extrusion PNC. Shear strain vs stress at the wall for neat PVAc and 11.1v% PNC with R_{NP} = 40 nm.

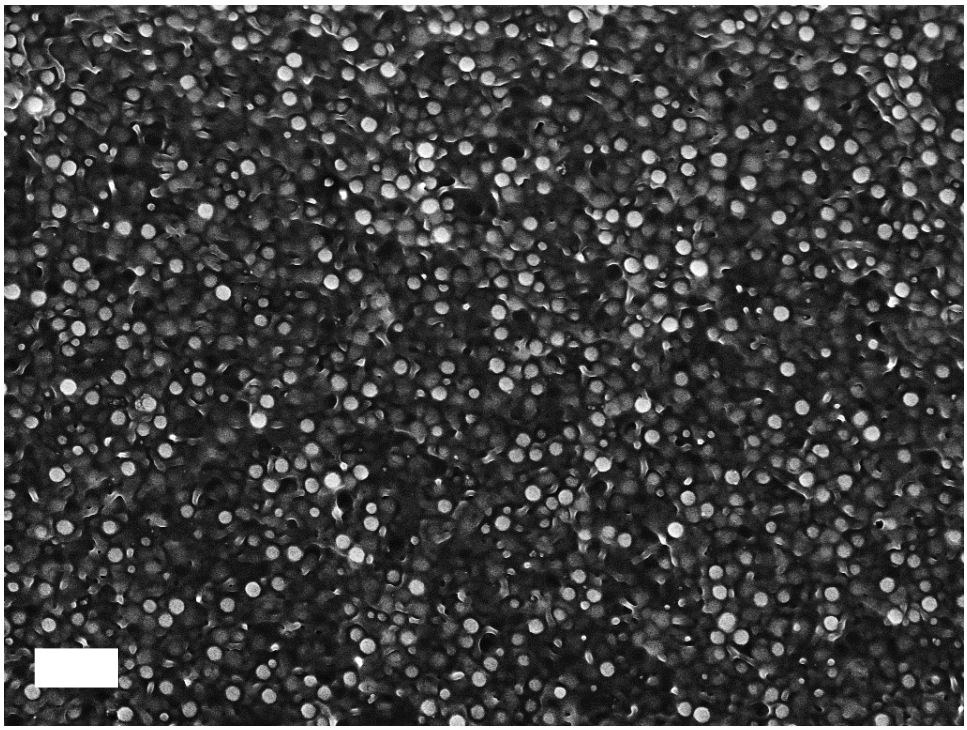

Figure 4.2: 11.1v% R_{NP} = 40 nm PNC extruded at applied pressure of 5 psi. Scale bar is 500 nm.

4.3.2 Effect of Polymer Stress on Characteristic Response

At the initial applied pressures, $\sigma = 0.02 – 0.06$ MPa, the flow regime is in the zero-shear response regime. As the applied pressure increases, and therefore the stress experienced by the PNC increases, the polymer flow response shifts, entering the shear-thinning regime. This transition is visible as the σ_{wall} exceeds 0.1 MPa in fig. 4.3, where dashed lines are provided to help guide the eye to visualize the slope changes on the extrusion curve, which also defines the scaling relationship between $\dot{\gamma}$ and σ. A potential slope change within the shear-thinning regime as pressure increases, albeit slight in the case of the 11.1v% PNC, would signify a deviation from the empirical Cox-Merz rule. While the magnitude of the strain rates and the resulting shear stress has decreased from the neat polymer to the PNC, a direct result of the non-deformable NPs occupying volume within the PNC extrudate, the curves exhibit similar regime transition values and shape, thus matching the observations of the SAOS master curves. Another method to show this stress relief within the PNC versus the neat polymer is to compare the amount of die swell between the PNC extrudate and the polymer extrudate across the same pressure range, which is shown in fig. 4.4. As the pressure increases, the comparable stress magnitude of the PNC relative to the neat polymer decreases as the presence of the NPs affects flow pathways in the confined space of the die. A noteworthy observation is that the NPs appear to be more clustered together in the extrudate during the shear-thinning regime as the polymer bulk works to relieve the stress, perhaps the result of a polymer mobility gradient between slower moving polymer trapped between the nanoparticles and the rest of the bulk, as shown in fig. 4.5. At the microscopic level, the face appears to show more frequent bands of smaller size, and on the nanoscale the NPs right at the surface appear to be more grouped with larger areas of open polymer present compared to the linear response regime. As the pressure is increased further, the NP dispersion does not appear to have changed

substantially for this φ_{NP}, as evidenced by fig. 4.6, although this could be due to the fact the slope change of the flow curve across these applied pressures is also minute.

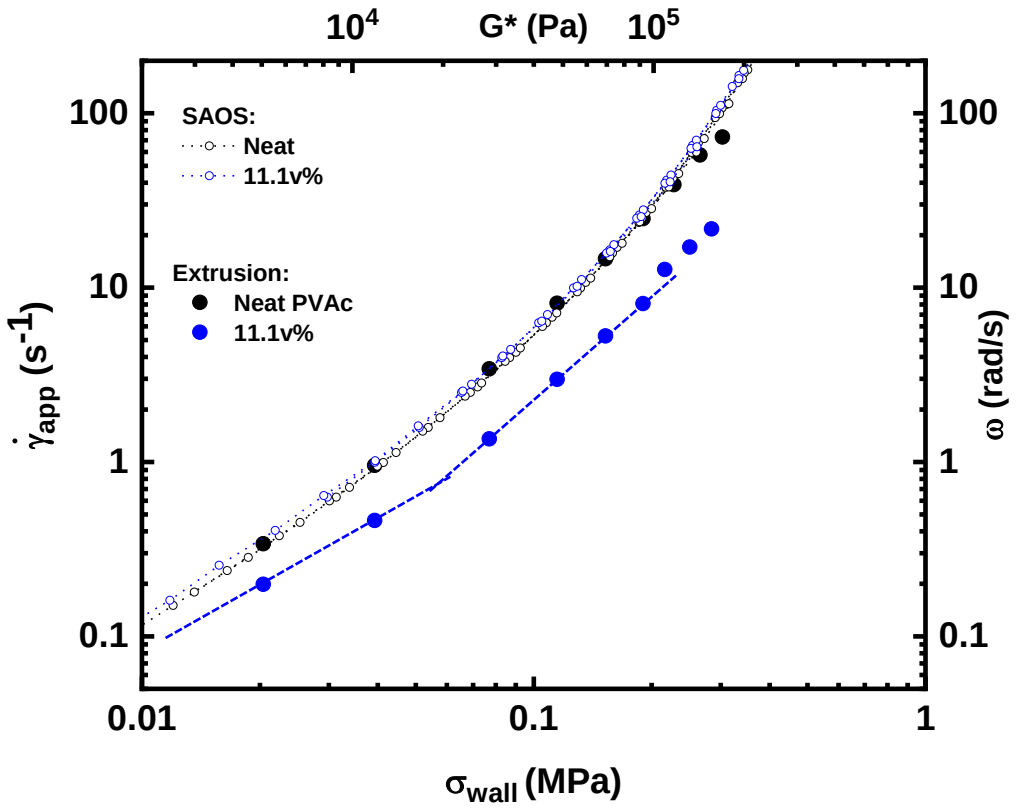

Figure 4.3: Extrusion flow curve for PNC with φ_{NP} = 11.1v% and R_{NP} = 40 nm. Shear strain vs stress at the wall for neat PVAc and 11.1v% PNC with R_{NP} = 40 nm.

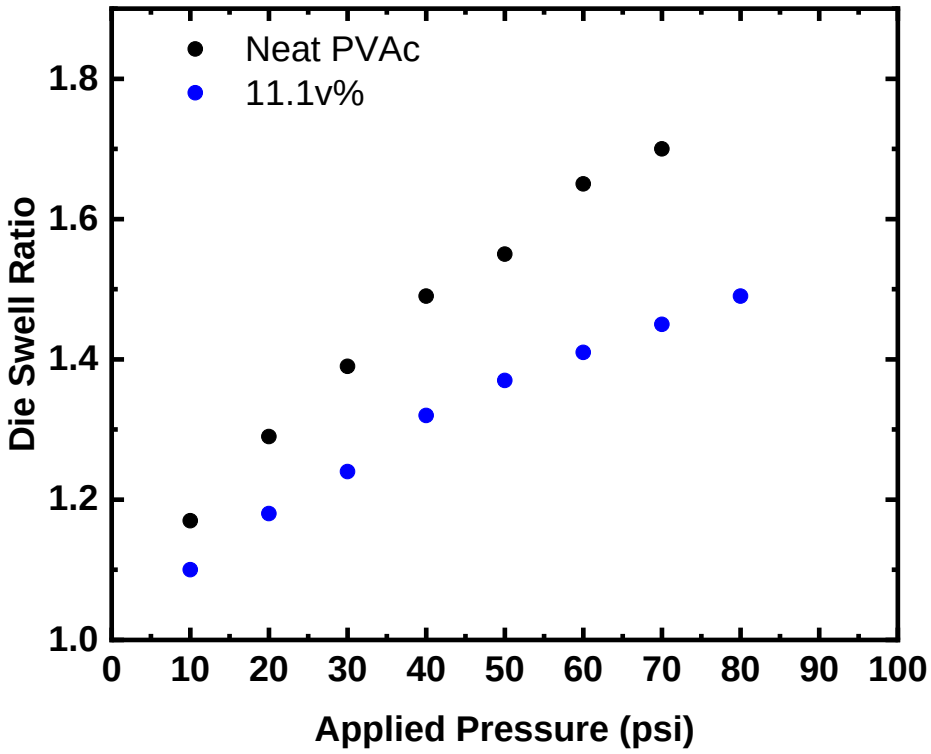

Figure 4.4: Die swell of PNC with φ_{NP} = 11.1v% and R_{NP} = 40 nm. Die swell vs applied pressure for neat PVAc and 11.1v% PNC with R_{NP} = 40 nm.

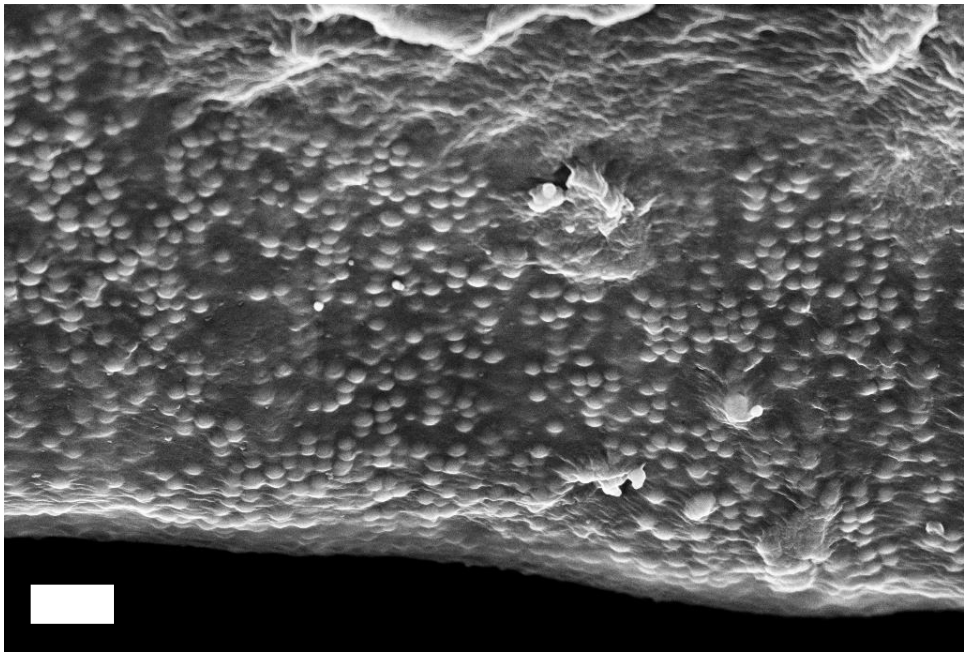

Figure 4.5: 11.1v% R_{NP} = 40 nm PNC extruded at applied pressure of 40 psi. Scale bar is 500 nm.

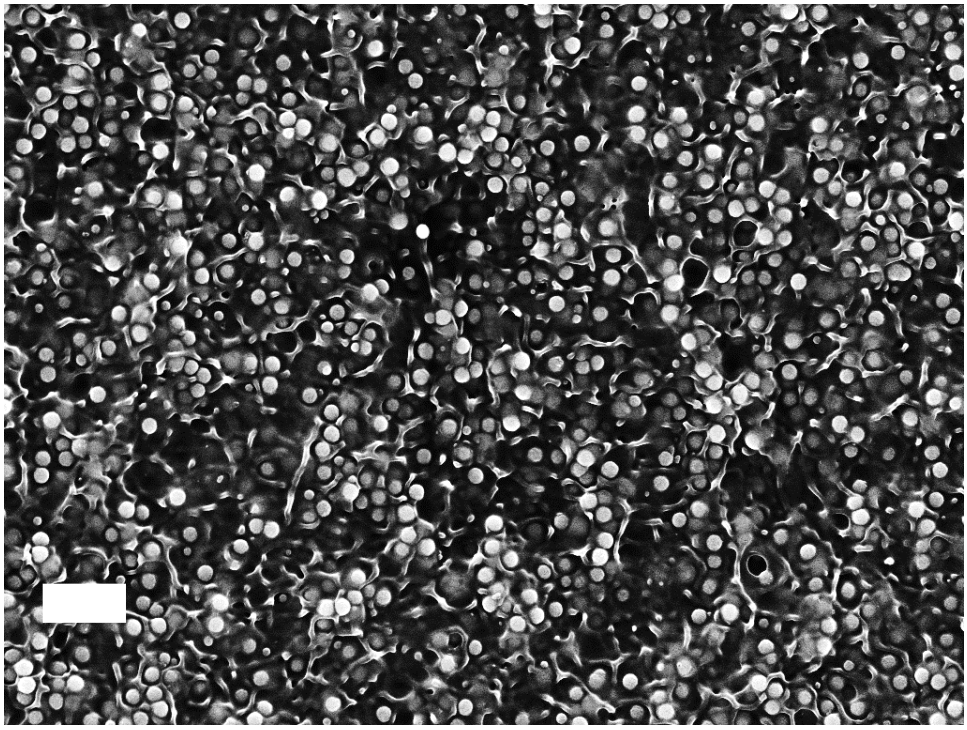

Figure 4.6: 11.1v% R_{NP} = 40 nm PNC extruded at applied pressure of 80 psi.
Scale bar is 500 nm.

4.3.3 Effect of Polymer Loading

Despite the similar flow curves, it is evident that the NPs influence the extrudate behavior and resultant properties. However, it is not immediately clear how the influence is scaled based on the presence of the NPs without measuring multiple systems of various φ_{NP}. Therefore, two additional PNCs were studied, with both significantly higher and lower volume fractions. Figs. 4.7 and 4.8 present the flow curves and die swell curves for all PNCs with R_{NP} = 40 nm compared to the neat PVAc curve. By reducing the concentration of the NPs present, the effects of the polymer flow field should be greater as there is less obstruction of the polymer response to stress. Interestingly, the linear flow regime of the 2.6v% sample appears to better match the neat polymer, while it shifts to match more closely the 11.1v% PNC as the stress is increased and yet does not clearly feature a shift in the chain stretching regime that would deviate from the Cox-Merz rule. By increasing the concentration of the NPs present, the flow obstruction is increased and ability

for the polymer to relieve stress is significantly limited, resulting in a significant shift in the flow curve and a massive reduction in the stress relieved upon exiting the die as evidenced by the lack of die swell. Additionally, the 33.3v% PNC has a significant shift in the slope between the shear-thinning regime and a chain-stretching regime present, showing a similar response of the 11.1v% PNC that indicates deviation from the Cox-Merz rule.

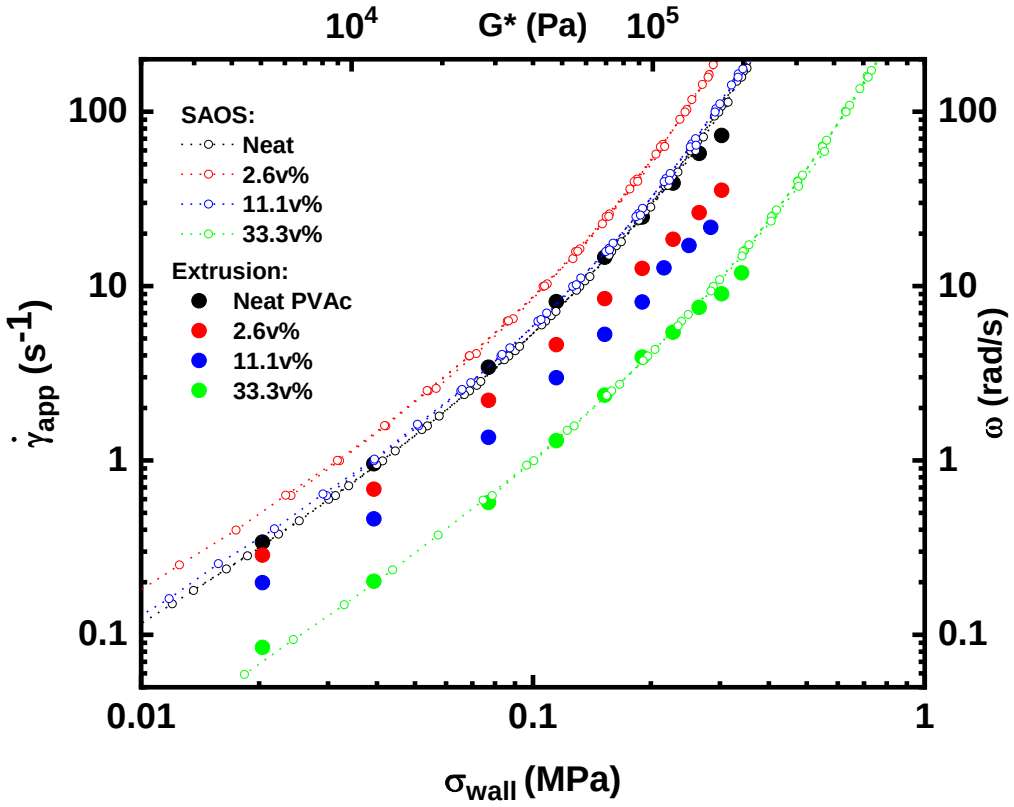

Figure 4.7: Extrusion flow curve for all PNCs with R_{NP} = 40 nm. Shear strain vs stress at the wall for neat PVAc and various PNCs with R_{NP} = 40 nm.

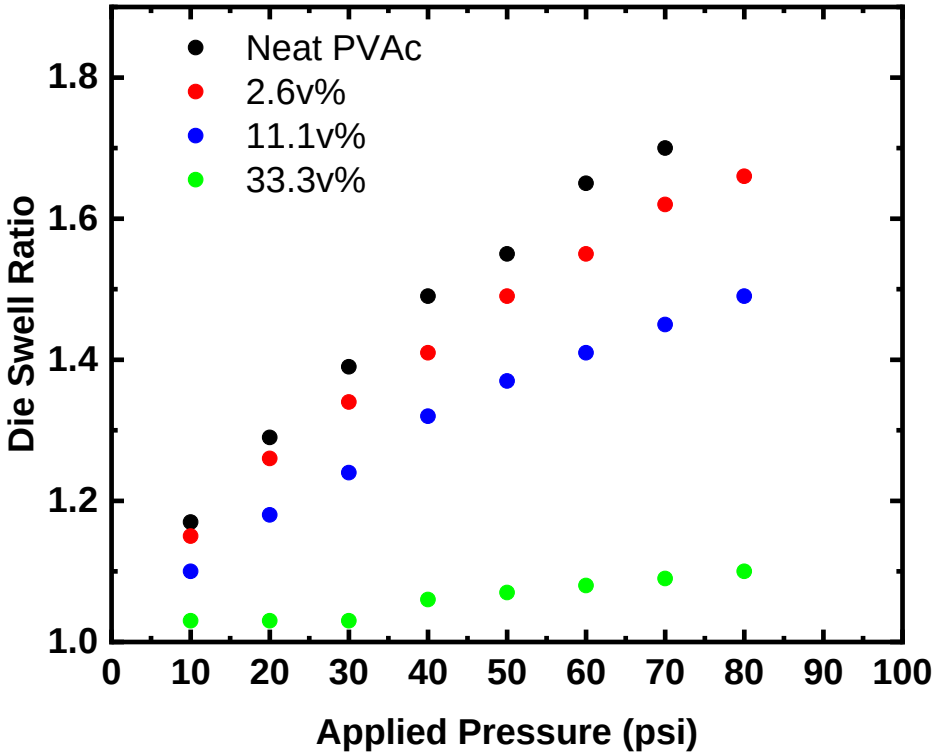

Figure 4.8: Die swell for all PNCs with R_{NP} = 40 nm.

Microscopically, the samples also exhibit fascinating changes in their respective NP dispersion. Even at the lowest pressures, the 2.6v% PNC exhibits NP agglomeration, specifically near the sample edge where there exists a thick border that runs consistently around the entire sample. Due to the localized increase in particle density at the edge, it is not surprising that the core of the sample has large areas of polymer without NPs visible; but perhaps it is more surprising therefore that the NPs observed in the core are still grouped into clusters more frequently than not. As the pressure is increased, the uniform thickness of the edge boundary region disappears and the overall thickness appears to shrink, although the packed edge is still present to some degree throughout the shear-thinning regime. Only at 80 psi are any areas of the edge not packed with NPs, and by this point there is also seemingly an increased presence of individual NPs observed interspersed with the clusters of the NPs within the core areas of the samples, which seemed to

correspond with the end of the shear-thinning regime into the beginning of the chain stretching regime as the first noticeable increase of individual NPs appeared at 60 psi. Images corresponding with these observations can be found in Appendix III. Observations for the 33.3v% PNC are more difficult due to the increased presence of the NPs throughout the sample; however, there are still clear observational differences in the appearance of this sample's edge and core regions as the pressure changes. In the two lower loadings, the appearance of bands across the cross-face of the extrudate signified the location of increased NP presence; however, in the 33.3v% cross-sectional face these regions have largely, but not entirely, disappeared due to the high concentration of particles in most areas. Whereas the 2.6v% PNC had a well-defined packed edge region and the 11.1v% PNC seemed to feature packed regions randomly spaced across the sample, it is therefore interesting to see that the 33.3v% sample at low strain rates appears to have a concentration gradient around the edge that is particle rich for large stretches while simultaneously particle sparse for other large stretches. As the pressure is increased into the shear-thinning regime, this gradient disappears, and the particle-sparse bands are observed to be narrow and spread out across the sample – as shown in fig. 4.9. Surprisingly, by the highest pressures, the edge gradient has returned, including its inconsistency with both NP-rich and NP-sparse regions and even the thickness of the band, at 2-3 μm, is consistent with the lower pressures. Thus, the high flow rate seems to prevent the NP clustering, in sharp contrast to the strong NP clustering at low flow rates. Imaging at higher magnification shows that the NPs are located across the entire face of the extrudate for the 35.3v% PNC, with the lower contrast areas merely covered by a layer of polymer, potentially indicating that the channels are not long-range pathways for the polymer, and a highly irregular flow field without an overarching shape in the transverse-flow plane exists. This would directly contradict the belief that the transverse flow field affects NP migration in a uniform manner; however,

without observing multiple cross-section faces from each pair of sample and pressure conditions this is merely a speculative observation. Once again, further images corresponding to these observations can be found in Appendix III.

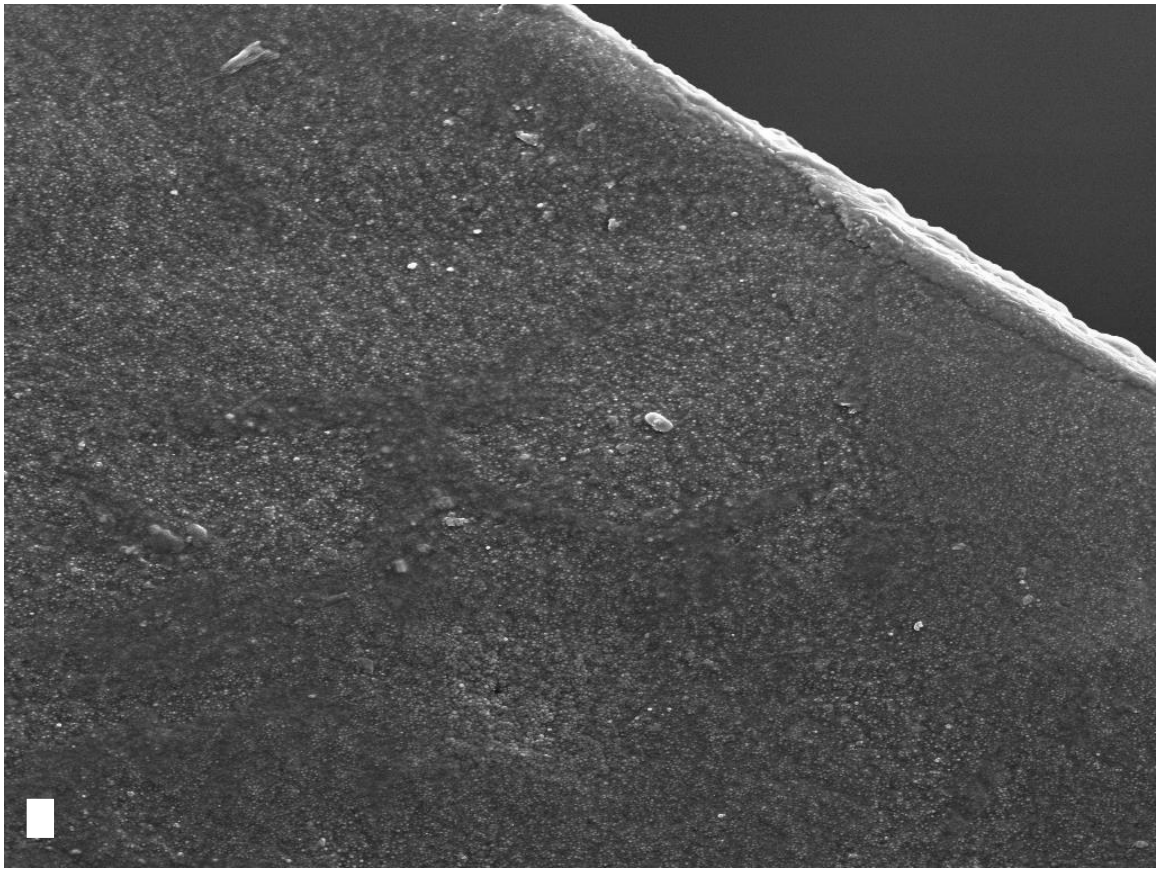

Figure 4.9: 33.3v% PNC with R_{NP} = 40 nm extruded at applied pressure of 40 psi. Scale bar is 500 nm.

4.3.4 Nanoparticle Size Effect

That the three different loadings with R_{NP} = 40 nm behaved so differently is surprising, though it has been mentioned that increasing the loading may actually help prevent some phase separation from occurring.[117] Additionally, it was stated that decreasing the NP size could have the same effect, so PNCs with similar φ_{NP} were made with NPs of R_{NP} = 23 nm. A comparison of the flow curves for these PNCs with differences in R_{NP} compared directly against one another are

featured in figs. 4.10, 4.11, and 4.12. The extrusion curves of the 2.4v% and 14.5v% (R_{NP} = 23 nm) in the shear-thinning regime closely align with the curves for the larger NP size; however, there is a difference at the highest loading, due to the curve's irregular non-linearity. The most important note though is the variance between the extrusion curves for the intermediate loadings in the zero-shear response regime. The φ_{NP} = 11.1v% (R_{NP} = 40 nm) sample images show NPs can be found along the edge at any applied pressure while appearing to decrease slightly in concentration with increased pressure, while the flow curve maintains a shape similar to that of the neat polymer while featuring noticeably lower strain values. Alternatively, for the φ_{NP} = 14.5v% (R_{NP} = 23 nm) sample a polymer-rich boundary originally exists at the lowest pressures, where the data points of the extrusion curve are more closely aligned with the neat polymer curve than its corresponding PNC. As the applied pressure increases the concentrations of the NPs at the edge are also increasing and the extrusion flow curve transitions towards a better fit with the corresponding R_{NP} = 40 nm PNC curve, as mentioned above. These differences, with representative images provided in fig. 4.13, could be because the extrusion process is directly measuring the sample interactions against the wall, as opposed to across the entire sample, so the variations in edge composition across samples, or even just non-uniformity along the edge within a single sample, becomes one of the key observations of these images. Given that, and the observation that the highest φ_{NP} PNCs appear most similar in edge characteristics, it is no surprise that in terms of die swell the 35.3v% (R_{NP} = 23 nm) PNC again behaves the most similarly to its large NP counterpart, as shown in fig. 4.14. Another layer of consideration for the smaller NPs is that there is a significant increase in interfacial area and bound polymer, which could lead to reduced polymer movement; however, the samples with smaller NPs have significantly improved the polymer's ability to relieve the stress as the 2.4v% and 14.5v% (R_{NP} = 23 nm) samples actually

feature greater die swell than similar loadings with larger NPs. Interestingly, the 2.4v% (R_{NP} = 23 nm) sample's die swell nearly matches the neat polymer across the entire pressure range. While the 14.5v% (R_{NP} = 23 nm) features a discrepancy in die swell values between its larger R_{NP} PNC, the curve shapes still closely mirror one another. Finally, at the highest loading, the NP size difference is not as impactful as the curves more closely resemble one another. This could be an indication that the high loading itself is obtruding polymer flow, as opposed to the increase in interfacial area and bound polymer reducing polymer movement.

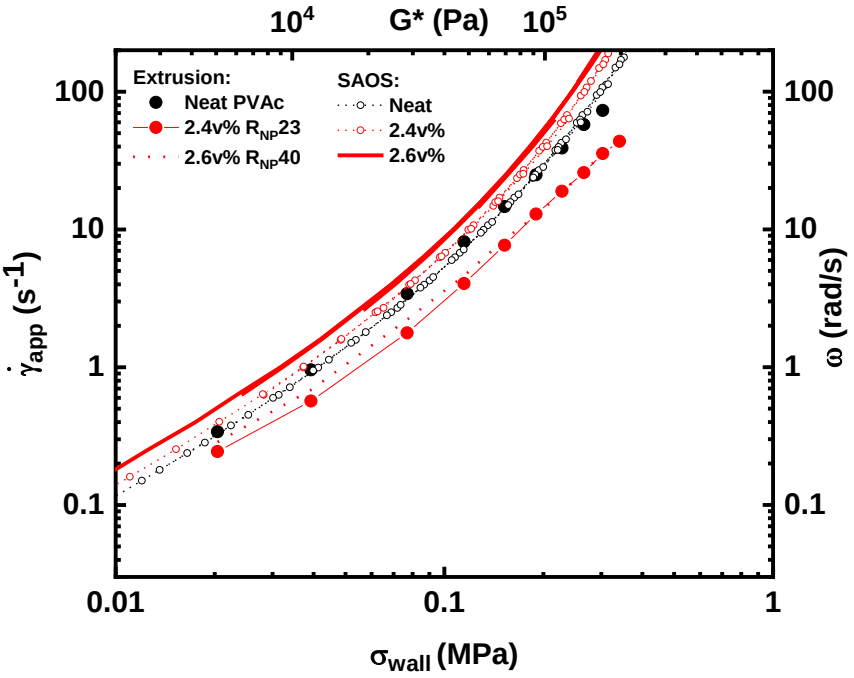

Figure 4.10: Flow curves comparison for lowest φ_{NP}. Stress-strain curves and overlapping portion of SAOS master curve shown for φ_{NP} = 2.4 v% with R_{NP} = 23 nm and φ_{NP} = 2.6 v% with R_{NP} = 40.

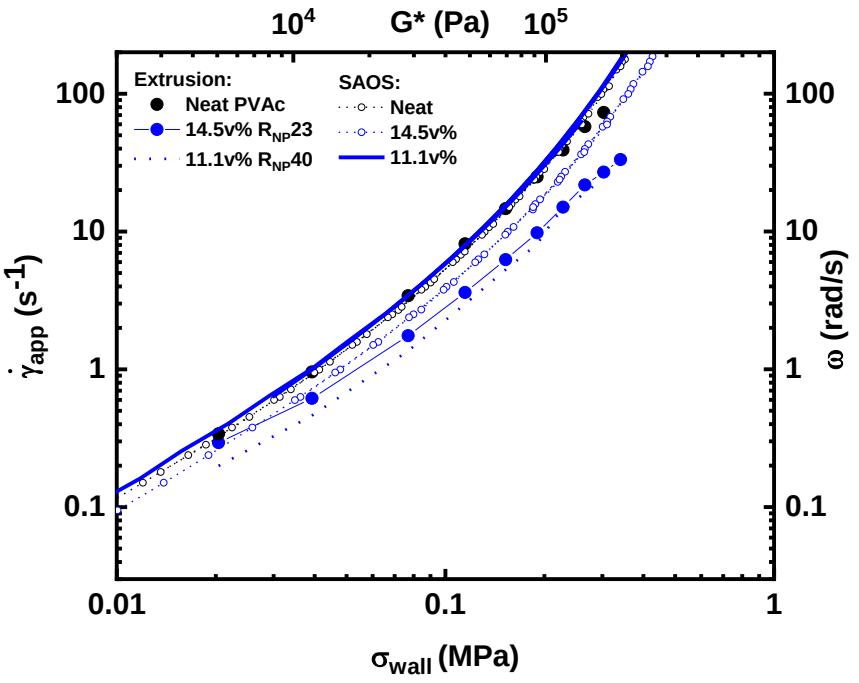

Figure 4.11: Flow curves comparison for intermediate φ_{NP}. Stress-strain curves and overlapping portion of SAOS master curve shown for φ_{NP} = 14.5 v% with R_{NP} = 23 nm and φ_{NP} = 11.1 v% with R_{NP} = 40.

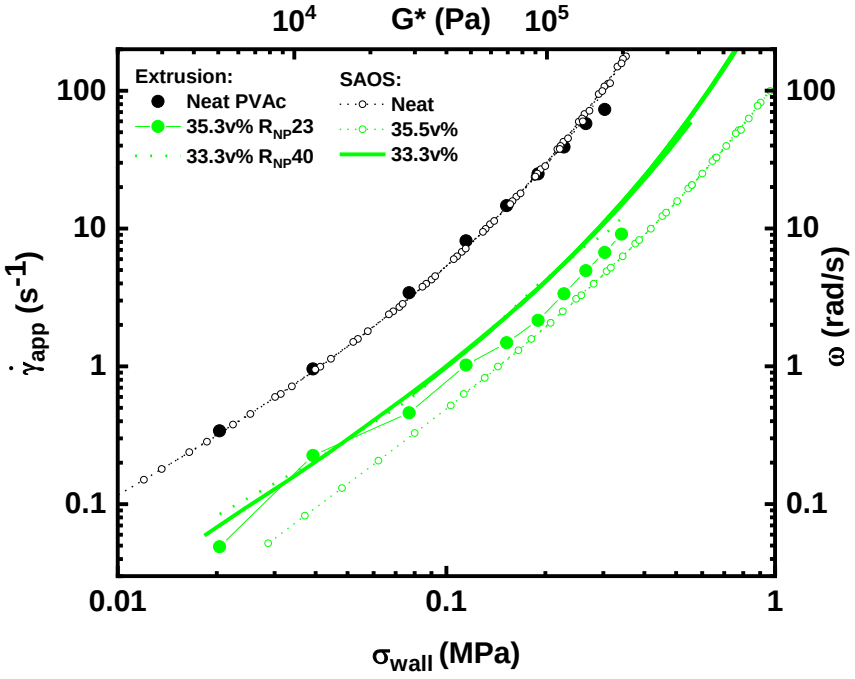

Figure 4.12: Flow curves comparison for highest φ_{NP}. Stress-strain curves and overlapping portion of SAOS master curve shown for φ_{NP} = 35.3 v% with R_{NP} = 23 nm and φ_{NP} = 33.3 v% with R_{NP} = 40.

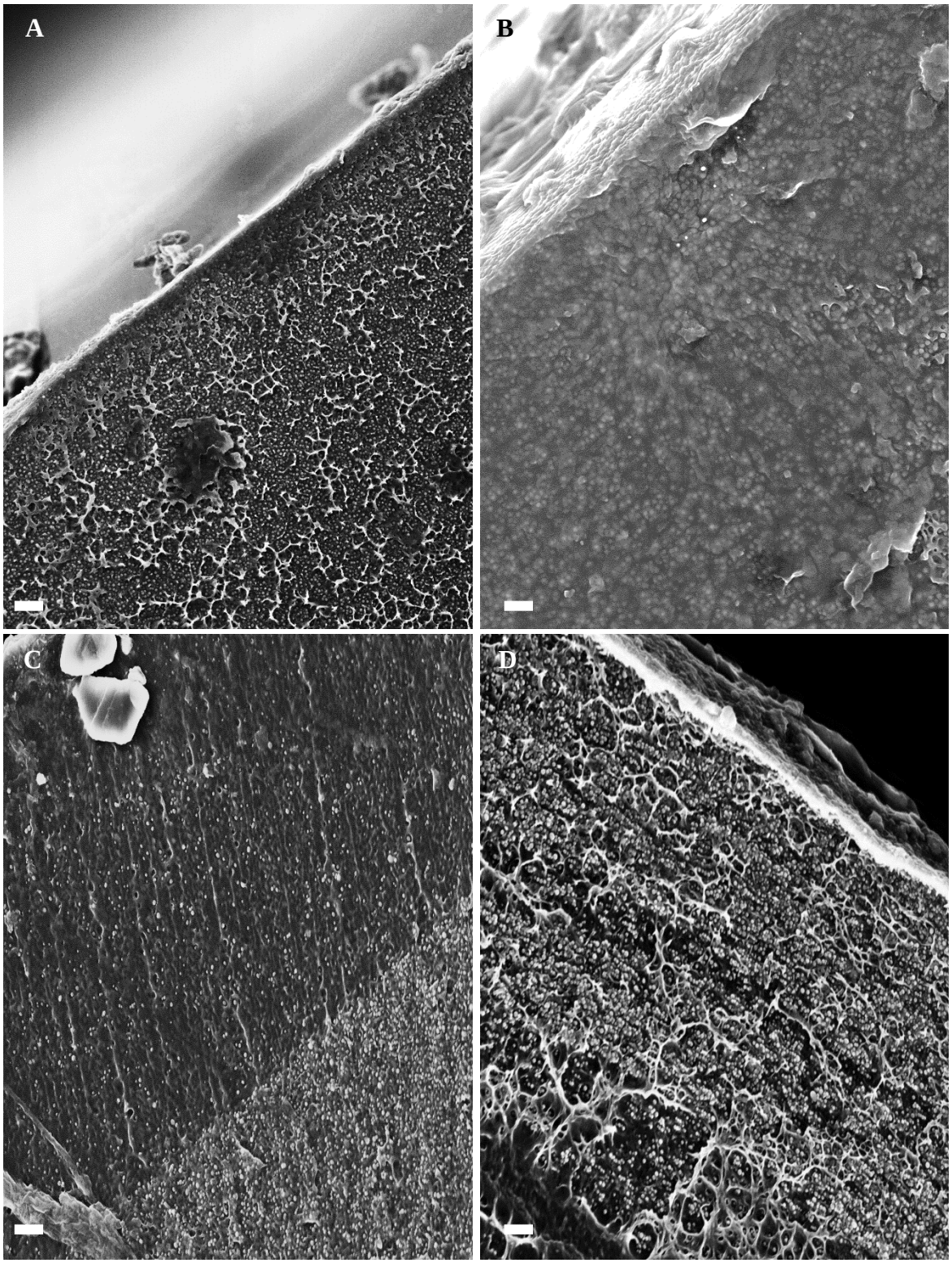

Figure 4.13: Comparison of edge evolution at intermediate φ_{NP}. Images show how the edge changes for φ_{NP} = 11.1v% R_{NP} = 40 nm from a) 5 psi to b) 80 psi applied pressure in comparison to φ_{NP} = 14.5v% R_{NP} = 23 nm from c) 5 psi to d) 80 psi with 500 nm scale bars.

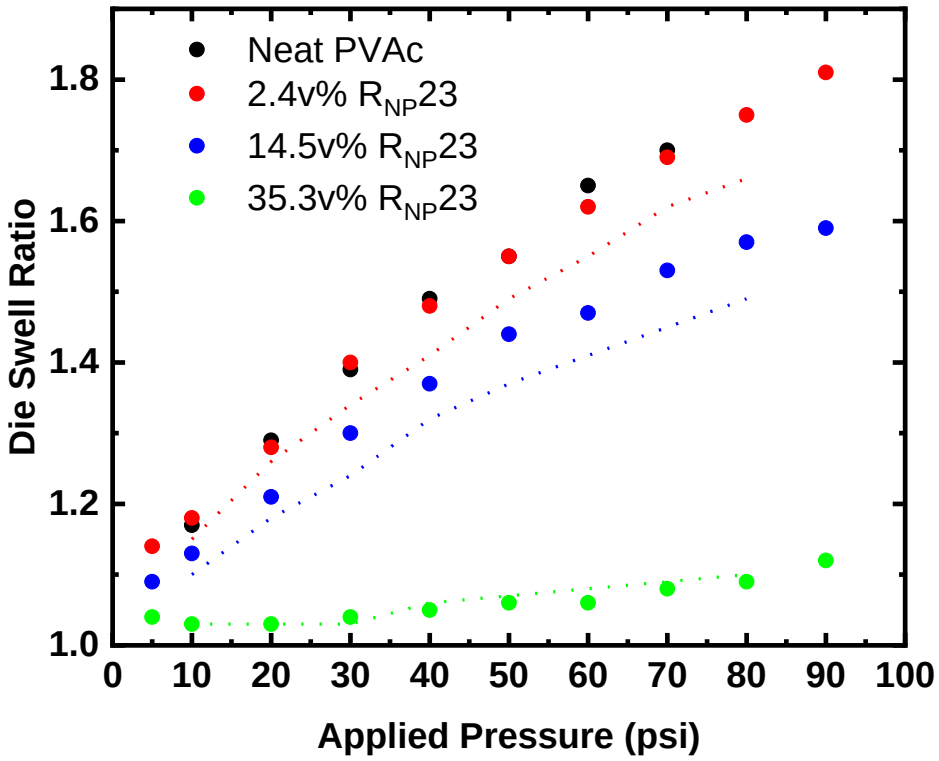

Figure 4.14: Die swell for all PNCs with R_{NP} = 23 nm. Data points show the R_{NP} = 23 nm curves while the dashed lines show R_{NP} = 40 nm.

The image-based observations of the R_{NP} = 23 nm group of samples also offer key differences to their larger-sized PNC corresponding samples, with images located within Appendix III. For 2.4v% (R_{NP} = 23 nm) the observations are immediate and stark: not only is there no NP aggregation at any pressure, but there is no discernable difference between the edge regions and core regions in the first flow regime. There are certainly still particle-dense and particle-sparse regions, but their locations on the sample exist randomly. As the applied pressure increases, the NPs migrate into smaller spaces with large regions dominated by the polymer bulk, although the NPs remain primarily individually dispersed within the matrix. Once in the shear-thinning regime, the edge becomes almost exclusively polymer. Additionally, at this point the bands of particle-dense regions have become more localized and are less consistent as they cut across the entire cross-sectional face of the sample, which could be an indication that the polymer flow has significantly increased randomness. It is important to note the polymer dynamics of the sample

have not been influenced by the change in NP size as the traditional SAOS curves, shown in fig. 4.15, are nearly identical for the lowest loading. This indicates that the change in NP migration is due to the NP size change, which is primarily a difference in total NP surface area / interaction volume and the NP spacing as smaller particles are present in greater quantities to make up the same total volume.

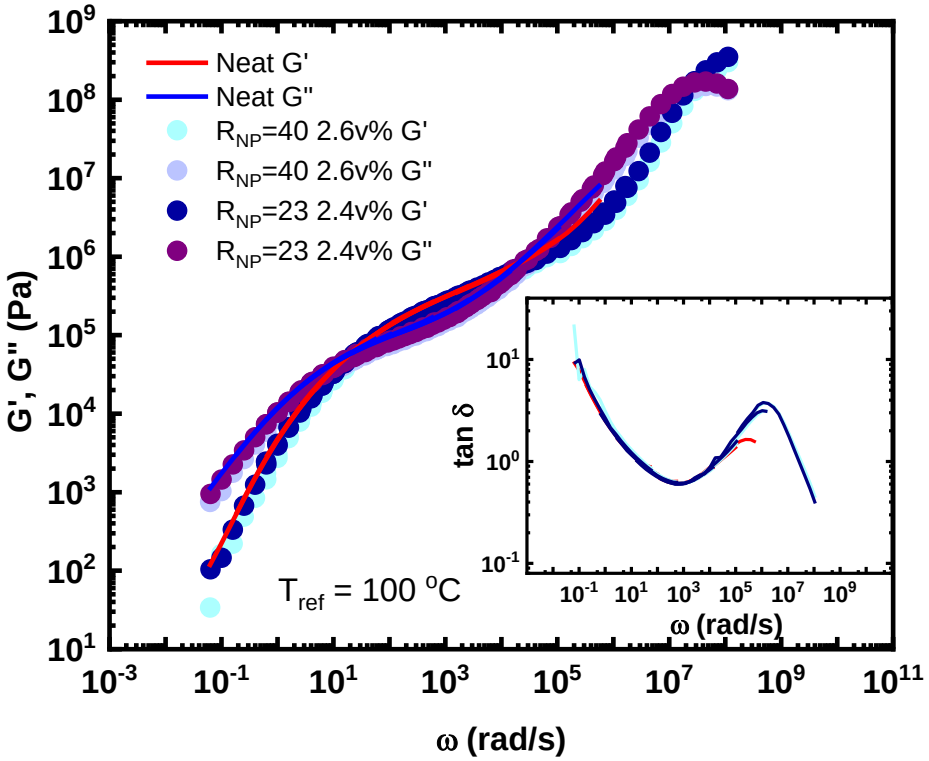

Figure 4.15: SAOS comparison for lowest φ_{NP}. Master curve comparison for the PNCs of varied NP size at low filler loading.

The moderate loading for R_{NP} = 23 nm, 14.5v%, offers yet another new perspective – different from both the 2.4v% (R_{NP} = 23 nm) PNC, but also the 11.1v% (R_{NP} = 40 nm) PNC – as the cross-sectional face of the zero-shear linear response regime has rings similar to the suggested formation of concentration gradients in Newtown fluids. However, unlike the observations of Newtonian fluids these rings are not uniformly spaced around the center of the channel, the rings themselves are actually particle-sparse and not particle rich, and lastly, the rings are not the major concentration gradients within the face as other boundaries exist. In addition to the rings, the edge

of the sample in the zero-shear linear response is a 5-9 μm thick polymer dominated region, which is considerably thicker than the bands in the 33.3v% (R_{NP} = 40 nm) PNC sample. As the extrusion process enters the shear-thinning regime, the once circular rings fold into themselves and the appearance of bands across the face becomes more prominent, although the appearance of rings is still visible even once the chain-stretching regime is reached for this sample. Yet while the cross-sectional appearance is maintained, the edge shifts from polymer dominated in the zero-shear response regime to particle dominated once well into the shear-thinning regime. Interestingly, the edges end up not well defined in the highest applied pressure, which is how the PNCs with larger NPs were observed to be as well with some sections highly populated and others more open. By the highest applied pressures, the broad appearance of the sample more closely resembles its counterpart with larger NPs as well, with a particle-dense edge and large areas of packed, yet individually dispersed, NPs surrounding smaller pockets of particle-sparse areas. Once again, despite the dramatic observational differences, the SAOS master curves of the similarly-loaded PNCs are remarkably similar across the NP sizes, as shown in fig. 4.16, leaving all shear-deformation response variations to the change in NP size and associated surface area.

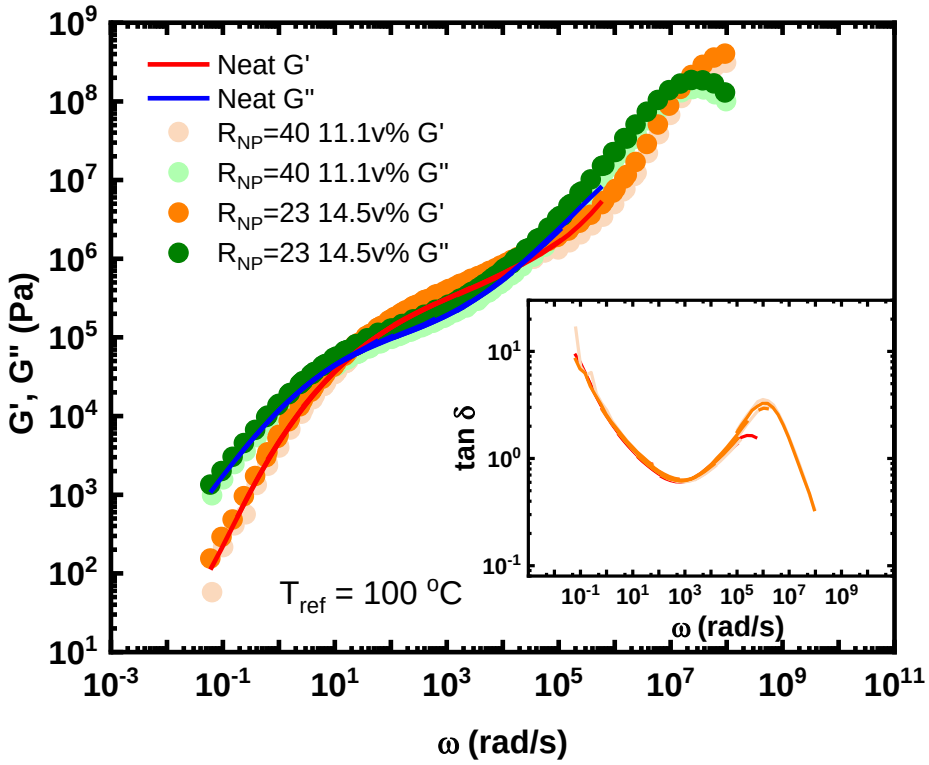

Figure 4.16: SAOS comparison for intermediate φ_{NP}. Master curve comparison for the PNCs of varied NP size at an intermediate filler loading.

Finally, a third R_{NP} = 23 nm PNC matching the highest loading, 35.3v% (R_{NP} = 23 nm), was extruded and imaged via SEM. From a flow curve standpoint this sample has the largest difference after reducing R_{NP}, as seen in both the extrusion curve in fig. 4.10 and the SAOS master curve in fig. 4.17 as well. Alternatively, the die swell curve and image observations between the samples are the closest. Initially, there are highly packed regions of the NPs throughout the face of the sample, with some on the edge as the core, but there are also areas with more pockets of polymer throughout the sample as well. This was true of the larger R_{NP} as well and was suggested that with such a high packing the polymer must flow through whatever space it can make and can no longer hold a preference for where those spaces are located. The number of large bands crossing the sample have also decreased, again potentially implying that the high turbidity of the flow field has dissolved any long-range flow channels. As was the case previously, while the cross-sectional faces still have highly contrasting regions the higher magnification images show that the darker

areas are not devoid of the NPs as is the case in PNCs with lower φ_{NP}. Rather, the particles are merely covered by a layer of polymer and appear to have similar packing densities as those closer to the surface, which was another similarity between this pair of PNCs.

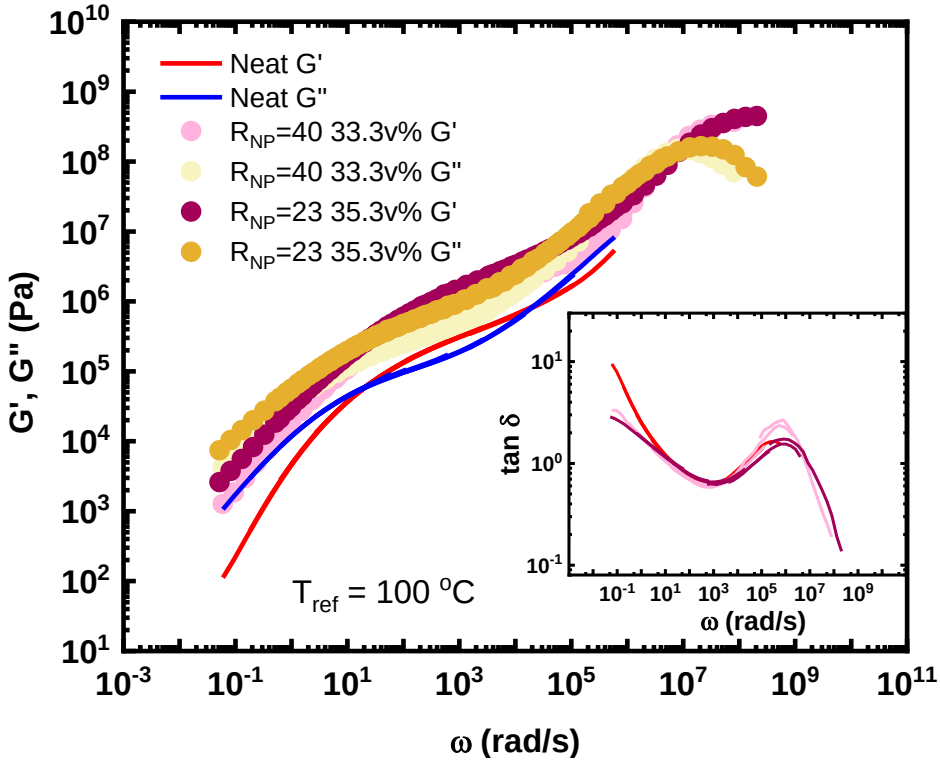

Figure 4.17: SAOS comparison for highest φ_{NP}. Master curve comparison for the PNCs of varied NP size at the highest volume fraction of filler loading.

4.4 Conclusions and Outlook

In a comparison between the SAOS master curves and the extrusion stress-strain curves, the neat PVAc and highest loadings for both NP sizes are in good agreement with one another while the lower and intermediate φ_{NP} composites have an apparent shift in their curves despite maintaining similar shapes. A few possibilities exist to explain this observation. First, the extrusion flow data for the PNCs have not been corrected using an orifice die, where the die entry pressure loss influence on the stress measurements can be accounted for by shifting the data against the curve of a die with the same entry angle and diameter but a length of 0. These corrections could bring the two curves into alignment with one another, though without performing the corrections

it is unknown how significant any potential shift would be, while also bringing the highest loading potentially out of alignment. A second alternative is that the disparity is real and caused by the thickness of the NPs at the edge of the extrudate samples. Unlike the SAOS curves, which are based on the response of the entire sample's polymer matrix, the extrusion measurements are only sensitive to the polymer at the wall. The formation of thick polymer edges as the applied pressure increases is therefore a significant observation. Likewise, a comparison of the difference in edges between similarly-loaded samples can aid the understanding with regard to extrusion flow curve differences across the NP sizes. Specifically, the contrast between the φ_{NP} = 11.1v% (R_{NP} = 40 nm) sample and the φ_{NP} = 14.5v% (R_{NP} = 23 nm) sample and the evolution of their edge against the comparison of their flow curves is particularly interesting and justifies the belief that the difference in the shape of the curve is at least partially the result of the NP concentration in edge regions. Ultimately, it is most likely that both of these conditions play a role to some degree, but without the orifice corrections it will remain unknown just what effect is due to the NPs at the edge and what is the result of die entry pressure loss. Despite this concession, it should already be considered a successful use of advanced imaging technology to make these direct-space observations of the extrudate phase separation behaviors of PNCs. Going forward, careful experimental design can utilize this technology to observe specific flow behaviors of PNCs, whether through the measurements of additional L/D dies to study stress relief, varied entryways to study the effects of entry pressure loss, or even simply imaging multiple cross-sections from various points of an extended isobaric run to observe flow field evolution and stabilization. This work opens the door for many exciting possibilities to better understand an important challenge relevant to polymer composite extrusion processing practices.

CHAPTER 5: CONCLUSIONS AND OUTLOOK

5.1 Conclusions

Polymer composites continue to grow in industrial importance due to the wide range of desirable functional properties and applications available. Understanding the relationships between processing, the microstructure of filler materials, and the final macroscopic properties is therefore crucial to developing a finished product that is fully optimized. This work has shown how the advanced imaging technology available in Scanning Electron Microscopes can be combined with small-angle scattering experiments to provide direct-space measurements of nanoparticle rearrangement across polymer deformation. Polymer composite behaviors during deformation can be very complex and are inherently dependent on the various aspects of deformation such as mode and rate. Because the nanoparticles are much larger in size than the polymer chains, their rearrangement is subject to the polymer deformation response and are independent of the much slower diffusion speeds, but unlike the individual polymers the particles are observable by advanced imaging techniques. Therefore, observation of the NP rearrangement during deformation provides crucial information to increase the understanding of the PNC deformation response, as well as provides the microstructural evolution of the PNC that the macroscopic properties are dependent on.

A review of the fundamentals of the SEM technology revealed how certain imaging parameters, such as the accelerating voltage, E_0, and various detection and imaging modes are able to be applied to optimize polymer images. Furthermore, it was shown how to determine the escape depth of the signal relative to a PNC sample and use the information to reveal the conditions when a single layer of nanoparticles within the PNC bulk would be observed. Modification of existing metals methodologies was then applied to determine the spacing of the NPs within the imaged

plane, even affording the ability to compare directly against small-angle scattering experimental results.

This new methodology was then applied to analyze the NP spacing during uniaxial extension measurements. The results provide interesting details of the polymer deformation behaviors, most importantly showing the deviation of nanoscale microstructural rearrangement from the macroscopic deformation field and the breakdown of the affine deformation principle in PNCs. These results also uncovered evidence of a strain rate affect within the NP rearrangement, as the NP rearrangement was strongly influenced by the applied strain rate. These observations reinforce the characteristics of hydrodynamics interactions between particles, wherein the combination of hydrodynamic forces and the externally applied deformation field result in unique trajectories for individual NPs as a product of their local environment. At lower strain rates the hydrodynamic forces dominate the particle rearrangement, sometimes leading to the formation of localized clusters. As the strain rate increases, the particles more closely follow the macroscopic deformation field, but are still affected by the hydrodynamic forces and as a result deviate from the affine prediction.

Advanced imaging techniques were also used to make phase evolution observations of PNCs across the complex shear deformation of an extrusion process. Although the flow curves have not been corrected for die entry pressure loss against an orifice die, the observations across loadings and NP sizes were still intriguing. The observed aggregation of larger NPs at small φ_{NP} and observed evolution of edge concentrations as a function of the applied pressure across several samples provide enough evidence of just how powerful this technology can be to aid the understanding of incredibly important industrial processing conditions and their influence on the end microstructure of PNCs. For the growing applications of polymer nanocomposites in additive

manufacturing, this demonstration of advanced imaging can open the door to future endeavors to directly observe the rearrangement of the nanoparticles in real space, promoting a greater ability to understand polymer nanocomposite response to shear deformation and crucially provide significant insight into how to optimize their macroscopic properties as result.

5.2 Future Outlook

The ideal use of a Scanning Electron Microscope with polymer nanocomposites would be *in-situ* tensile testing in order to directly track NP rearrangement across uniaxial deformation in real time. As stated towards the end of chapter 2, the sample and relevant imaging conditions must be carefully selected in order to make this a reality and perhaps common SEM columns are not yet able to achieve high enough resolution at a low enough beam current to avoid issues common to imaging polymers. However, even without the ability to perform direct NP tracking the advanced imaging technology is ready to be more utilized by polymer science.

The first proposed future work is to continue the use of *ex-situ* NP spacing distribution analysis following the methodologies laid out in this dissertation to further study the influence of the hydrodynamic forces between NPs on their subsequent rearrangement during uniaxial deformation. This continuation should include several experimental factors to fully explore this effect: (i) A significantly high filler fraction, such as $\varphi_{NP} \approx 15$v%, should follow the same procedure laid out in chapter 3. With just over double the volume fraction of the studied 7.4v% PNC, there should be a significant increase in the hydrodynamic forces. At deformation rates $Wi << 1$ this could result in seeing increased aggregation based on the initial observations but it will also be interesting to observe the magnitude of deviation at rates $Wi >> 1$ when that was able to maintain affine principles for larger elongation ratios, λ. (ii) A pair of samples similarly loading with varied NP dispersion at the beginning, such as a 5v% PNC with individually dispersed NPs

and another 5v% PNC with pre-aggregated particles in randomly dispersed clusters. The idea is to provide enough NPs to find several aggregated clusters within the normal field of view, while the other sample serves as the control to match against the initial results. Depending on the size of the clusters, and therefore the volume of polymer trapped within the aggregate, it would be interesting to observe both how the clusters move relative to one another as well as how the particles within the cluster rearrange during deformation. (iii) A sample within the dilute limit, likely $\varphi_{NP} \leq 1$v%, to observe the limits of the hydrodynamic forces. As NPs are spaced further away from one another in the initial dispersion, their influence on one another during deformation should decrease and there could be a critical loading below which the affine deformation principles are microscopically followed. This test would aim to find out if that is the case. Although there must be sufficient NPs within the field of view to perform distribution analysis, which might require a high loading, if the results for $Wi >> 1$ are able to more closely mirror the macroscopic deformation field beyond $\lambda \approx 4$ at any significantly lower loading it should also imply the influence of the hydrodynamic forces as the cause of the deviation from affine NP rearrangement while potentially confirming the existence of a critical loading simultaneously. Any of these three experiments has sufficient merit to be undertaken, and the combination of their results would benefit the understanding of the NP rearrangement during tensile deformation to usher in more complete theories of the behaviors of polymer nanocomposites.

With regard to the next steps in understanding the phase separation behaviors of polymer nanocomposites during shear deformation, further experimentation should also be performed. The current work should have the corrections for die entry pressure loss applied, to guide the observations of the imaged samples more definitively, but there are also additional methods to be tested as well. Notably, since the control of the NP dispersion is a desirable aspect to optimize

many different properties, a study aiming to determine the degree to which phase separation can be controlled is valuable. For example, using functionalized NPs to promote interaction and adhesion between the polymer and the NPs and comparing that to a similarly loaded PNC with particles of the same size but without the surface modifications would be beneficial. If it turns out that NP packing can be reliably tuned to any degree, then the ability to optimize processing practices should benefit industrial applications immensely as the understanding of polymer nanocomposites grows.

In the end, there are still many important challenges in understanding the complex relationships between polymer nanocomposite processing practices, the microstructure of the nanoparticles, and the final macroscopic properties. However, the methodologies discussed and observations made herein promote intriguing possibilities towards uncovering how the microstructural rearrangement of polymer nanocomposites occurs during deformation and how these advanced techniques can be further leveraged to increase the scientific understanding in a manner relevant to the current use of polymer composites.

APPENDICES

APPENDIX A

Delaunay Triangulation Images

A Note Regarding the Organization of Subsequent Images:

This appendix provides the representative images relevant to Delaunay Triangulation analysis. For each sample, multiple images were taken at randomly selected locations within the sample. For each rate and elongation ratio combination three of these locations will be featured below and will present the original Scanning Electron Microscope image, the binary image representing the nanoparticles as black dots on a white field, and the Delaunay Triangulation mapping for that binary image. Most SEM images feature a 500 nm scale bar and a red square with sides representing 500 nm is present on each binary image and SEM images that did not already have a scale bar present. The analytical results are based on the averaged data from all locations, including calculated error based on the number of locations surveyed, since there is a range of nanoparticles present between images based on localized particle concentration fluctuations. However, the observed trends of general spacing distribution should be noticeable in the comparison of these images.

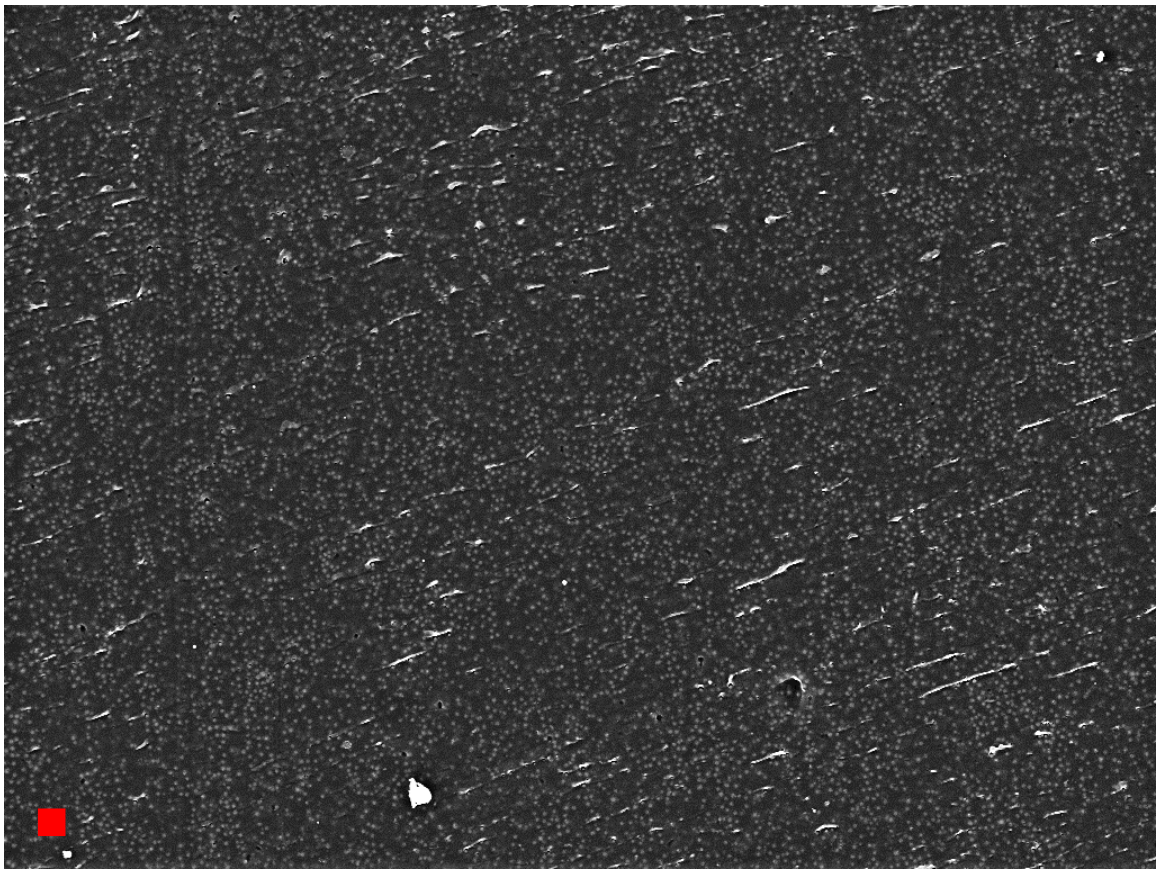

Figure A.1: Undeformed PNC, elongation ratio λ = 1.0: Location 1. This figure contains the original SEM image, corresponding binary image, and Delaunay Triangulation plot of the conditions from the figure title. Scale bars are 500 nm.

Figure A.1 (cont.)

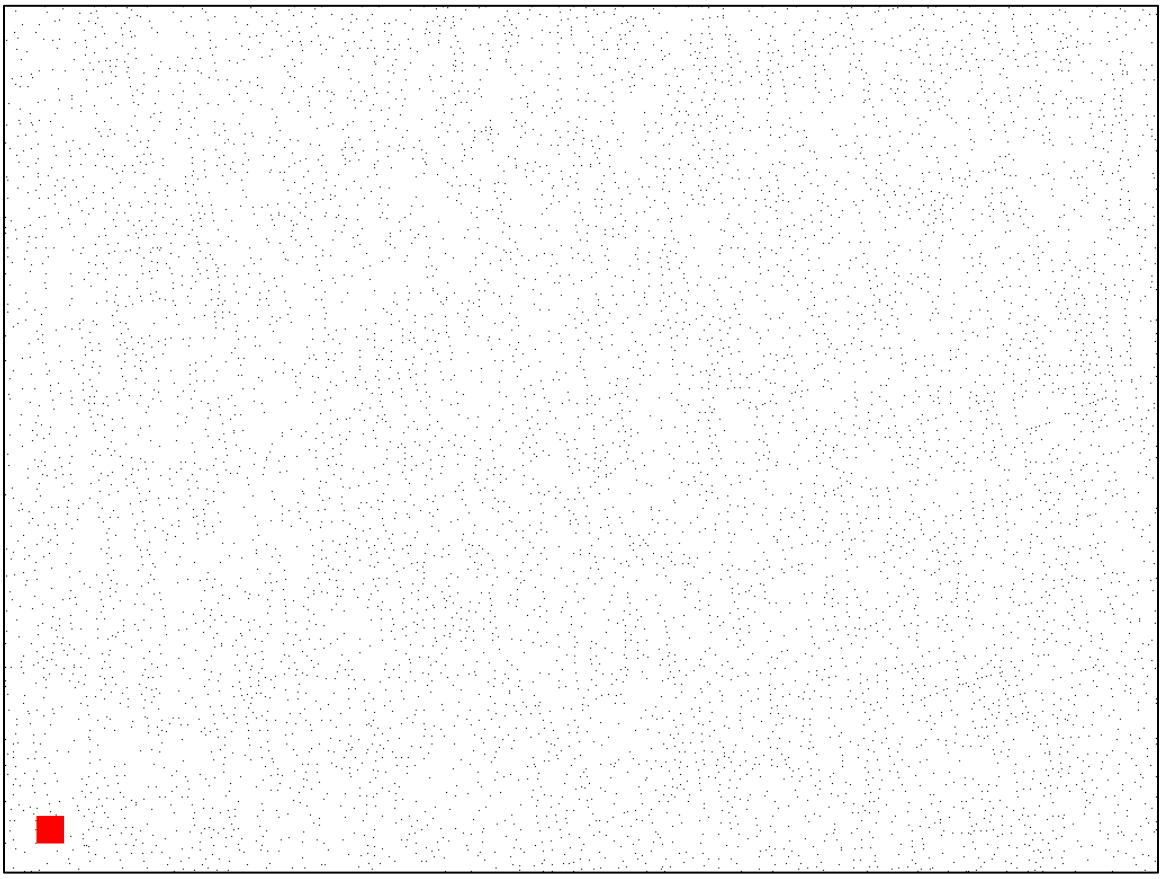

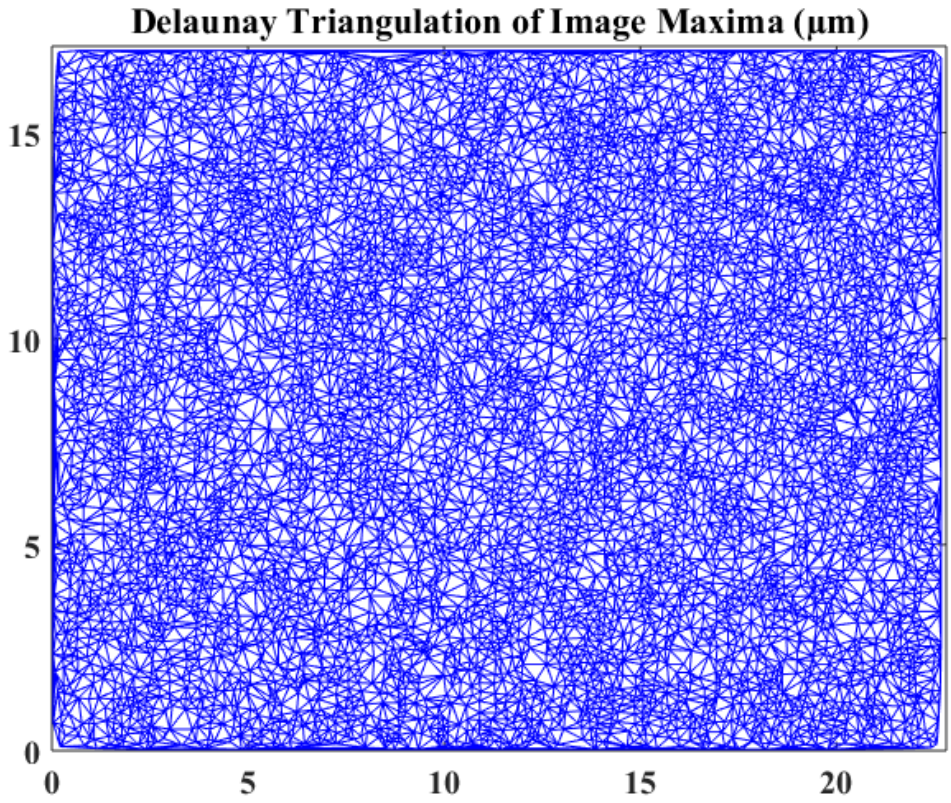

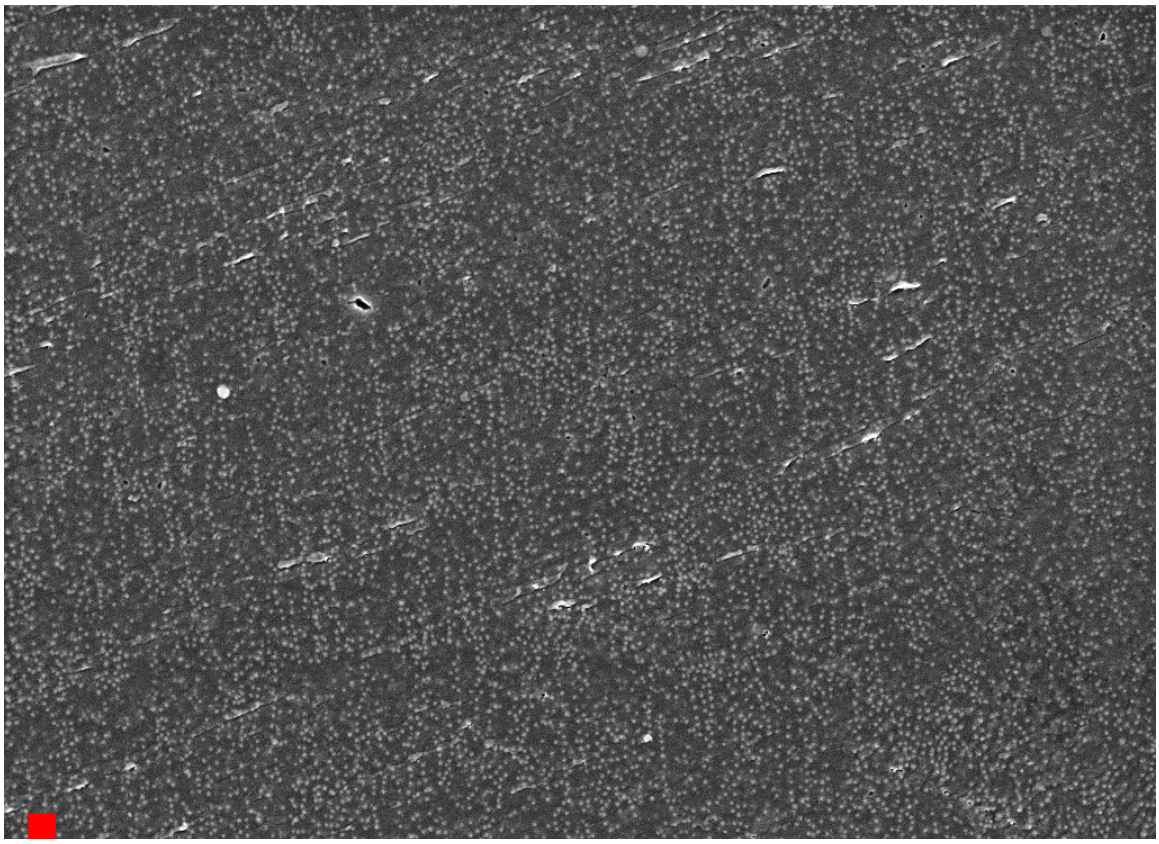

Figure A.2: Undeformed PNC, elongation ratio λ = 1.0: Location 2. This figure contains the original SEM image, corresponding binary image, and Delaunay Triangulation plot of the conditions from the figure title. Scale bars are 500 nm.

Figure A.2 (cont.)

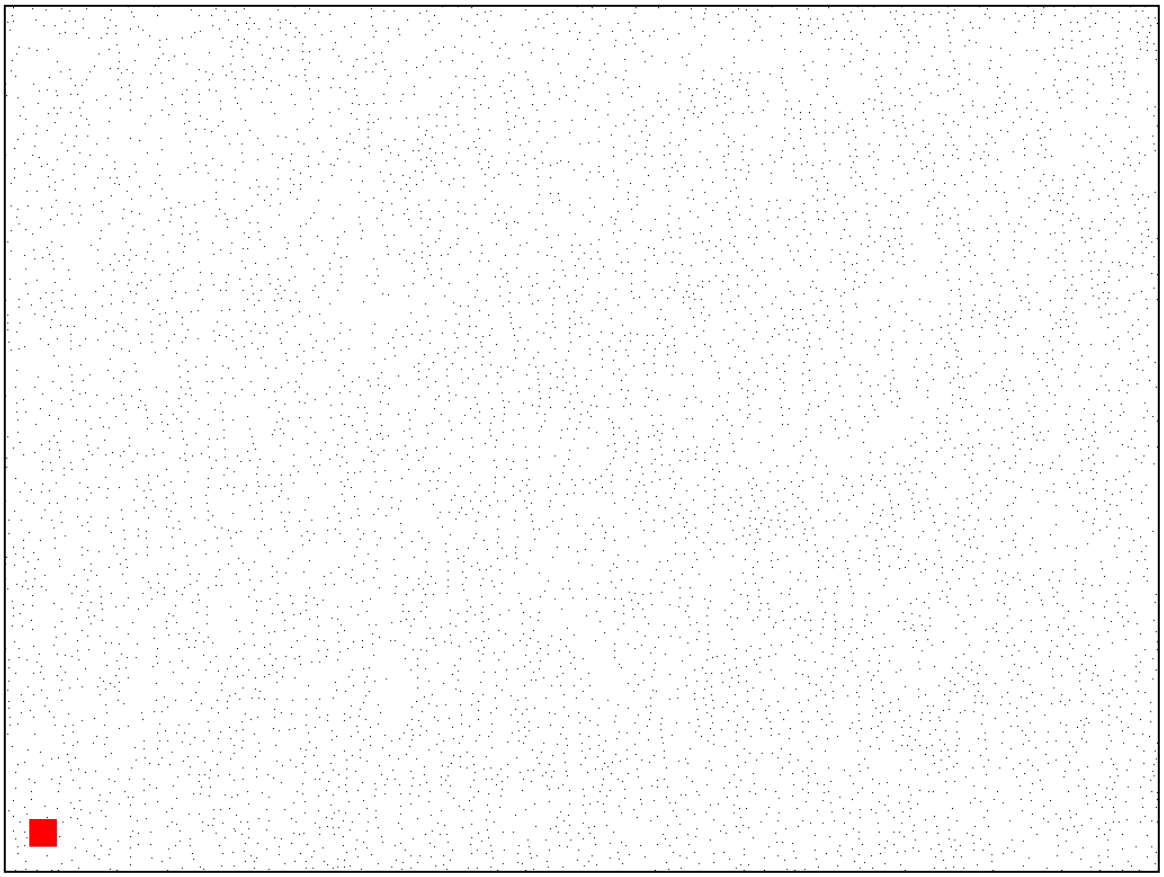

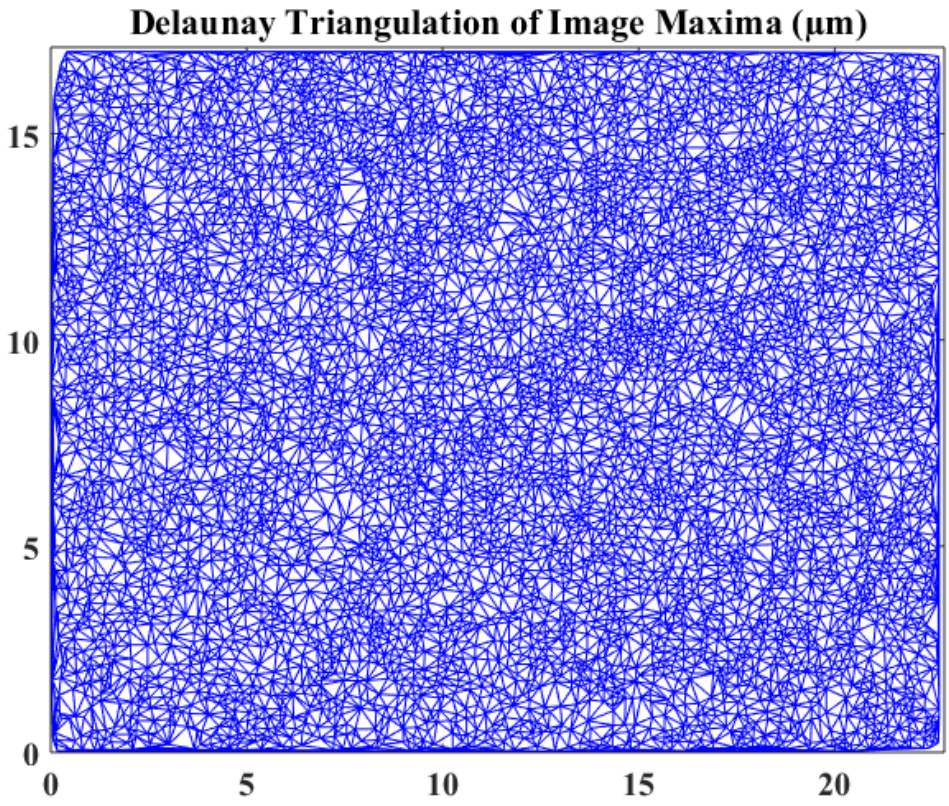

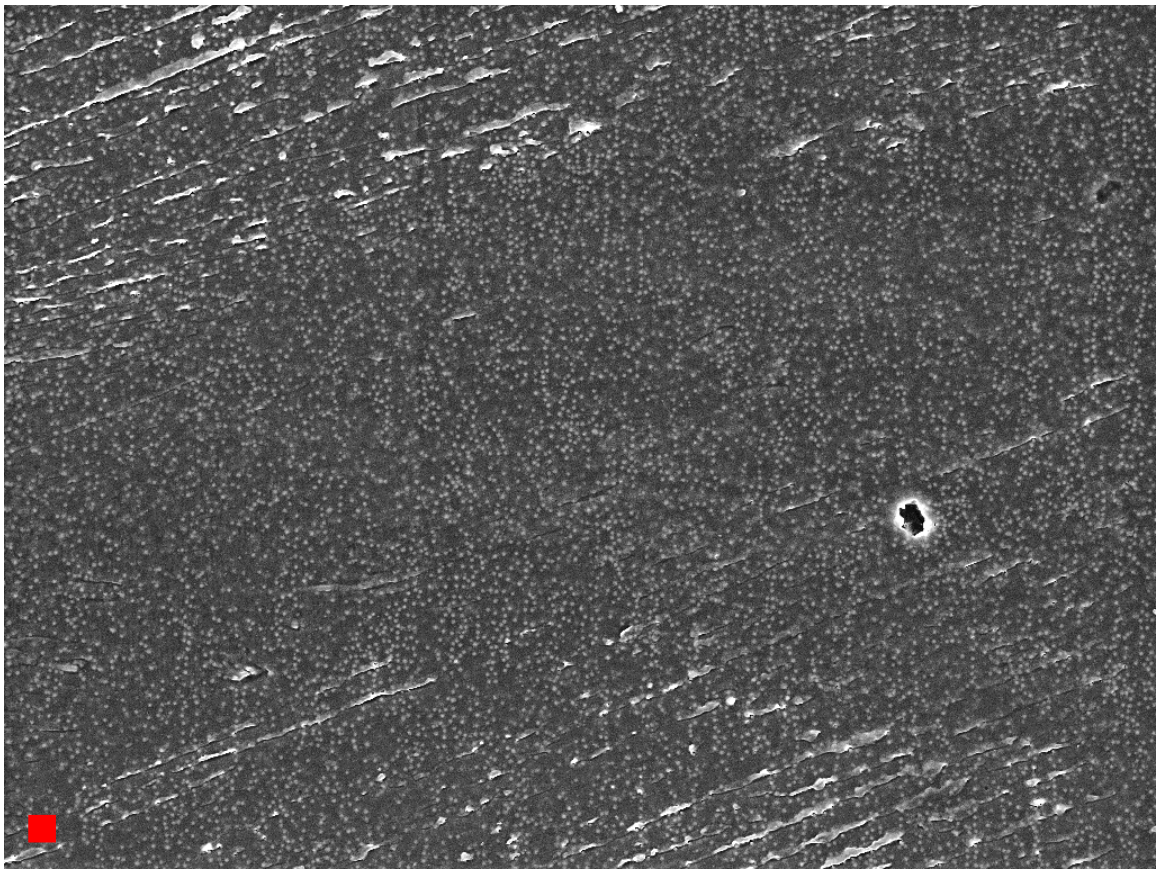

Figure A.3: Undeformed PNC, elongation ratio λ = 1.0: Location 3. This figure contains the original SEM image, corresponding binary image, and Delaunay Triangulation plot of the conditions from the figure title. Scale bars are 500 nm.

Figure A.3 (cont.)

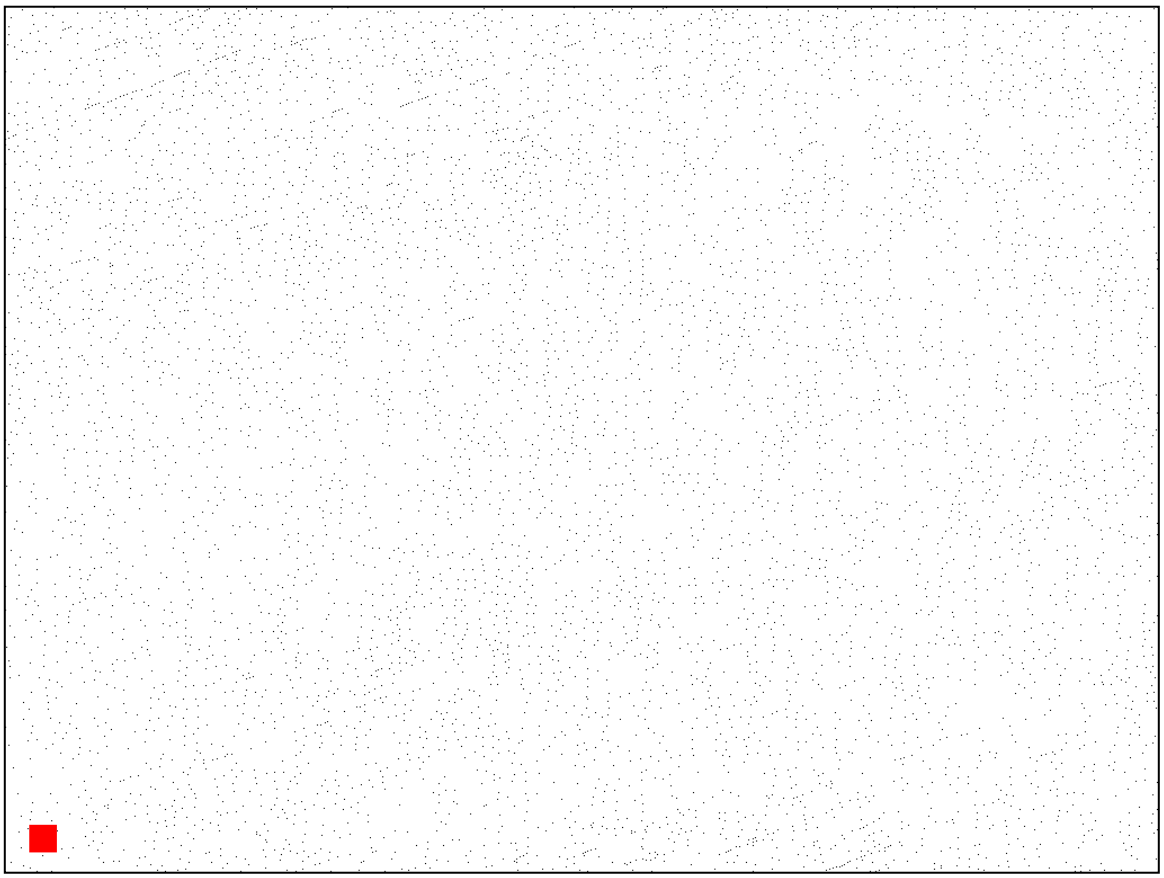

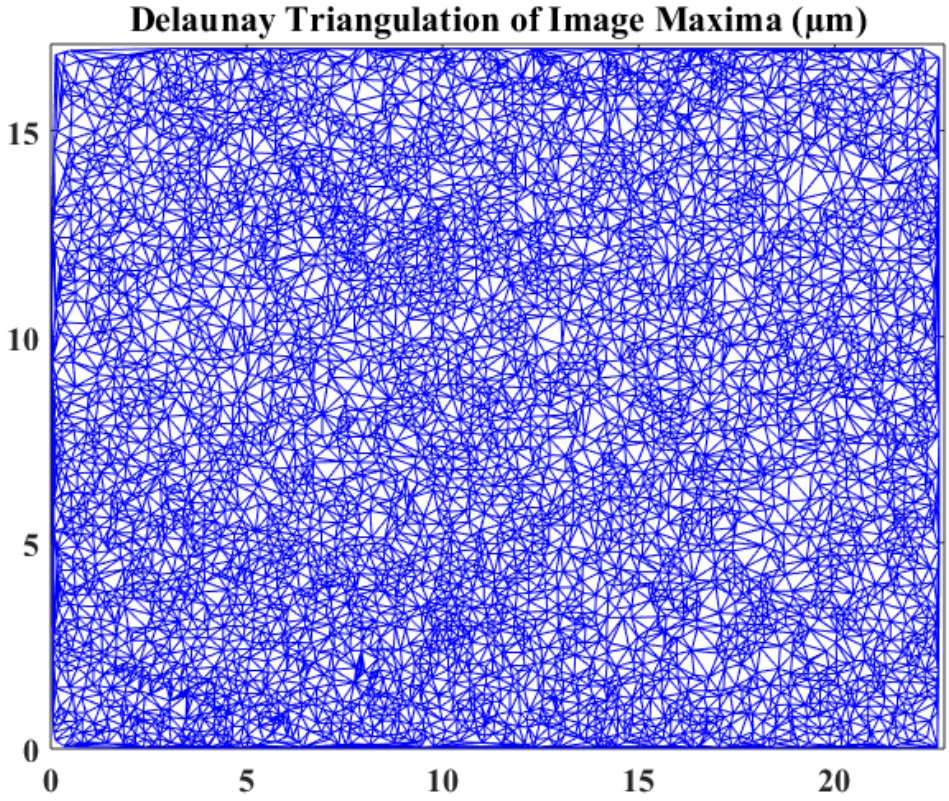

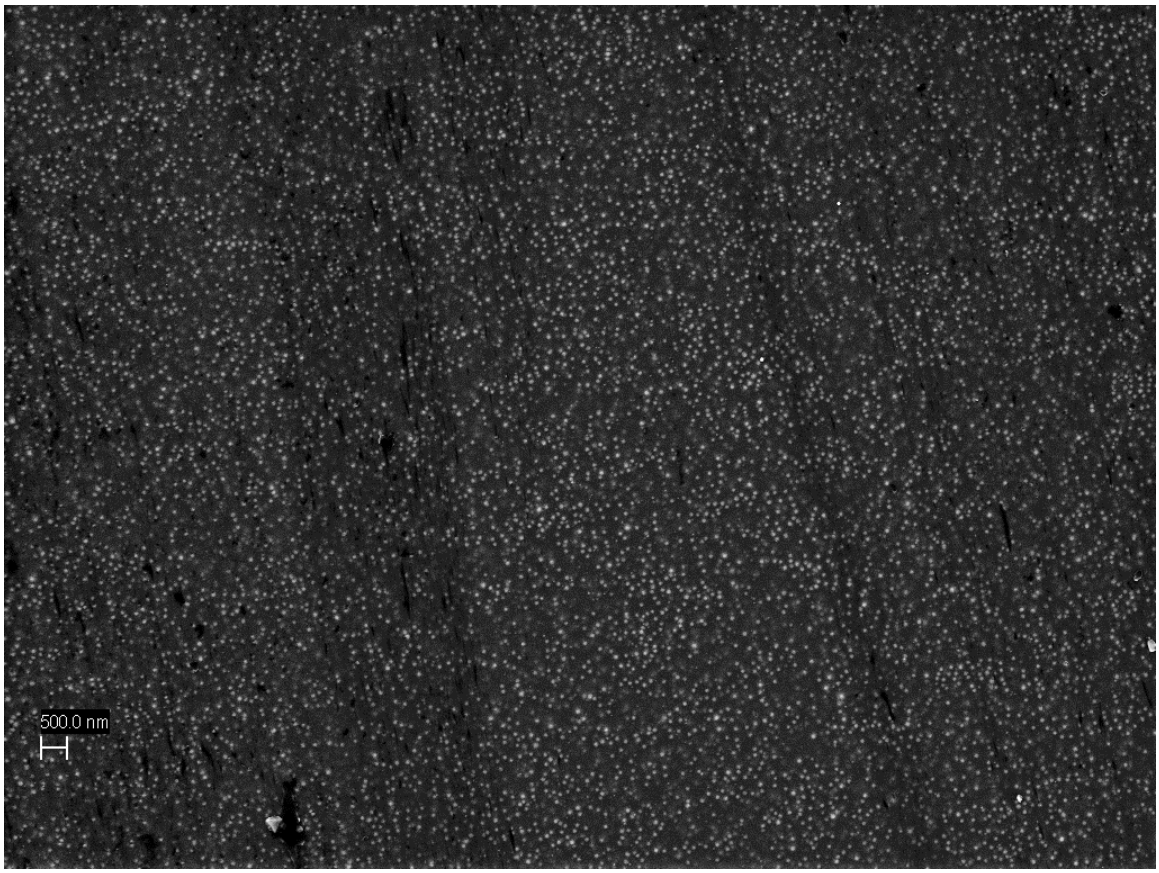

Figure A.4: Deformation rate *Wi* = 0.06, elongation ratio λ = 1.5: Location 1. This figure contains the original SEM image, corresponding binary image, and Delaunay Triangulation plot of the conditions from the figure title. Scale bars are 500 nm.

Figure A.4 (cont.)

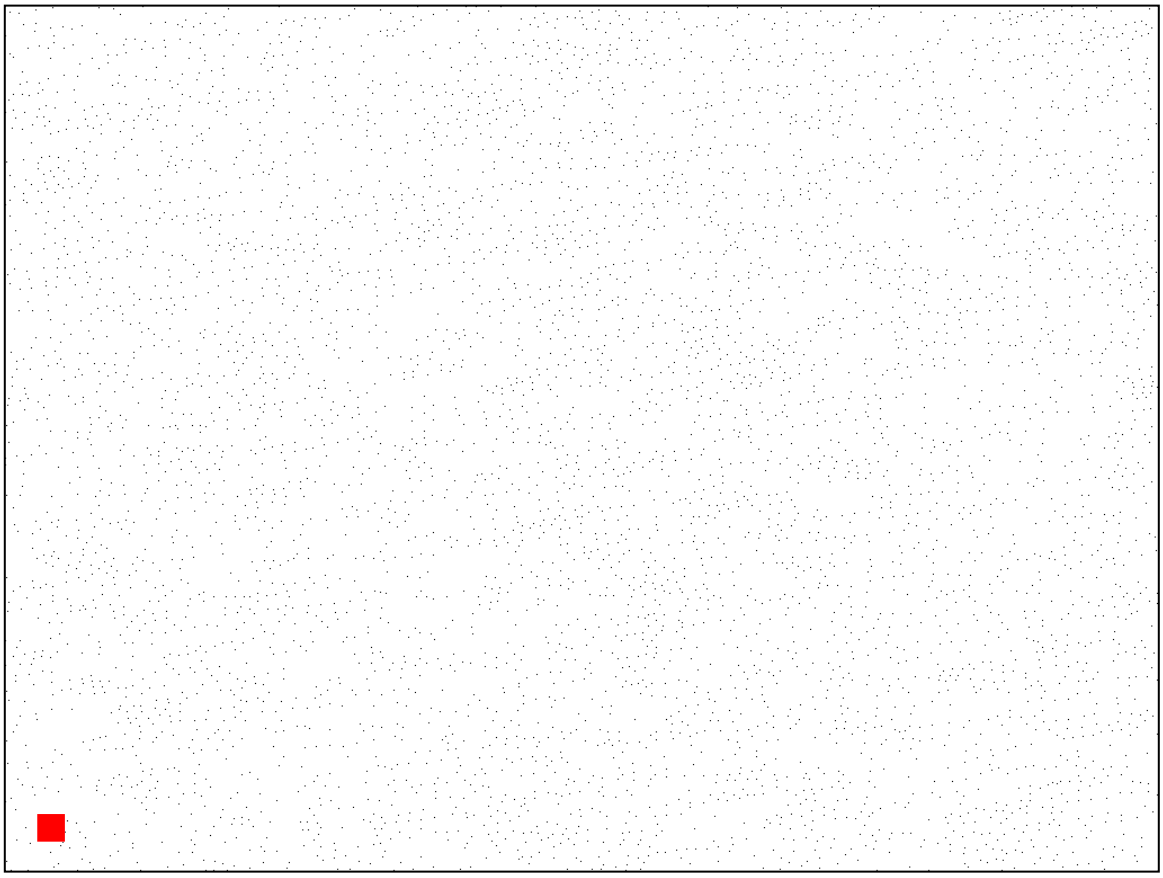

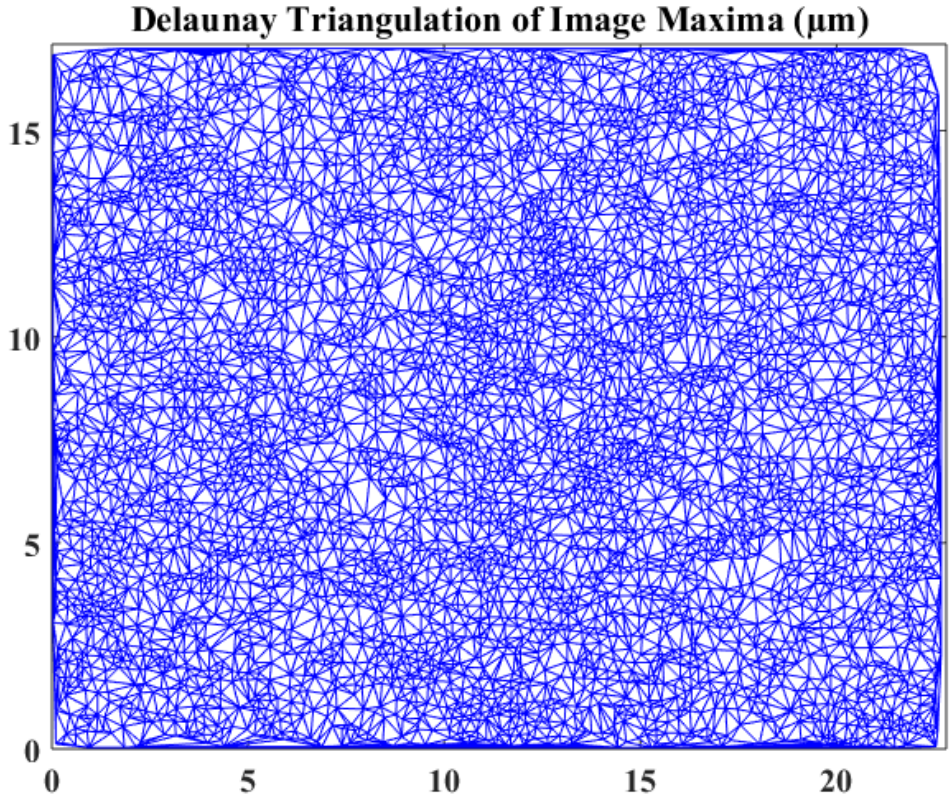

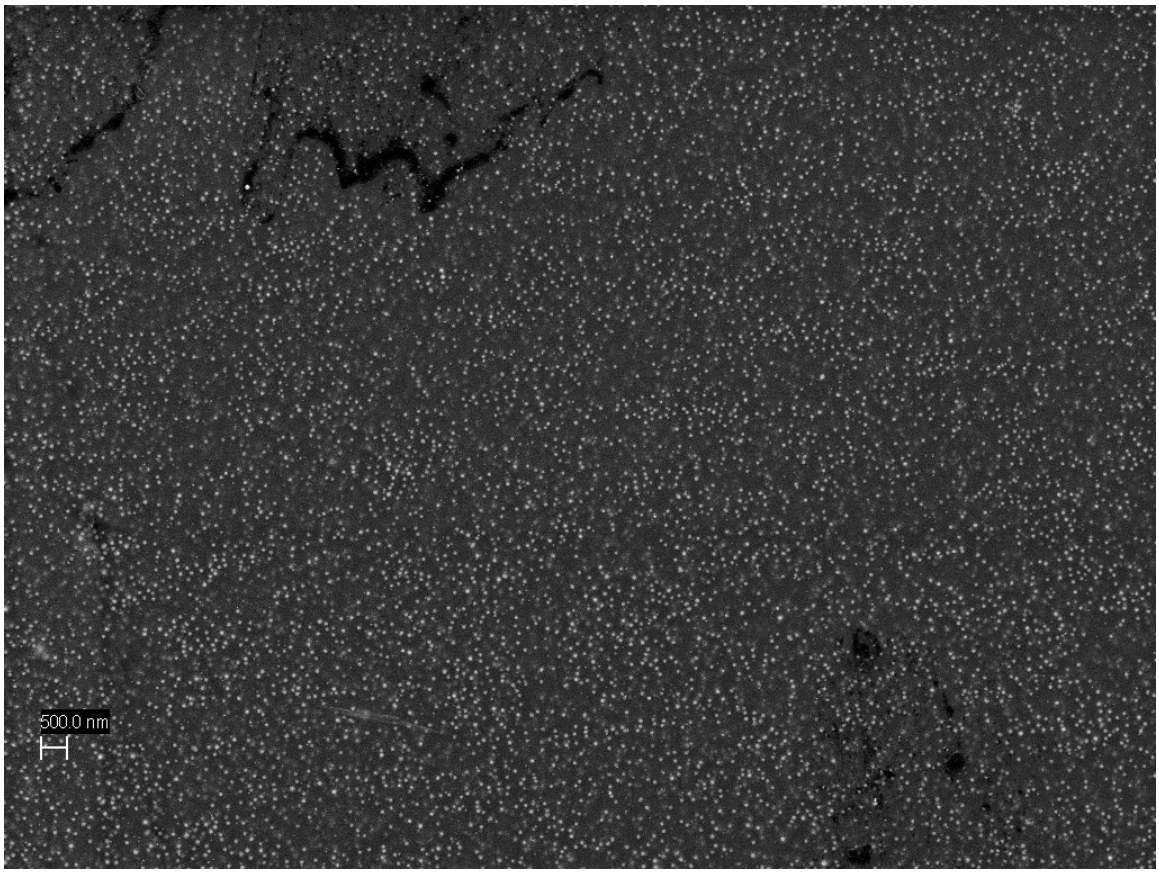

Figure A.5: Deformation rate *Wi* = 0.06, elongation ratio λ = 1.5: Location 2. This figure contains the original SEM image, corresponding binary image, and Delaunay Triangulation plot of the conditions from the figure title. Scale bars are 500 nm.

Figure A.5 (cont.)

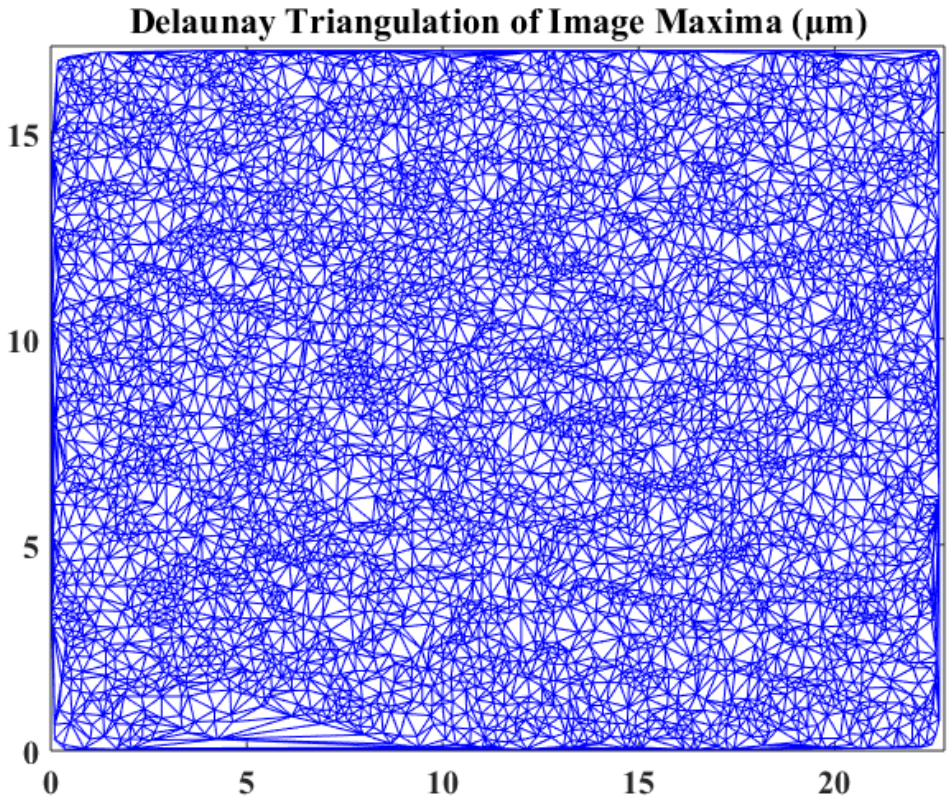

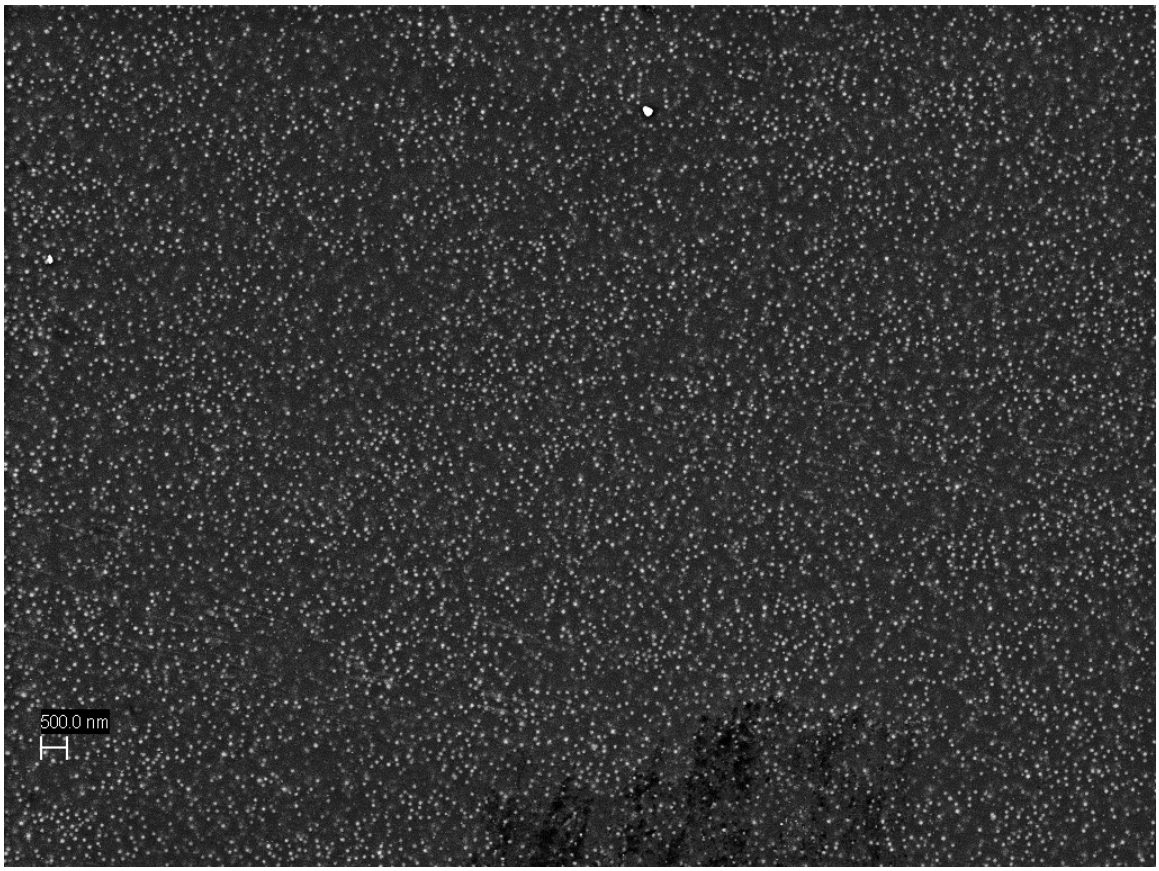

Figure A.6: Deformation rate *Wi* = 0.06, elongation ratio λ = 1.5: Location 3. This figure contains the original SEM image, corresponding binary image, and Delaunay Triangulation plot of the conditions from the figure title. Scale bars are 500 nm.

Figure A.6 (cont.)

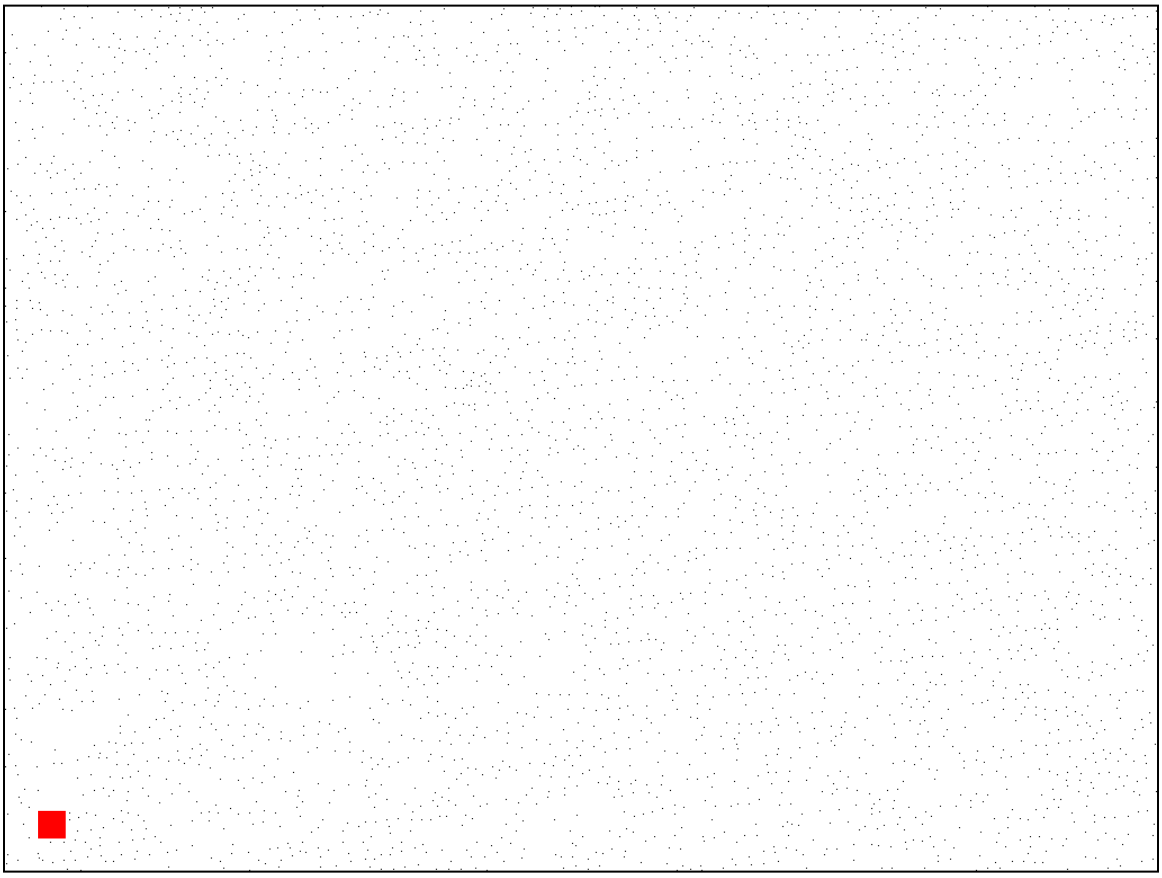

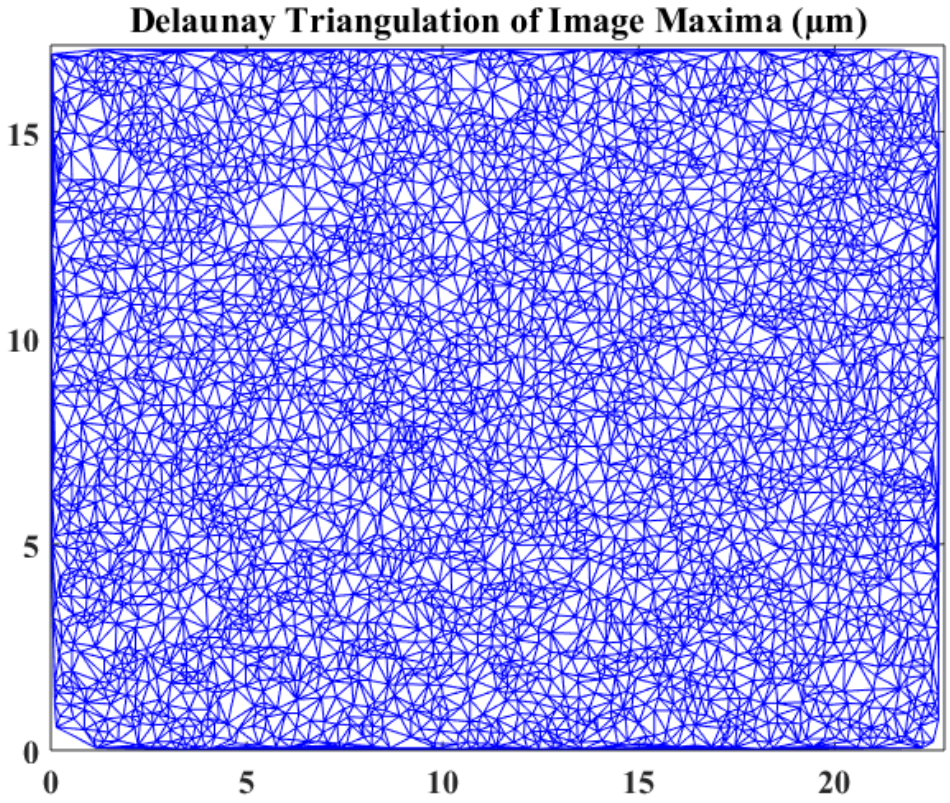

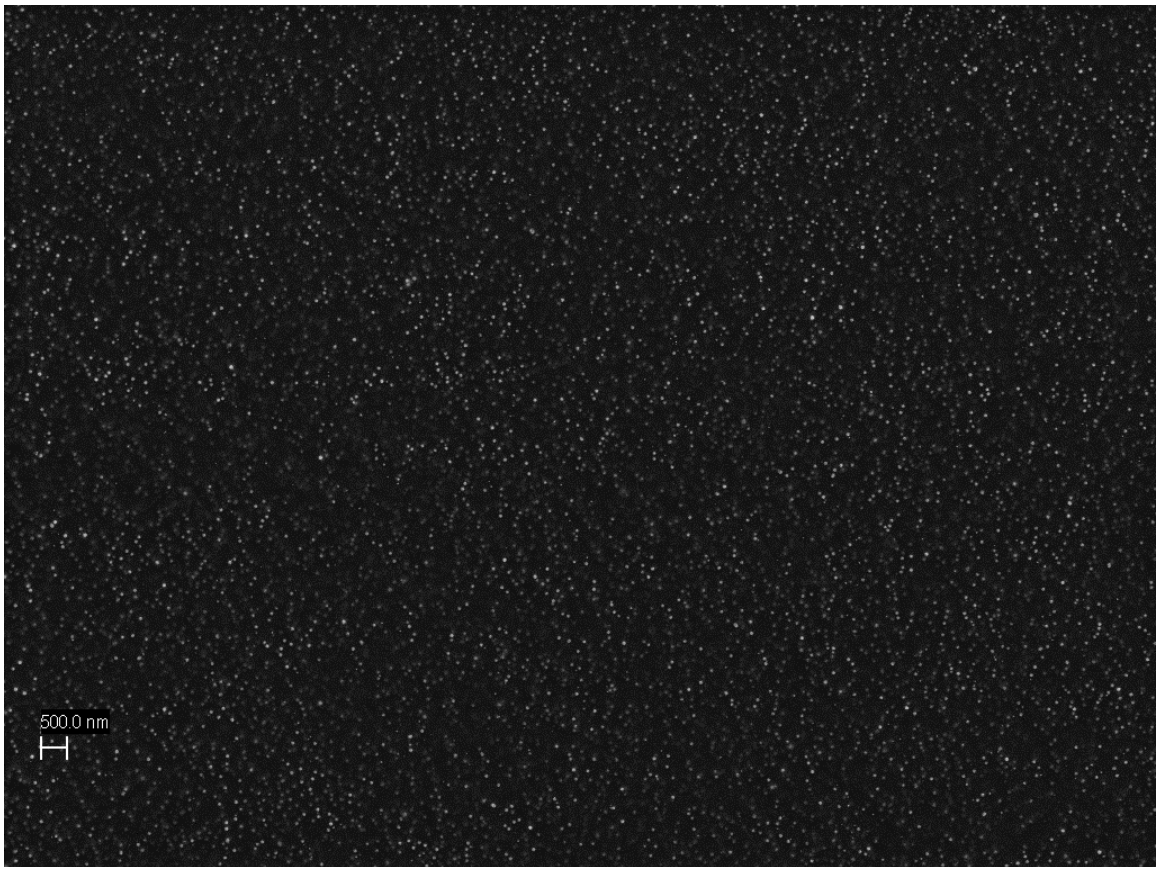

Figure A.7: Deformation rate *Wi* = 0.06, elongation ratio λ = 2.5: Location 1. This figure contains the original SEM image, corresponding binary image, and Delaunay Triangulation plot of the conditions from the figure title. Scale bars are 500 nm.

Figure A.7 (cont.)

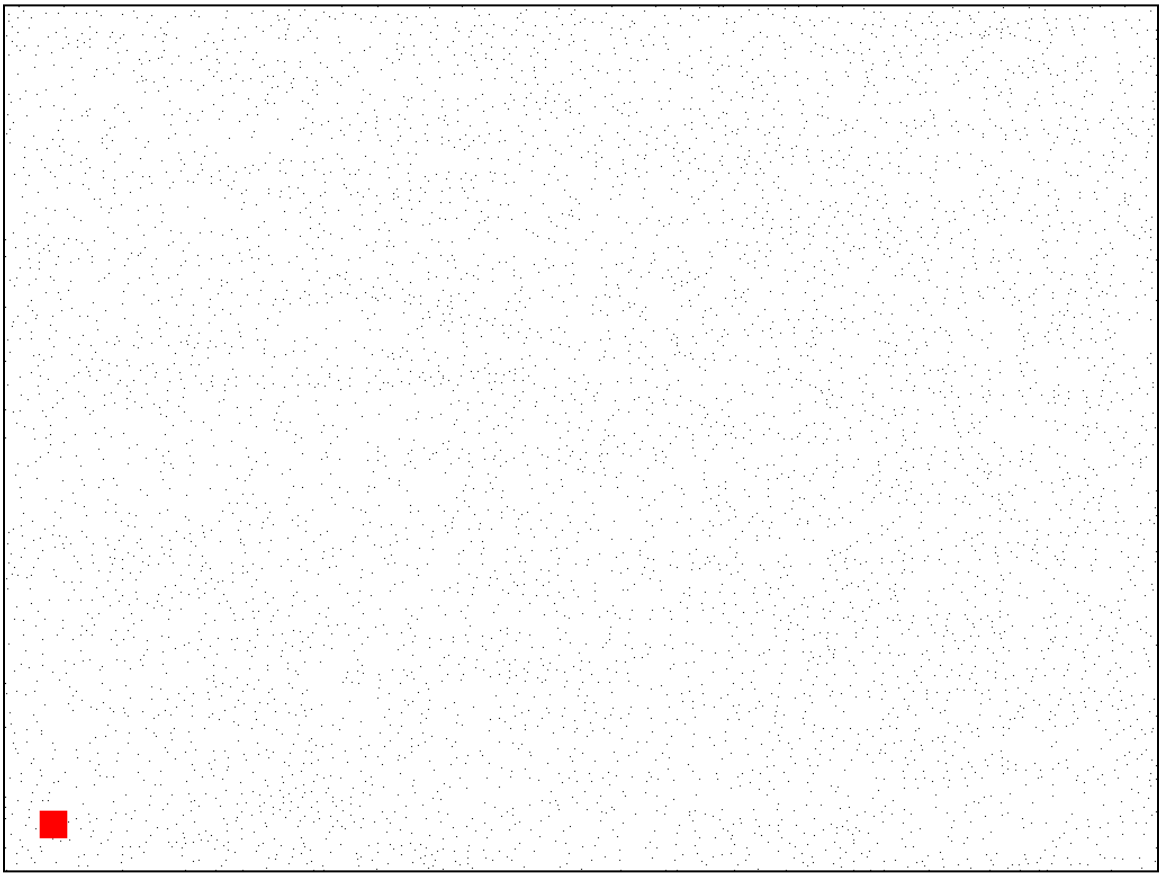

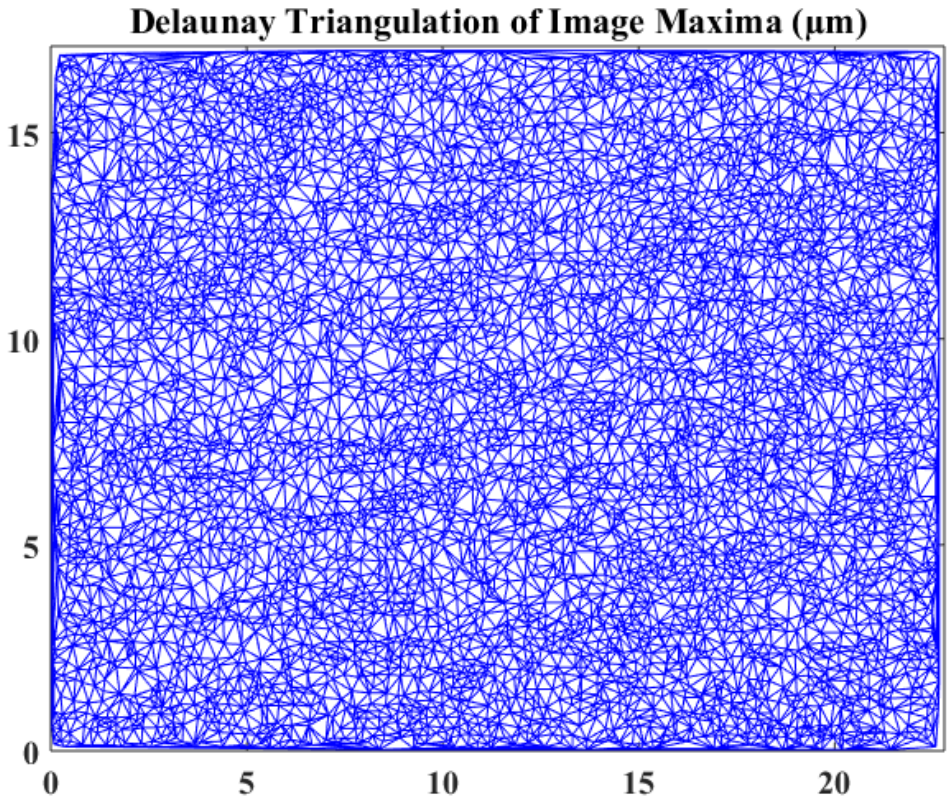

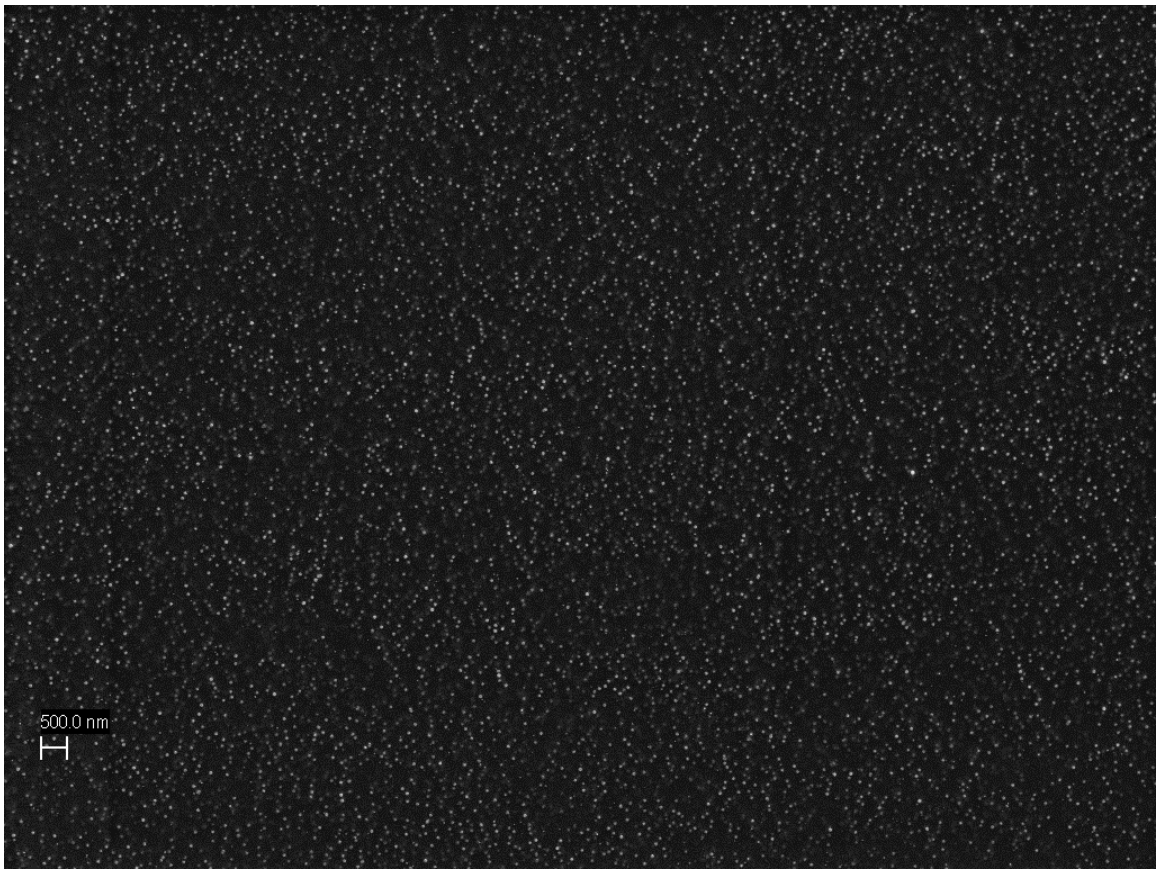

Figure A.8: Deformation rate *Wi* = 0.06, elongation ratio λ = 2.5: Location 2. This figure contains the original SEM image, corresponding binary image, and Delaunay Triangulation plot of the conditions from the figure title. Scale bars are 500 nm.

Figure A.8 (cont.)

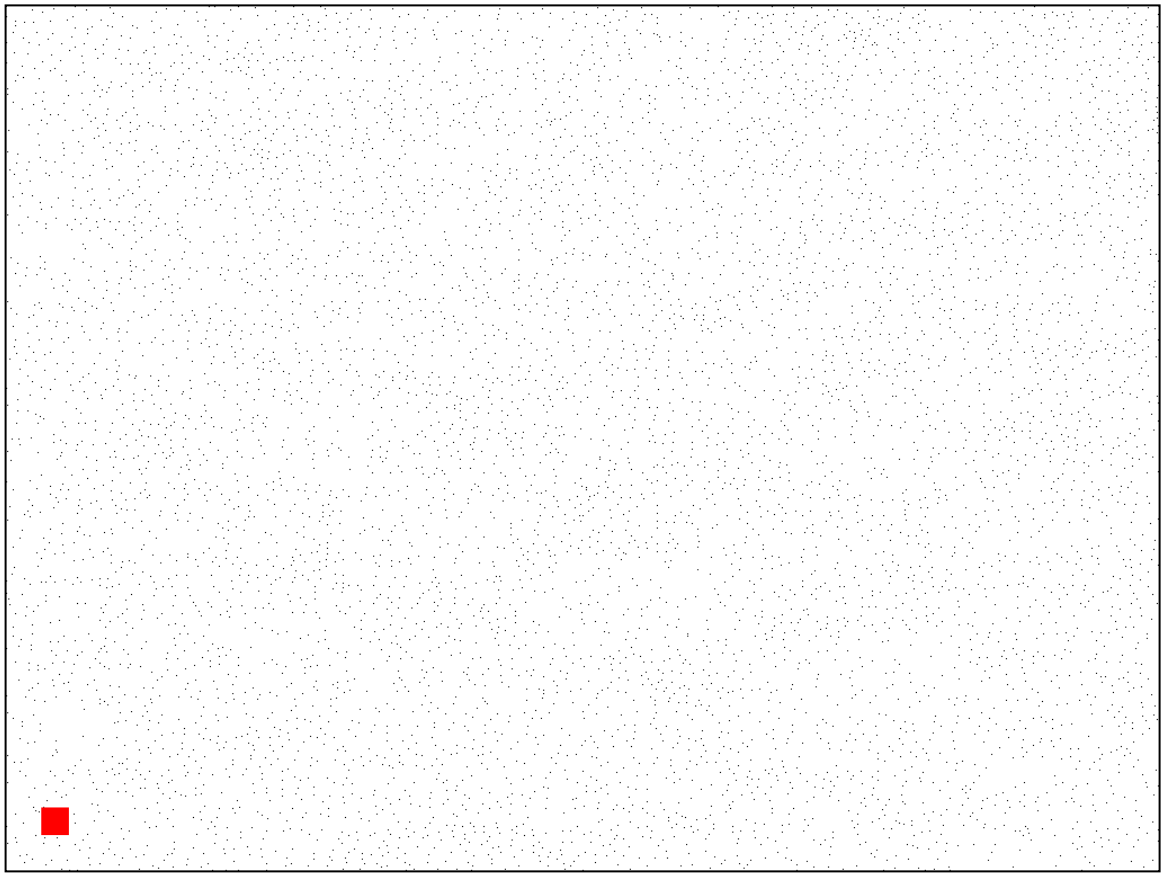

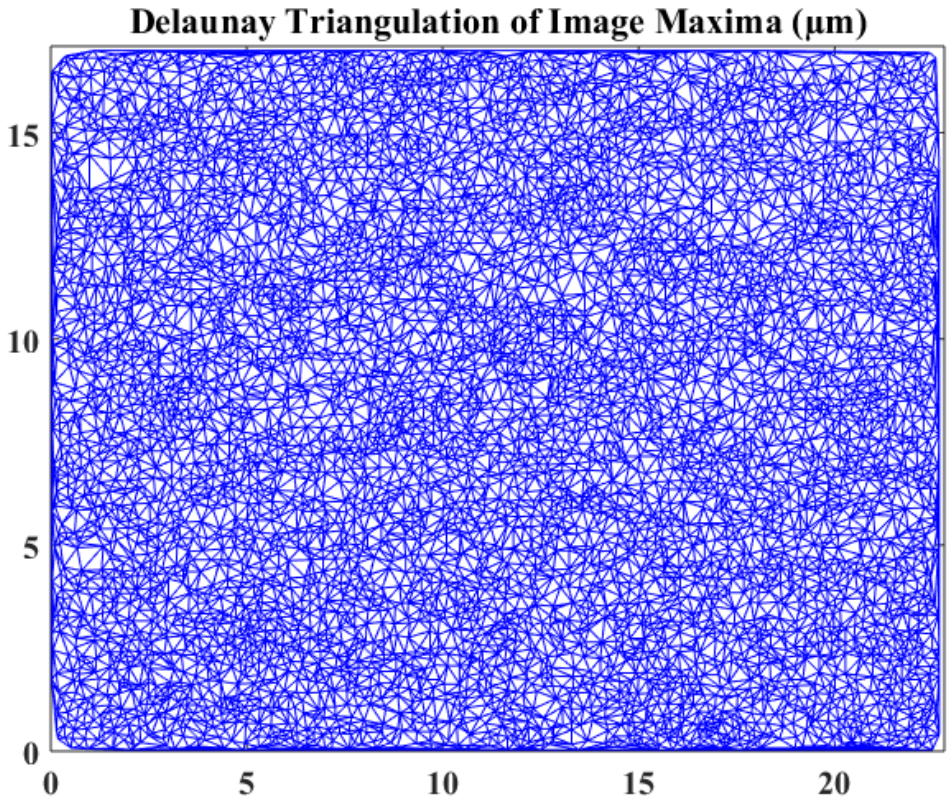

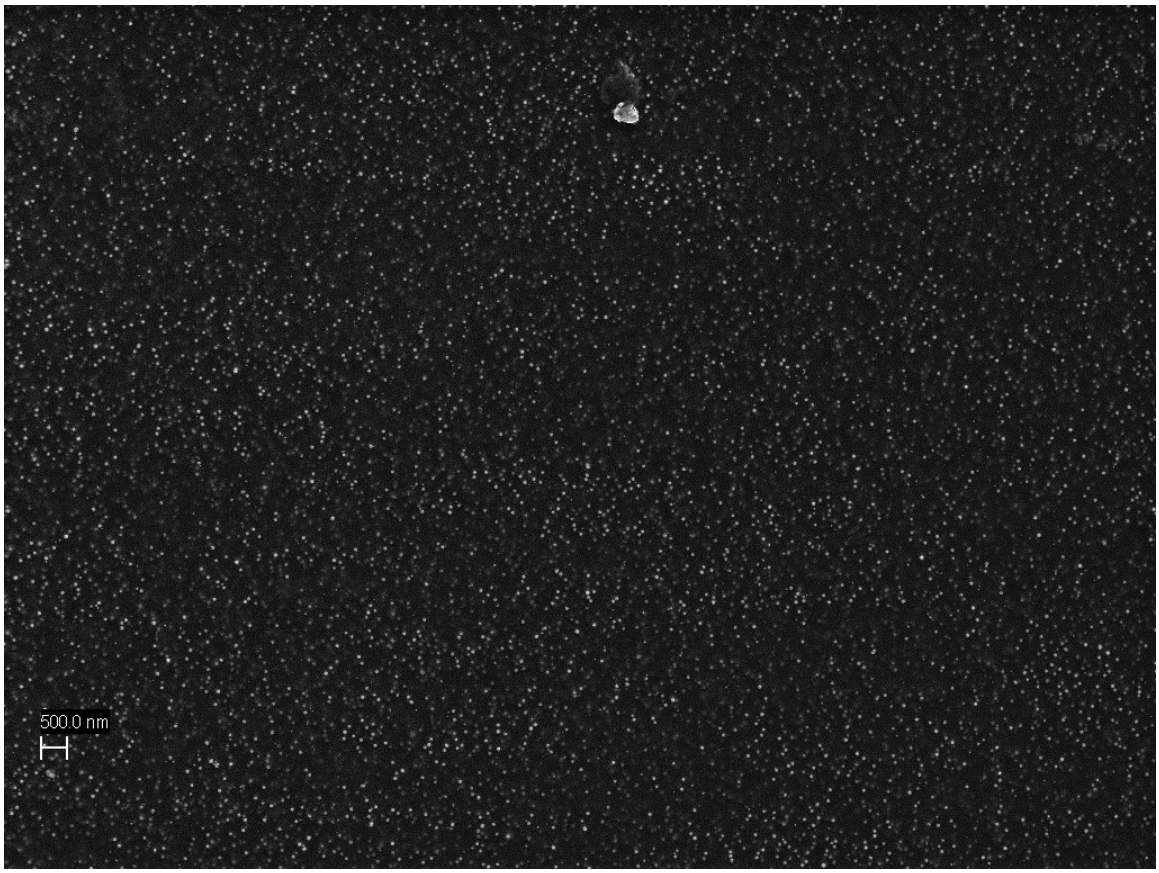

Figure A.9: Deformation rate *Wi* = 0.06, elongation ratio λ = 2.5: Location 3. This figure contains the original SEM image, corresponding binary image, and Delaunay Triangulation plot of the conditions from the figure title. Scale bars are 500 nm.

Figure A.9 (cont.)

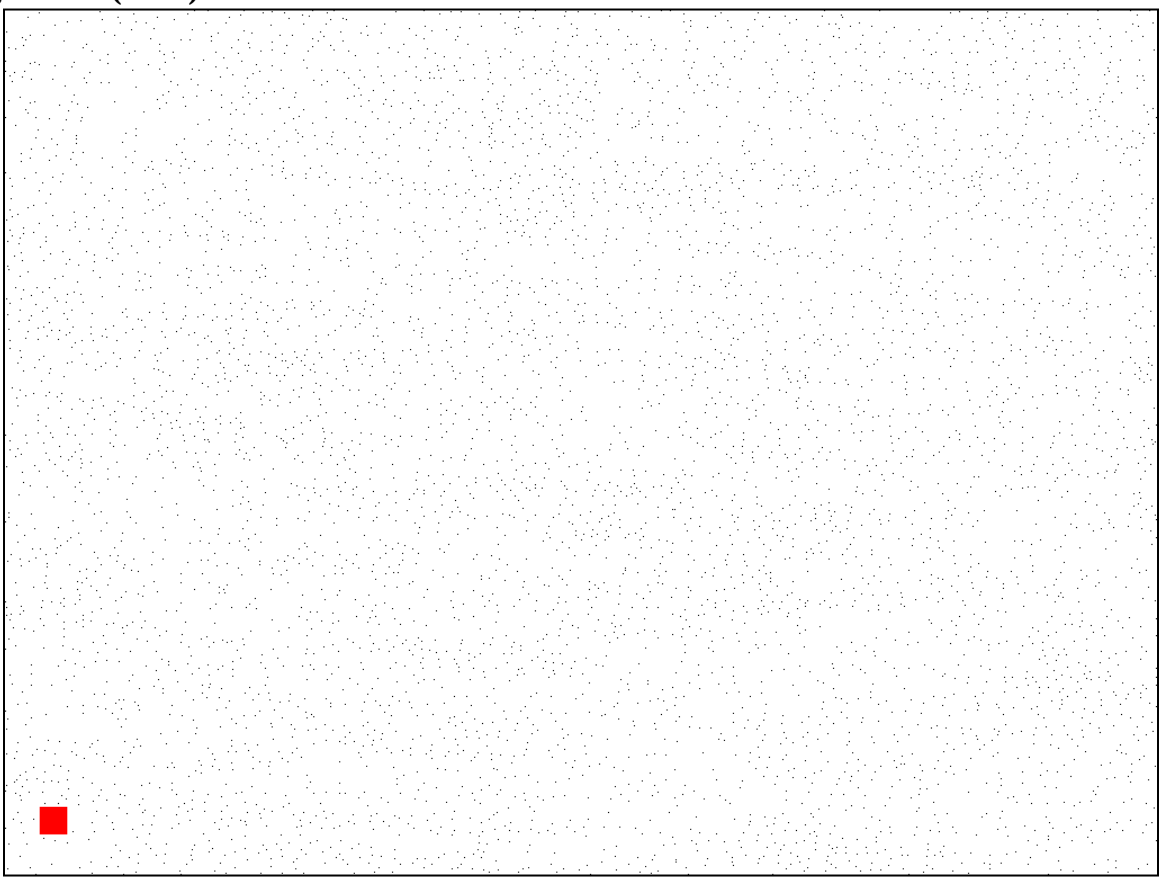

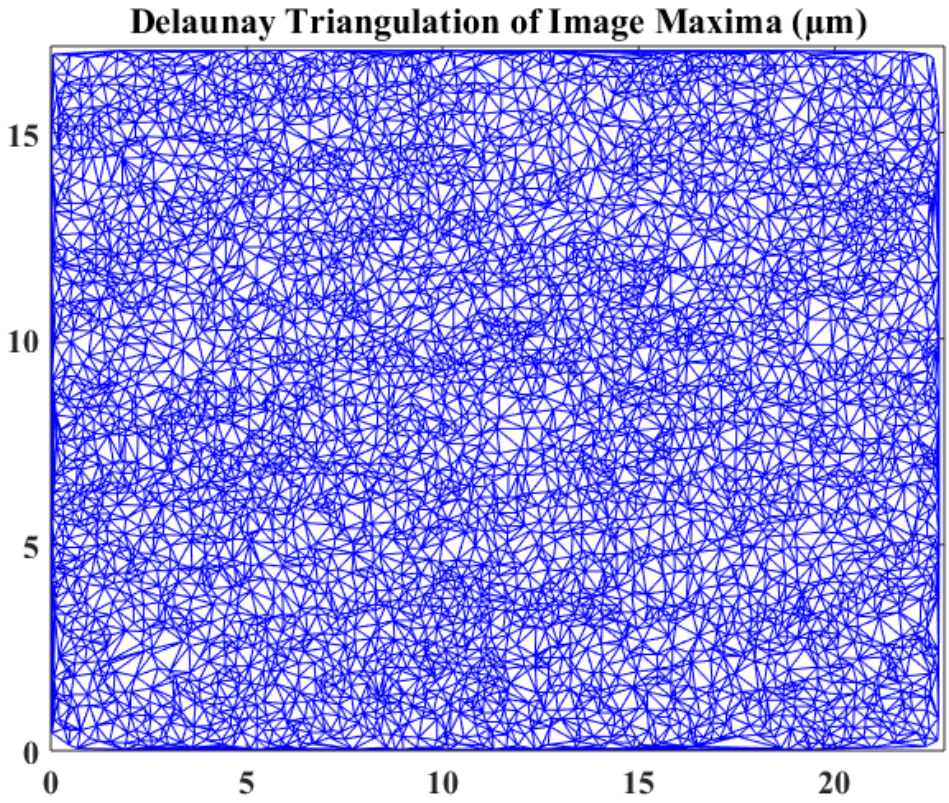

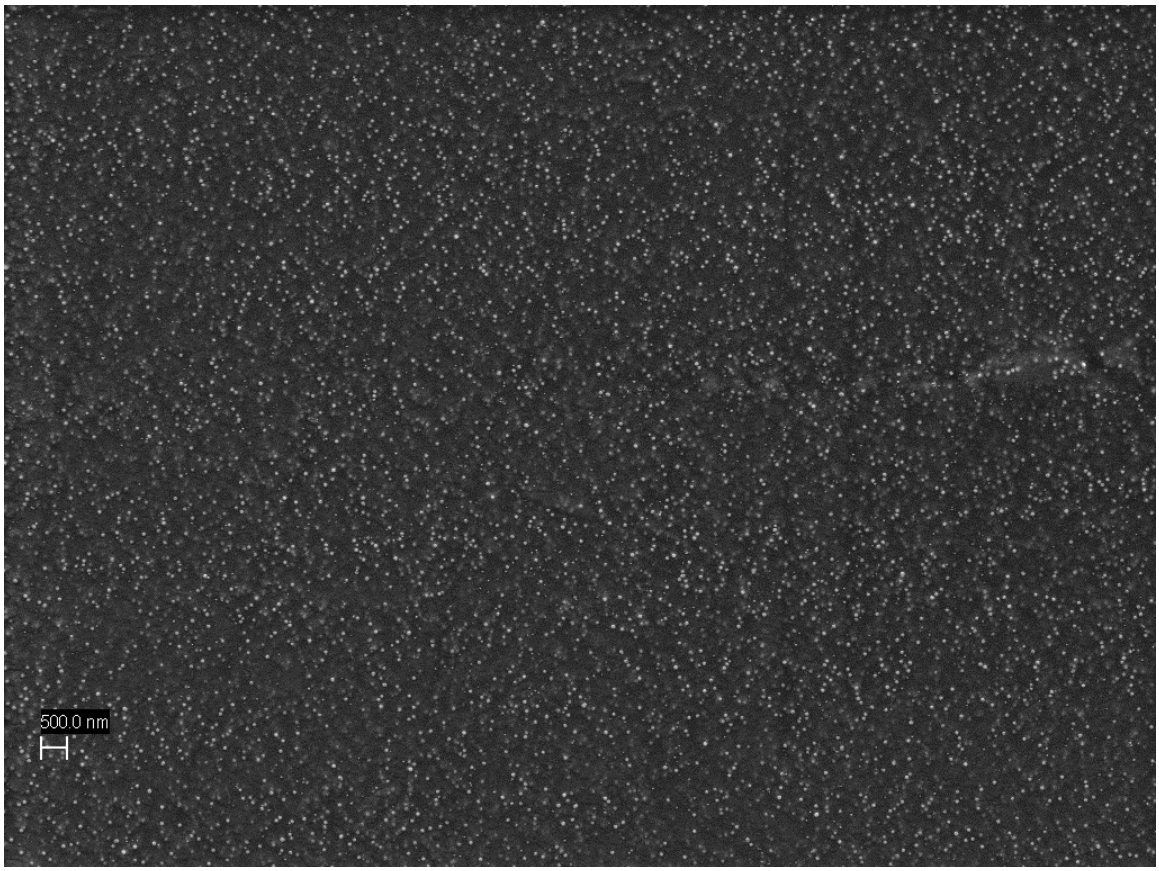

Figure A.10: Deformation rate *Wi* = 0.06, elongation ratio λ = 4.0: Location 1. This figure contains the original SEM image, corresponding binary image, and Delaunay Triangulation plot of the conditions from the figure title. Scale bars are 500 nm.

Figure A.10 (cont.)

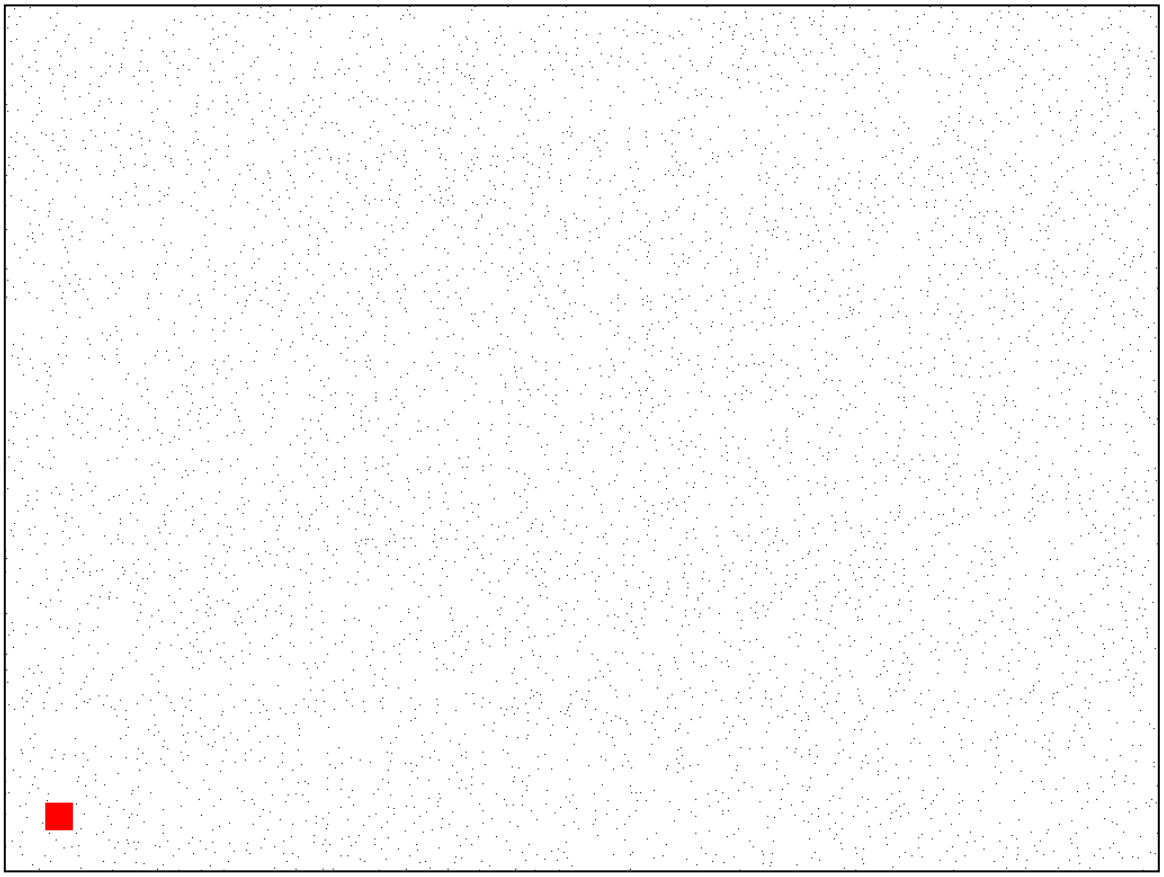

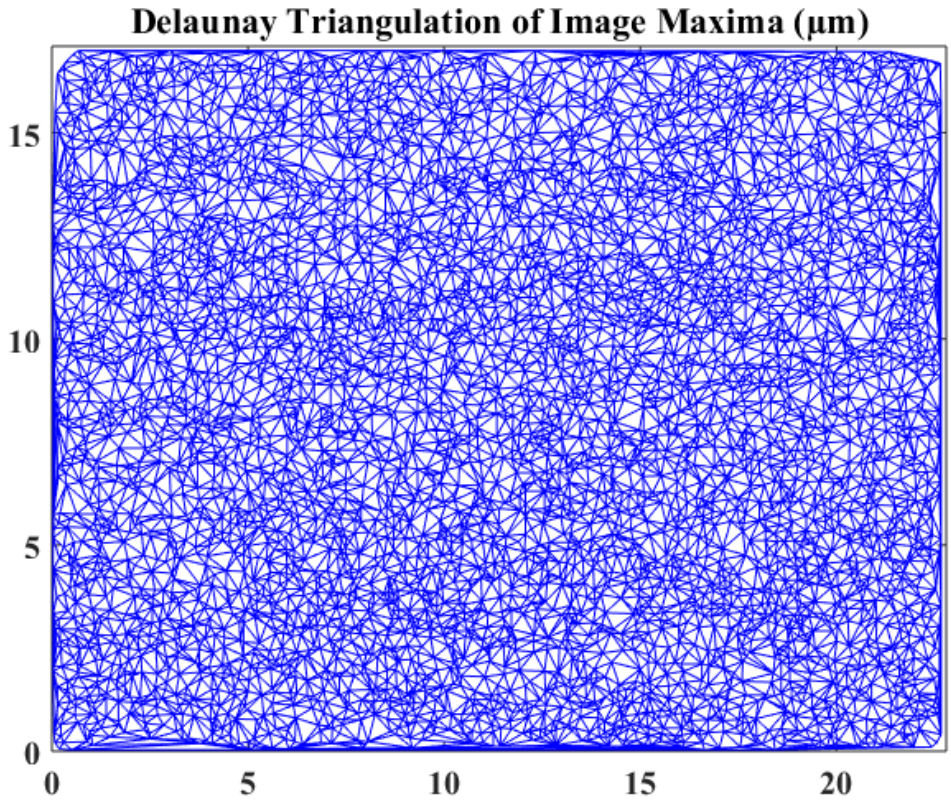

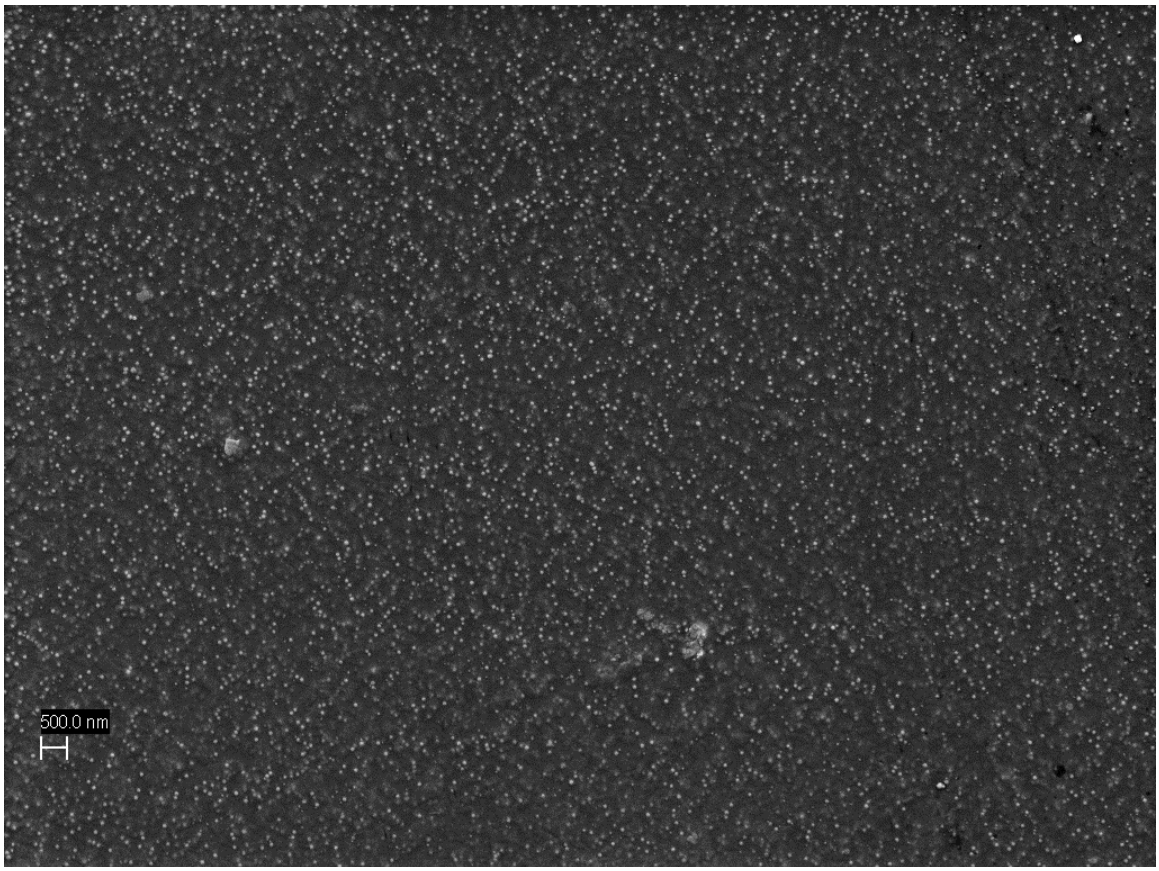

Figure A.11: Deformation rate *Wi* = 0.06, elongation ratio λ = 4.0: Location 2. This figure contains the original SEM image, corresponding binary image, and Delaunay Triangulation plot of the conditions from the figure title. Scale bars are 500 nm.

Figure A.11 (cont.)

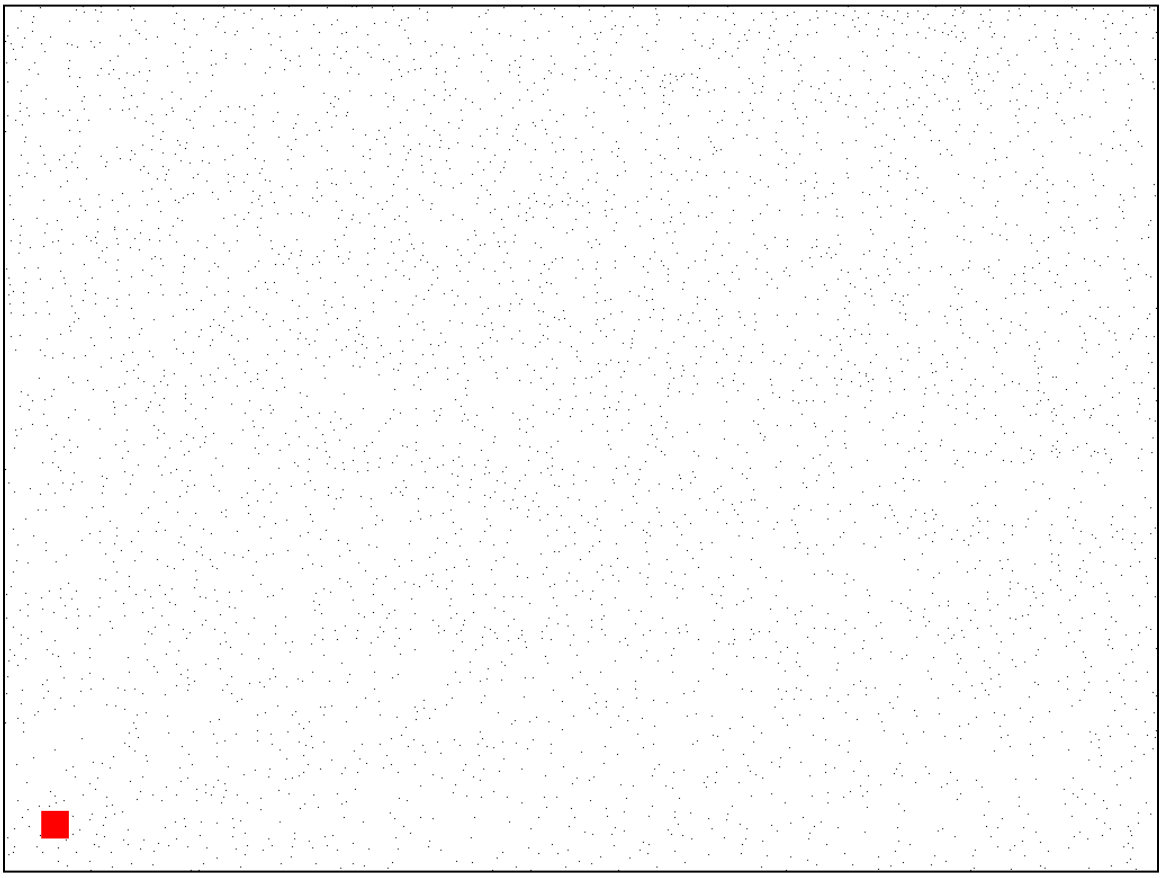

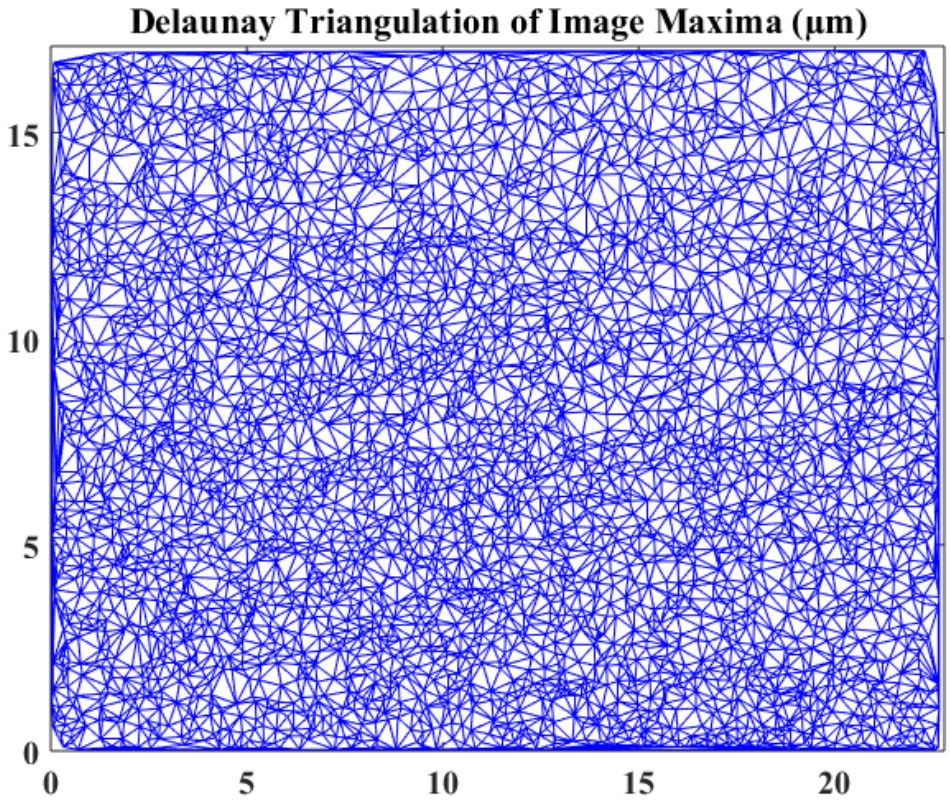

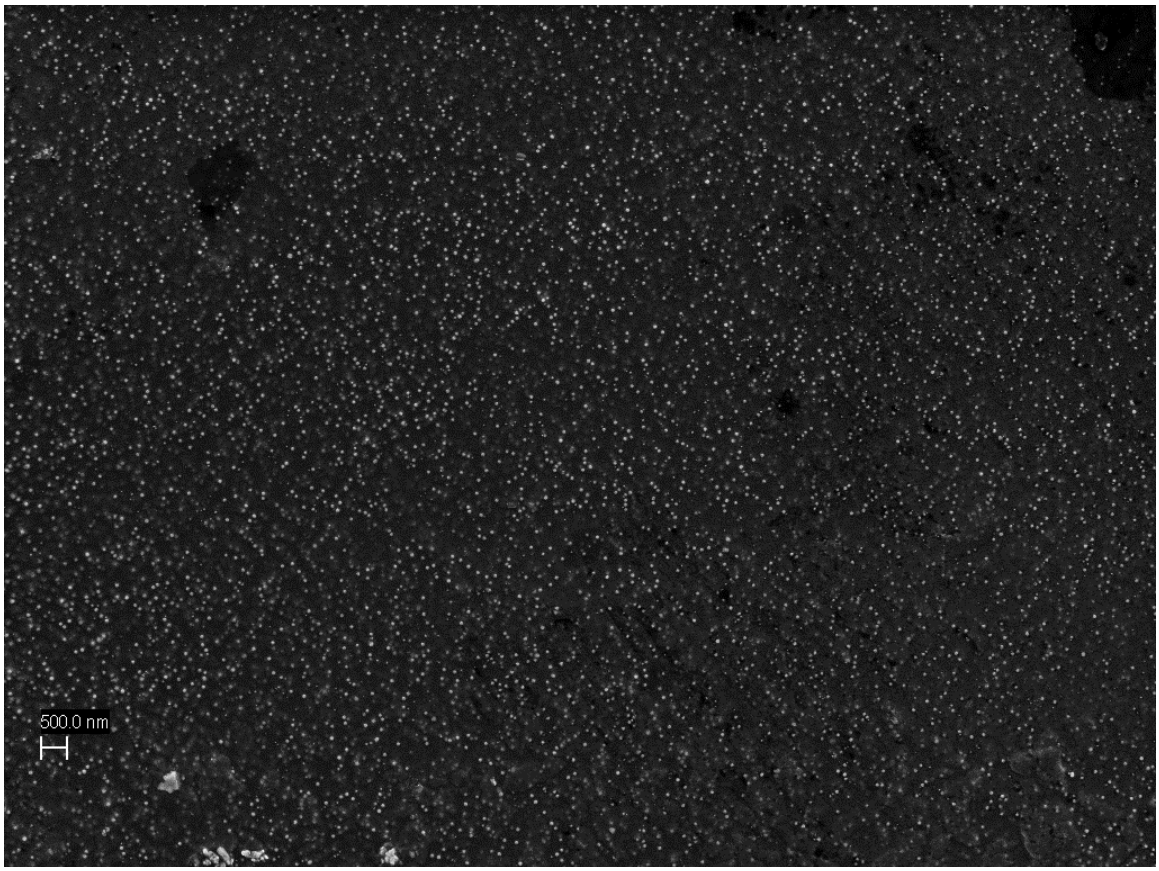

Figure A.12: Deformation rate *Wi* = 0.06, elongation ratio λ = 4.0: Location 3. This figure contains the original SEM image, corresponding binary image, and Delaunay Triangulation plot of the conditions from the figure title. Scale bars are 500 nm.

Figure A.12 (cont.)

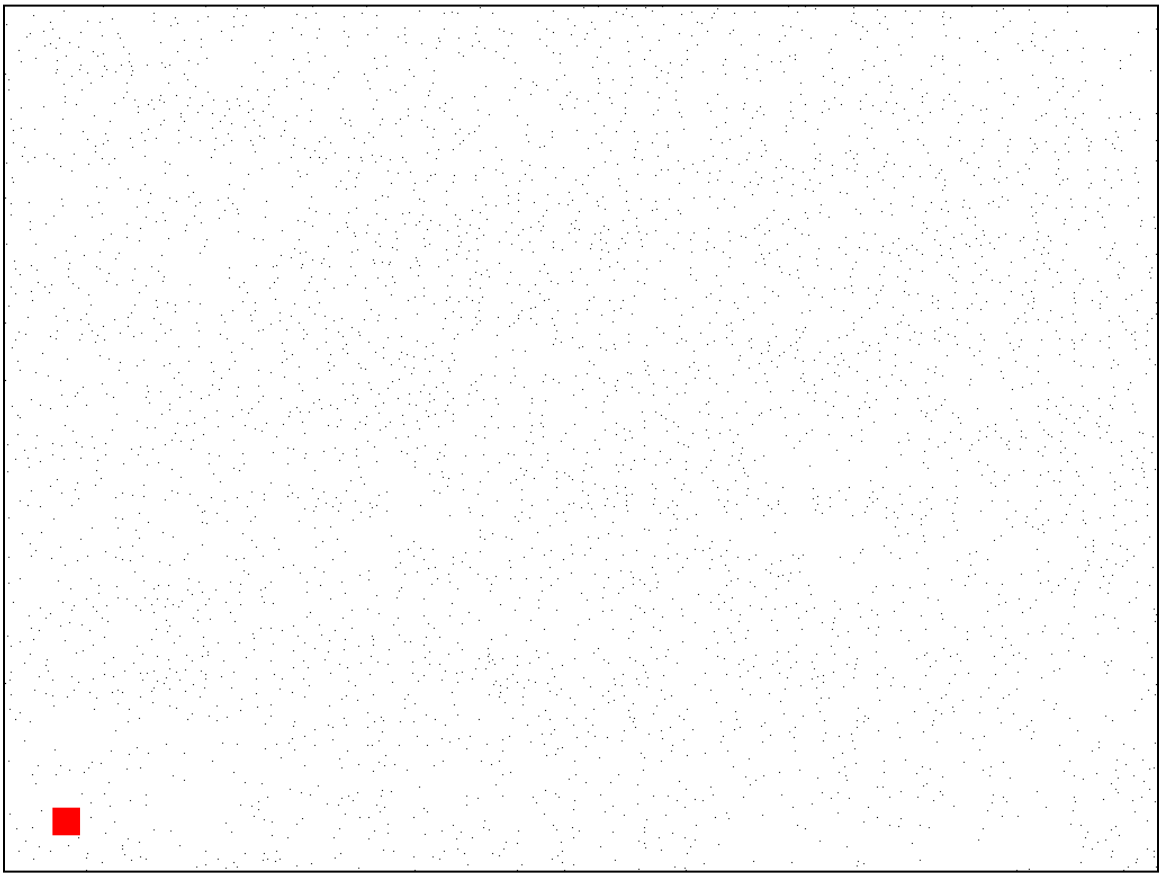

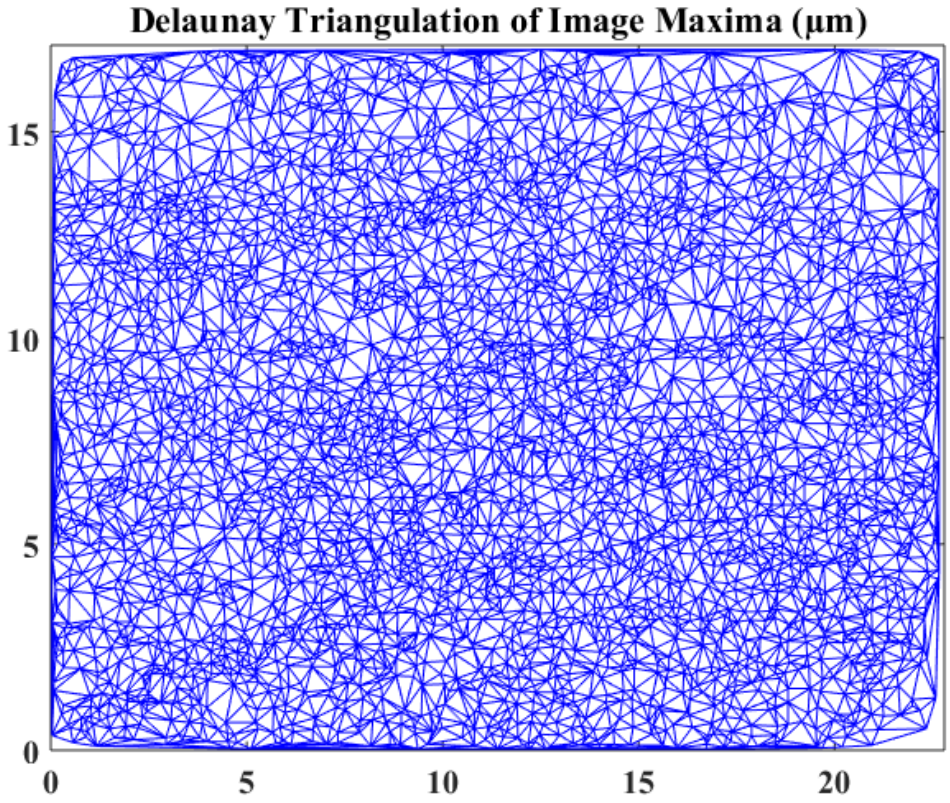

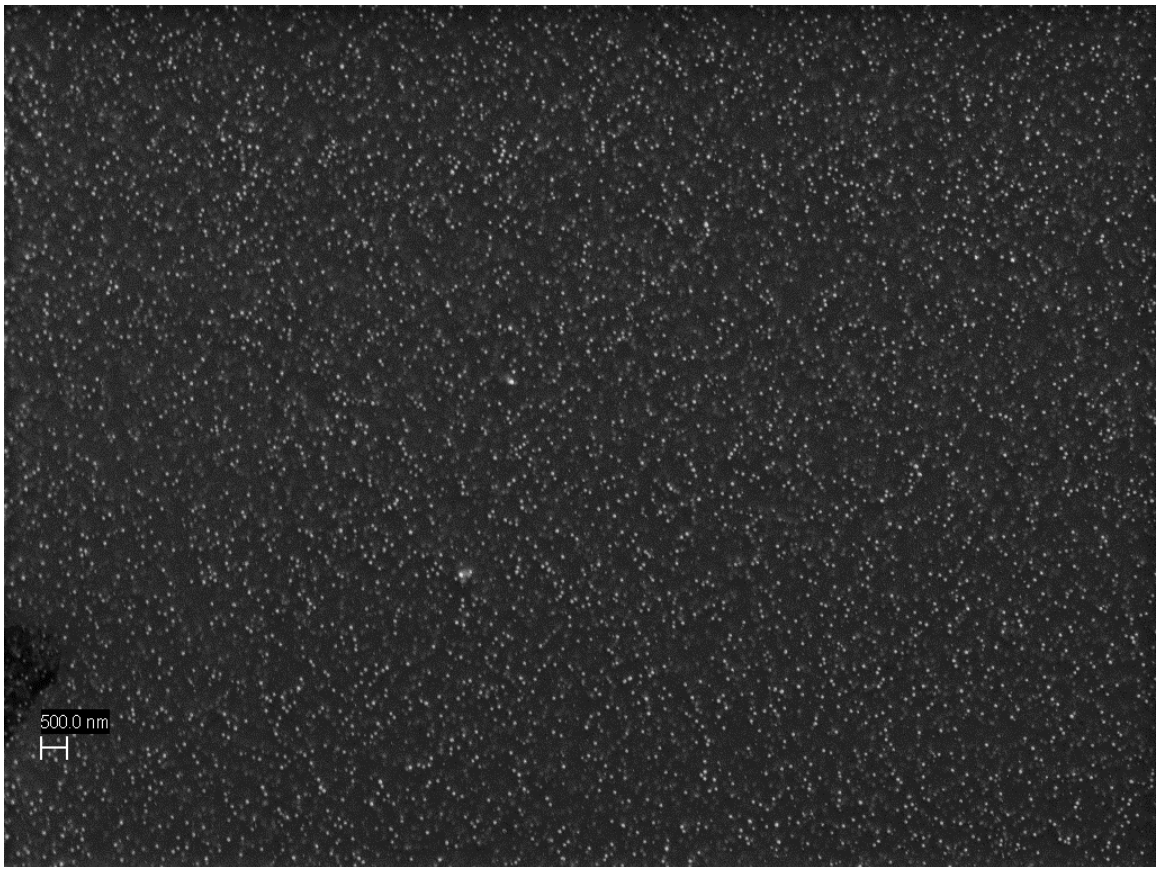

Figure A.13: Deformation rate *Wi* = 0.06, elongation ratio λ = 5.0: Location 1. This figure contains the original SEM image, corresponding binary image, and Delaunay Triangulation plot of the conditions from the figure title. Scale bars are 500 nm.

Figure A.13 (cont.)

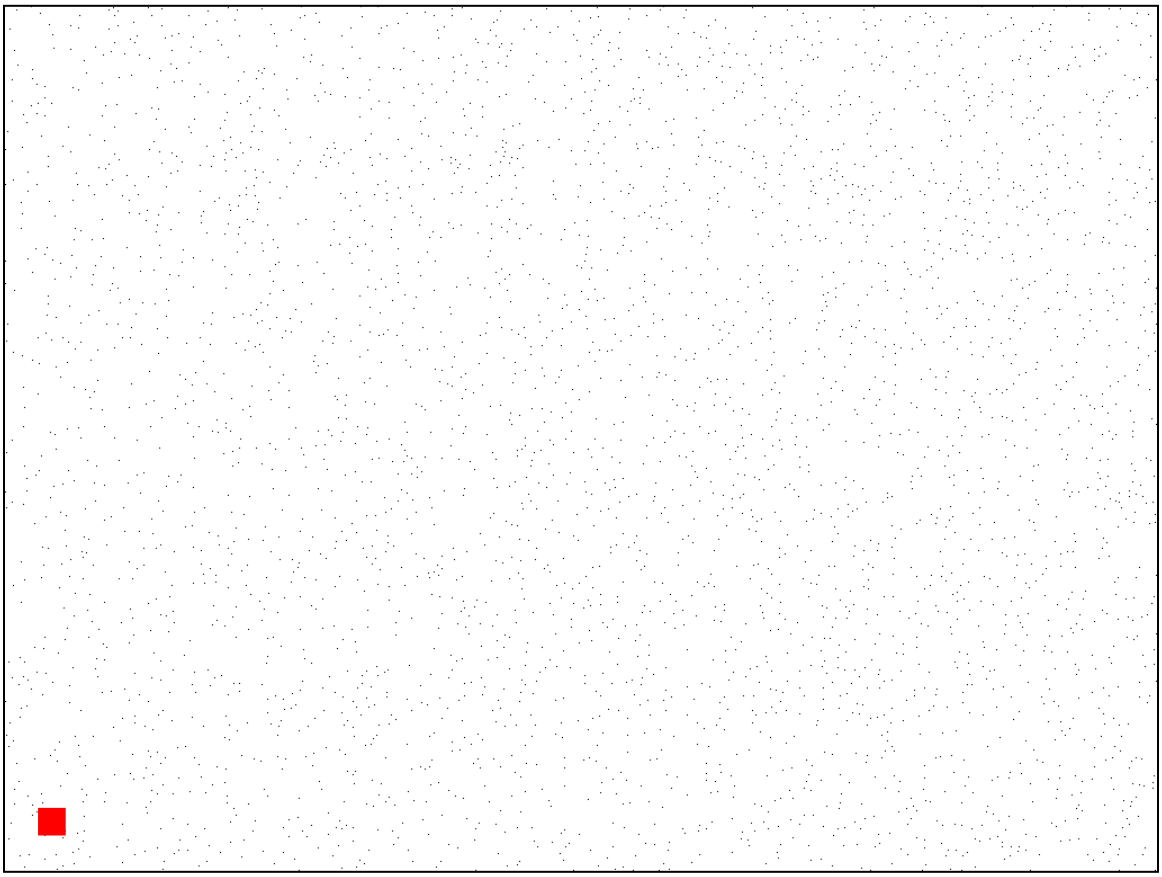

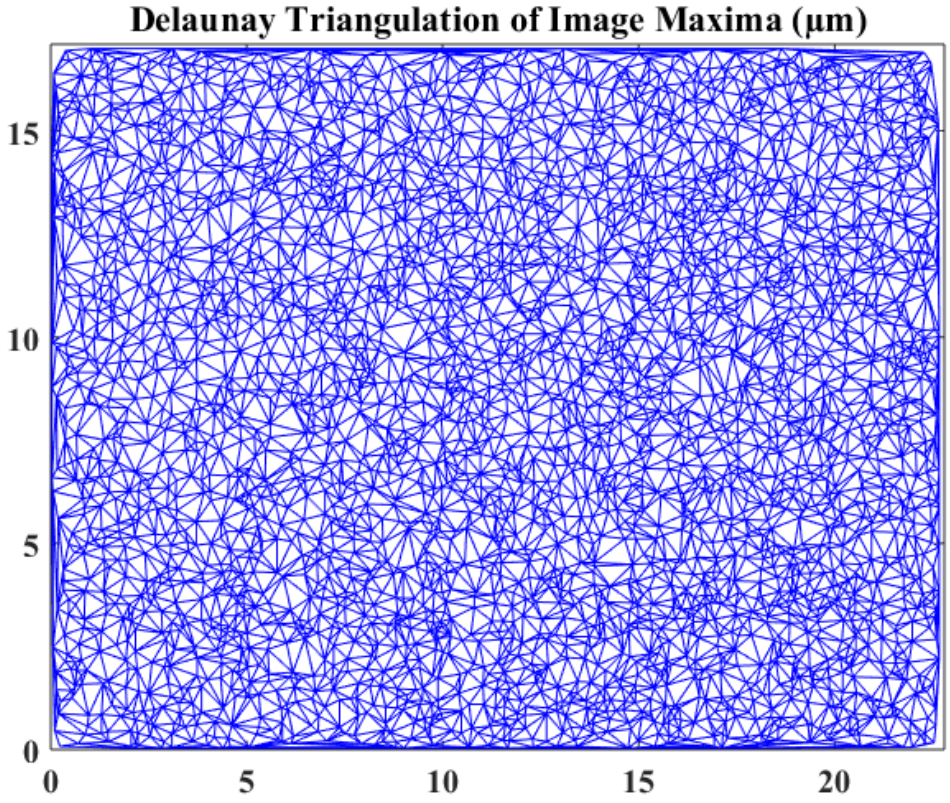

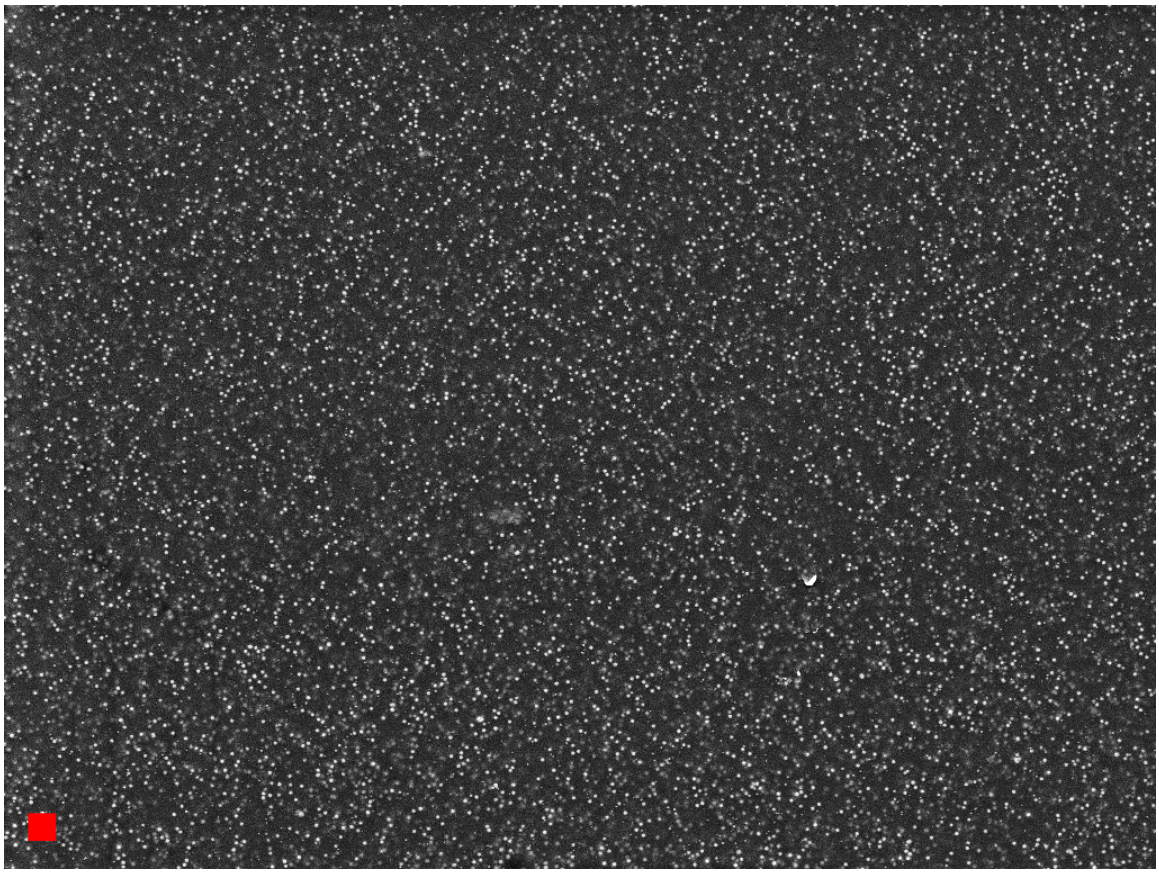

Figure A.14: Deformation rate *Wi* = 0.06, elongation ratio λ = 5.0: Location 2. This figure contains the original SEM image, corresponding binary image, and Delaunay Triangulation plot of the conditions from the figure title. Scale bars are 500 nm.

Figure A.14 (cont.)

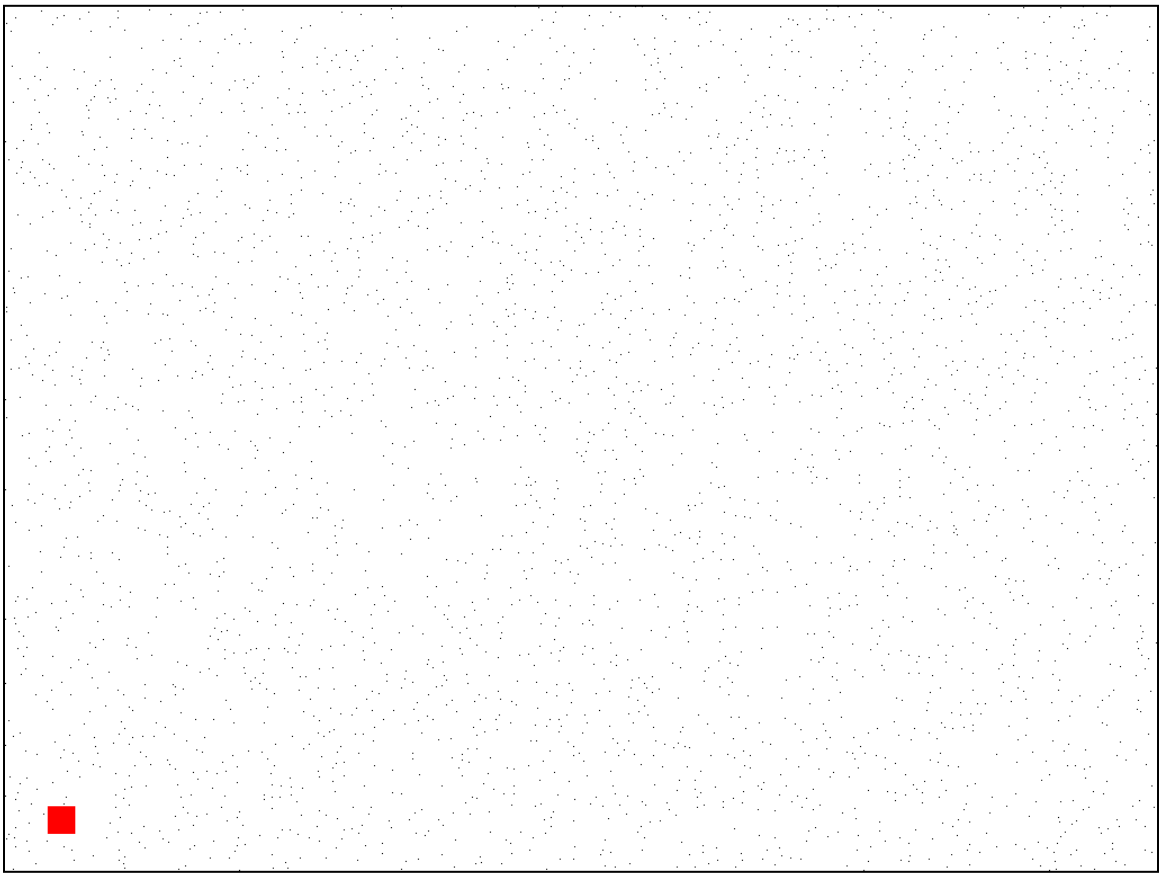

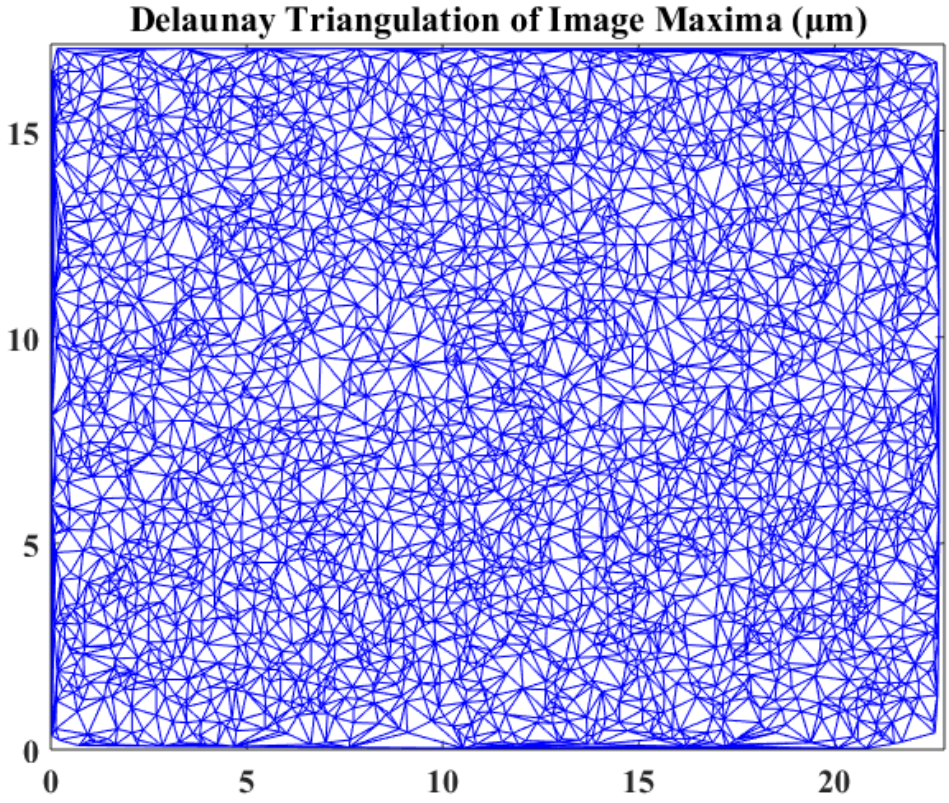

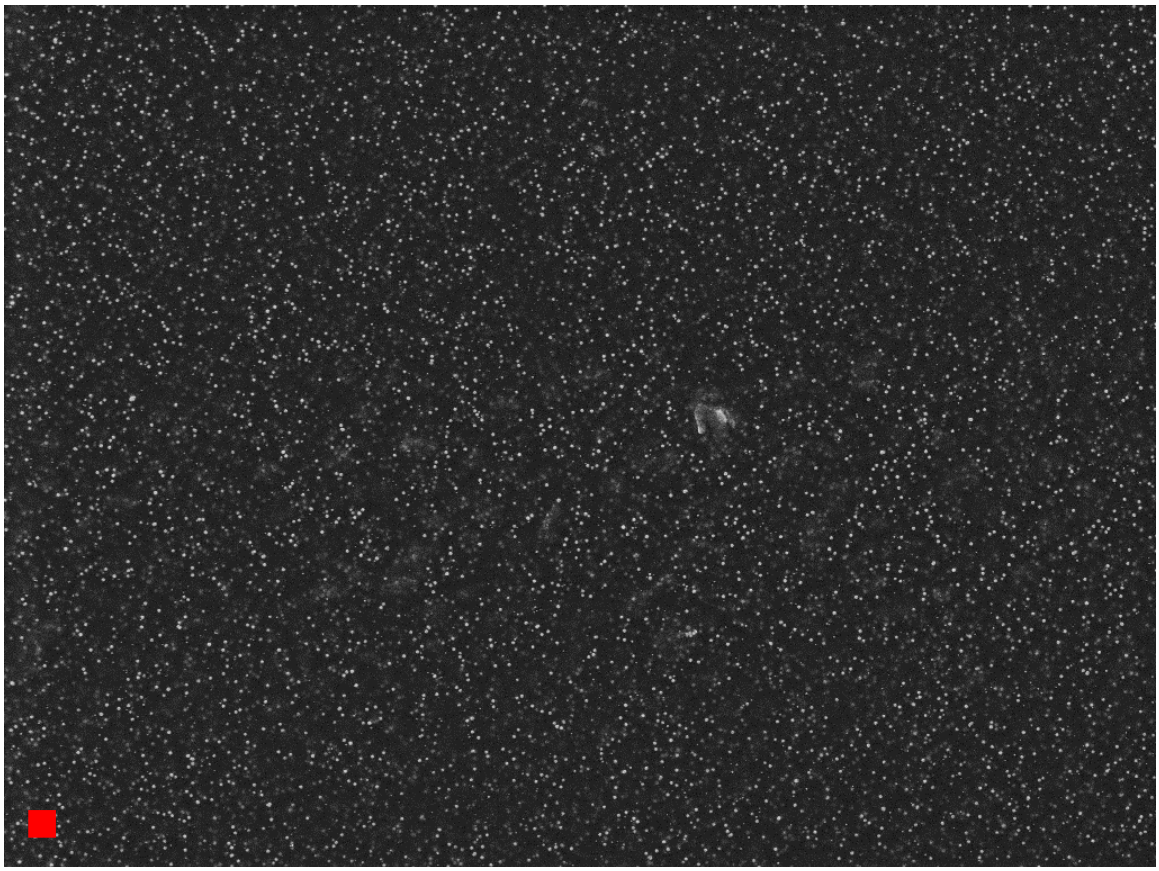

Figure A.15: Deformation rate *Wi* = 0.06, elongation ratio λ = 5.0: Location 3. This figure contains the original SEM image, corresponding binary image, and Delaunay Triangulation plot of the conditions from the figure title. Scale bars are 500 nm.

Figure A.15 (cont.)

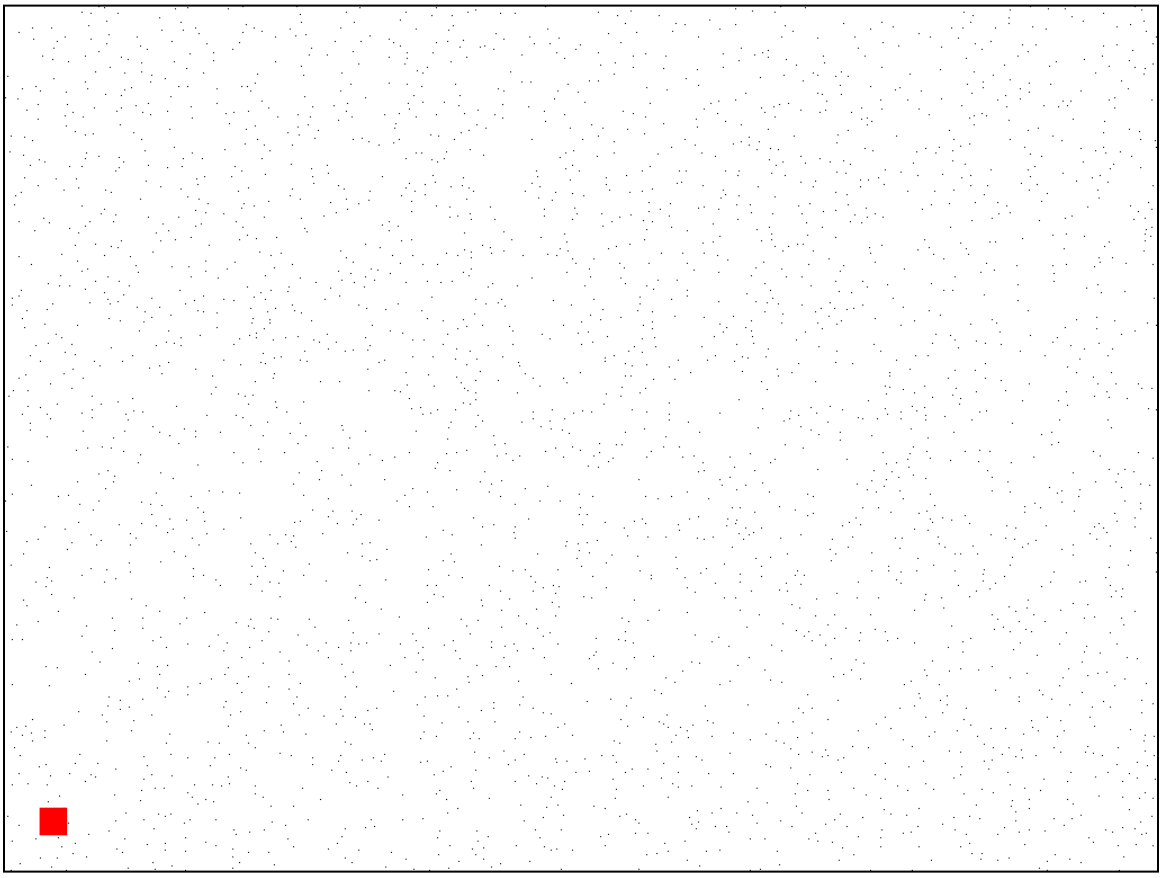

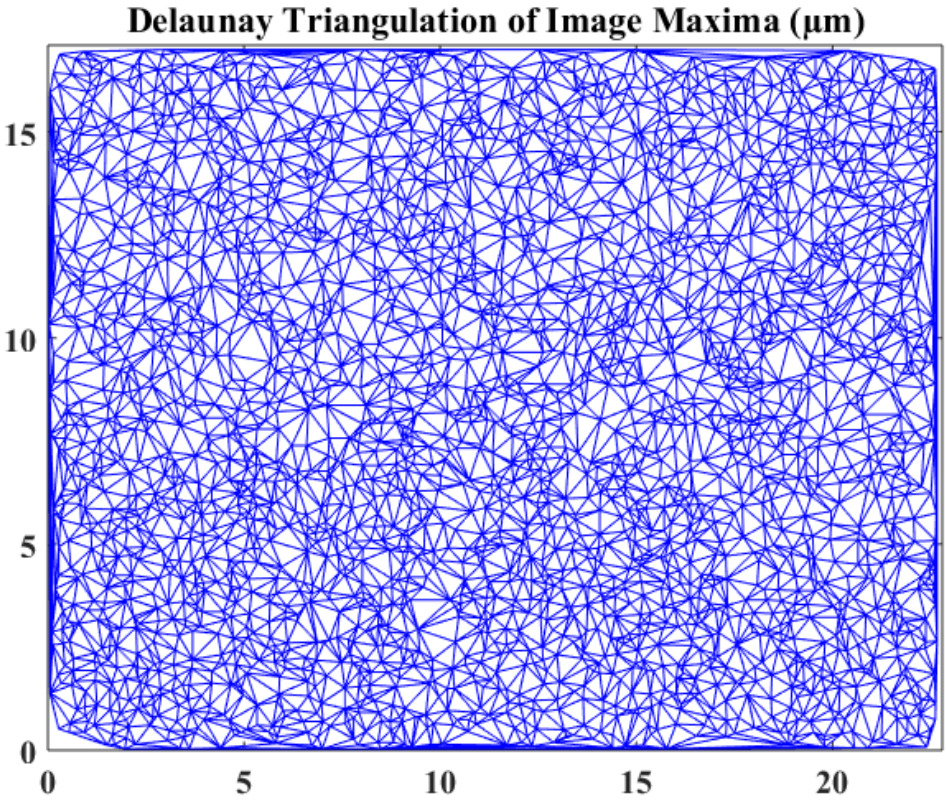

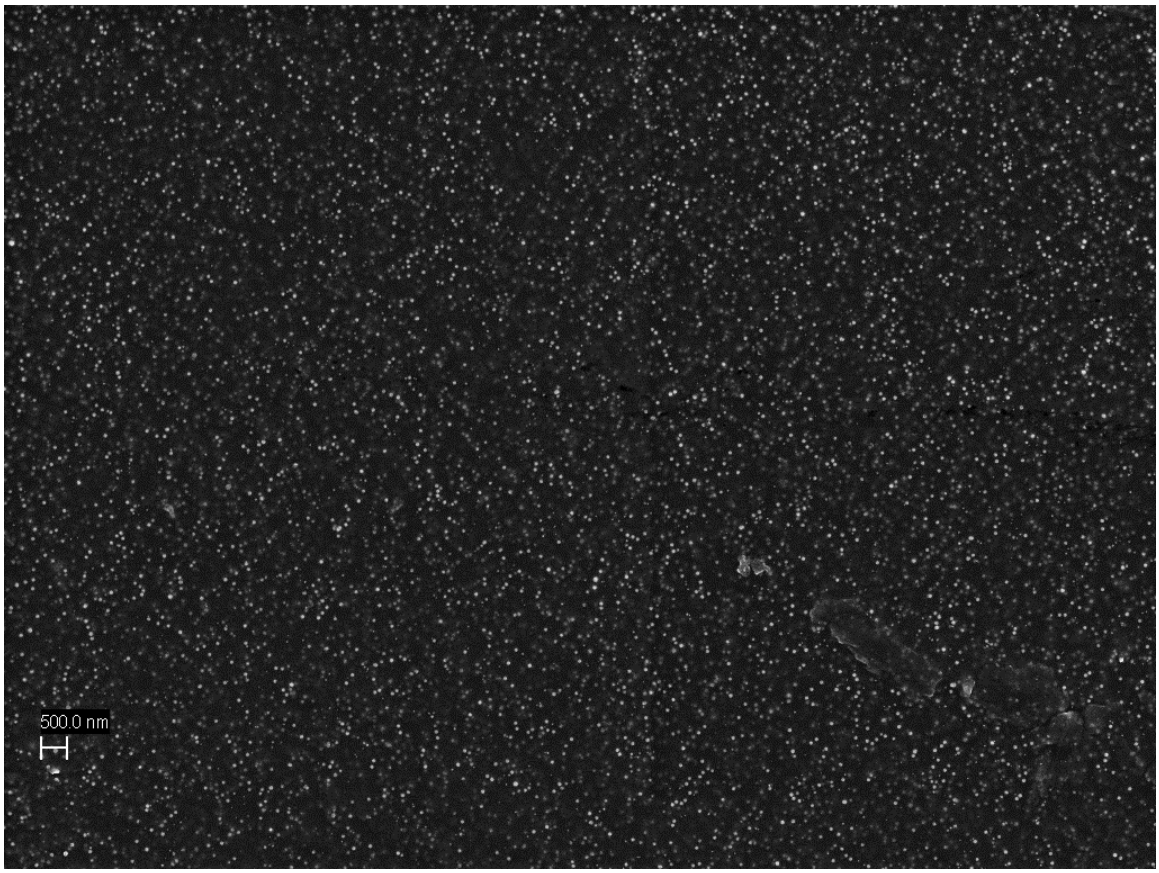

Figure A.16: Deformation rate *Wi* = 0.06, elongation ratio λ = 7.0: Location 1. This figure contains the original SEM image, corresponding binary image, and Delaunay Triangulation plot of the conditions from the figure title. Scale bars are 500 nm.

Figure A.16 (cont.)

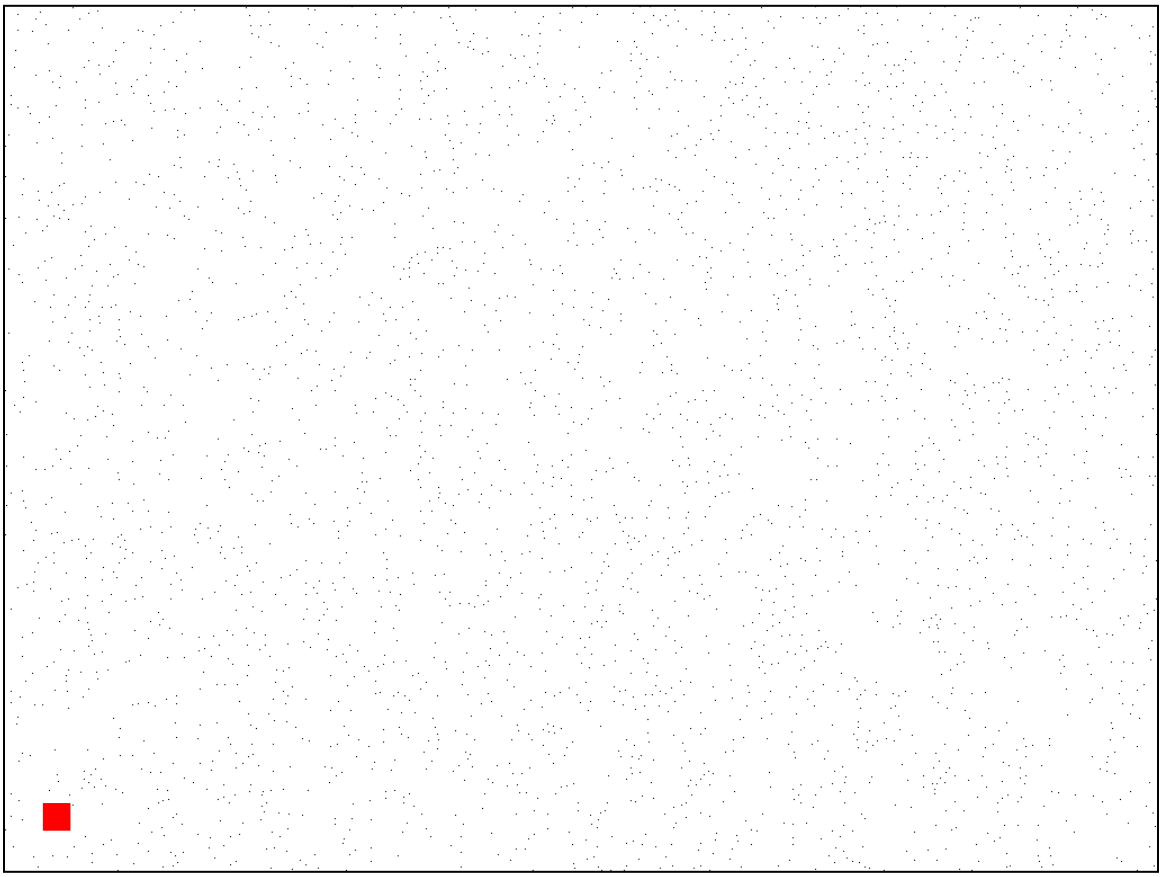

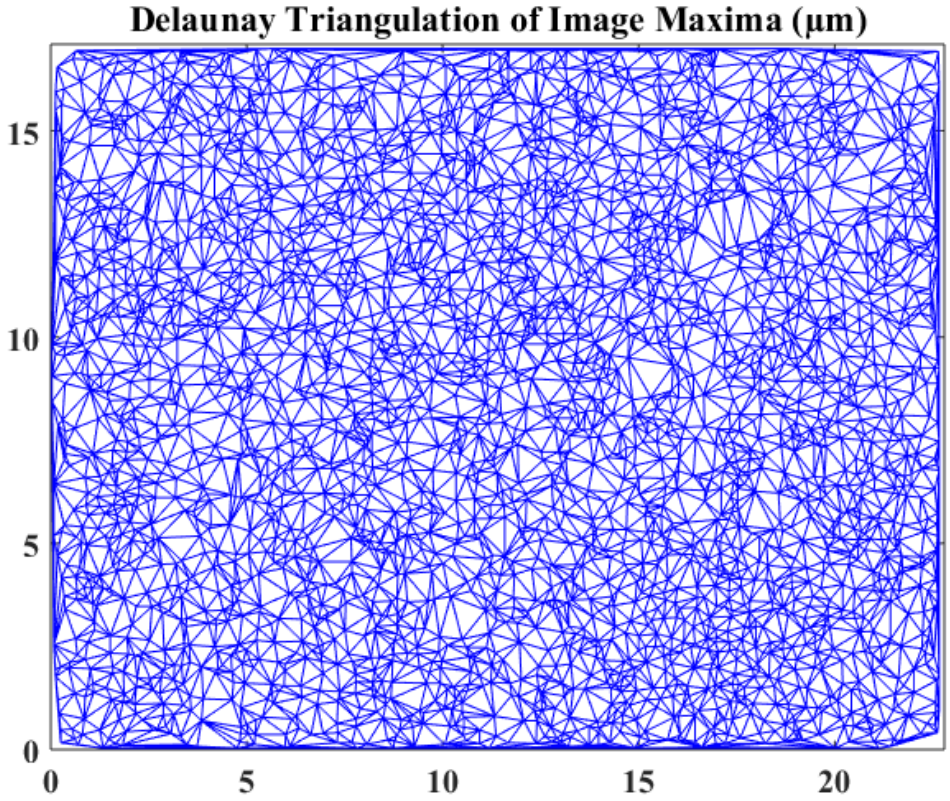

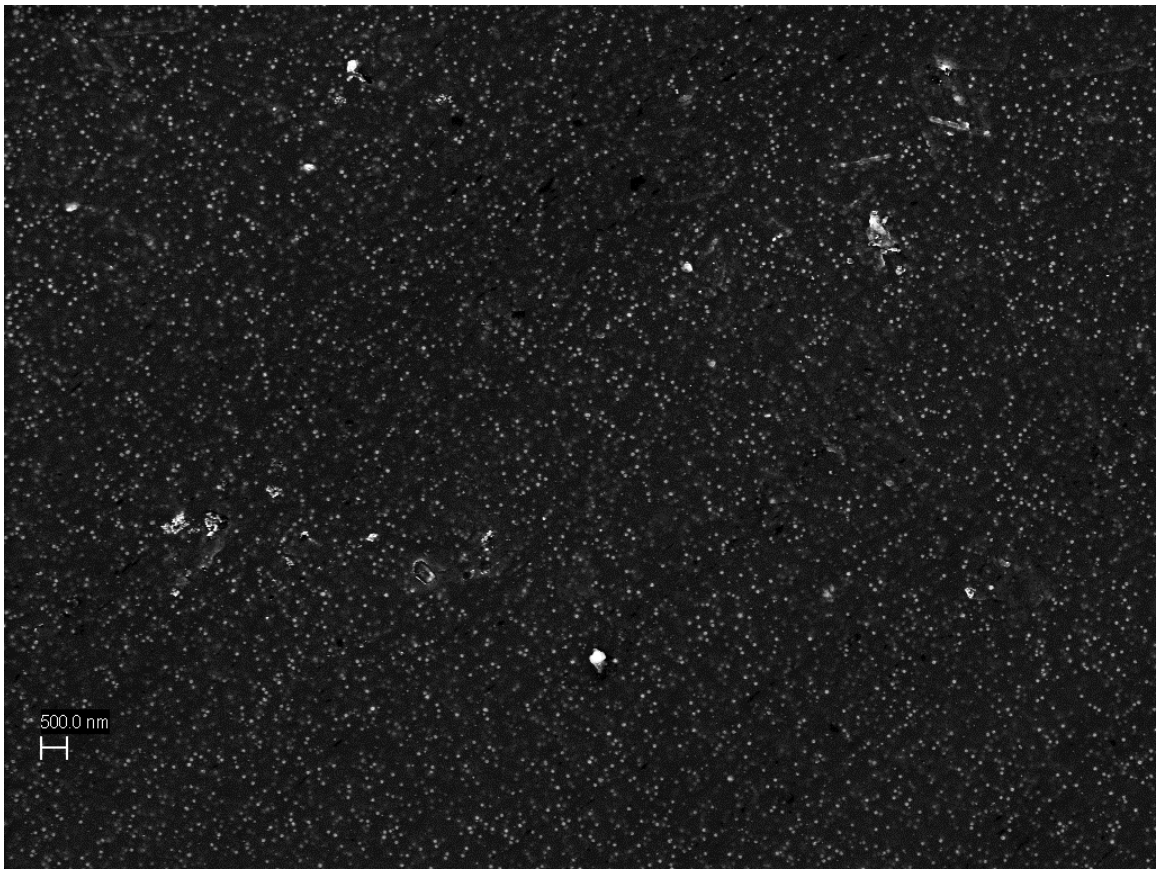

Figure A.17: Deformation rate *Wi* = 0.06, elongation ratio λ = 7.0: Location 2. This figure contains the original SEM image, corresponding binary image, and Delaunay Triangulation plot of the conditions from the figure title. Scale bars are 500 nm.

Figure A.17 (cont.)

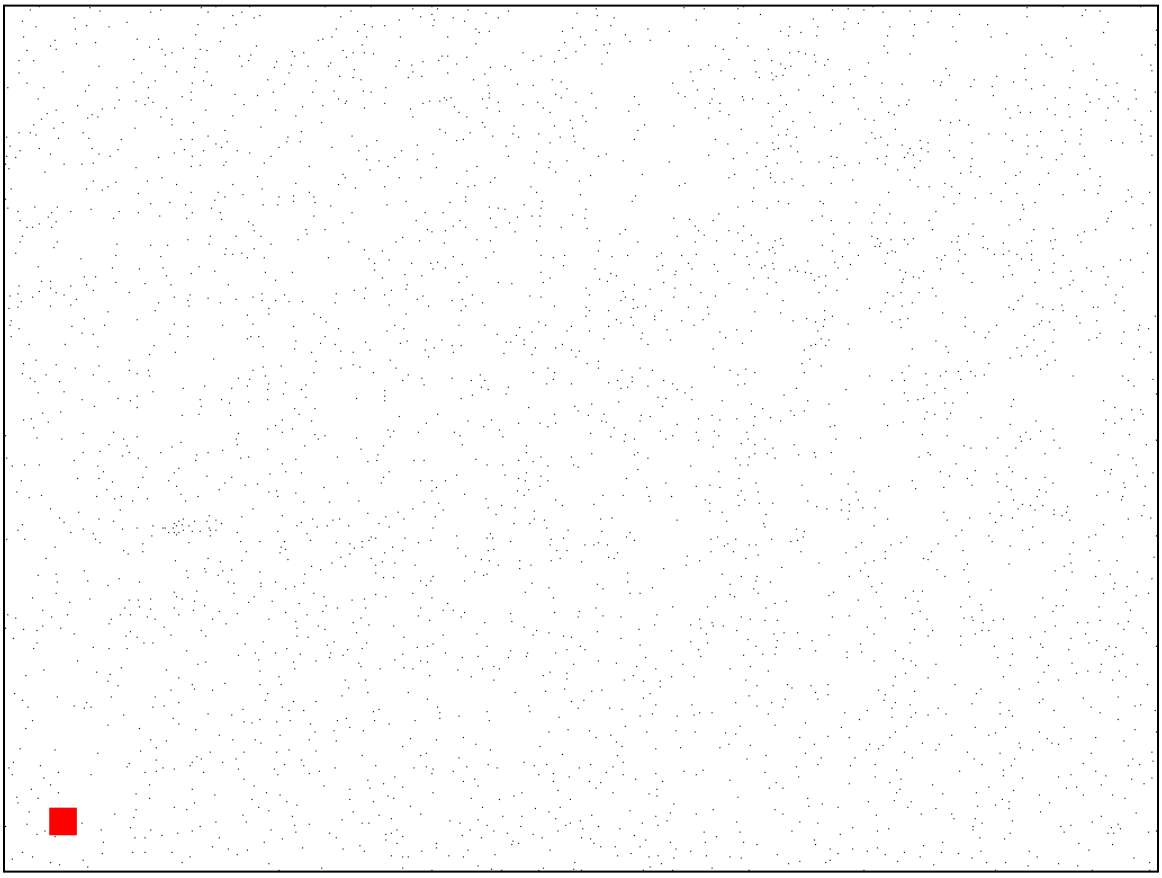

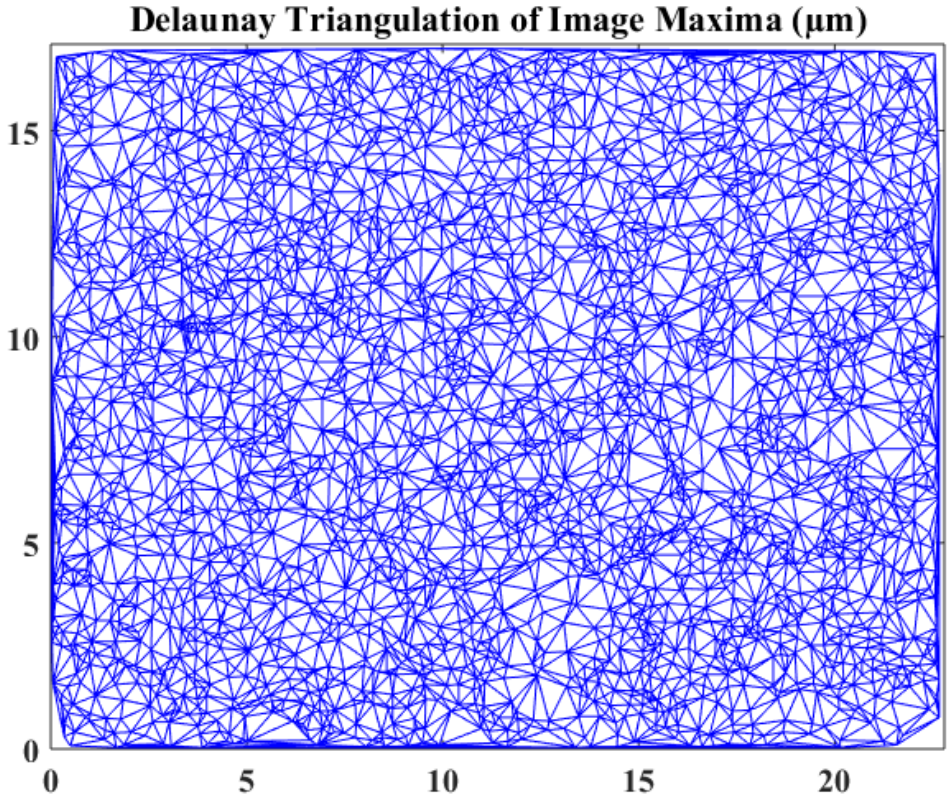

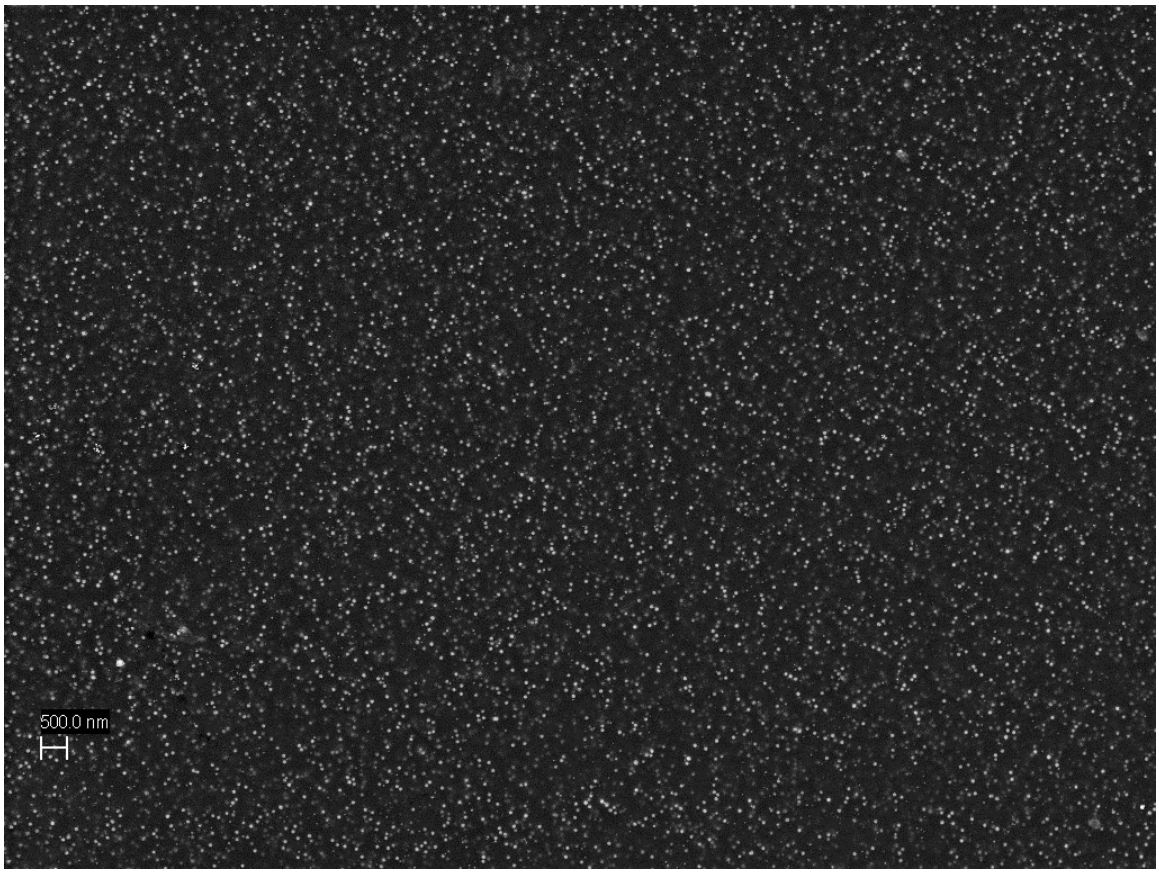

Figure A.18: Deformation rate *Wi* = 0.06, elongation ratio λ = 7.0: Location 3. This figure contains the original SEM image, corresponding binary image, and Delaunay Triangulation plot of the conditions from the figure title. Scale bars are 500 nm.

Figure A.18 (cont.)

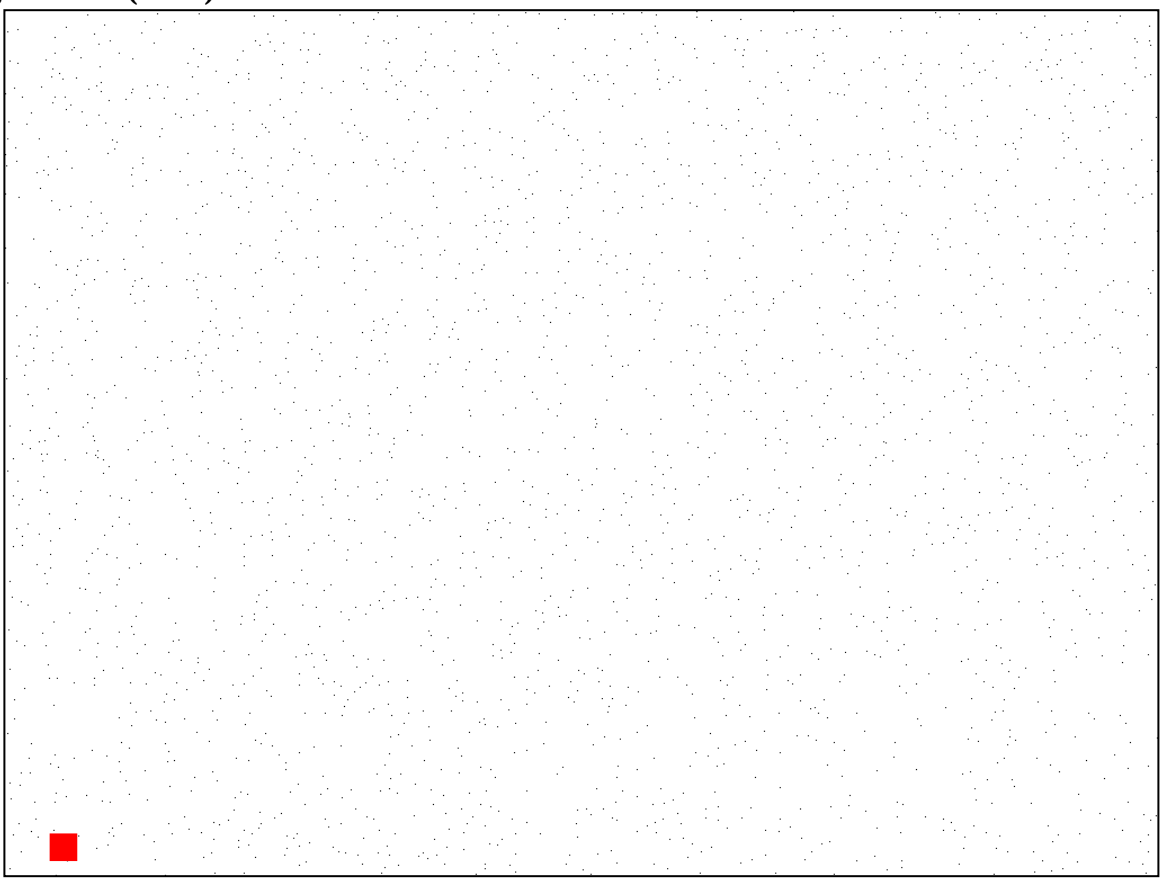

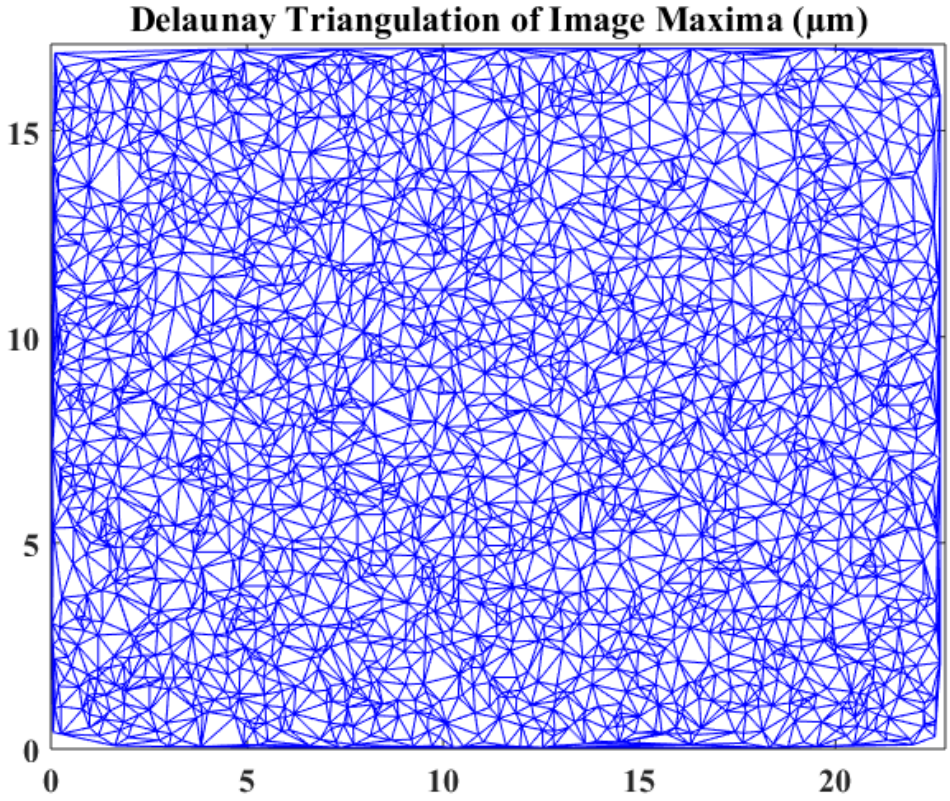

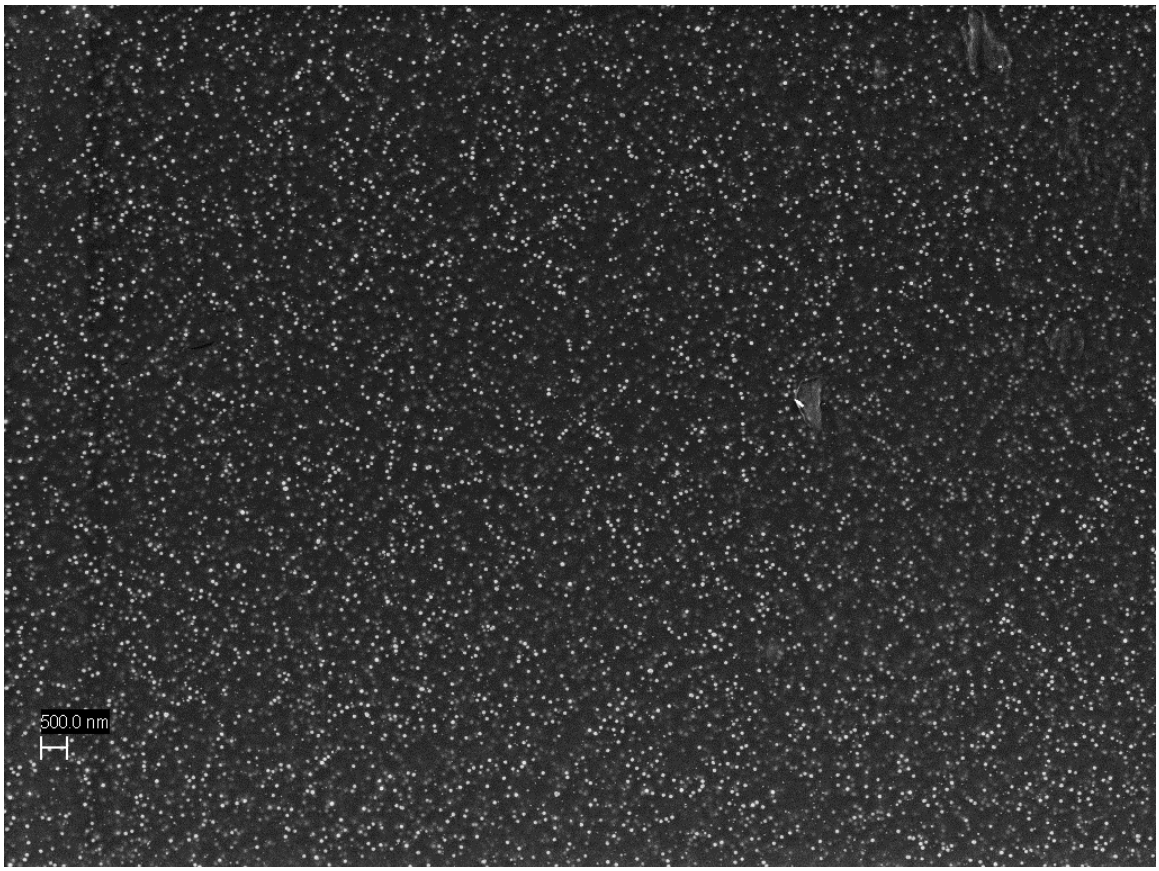

Figure A.19: Deformation rate *Wi* = 0.06, elongation ratio λ = 9.0: Location 1. This figure contains the original SEM image, corresponding binary image, and Delaunay Triangulation plot of the conditions from the figure title. Scale bars are 500 nm.

Figure A.19 (cont.)

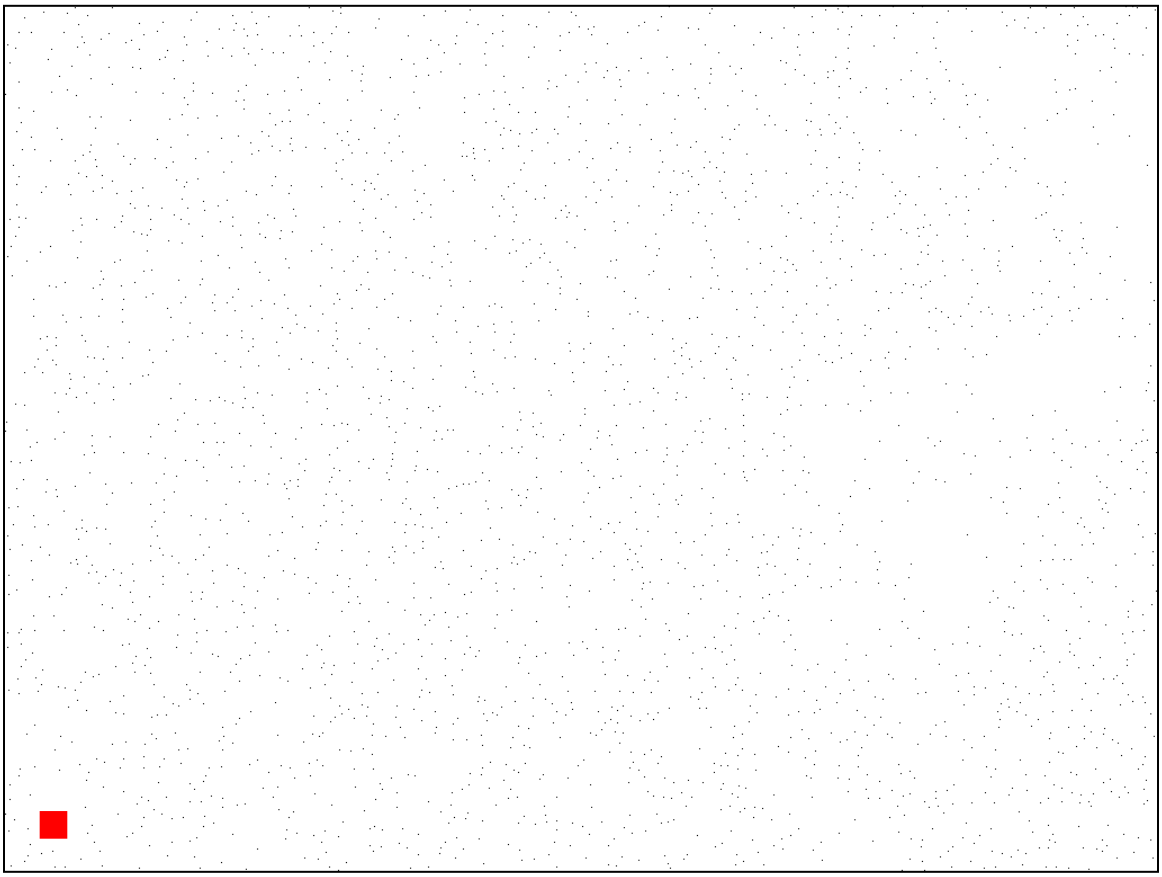

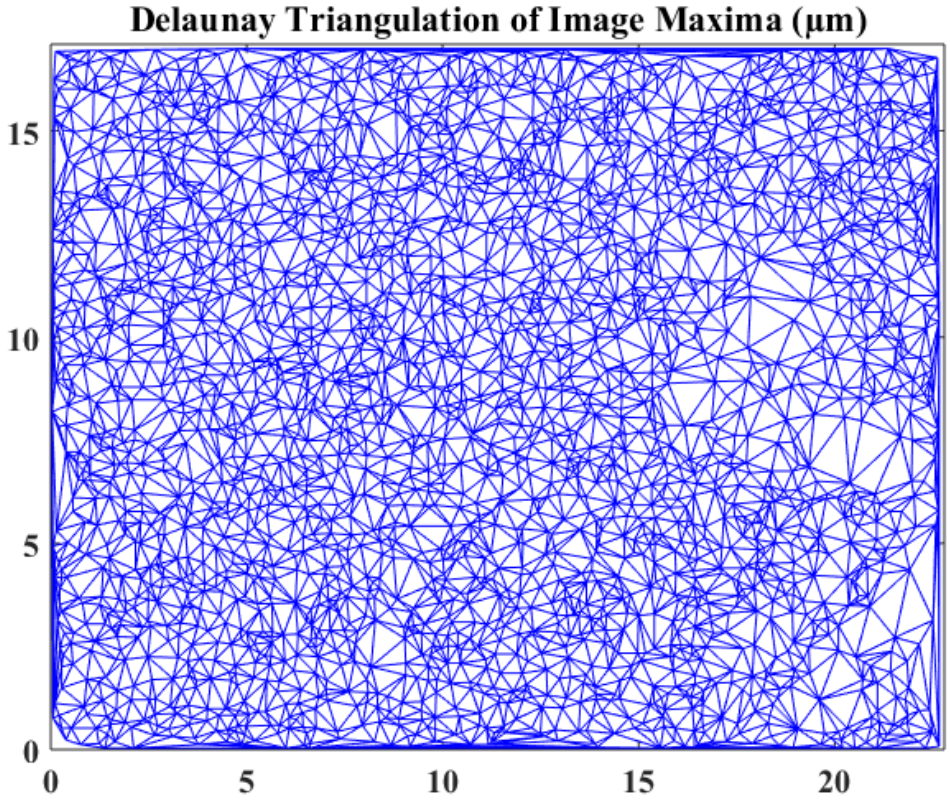

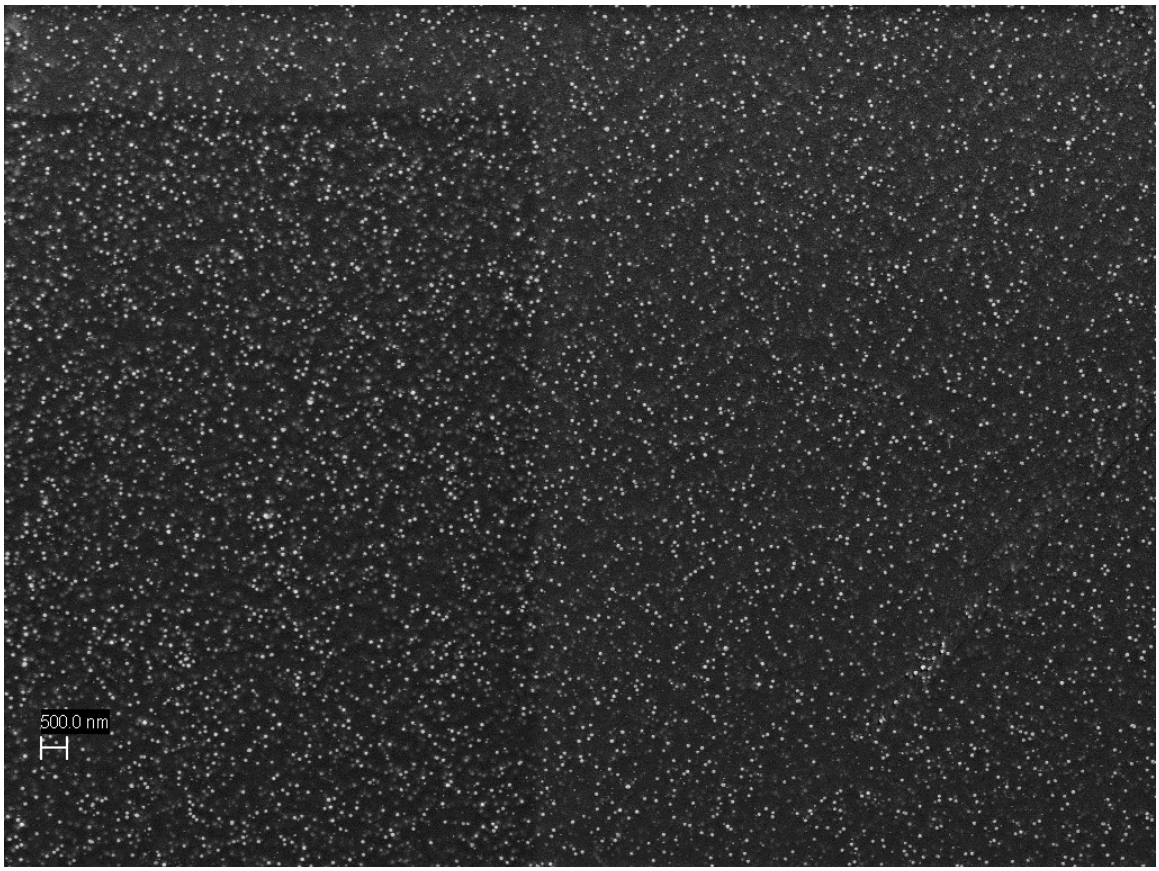

Figure A.20: Deformation rate *Wi* = 0.06, elongation ratio λ = 9.0: Location 2. This figure contains the original SEM image, corresponding binary image, and Delaunay Triangulation plot of the conditions from the figure title. Scale bars are 500 nm.

Figure A.20 (cont.)

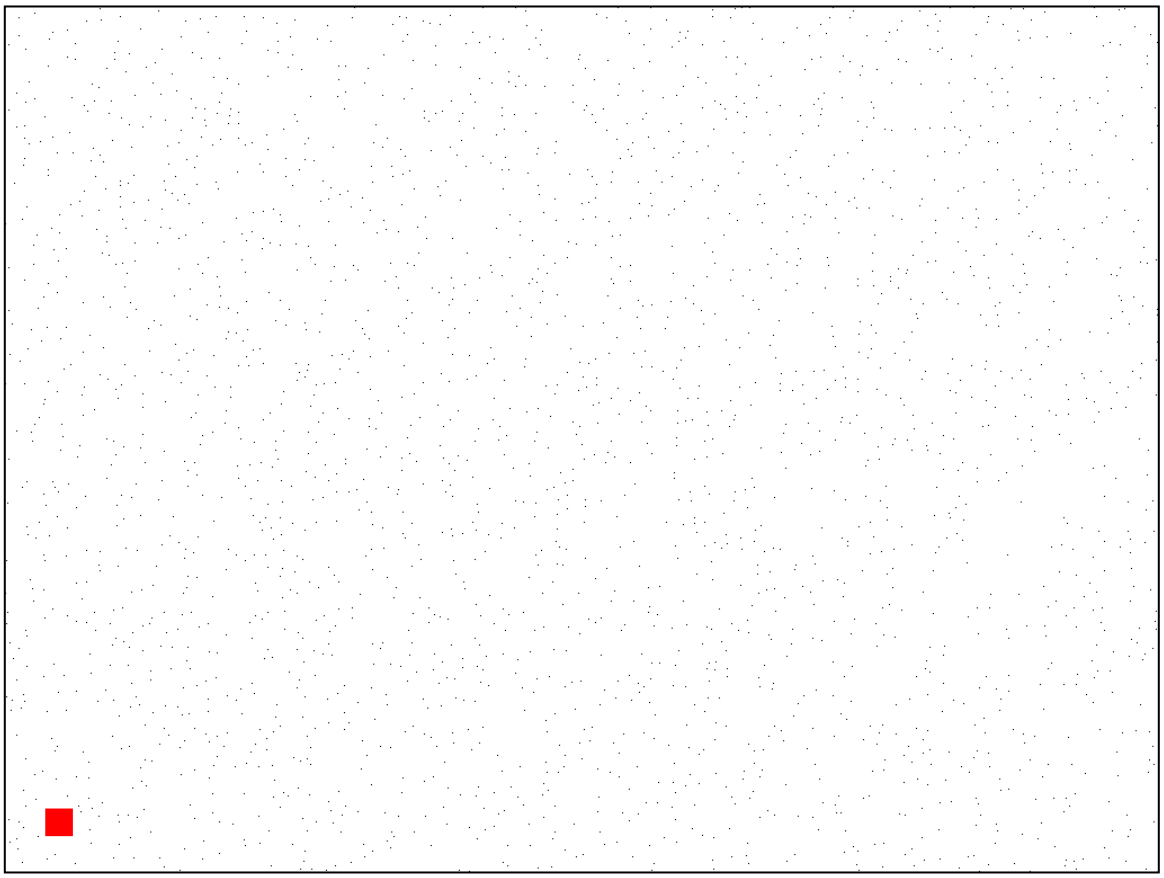

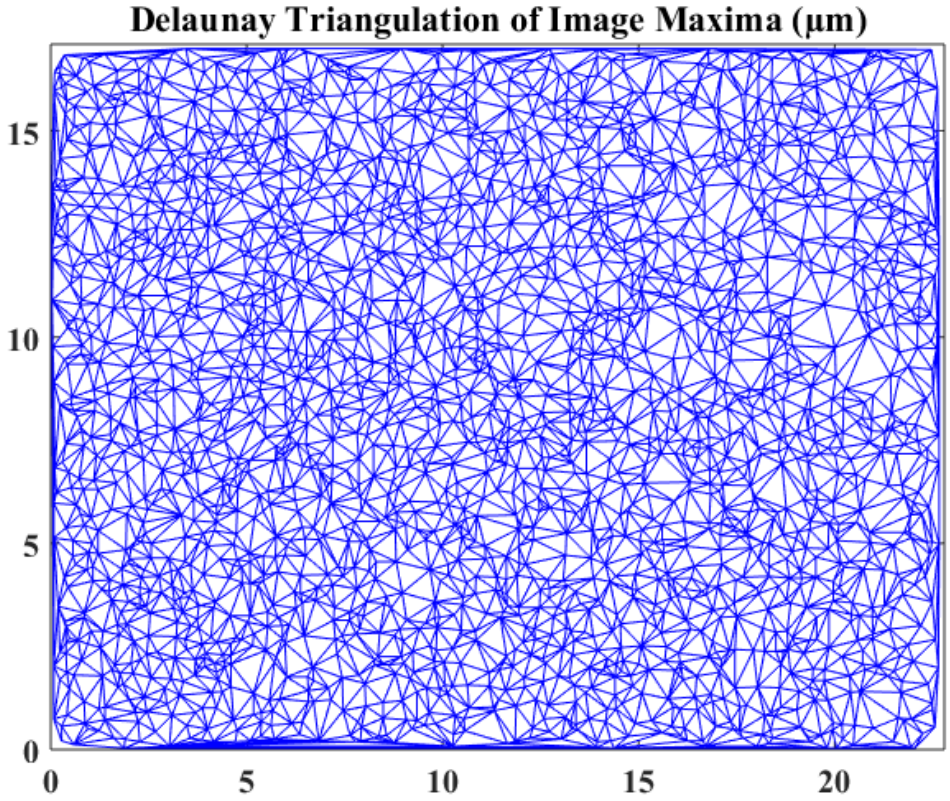

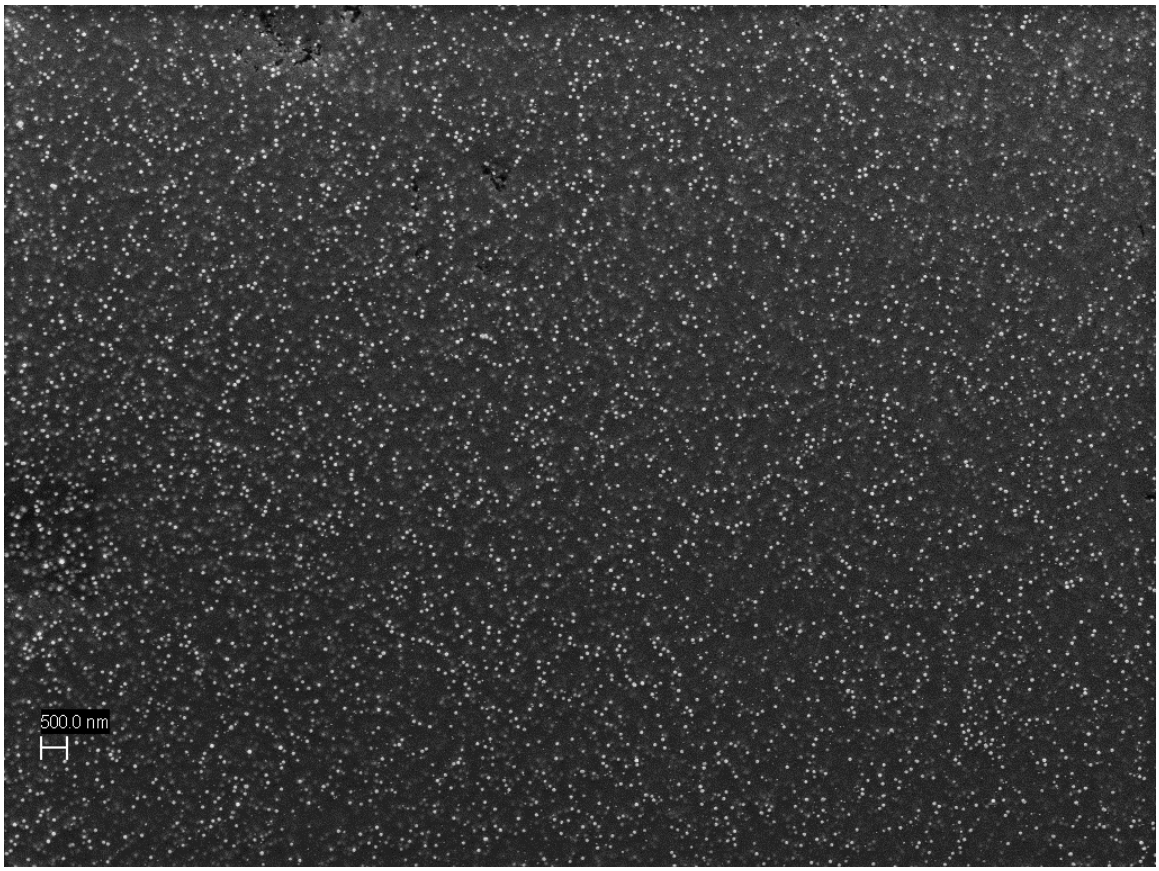

Figure A.21: Deformation rate *Wi* = 0.06, elongation ratio λ = 9.0: Location 3. This figure contains the original SEM image, corresponding binary image, and Delaunay Triangulation plot of the conditions from the figure title. Scale bars are 500 nm.

Figure A.21 (cont.)

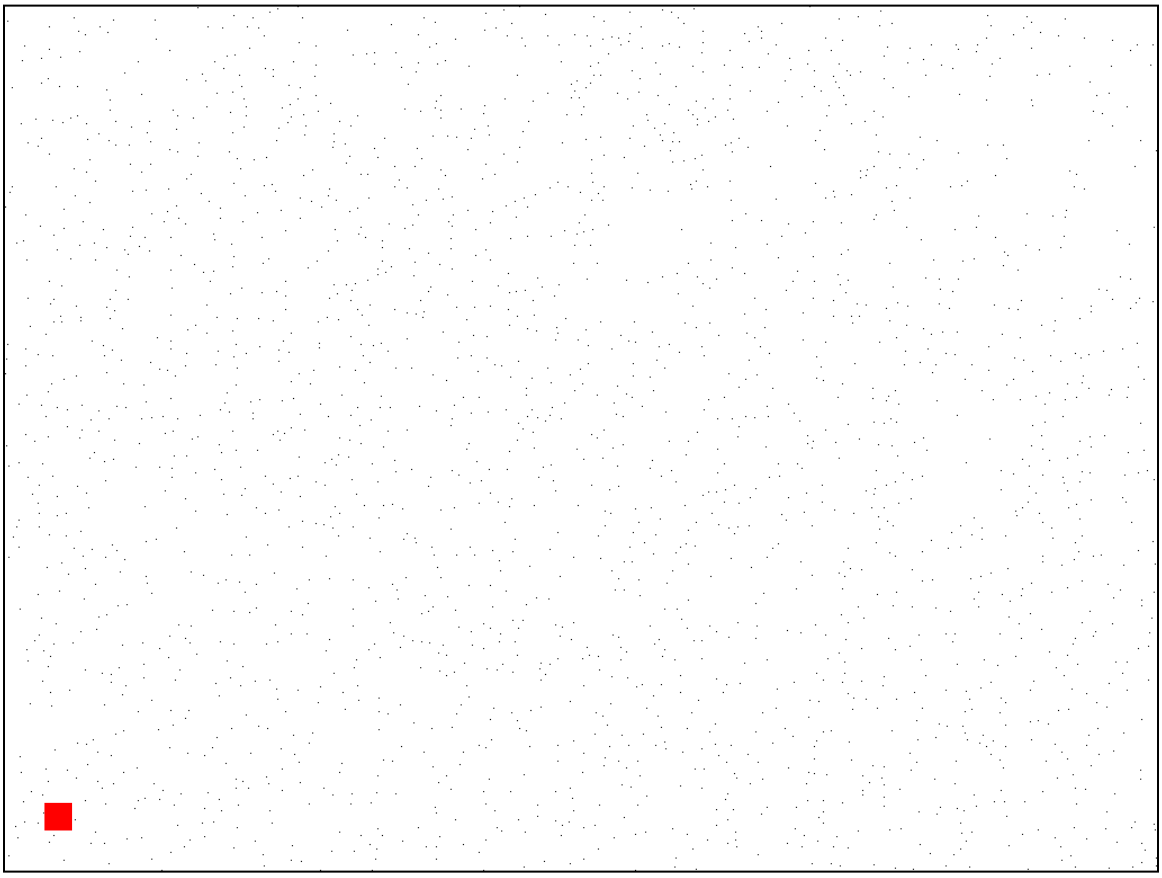

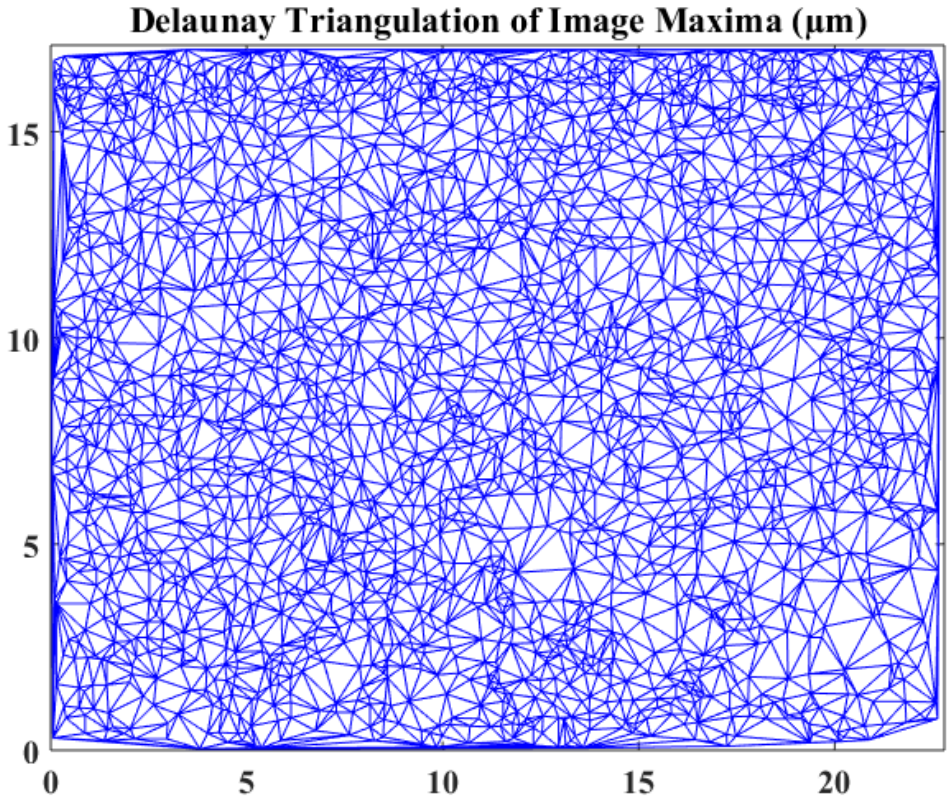

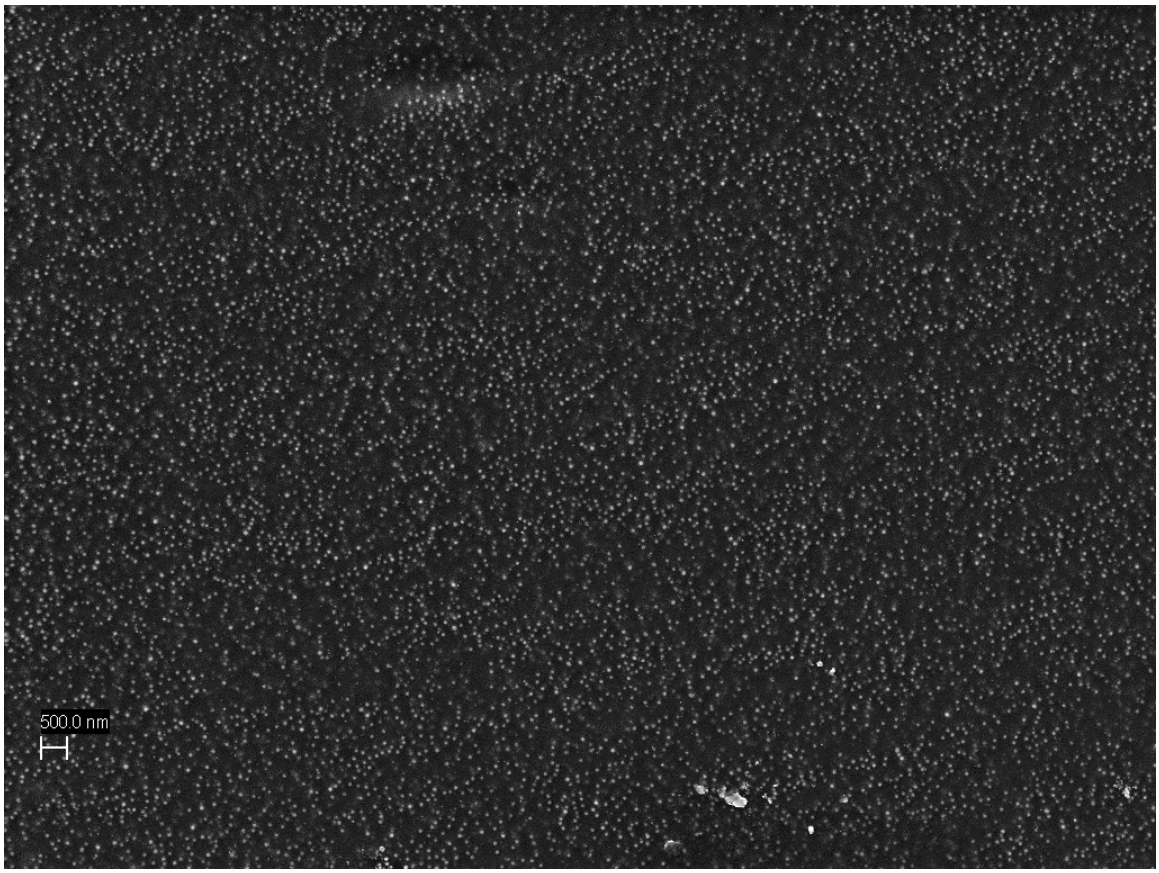

Figure A.22: Deformation rate *Wi* = 20, elongation ratio λ = 1.5: Location 1. This figure contains the original SEM image, corresponding binary image, and Delaunay Triangulation plot of the conditions from the figure title. Scale bars are 500 nm.

Figure A.22 (cont.)

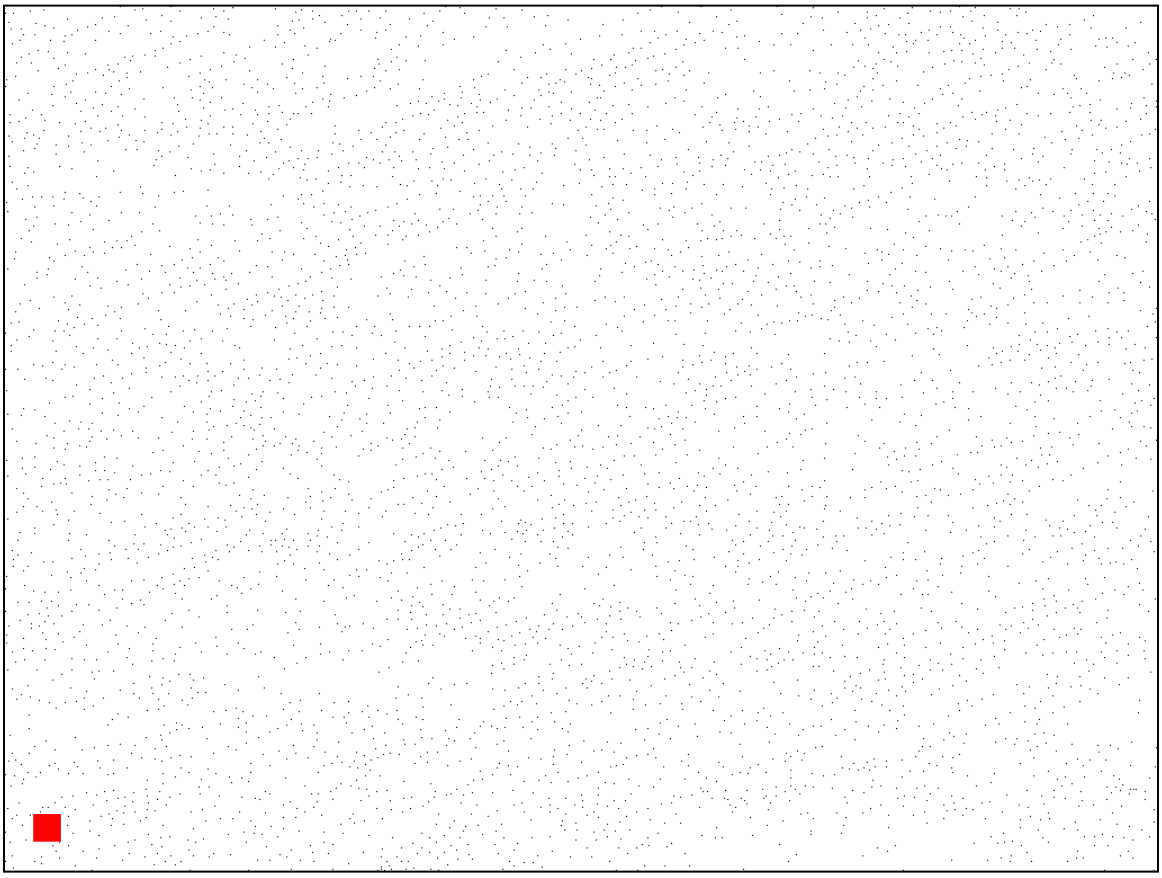

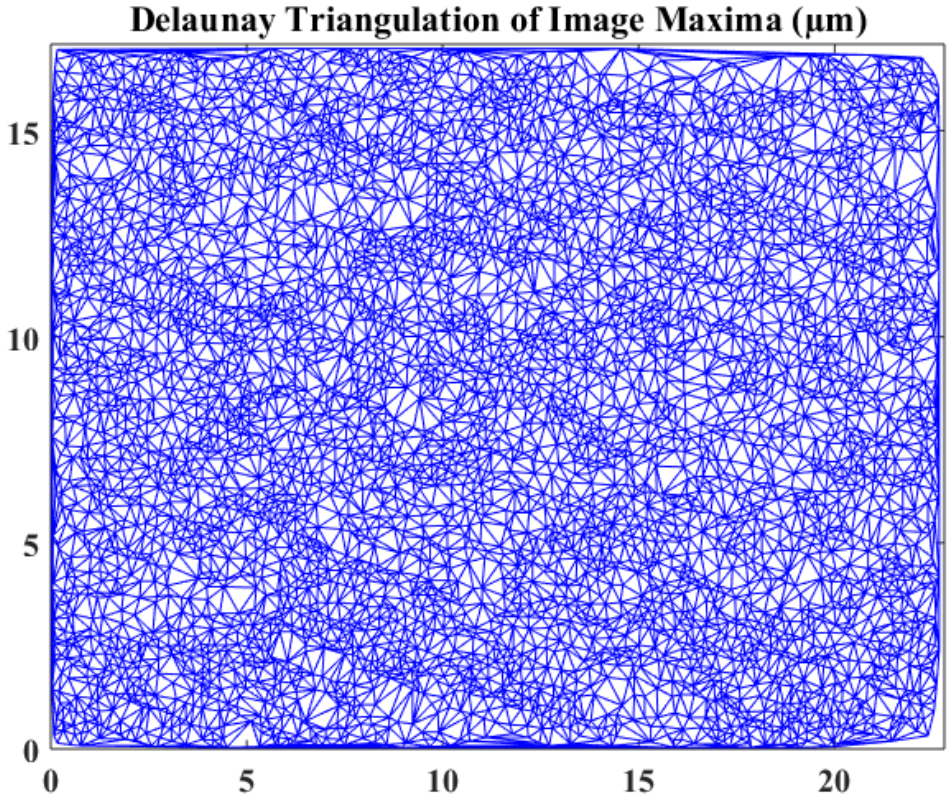

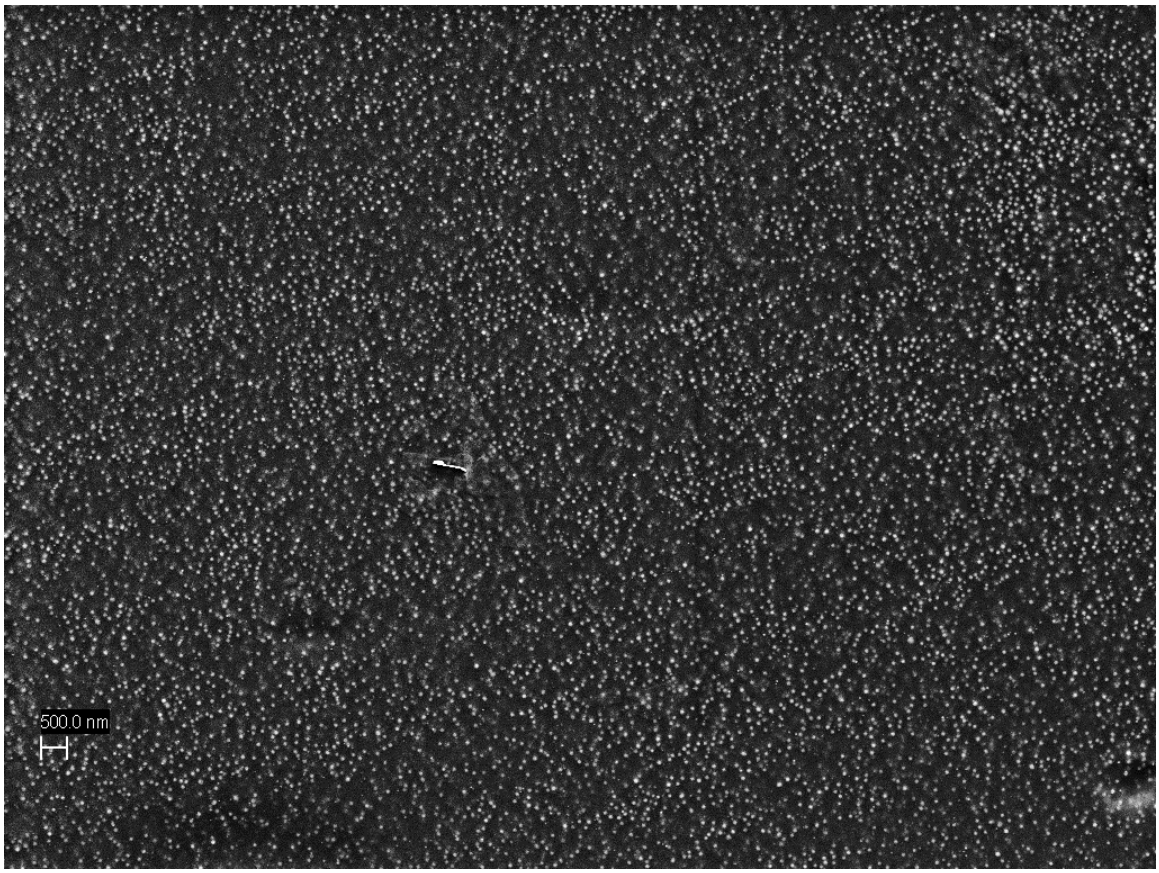

Figure A.23: Deformation rate *Wi* = 20, elongation ratio λ = 1.5: Location 2. This figure contains the original SEM image, corresponding binary image, and Delaunay Triangulation plot of the conditions from the figure title. Scale bars are 500 nm.

Figure A.23 (cont.)

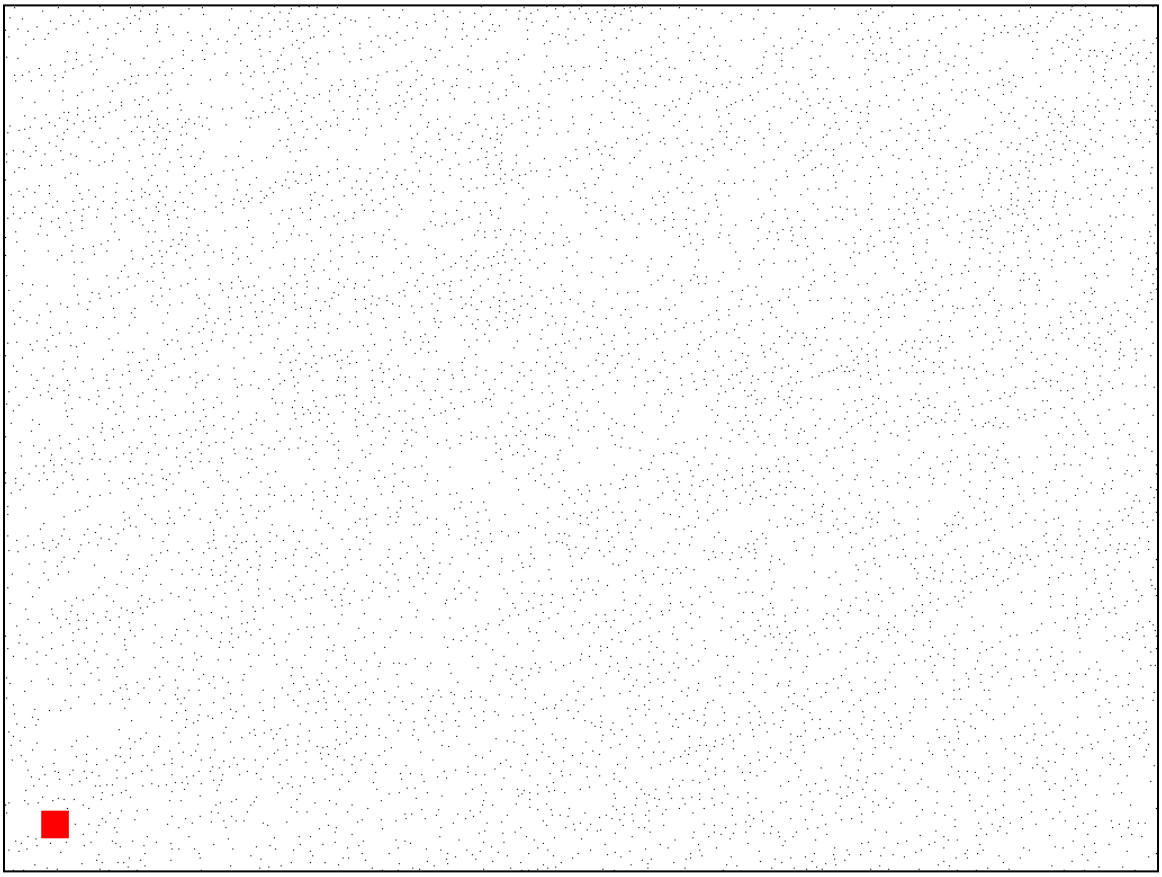

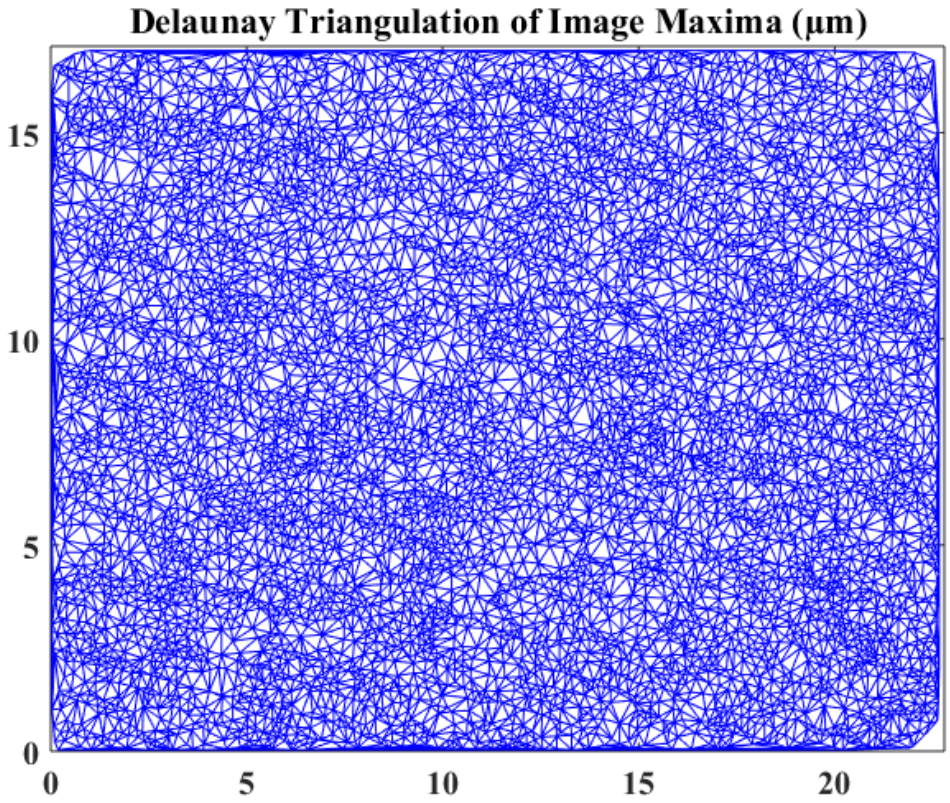

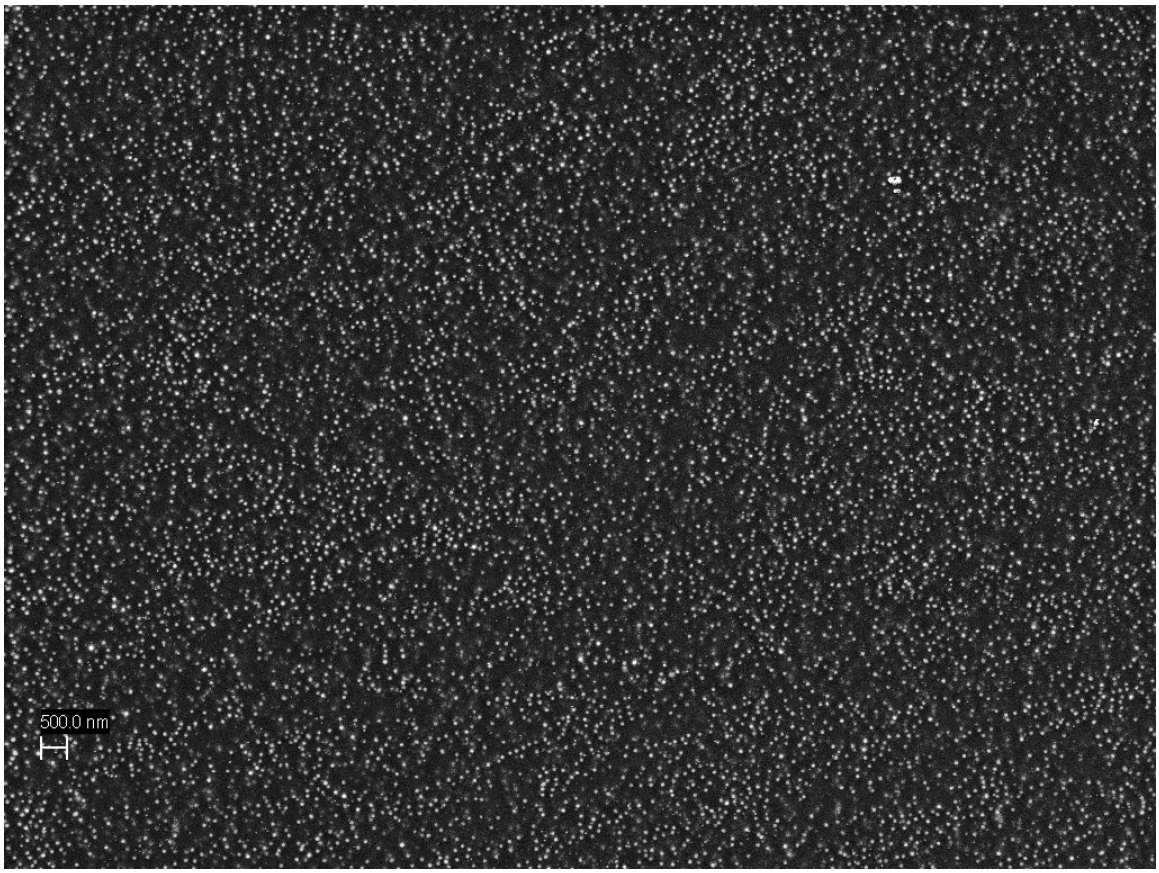

Figure A.24: Deformation rate *Wi* = 20, elongation ratio λ = 1.5: Location 3. This figure contains the original SEM image, corresponding binary image, and Delaunay Triangulation plot of the conditions from the figure title. Scale bars are 500 nm.

Figure A.24 (cont.)

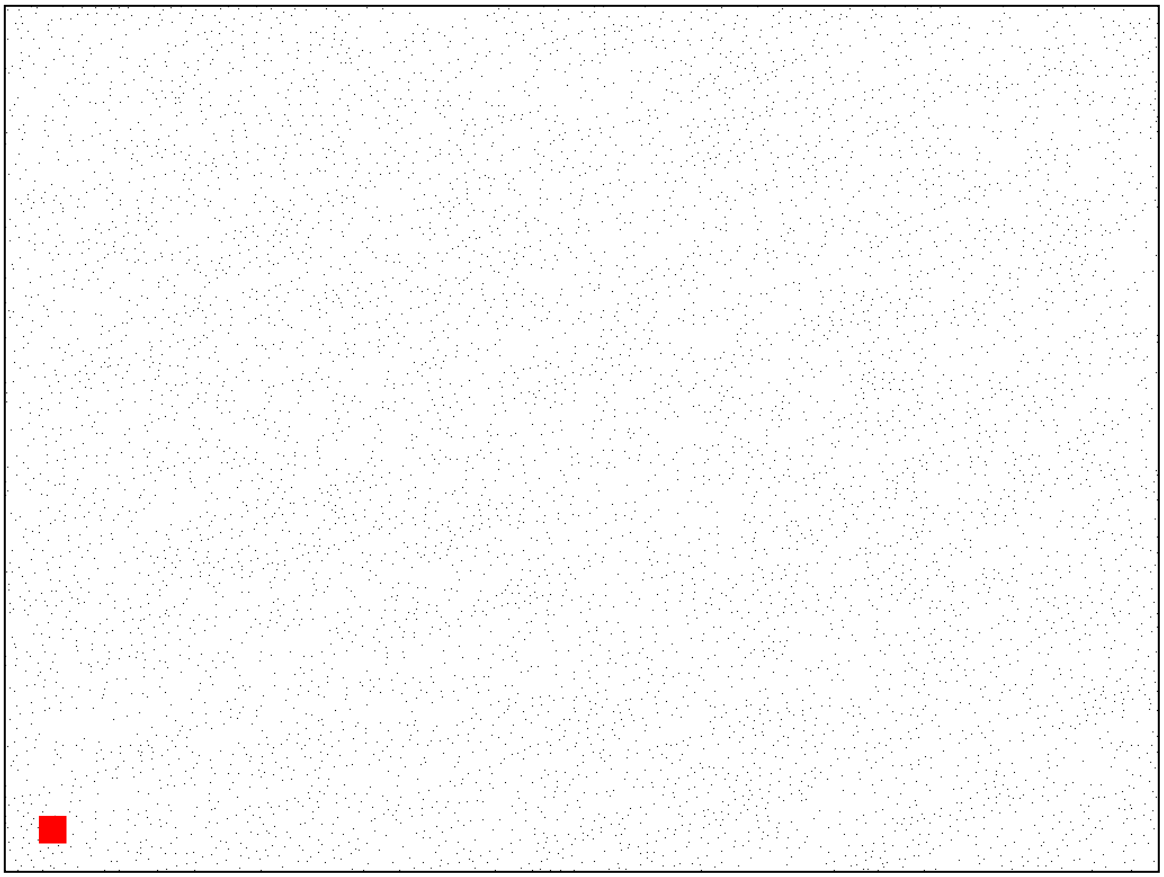

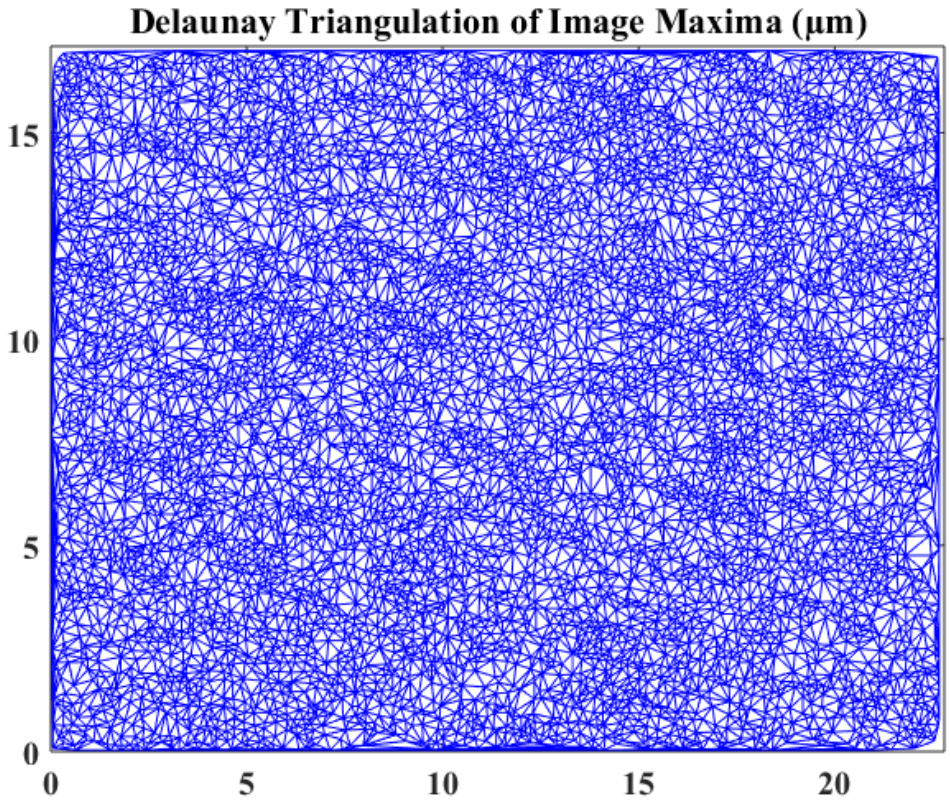

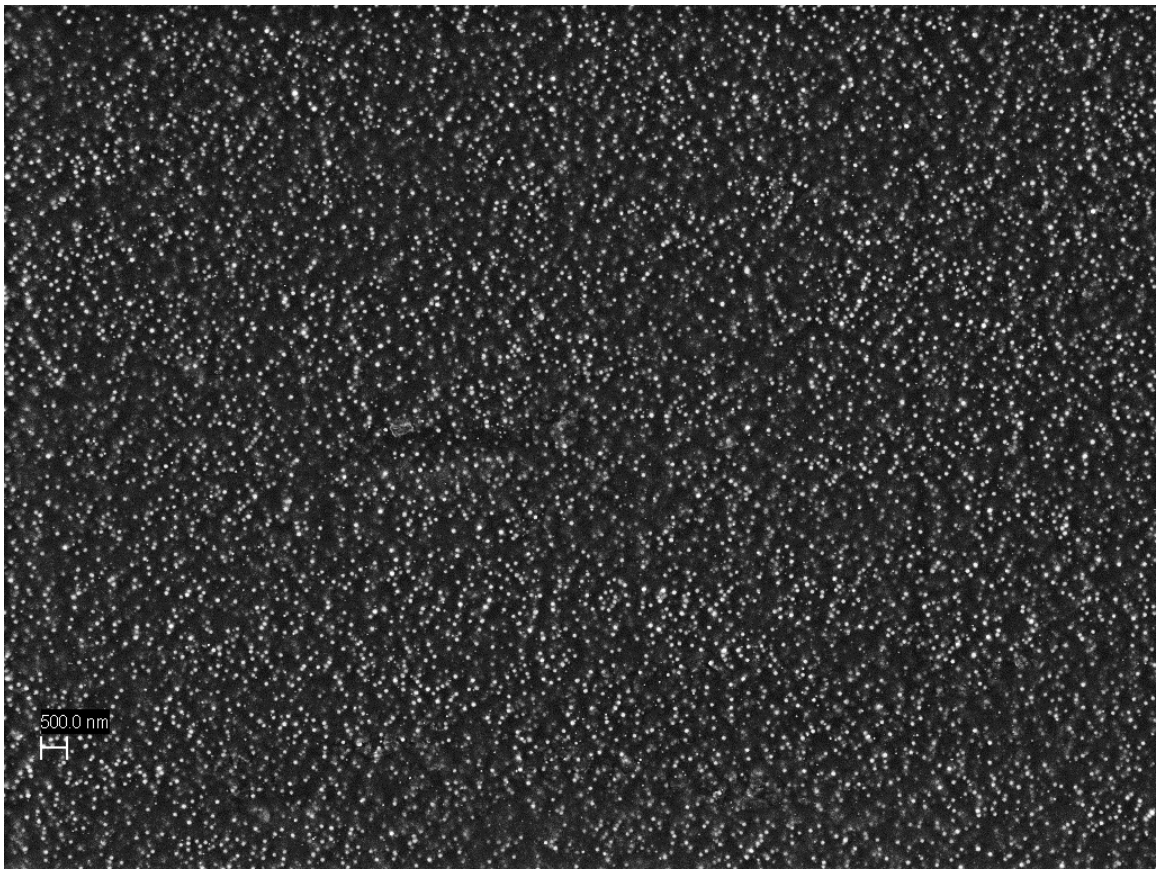

Figure A.25: Deformation rate *Wi* = 20, elongation ratio λ = 2.5: Location 1. This figure contains the original SEM image, corresponding binary image, and Delaunay Triangulation plot of the conditions from the figure title. Scale bars are 500 nm.

Figure A.25 (cont.)

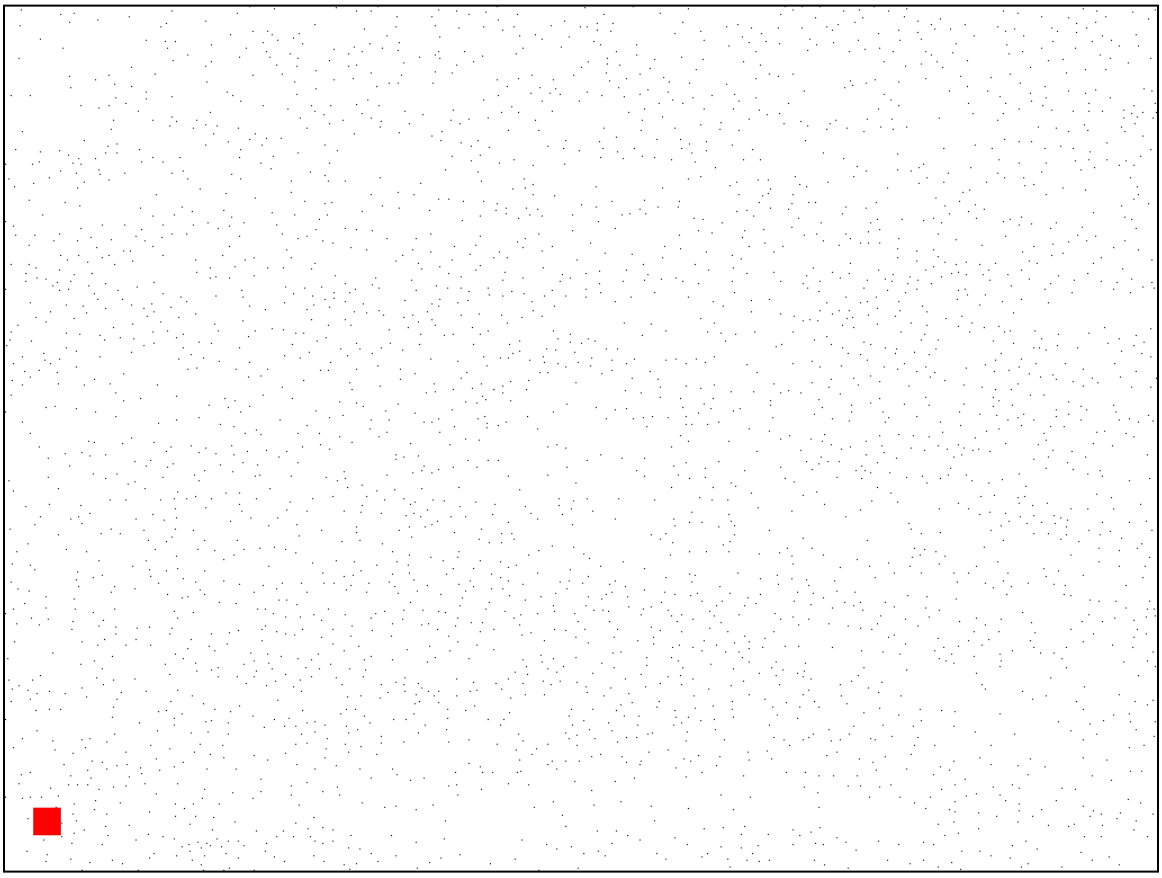

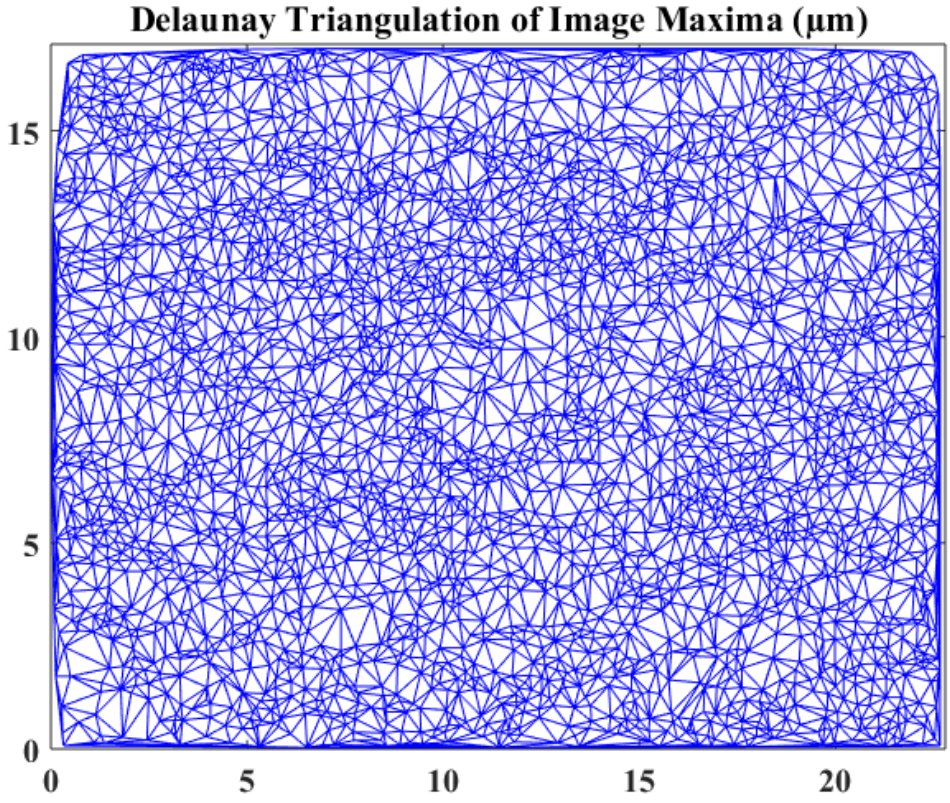

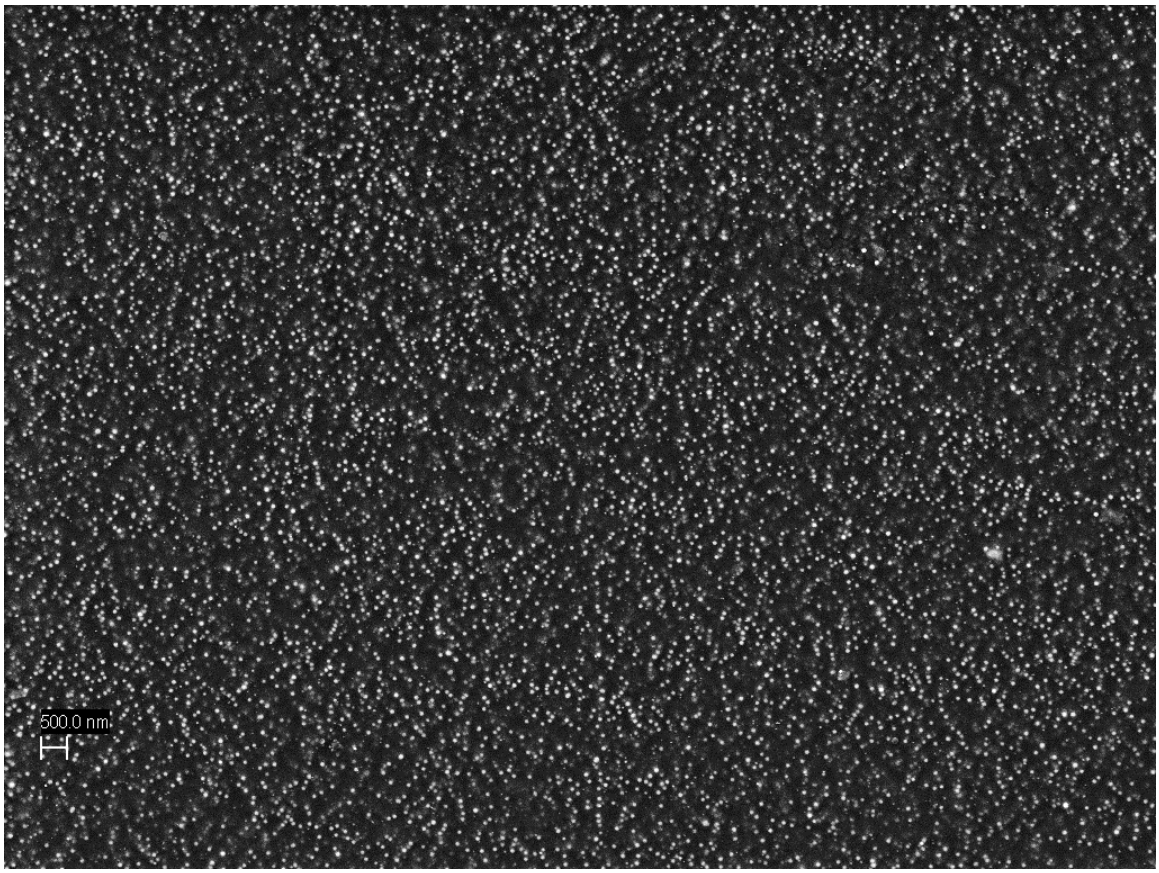

Figure A.26: Deformation rate *Wi* = 20, elongation ratio λ = 2.5: Location 2. This figure contains the original SEM image, corresponding binary image, and Delaunay Triangulation plot of the conditions from the figure title. Scale bars are 500 nm.

Figure A.26 (cont.)

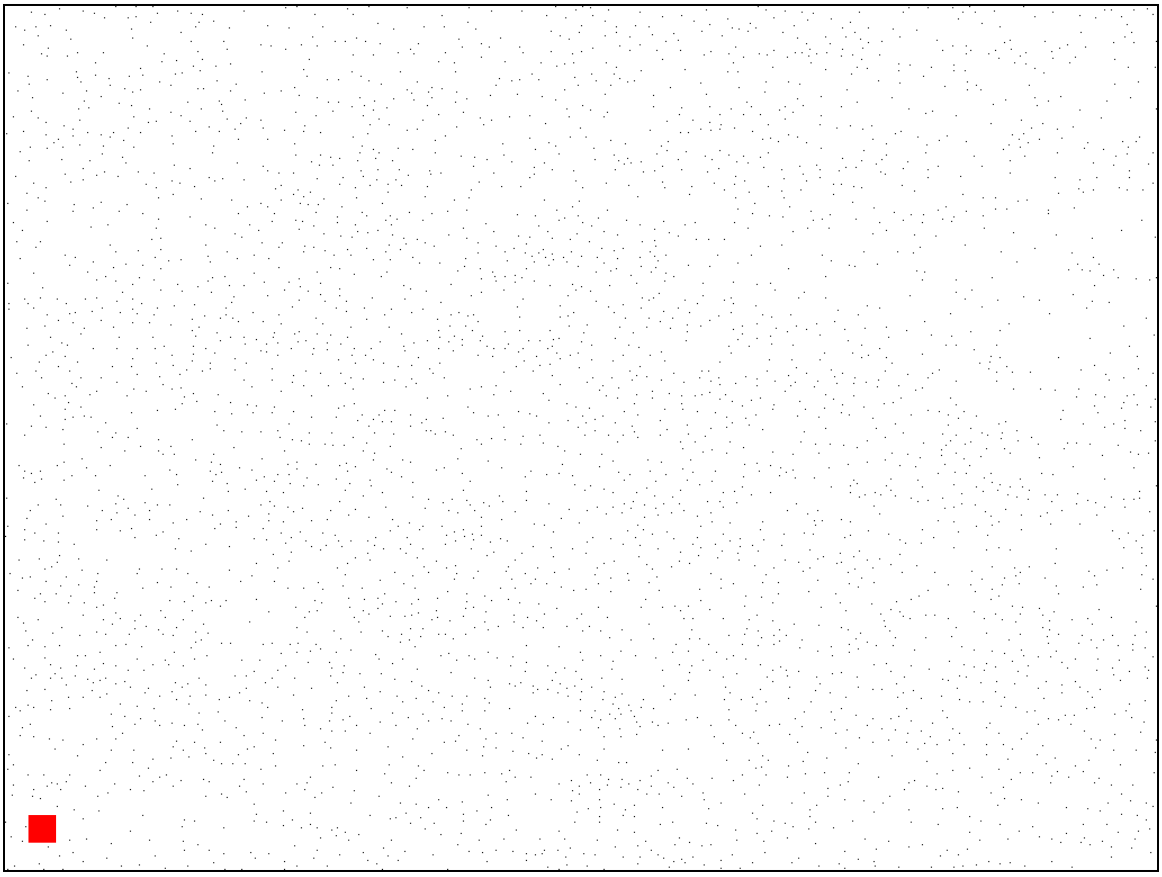

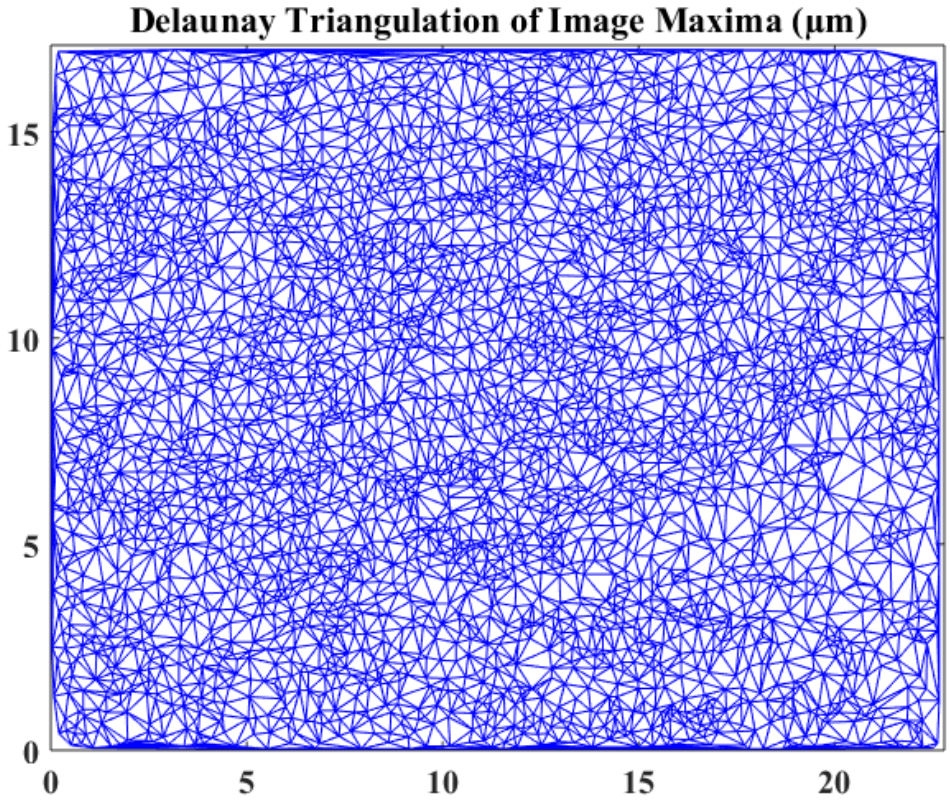

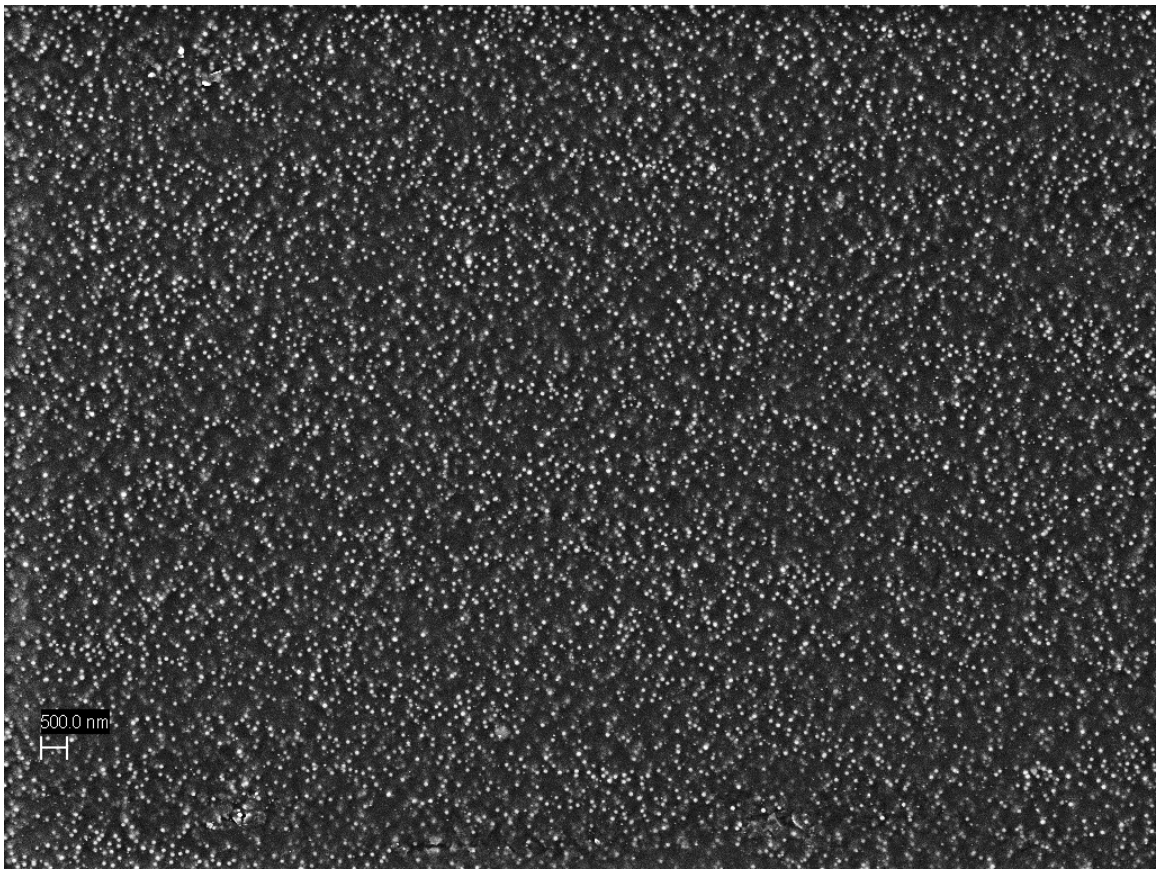

Figure A.27: Deformation rate *Wi* = 20, elongation ratio λ = 2.5: Location 3. This figure contains the original SEM image, corresponding binary image, and Delaunay Triangulation plot of the conditions from the figure title. Scale bars are 500 nm.

Figure A.27 (cont.)

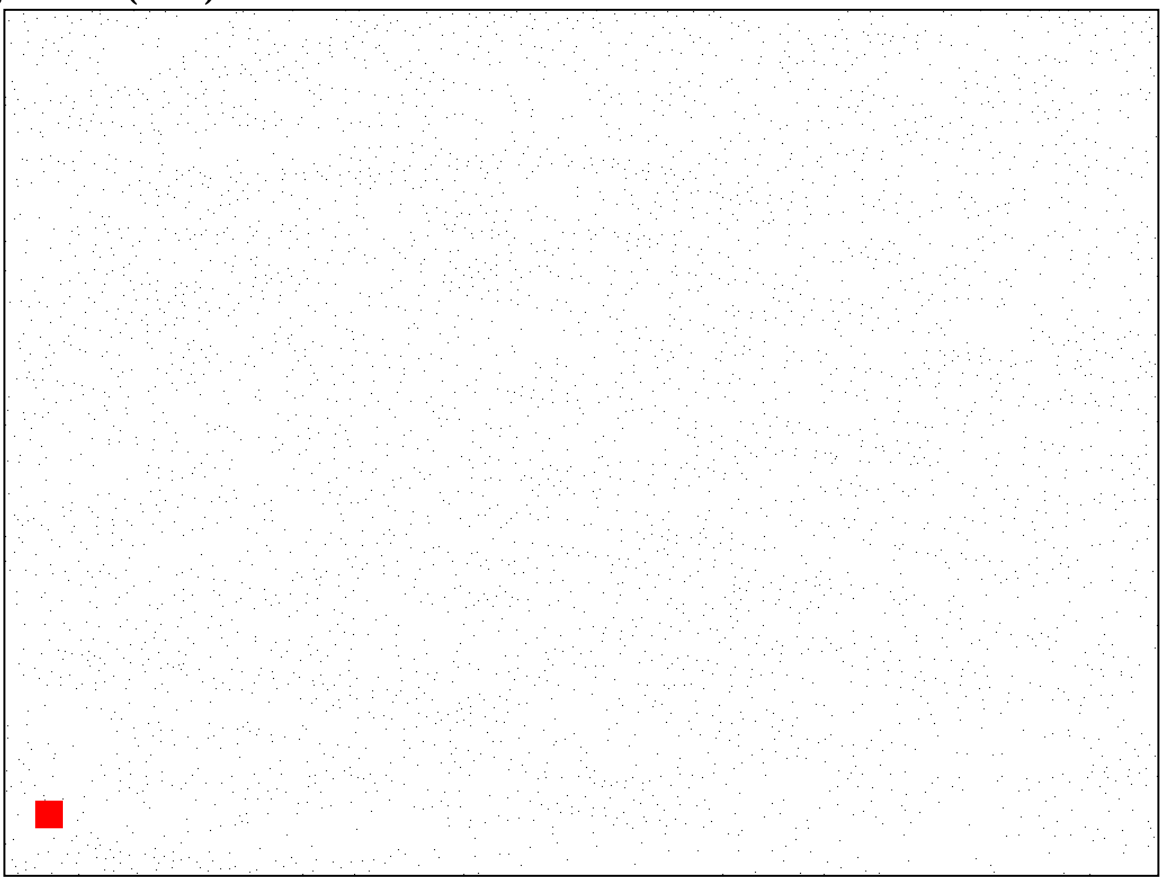

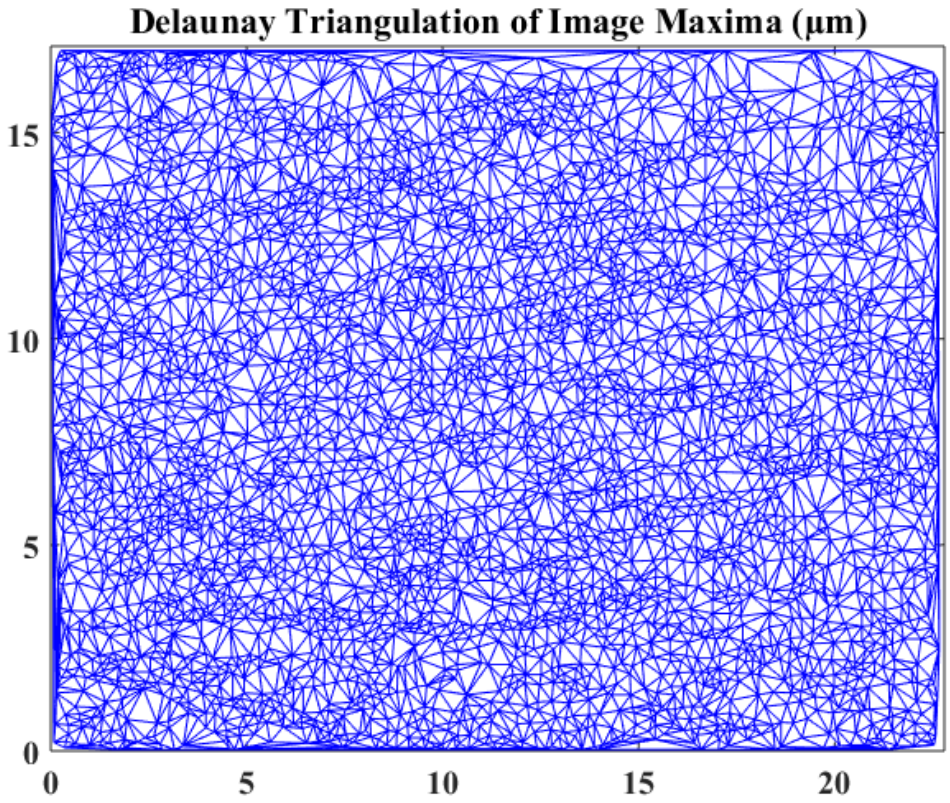

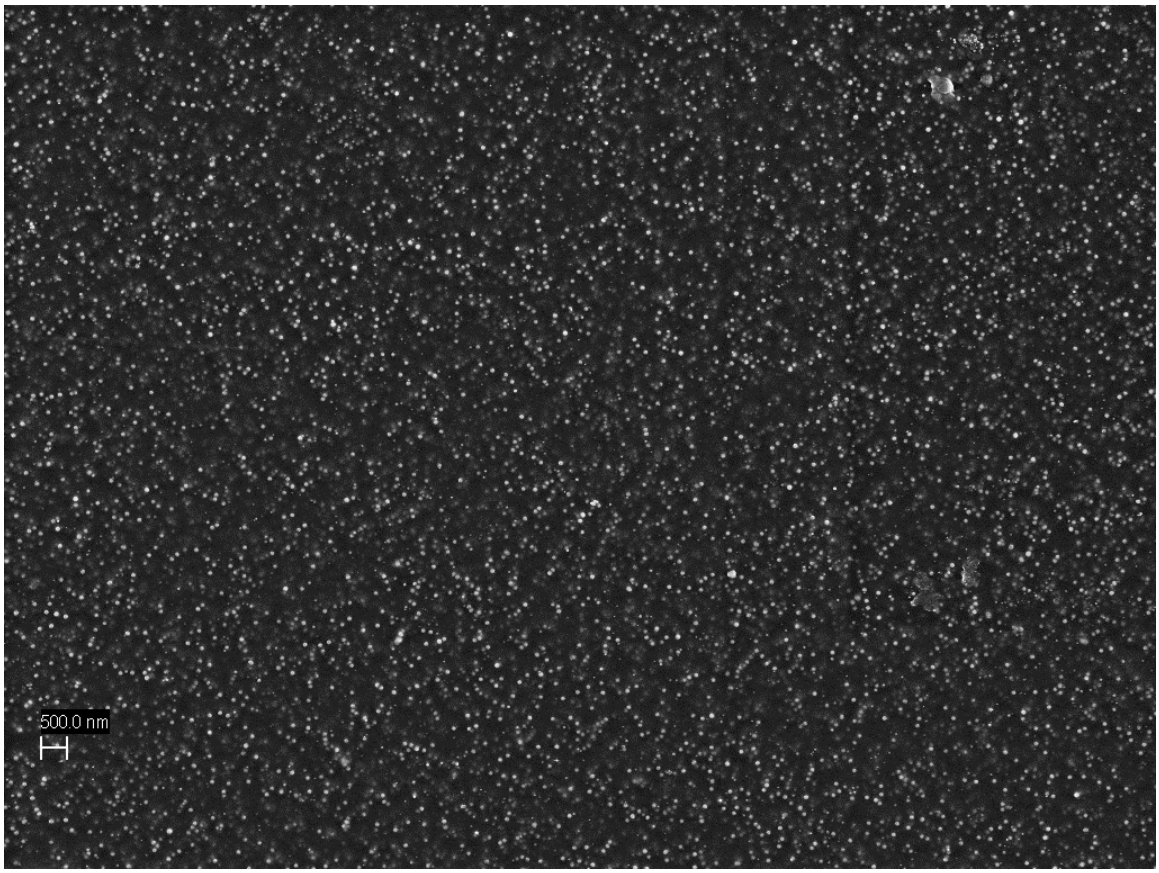

Figure A.28: Deformation rate *Wi* = 20, elongation ratio λ = 4.0: Location 1. This figure contains the original SEM image, corresponding binary image, and Delaunay Triangulation plot of the conditions from the figure title. Scale bars are 500 nm.

Figure A.28 (cont.)

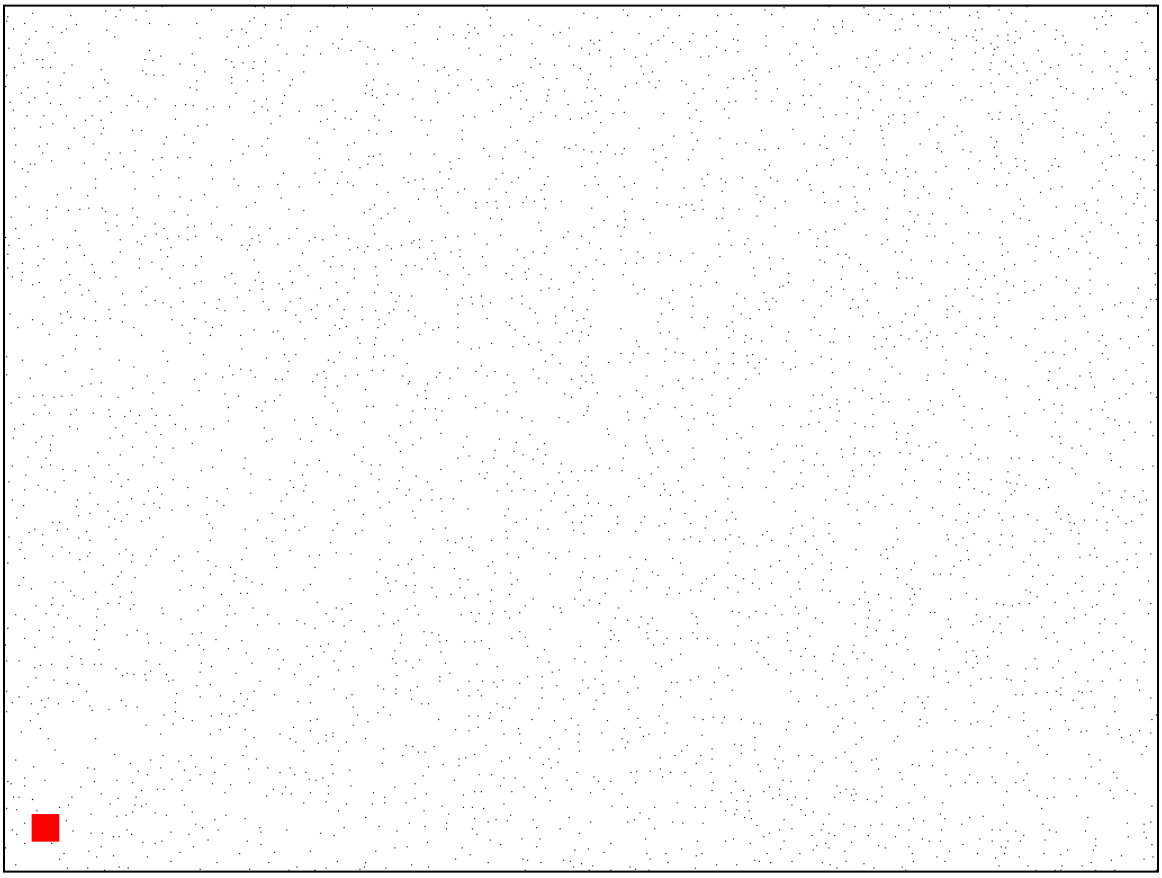

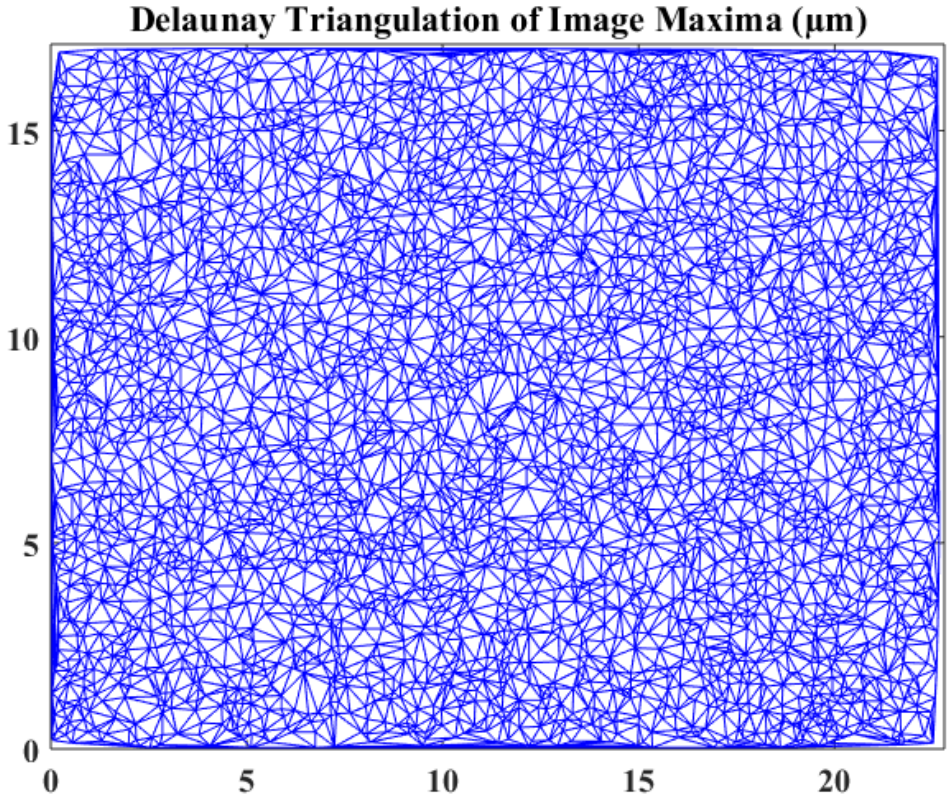

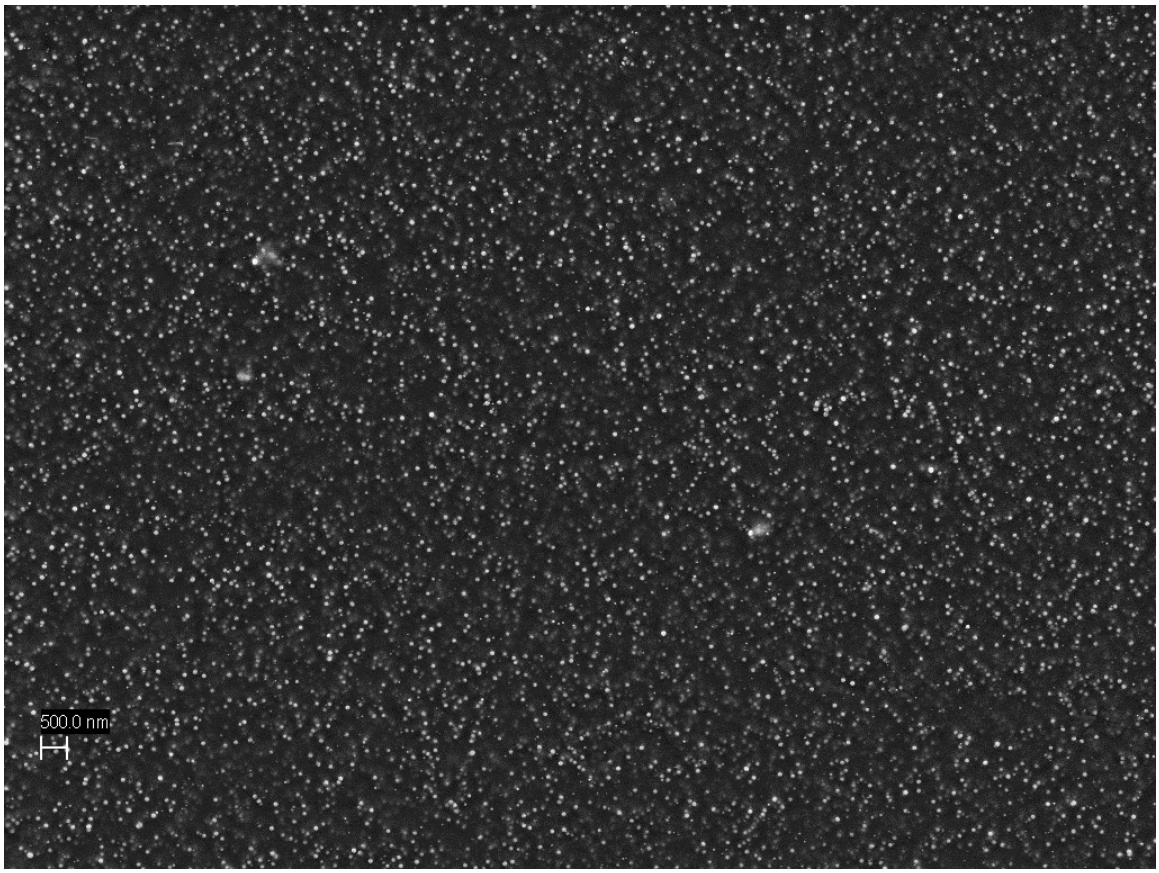

Figure A.29: Deformation rate *Wi* = 20, elongation ratio λ = 4.0: Location 2. This figure contains the original SEM image, corresponding binary image, and Delaunay Triangulation plot of the conditions from the figure title. Scale bars are 500 nm.

Figure A.29 (cont.)

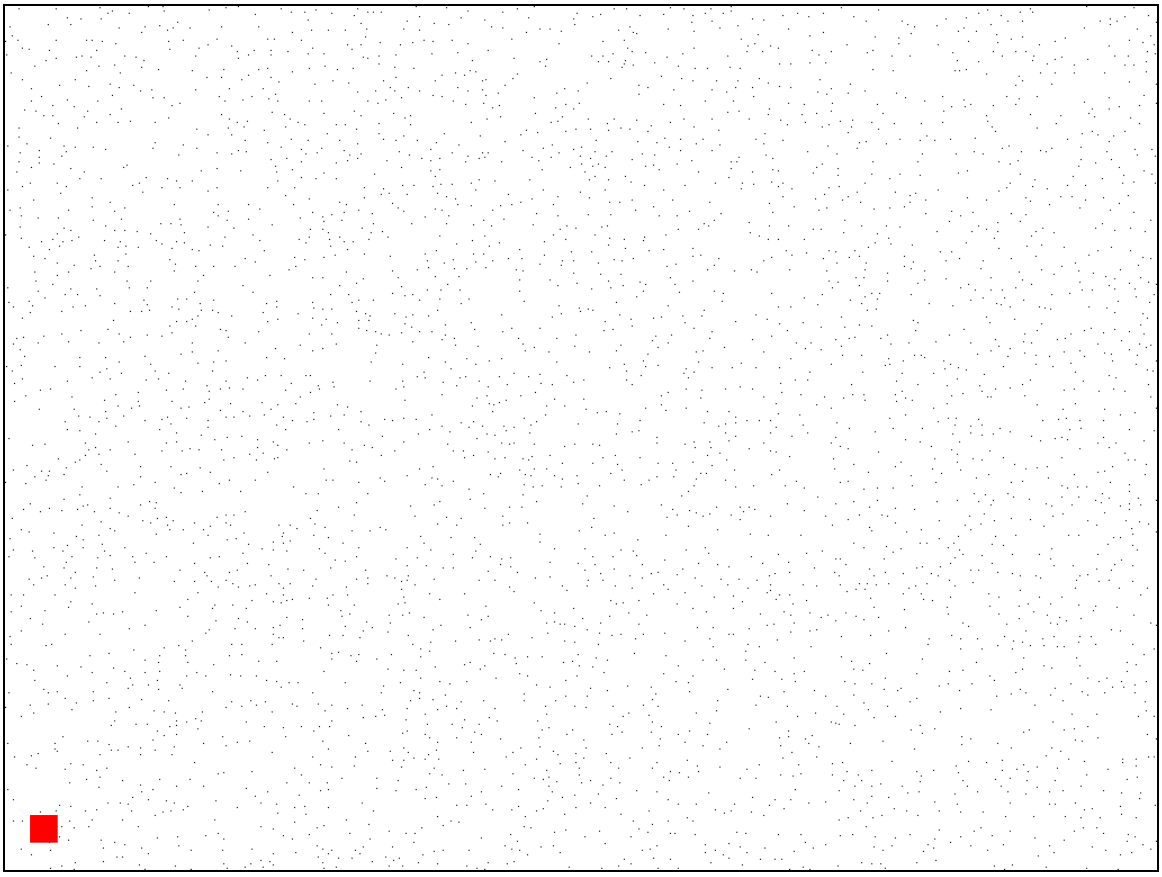

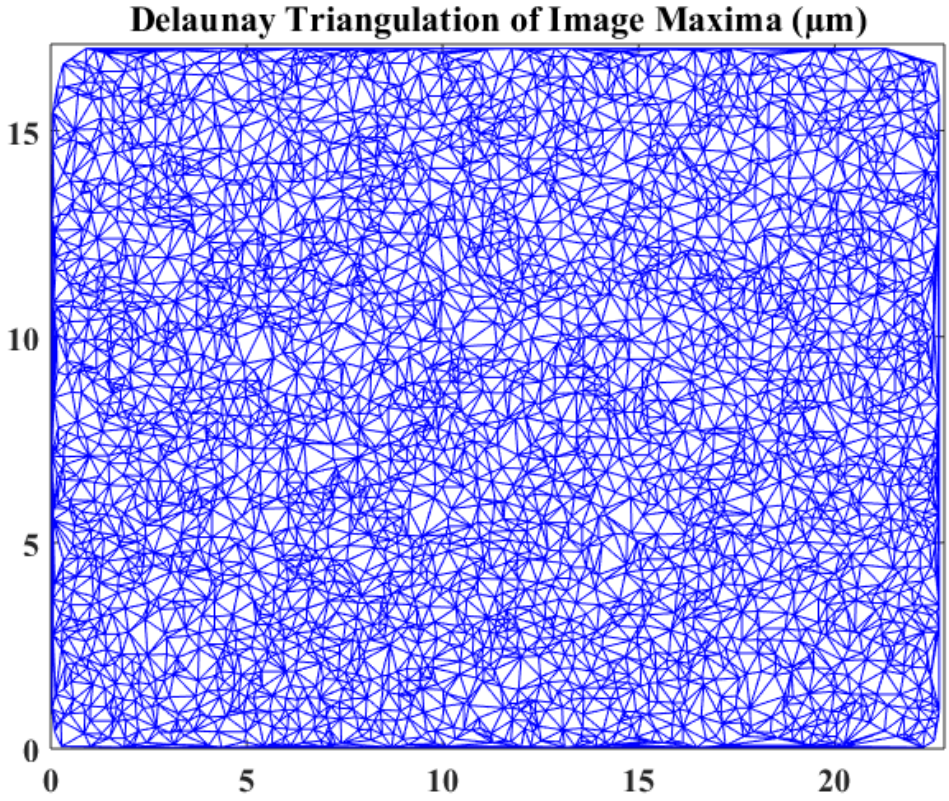

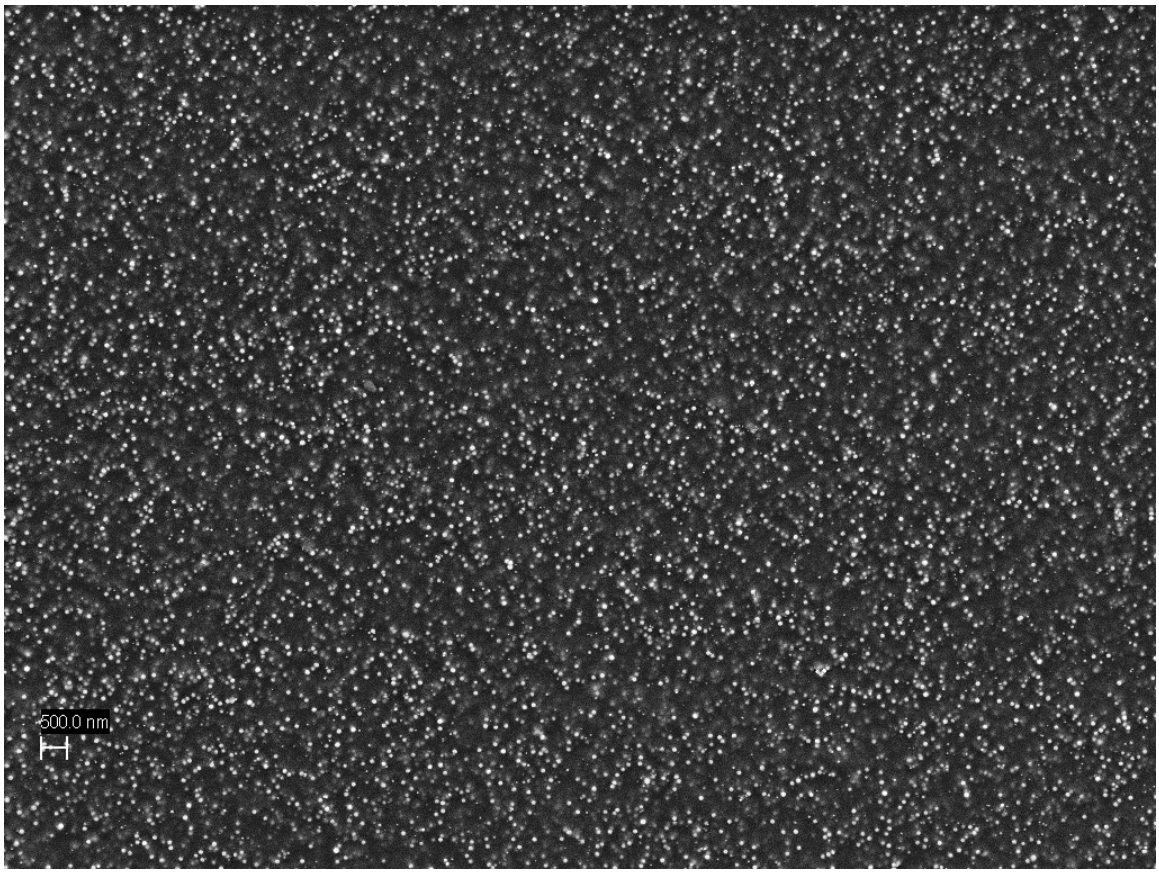

Figure A.30: Deformation rate *Wi* = 20, elongation ratio λ = 4.0: Location 3. This figure contains the original SEM image, corresponding binary image, and Delaunay Triangulation plot of the conditions from the figure title. Scale bars are 500 nm.

Figure A.30 (cont.)

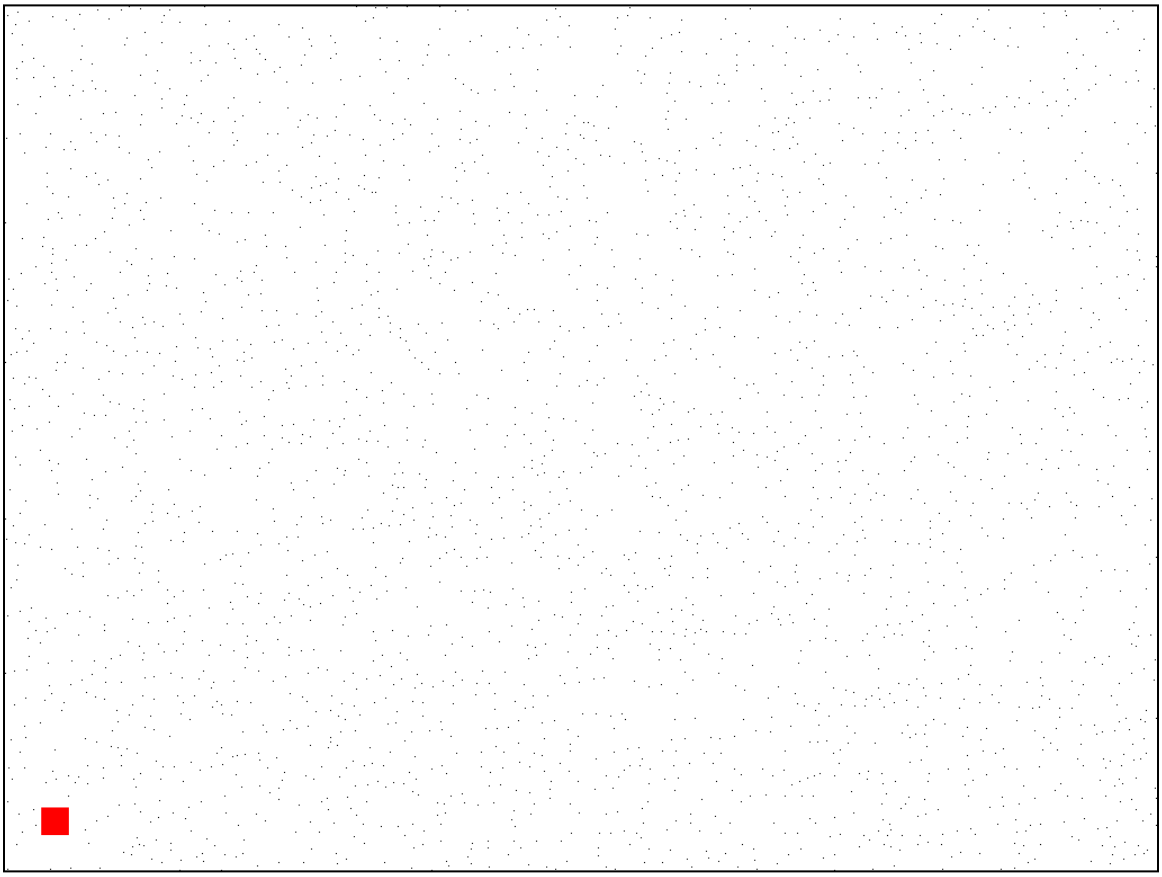

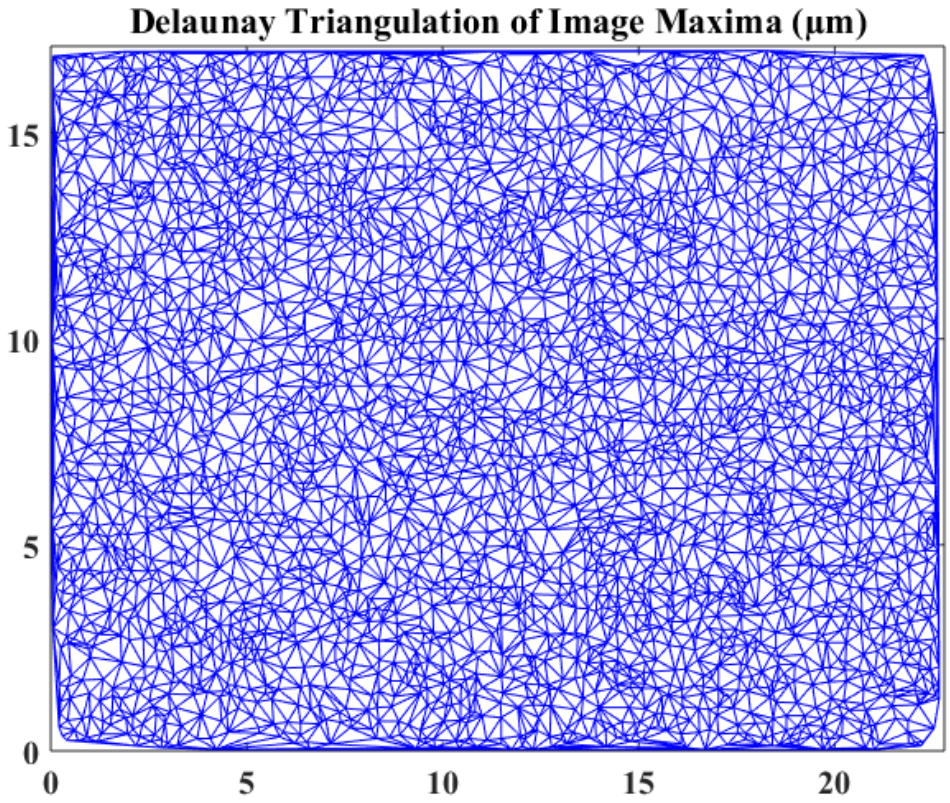

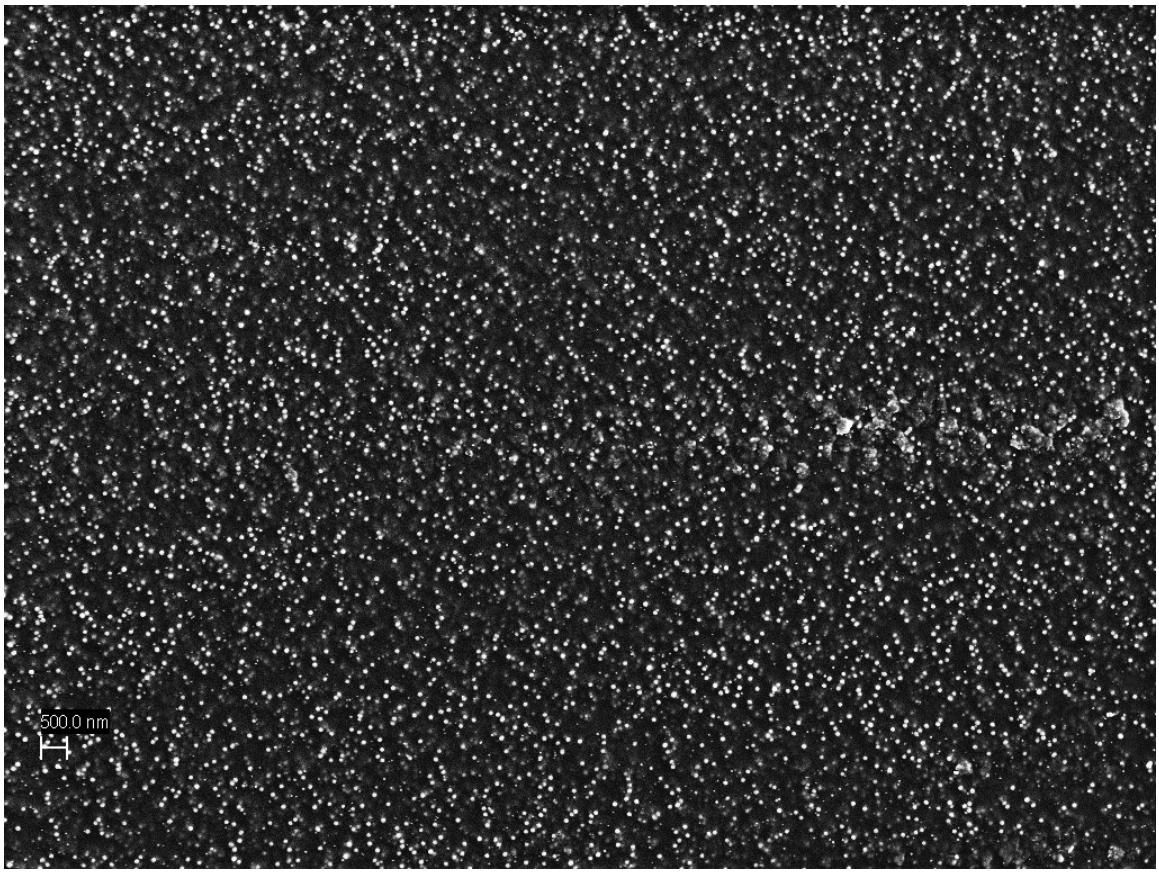

Figure A.31: Deformation rate *Wi* = 20, elongation ratio λ = 5.0: Location 1. This figure contains the original SEM image, corresponding binary image, and Delaunay Triangulation plot of the conditions from the figure title. Scale bars are 500 nm.

Figure A.31 (cont.)

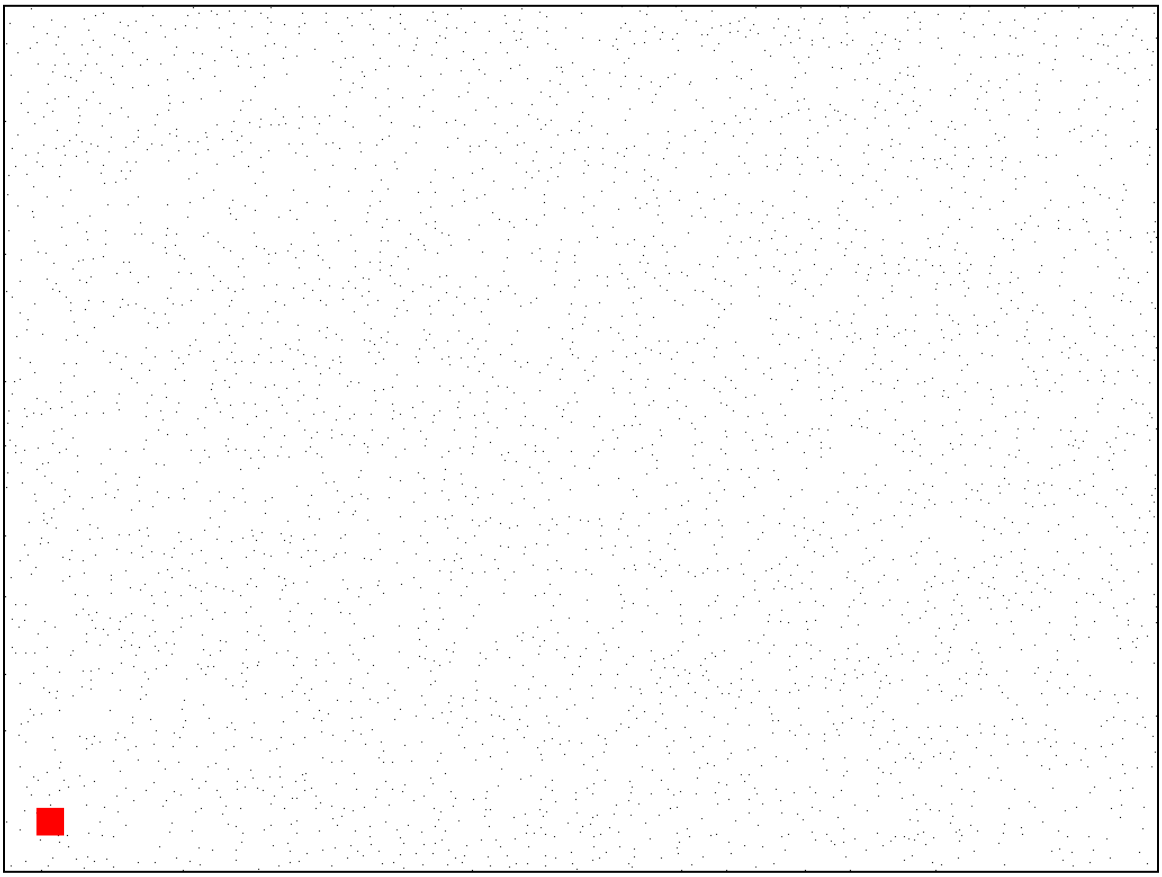

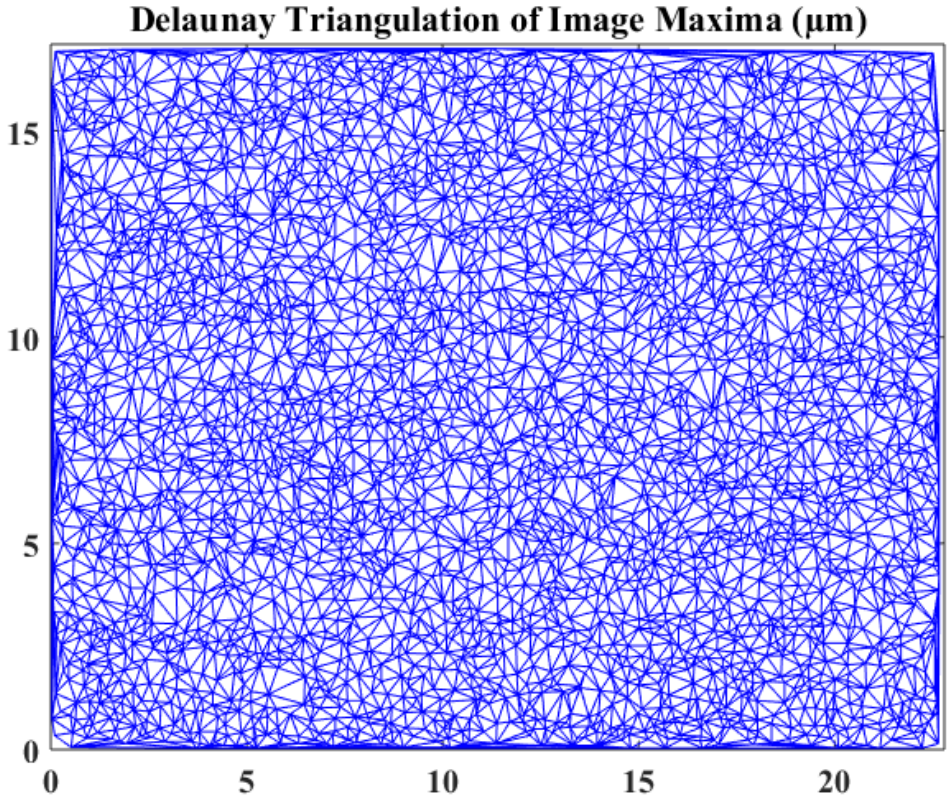

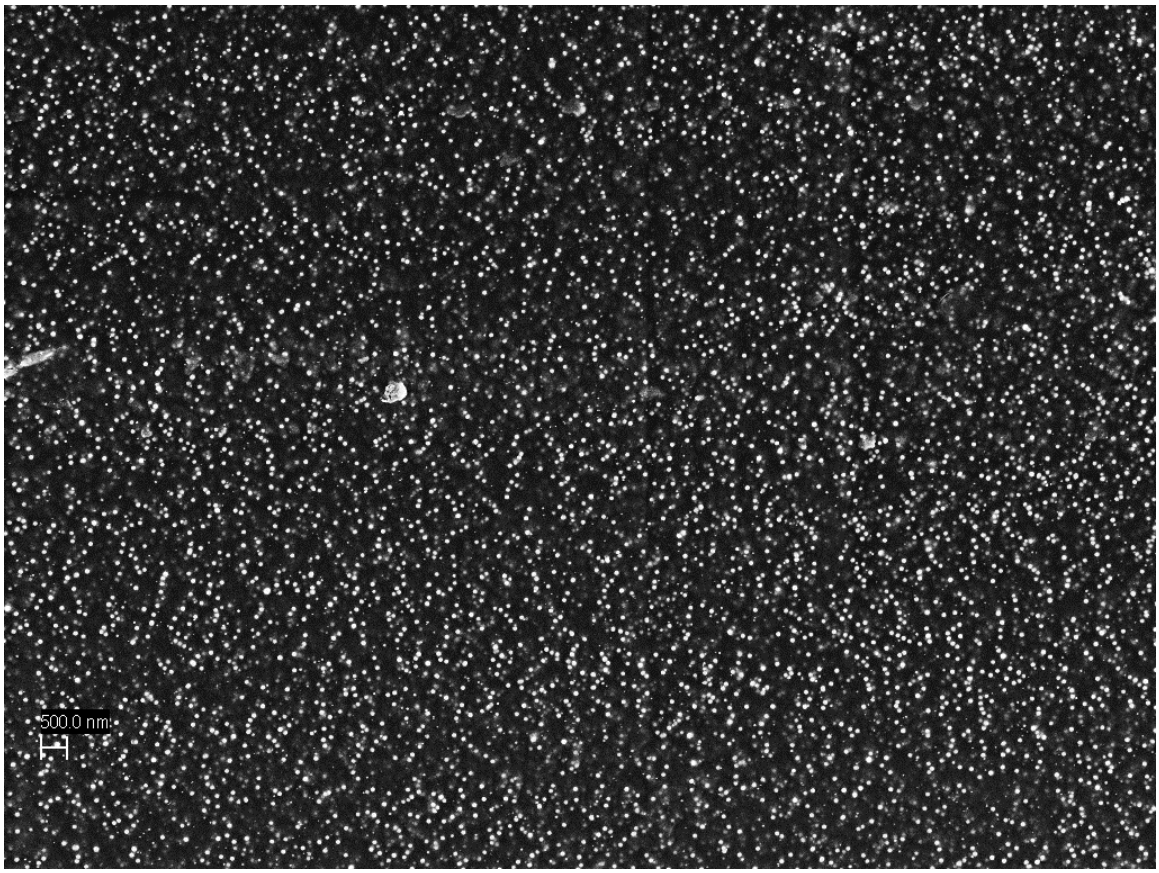

Figure A.32: Deformation rate *Wi* = 20, elongation ratio λ = 5.0: Location 2. This figure contains the original SEM image, corresponding binary image, and Delaunay Triangulation plot of the conditions from the figure title. Scale bars are 500 nm.

Figure A.32 (cont.)

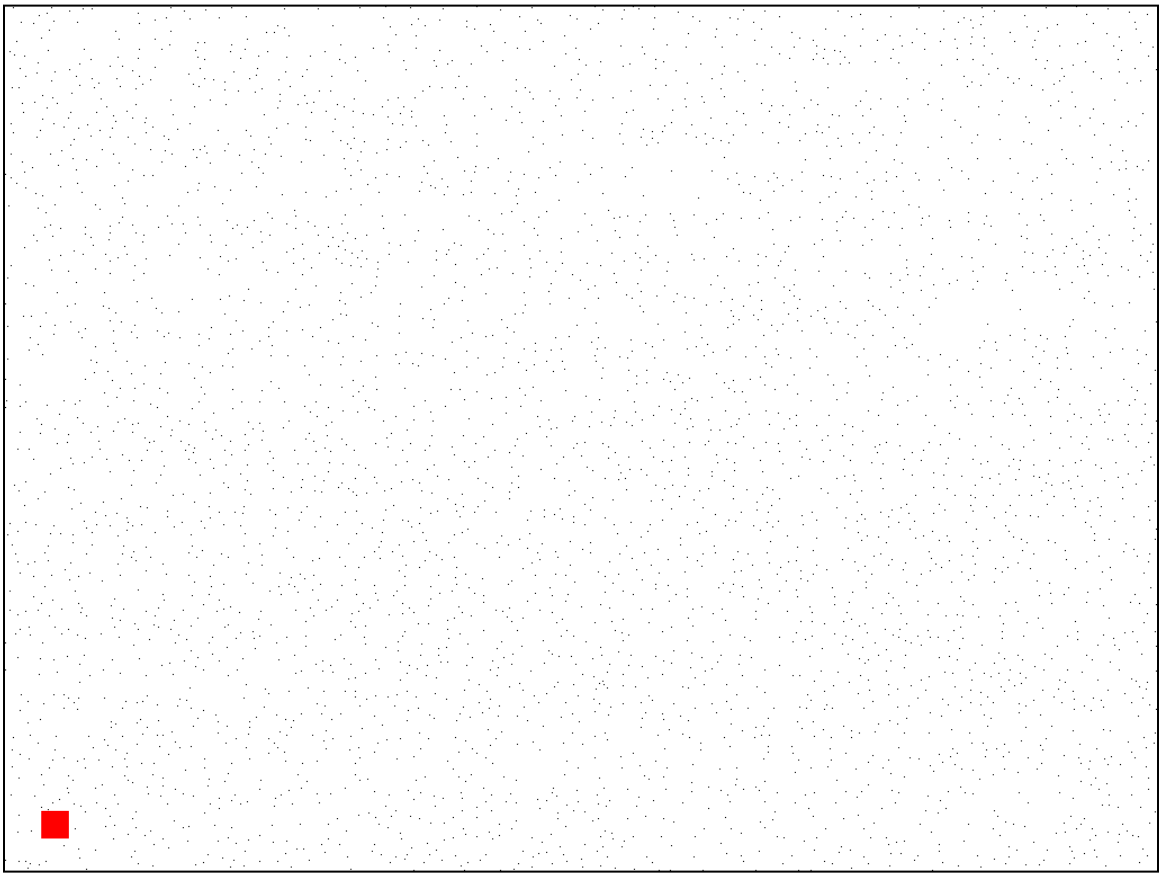

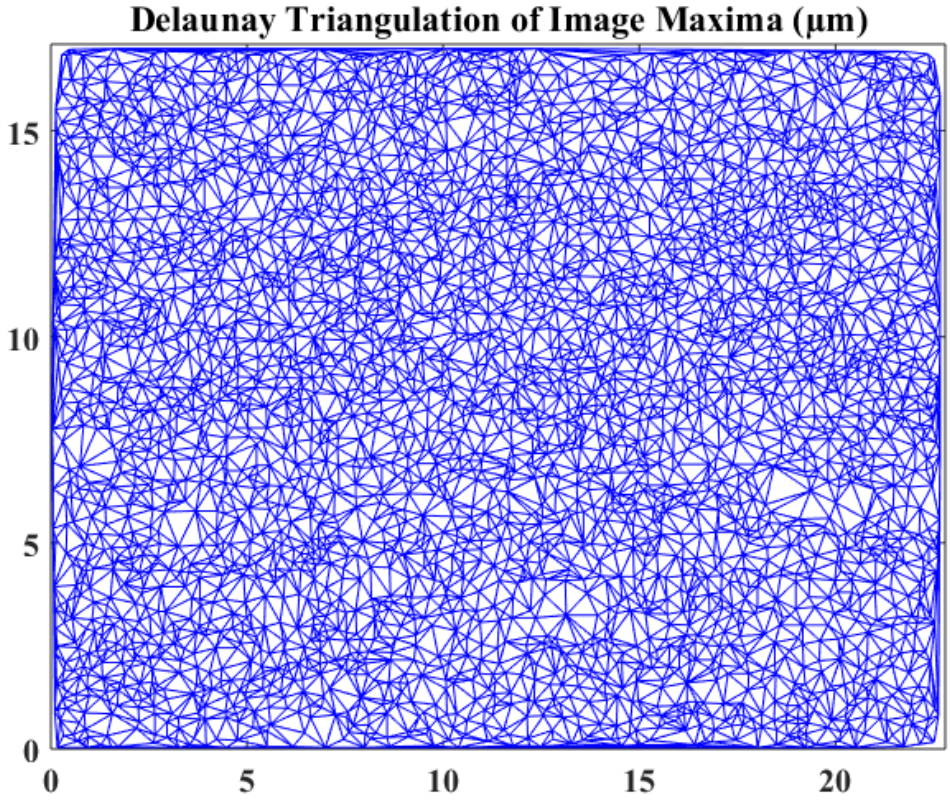

Figure A.33: Deformation rate *Wi* = 20, elongation ratio λ = 5.0: Location 3. This figure contains the original SEM image, corresponding binary image, and Delaunay Triangulation plot of the conditions from the figure title. Scale bars are 500 nm.

Figure A.33 (cont.)

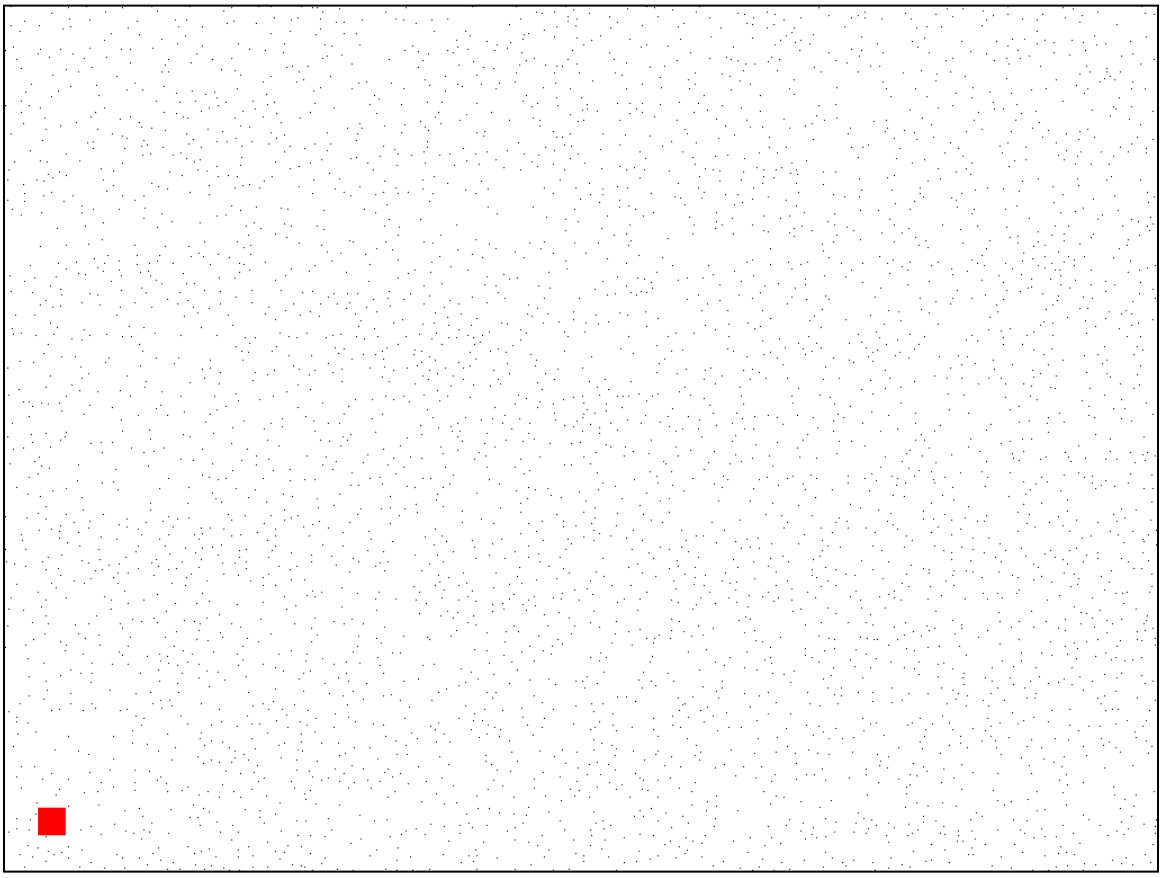

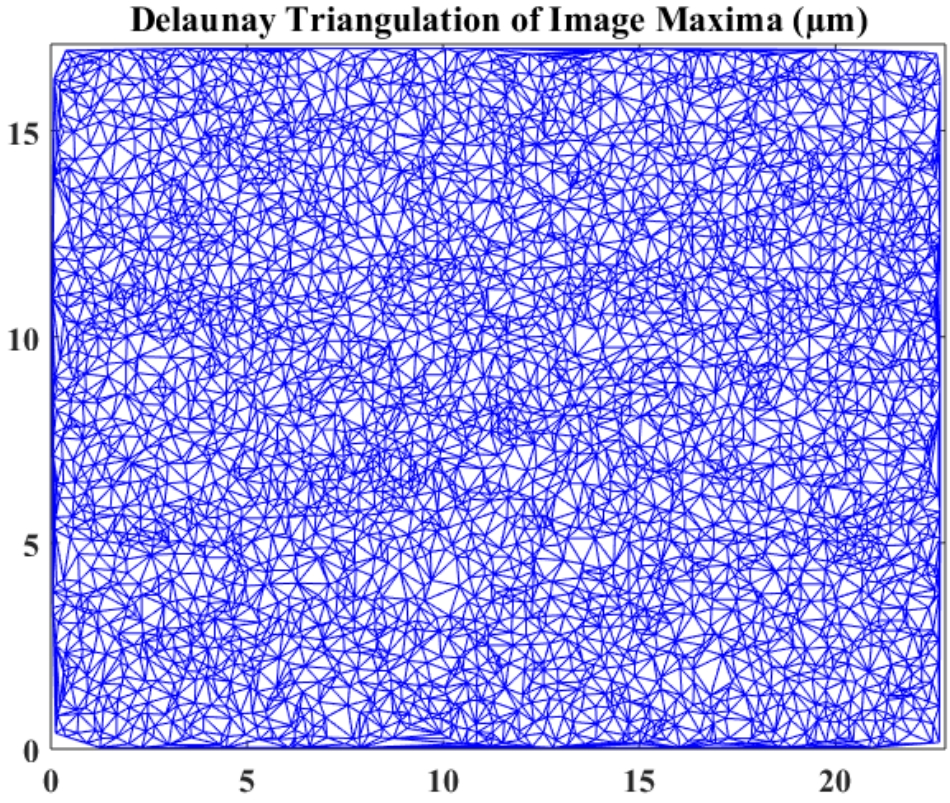

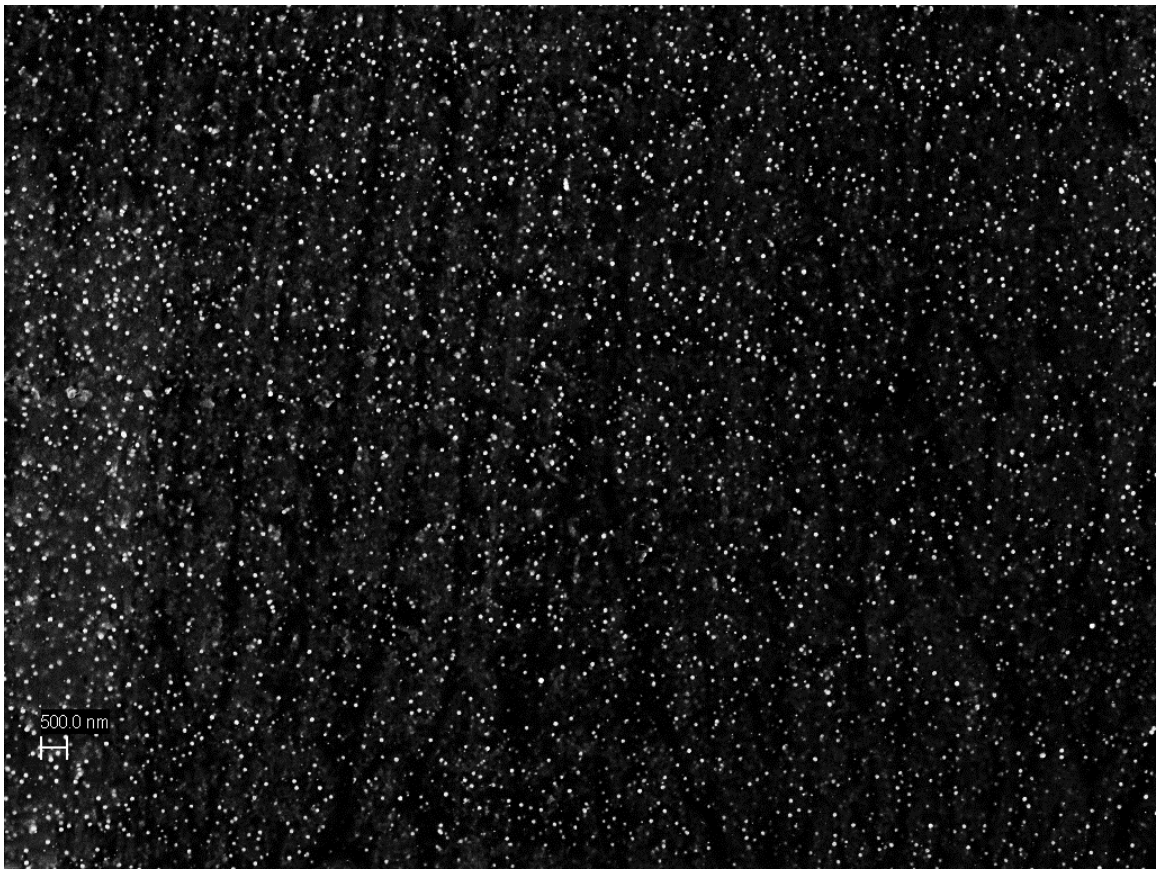

Figure A.34: Deformation rate *Wi* = 20, elongation ratio λ = 7.0: Location 1. This figure contains the original SEM image, corresponding binary image, and Delaunay Triangulation plot of the conditions from the figure title. Scale bars are 500 nm.

Figure A.34 (cont.)

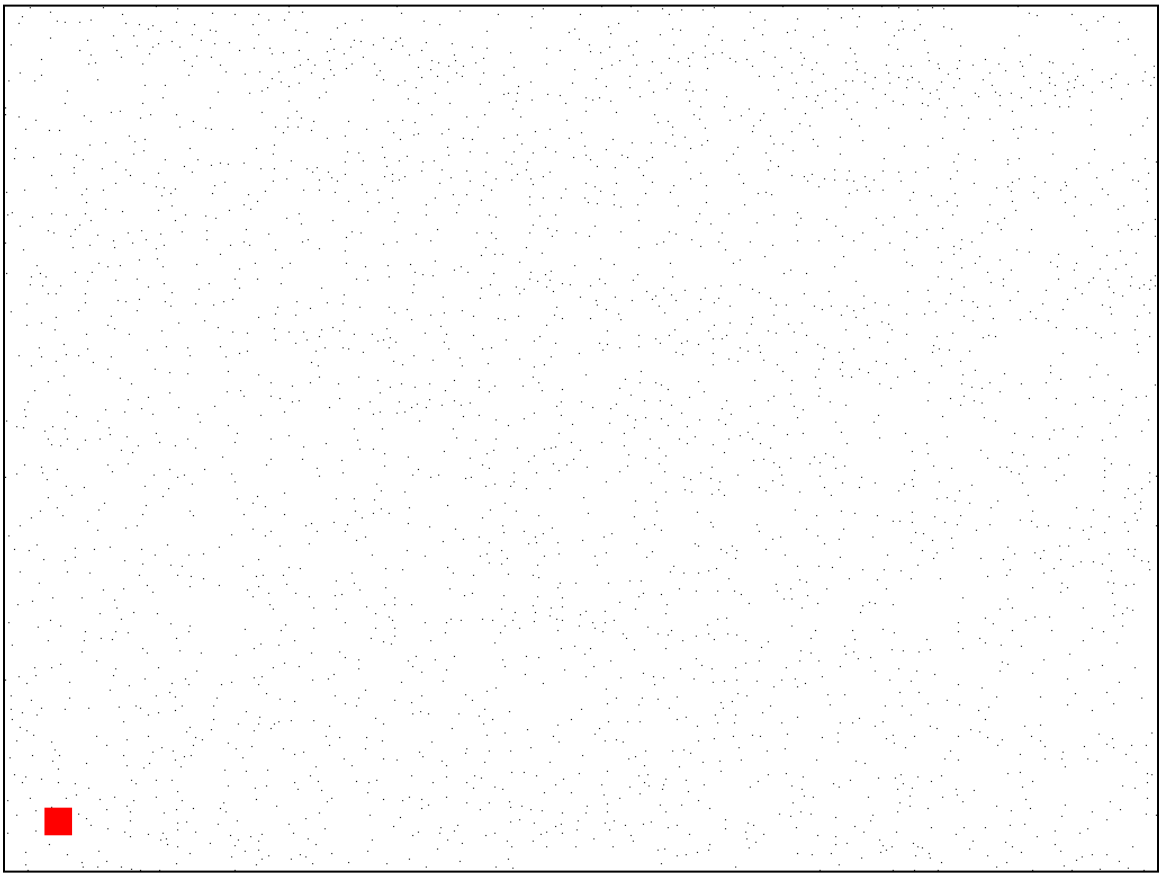

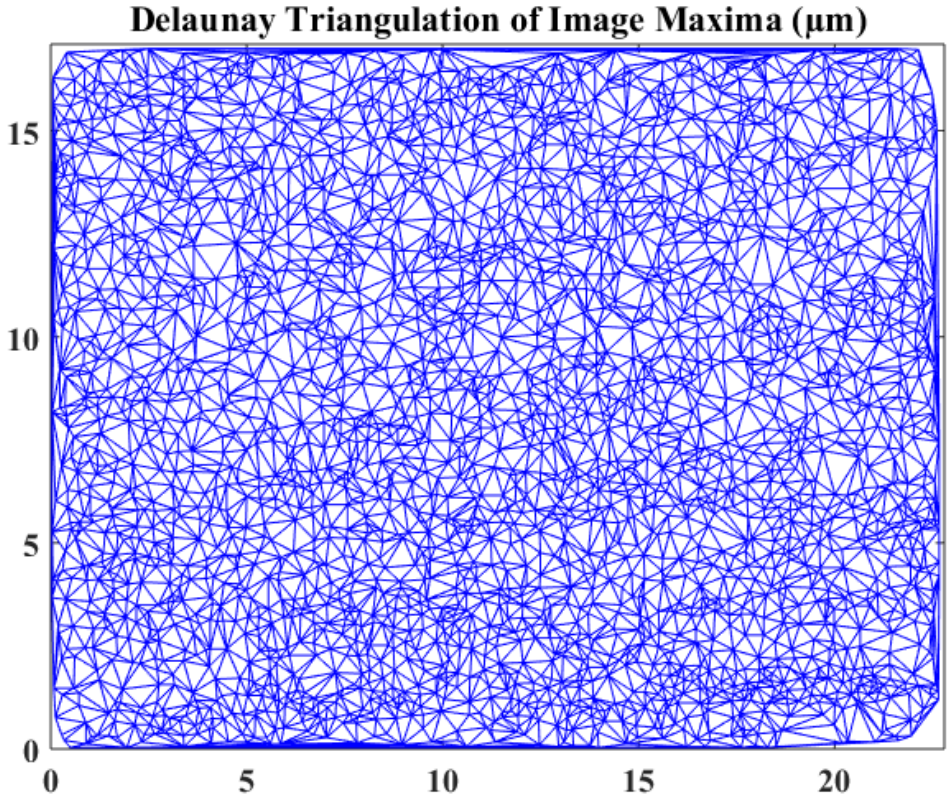

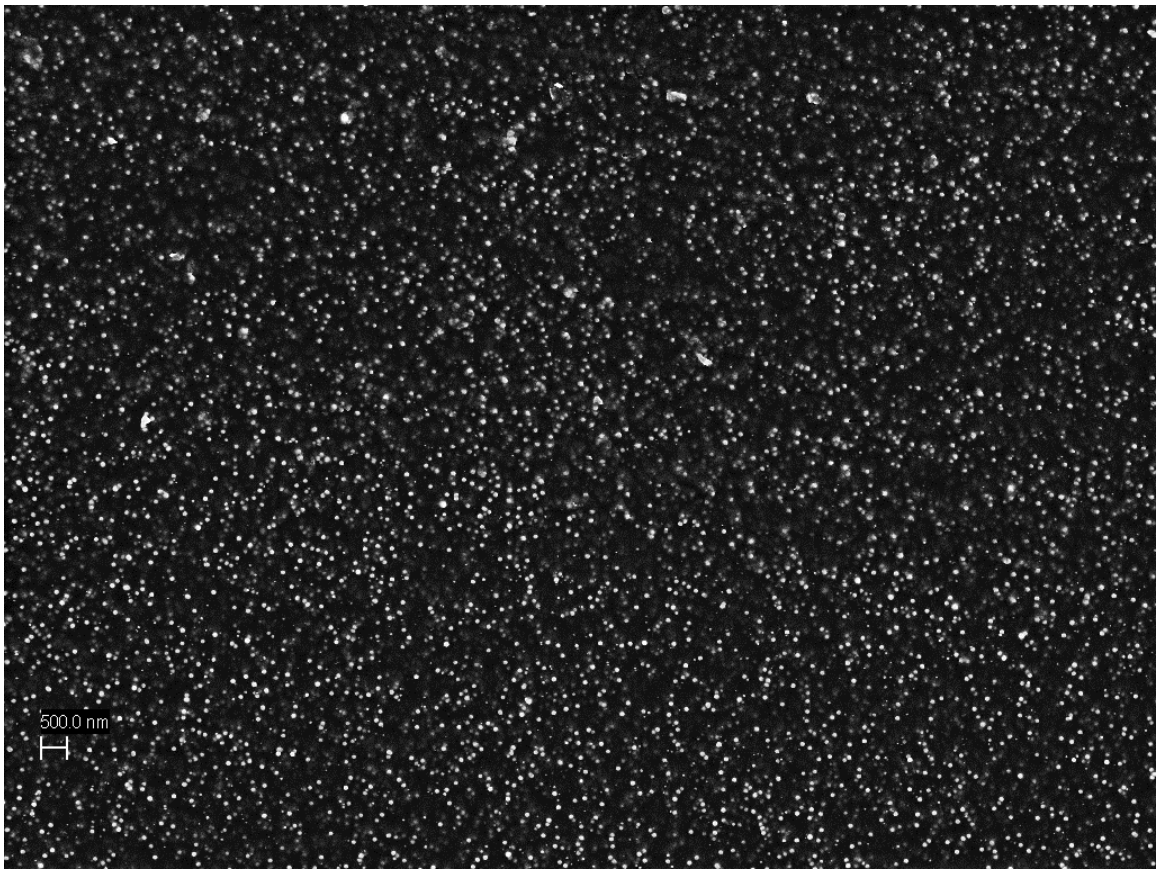

Figure A.35: Deformation rate *Wi* = 20, elongation ratio λ = 7.0: Location 2. This figure contains the original SEM image, corresponding binary image, and Delaunay Triangulation plot of the conditions from the figure title. Scale bars are 500 nm.

Figure A.35 (cont.)

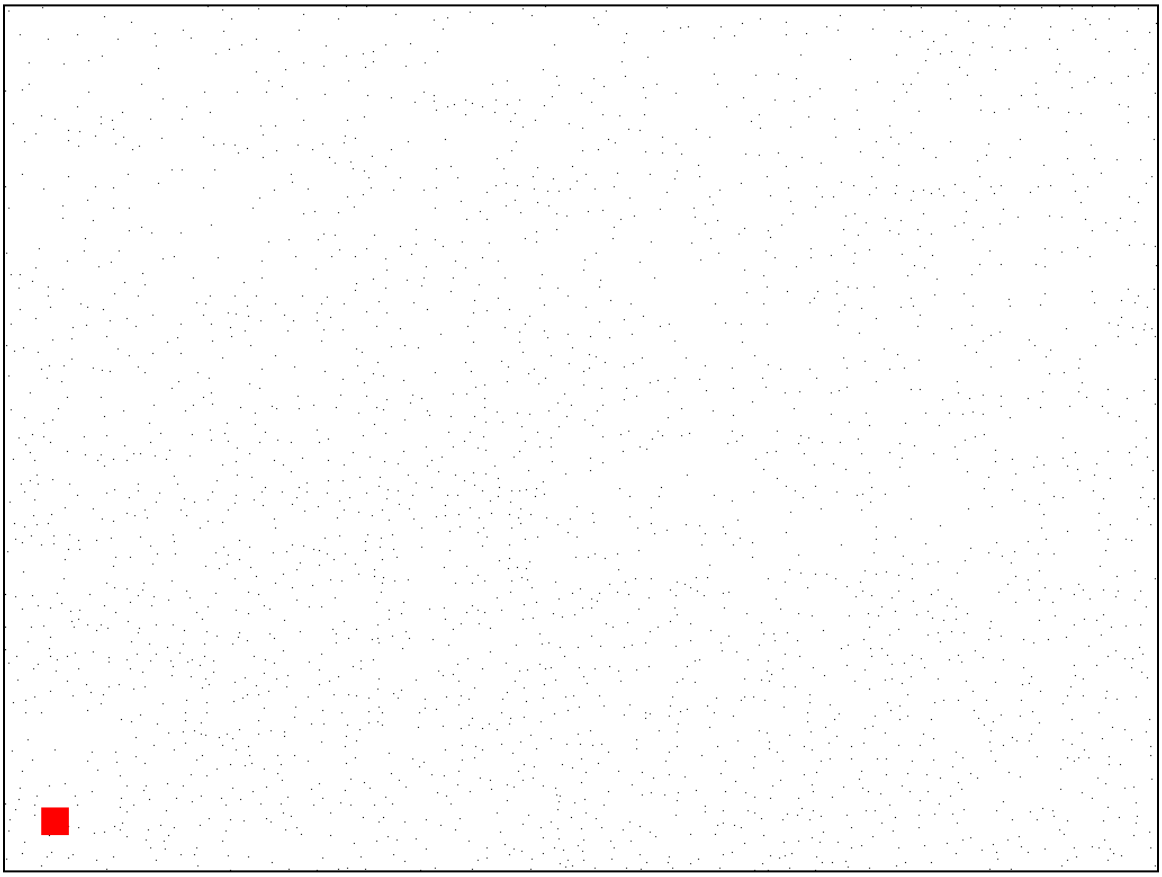

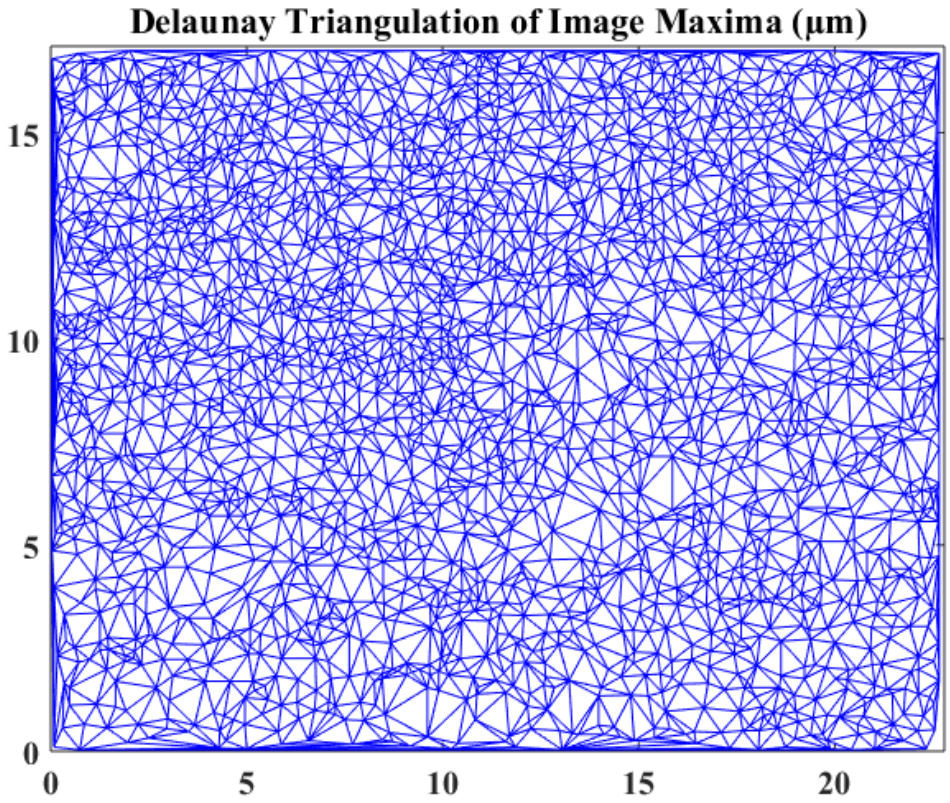

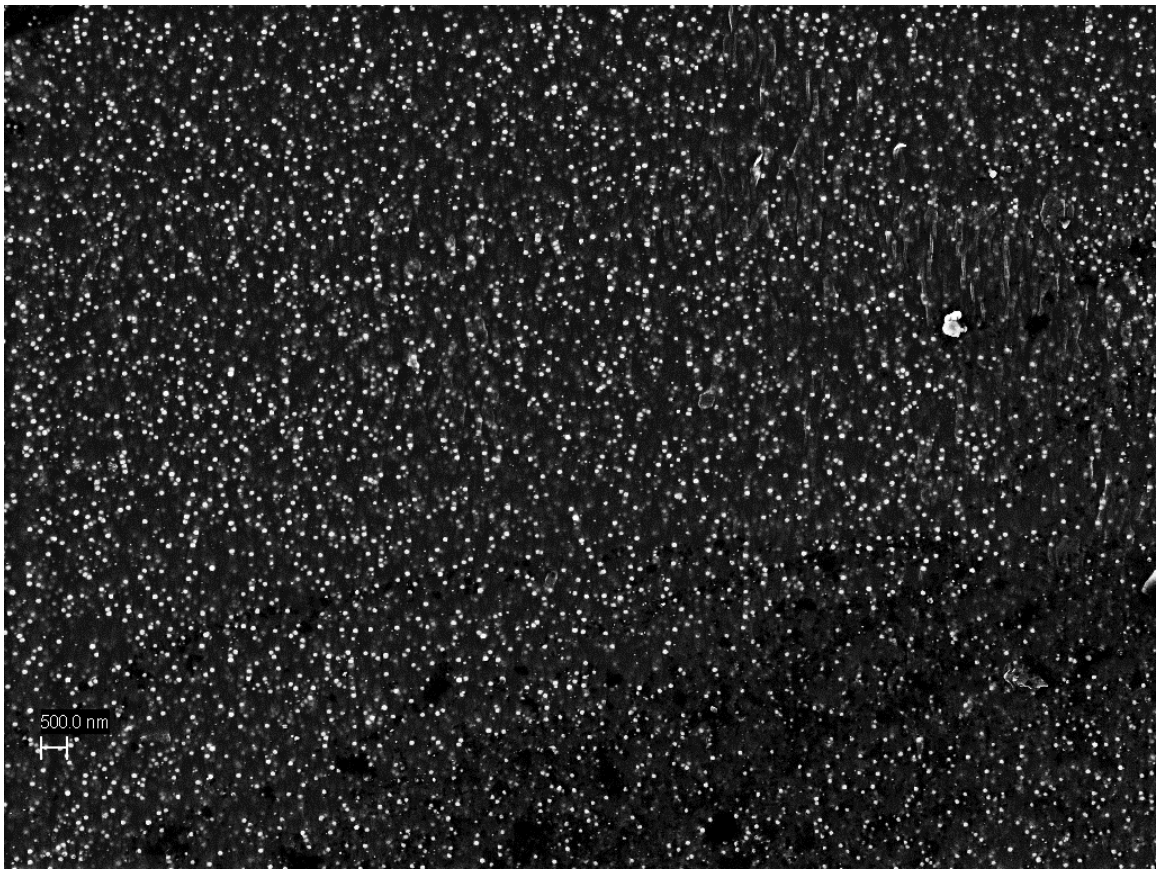

Figure A.36: Deformation rate *Wi* = 20, elongation ratio λ = 7.0: Location 3. This figure contains the original SEM image, corresponding binary image, and Delaunay Triangulation plot of the conditions from the figure title. Scale bars are 500 nm.

Figure A.36 (cont.)

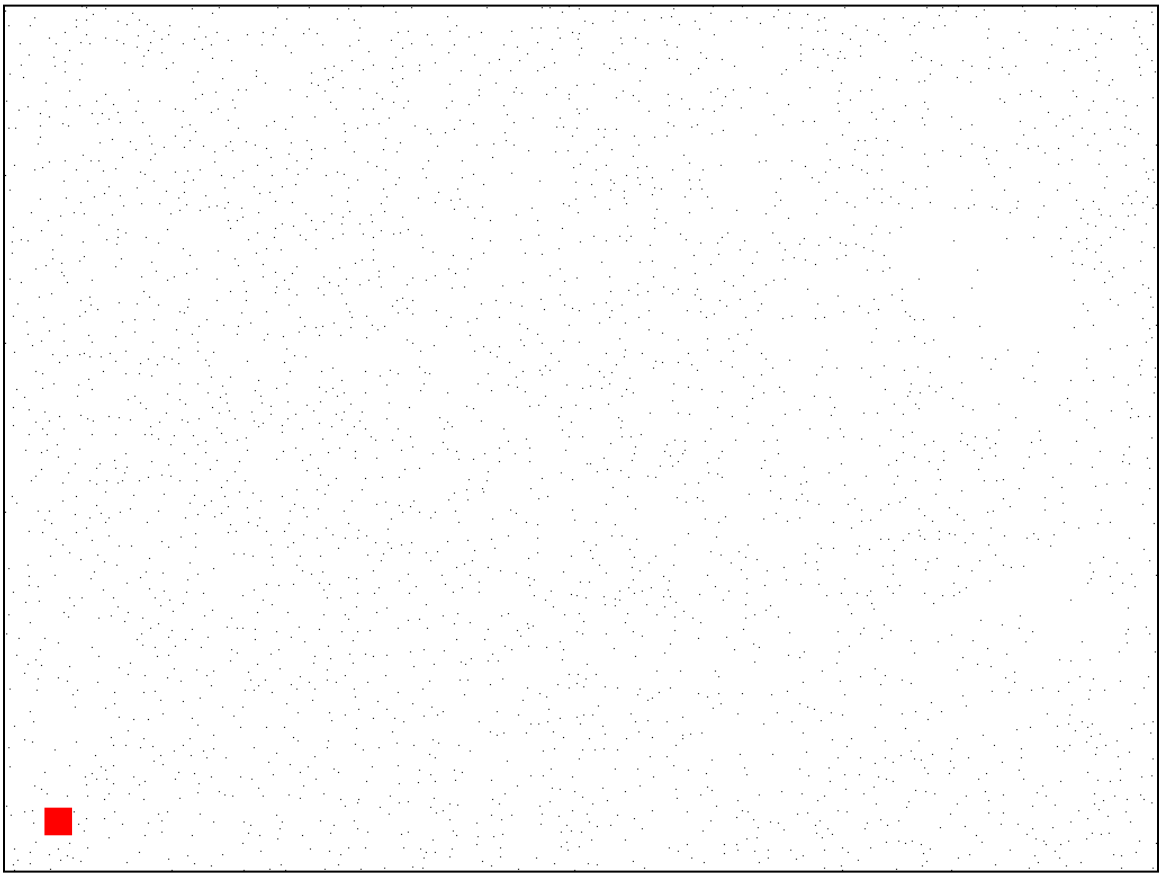

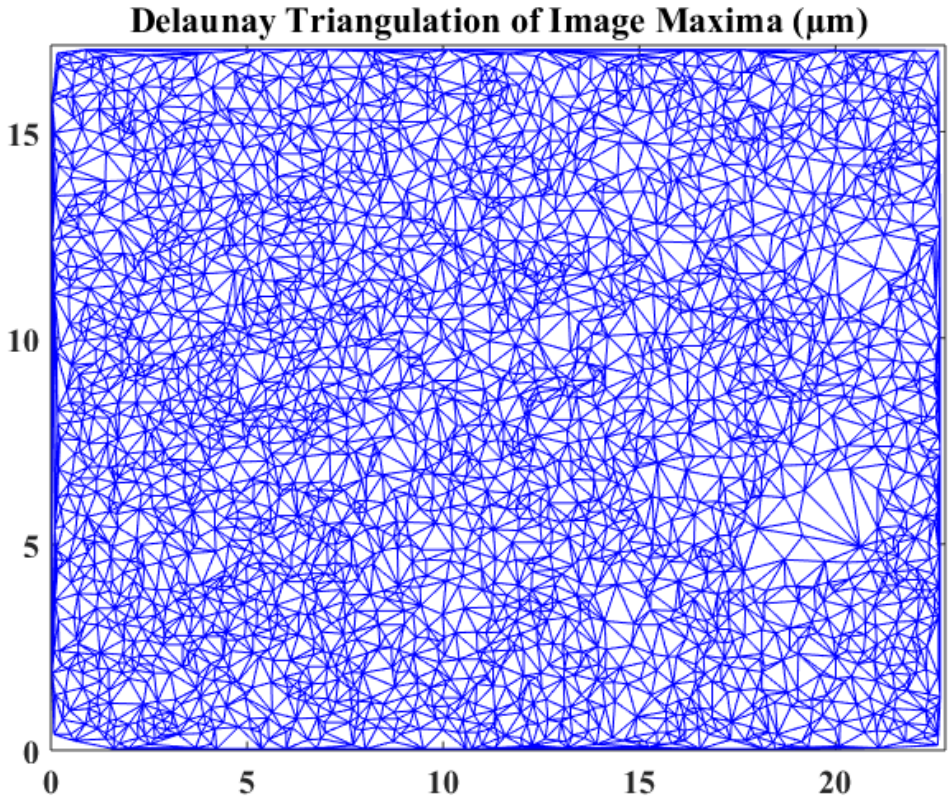

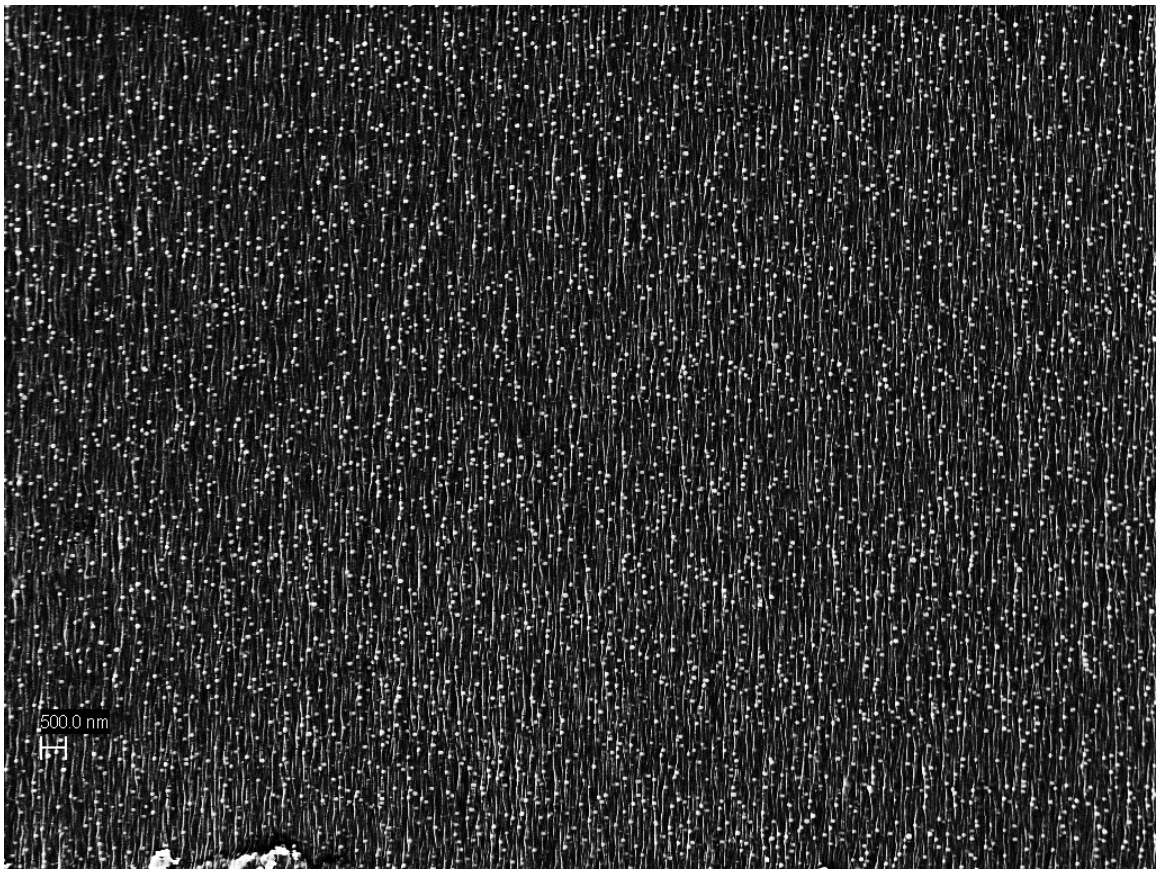

Figure A.37: Deformation rate *Wi* = 20, elongation ratio λ = 9.0: Location 1. This figure contains the original SEM image, corresponding binary image, and Delaunay Triangulation plot of the conditions from the figure title. Scale bars are 500 nm.

Figure A.37 (cont.)

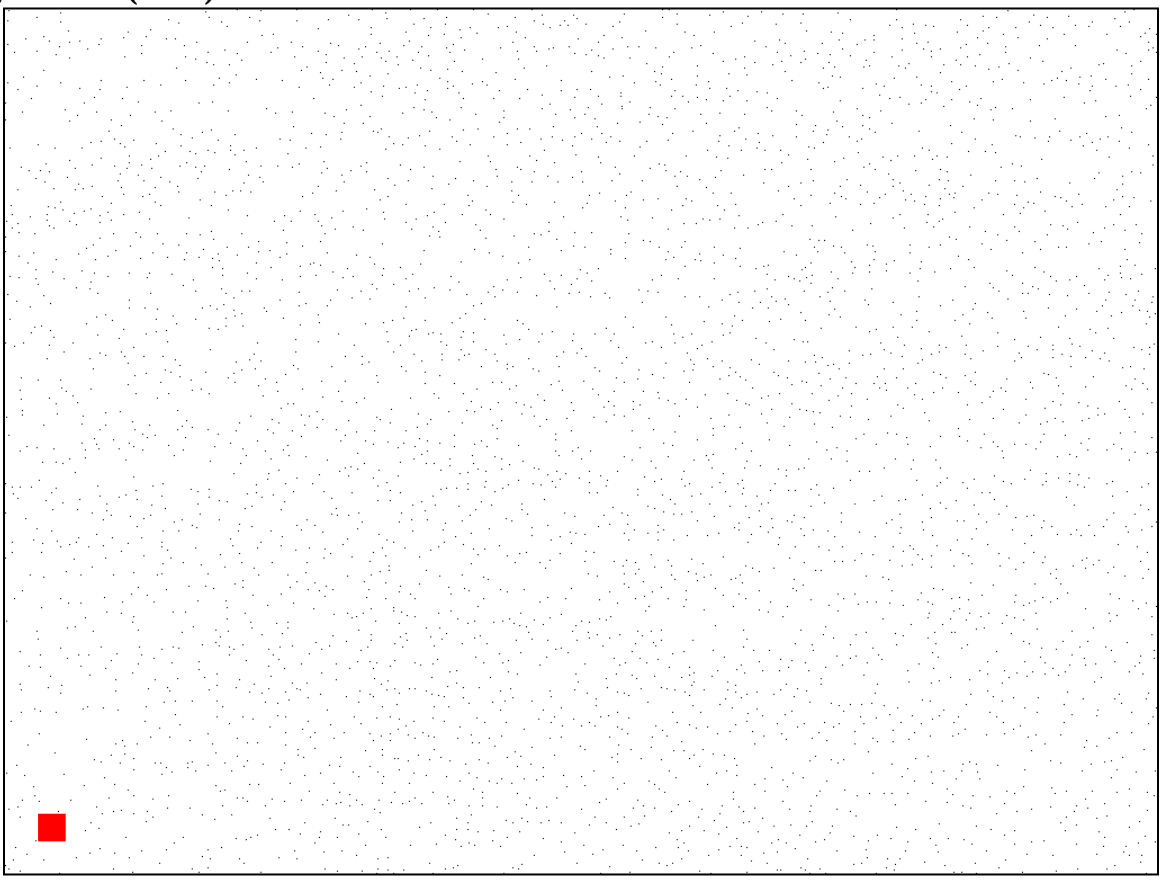

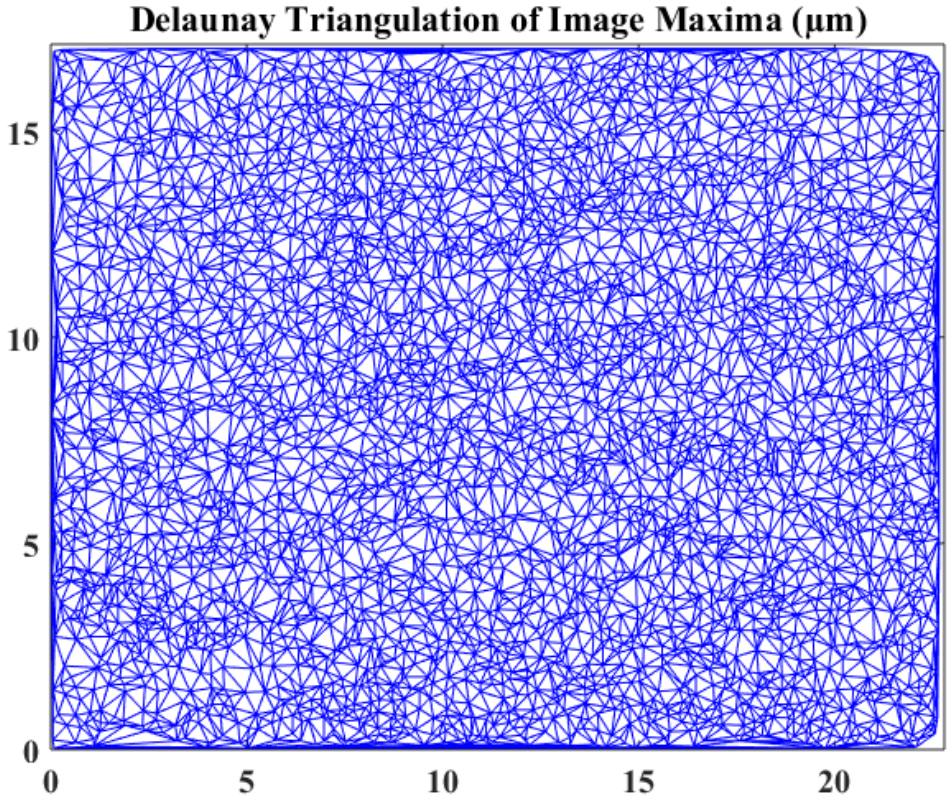

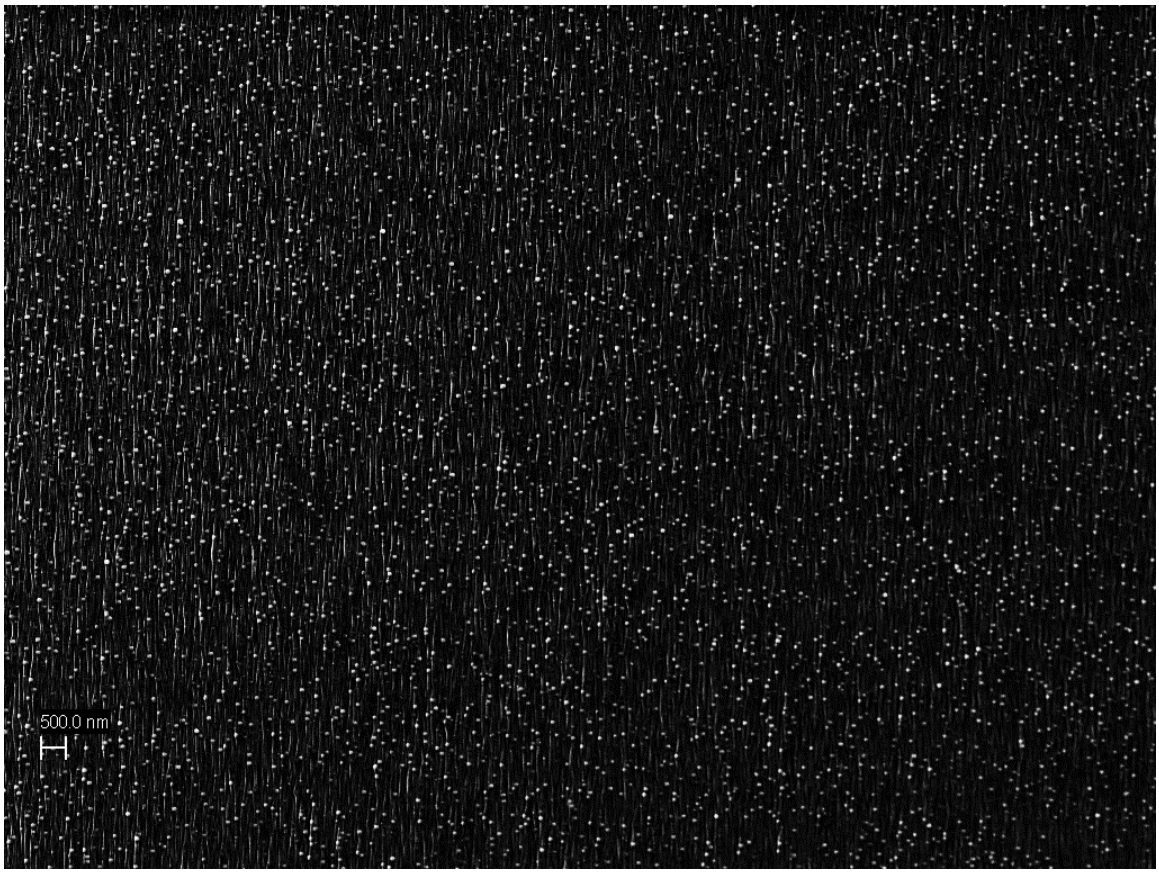

Figure A.38: Deformation rate *Wi* = 20, elongation ratio λ = 9.0: Location 2. This figure contains the original SEM image, corresponding binary image, and Delaunay Triangulation plot of the conditions from the figure title. Scale bars are 500 nm.

Figure A.38 (cont.)

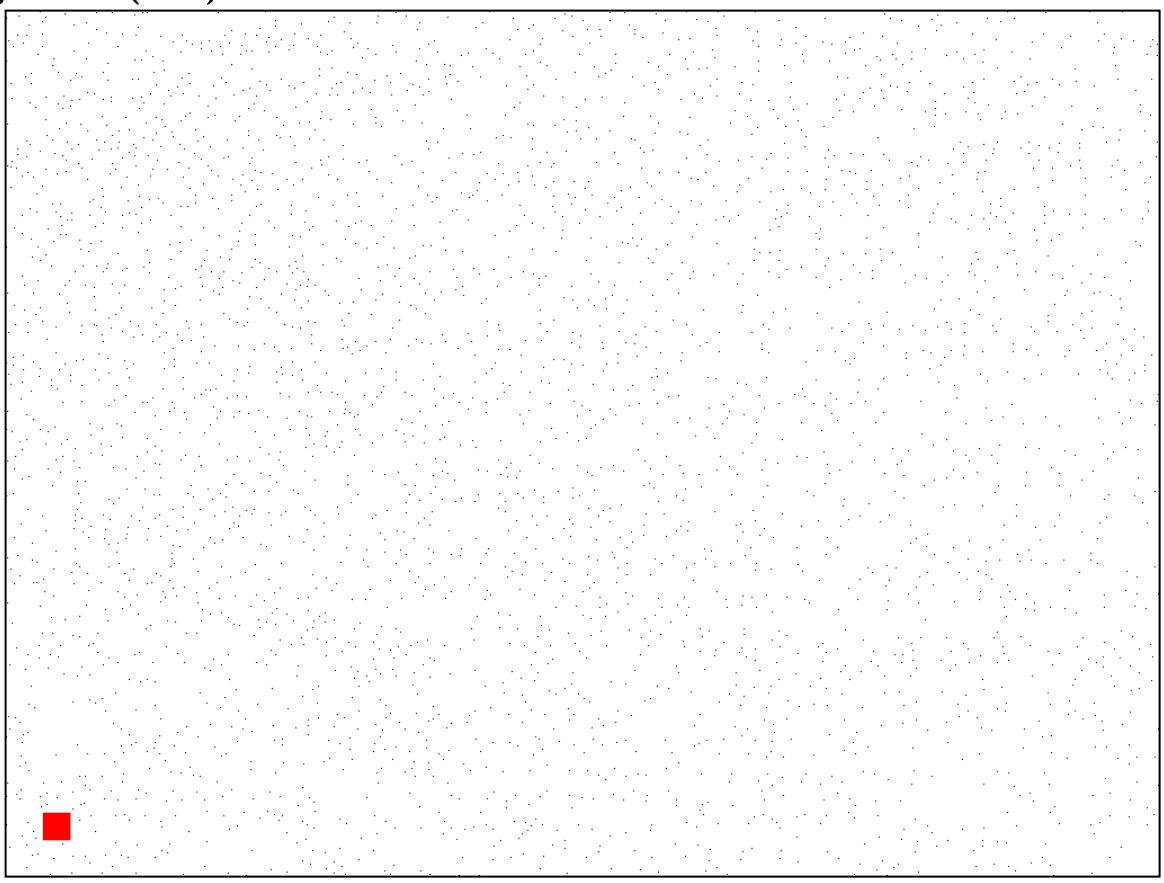

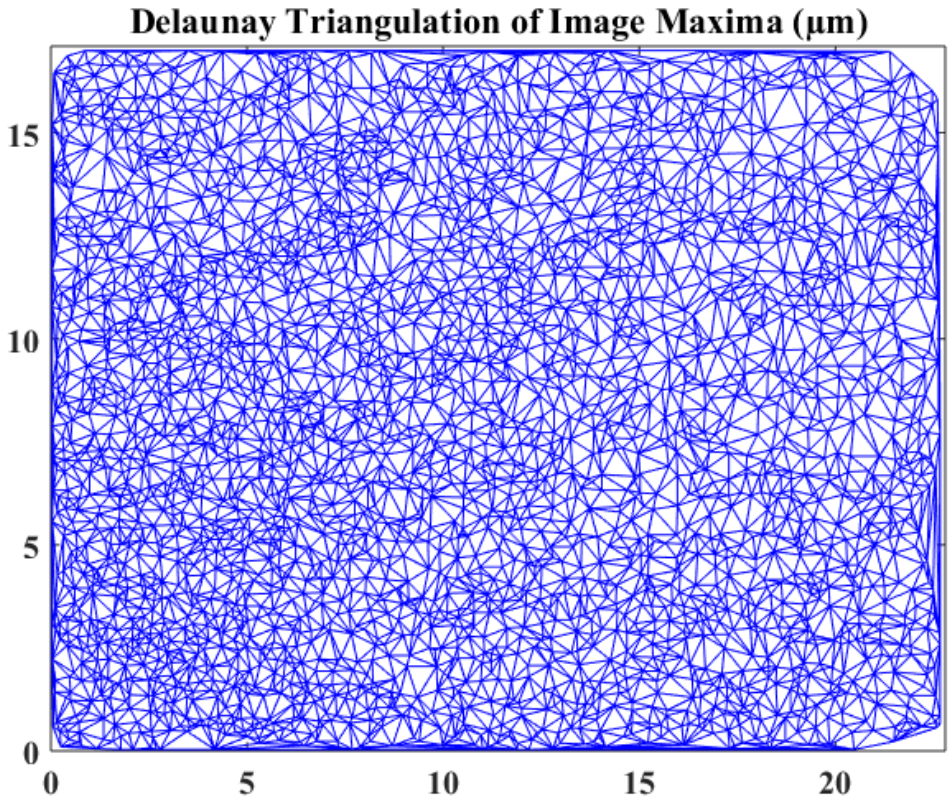

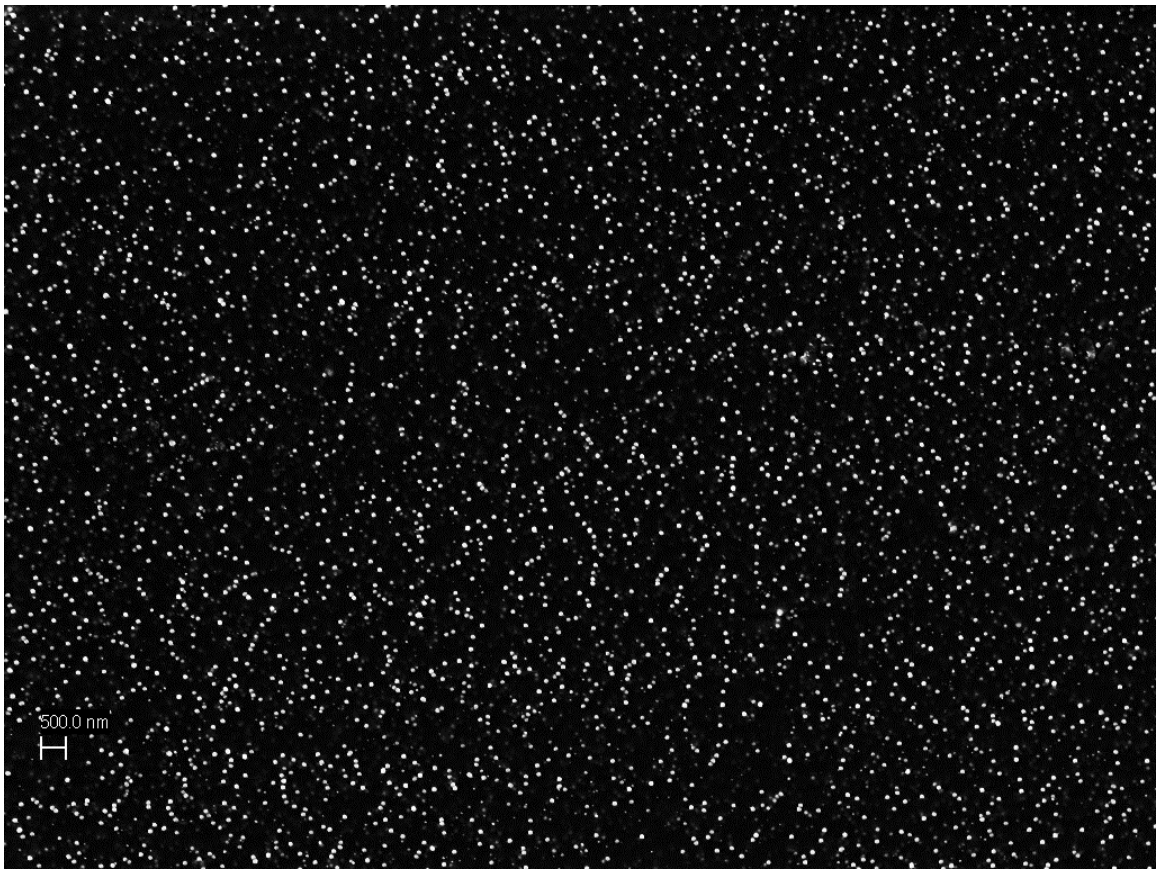

Figure A.39: Deformation rate *Wi* = 20, elongation ratio λ = 9.0: Location 3. This figure contains the original SEM image, corresponding binary image, and Delaunay Triangulation plot of the conditions from the figure title. Scale bars are 500 nm.

Figure A.39 (cont.)

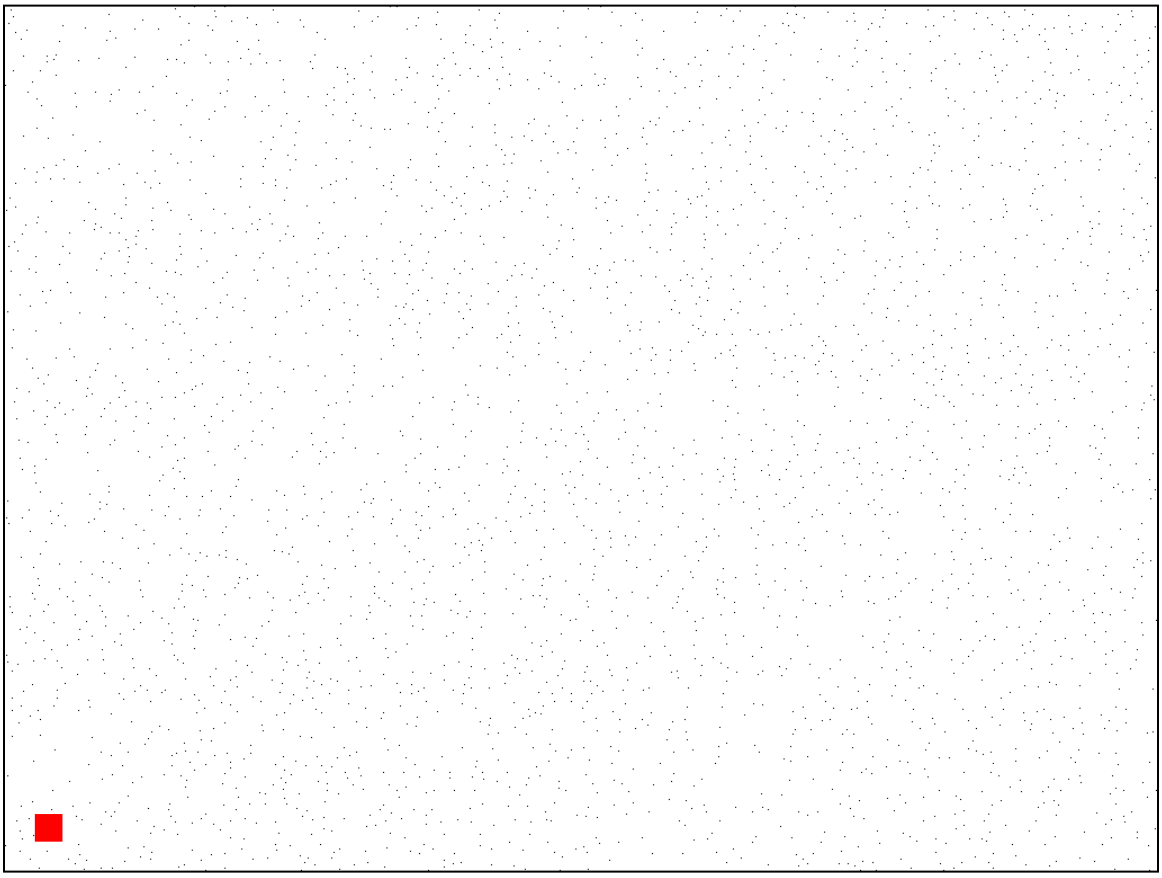

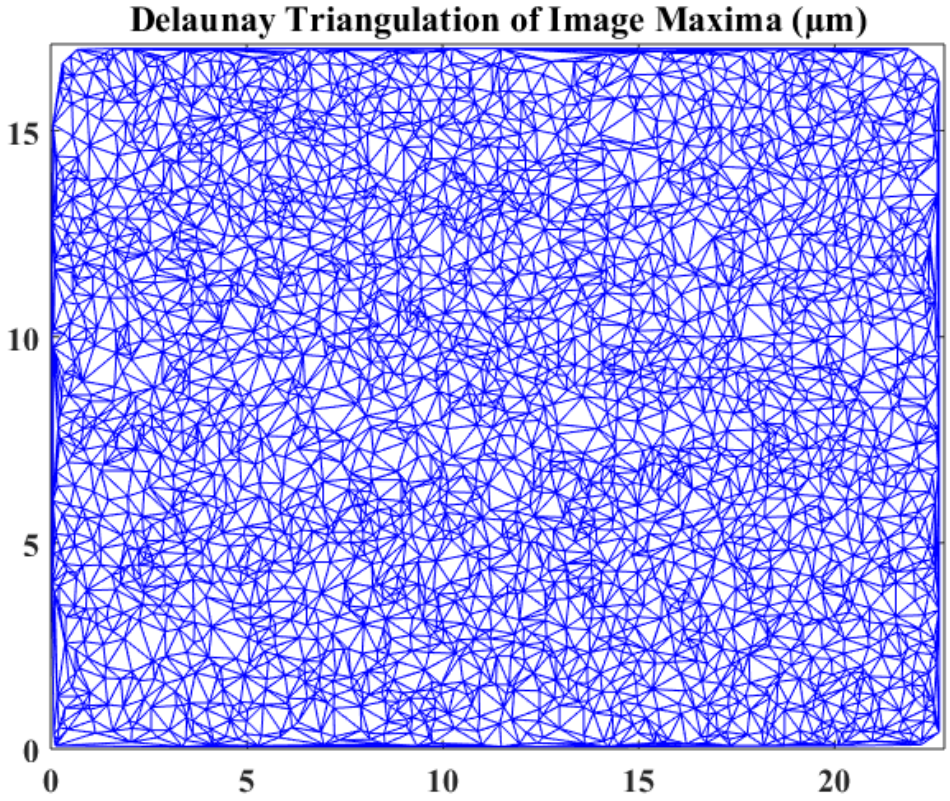

APPENDIX B

Additional Delaunay Triangulation Analytical Results

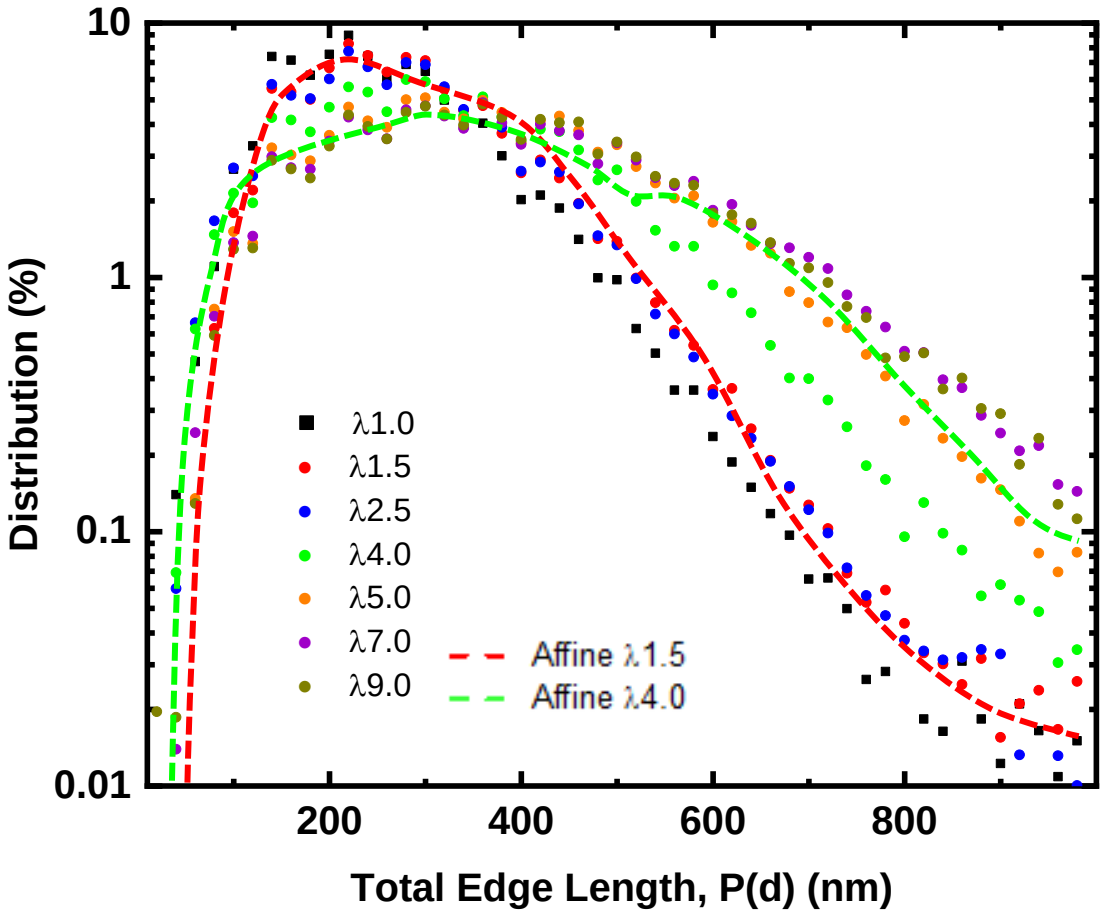

Figure B.1: Total edge length for *Wi* = 0.06, all λ.

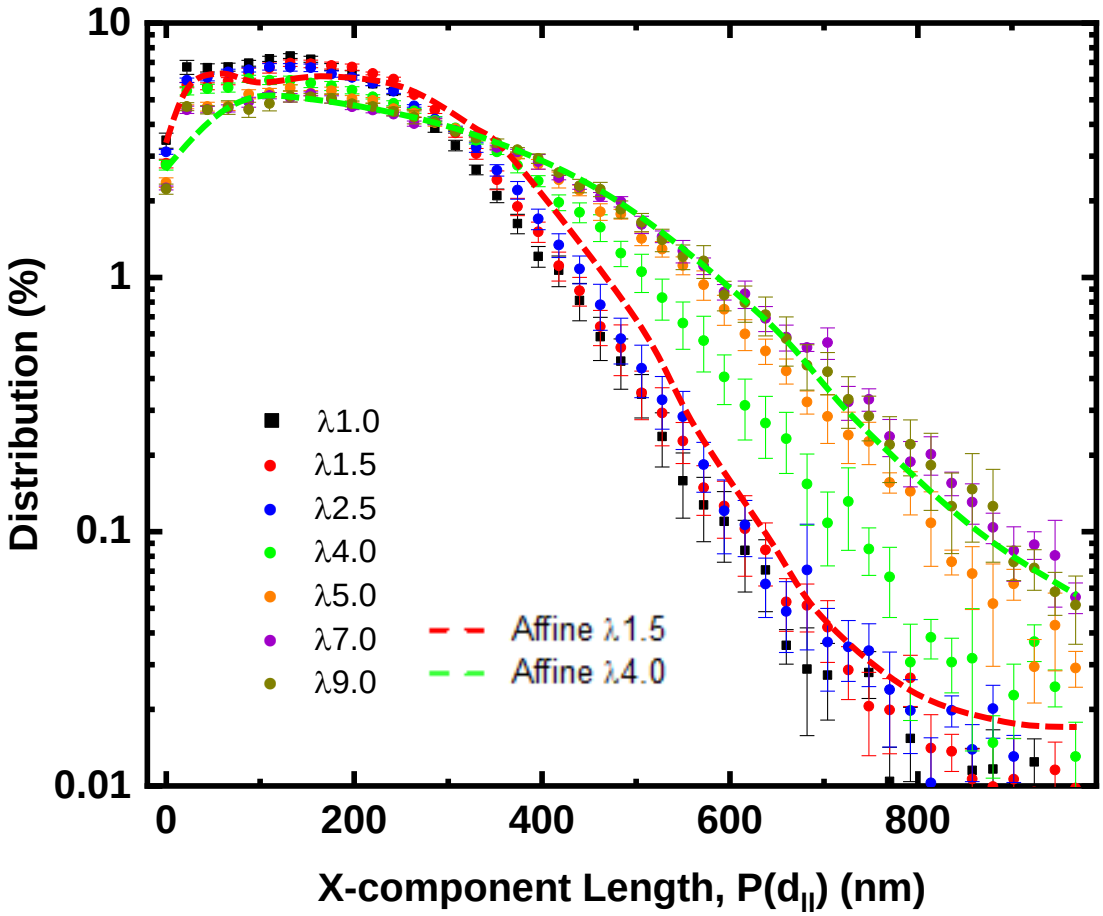

Figure B.2: X-component length for *Wi* = 0.06, all λ.

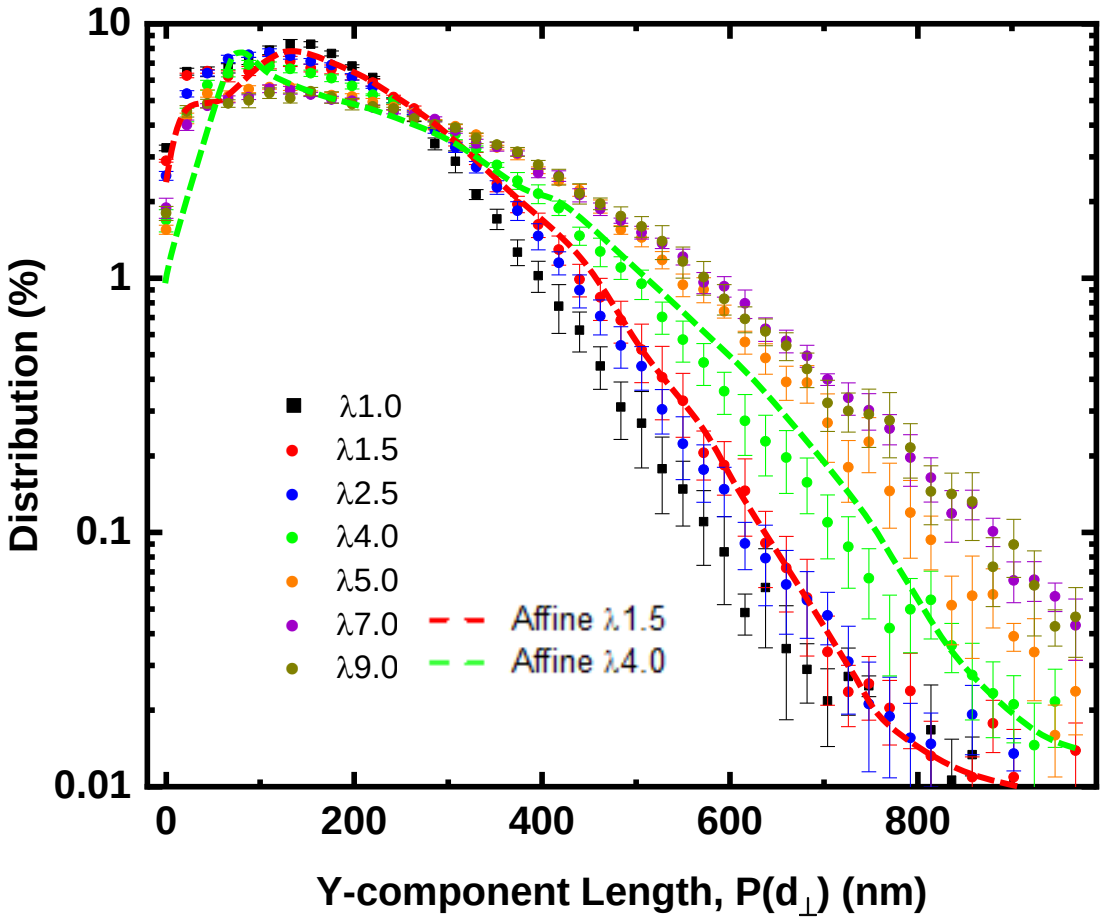

Figure B.3: Y-component length for *Wi* = 0.06, all λ.

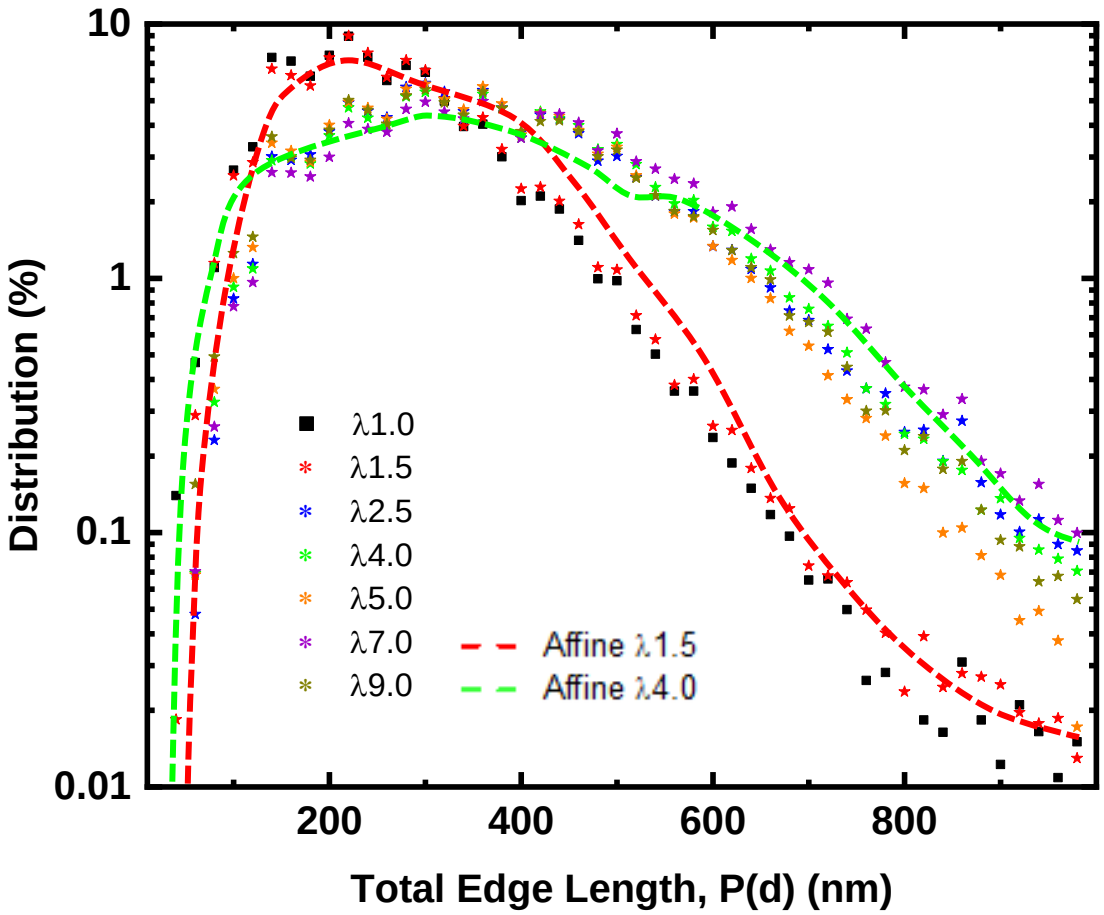

Figure B.4: Total edge length for *Wi* = 20, all λ.

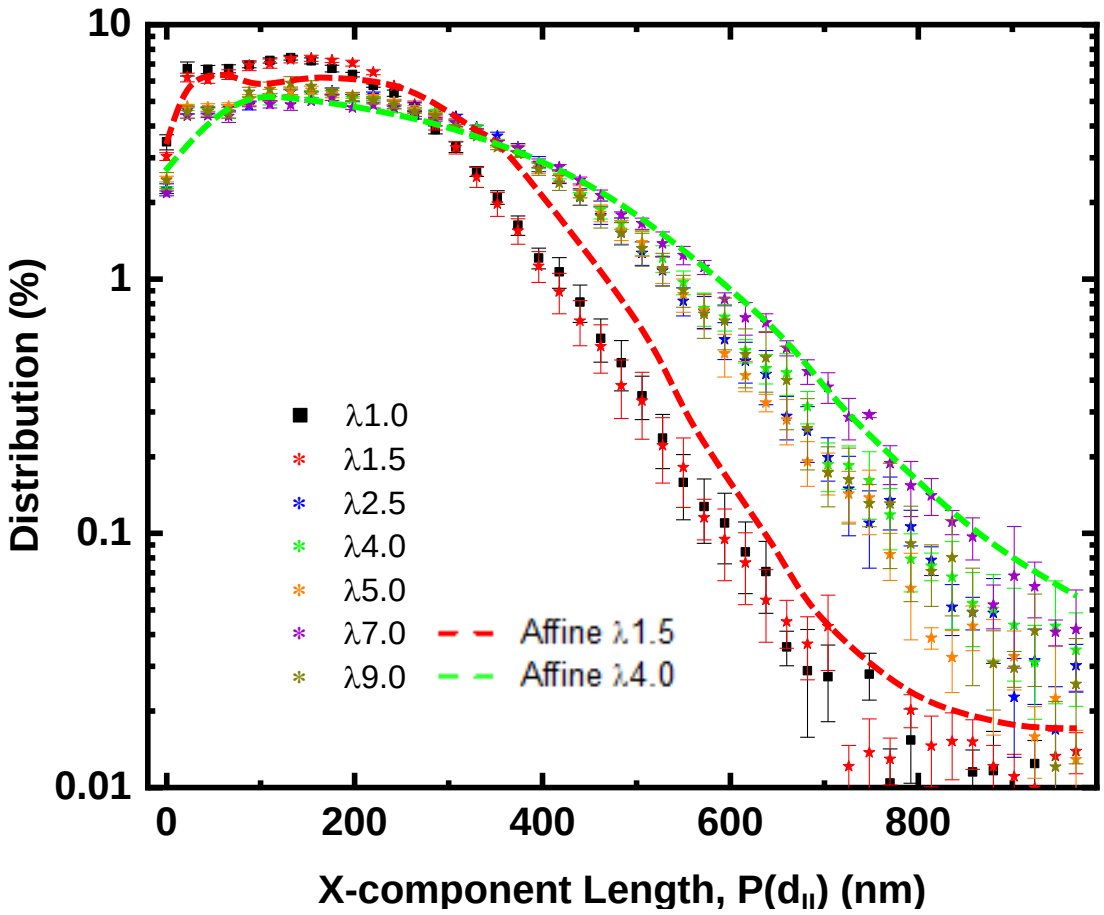

Figure B.5: X-component length for *Wi* = 20, all λ.

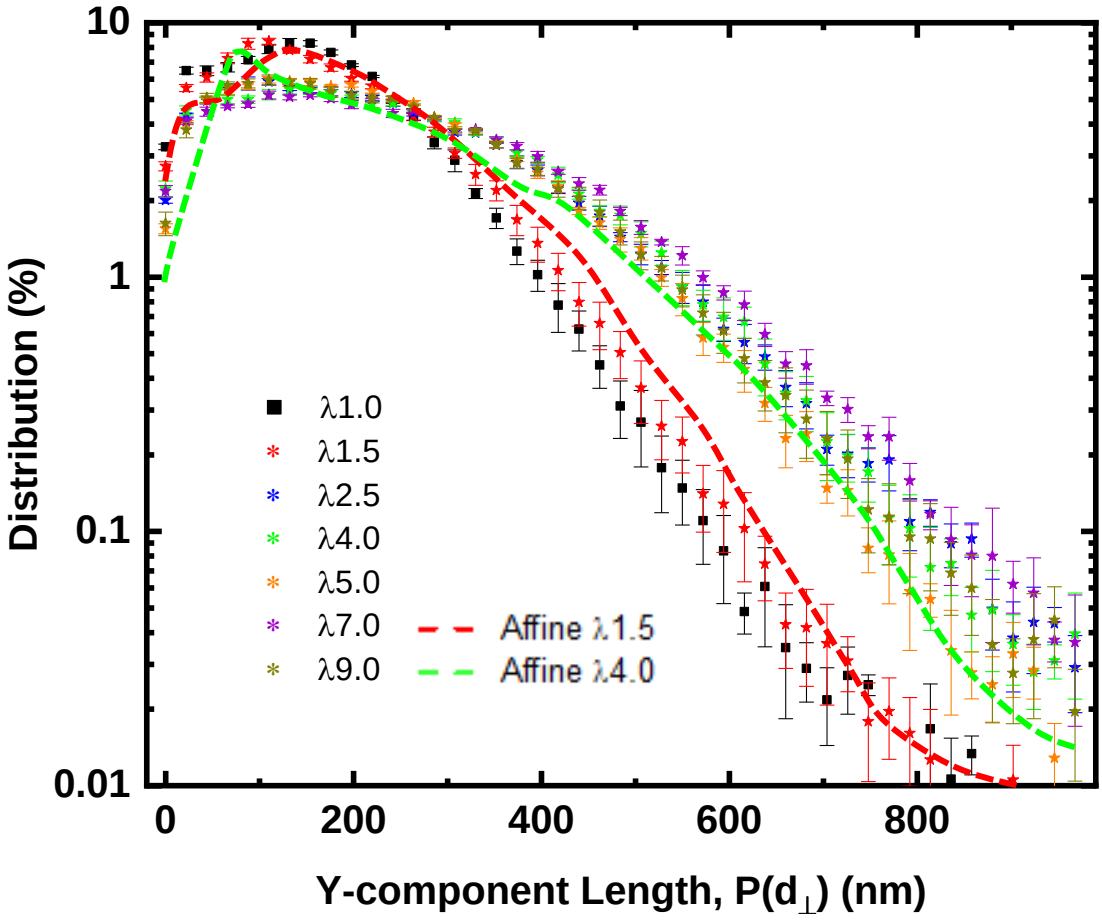

Figure B.6: Y-component length for *Wi* = 20, all λ.

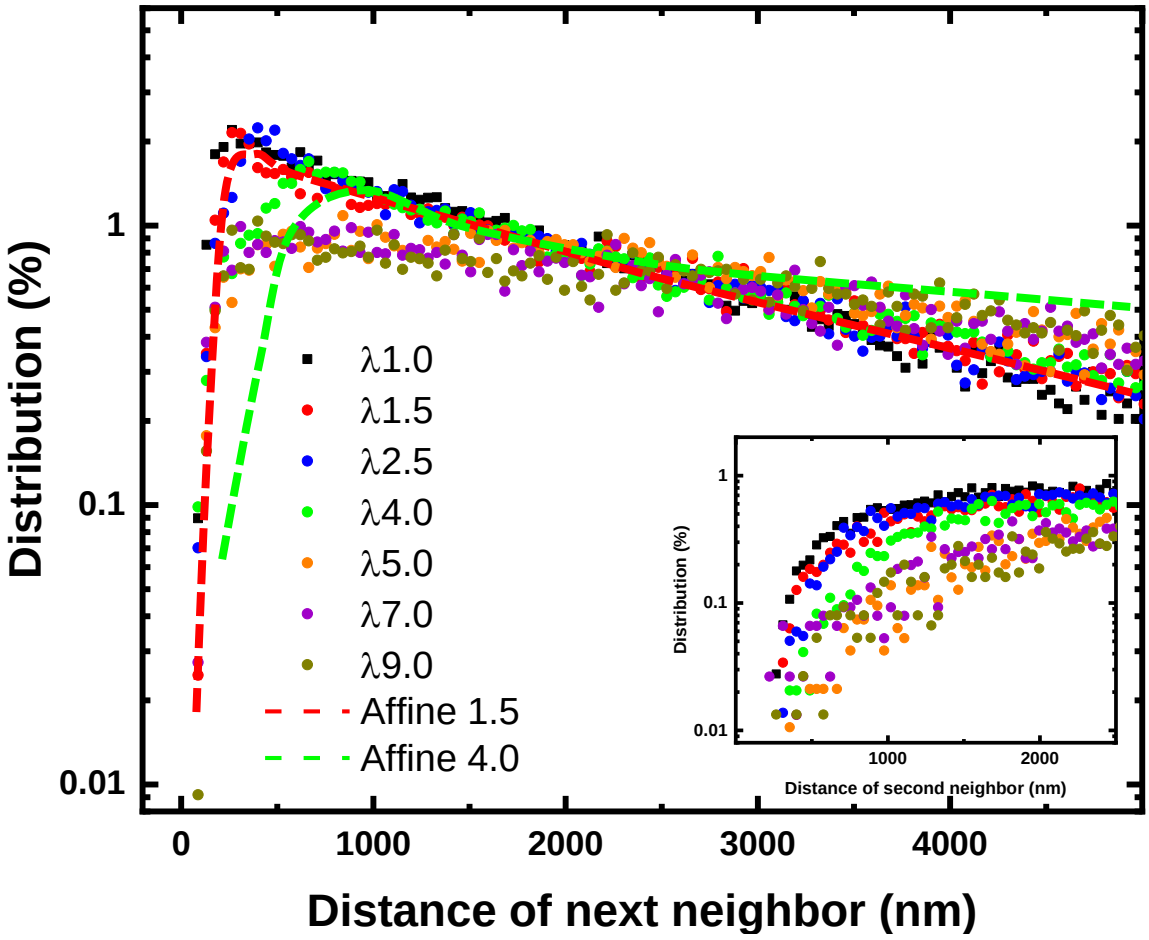

Figure B.7: Nearest neighbor in direction of stretching for *Wi* = 0.06, all λ.

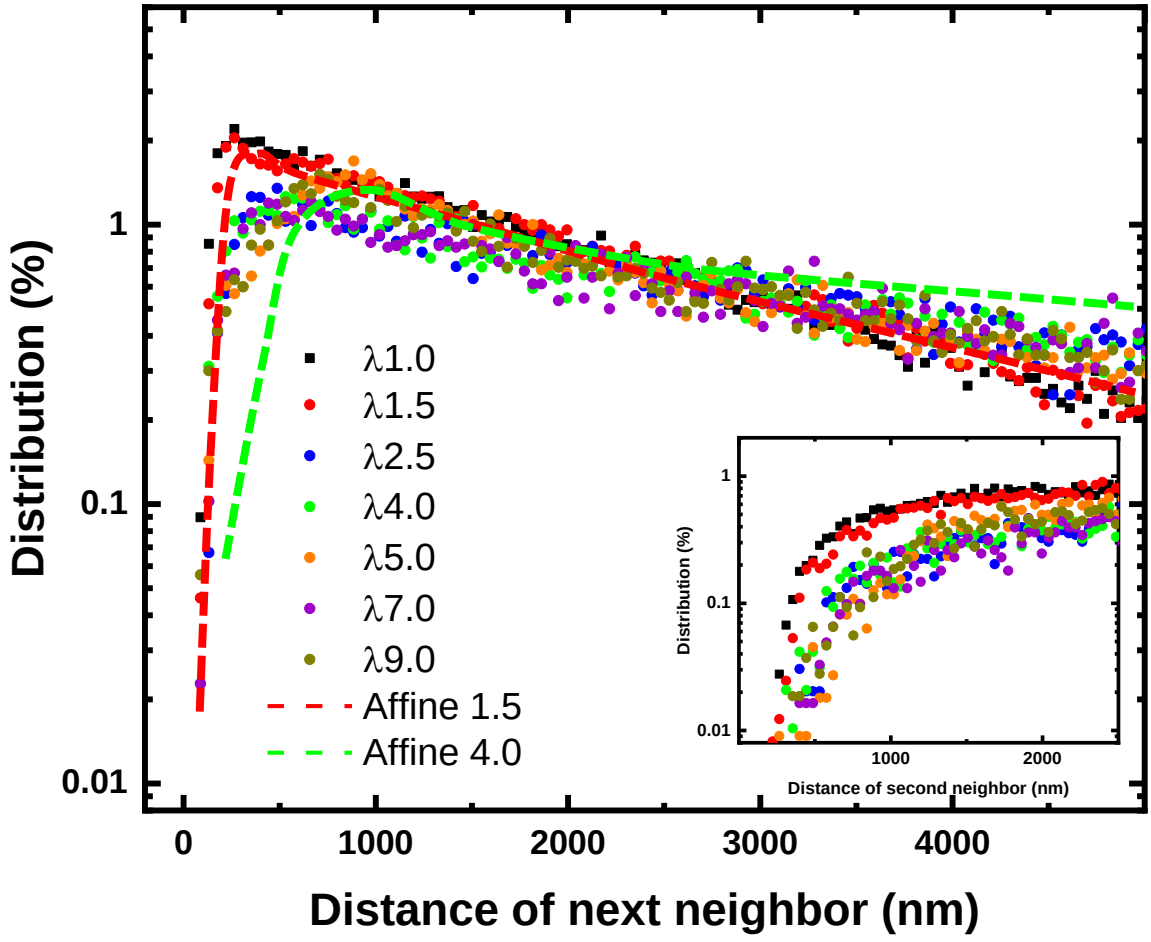

Figure B.8: Nearest neighbor in direction of stretching for *Wi* = 20, all λ.

APPENDIX C

SEM Images of Extrusion Sample Cross-Section Faces

A Note Regarding the Organization of Subsequent Images:

In this section, images for various sets of extrusion conditions will be provided in order of ascending pressure. The first image presented in a figure will always be the cross-section overview, which will have a few colored circles on it. These circles denote the locations of the subsequent images presented and will always follow a rainbow pattern (red first, followed by orange, followed by yellow for every sample. Next would be green, followed by blue, followed by purple as necessary). All sample overview scale bars are 100 μm, all other scale bars are 500 nm.

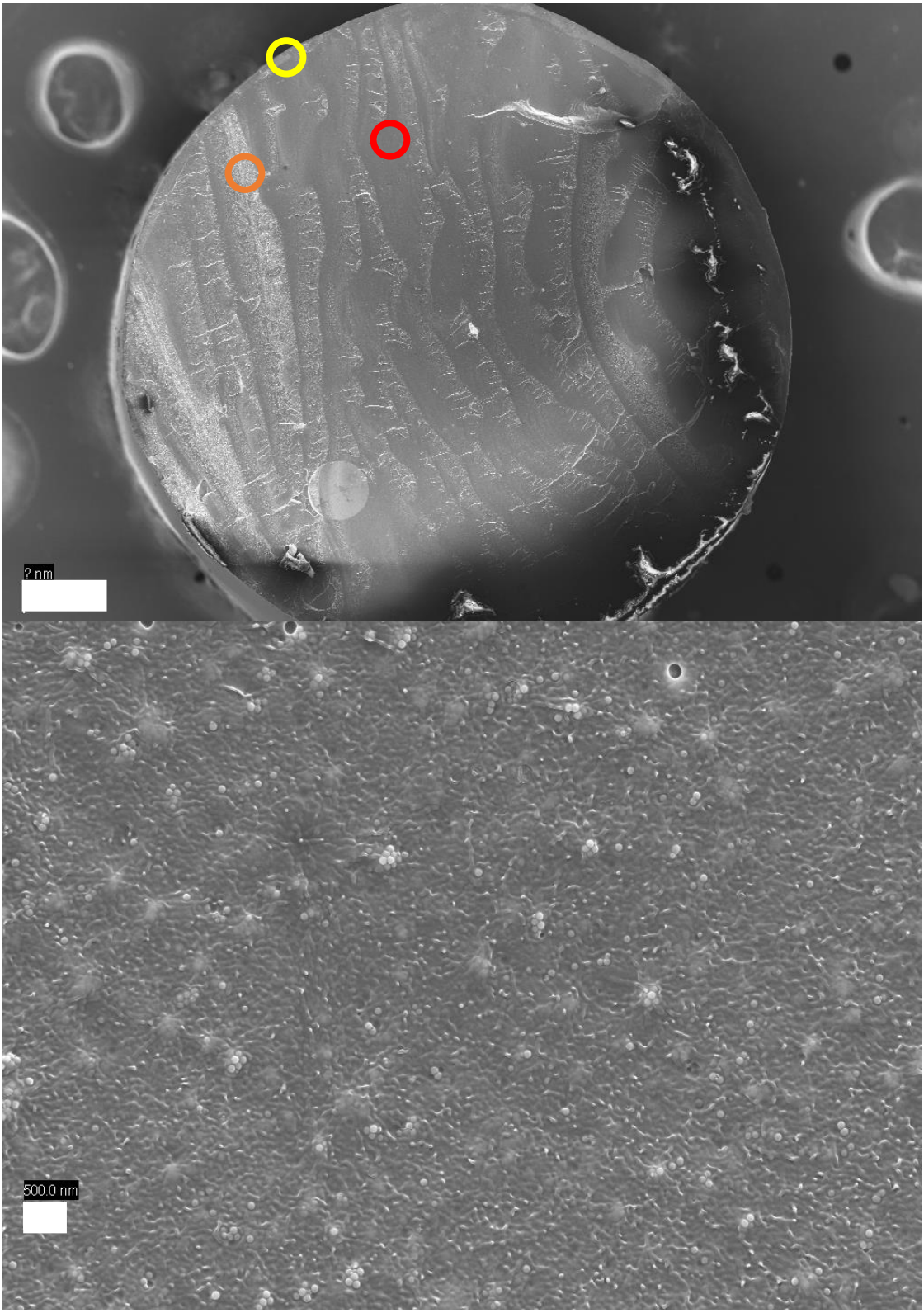

Figure C.1: 2.6v% R_{NP} = 40 nm images; Applied pressure of 5 psi.

Figure C.1 (cont.)

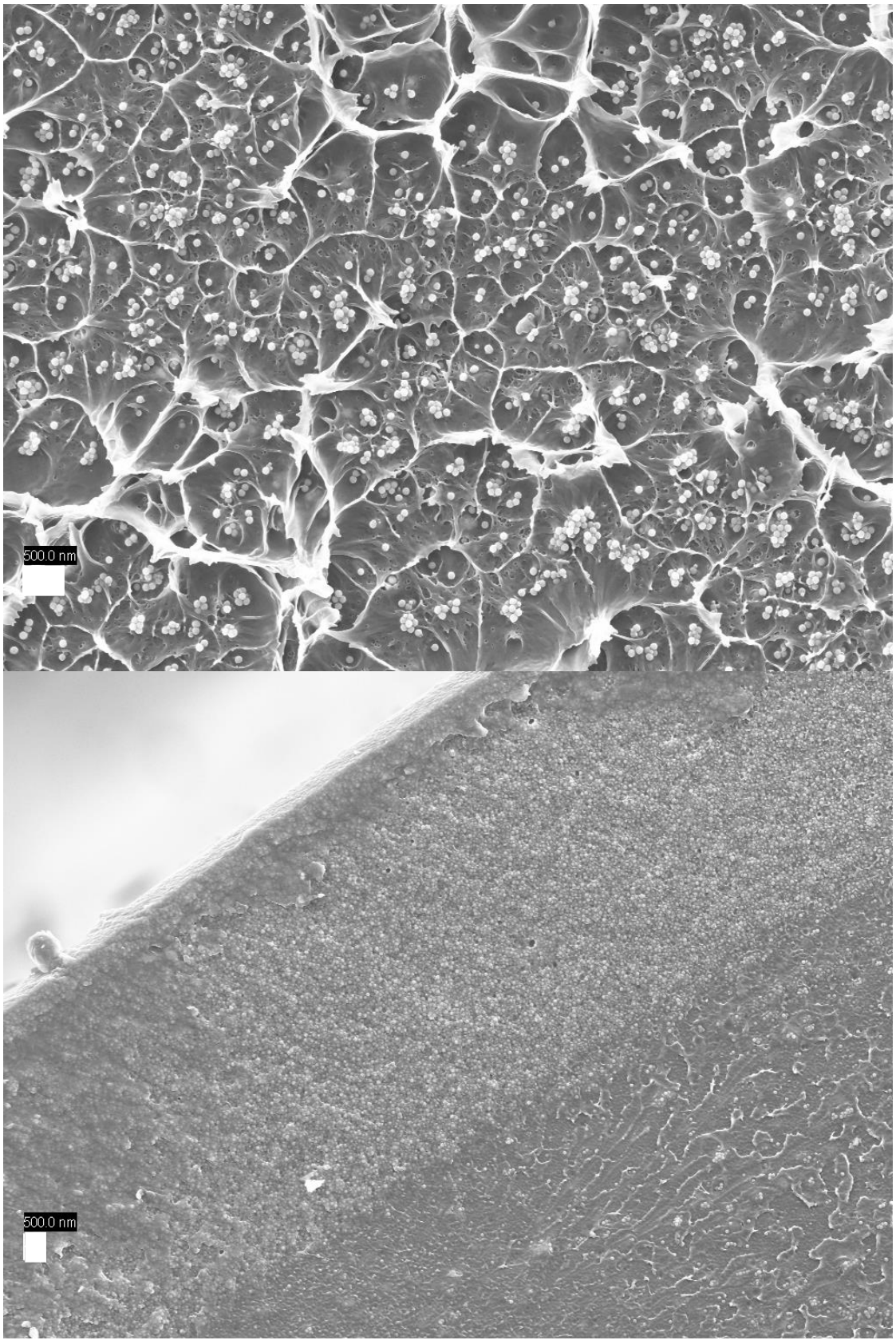

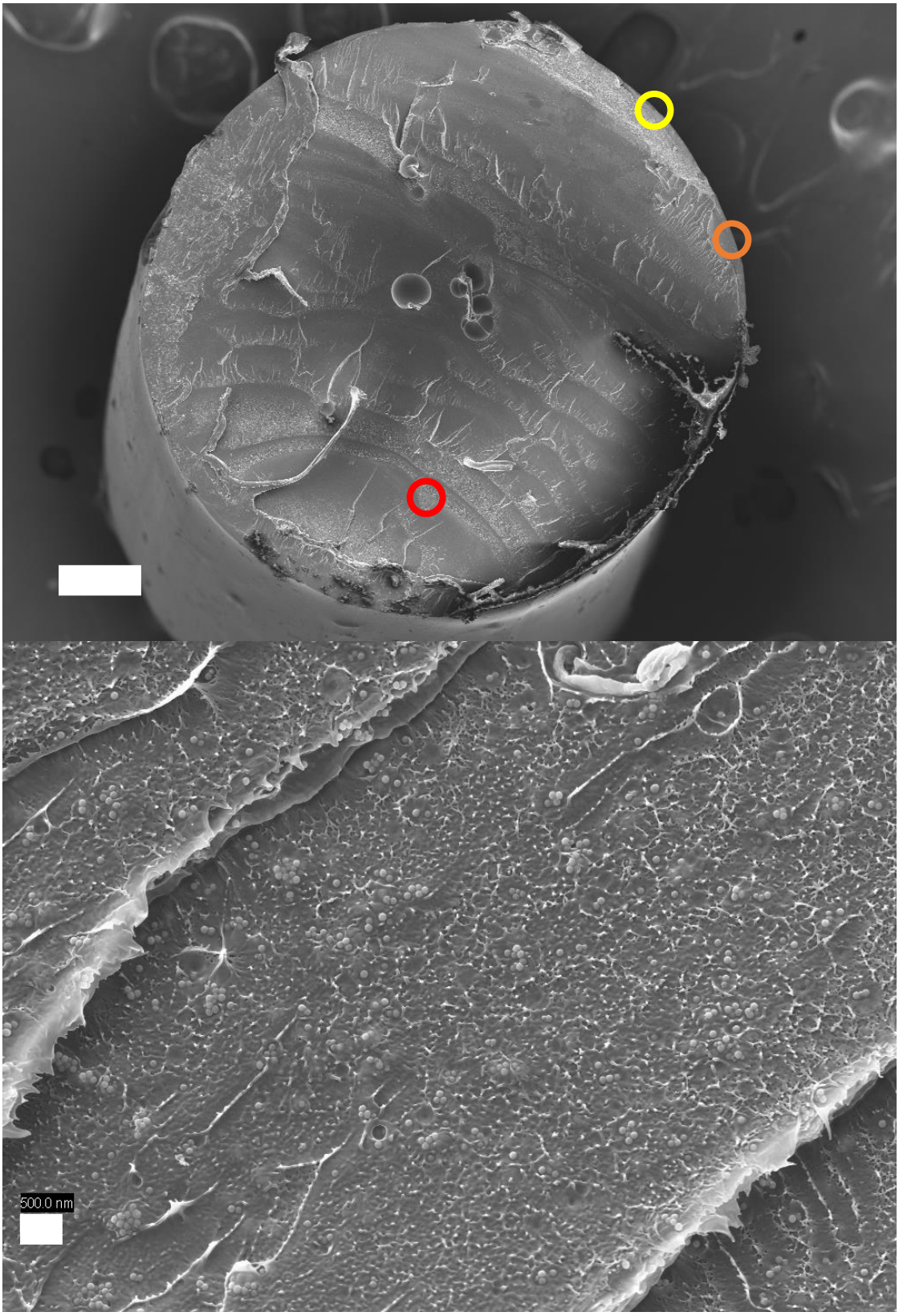

Figure C.2: 2.6v% R_{NP} = 40 nm images; Applied pressure of 20 psi.

Figure C.2 (cont.)

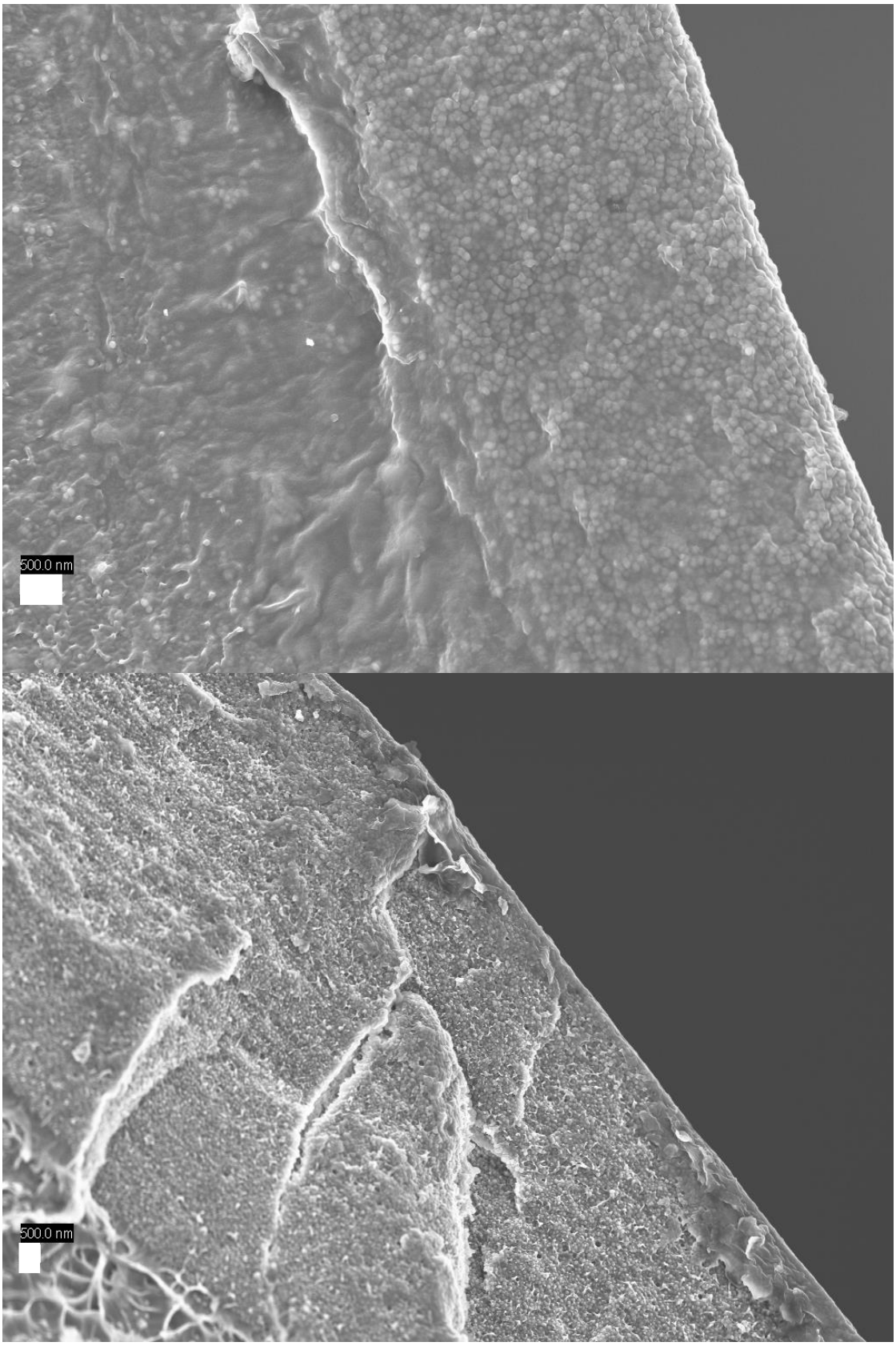

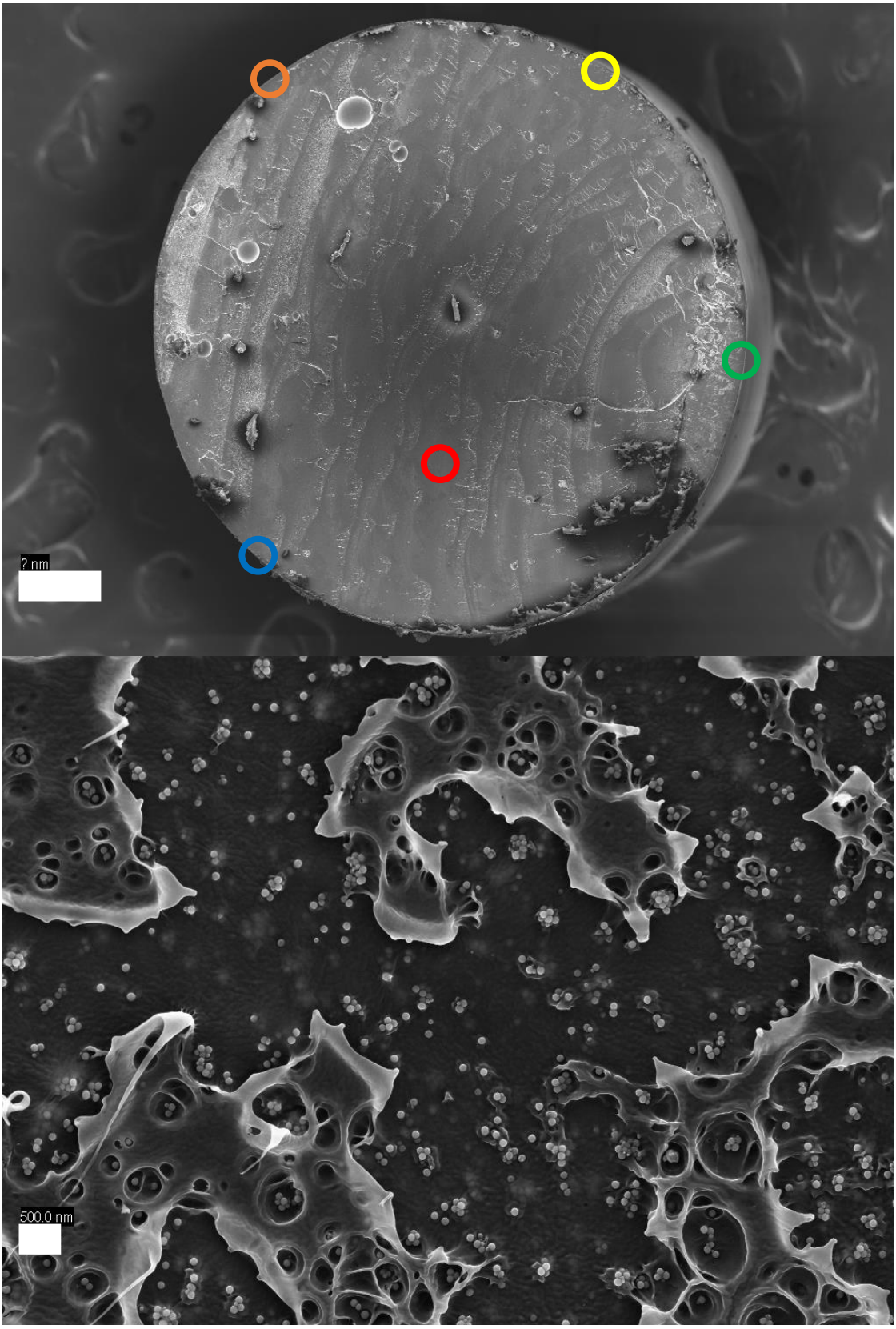

Figure C.3: 2.6v% R_{NP} = 40 nm images; Applied pressure of 60 psi.

Figure C.3 (cont.)

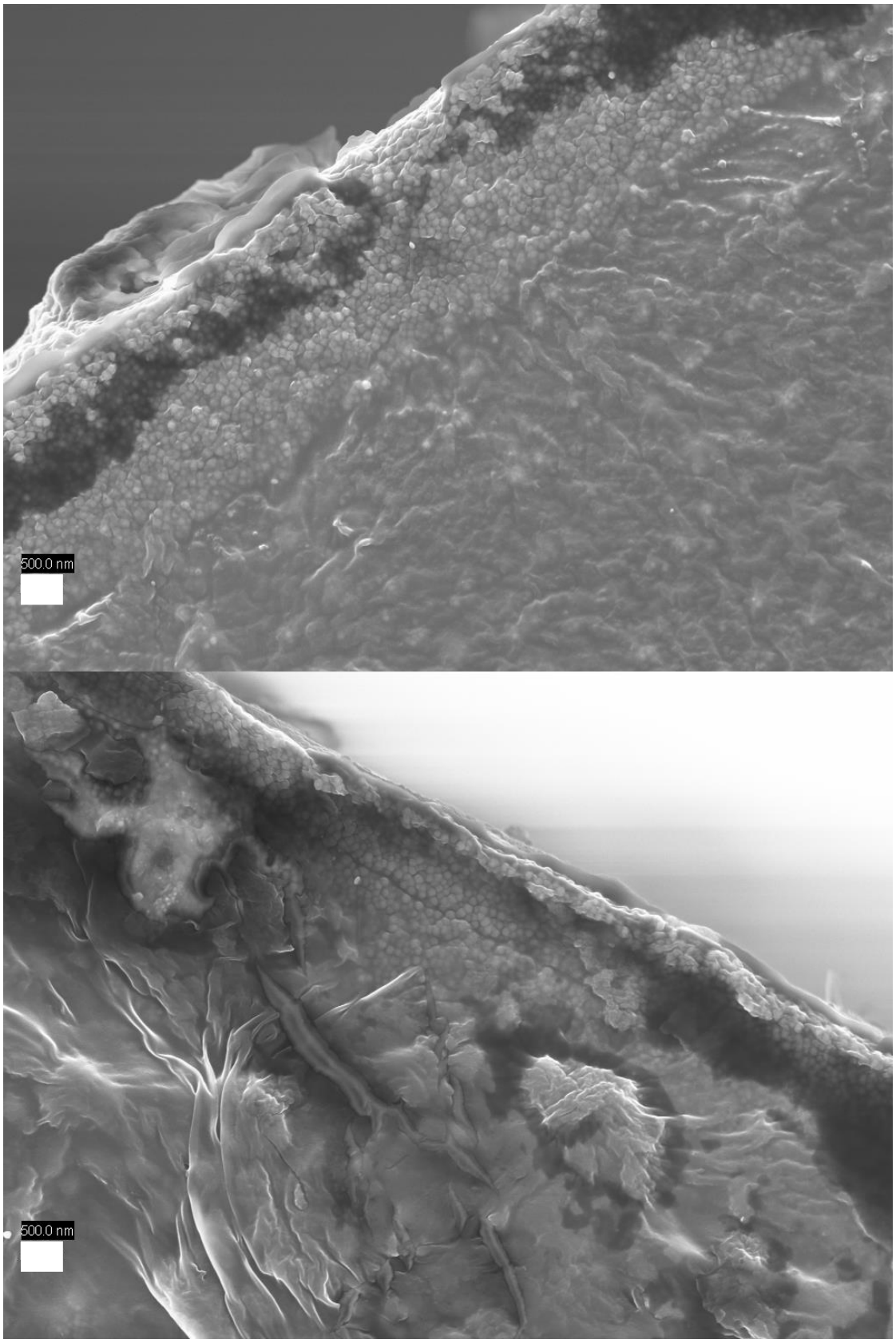

Figure C.3 (cont.)

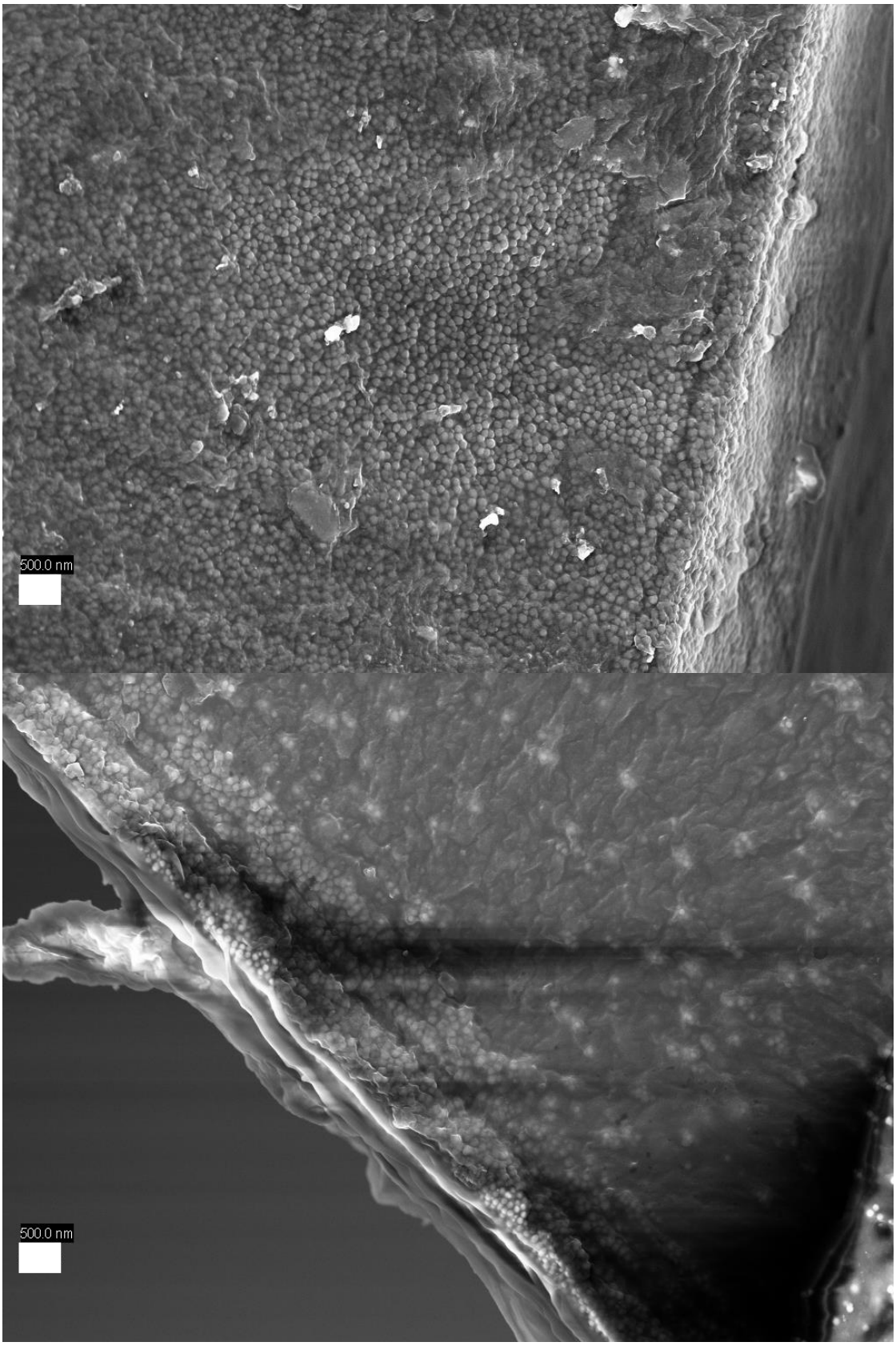

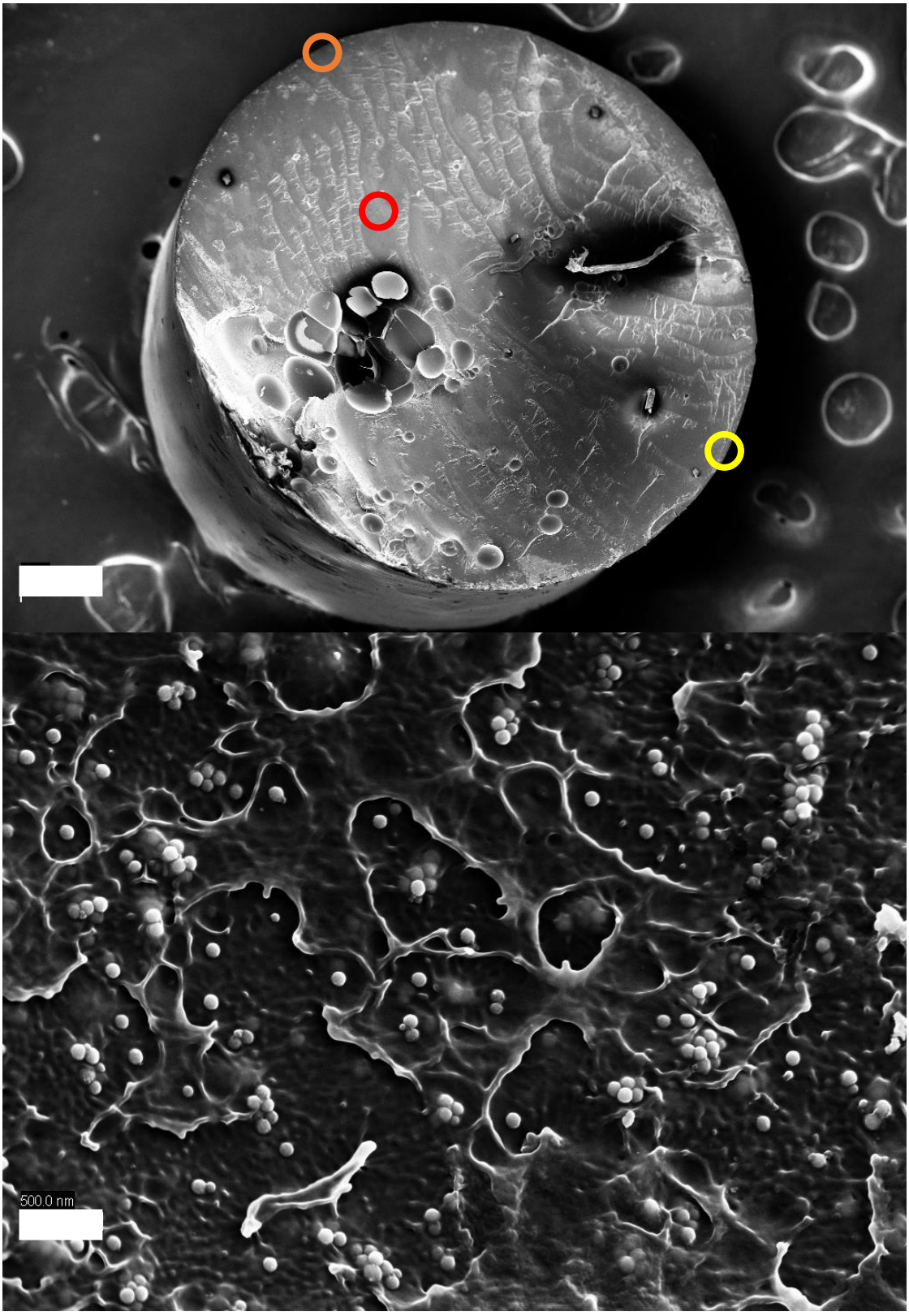

Figure C.4: 2.6v% R_{NP} = 40 nm images; Applied pressure of 80 psi.

Figure C.4 (cont.)

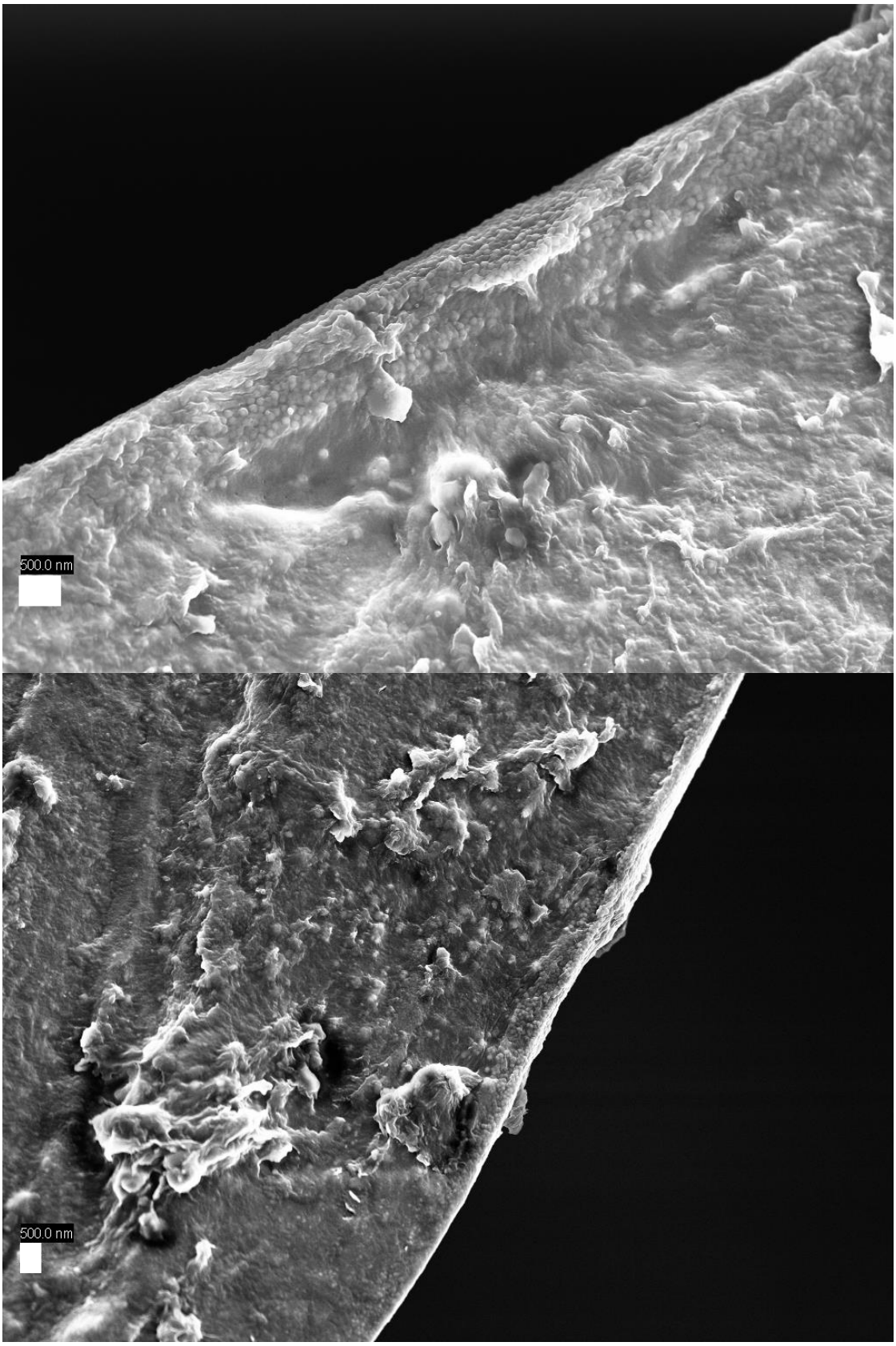

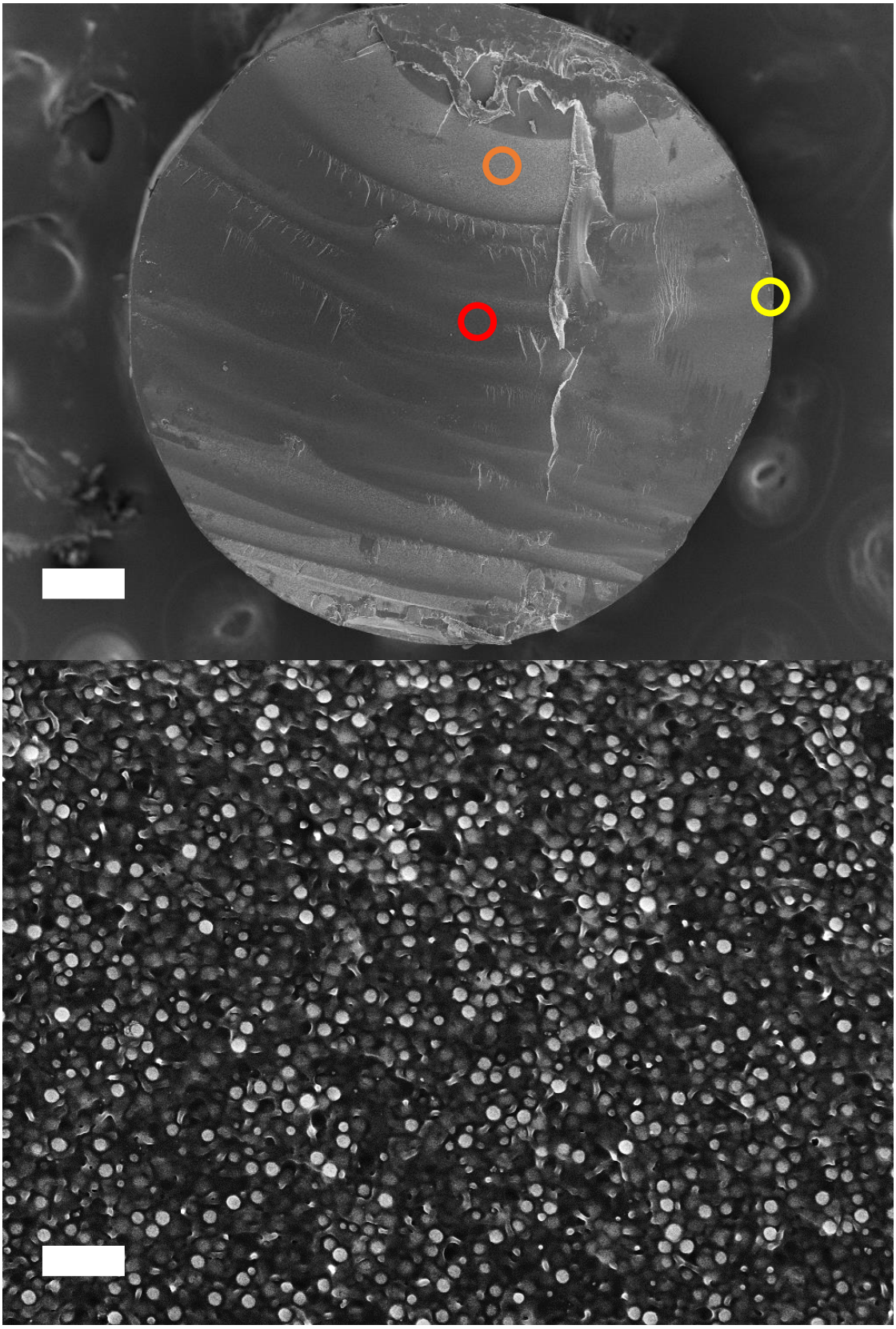

Figure C.5: 11.1v% R_{NP} = 40 nm images; Applied pressure of 5 psi.

Figure C.5 (cont.)

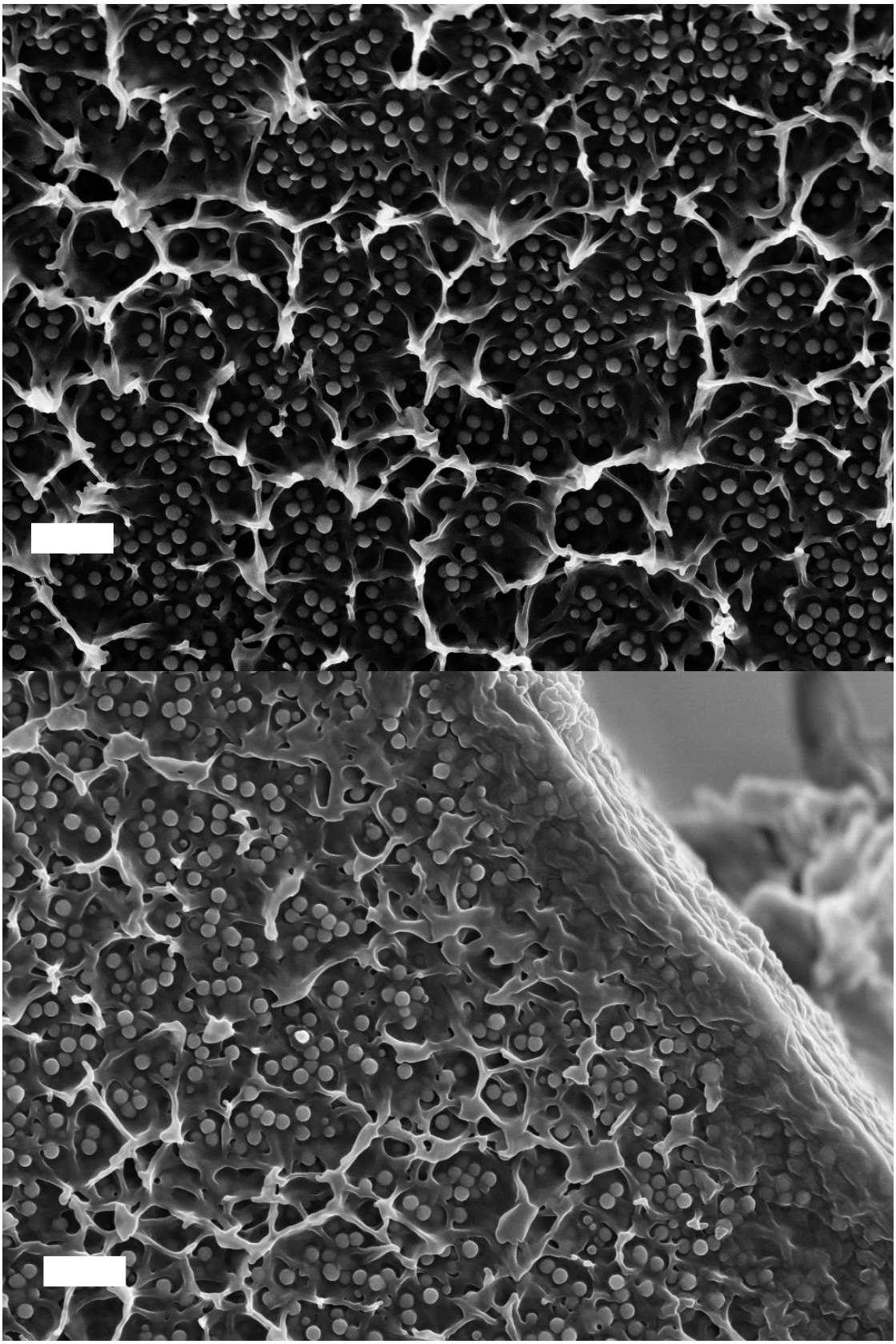

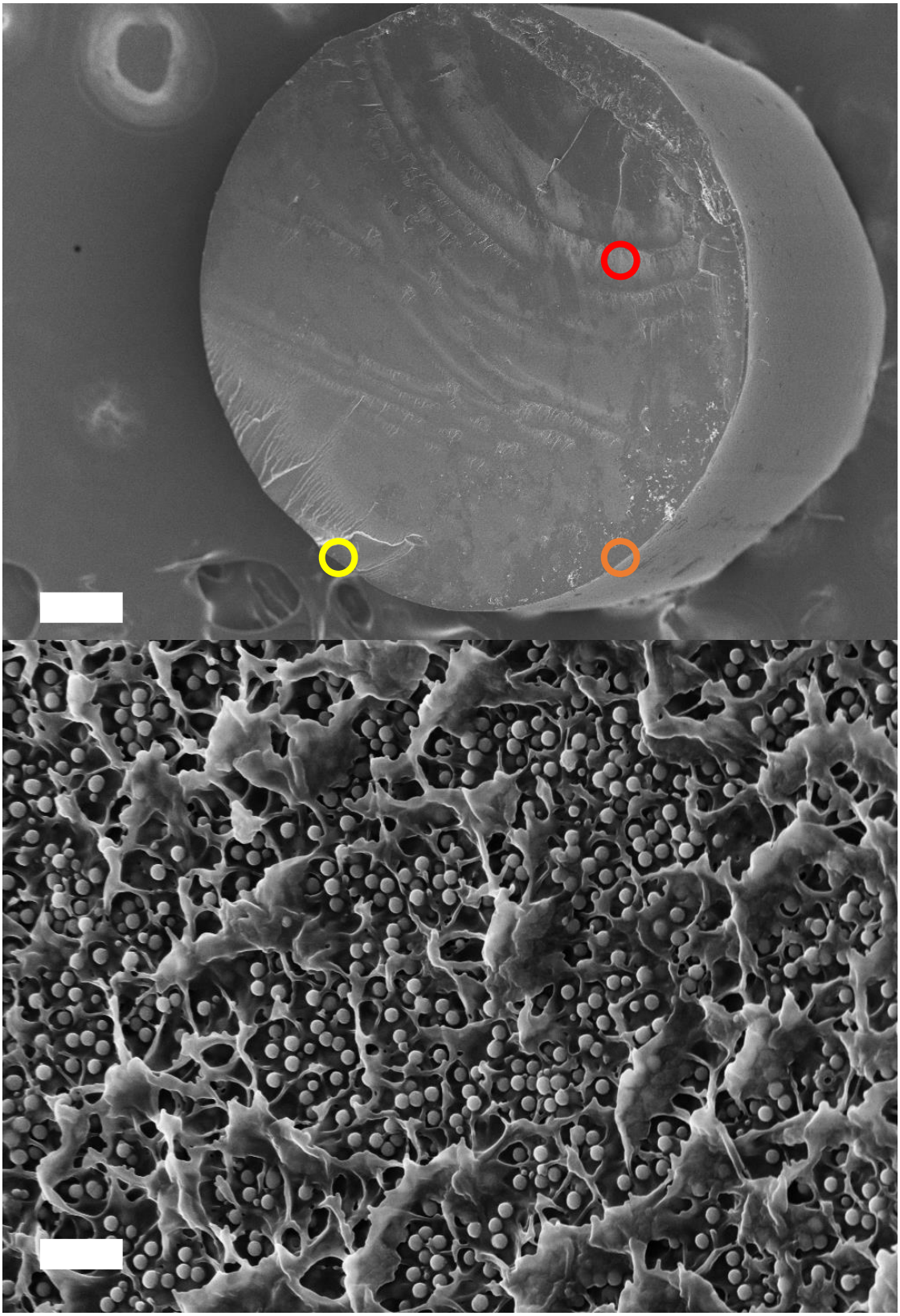

Figure C.6: 11.1v% R_{NP} = 40 nm images; Applied pressure of 20 psi.

Figure C.6 (cont.)

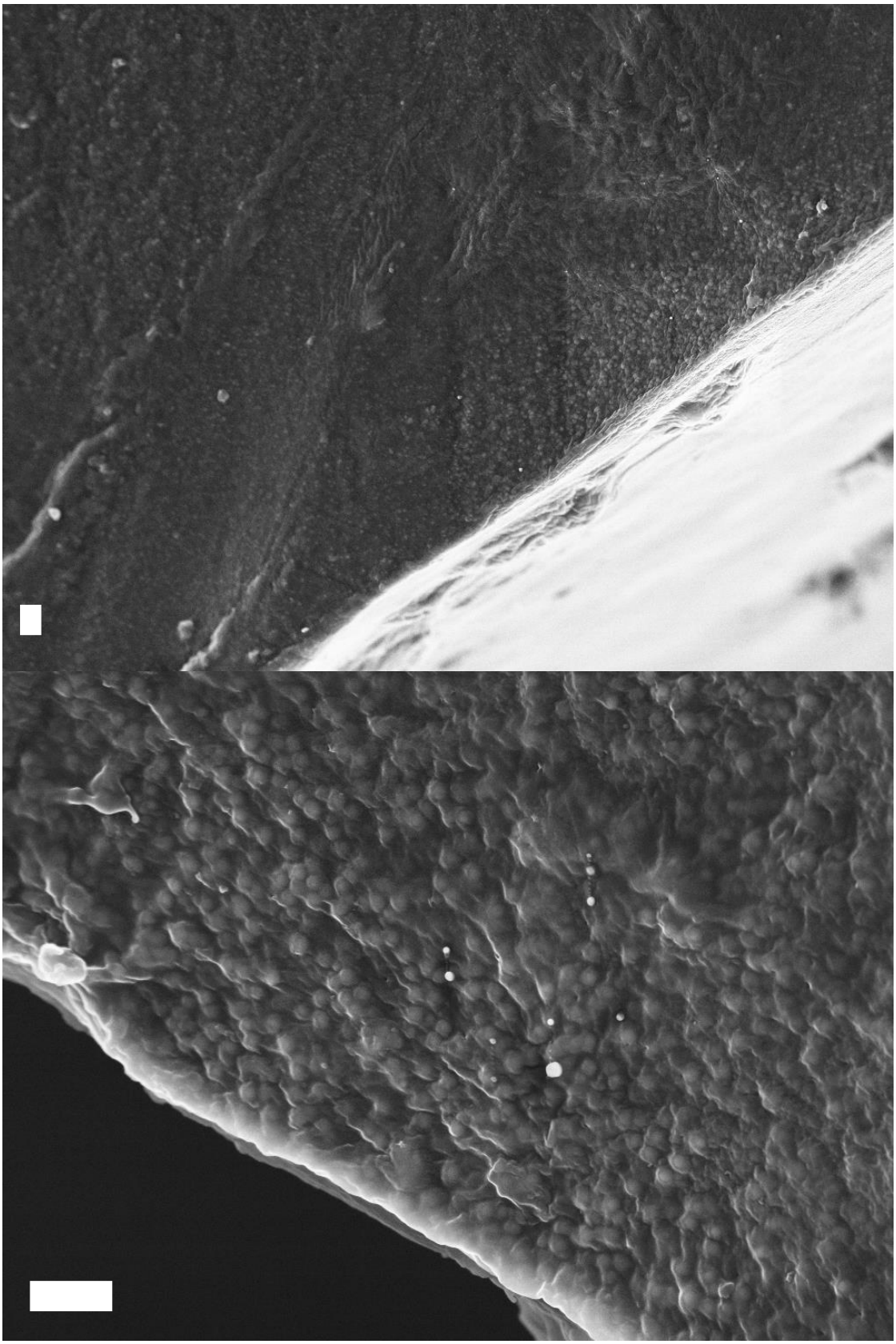

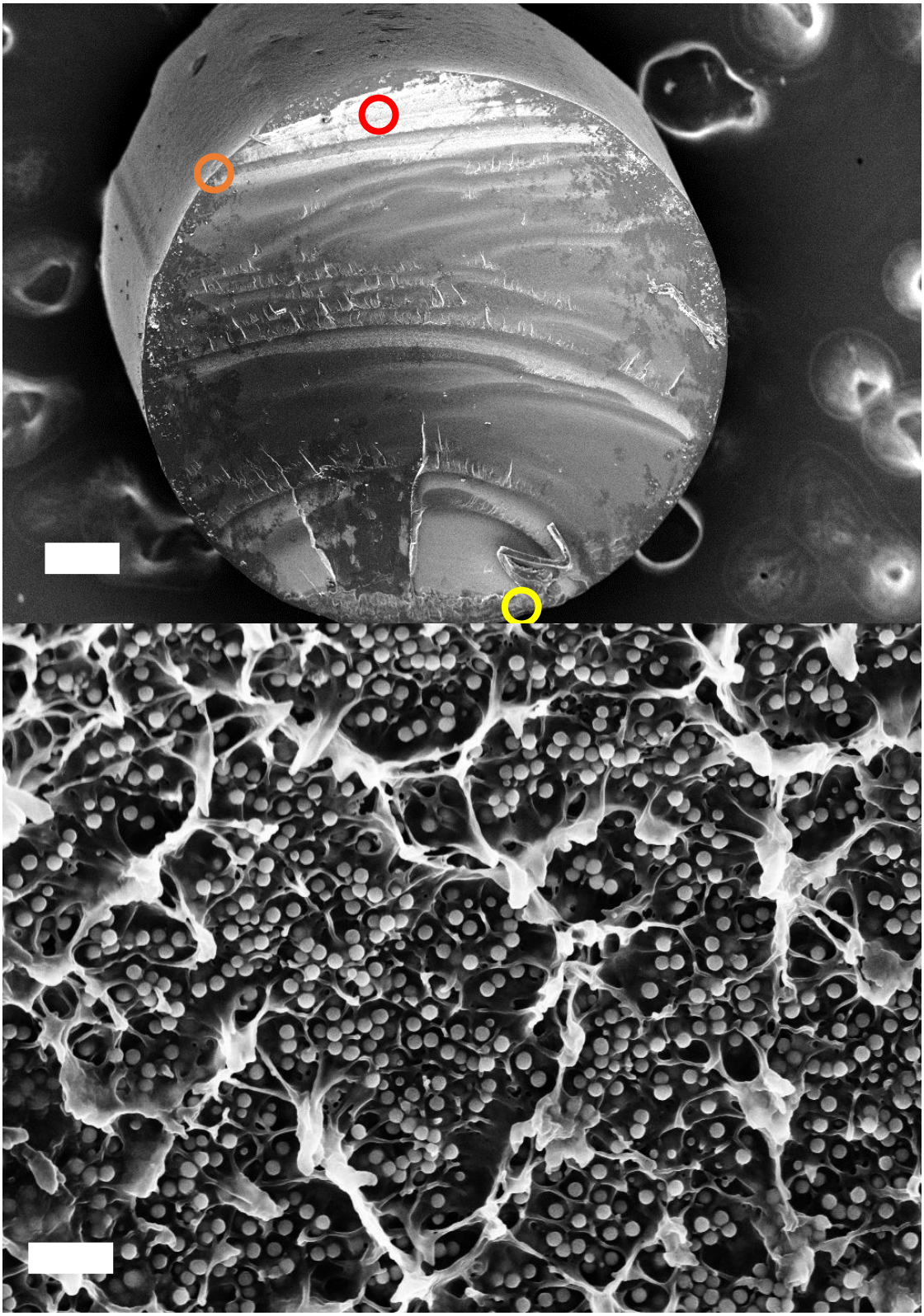

Figure C.7: 11.1v% R_{NP} = 40 nm images; Applied pressure of 40 psi.

Figure C.7 (cont.)

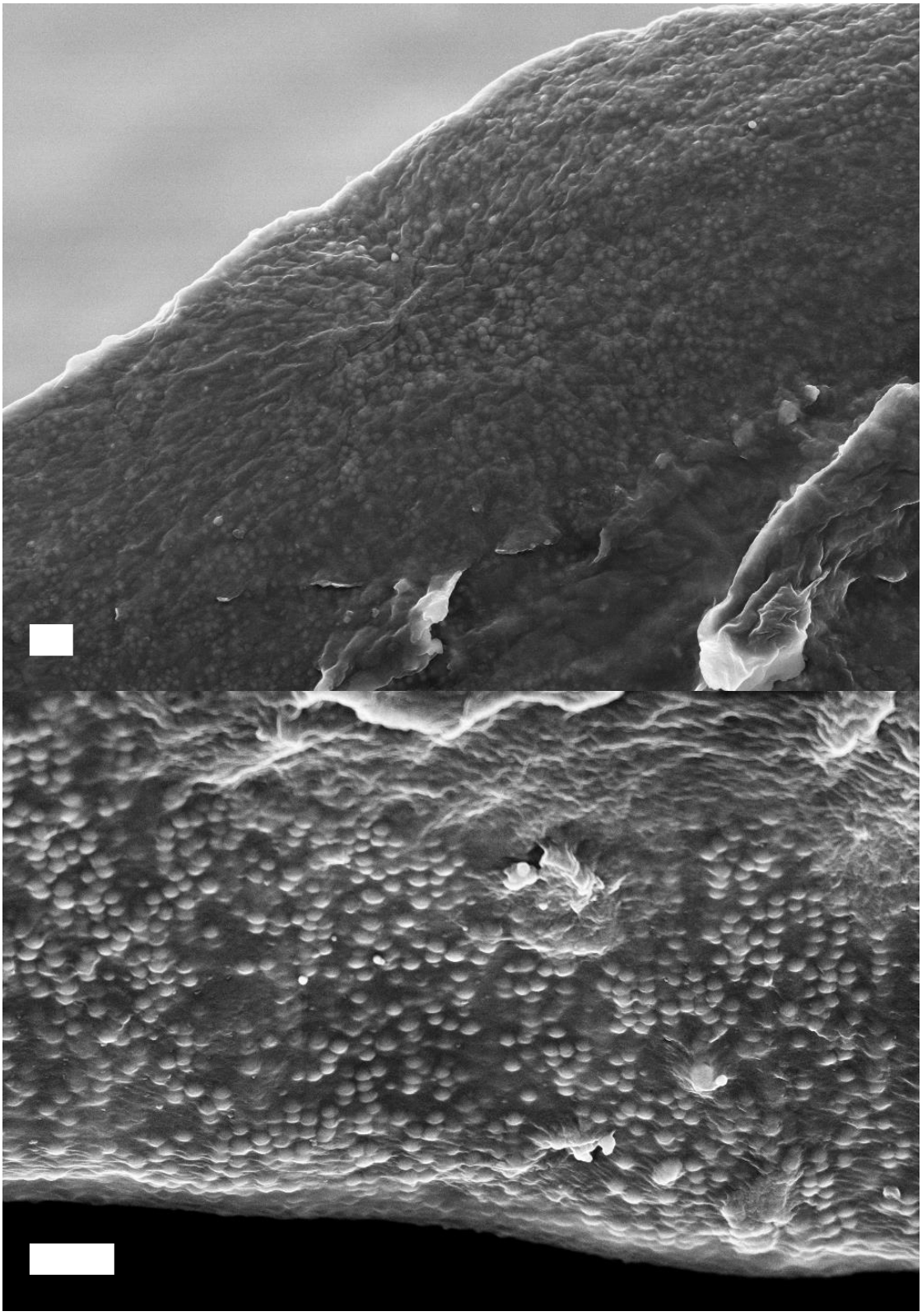

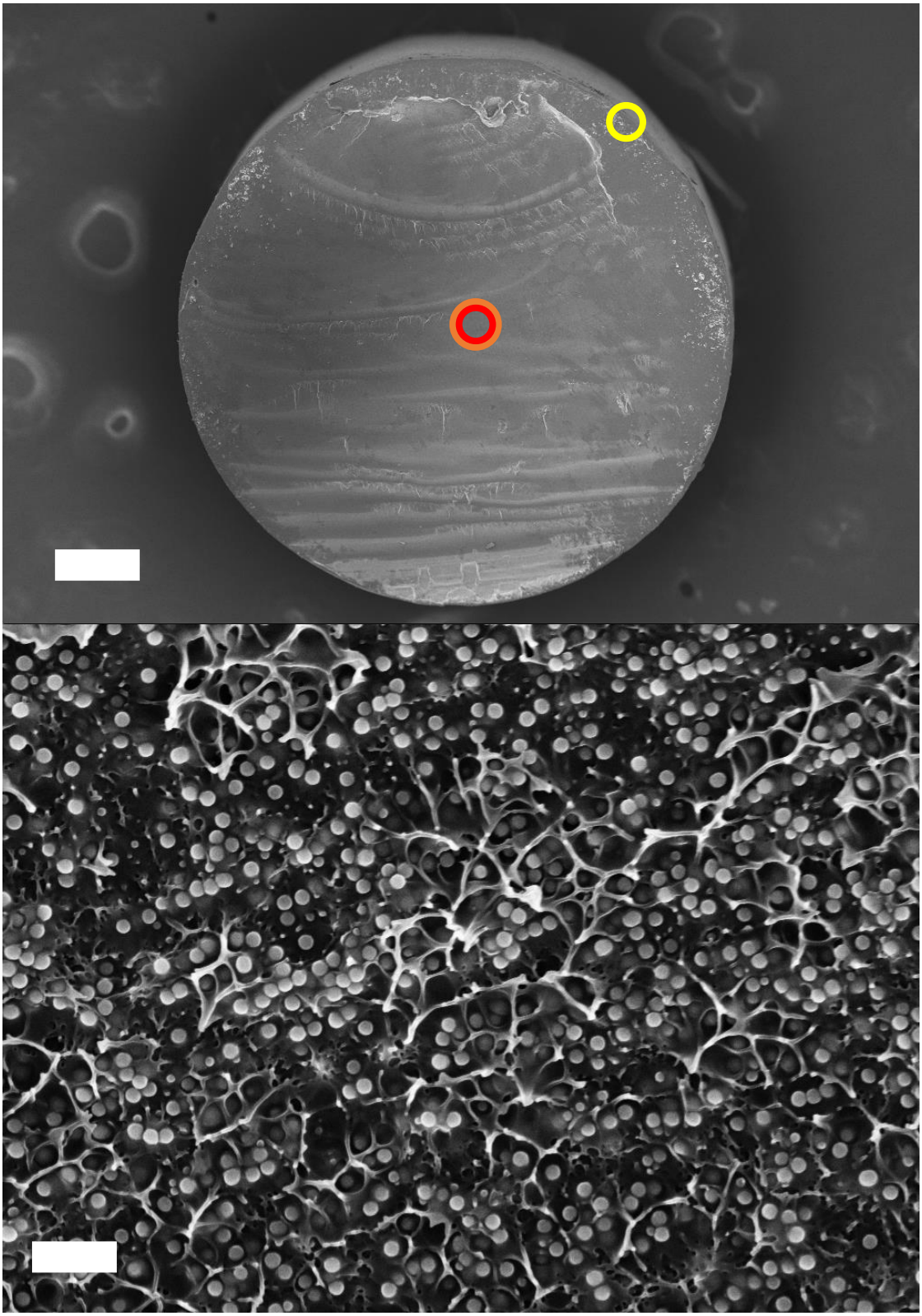

Figure C.8: 11.1v% R_{NP} = 40 nm images; Applied pressure of 60 psi.

Figure C.8 (cont.)

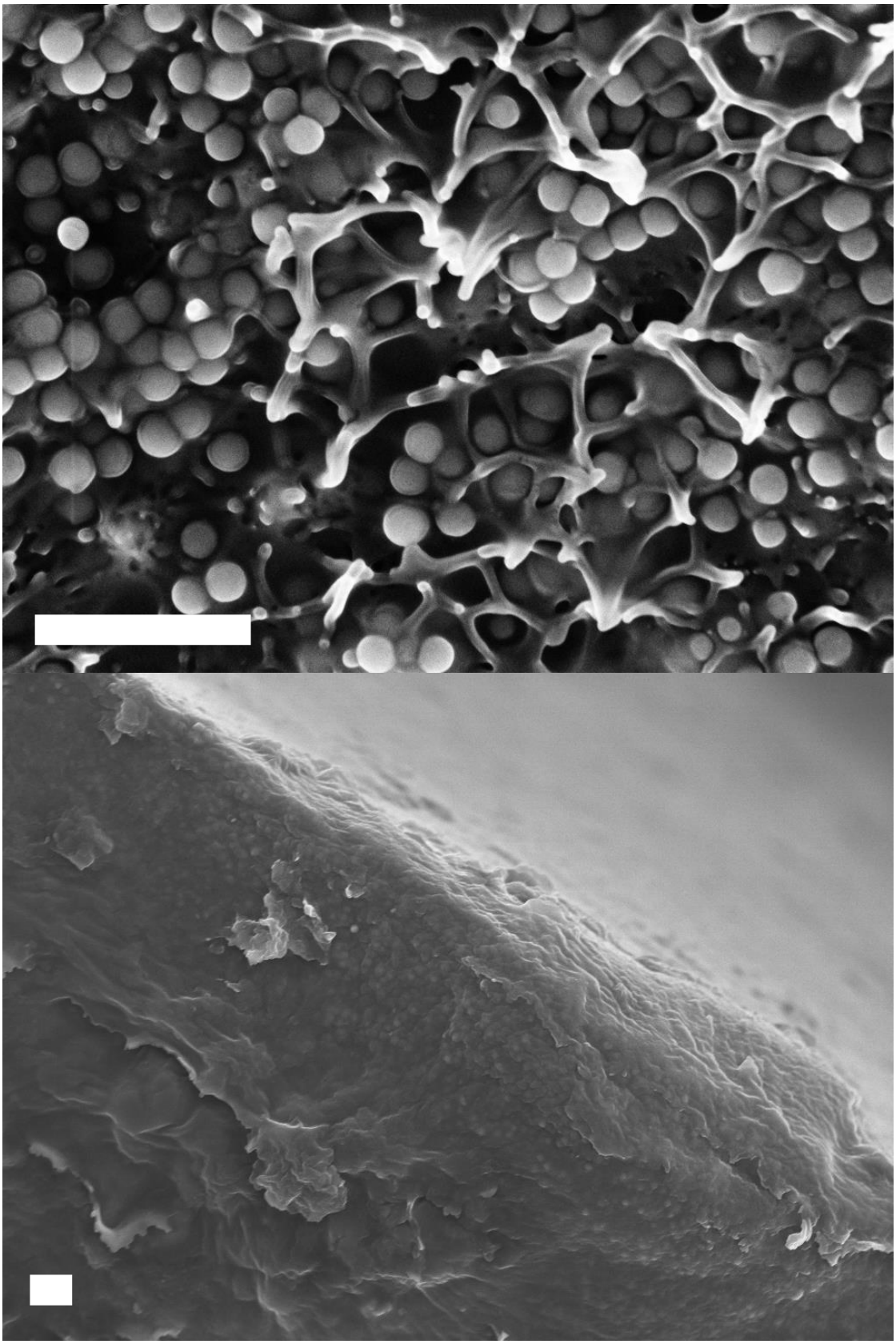

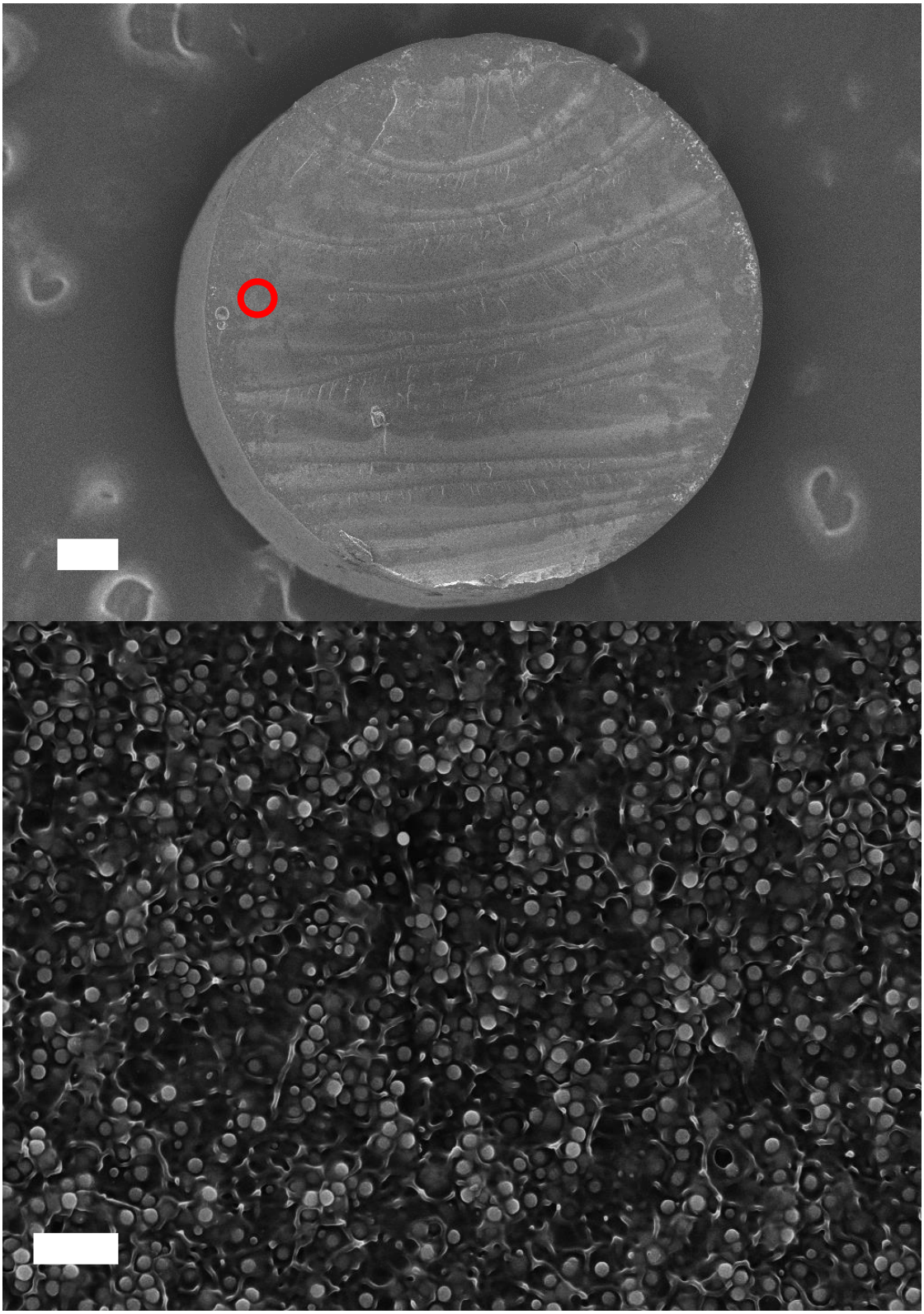

Figure C.9: 11.1v% R_{NP} = 40 nm images; Applied pressure of 80 psi.

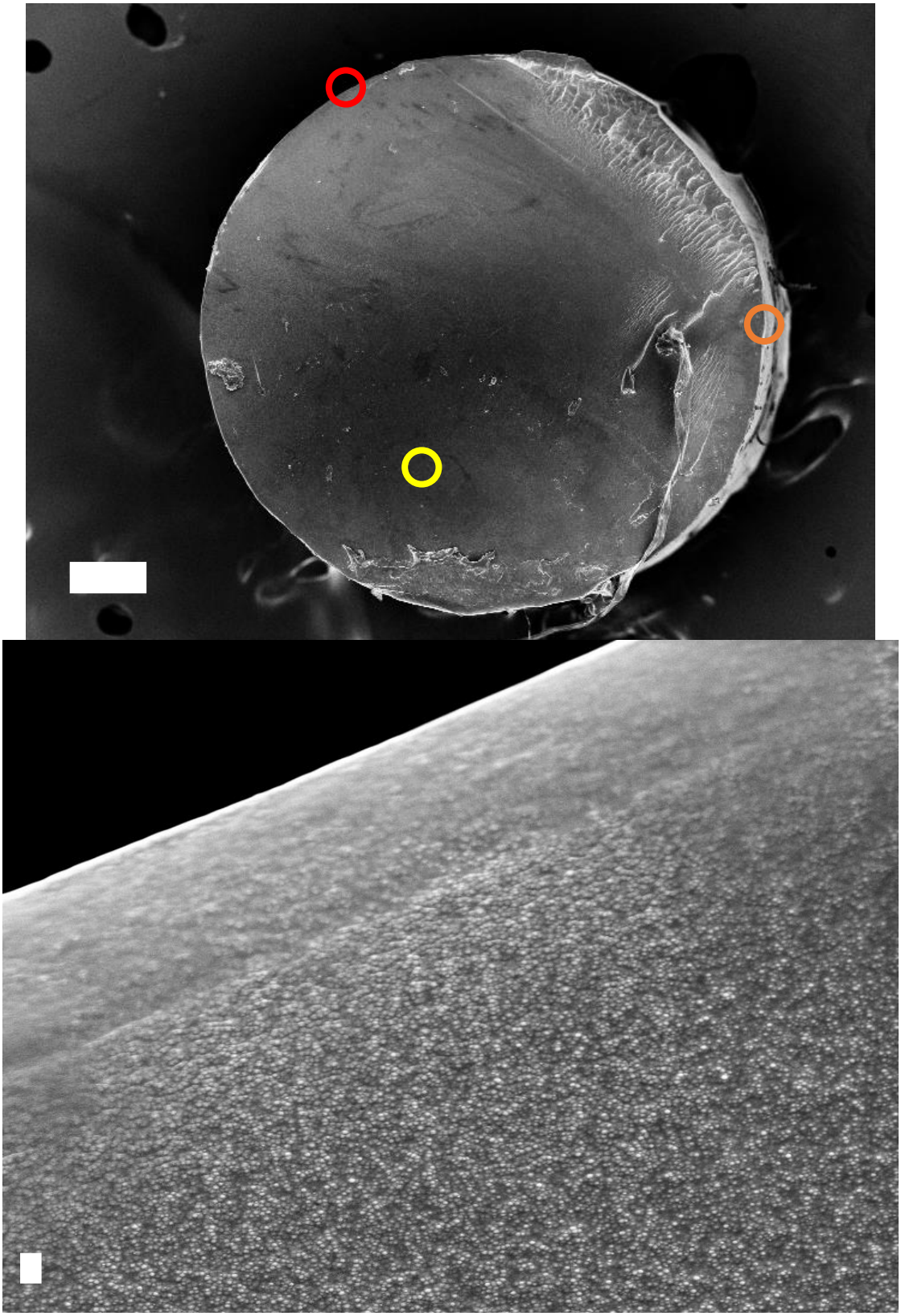

Figure C.10: 33.3v% R_{NP} = 40 nm images; Applied pressure of 10 psi.

Figure C.10 (cont.)

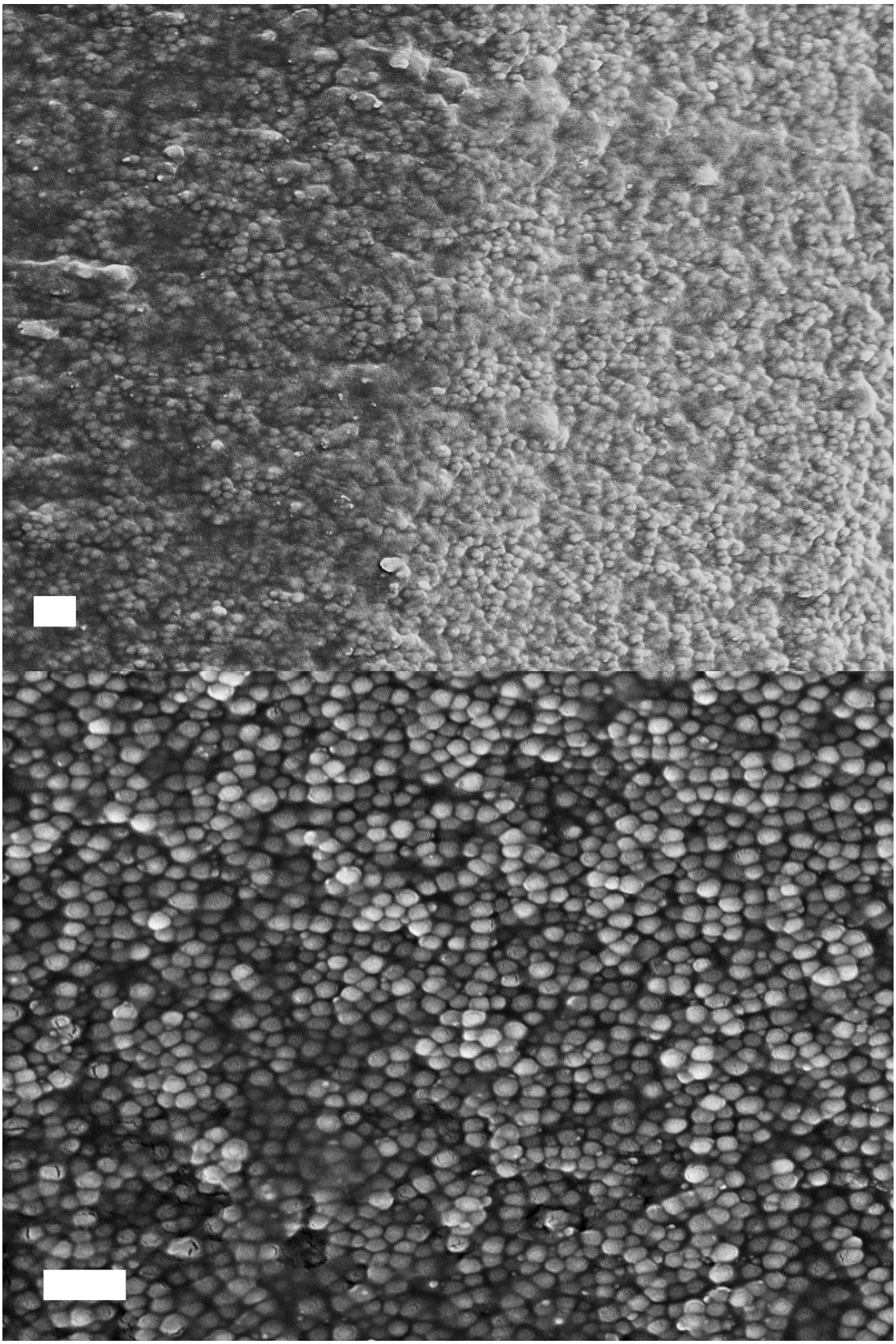

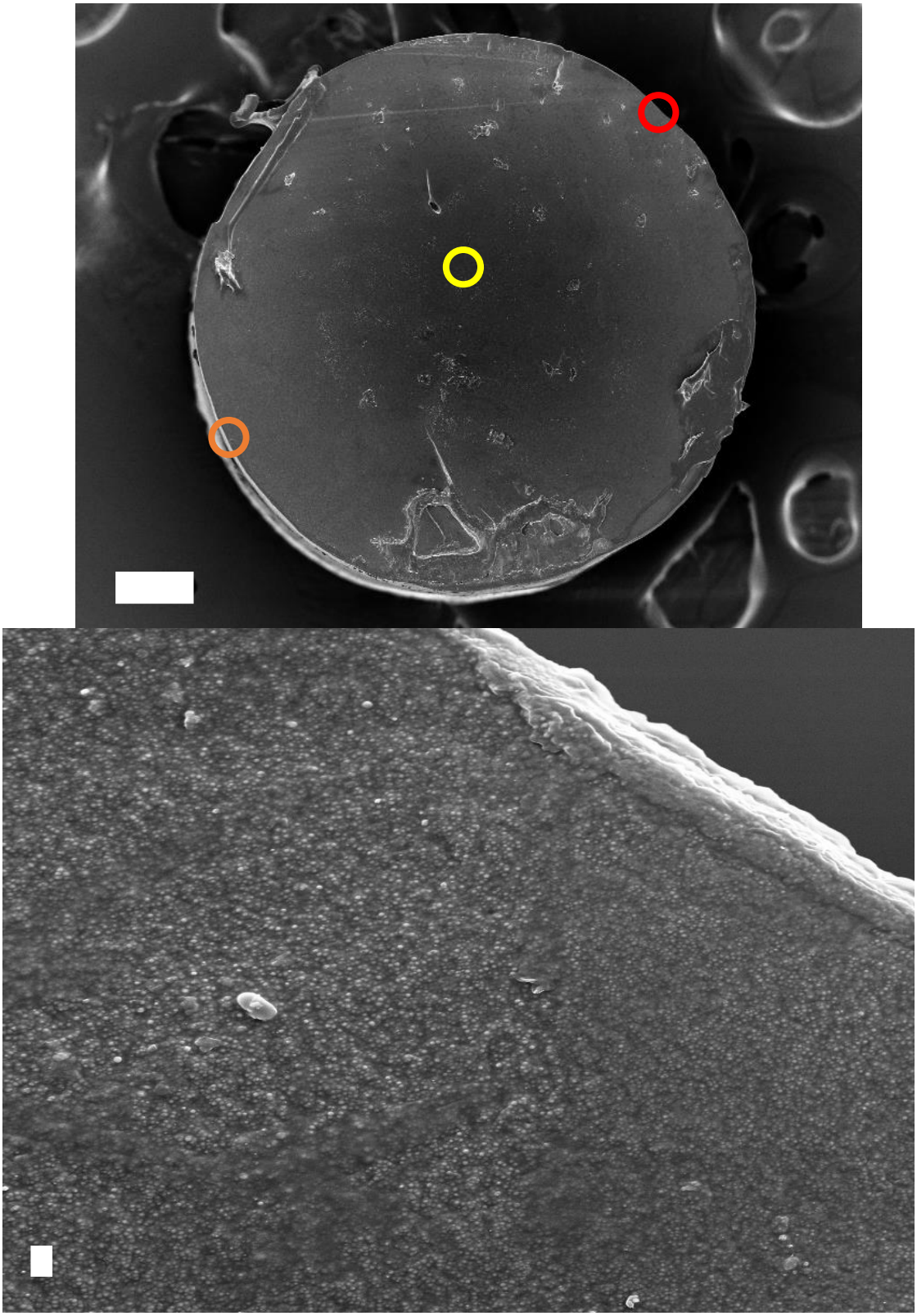

Figure C.11: 33.3v% R_{NP} = 40 nm images; Applied pressure of 40 psi.

Figure C.11 (cont.)

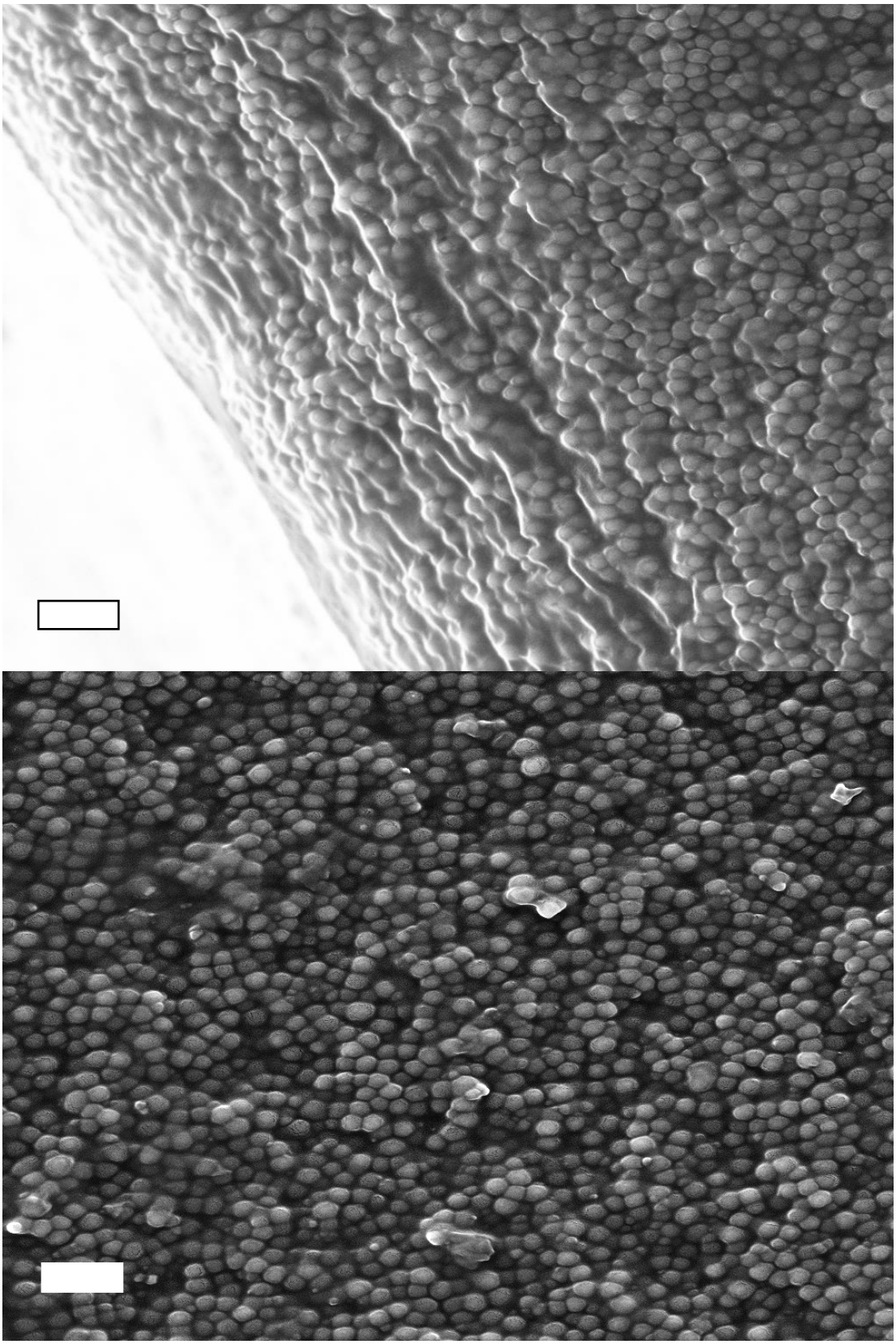

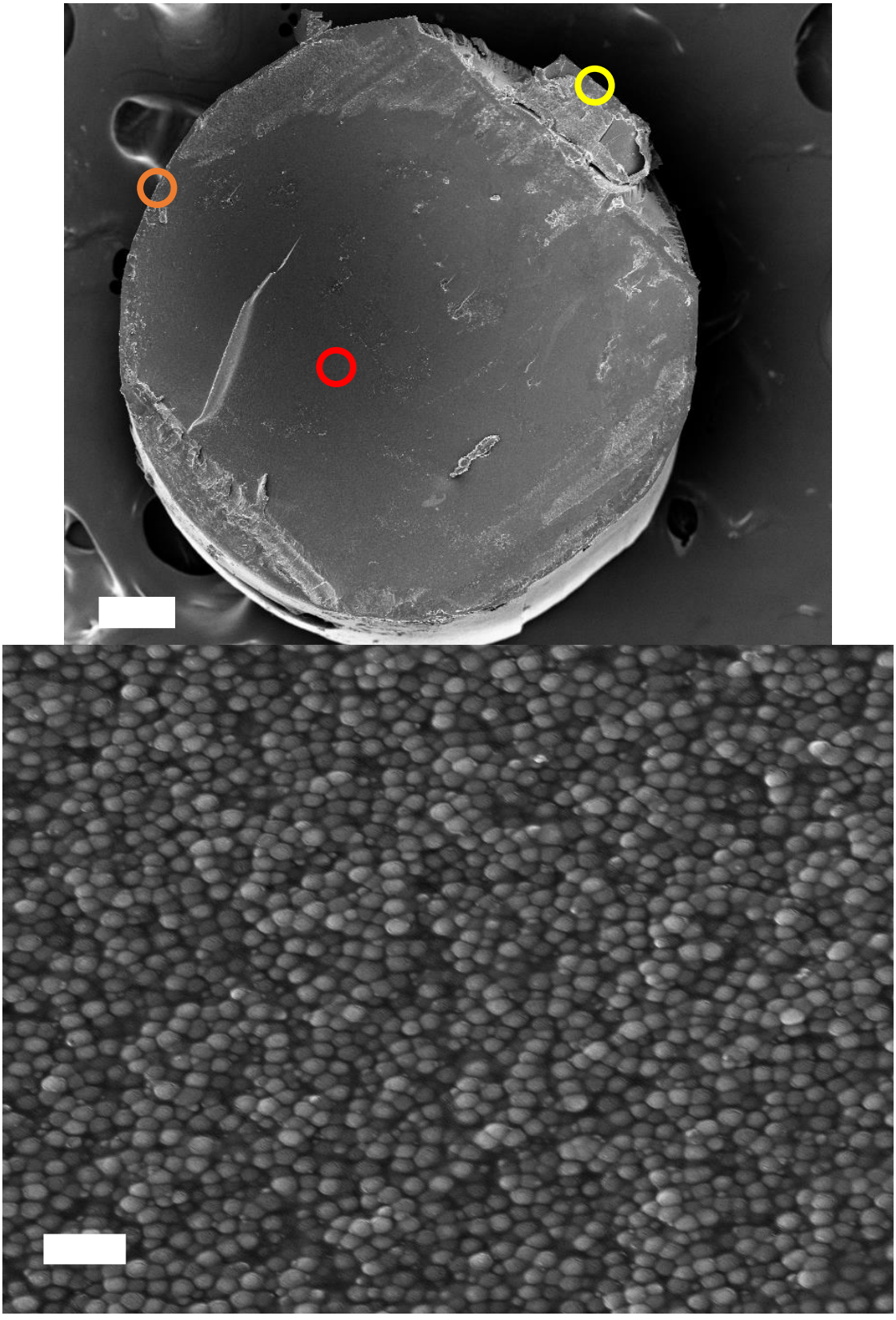

Figure C.12: 33.3v% R_{NP} = 40 nm images; Applied pressure of 60 psi.

Figure C.12 (cont.)

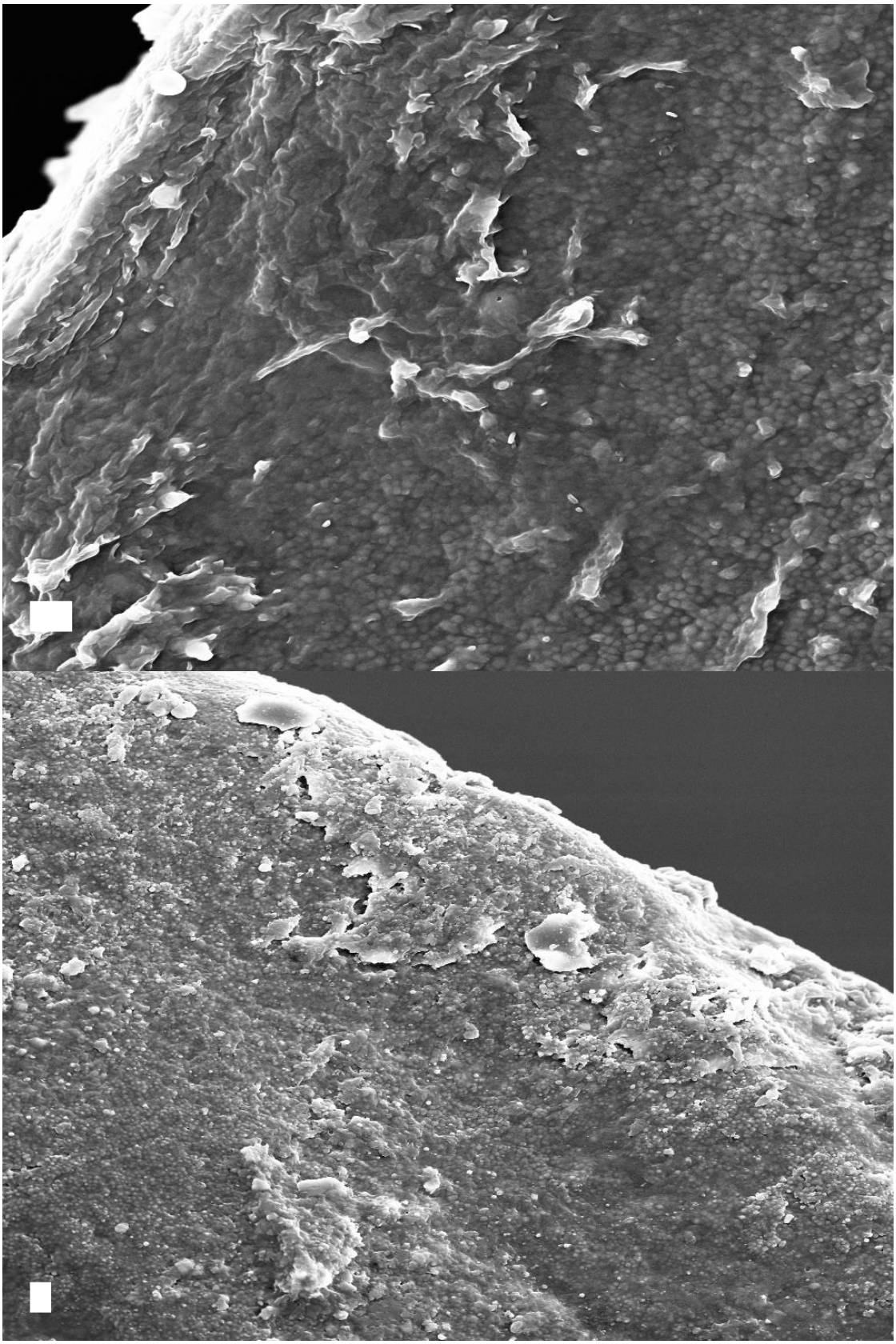

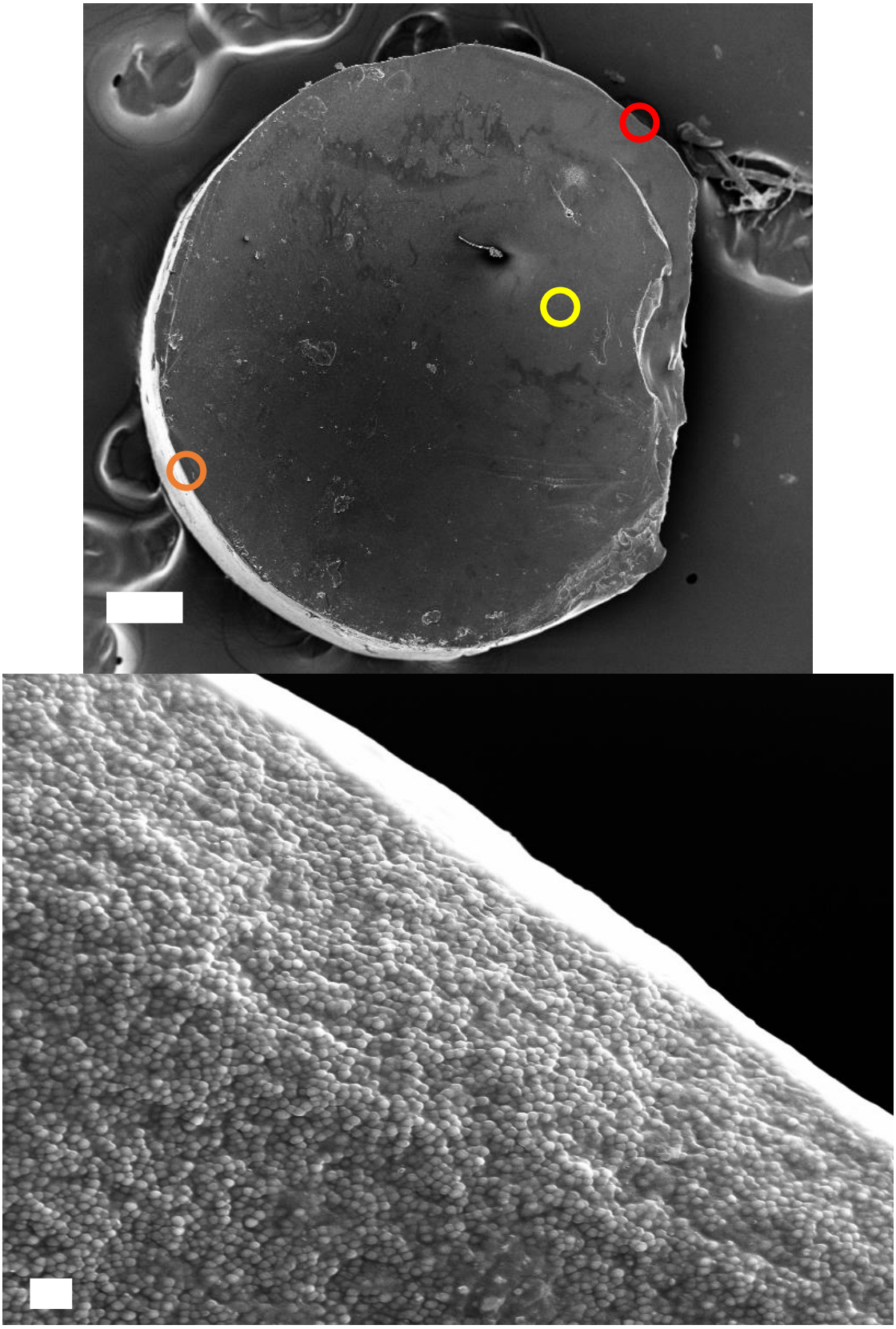

Figure C.13: 33.3v% R_{NP} = 40 nm images; Applied pressure of 80 psi.

Figure C.13 (cont.)

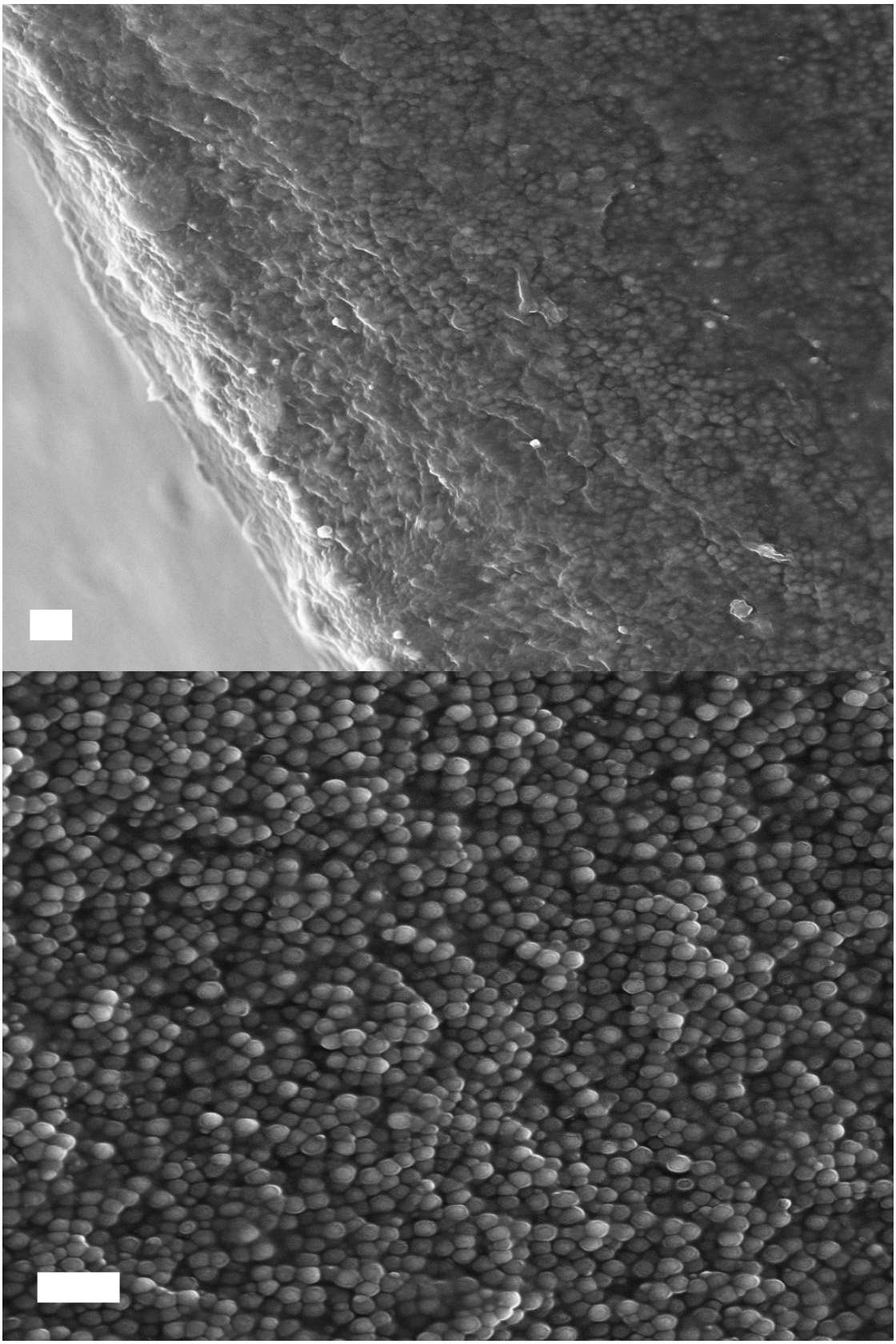

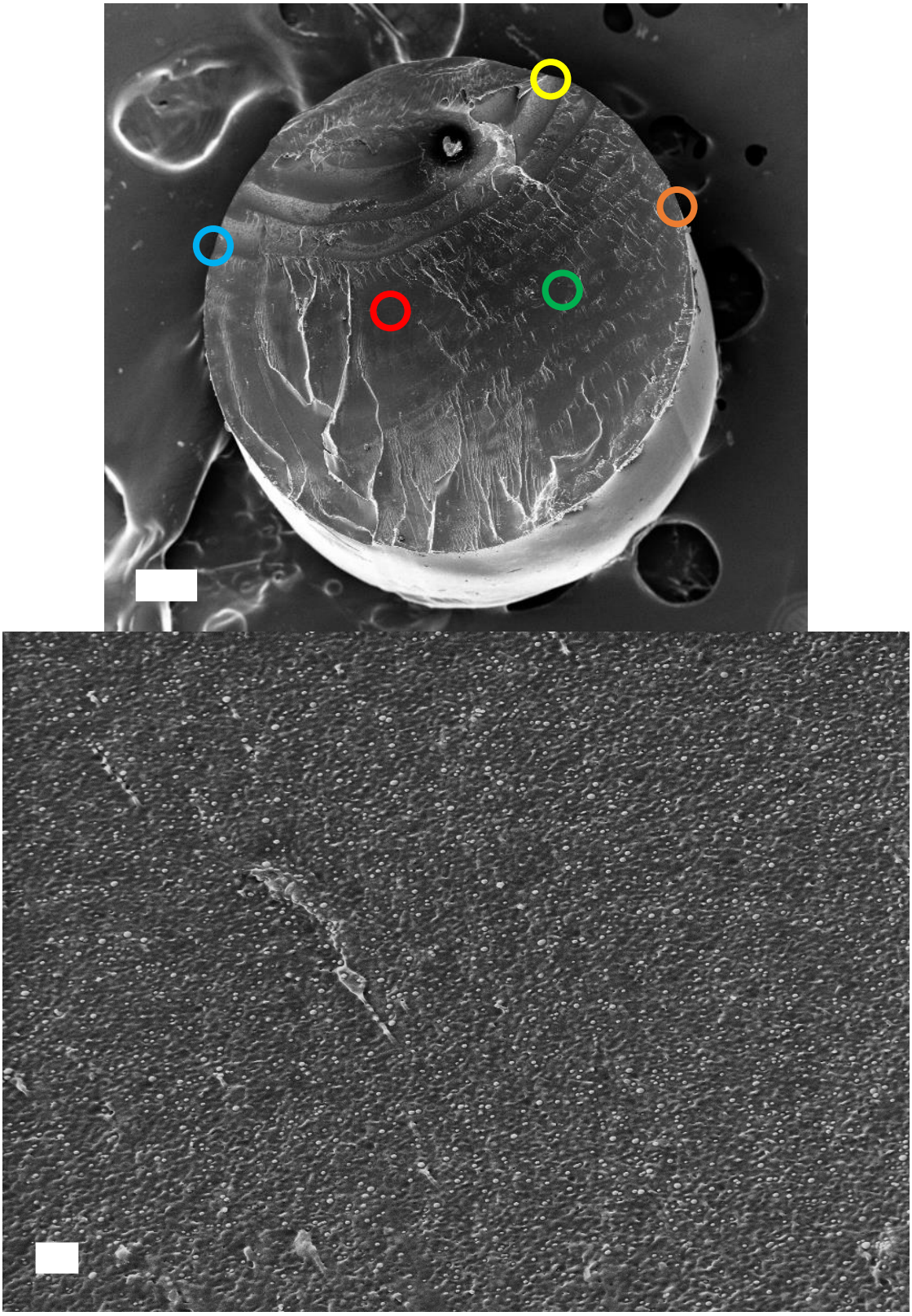

Figure C.14: 2.4v% R_{NP} = 23 nm images; Applied pressure of 5 psi.

Figure C.14 (cont.)

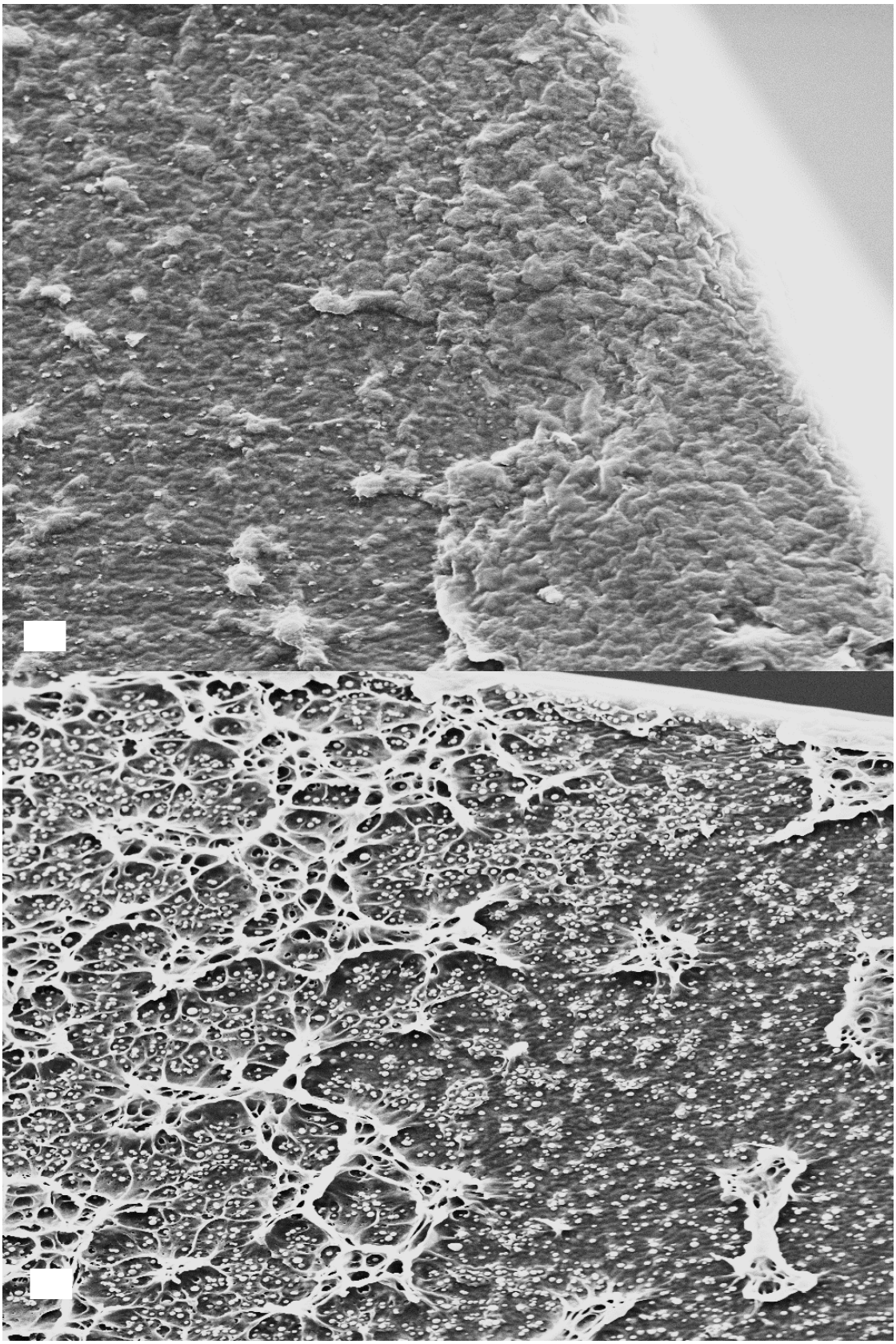

Figure C.14 (cont.)

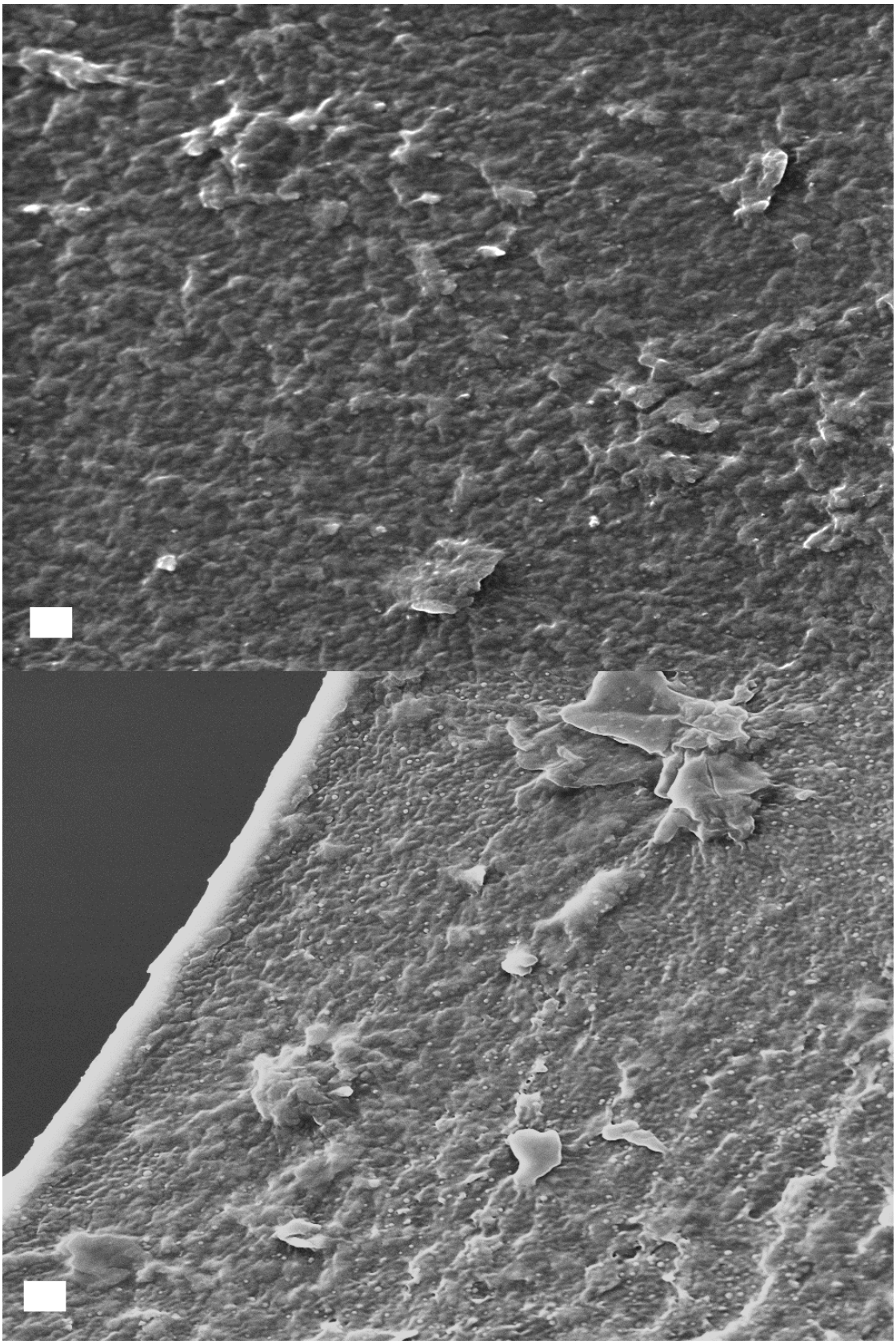

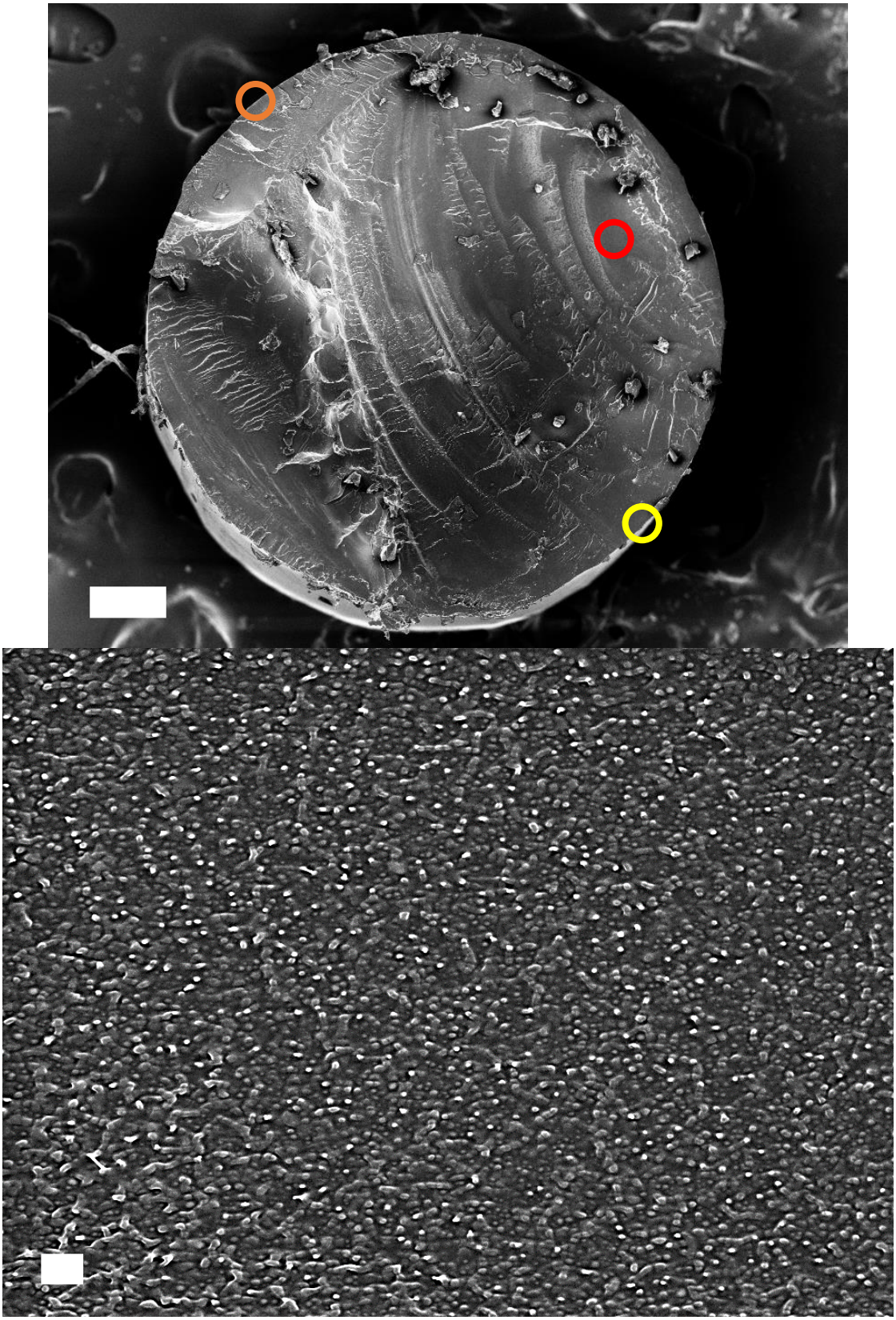

Figure C.15: 2.4v% R_{NP} = 23 nm images; Applied pressure of 10 psi.

Figure C.15 (cont.)

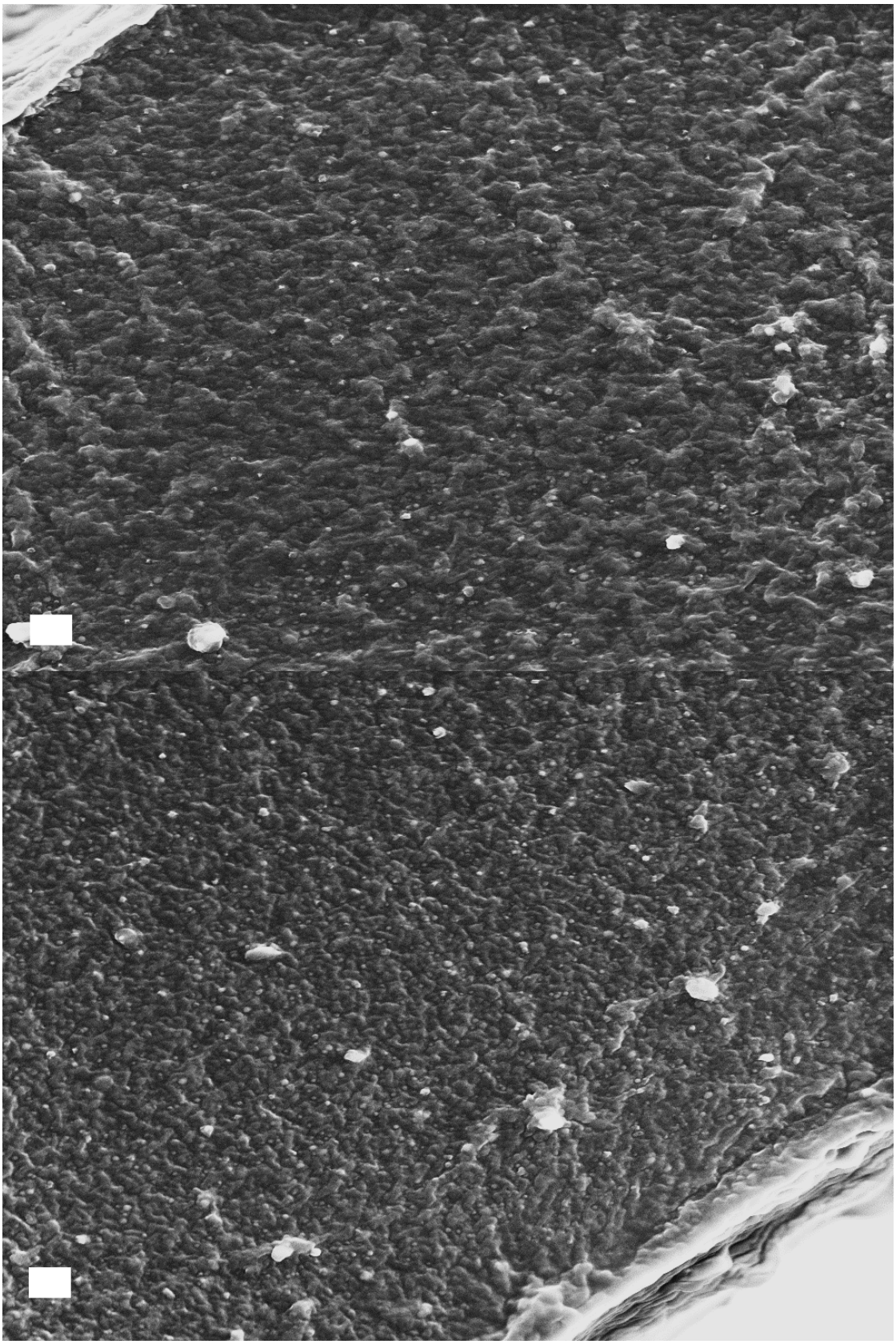

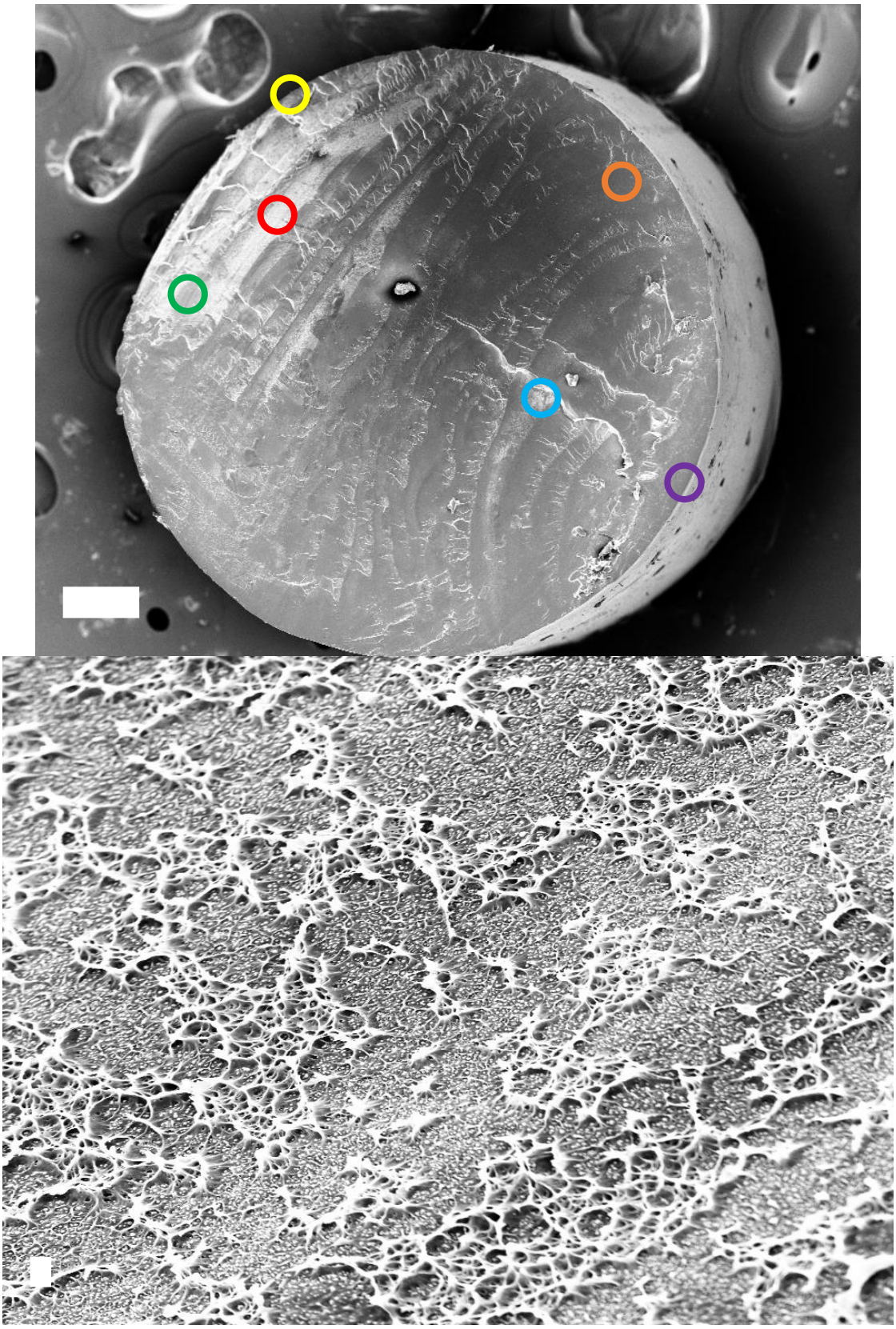

Figure C.16: 2.4v% R_{NP} = 23 nm images; Applied pressure of 20 psi.

Figure C.16 (cont.)

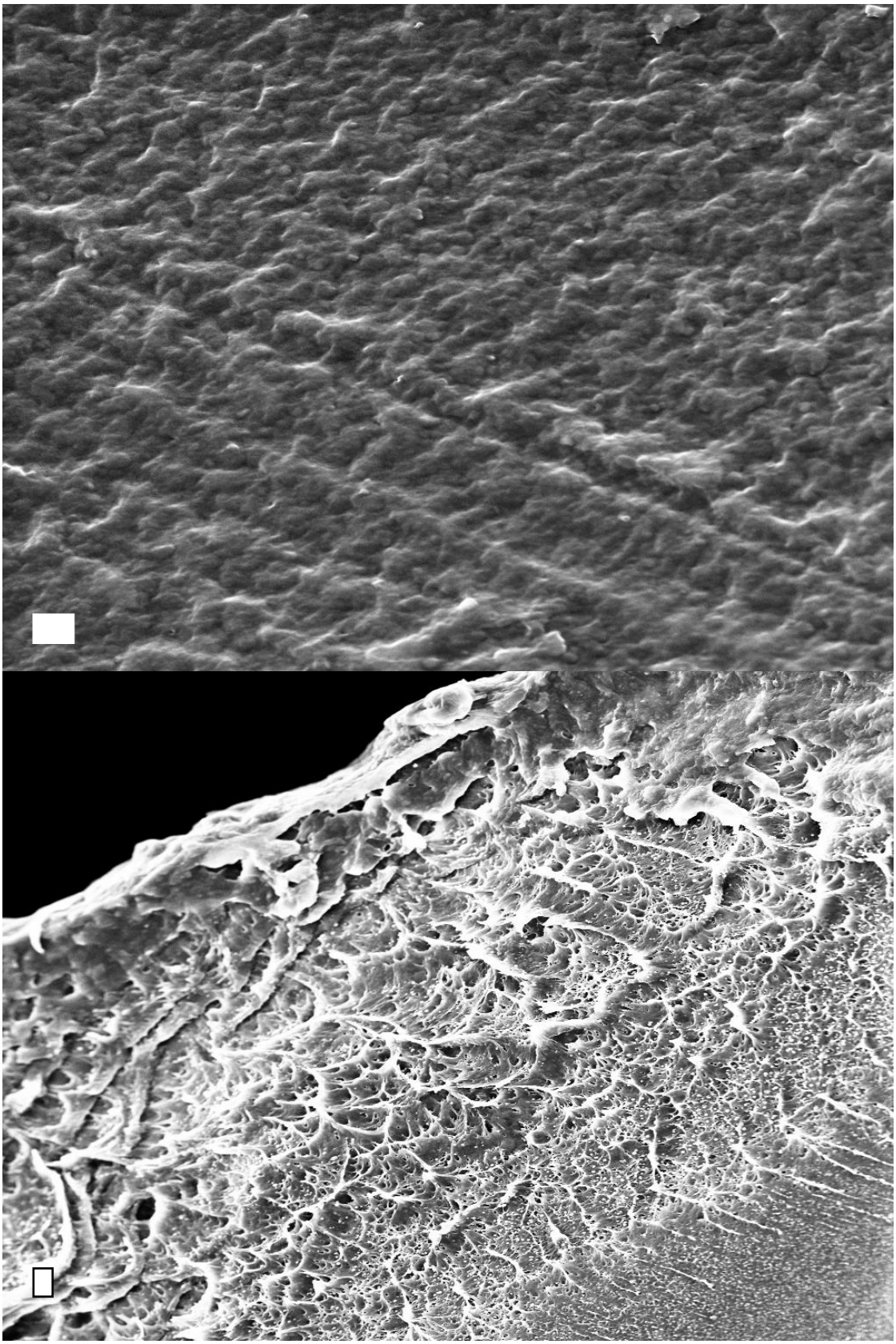

Figure C.16 (cont.)

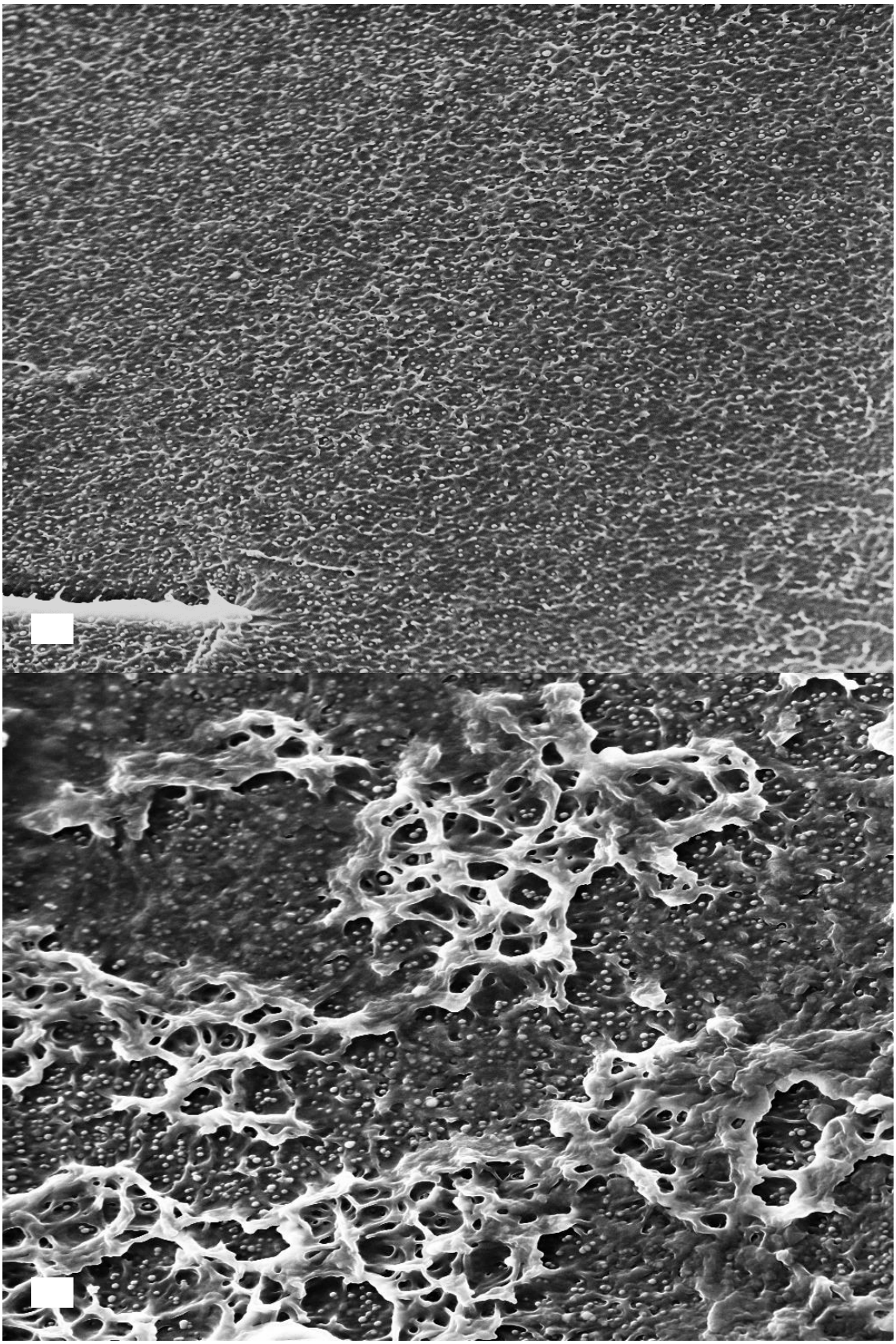

Figure C.16 (cont.)

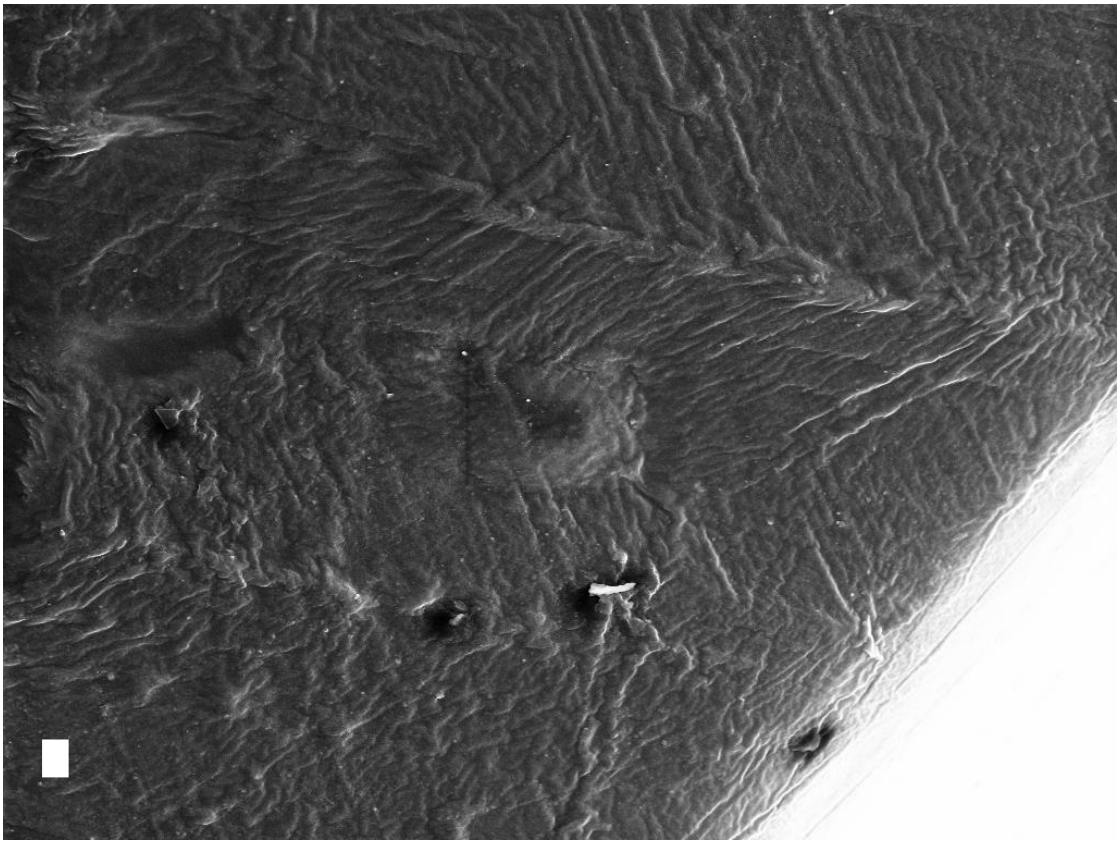

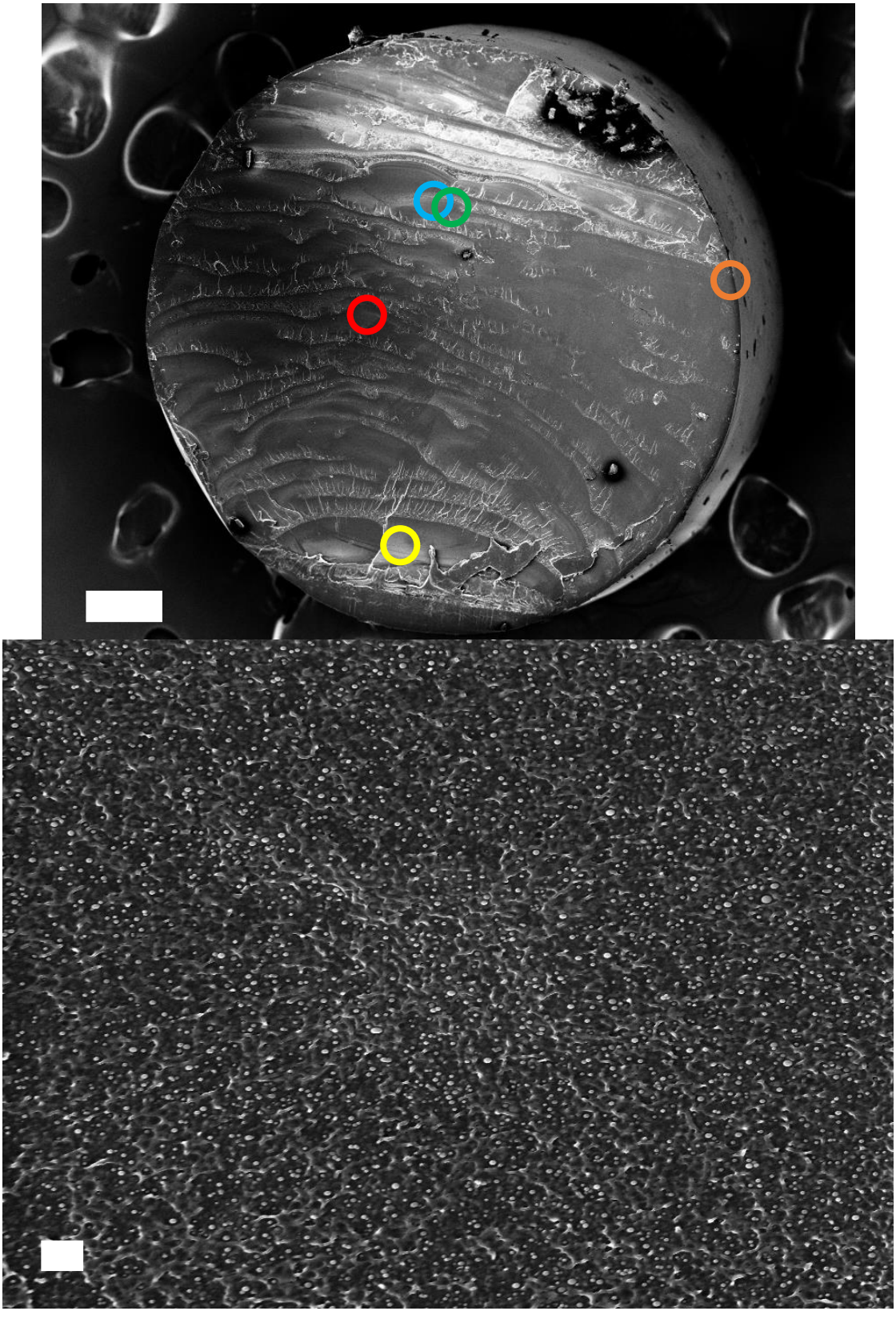

Figure C.17: 2.4v% R_{NP} = 23 nm images; Applied pressure of 40 psi.

Figure C.17 (cont.)

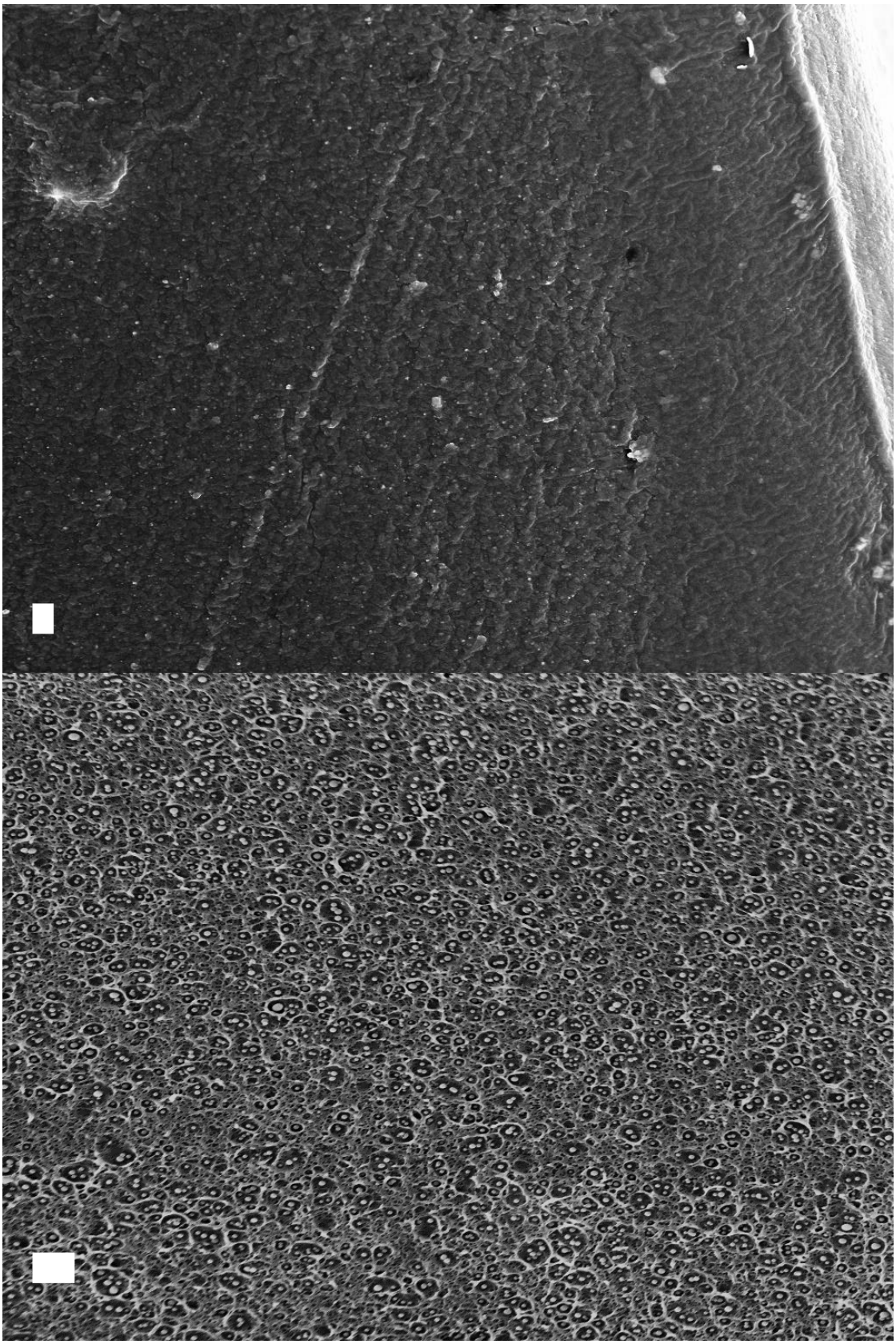

Figure C.17 (cont.)

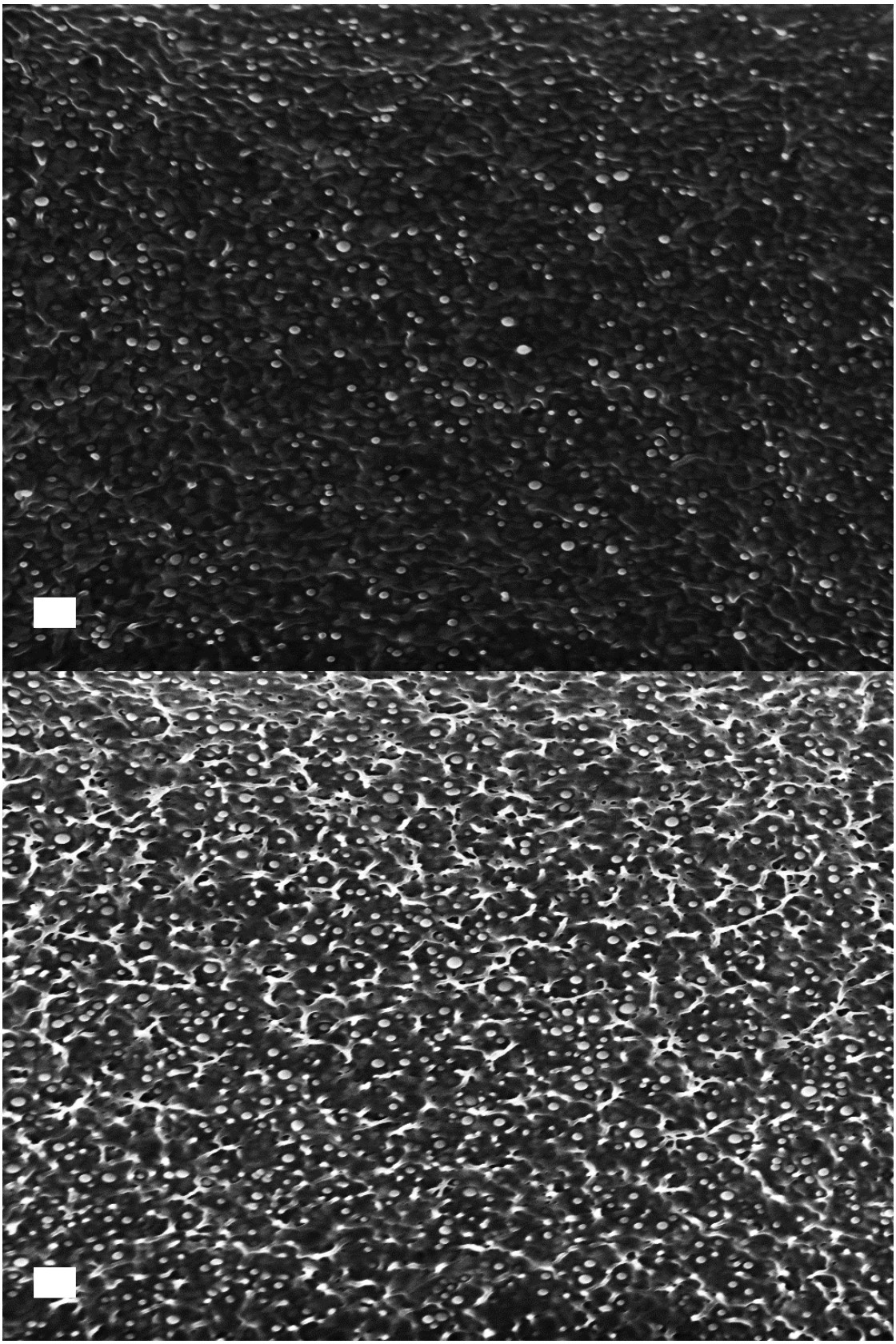

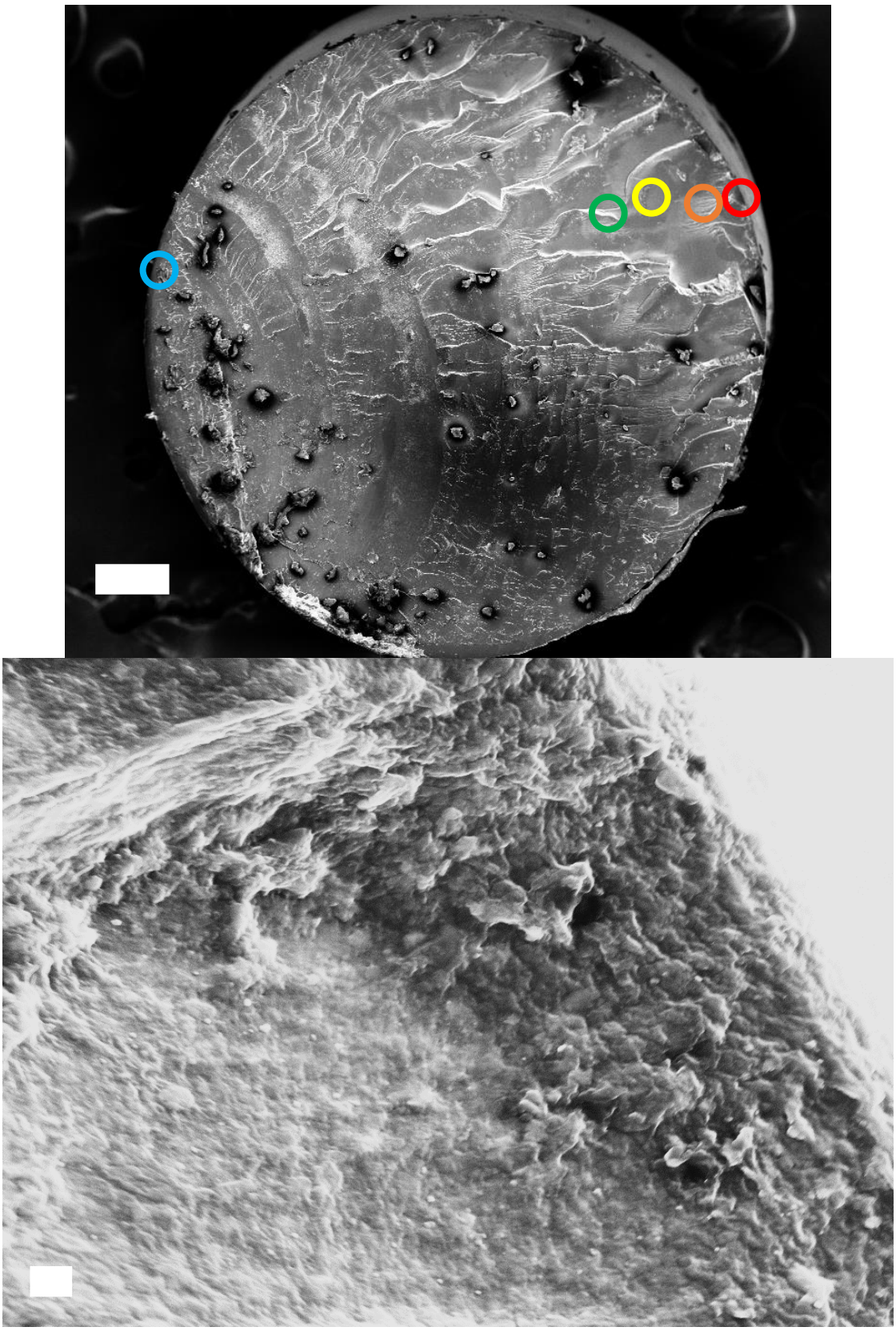

Figure C.18: 2.4v% R_{NP} = 23 nm images; Applied pressure of 80 psi.

Figure C.18 (cont.)

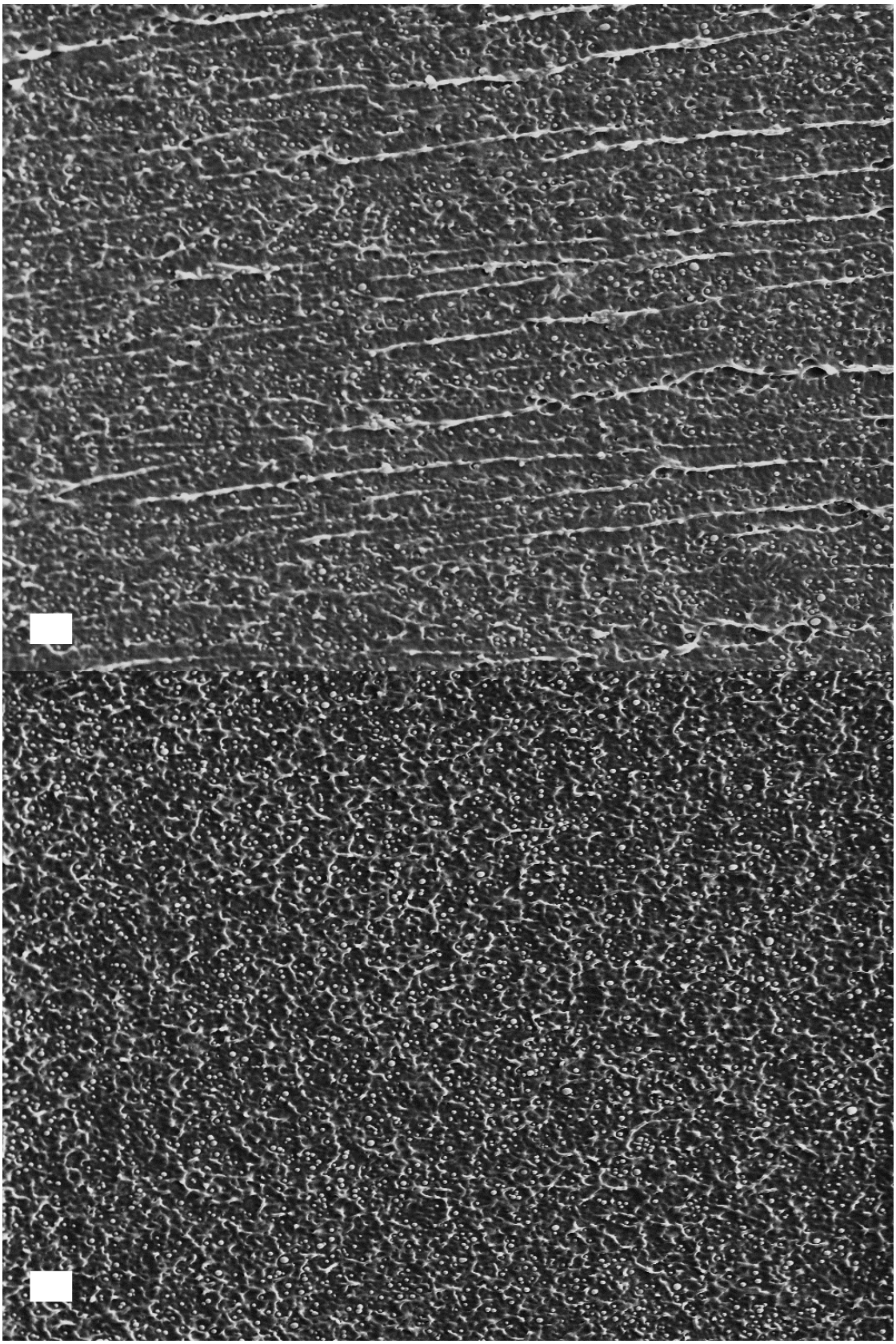

Figure C.18 (cont.)

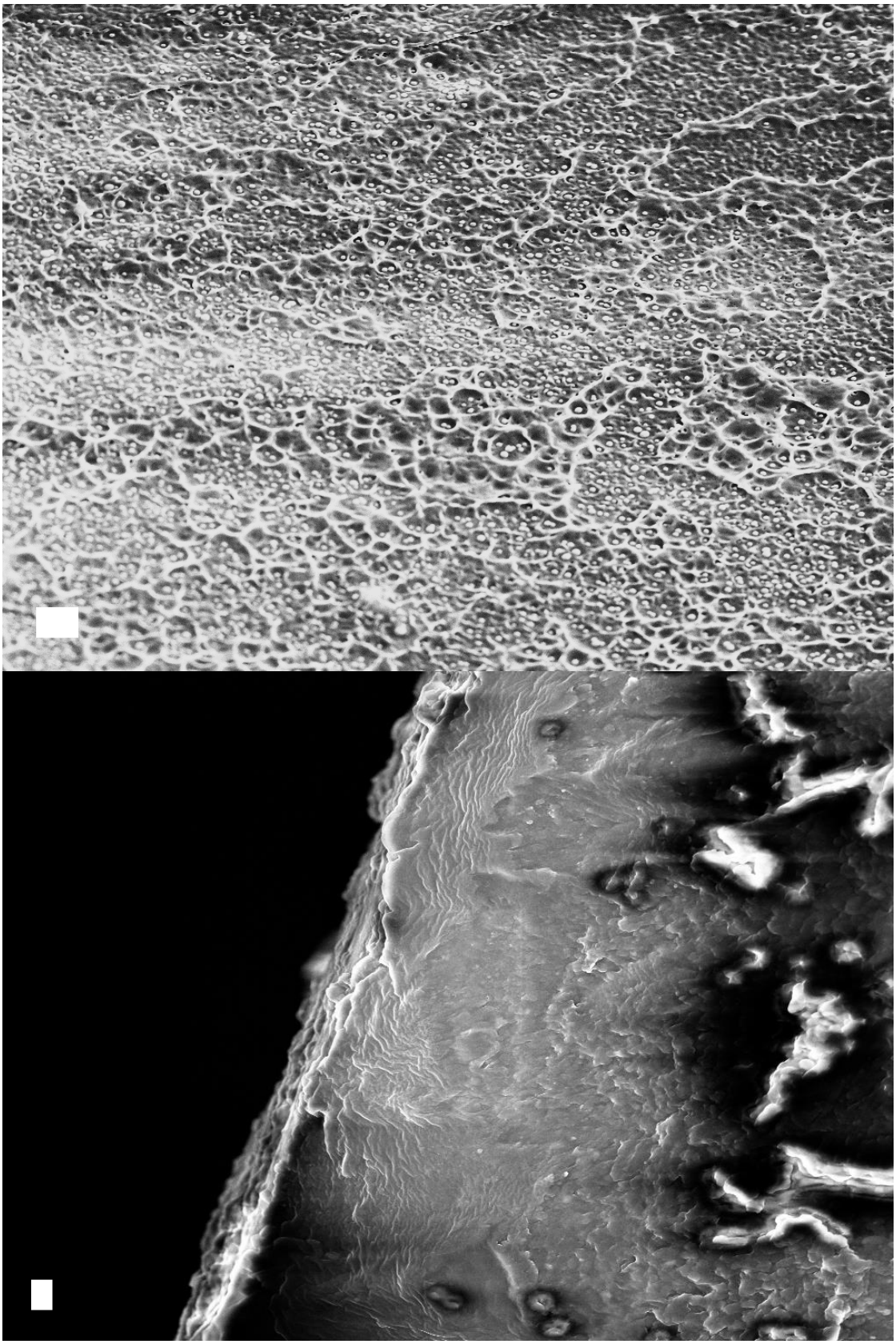

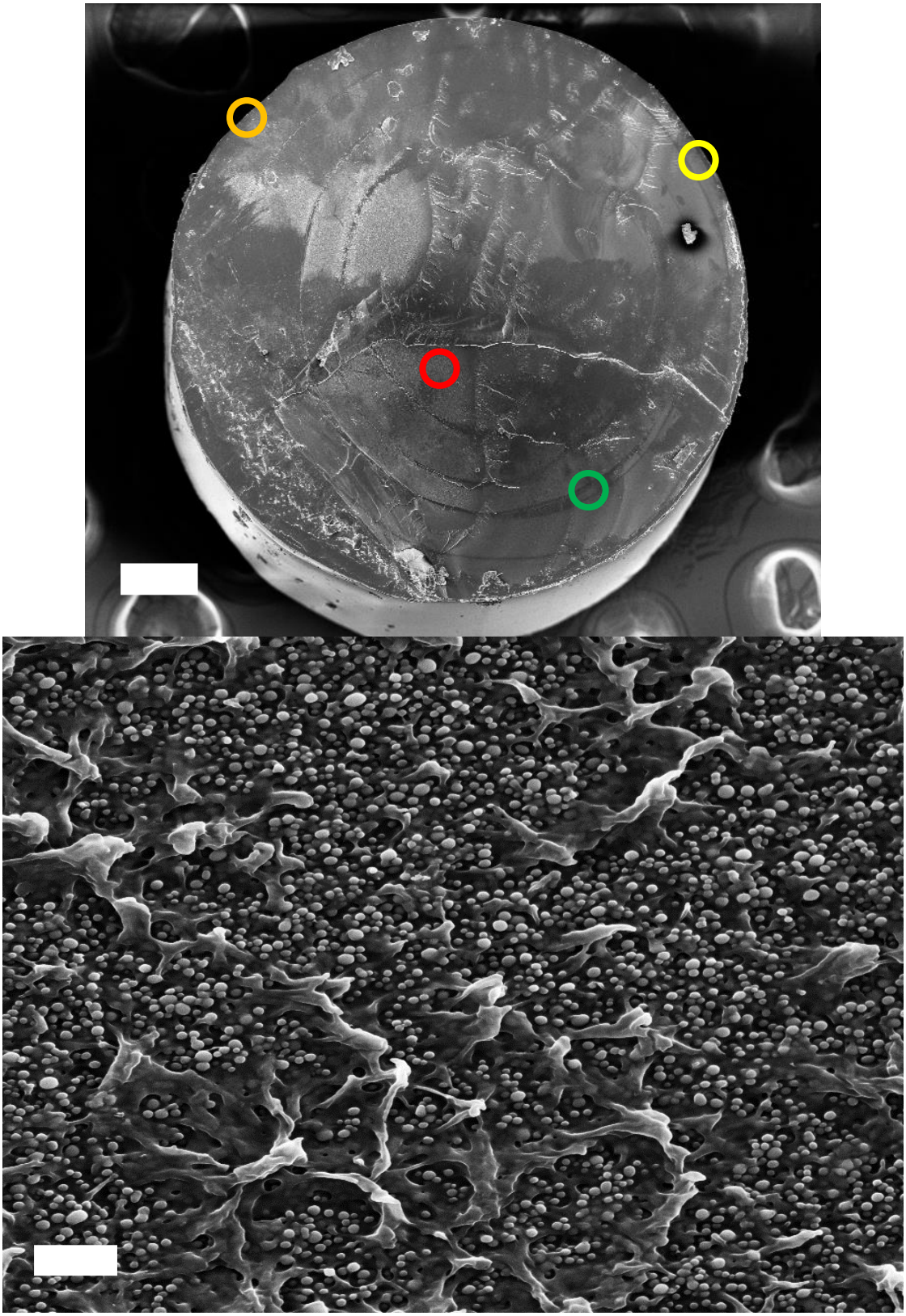

Figure C.19: 14.5v% R_{NP} = 23 nm images; Applied pressure of 5 psi.

Figure C.19 (cont.)

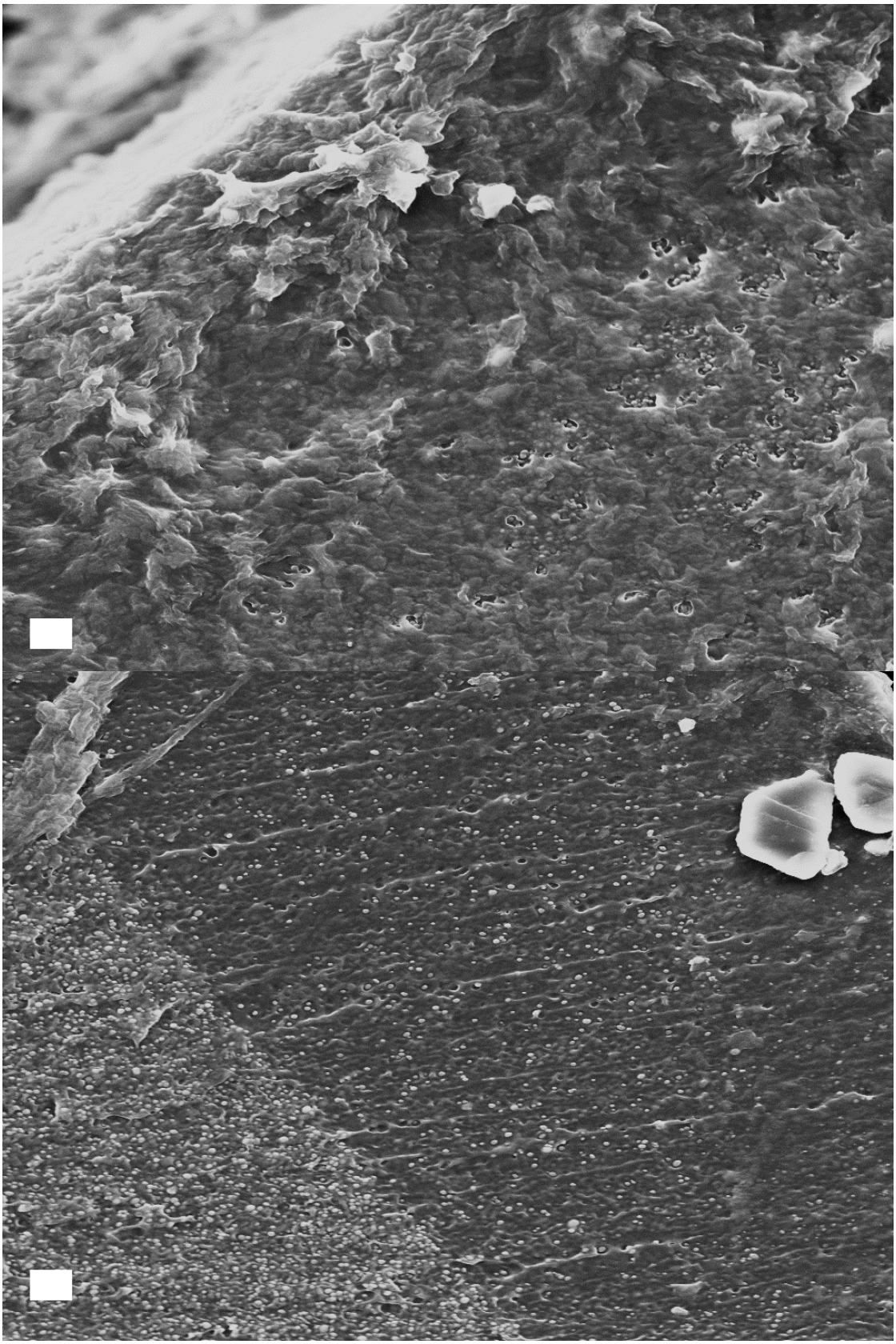

Figure C.19 (cont.)

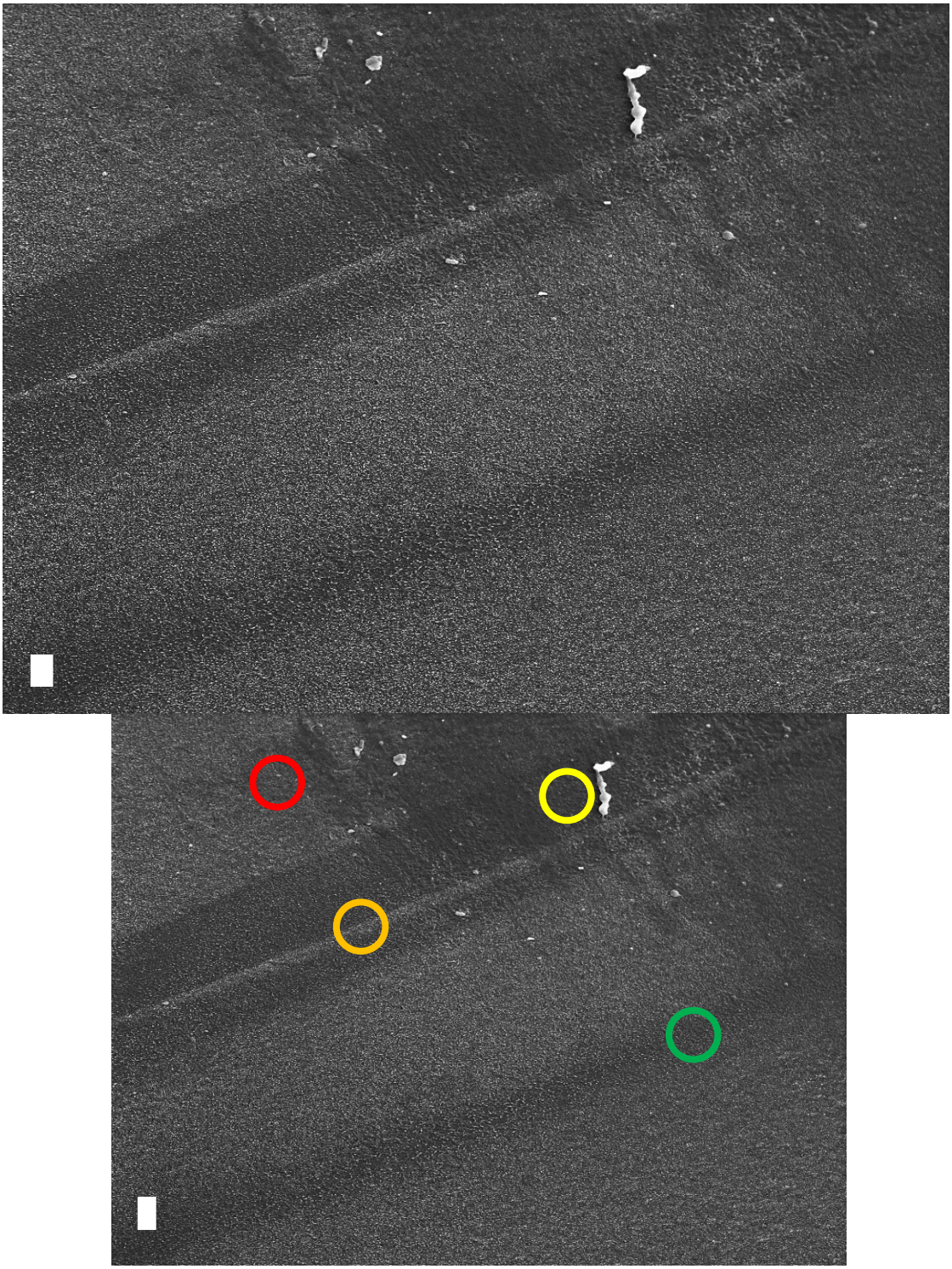

Note regarding the next sequence of this figure: While the top image on this page is the 'green' circle of the first image, all subsequent images for this sample are higher magnifications of regions of this image and the sequence of colored circles has been restarted on a smaller copy of the same image for clarification purposes. The scale bars are still 500 nm.

Figure C.19 (cont.)

Figure C.19 (cont.)

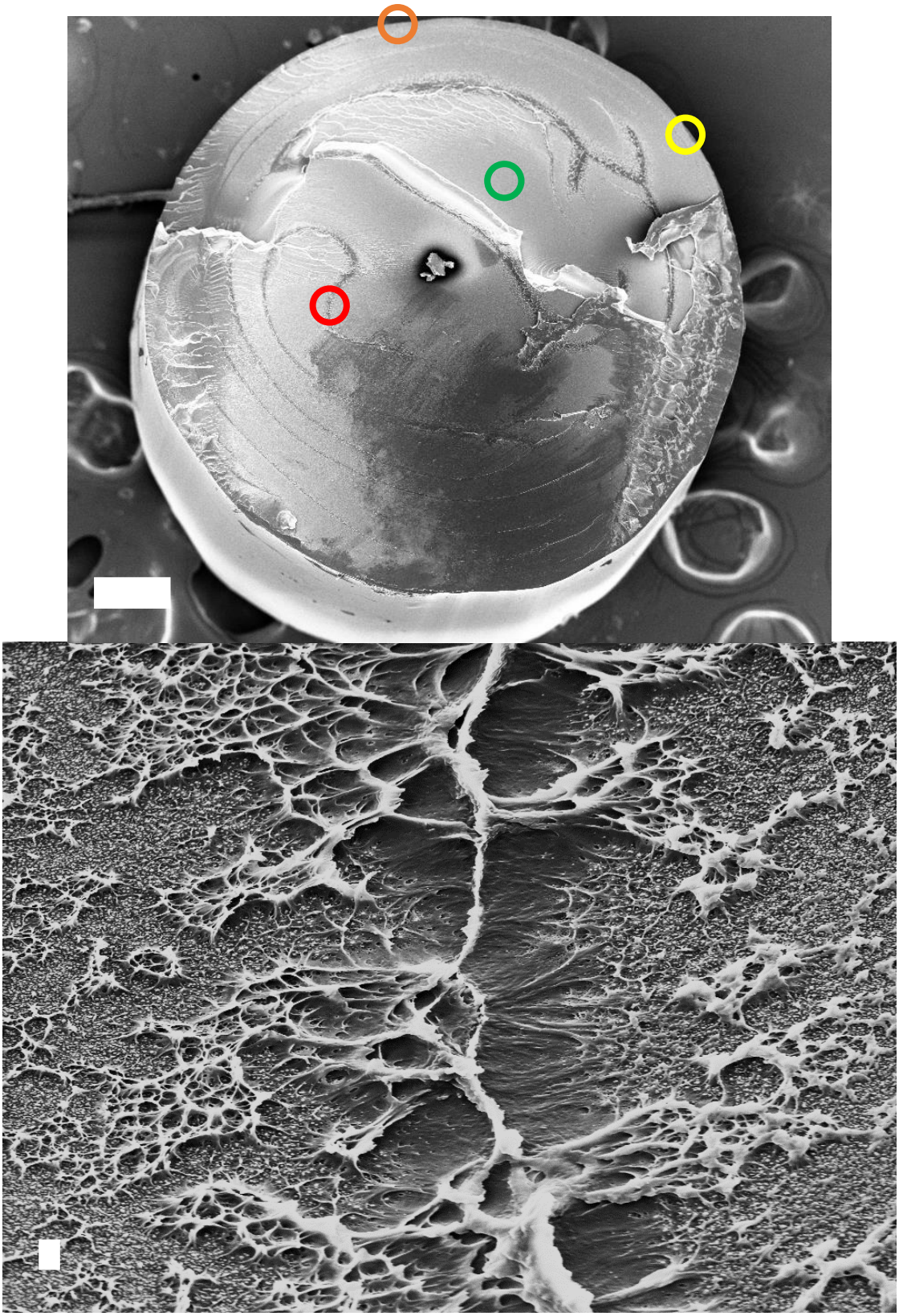

Figure C.20: 14.5v% R_{NP} = 23 nm images; Applied pressure of 10 psi.

Figure C.20 (cont.)

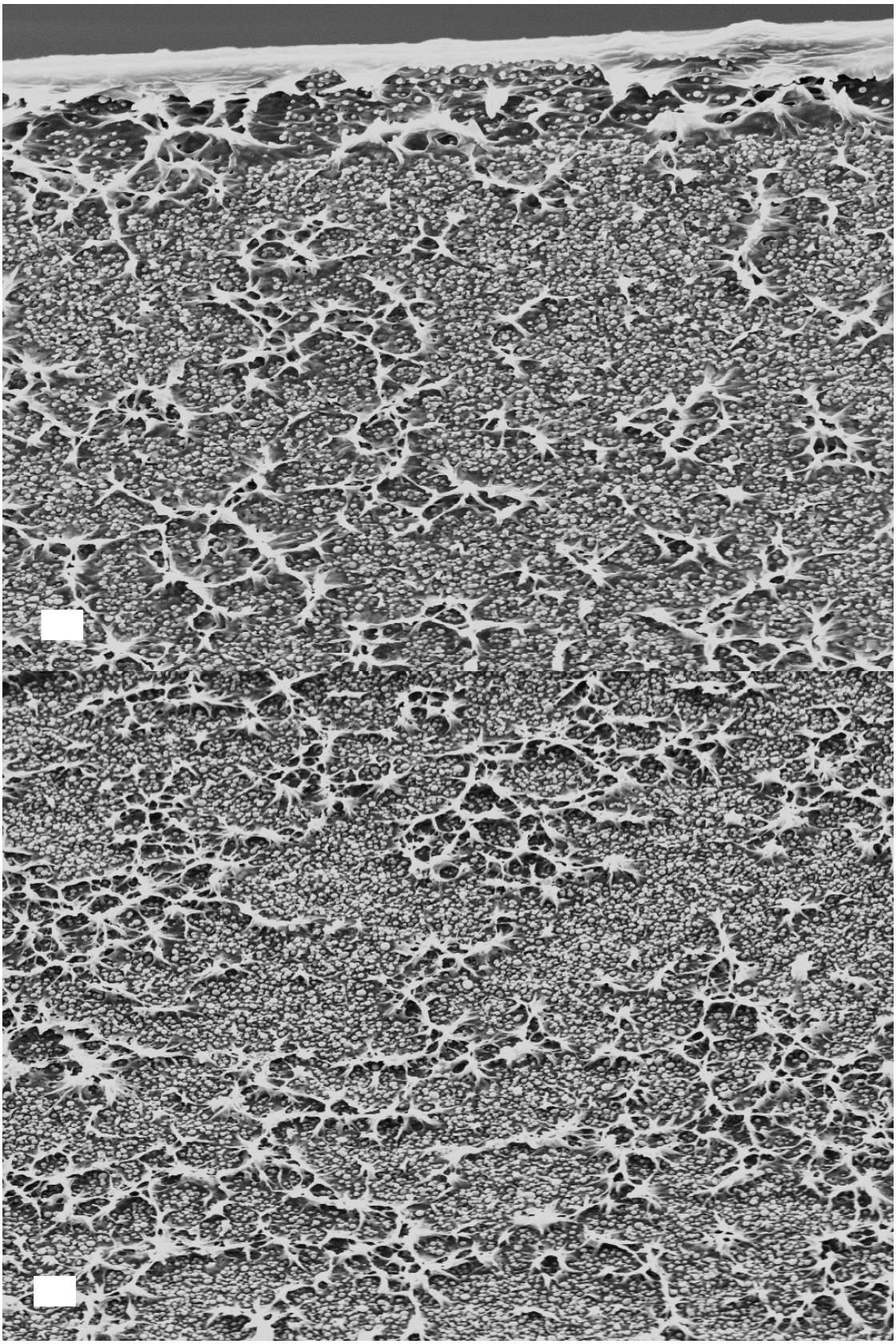

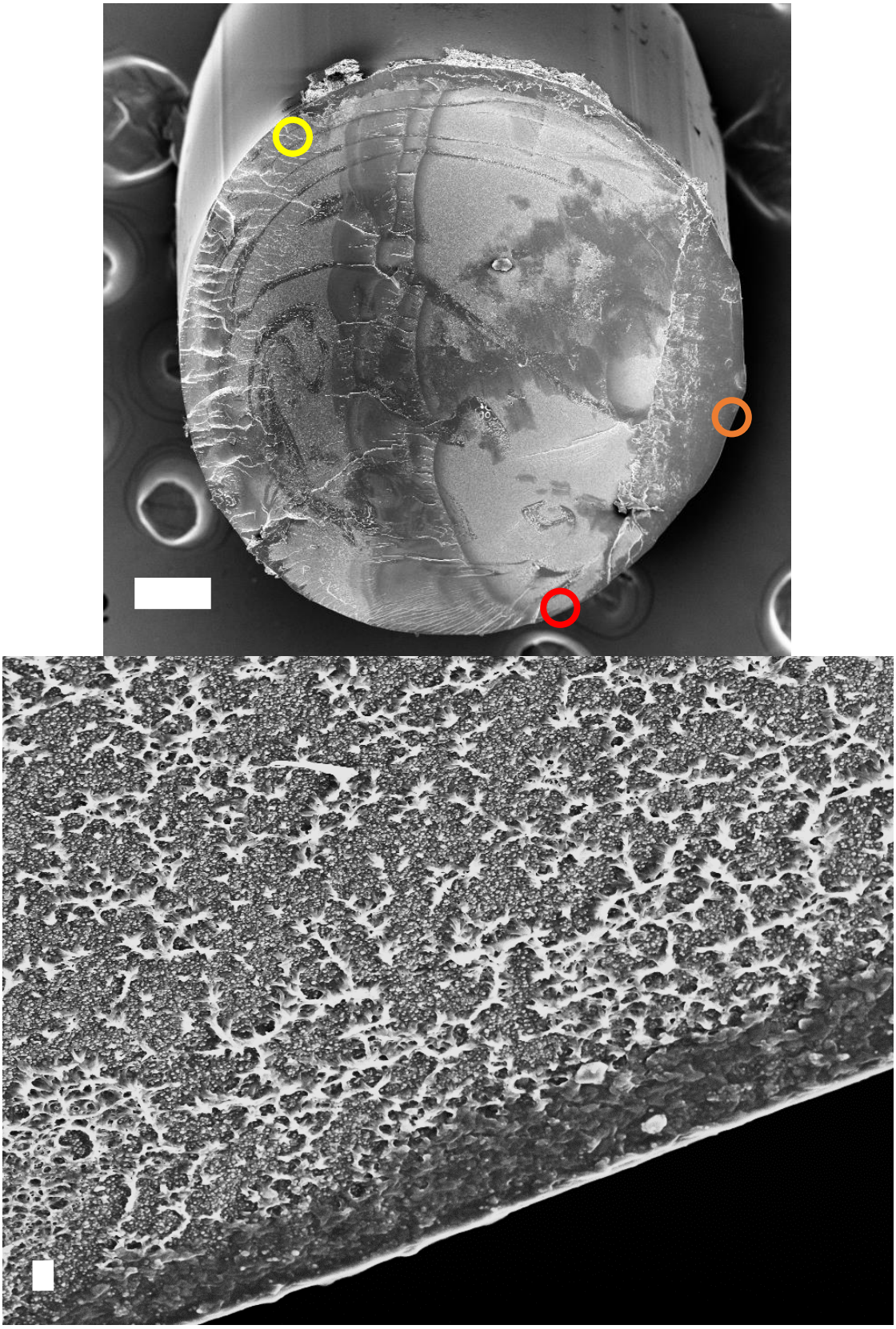

Figure C.21: 14.5v% R_{NP} = 23 nm images; Applied pressure of 20 psi.

Figure C.21 (cont.)

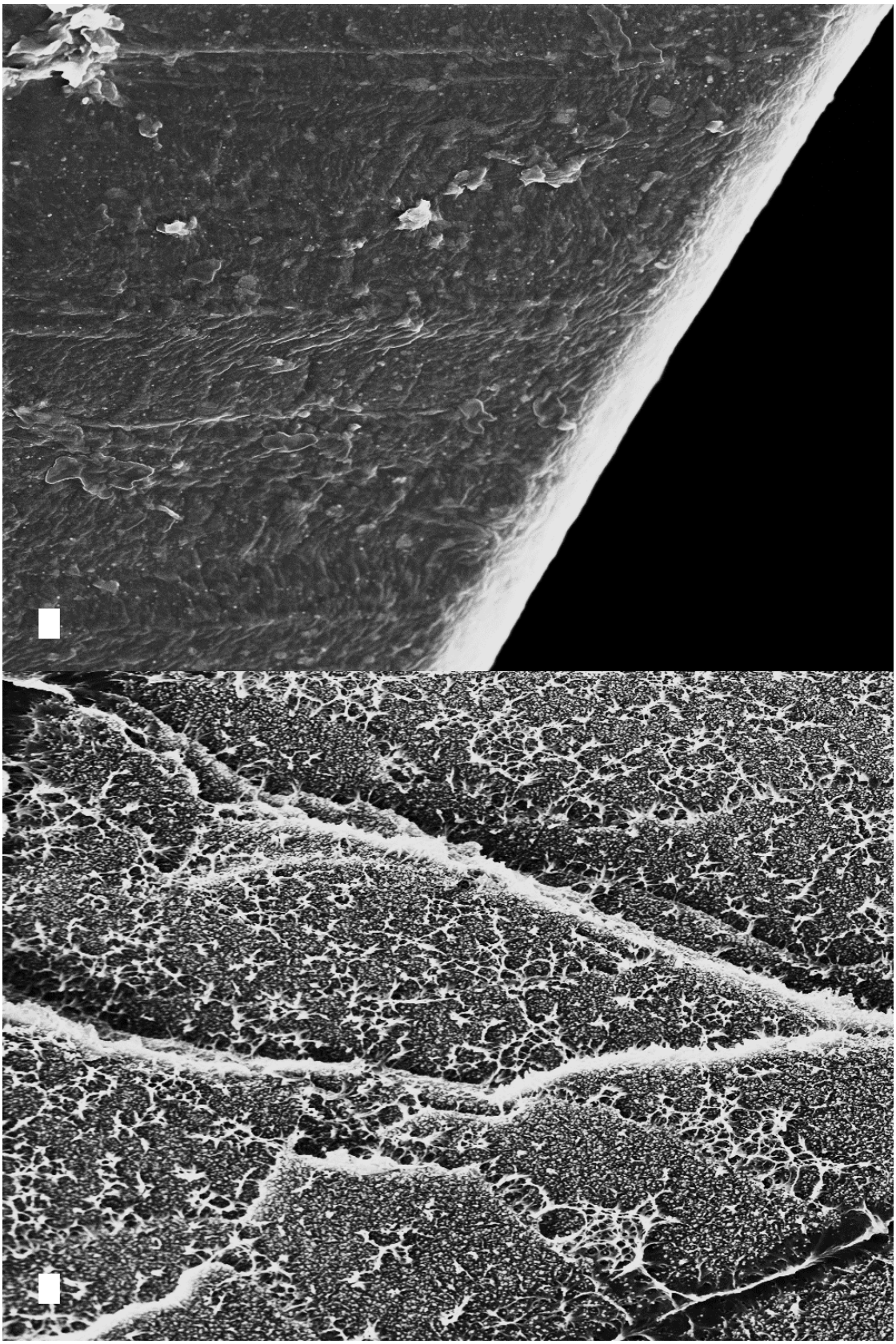

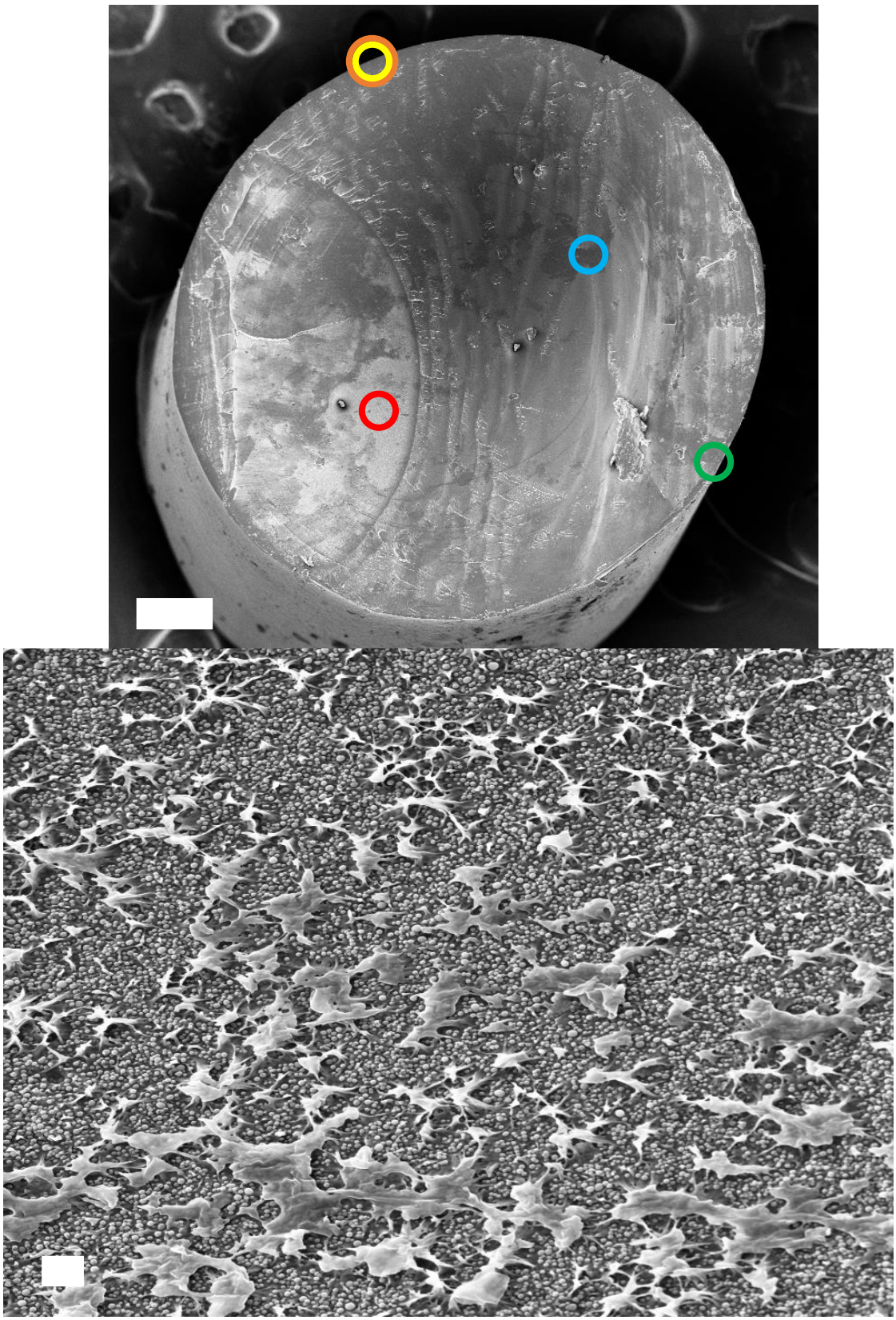

Figure C.22: 14.5v% R_{NP} = 23 nm images; Applied pressure of 60 psi.

Figure C.22 (cont.)

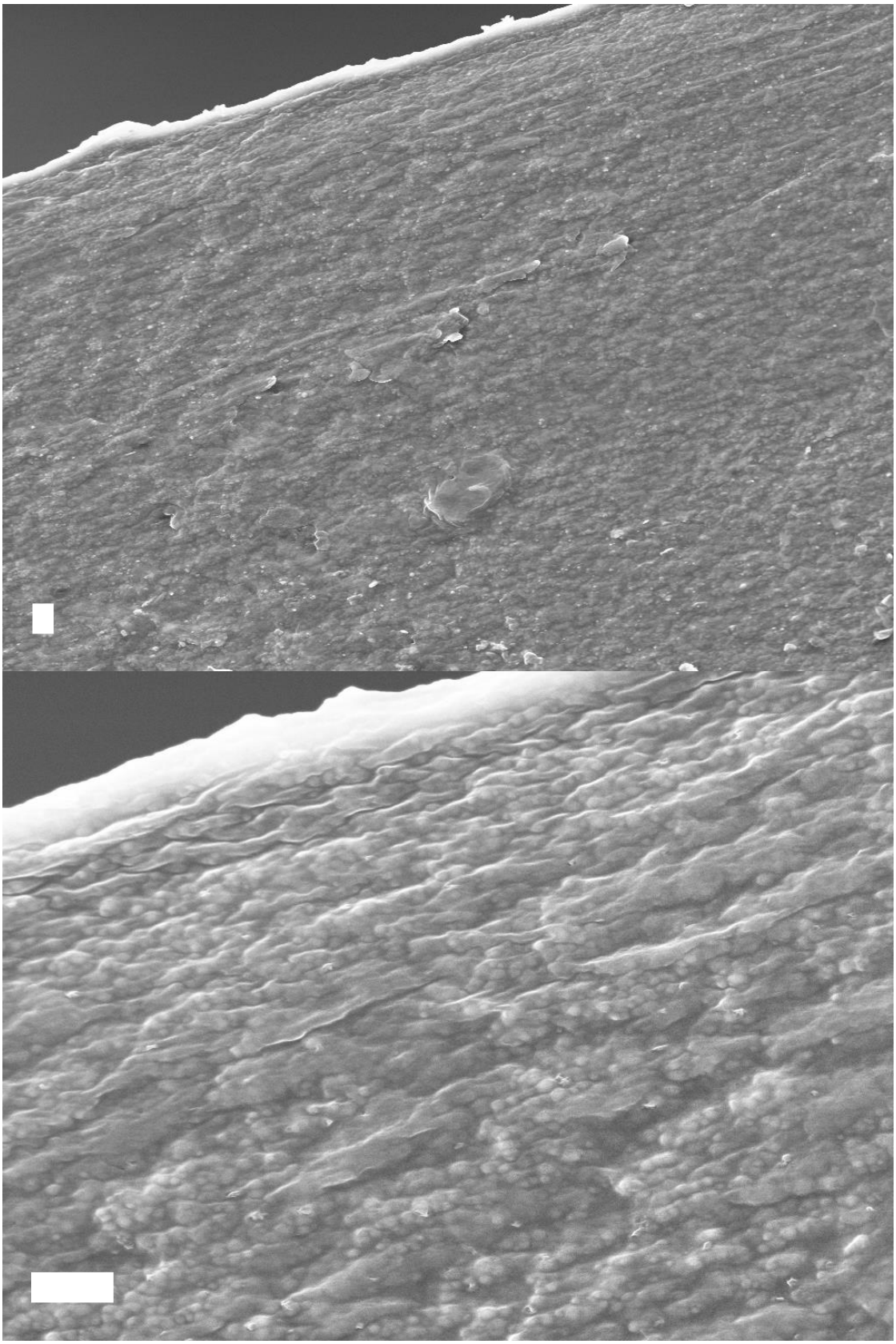

Figure C.22 (cont.)

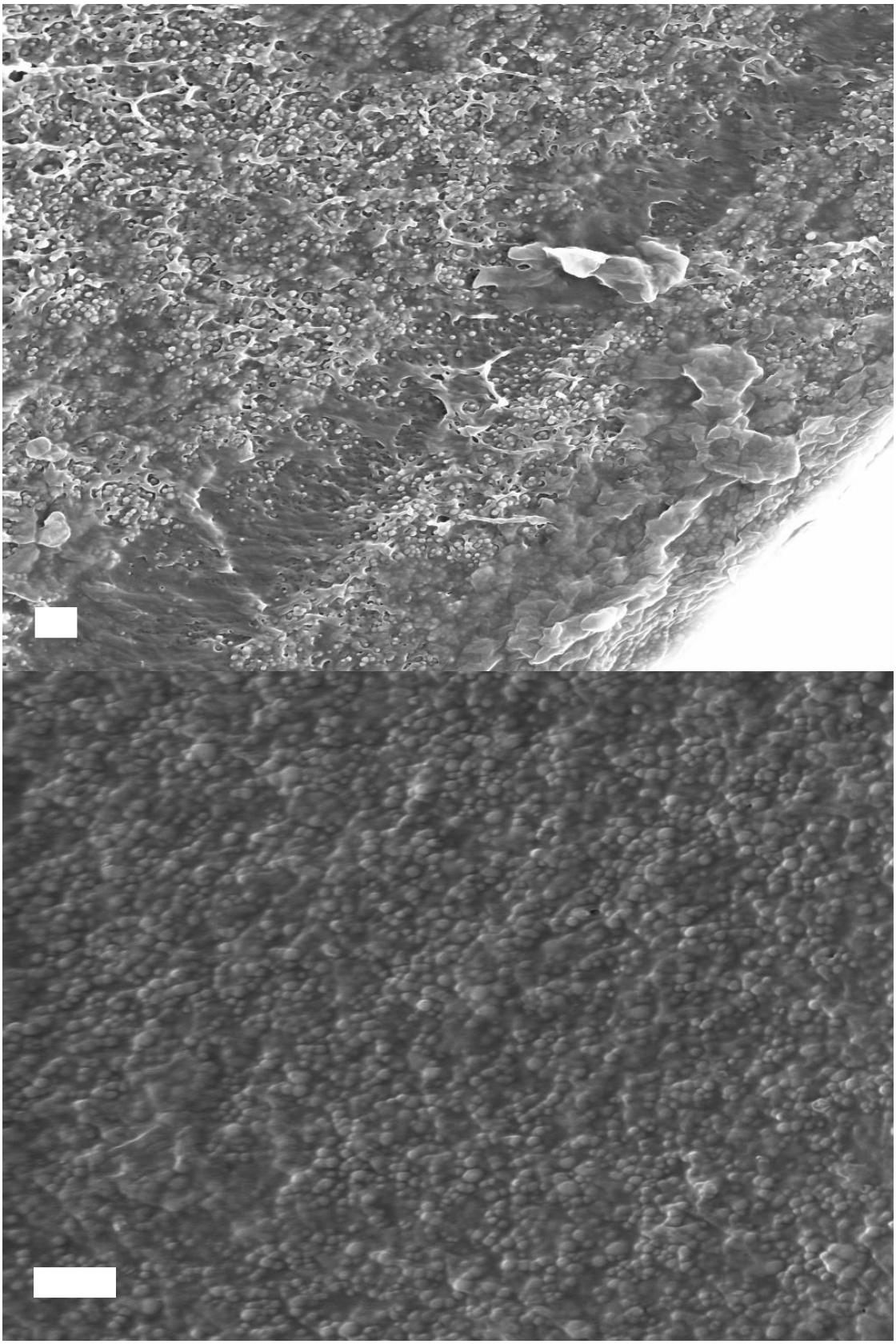

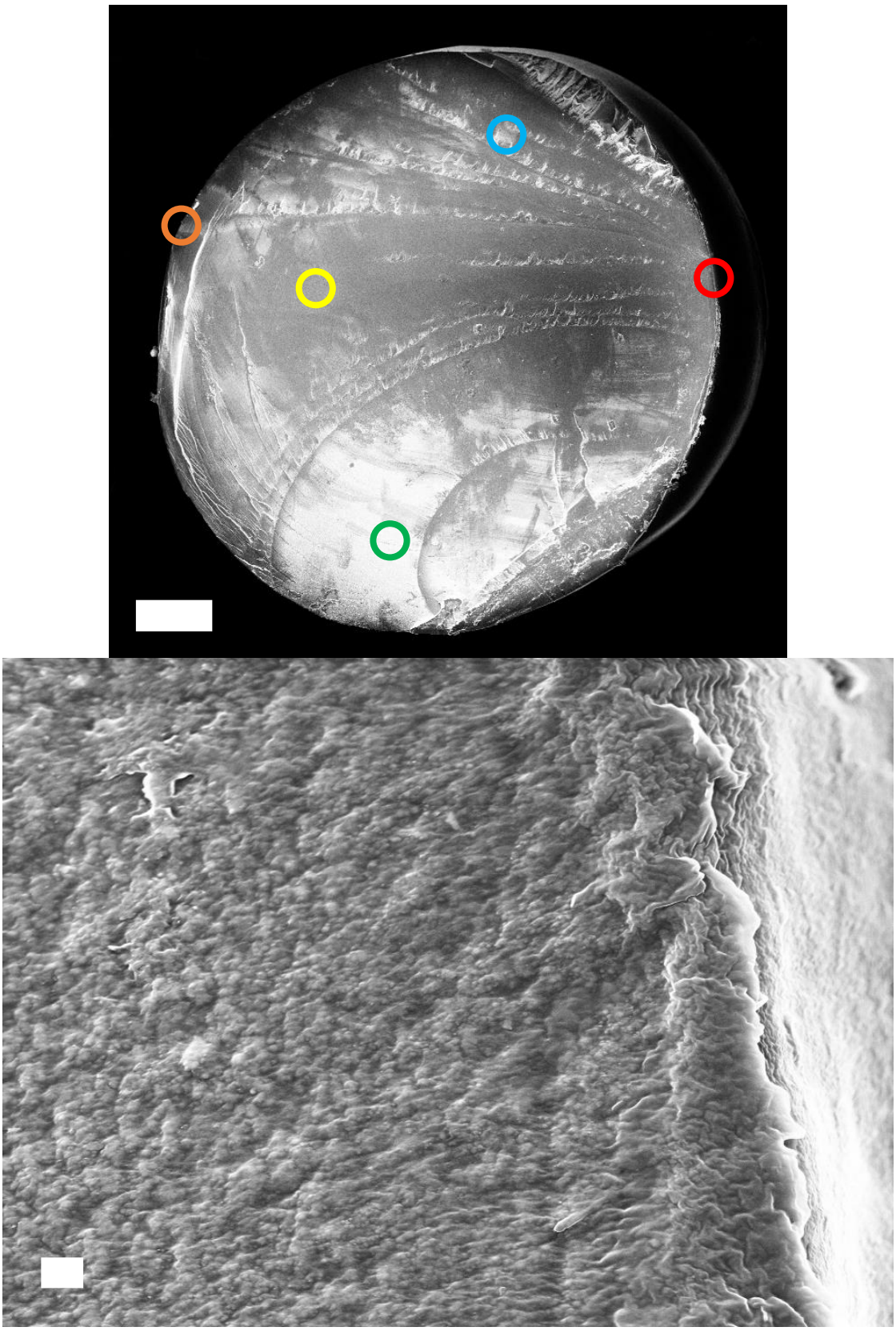

Figure C.23: 14.5v% R_{NP} = 23 nm images; Applied pressure of 80 psi.

Figure C.23 (cont.)

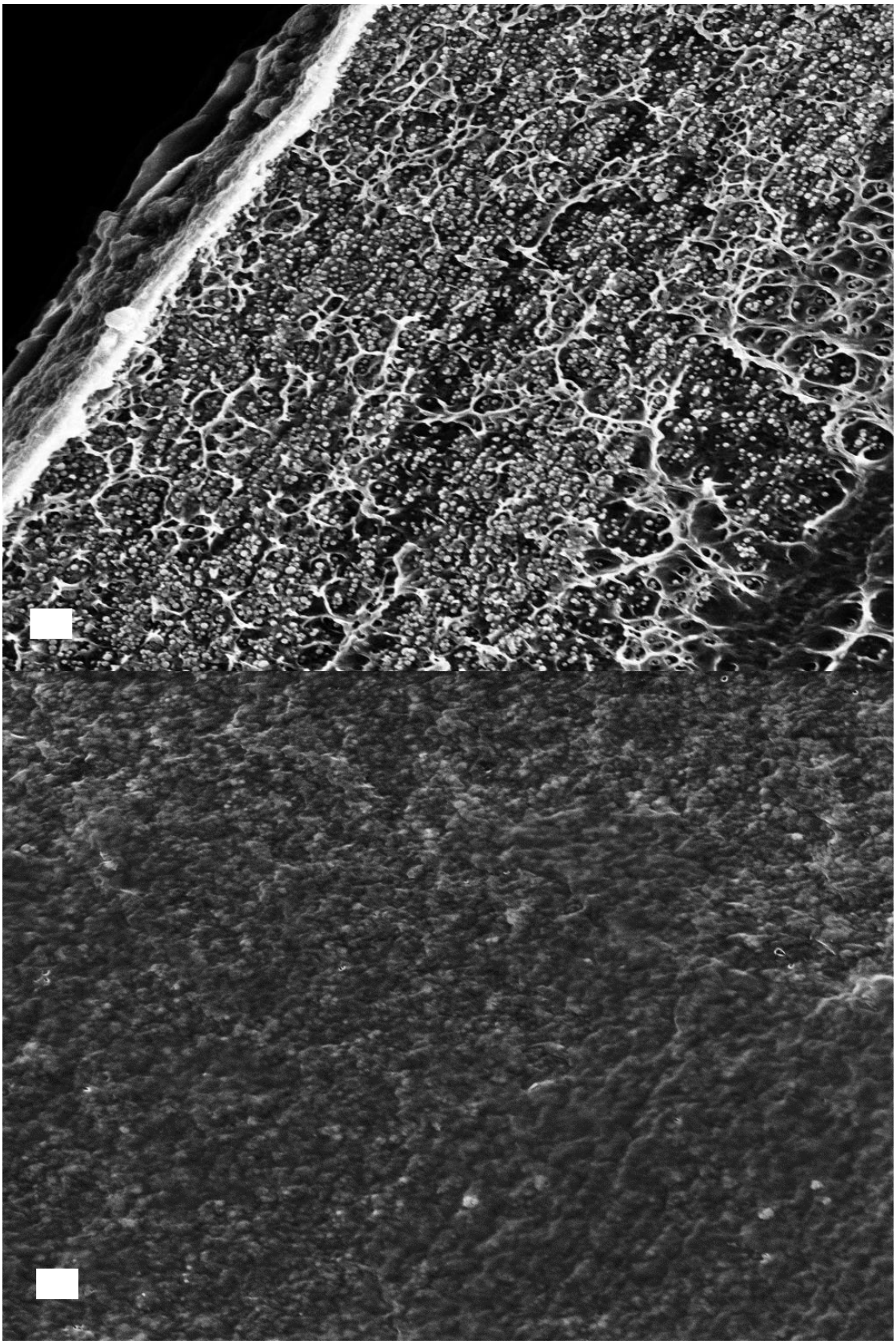

Figure C.23 (cont.)

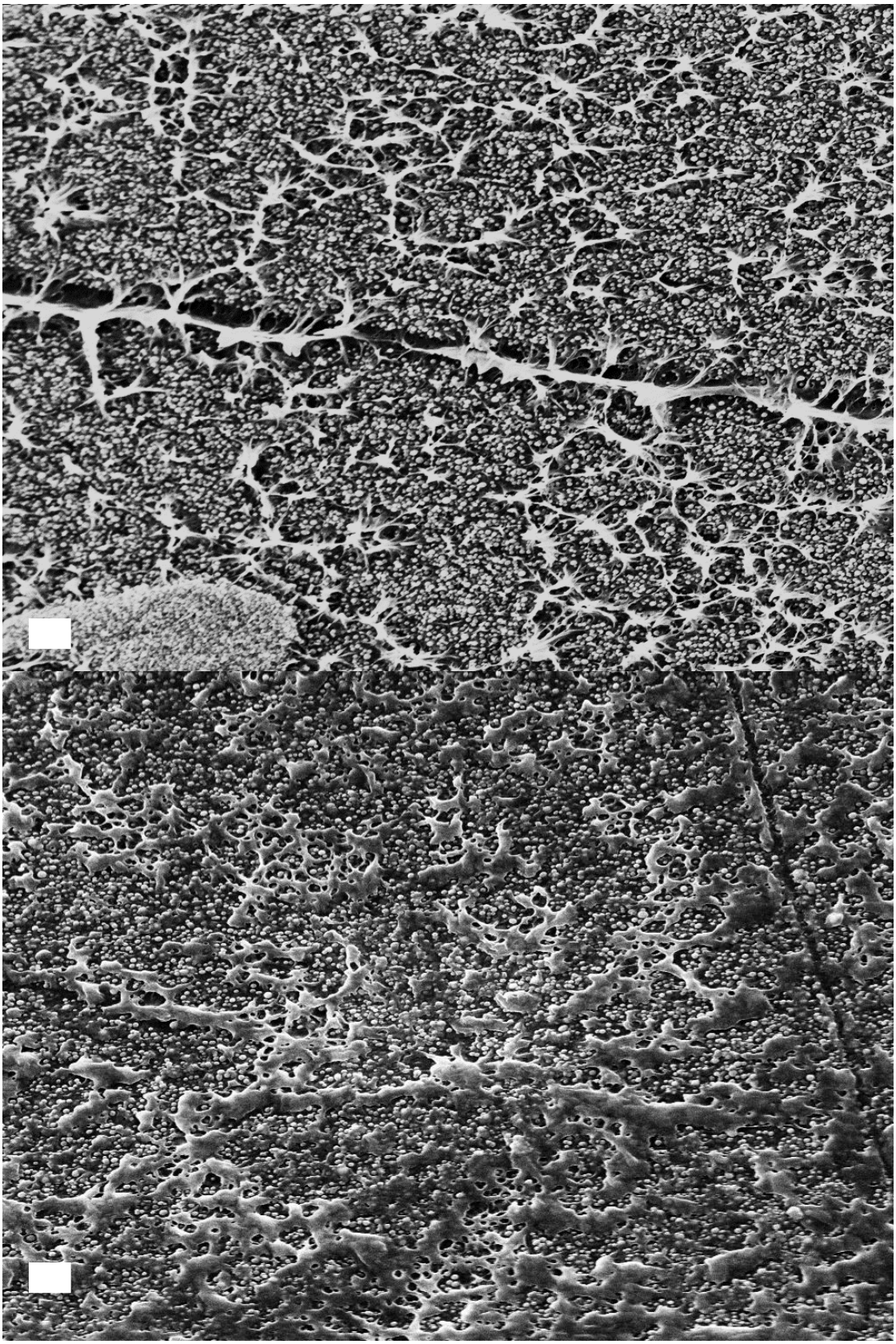

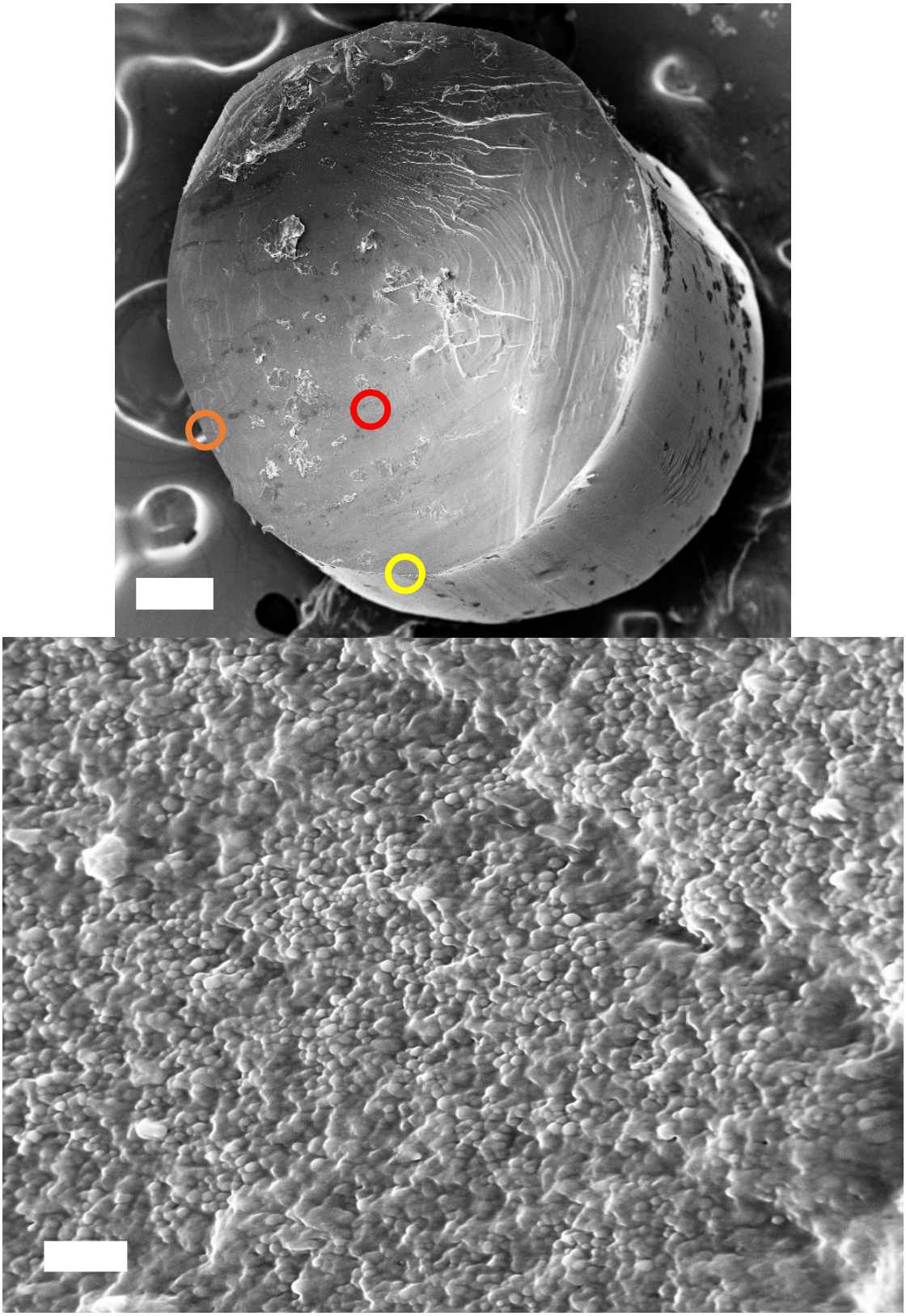

Figure C.24: 35.3v% R_{NP} = 23 nm images; Applied pressure of 10 psi.

Figure C.24 (cont.)

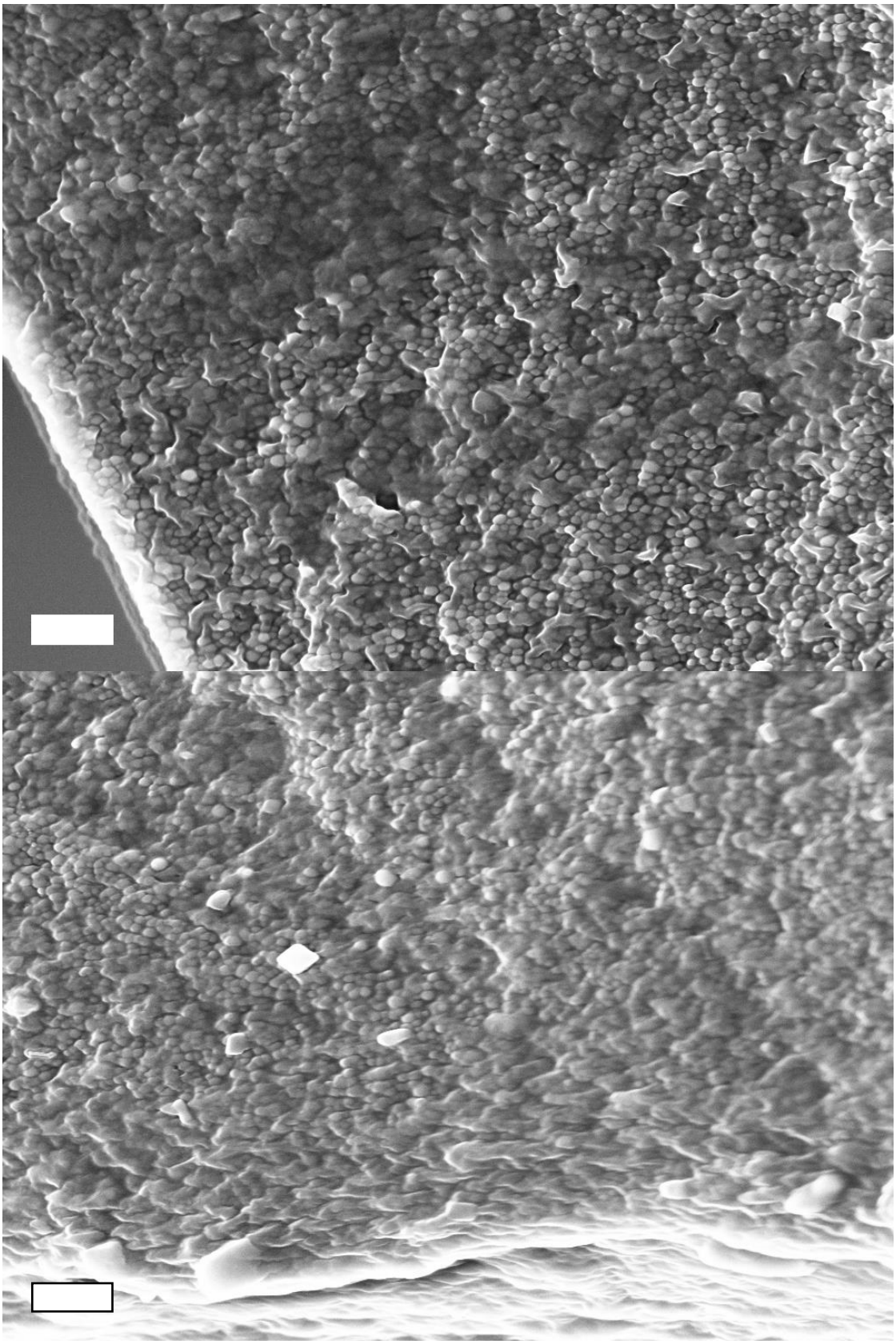

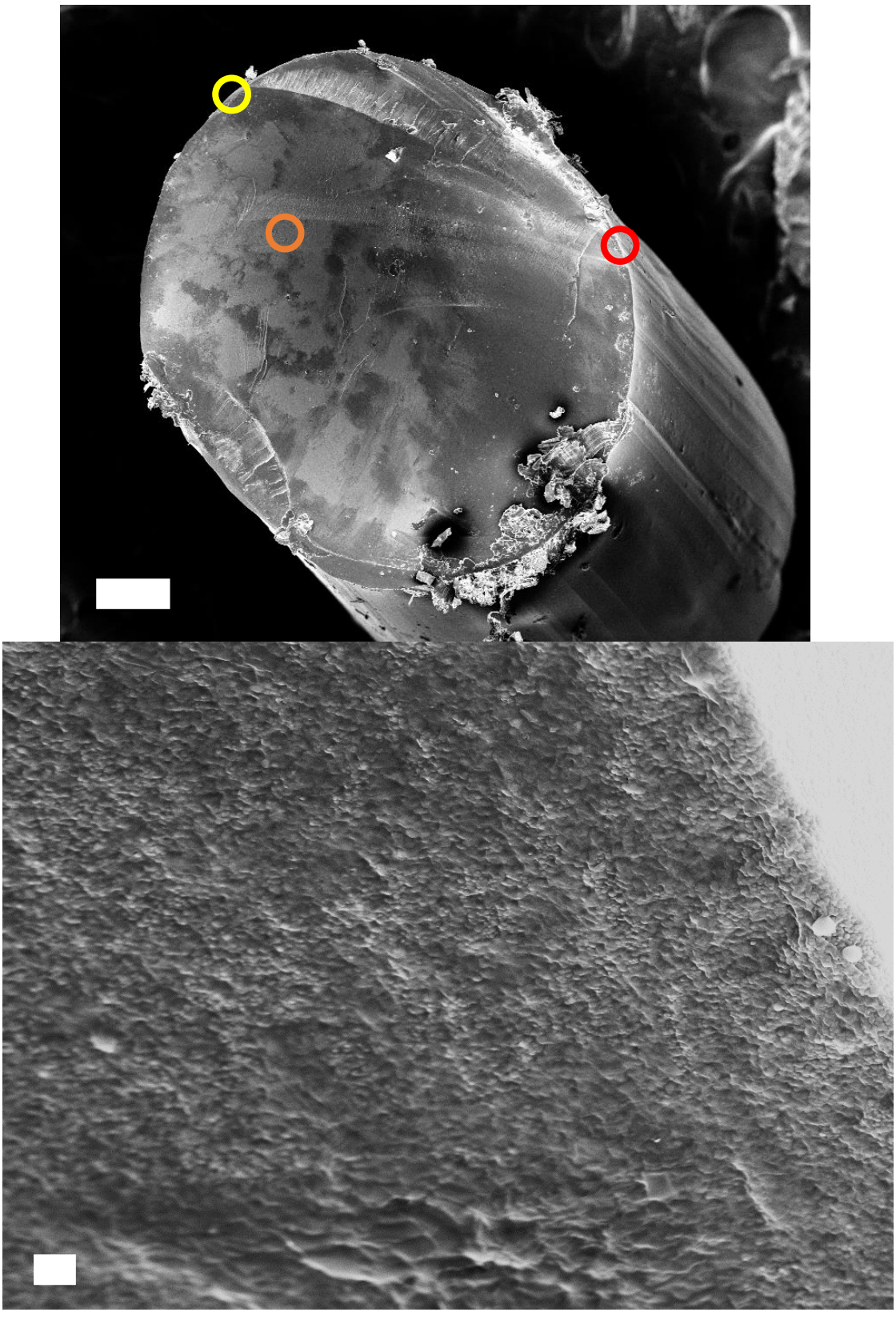

Figure C.25: 35.3v% R_{NP} = 23 nm images; Applied pressure of 20 psi.

Figure C.25 (cont.)

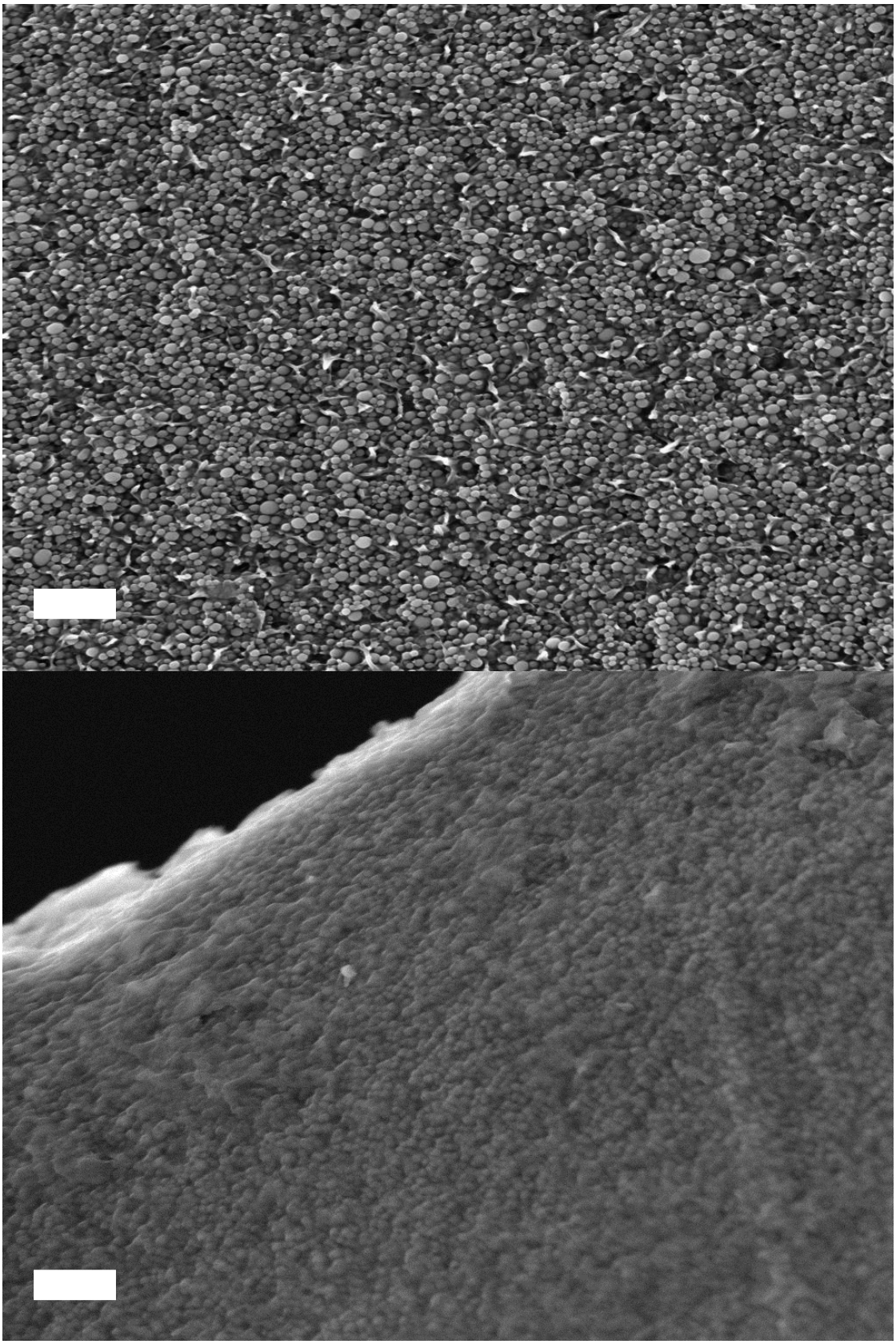

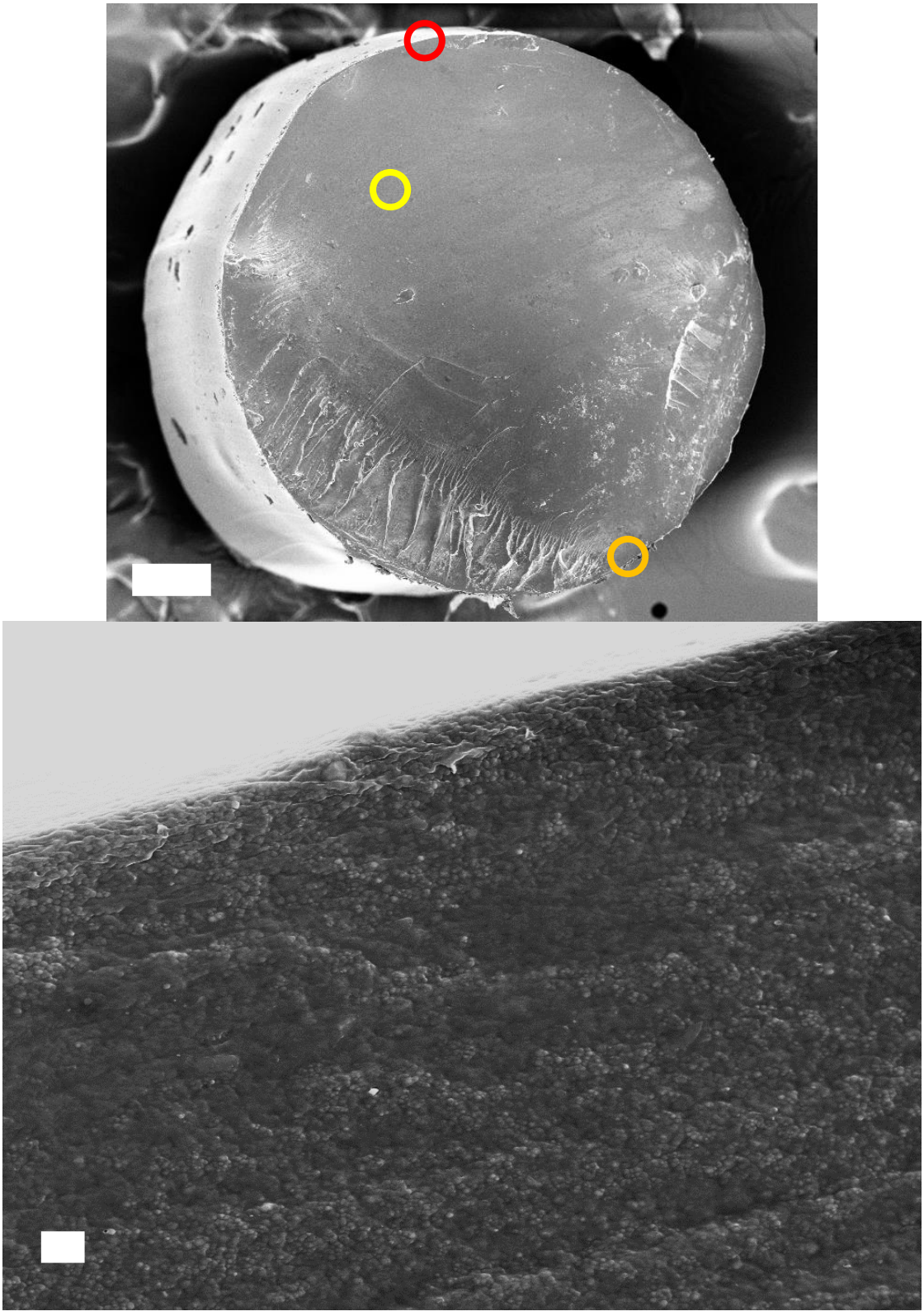

Figure C.26: 35.3v% R_{NP} = 23 nm images; Applied pressure of 40 psi.

Figure C.26 (cont.)

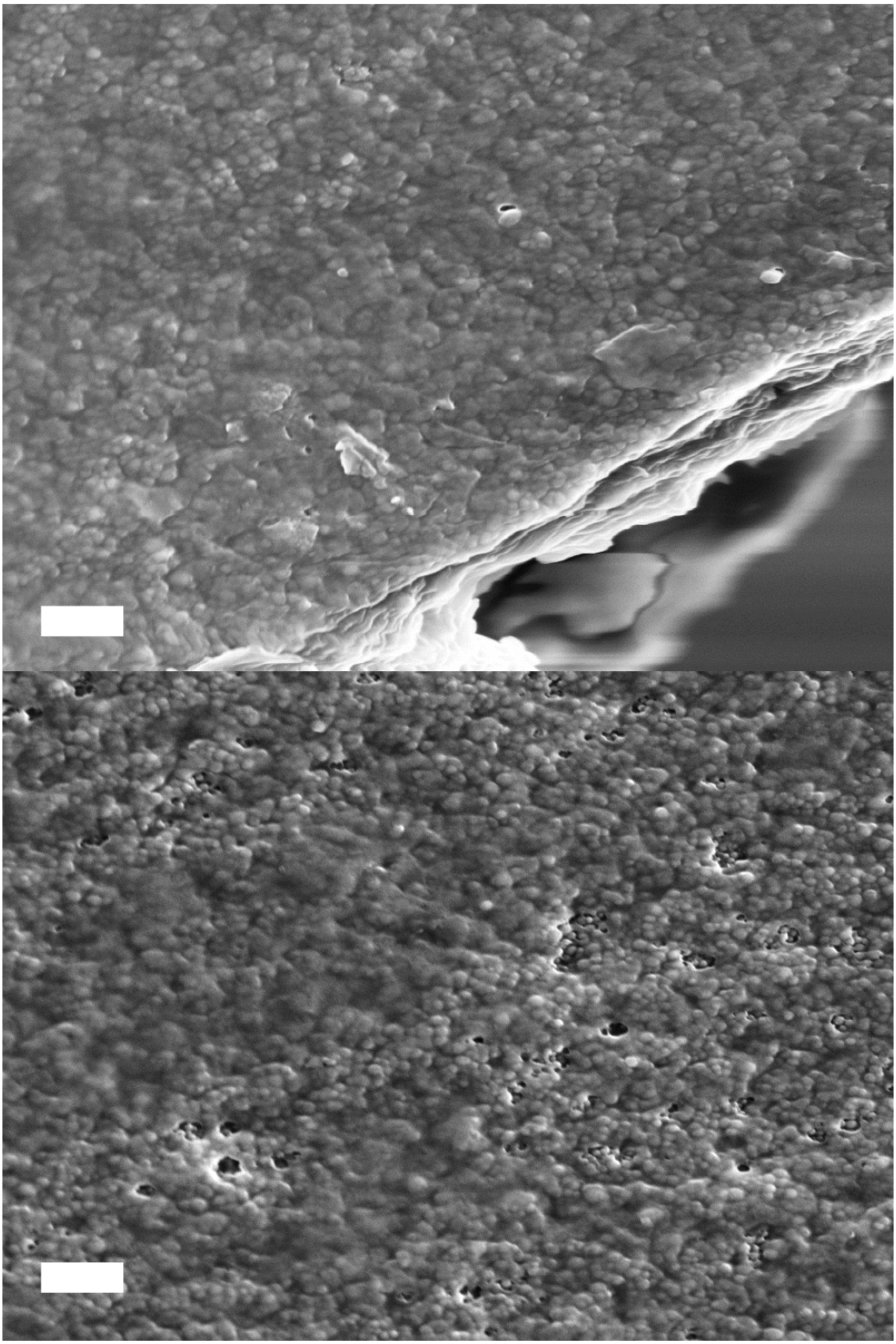

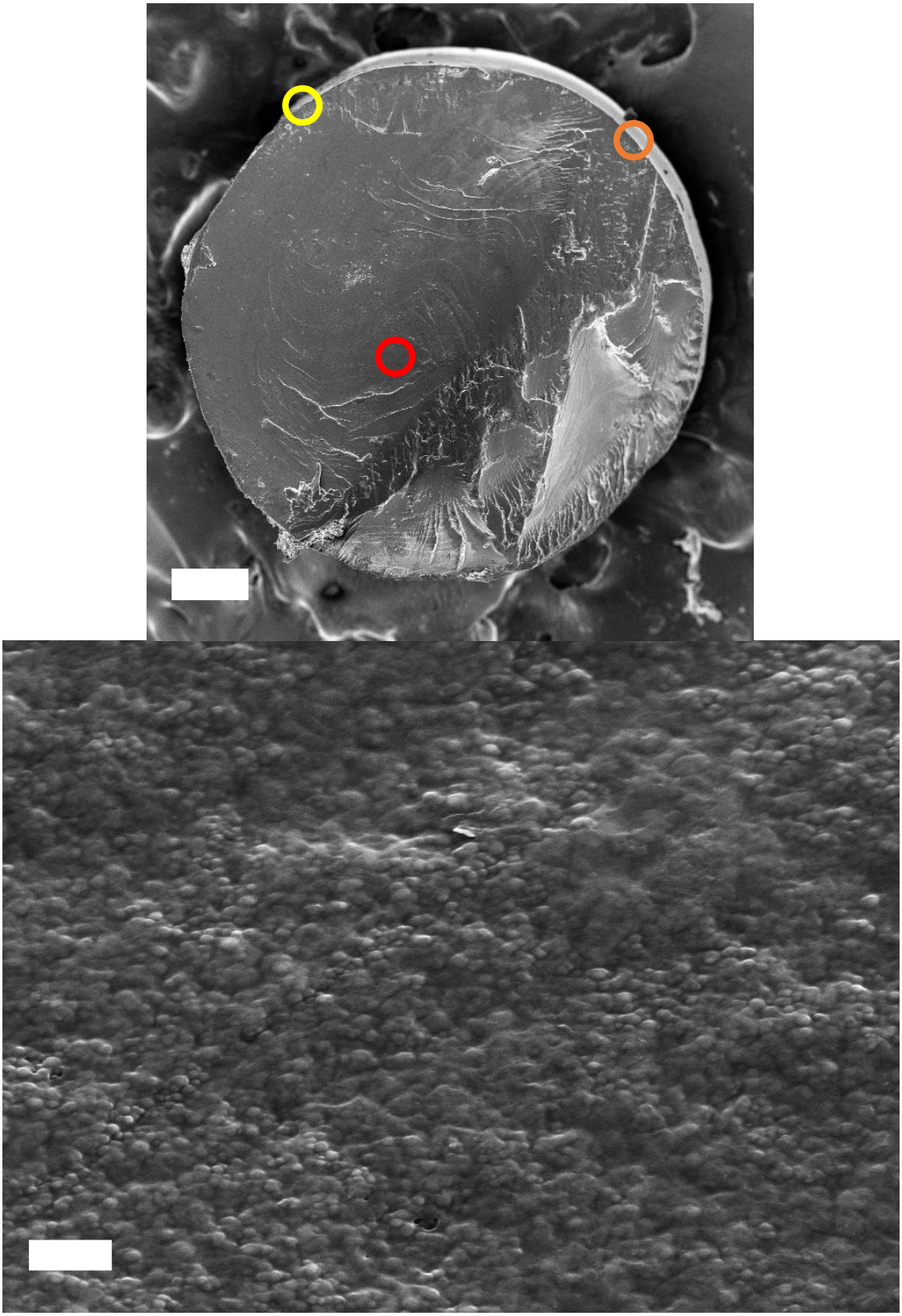

Figure C.27: 35.3v% R_{NP} = 23 nm images; Applied pressure of 60 psi.

Figure C.27 (cont.)

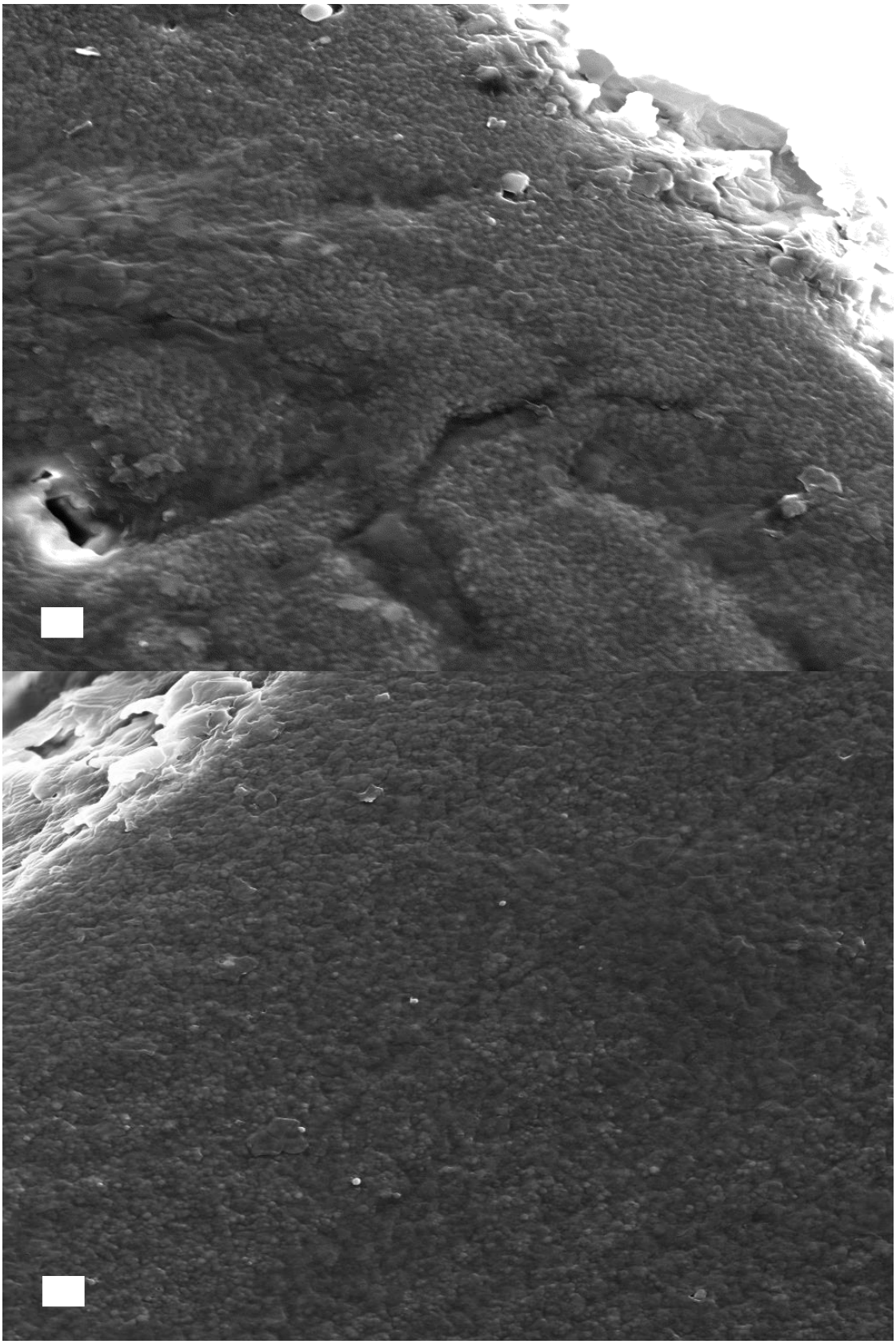

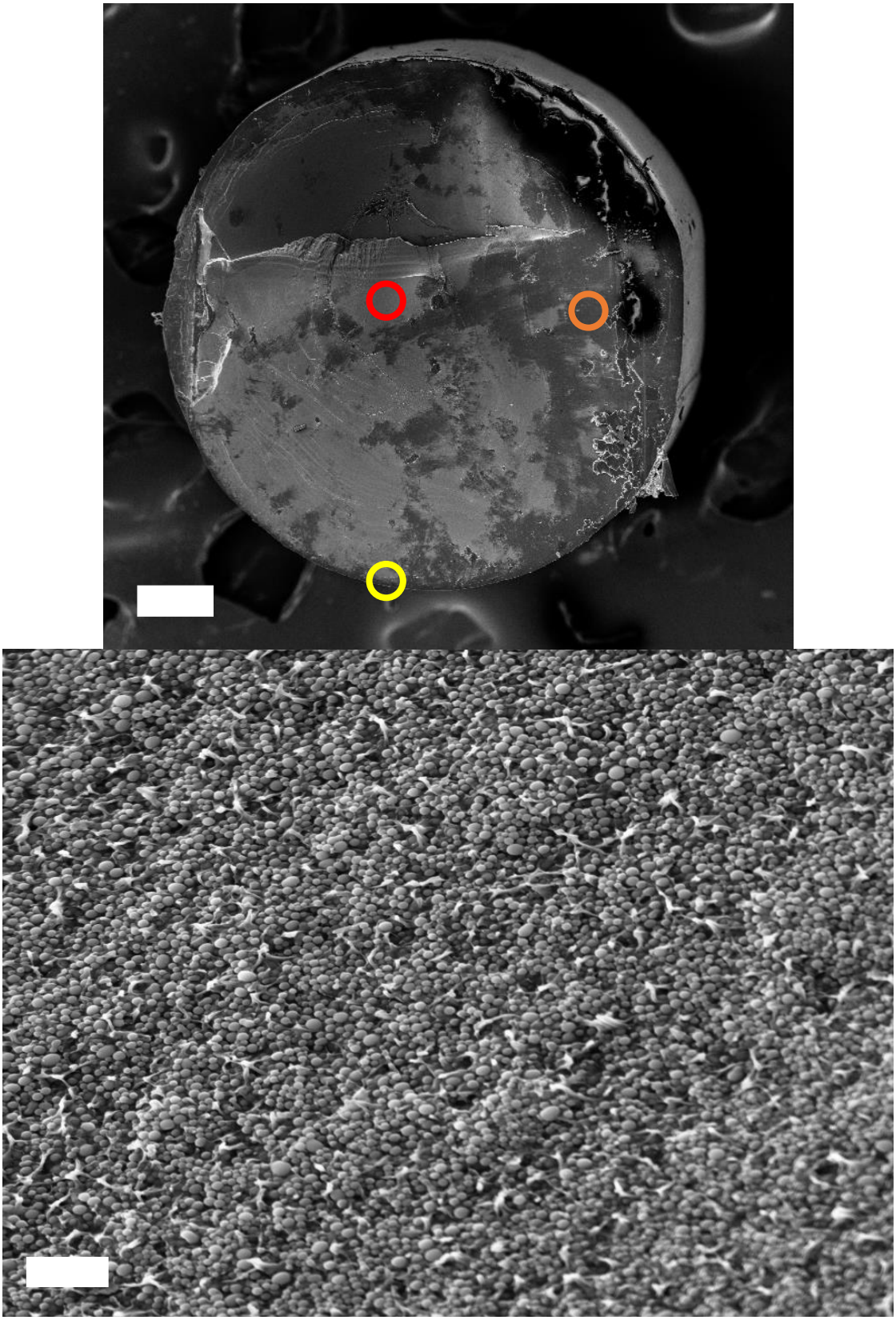

Figure C.28: 35.3v% R_{NP} = 23 nm images; Applied pressure of 80 psi.

Figure C.28 (cont.)

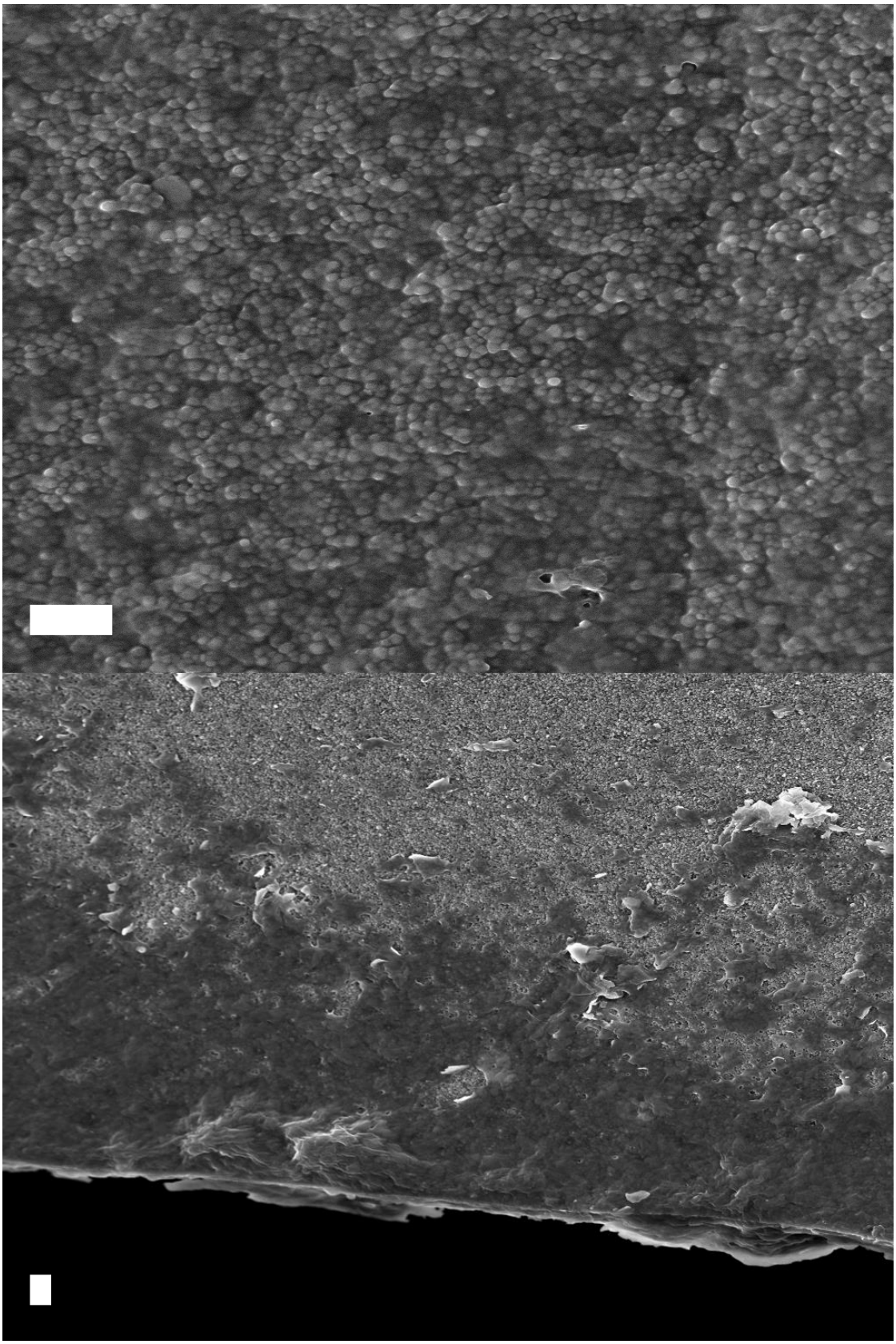

BIBLIOGRAPHY

BIBLIOGRAPHY

1. Kojima, Y.; Usuki, A.; Kawasumi, M.; Okada, A.; Fukushima, Y.; Kurauchi, T.; Kamigaito, O., Mechanical-Properties of Nylon 6-Clay Hybrid. *J. Mater. Res*. **1993**, *8*, 1185−89.

2. Njuguna, J.; Plielichowski, K., Polymer Nanocomposites for Aeroscpace Application: Properties. *Adv. Eng. Mater.* **2003**, *5* (11), 769-778.

3. Siang Soh, M.; Sellinger, A.; Yap, A.U.J., Dental Nanocomposites. *Curr. Nanosci.* **2006**, *2* (4), 373-381.

4. Khalid, A.; Al-Juhani, A.A.; Al-Hamouz, O.C.; Laoui, T.; Khan, Z.; Atieh, M.A., Preparation and properties of nanocomposite polysulfone/multi-walled carbon nanotubes membranes for desalination. *Desalination*. **2015**, *367*, 134-144.

5. Li, Q.; Wood, E.; Ardebili, H., Elucidating the mechanism of ion conductivity enhancement in polymer nanocomposite electrolytes for lithium ion batteries. *Appl. Phys. Lett.* **2013**, *102* (24), 243903.

6. Pradhan, D.K.; Choudhary, R.N.P.; Samantaray, B.K., Studies of Dielectric Relaxation and AC Conductivity Behavior of Plasticized Polymer Nanocomposite Electrolytes. *Int. J. Electrochem. Sci.* **2008**, *3*, 597-608.

7. Huang, C.; Qian, X.; Yang, R., Thermal conductivity of polymers and polymer nanocomposites. *Mater. Sci. Eng. R Rep.* **2018**, *132*, 1-22.

8. Srivastava, S.; Haridas, M.; Basu, J.K., Optical properties of polymer nanocomposites. *Bull. Mater. Sci.* **2008**, *31* (3), 213-217.

9. Tjong, S.C., Structural and mechanical properties of polymer nanocomposites. *Mater. Sci. Eng. R Rep.* **2006**, *53* (3-4), 73-197

10. Feldman, D., Polymer Nanocomposite Barriers. *J. Macromol. Sci. A.* **2013**, *50*, 441-448.

11. Bogue, R., Nanocomposites: a review of technology and applications. *Assem. Autom.* **2011**, *31* (2), 106-112.

12. AIP Precision Machining. **2017**. Advantages of Polymer Component over Metallic Materials for Machined Parts. [03/2019; 01/27/2022]. https://aipprecision.com/the-advantage-of-plastics-over-metals-for-custom-parts/

13. "3. Manufacturing: Materials and Processing." National Research Council. **1994**. *Polymer Science and Engineering: The Shifting Research Frontiers*. Washington, DC: The National Academies Press. doi: 10.17226/2307.

14. Vinyas, M.; Athul, S.J.; Harursampath, D.; Loja, M.; Thoi, T.N., A comprehensive review on analysis of nanocomposites: from manufacturing to properties characterization. *Mater. Res. Express*. **2019**. 6, 092002.

15. ChemAnalyst. **2021**. Polymer Market Analysis: Plant Capacity, Production, Operating Efficiency, Demand & Supply, Product Type, Application, Distribution Channel, Region, Competition, Trade, Market Analysis, 2015-2030. [08/2021; 1/27/2022]. https://www.chemanalyst.com/industry-report/polymer-market-306.

16. Mittal, V.; Chaudhry, A.U., Polymer – graphene nanocomposites: effect of polymer matrix and filler amount on properties. *Macromol Mater Eng.* **2015**, *300*, 510-521.

17. Alonso-Redondo, E.; Belliard, L.; Rolle, K.; Gracykowski, B.; Tremel, W.; Djafari-Rouhani, B.; Fytas, G., Robustness of elastic properties in polymer nanocomposite films examined over the full volume fraction range. *Sci. Rep.* **2018**, *8*, 16986.

18. Liu, J.; Gao, Y.; Cao, D.; Zhang, L.; Guo, Z. Nanoparticle Dispersion and Aggregation in Polymer Nanocomposites: Insights from Molecular Dynamics Simulation. *Langmuir*. **2011**, *27*, 7926-7933.

19. Wang, Y.U.; Tan, D.Q., Computational study of filler microstructure and effective property relations in dielectric composites. *J. Appl. Phys.* **2011**, *109*, 104102.

20. Ashraf, M.A.; Peng, W.; Zare, Y.; Rhee, K.Y., Effects of Size and Aggregation/Agglomeration of Nanoparticles on the Interfacial/Interphase Properties and Tensile Strength of Polymer Nanocomposites. *Nanoscale Res. Lett.* **2018**, *13*, 214.

21. Mittal, V., **2010**. *Optimization of Polymer Nanocomposite Properties*. Weinheim, Germany: Wiley-VCH. doi: 10.1002/9783527629275.

22. Kharbas, H.; Nelson, P.; Yuan, M.; Gong, S.; Turng, L.; Spindler, R., Effects of nano-fillers and process conditions on the microstructure and mechanical properties of microcellular injection molded polyamide nanocomposites. *Polym. Compos*. **2003**, *24* (6), 655-671.

23. Rider, A.N.; An, Q.; Brack, N.; Thostenson, E.T., Polymer nanocomposite – fiber model interphases: Influence of processing and interface chemistry on mechanical performance. *Chem. Eng. J*. **2015**, *269*, 121-134.

24. "Polymer Processing." Baird, D.G,. **2003**. *Encyclopedia of Physical Science and Technology (Third Edition)*. San Diego, CA: Academic Press. ISBN: 978-0-12-227410-7.

25. Strobl, G., **2007**. *The Physics of Polymers (Third Edition)*. Berlin, Germany: Springer-Verlag. doi 10.1007/978-3-540-68411-4.

26. Rubinstein, M.; Colby, R.H., **2007**. *Polymer Physics*. Oxford, England: Oxford University Press. ISBN-10: 0-19-852059-X.

27. Liu, J.; Cao, D.; Zhang, L.; Wang, W., Time-Temperature and Time-Concentration Superposition of Nanofilled Elastomers: A Molecular Dynamics Study. *Macromolecules*. **2009**, *42* (7), 2831-2842.

28. Guth, E., Theory of Filler Reinforcement. *J. Apply. Phys.* **1945**. 16, 20-25.

29. Cheng, S.; Bocharova, V.; Belianinov, A.; Xiong, S.; Kisliuk, A.; Somnath, S.; Holt, A.P.; Ovchinnikova, O.S.; Jesse, S.; Martin, H.; Etampawala, T.; Dadmun, M.; Sokolov, A.P., Unraveling the Mechanism of Nanoscale Mechanical Reinforcement in Glassy Polymer Nanocomposites. *Nano Lett*. **2016**. *16* (6), 3630-3637.

30. AZO Materials. **2001**. Silica – Silicon Dioxide (SiO_2) property data. [1/28/2022] https://www.azom.com/article.aspx?ArticleID=1114.

31. Lopez-Pamies, O.; Goudarzi, T.; Nakamura, T., The nonlinear elastic response of suspensions of rigid inclusions in rubber: I—An exact result for dilute suspensions. *J. Mech Phys Solids.* **2013**. 61. 1-18.

32. Smallwood, H.M., Limiting Law of the Reinforcement of Rubber. *J. Appl. Phys*. **1944**. *15* (11), 758-766.

33. Einstein, A., Eine neue Bestimmung der Moleküldimensionen. *Ann. d. Physik*. **1906**, *324* (2), 289-306.

34. Einstein, A., Berichtigung zu meiner Arbeit: "Eine neue Bestimmung der Moleküldimensionen". *Ann. d. Physik*. **1911**, *339*(3), 591-592.

35. Mullins, L.; Tobin, N.R., Stress softening in rubber vulcanizates. Part I. Use of a strain amplification factor to describe the elastic behavior of filler-reinforce vulcanized rubber. *J. Appl. Polym. Sci*. **1965**, *9* (9), 2993-3009.

36. Domurate, J.; Sapiannikova, M.; Ausias, G.; Heinrich, G., Modelling of stress and strain amplification effect in filled polymer melts. *J. Non-newton Fluid Mech*. **2012**, *171-172,* 8-16.

37. Botti, A.; Pyckhout-Hintzen, W.; Richter, D.; Urban, V.; Straube, E., A microscopic look at the reinforcement of silica-filler rubbers. *J. Chem. Phys*. **2006** *124* (17), 174908.

38. Joualt, N.; Dalmas, F.; Said, S.; Di Cola, E.; Schweins, R.; Jestin, J.; Boué, F., Direct small-angle-neutron-scattering observation of stretched chain conformation in nanocomposites: More insight on polymer contributions in mechanical reinforcement. *Phys. Rev E.* **2010**, *82* (3), 031801.

39. Westermann, S.; Kreitschmann, M.; Pyckhout-Hintzen, W.; Richter, D.; Straube, E.; Farago, B.; Goerigk, G., Matrix Chain Deformation in Reinforced Networks: a SANS Approach. *Macromolecules.* **1999**, *32* (18), 5793-5802.

40. Filippov, A.A., Effect of the Size of Silica Nanoparticle on the Mechanical Characteristics of Heterogeneous Epoxy Resin Materials. **2008**. *AIP Conference Proceedings 2053,* 030014.

41. Kutvonen, A.; Rossi, G.; Puisto, S.R.; Rostedt, N.K.J.; Ala-Nissila, T., Influence of nanoparticle size, loading, and shape on the mechanical properties of polymer nanocomposites. *J. Chem. Phys*. **2012**. *137*, 214901.

42. Baeza, G.P.; Dessi, C.; Costanzo, S.; Zhao, D.; Gong, S.; Alegria, A.; Colby, R.H.; Rubinstein, M.; Vlassopoulos, D.; Kumar, S.K., Network dynamics in nanofilled polymers. *Nat. Commun.* **2016**, *7*, 11368.

43. Yang, J.; Melton, M.; Sun, R.Q.; Yang, W.; Cheng, S., Decoupling the Polymer Dynamics and the Nanoparticle Network Dynamics of Polymer Nanocomposites through Dielectric Spectroscopy and Rheology. *Macromolecules*. **2020**, *53* (1), 302-311.

44. Chen, Q.; Gong, S.; Moll, J.; Zhao, D.; Kumar, S.K.; Colby, R.H., Mechanical Reinforcement of Polymer Nanocomposites from Percolation of a Nanoparticle Network. *ACS Macro Lett.* **2015**, *4*, 398-402.

45. Huber, G.; Vilgis, T.A., On the Mechanism of Hydrodynamic Reinforcement in Elastic Composites. *Macromolecules*. **2002**. *35*, 9204-9210.

46. Sternstein, S.S.; Zhu, A.J., Reinforcement Mechanism of Nanofilled Polymer Melts As Elucidated by Nonlinear Viscoelastic Behavior. *Macromolecules*. **2002**, *35*, 7262-7273.

47. Mark, J.E.; Binder, K.; Erman, B.; Roe, R.J., **2000**. *Methods of X-ray and Neutron Scattering in Polymer Science*. New York, NY: Oxford University Press. ISBN: 9780195113211.

48. Wang, K.H.; Chung, I.J.; Jang, M.C.; Keum, J.K.; Song, H.H., Deformation Behavior of Polyethylence/Silicate Nanocomposites As Studied by Real-Time Wide-Angle X-ray scattering. *Macromolecules*. **2002**, *35* (14), 5529-5535.

49. Genix, A.-C.; Oberdisse, J., Structure and dynamics of polymer nanocomposites studied by X-ray and neutron scattering techniques. *Curr. Opin. Colloid Interface Sci*. **2015**, *20*, 293-303.

50. Sun, R.; Melton, M.; Zuo, X.; Cheng, S., Nonmonotonic Strain Rate Dependence on the Strain Hardening of Polymer Nanocomposites. *ACS Macro Lett*. **2020**, *9*, 1224-1229.

51. Pal, R.; Sikder, A.L.; Saito, K.; Funston, A.M.; Bellare, J.R., Electron energy loss spectroscopy for polymer: a review. *Polym. Chem.* **2017**, *8*, 6927-6937.

52. Huang, J.; Xiao, Y.; Xu, T., Achieving 3-D Nanoparticle Assembly in Nanocomposite Thin Films via Kinetic Control. *Macromolecules*. **2017**, *50* (5), 2183-2188.

53. Roy, S.; Ryan, J.; Webster, S.; Nepal, D., A Review of In Situ Mechanical Characterization of Polymer Nanocomposites: Prospect and Challenges. *Appl. Mech. Rev.* **2017**, *69* (5), 050802.

54. Kim, G.M.; Lach, R.; Michler, G.H.; Pötschke, P.; Albrecht, K., Relationships between phase morphology and deformation mechanisms in polymer nanocomposite nanofibres prepared by an electrospinning process. *Nanotechnology*. **2006**, *17* (4), 963-972.

55. Haque, M.A.; Saif, M.T.A., In-Situ Tensile Testing of Nano-scale Specimens in SEM and TEM. *Exp. Mech*. **2002**, *42* (1), 123-128.

56. Thomas, C.; Ferreiro, V.; Coulon, G.; Seguela, R., *In situ* AFM investigation of crazing in polybutene spherulites under tensile drawing. *Polymer*. **2007**, *48* (20), 6041-6048.

57. Hang, F.; Lu, D.; Bailey, R.J.; Jimenez-Palomar, I.; Stachewicz, U.; Corster-Ballesteros, B.; Davies, M.; Zech, M.; Bödefeld, C.; Barber, A.H., *In situ* tensile testing of nanofibers by combining atomic force microscopy and scanning electron microscopy. *Nanotechnology*. **2011**, *22* (36), 365708.

58. Kammers, A.; Daly, S., **2011.** Experimental Investigation of Deformation Mechanisms Present in Ultrafine-Grained Metals. In: Proulx, T., *MEMS and Nanotechnology, Volume 4. Conference Proceedings for the Society for Experimental Mechanics Series*. New York, NY: Springer. doi: 10.1007/978-1-4614-0210-7_15.

59. Allison, P.G.; Moser, R.D.; Schirer, J.P.; Martens, R.L.; Jordon, J.B.; Chandler, M.Q., In-Situ nanomechanical studies of deformation and damage mechanisms in nanocomposites monitored using scanning electron microscopy. *Mater. Lett*. **2014**, *131*, 313-316.

60. Deuschle, J.K.; Buerki, G.; Deuschle, H.M.; Enders, S.; Michler, J.; Arzy, E., In Situ Indentation Testing of Elastomers. *Acta Mater*. **2008**, *56* (16), 4390-4401.

61. Sutton, M.A.; Li, N.; Joy, D.C.; Reynolds, A.P.; Li, X., Scanning Electron Microscopy for Quantitative Small and Large Deformation Measurements Part I: SEM Imaging at Magnification from 200 to 10,000. *Exp. Mech.* **2007**, *47*, 775-787.

62. Sutton, M.A.; Li, N.; Garcia, D.; Cornille, N.; Orteu, J.J.; McNeill, S.R.; Schreier, H.W.; Li, X.; Reynolds, A.P., Scanning Electron Microscopy for Quantitative Small and Large Deformation Measurements Part II: Experimental Validation for Magnifications from 200 to 10,000. *Exp. Mech.* **2007**, *47*, 789-804.

63. Kammers, A.D.; Daly, S., Digital Image Correlation under Scanning Electron Microscopy: Methodology and Validation. *Exp. Mech*. **2013**, *53*, 1743-1761.

64. Jerabek, M.; Major, Z.; Lang, R.W., Strain Determination of Polymer Materials Using Digital Image Correlation. *Polym. Test*. **2010**, *29* (3), 407-416.

65. Naskar, A.K.; Keum, J.K.; Boeman, R.G., Polymer matrix nanocomposites for automotive structural components. *Nat. Nanotechnol*. **2016**, *11* (12), 1026-1030.

66. Leung, S.N., Thermally conductive polymer composites and nanocomposites: Processing-structure-property relationships. *Compos. B. Eng.* **2018**, *150*, 78-92.

67. Grzelczak, M., Directed Self-Assembly of Nanoparticles. *ACS Nano*. **2010**, *4* (7), 3591-3605.

68. Chen, B.; Zhou, X.Y.; Zhang, B.; Kondoh, K.; Li, J.S.; Qian, M., Microstructure, tensile properties and deformation behaviors of aluminium metal matrix composites co-reinforce by ex-situ carbon nanotubes and in-situ alumina nanoparticles. *Mater. Sci. Eng*. **2020**, *795*, 139930

69. Jouault, N.; Dalmas, F.; Boué, F.; Jestin, J., Nanoparticles reorganizations in polymer nanocomposites under large deformation. *Polymer*. **2014**, *55* (10), 2523-2534.

70. Zare, Y.; Rhee, K.Y., Tensile modulus prediction of carbon nanotubes-reinforce nanocomposites by a combined model for dispersion and networking of nanoparticles. *J. Mater. Res. Technol*. **2020**, *9* (1), 22-32.

71. Macosko, C.W., **1994**. *Rheology: Principles, Measurements, and Applications*. New York, NY: Wiley-VCH. ISBN: 0-471-18575-2.

72. Wang, S.Q., **2017**. *Nonlinear polymer rheology: macroscopic phenomenology and molecular foundation*. Hoboken, NJ: Wiley. LCCN: 2017036798.

73. Jouibari, I.S.; Haddadi-Asl, V.; Mirhosseini, M.M., Formulation of micro-phase separation kinetics of polyurethan nanocomposites. *Polym Adv Technol.* **2018**, *29* (12), 2909-2916.

74. Starr, F.W.; Douglas, J.F., Origin of particle clustering in a simulated polymer nanocomposite and its impact on rheology. *J. Chem. Phys*. **2003**, *199*, 1777.

75. Li, G.; McKinley, G.H.; Ardekani, A.M., Dynamics of the particle migration in channel flow of viscoelastic fluids. *J. Fluid Mech*. **2015**, *785*, 486-505.

76. Valino, A.D.; Dizon, J.R.C.; Espera Jr., A.H.; Chen, Q.; Messman, J.; Advincula, R.C., Advances in 3D printing of thermoplastic polymer composites and nanocomposites. *Prog. Polym. Sci*. **2019**, *98*, 101162.

77. Instron. **2022**. Bagley Correction. [1/31/2022] https://www.instron.com/en/our-company/library/glossary/b/bagley?region=Global%20Site.

78. Göttfert. **2022**. Corrections of Capillary Rheometer Experiments. [1/31/2022] https://www.goettfert.com/application-knowledge/rheo-info/for-capillary-rheometer/corrections-of-capillary-rheometer-experiments.

79. Michler, G.H., **2008**. *Electron Microscopy of Polymers*. Berlin, Germany: Springer-Verlag. doi 10.1007/978-3-540-36352-1.

80. Goldstein, J.I.; Newbury, D.E.; Michael, J.R.; Ritchie, N.W.M.; Scott, J.H.J.; Joy, D.C., **2018**. *Scanning Electron Microscopy and X-Ray Microanalysis (Fourth Edition)*. New York, NY: Springer. doi 10.1007/978-1-4939-6676-3.

81. Nguyen-Truong, H.T., Analytical Formula for High-Energy Electron Inelastic Mean Free Path. *J. Phys. Chem. C*. **2015**, *119*, 23627-23631.

82. Bethe, H. Zur Theorie des Durchgangs schneller Korpus-kularstrahlen durch Materie. *Ann. Phys.* **1930**, *397* (3), 325-400.

83. Kanaya, K.; Okayama, S., Penetration and energy-loss theory of electrons in solid targets. *J. Phys. D: Appl. Phys*. **1972**, *5*, 43-58.

84. Lide, D.R., ed. **2005**. *CRC Handbook of Chemistry and Physics (86th edition)*. Boca Raton, FL: CRC Press. ISBN 0-8493-0486-5.

85. Robinson, M.T.; Oen, O.S., The Channeling of Energetic Atoms in Crystal Lattices. *Appl. Phys. Lett.* **1963**, *2* (2), 30-32.

86. Babu, S.R.; Badiger, N.M., Experimental Determination of Electron Interaction Parameters of Medically Significant Polymers. *RA J. Appl. Res*. **2018**, *4* (4), 1656-1661.

87. Rasband, W.S., ImageJ. **2018**. Bethesda, MD: U.S. National Institutes of Health. https://imagej.nih.gov/ij/.

88. MATLAB®. **2017**. R2017a. Natick, MA: The MathWorks Inc.

89. Baggethun, P. **2009**. Radial Profile Plot. [05/14/2009; 2/11/2022]. https://imagej.nih.gov/ij/plugins/radial-profile.html.

90. Lee, D.T.; Lin, A.K., Generalized Delaunay triangulation for planer graphs. *Discrete Comput. Geom.* **1986**, *1*, 201-217.

91. Bebis, G.; Deaconu, T.; Georgiopoulos, M., Fingerpring identification using Delaunay triangulation. **1999**. *Proceedings 1999 International Conference on Information Intelligence and Systems (Cat. No.PR00446)*, 452-459.

92. Nowak, M.; Maj, M., Determination of coupled mechanical and thermal fields using 2D digital image correlation and infrared thermography: Numerical procedures and results. *Arch. Civ. Mech. Eng*. **2017**, *18*, 630-644.

93. Silvani, C.; Réthoré, J.; Bonelli, S., Measuring rockfill deformation by digital image correlation. **2015**. *9th European Solid Mechanic Conference (ESMC 2015)*. Hal-01299362.

94. Kumar, S.K.; Benicewicz, B.C.; Vaia, R.A.; Winey, K.I., Are Polymer Nanocomposites Practical for Applications? *Macromolecules*. **2017**, *50*, 714-731.

95. Bouty, A.; Petitjean, L.; Chatard, J.; Matmour, R.; Degrandcourt, C.; Schweins, R.; Meneau, F.; Kwasniewski, P.; Boue, F.; Couty, M.; Jestin, J., Interplay between polymer chain conformation and nanoparticle assembly in model industrial silica/rubber nano-composites. *Faraday Discuss.* **2016**, *186*, 325-343.

96. Moll, J.; Kumar, S.K.; Snijkers, F.; Vlassopoulos, D.; Rungta, A.; Benicewicz, B.C.; Gomez, E.; Ilavsky, J.; Colby, R.H., Dispersing Grafted NanoparticleAssemblies into Polymer Melts through Flow Fields. *ACS Macro Lett*. **2013**, *2*, 1051-1055.

97. “Recent advances in the theory of filler networking in elastomers.” Heinrich, G.; Klüppel, M., **2002**. *Filled Elastomers Drug Delivery Systems*. Berlin, Germany: Springer-Verlag. ISBN: 3-540-43052-0.

98. Wang, M.J., Effect of polymer-filler and filler-filler interactions on dynamic properties of filled vulcanizates. *Rubber Chem. Technol.* **1998**, *71*, 520-589.

99. Hagita, K.; Arai, T.; Kishmoto, H.; Umesaki, N.; Shinohara, Y.; Amemiya, Y., Two-dimensional pattern reverse Monte Carlo method for modelling the structures of nano-particles in uniaxial elongated rubbers. *J. Condens. Matter Phys*. **2007**, *19* (33), 335217.

100. Puech, N.; Mora, S.; Phou, T.; Porte, G.; Jestin, J.; Oberdisse, J., Mocroemulsion nanocomposites: phase diagram, rheology, and structure using a combined small angle neutron scattering and reverse Monte Carlo approach. *Soft Matter*. **2010**, *6*, 5605-5614.

101. “Chapter 2.1.3 – Scanning probe microscopy (SPM).” Feltin, N.; Ducourtieux, S.; Crouzier, L.; Delvallée, A.; Dirscherl, K.; Zeng, G., **2020**. *Characterization of Nanoparticles: Measurement Processes for Nanoparticles*. Cambridge, MA: Elsevier. ISBN: 978-0-12-814182-3.

102. Cheng, S.; Holt, A.P.; Wang, H.; Fan, F.; Bocharova, V.; Martin, H.; Etampawala, T.; White, B.T.; Saito, T.; Kang, N.-G.; Dadmun, M.D.; Mays, J.W.; Sokolov, A.P., Unexpected Molecular Weight Effect in Polymer Nanocomposites. *Phys. Rev. Lett*. **2016**, *116*, 038302.

103. Baeza, G. P.; Genix, A.-C.; Degrandcourt, C.; Petitjean, L.; Gummel, J.; Couty, M.; Oberdisse, J., Multiscale Filler Structure in Simplified Industrial Nanocomposite Silica/SBR Systems Studied by SAXS and TEM. *Macromolecules*. **2013,** *46* (1), 317-329.

104. Sun, R.; Melton, M.; Safaie, N.; Ferrier, Jr., R.C.; Cheng, S.; Liu, Y.; Zuo, X.; Wang, Y., Molecular View on Mechanical Reinforcement in Polymer Nanocomposites. *Phys. Rev. Lett.* **2021**, *126* (11), 117801.

105. Onuki, A., Phase transitions of fluids in shear flow. *J. Phys.: Condens. Matter*. **1997**, *9*, 6119-6157.

106. Tanaka, H.; Araki, T., Viscoelastic phase separation in soft matter: Numerical-simulation study on its physical mechanism. *Chem. Eng. Sci*. **2006**, *61*, 2108-2141.

107. Stevens, M.J.; Covas, J.A., **1995**. *Extruder Principles and Operation (Second Edition)*. London, U.K.: Springer-Science. ISBN: 978-94-010-4247-5.

108. Vera-Sorroche, J.; Kelly, A.; Brown, E.; Coates, P.; Karnachi, N.; Harkin-Jones, E.; Li, K.; Deng, J., Thermal optimization of polymer extrusion using in-process monitoring techniques. *Appl. Therm. Eng*. **2013**, *53* (2), 405-413.

109. Thien, N.P.; Tenner, R.I., A new constitutive equation derived from network theory. *J. Non-Newtonian Fluid Mech.* **1977**, *2* (4), 353-365.

110. Doi, M.; Edwards, S.F., **1986**. *The Theory of Polymer Dynamics*. New York, NY: Oxford University Press. ISBN: 0-19-852033-6.

111. Rubenstein, M.; Panyukov, S., Elasticity of Polymer Networks. *Macromolecules*. **2002**, *35* (17), 6670-6686.

112. Wang, S.Q.; Wang, Y.; Cheng, S.; Li, X.; Zhu, X.; Sun, H., New experiments for improved theoretical description of nonlinear rheology of entangled polymers. *Macromolecules*. **2013**, *46* (8), 3147-3159.

113. Xie, S-J.; Schqeizer, K.S., Consequences of Delayed Chain Retraction on the Rheology and Stretch Dynamics of Entangled Polymer Liquids under Continuous Nonlinear Shear Deformation. *Macromolecules*. **2018**, *51* (11), 4185-4200.

114. Becerra, D.; Córdoba, A.; Schieber, J.D., Examination of Nonuniversalities in Entangled Polymer Melts during the Start-Up of Steady Shear Flow. *Macromolecules*. **2021**, *54* (17), 8033-8042.

115. Rueda, M.M.; Auscher, M-C.; Fulchiron, R.; Périé, T.; Martin, G.; Sonntag, P.; Cassagnau, P., Rheology and applications of highly filled polymer: A review of current understanding. *Prog. Polym. Sci*. **2017**, *66*, 22-53.

116. Li, G.; McKinley, G.H.; Ardekani, A.M., Dynamics of particle migration in channel flow of viscoelastic fluids. *J. Fluid Mech.* **2015**, *785*, 486-505.

117. Yang, X.; Wang, S-Q.; Halasa, A.; Ishida, H., Fast flow behavior of highly entangled monodisperse polymers. *Rheol. Acta*. **1998**, *37* (5), 415-423.

118. Xu, Z.; Sun, R.; Lu, W.; Mays, J.; Schweizer, K.S.; Cheng, S., Nature of Steady-State Fast Flow in Entangled Polymer Melts: Chain Stretching, Viscosity Scaling, and Stress-Induced Disentanglement. *Proc. Natl. Acad. Sci. U.S.A.* **Manuscript in review as of 4/15/2022**.

119. Kalyon, D.M.; Aktas, S., Factors Affecting the Rheology and Processability of Highly Filled Suspensions. *Annu. Rev. Chem. Biomol. Eng*. **2014**, *5*, 229-254.